Unsteady Fluid Mechanics of Annular Swirling Shear Layers

by

David Dunham

A Doctoral Thesis

Submitted in partial fulfillment of the requirements for the award of
Doctor of Philosophy of Loughborough University
Department of Aeronautical and Automotive Engineering

June 2011

Abstract

The vast majority of gas turbine combustor systems employ swirl injectors to produce a central toroidal recirculation zone (CTRZ) which entrains and recirculates a portion of the hot combustion gases to provide continuous ignition to the incoming air-fuel mix. In addition to these primary functions, swirl injectors often generate multiple aerodynamic instability modes which are helical in nature with characteristic frequencies that can differ by many orders of magnitude. If any of these frequencies are consistent with prevalent acoustic modes within the combustor there is a potential for flow-acoustic coupling which may reinforce acoustic oscillations and drive combustion instabilities via the Rayleigh criterion. The aerodynamic performance of the swirl injector is thus of great practical importance to the design and development of combustion systems and there is a strong desire within industry for reliable computational methods that can predict this highly unsteady behaviour. This assessment can be made under isothermal conditions which avoids the complex interactions that occur in reacting flow.

The goal of the present work was to compare and contrast the performance of Unsteady Reynolds-Averaged Navier-Stokes (URANS) and Large-Eddy Simulation (LES) CFD methodologies for a combustion system equipped with a derivative of an industrial Turbomeca swirl injector as this exhibits similar unsteady aerodynamic behaviour under reacting and isothermal conditions. The influence of the level of swirl, $S_{\mathrm{N}} = 0.51 - 0.8$, was first investigated experimentally using Particle Image Velocimetry (PIV) by varying the inlet swirl vane angle. Based on a qualitative assessment of instantaneous velocity data, and a range of coherent structure eduction techniques, it was found that $\alpha_1 = 30^\circ$ ($S_{\mathrm{N}} \approx 0.8$) would be the most challenging test case for LES and URANS as this contained near and far-field instability modes that differ in frequency by around two orders of magnitude and the highest levels of normal Reynolds-stress anisotropy. Based on extensive simulations performed with both in-house (LULES and Delta) and commercial (Fluent) CFD codes it was found that, despite the relative modest computational cost of URANS which is between one-third (RST) to an order of magnitude ($k-\epsilon$) less than that demanded by LES, only LES captures the all-important frequency content in accordance with experimental evidence and, thus, only LES can be recommended for use in swirl injector flows. The increased cost is believed to be an absolutely worthwhile expense because of the high fidelity of the predicted results in the important area of flow instabilities.

keywords: Gas-Turbine Swirl Injectors, Large-Eddy Simulation, Unsteady Reynolds-Averaged Navier-Stokes, Particle Image Velocimetry, Coherent Structures, Helical Instabilities, Shear-Layer Vortices, Precessing Vortex Core

Acknowledgements

Firstly, I would like to thank Rolls-Royce and EPSRC for providing the funding that has made this research possible. I would also like to thank all members of the UTC, both past and present, who have always been willing to share with me their considerable collective knowledge and, importantly, their friendship. In particular, I express my sincere gratitude to Prof Jim McGuirk and Dr Adrian Spencer for their continual support, encouragement and enthusiasm throughout the entire course of this project and their many helpful suggestions on earlier drafts of this thesis.

The Ph.D. viva is a daunting prospect for any candidate and the one relating to this thesis was certainly no exception. I would therefore like to acknowledge Prof. Jochen Fröhlich and Dr Gary Page for the constructive manner in which it was conducted, making it, dare I say, an enjoyable experience. The many points raised during this process will provide food for thought for some time to come.

Away from the UTC, the constant support and encouragement I have received from friends and family has been immeasurable. In the case of my parents, Ann and Gerry Dunham, this extends far beyond my time as a Ph.D. student and has always been something I can rely on. My decision to undertake a Ph.D. at Loughborough was fully supported by my Grandparents, Mary and Maurice Pocock. They always showed a genuine interest in my studies throughout my education and Im sure that would be as strong today and it always was. Last, but not least, I would like to thank my partner, Anna Gregory, whose inexhaustible optimism was particularly beneficial during the more challenging moments encountered when composing this thesis.

Contents

List of Figures

List of Tables

Nomenclature

Symbols

a	Acceleration
A	Area
A^+	van Driest constant
b_0	Side width of image plane
B_0	Side width of object plane
C	Confidence factor
C_{ij}	Mean flow convection tensor (RST model)
C_s	Smagorinsky coefficient
d_{diff}	Diffraction limited particle image diameter
d_{ijk}	Diffusion tensor (RST model)
d_p	Tracer particle diameter
d_r	Pixel width
d_s	Absolute particle image shift
d_τ	Particle image diameter
D	Characteristic diameter
E	Expansion ratio, $E = D_{ex}/D_s$
f	Frequency
f_s	Sampling frequency, $f = 1/\Delta t$
$f^\#$	Lens F-number (ratio of focal length to lens aperture diameter)
G	LES convolution kernel
$\dot{G}_\theta$	Tangential momentum flow rate
$\dot{G}_x$	Axial momentum flow rate
h_i	Scale factor between Cartesian and curvilinear coordinate systems
$H_i(j)$	Coordinate curvature terms in curvilinear system
I	Intensity of incidence light
k	Turbulent kinetic energy
ℓ	Characteristic eddy size
ℓ_0	Lengthscale of largest eddies

${}^{k}L_{ij}$	Integral length scale defined by R_{ij} in k co-ordinate direction
$\dot{m}$	Mass flow rate
M	Magnification
n	Normal direction
N	Number of samples
N_a	Number of samples per PDF bin
N_c	Number of samples in conditionally-averaged subset
N_{I}	Number of statistically independent samples
N_{PI}	Number of particle image pairs per interrogation cell
N_{T}	Total number of samples
p	Pressure
p^*	Modified pressure
P	Cross-correlation value
P_{ij}	Production tensor (RST model)
P_k	Rate of production of turbulent kinetic energy
q	Scattered light intensity, heat release
Q	Q-ratio (PIV signal to noise indicator), Q-criterion
$\dot{Q}$	Volumetric flow rate
$\mathbf{r}$	Generalised separation vector
R	Characteristic radius
R_{ij}	2^{nd} order 2-point 2-time correlation
Re	Reynolds number $Re = U_{\mathrm{ref}} D_{\mathrm{ref}} / \nu$
S_{ij}	Strain tensor
S_{N}	Swirl number
S_t	Strouhal number
$S_{t_{\dot{Q}}}$	Volumetric Strouhal number
t	Time
T	Characteristic time period, temperature
T_s	Characteristic timescale at swirler exit
T_r	Residence time
T_{ij}	Integral timescale
Δt	Interframe time (PIV), computational time step size (CFD)
ΔT	Sampling interval
u_i	Instantaneous velocity component in i direction
u_i'	Fluctuating instantaneous velocity component in i direction
$\widetilde{u}_i$	Filtered instantaneous velocity component in i direction
$\hat{u}_i$	Peak / intermediate (LULES) / coherent velocity component in i direction

$\langle u_i \rangle$	Statistically-averaged velocity component in i direction equivalent to time-averaging, $\overline{u}_i$ unless indicated by subscript
$\langle u_i' \rangle$	r.m.s velocity component in i direction
$\langle u_i' u_j' \rangle$	Components of Reynolds stress tensor
u_τ	Friction velocity
$U_{i,s}$	Swirler exit bulk average velocity component in i direction, $U_{x,s} = \dot{m}/\rho A_s$
U_p	Particle velocity lag
x, y, z	Cartesian coordinates
x, r, θ	Polar cylindrical coordinates
Δx	Particle image displacement (PIV), computational cell size (CFD)
ΔX , ΔY	Interrogation cell dimension
y^*, y^+	Non-dimensional near-wall distance
z	Confidence interval coefficient
z_0	Lens focal length
Z_0	Object distance
δ_z	Depth of field
∇	Vector differential operator

Greek Symbols

α	Modular swirler angle, camera viewing angle ($x-z$ plane), pressure-velocity linkage coefficient (Delta)
β	Camera viewing angle ($y-z$ plane)
Γ_i	Circulation in i direction
δ_{ij}	Kronecker delta ($\delta_{ij} = 1$ if $i = j$ and $\delta_{ij} = 0$ if $i \neq j$)
Δ	LES filter width
ϵ	Turbulent kinetic energy dissipation rate
ϵ_{ds}	Pixel displacement uncertainty
ϵ_i	2C-PIV perspective projection error in i direction
$\epsilon_{u,i}$	Confidence interval limits for mean velocity component in i direction
$\epsilon_{u',i}$	Confidence interval limits for r.m.s velocity component in i direction
ϵ_{ij}	Dissipation tensor (RST model)
η	Kolmogorov length scale
λ	Wavelength of incident laser light
λ_2	Swirl strength of Jeong and Hussian [1]
${}^k\lambda_{ij}$	Taylor micro-scale in k co-ordinate direction
μ	Molecular viscosity
ν	Kinematic viscosity
ν_t	URANS eddy viscosity

ν_{sgs}	LES sub-grid viscosity
ρ	Fluid density
ρ_p	Particle density
σ	Standard deviation
τ	Characteristic turbulent timescale
$\vec{\tau}$	Temporal separation vector
τ_p	Particle response time
τ_w	Wall shear stress
τ_η	Kolmogorov time scale
ϕ	Instantaneous variable of turbulent system, residual of pressure equation
ϕ_{pz}	Primary zone equivalence ratio
ϕ_{ij}	Pressure-rate-of-strain tensor
ψ_i	Convective and diffusive terms
ω	Angular velocity
ω_i	Vorticity component in i direction
$\vec{\omega}$	Vorticty vector
Ω_{ij}	Vorticity tensor

Subscripts and Brackets

1	Modular swirler inlet vane angle
2	Modular swirler inner wall angle
3	Modular swirler outer wall angle
down	Downstream
ex	Expansion chamber
mod	Modelled value
meas	Measured value including experimental bias errors
res	Resolved value, resolution
rot	Rotationally-averaged
s	Swirl stream
SC	Swirl cone
tot	Total value
true	Best estimate of actual value with experimental bias accounted for
up	Upstream
x, r, θ	Cylindrical polar coordinates
$\langle \cdots \rangle_{\text{rot}}$	Rotationally-average quantity
$\langle \cdots \rangle_N$	Statistical average of a subset based on N members
$\langle \cdots \rangle_P$	Estimation of statistically-averaged populatin parameters

Abbreviations

2C	Two Component
3C	Three Component
ACF	Autocorrelation Function
AoI	Area of Interest
CAEP	Committee on Aviation Environmental Protection
CCD	Charged Coupled Device
CCF	Cross Correlation Function
CFD	Computational Fluid Dynamics
CFL	Courant-Friedrichs-Lewy condition
CPU	Central Processing Unit
CS	Coherent Structure
CTRZ	Central Toroidal Recirculation Zone
CRZ	Corner Recirculation Zone
CV	Control Volume
CW	Continuous Wave
DFS	Diffusive Stability
DNS	Direct Numerical Simulation
FFT	Fast Fourier Transform
FoV	Field of View
FV	Finite Volume
HMN	Hoest-Madsen and Nielsen SGF compensation method
HWA	Hot Wire Anamometry
HS	High Speed
ICAO	International Civil Aviation Organisation
K-H	Kelvin-Helmholtz
LDA	Laser Doppler Anemometry
LDV	Laser Doppler Velocimetry
LES	Large Eddy Simulation
LPP	Lean Premixed Prevapourised
MPI	Message Passing Interface
NO_x	Nitrogen Oxide
Nd-YAG	Neodym Yttrium Aluminium Garnet (laser)
PDE	Partial Differential Equations
PDF	Probability Density Function
PIV	Particle Imaging Velocimetry
PLIF	Planar Laser Induced Fluorescence
POD	Proper Orthogonal Decomposition

PSD	Power Spectral Density
PTV	Particle Tracking Velocimetry
PVC	Precessing Vortex Core
RANS	Reynolds-Averaged Navier-Stokes
r.m.s	Root Mean Square
RST	Reynolds Stress Transport
SGF	Sub-Grid Filtering
SGS	Sub-Grid Scale
SNR	Signal to Noise Ratio
SVC	Spatial Velocity Correlation
SVD	Singular Value Decomposition
TKE	Turbulent Kinetic Energy
TI	Turbulence Intensity
URANS	Unsteady Reynolds-Averaged Navier-Stokes

Chapter 1

Introduction

1.1 Design and Development of Combustion Systems

A fundamental issue affecting gas turbine design is the stage of the development process at which combustion instabilities become apparent [2]. As a certain degree of unsteadiness is always present in practical systems it is important to make a distinction between stable and unstable combustion. Stable combustion is associated with small-amplitude pressure (including acoustic) oscillations which are typically less than $\approx 5\%$ of the mean chamber pressure [3]. Combustion with large-amplitude pressure oscillations exhibiting strong periodic frequencies is classified as unstable. Instabilities may develop spontaneously within the system or be initiated by perturbations external to it. In both cases they can be an undesirable feature which can generate an externally auidible tone at intolerable levels and, if allowed to reach a certain amplitude, interfere with engine operation. In extreme cases, combustion instabilities can result in system failure due to excessive vibration and heat transfer to the chamber wall as shown in Figure 1.1. It is well known that acoustic pressure oscillations can be excited and sustained by the addition of heat energy. This is known as the Rayleigh criterion and is expressed mathematically by Putnam [4] as:

$$\frac{1}{T}\int_0^T p'(t)q'(t)dt > 0 \tag{1.1}$$

where p' and q' are fluctuating pressure and heat release respectively and T is the time period of one acoustic cycle. Equation 1.1 implies that the instability will be amplified when heat is supplied while the pressure is maximum and that suppression occurs for the reverse condition. In addition to the Rayleigh criterion, the rate of heat addition must exceed the rate of acoustic energy dissipation. Thus, by increasing the absorption (i.e. damping) of acoustic waves, no-self sustaining thermo-acoustic oscillation (of large enough amplitude to be problematic) will result. In conventional diffusion-flame combustors acoustic damping can be achieved through changes to the fueling system and operating characteristics [2] and instabilities are not considered to be an

issue of heightened concern. Unfortunately, this type of combustor usually produces unacceptably high levels of thermal NO_x and increasingly strict regulation for pollutant emission has recently led engine manufacturers to develop combustors that meet various regulatory requirements [1]. It is unfortunate that these systems, such as the lean premixed prevapourised (LPP) concept, suffer from persistent instability problems that are only partially alleviated with the application of empirical tools and controls. Figure 1.2 shows schematics comparing diffusion-flame and LPP combustors for aeronautical applications.

Although many thermo-acoustic problems are not aerodynamically related, since the late 1970's there has been a growing interest in what are variously referred to as large eddies, organised structures, coherent structures, or simply turbulent vortices [6]. Although quite difficult to define rigorously, an eddy, according to Pope [7], is a turbulent motion, localised within a region of size ℓ, that is at least moderately coherent over this region. For the remainder of this thesis, coherent structures, referred to for brevity as CS, is the preferred nomenclature. Although earlier indications of the importance of CS in combustion systems exist (for example, see Rogers and Marble [8]), Coats [6] identifies several factors that have lead to a renewed interest in them. These include:

- The discovery that, under appropriate conditions, free turbulent shear-layers of the type found in many practical combustion system naturally contain large quasi-two-dimensional vortical structures which grow in size as they convect with the flow and persist to the highest Reynolds numbers accessible by experiments.
- Environmental pressures to develop cleaner and more efficient combustion systems which retain good ignition, flame stability and turn-down characteristics.
- The availability of supercomputers and methodologies which allow the development of vortical motions and their interaction with the combustion process to be simulated numerically.

In practice, most emission-control strategies depend on the control of air-fuel mixing in the primary zone and the vast majority of systems employ swirl injectors with axial or radial vanes (Figure 1.3) to achieve this. These produce a central toroidal recirculation zone (CTRZ) such as that shown in Figure 1.4, which entrains and recirculates a portion of the hot combustion gases to provide continuous ignition to the incoming air-fuel mix. In addition to this primary function, swirl injectors often generate multiple aerodynamic instability modes which are helical

[1] For aeronautical applications the standard for NO_x was adopted by the International Civil Aviation Organisation (ICAO) in 1981 and became effective in 1986. Since then ICAO has increased the stringency of international NO_x standards by about 40% for newly certified aircraft engines [5]. The most recent standard, CAEP/7, sets out medium- and long-term technology goals, of 10 and 20 years respectively, for NO_x reduction. In relation to mid-term goals (2016) the group estimated a 45% reduction on current standards. As for the long-term goal (2026), it estimated that a reduction of some 60% would be attainable.

in nature and exhibit characteristic frequencies that can differ by many orders of magnitude. An example of a typical swirl injector helical instability is shown in Figure 1.5. The interaction of these instabilities with combustion and heat release has been investigated experimentally by numerous authors for swirl-stabilised systems. For example, Paschereit et al. [9] identified several axisymmetric and helical instability modes for fully premixed and partially premixed/diffusion combustion. The axisymmetric mode showed a large variation of heat release during one cycle of oscillations, while the helical modes showed variations in the radial location of maximum heat release. Similarly, Li and Gutmark [10] detected large vortices which were closely coupled with flame and pressure oscillations. In the context of non-swirling flows, Schadow and Gutmark [11] have suggested that fluctuating heat release, which can be associated with burning inside vortices, can feed energy into acoustic pressure oscillations via the Rayleigh criterion and as these are amplified they can drive the velocity field (flow-acoustic coupling) which futher enhances the generation of CS. In this way a self-sustaining feedback loop of thermo-acoustic instability is established which also depends on the aerodynamic characteristics of the system.

The aerodynamic performance of swirl injectors, particularly the role of associated CS, is clearly of great practical importance and directly affects the pollutant emissions and stability characteristics of gas turbine combustion systems. Traditionally, the design and development of combustion systems has relied heavily on extensive rig testing programs conducted at engine representative temperatures and pressures. Although this is essential at some point during the design cycle it is undesirable at a preliminary stage since it is both extremely expensive and time consuming. Furthermore, when combustion occurs, the flow is complicated by the variations in the air-fuel distribution, local combustion intensity and temperature field. As an alternative, isothermal testing based on appropriate experimental and computational methods allows the aerodynamic behaviour of the system to be isolated and understood, without the complex interactions that occur in reacting flow. However, it should be noted that reaction may alter aerodynamically related processes. This is highlighted by Janus et al. [12] who performed point-based Laser Doppler Anemometry (LDA) measurements on a slightly modified version of an industrial Turbomeca swirl injector (original and modified designs are shown schematically in Figure 1.6(a) and (b)) under isothermal and reacting conditions. A similar unsteady behaviour was observed in both cases and characterised by distinct peaks appearing in near-field velocity spectra at $S_t = 0.84$ and 1.78 (see Equation 1.5) as shown in Figure 1.6(c). In the reacting case an additional frequency of $S_t = 0.31$ not observed under isothermal conditions was also present which may be related to thermo-acoustic instabilities. In this example, isothermal testing is clearly not able to capture *all* instabilities frequencies that occur under reacting conditions, however, those attributed to purely aerodynamic modes (i.e. $S_t = 0.84$ and 1.78) that may prove problematic at later stages of development are identified. Particle Image Velocimetry (PIV), which is considered further in Section 2.3, is an optically-based measurement technique that holds a considerable

advantage over LDA in the sense that it has the ability to provide spatially and temporally resolved velocity data. This was used extensively by Midgley [13] and Midgley et al. [14, 15] to investigate the Turbomeca design reported in [12] under a variety of isothermal test conditions. Unlike [12] these measurements were able to link directly peaks appearing in velocity spectra to near-field CS emerging from within the swirl duct.

One of the limitations of PIV, indeed shared by all optically-based methods, is that access to particular regions of the flow may be extremely difficult. In such cases the ability to perform complete measurements is lost and important information may be unavailable. Other techniques are also difficult because of the hostile environment. Furthermore, it is also difficult to extrapolate from necessarily incomplete planar data to explain fully 3D flow behaviour. Computational fluid dynamics (CFD), which is discussed in Section 3.1, is a numerical approach that has the potential to predict this complex behaviour on both an instantaneous and a time-mean basis. An attractive property of CFD is that full volumetric information is available and issues regarding access do not arise (though data handling does). In an attempt gain an improved understanding of the role of CS within combustion systems and reduce initial development costs there is a strong desire within industry to utilise CFD. Following a comprehensive literature review presented in Section 1.3 it was found that the suitability of various CFD methodologies in relation to swirl-stabilised systems is still a matter of fundamental debate and it is this topic that forms the central theme of this thesis.

1.2 Swirling Flows

According to Gupta [16], swirling flows always possess a central core of solid body rotation in which tangential velocity, u_θ, increases linearly with radius. Outside the central region, free vortex conditions may prevail in which the flow is irrotational. The central forced vortex region exhibits flowfield and turbulence characteristics which appear to be significantly different from those displayed by the surrounding irrotational vortex flowfield. Specifically, the vortex core is described as being shear or strain free but not vorticity free [17]. Assuming axisymmetric conditions with zero axial and radial velocity components, u_x and u_r respectively, u_θ is a function of radius, r, only and represented by the following Rankine distribution:

$$u_\theta = \begin{cases} \hat{u}_\theta \frac{r}{R} & \text{if } 0 \leq r < R, \\ \hat{u}_\theta \frac{R}{r} & \text{if } r \geq R. \end{cases} \tag{1.2}$$

where R is the radius of the central vortex core and $\hat{u}_\theta$ is the maximum tangential velocity component at R. In a simple swirling flow, radial pressure gradients are necessary to balance centripetal acceleration:

$$\frac{\partial p}{\partial r} = -\rho \frac{u_\theta^2}{r} \tag{1.3}$$

The level of swirl intensity is usually assessed via the non-dimensional swirl number, S_{N}, which is defined as the ratio of tangential momentum flow rate, $\dot{G}_\theta$, to the product of axial momentum flow rate, $\dot{G}_x$, and a characteristic radius, R. Assuming no density variation and a negligible pressure contribution, the following equation proposed by Kerr and Fraser [18] is widely used in swirl injector design:

$$S_{\mathrm{N}} = \frac{\dot{G}_\theta}{R\dot{G}_x} = \frac{\int_0^R \langle u_x \rangle \langle u_\theta \rangle r^2 dr}{\int_0^R \langle u_x \rangle^2 r dr} \tag{1.4}$$

Sufficiently high levels of swirl ($S_{\mathrm{N}} > 0.6$ [16]) leads to the phenomenon of vortex breakdown which is described in the following subsection.

1.2.1 Vortex Breakdown

The vortex breakdown phenomenon is defined by Ruith et al. [19] as an abrupt change in the structure of the nominally axisymmetric core of a swirling jet. For relatively low levels of swirl, $S_{\mathrm{N}} < 0.6$, although significant radial pressure gradient may exists (see Equation 1.3), they only give rise to a slight axial pressure gradient which is not sufficient to cause axial recirculation. Under these conditions there is no coupling between axial and tangential velocity components [20]. For increased levels of swirl, i.e. $S_{\mathrm{N}} > 0.6$, a strong coupling develops between axial and tangential velocity components and a point is reached where the axial pressure gradient is such that the kinetic energy of the approaching flow is not sufficient to overcome it, resulting in the formation of a CTRZ as shown in Figure 1.4. Figure 1.7 shows a series of images obtained by Escuider [21] describing the evolution of a bubble-type breakdown resulting from an axisymmetric swelling of the vortex core in a confined cylindrical tube. Gupta [16] states that in a gas turbine combustor application, a stable recirculation bubble will generally be established if $S_{\mathrm{N}} > 0.6$ and $Re > 1.8 \times 10^4$. Further increases in Re yield no significant change in the flowfield, as shown by Li and Tomita [22] and Dellenbeck et al. [23]. The formation of the CTRZ is a form of vortex breakdown as a change in flow structure (the appearance of a vortex) is initiated by a variation in the characteristic ratio of tangential to axial velocity components. Experimentally, Sarpkaya [24] [25] observed three types of vortex breakdown in laminar swirling pipe flows: axisymmetric, spiral and double helix. The bubble mode usually prevails at high S_{N}, while the spiral mode occurs at low S_{N} [3]. Further work by Leibovich [26] and Faler and Leibovich [27] [28] revealed seven distinct modes of vortex breakdown over a wide range of Re and S_{N}. At higher Re, such as those considered in this thesis ($Re = O[10^4 - 10^5]$), the only characteristic geometric forms

are the bubble and spiral modes which are shown in Figure 1.8 in cylindrical and diverging tubes.

The widespread occurance of vortex breakdown in high S_N flows has resulted in considerable efforts being devoted to achieving a better understanding of the phenomenon. This has lead to the emergence of several different theories which can roughly be categorised according to the following underlying ideas. Due to the abruptness of vortex breakdown, Benjamin [29] proposed the existence of a critical state which separates a supercritical and subcritical flow state. In supercritical flows, disturbances can only propagate downstream, whereas in subcritical flows, standing waves exist with disturbances propagating both upstream and downstream. Hall [30] considered vortex breakdown to be analogous to boundary separation or flow stagnation under the influence of an adverse pressure gradient. Finally, the concept of hydrodynamic instabilities has been proposed by numerous authors, including Howard and Gupta [31] and Leibovich and Stewartson [32]. This is based on the observations of Rayleigh [33] that a system is stable if $\rho u_\theta r$ increases locally with r (isothermal forced vortex), neutrally stable if $\rho u_\theta r$ is constant (isothermal free vortex) and unstable if $\rho u_\theta r$ decreases with r. Although the above theories have improved understanding of vortex breakdown, none of them is able to completely and accurately describe all of its features. Comprehensive reviews of the literature available on vortex breakdown are given by Hall [34], Leibovich [35] and more recently by Lucca-Negro and O'Doherty [20].

1.2.1.1 Precessing Vortex Core

The precessing vortex core (PVC) is a three-dimensional unsteady asymmetric flow structure which develops when the central vortex core starts to precess about the axis of symmetry. Figure 1.9 shows an example PVC deduced from the PIV data of Grosjean et al. [36] in a confined pipe flow. In Figure 1.9, it can be seen that the aerodynamic centre of the PVC does not coincide with the geometric centre of the pipe which is indicated by the red cross. At other instants in time the aerodynamic centre of the PVC was observed to move circumferentially about the geometric centre with a precessional frequency that is a function of S_N and chamber configuration and increases linearly with flow rate. The non-dimensional Strouhal number, S_t, is often used to characterise the precessional frequency, f, and is defined as:

$$S_t = f\frac{D_{\text{ref}}}{U_{\text{ref}}} \tag{1.5}$$

where f is the PVC precession frequency and U_{ref} and D_{ref} are reference velocity and length scales respectively. Based on previous work by Claypole and Syred [37], Syred et al. [38] plotted the Strouhal number of the PVC as a function of Re and S_N for a tangential inlet swirl burner as shown in Figure 1.10. The Strouhal number used in [38] is based on volumetric flow rate, $\dot{Q}$, and is a factor of $4/\pi$ greater than that defined in Equation 1.5:

$$S_{t_{\dot{Q}}} = f\frac{D_{\text{ref}}^3}{\dot{Q}} = \frac{4}{\pi}S_t \tag{1.6}$$

Figure 1.10 shows that $S_{t_{\dot{Q}}}$ increases with S_{N} but is independent of Re at values greater than 1.5×10^4. In diffusion-flame systems, combustion tends to damp the PVC instability to the extent that it ceases to be of any practical importance [6]. However, when reactants are premixed, combustion tends to increase both the amplitude and frequency of the precession. A recent review on PVC oscillation mechanisms in swirl combustors is given by Syred [39].

1.2.2 Shear Layers

As flow expands from the injector and evolves downstream, strong shear-layers develop due to the velocity difference between the jet flow and CTRZ. CS are generated in these regions due to various instability mechanisms, such as Kelvin-Helmholtz (K-H) instabilities. As already noted in Section 1.1, these aerodynamic modes can exert a significant influence on the combustion process by modulating the mixing process between fuel, air and hot combustion products. Unlike shear-layer instabilities in non-swirling flows, which are usually predominantly axisymmetric, swirl enhances asymmetric flow structures. These differences are highlighted by the experimental work of Liang and Maxworthy [40] who investigated swirling jets at $Re = 1000$ for a range of S_{N}. Without swirl, K-H instabilities caused the laminar shear-layer shed from the nozzle exit to roll up into discrete axisymmetric vortex rings which grew in the streamwise direction. However, after the introduction of swirl the combined axial and azimuthal shear-layers became unstable to a modified K-H instability and strong helical waves with windings opposed to the bulk flow replace the vortex rings as the dominant structure. Midgley [13] and Midgley et al. [15] also observed the near-field frequency characteristics of a derivate of an industrial Turbomeca swirl injector to be highly dependent on S_{N}.

1.3 Numerical Simulation of Swirling Flows

Due to the high Re encountered in swirl-stabilised combustors ($O[10^4 - 10^5]$), Direct Numerical Simulation (DNS) is not realistic given current and near future computing power. Unsteady Reynolds-Averaged Navier-Stokes (URANS) and Large-Eddy Simulation (LES) are two widely used and well established CFD methodologies that provide a more economical alternative to DNS and are more relevant to industrial applications. The inherent difference between LES and URANS is that whilst the former preserves the stochastic nature of turbulence through a low-pass spatial filter (Δ), the latter only provides the coherent, or phase-averaged, component of fluctuating motion with the stochastic contribution accounted for via a turbulence model. For a detailed discussion of the mathematical background of URANS and LES the reader is referred to Sections 3.1.1 and 3.1.2. The purpose of this section is to provide a comprehensive literature

review of studies which have sought to simulate swirling flowfields using these approaches. Particular emphasis is placed on the complex CS associated with swirl flow discussed in Section 1.2 and the level of fidelity to which they can be resolved.

1.3.1 Unsteady Reynolds-Averaged Navier-Stokes

Guo et al. [41] used the standard k-ϵ model to investigate the effect of S_{N} on the unsteady behaviour of a swirling round jet in an axisymmetric geometry with an expansion ratio of $E = 1.96$. It was found that for $S_{\mathrm{N}} < 0.044$, initial disturbances were damped and a steady state solution was reached. However, for $0.044 < S_{\mathrm{N}} < 0.13$, time traces of velocity and pressure recorded downstream of the expansion at the geometric centre exhibited strong oscillatory behaviour, indicating the presence of a PVC. When $S_{\mathrm{N}} = 0.13$, a higher-order frequency oscillation, approximately an order of magnitude greater than the PVC, was also present and thought by the authors to be associated with eddy shedding. Further increases in S_{N} resulted in a variation of the observed unsteady flow dynamics, which included an almost complete suppression of the low frequency precession and a change in rotational direction of the PVC at $S_{\mathrm{N}} = 0.17$ and 0.22 respectively. At $S_{\mathrm{N}} = 0.48$, the formation of a CTRZ due to vortex breakdown completely eliminated any precessional motion. The authors report these observations to be in good agreement with the experimental investigations of Hallett and Gunther [42] and Dellenback et al. [43]. A later study by the same authors [44], again using the standard k-ϵ model, investigated an identical S_{N} range for a similar axisymmetric geometry but with the expansion ratio increased from $E = 1.96$ to $E = 5$. In contrast to that reported in [41] the flow was found to be highly unstable for all S_{N}, even after the vortex breakdown event. Although these studies [41, 44] provide an interesting insight into the performance of URANS, the practical significance is questionable given that the highest S_{N} investigated is below that given by Gupta [16] ($S_{\mathrm{N}} > 0.6$) as being sufficient for a stable recirculation bubble in gas turbine applications. Furthermore, no comparison of time-mean flow statistics against experiment was given.

Wegner et al. [45] evaluated the performance of URANS (standard $k - \epsilon$ and RST turbulence closures) and LES against LDV in predicting a PVC for an *unconfined* swirling flow based on the TECFLAM experiment (see, for example Schneider [46]) at $S_{\mathrm{N}} = 0.75$. Although simulations performed using the standard k-ϵ model showed some periodic behaviour during an early stage, the initial instabilities decayed and a steady-state solution was eventually reached. The authors report similar observations by Bowen et al. [47]. For LES calculations, a sequence of instantaneous axial velocity isosurfaces revealed a CRTZ that reached upstream into the swirler device together with two helical vortices shed off the outside edge of the swirler exit. A similar plot was not presented for the RST model, however velocity vectors in a plane downstream of the swirler exit ($x/D_s = 0.5$ based on $D_s = 0.06$m from schematic in [45]) indicate a time-dependent vortex structure. For the RST model, mean velocity profiles ($\langle u_x \rangle$ and $\langle u_\theta \rangle$) were in reasonable agree-

ment with experiment but levels of turbulent kinetic energy were found to be much lower than expected. The authors attribute this to the fact that the coherent velocity fluctuations obtained from URANS were considerably lower than those obtained from phase-averaged LES. Spectral analysis, based on velocity time-series obtained close to the swirler exit ($x = 1$mm, $r = 20$mm) revealed the presence of coherent motions represented by discrete spikes in the frequency spectra at ≈37 and 75Hz for LES, URANS and LDV.

Jochman et al. [48] employed the standard k-ϵ and an RST model (Speziale, Sakar and Gatski [49]) to perform URANS simulations of a swirling flow with a confinement ratio of $E = 5$ at $S_{\mathrm{N}} = 0.52$. It is interesting to note that, unlike the unconfined results of Wegner et al. [45], *both* k-ϵ and RST models were now able to reproduce the spatial and temporal dynamics of the flow. These were characterised by a CTRZ due to the vortex breakdown phenomenon, which exhibited both axisymmetric and spiral modes close the centreline, and a single helical structure emerging from within the swirler. This high degree of similarity is despite the fact that turbulent viscosity ($\mu_t = \rho C_\mu k^2/\epsilon^2$) was three to four times higher for the $k-\epsilon$ model compared to the SSG model. It is argued by the authors that one of the reasons for the similar results between the two turbulence models is due to the fact that vortex breakdown is an inviscid phenomenon dominated by inertial terms and, therefore, details of the models may not be important. The presence of both a PVC and rotating helical structures were evident in power spectral density (PSD) plots deduced from LDA measurements and URANS solutions, occurring at $S_t = 0.15$, 0.51 and 0.66. These were interpreted as the lower S_t being due to an axial oscillation of the front stagnation point of the CTRZ and the highest being the precession frequency. Although S_t obtained from URANS were in good agreement with measured data; the energy associated with the periodic fluctuations was much lower. This was correctly assigned to the fact that in the URANS approach the main part of the turbulent spectrum is modelled and, therefore, this fraction is not included in the spectra. Profiles of axial velocity were compared against LDA for the RST model at a number of locations downstream of the swirler exit. Although these displayed similar overall characteristics, deviations of up to 15% existed.

Recently, Dunham et al. [50] used the standard $k-\epsilon$ model and LES to investigate an industrial Turbomeca gas turbine combustor (see Figure 1.6(b)) based on the experimental data (2C-PIV and HWA) of Midgley [13] and Midgley et al. [14]. Two test conditions were considered and termed with-jet and no-jet respectively. In the with-jet condition, a non-swirling axial jet surrounded by an annular swirl flow of $S_{\mathrm{N}} = 0.78$ issued into a dump expansion chamber of expansion ratio $E = 3.72$. In the no-jet condition, an identical geometry and S_{N} was applied with the central jet flow isolated. In both cases, radial profiles of $\langle u_x \rangle$ downstream of the swirler exit from URANS were in reasonable agreement with experiment, however, $\langle u_\theta \rangle$ provided a poor representation tending towards an incorrect solid body rotation rather than the expected Rank-

ine distribution. Under with-jet conditions, a Reynolds-decomposition of the PIV velocity field (i.e. subtraction of the time-mean flow from each instantaneous realisation) in a plane normal to the injector exit at $x/D_s = 0.02$ revealed the presence of four vortical structures with distinct characteristic frequencies of $S_t = 1.24$ and 2.48 which were postulated [13] to form due to flow separation from the inner wall of the swirl duct. Although similar vortical structures were also observed under no-jet conditions, their characteristic frequencies were $S_t = 0.62$ and 1.24. These differences were attributed to the presence of a low-frequency PVC in the no-jet condition which interacted with the near-field vortices and reduced their spatial and temporal coherence. Initially, it was found that $k - \epsilon$- based URANS was able to capture the experimentally observed vortex structure emerging from within the swirler, however, the fully-developed, self-sustained solution reached after further timesteps did not reflect measured dynamics with no spectral differences between test cases. Moreover, spectral analysis of near-field velocity traces suggested that URANS was not able to capture the expected PVC under no-jet conditions which is characterised by an accumulation of energy at low frequencies ($S_t \approx 0.01$ in the present case). This was in stark contrast to LES in which profiles of $\langle u_x \rangle$ and $\langle u_\theta \rangle$ and spectral characteristics observed experimentally were faithfully reproduced for both test cases.

1.3.2 Large Eddy Simulation

A preliminary study by Tang et al. [51] investigated the application of LES to an LPP-type geometry which consisted of a central non-swirling axial jet and two radially-inflowing swirl streams. Random perturbation prescribed at the inlet were found to decay rapidly and large-scale unsteadiness observed downstream in the pre-mixing duct was attributed to instabilities arising in shear layers formed between incoming swirl-streams and between the central jet and annular swirling flow. Wang et al. [52] also found the effect of broadband inlet turbulence on the downstream flow development to be relatively modest in comparison to the influence of strong shear-layers inherent in swirling flowfields. Despite not having reached a statistically-stationary state, reasonable agreement with LDA data was obtained in the pre-mixing duct with discrepancies thought to be due to inlet conditions, in particular the level of inlet swirl which is difficult to prescribe accurately in the absence of experimental data in this region. Other features associated with confined swirl flow, such as the formation of a corner recirculation zone (CRZ) and CTRZ, were present in the mean field. A more detailed assessment of the time-dependent flow features arising in the LPP-type geometry considered in [51] is presented by the same authors in a later work [53]. It was found that although negative velocities associated with the CTRZ did not enter the pre-mixing duct on a time-mean basis; instantaneous realisation of the velocity field revealed 'tongues' of negative axial velocity penetrating this upstream region. Time-traces of velocity recorded within the pre-mixing duct and close to the centreline in the recirculation region proved particularly insightful as they clearly indicate the broadband frequency content present across the flow domain. Spectral analysis, based on a somewhat limited record of velocities obtained

within the pre-mixing duct, showed signs of coherent motion at relatively low frequency (several hundred hertz) in addition to the more familiar turbulent shape (-5/3) in the kilohertz range. Due to the limited duration considered, it is difficult to precisely deduce the underlying mechanisms of the coherence but it is suggested by the authors that it may be indicative of flowfield precession. Once again reasonable agreement with experimental velocity profiles was obtained.

Garcia-Villalba and Fröhlich [54] used LES to investigate the influence of S_{N} and the presence of a central round jet on the CS associated with unconfined annular swirl flow. Initially, the central jet was not considered and the central inner body consisted of a solid cylinder. The level of swirl was varied from $S_{\mathrm{N}} = 0-1.2$ which lead to the formation of a CTRZ whose front stagnation point moved further upstream with increasing S_{N}. For $S_{\mathrm{N}} = 1.2$ radial profiles of mean and r.m.s velocities (axial and tangential components) were in good agreement with experiment downstream of the swirler exit. Iso-surfaces of fluctuating pressure ($p' = p - \langle p \rangle$) at $S_{\mathrm{N}} = 0.55$ revealed the presence of two spiral structures embedded within the inner shear-layer formed between the annular swirl jet and CTRZ. For $S_{\mathrm{N}} < 0.55$ no spiral structures were detected and increasing to $S_{\mathrm{N}} = 0.7$ resulted in only a single spiral structure within the inner shear-layer with an additional spiral structure in the outer shear-layer. At $S_{\mathrm{N}} = 1$ and 1.2, the irregularity of the flow increased which was characterised by a variation in the number of CS. In Garcia-Villalba et al. [55] the authors suggests that both families of structures are the result of K-H instabilities as they are perpendicular to the mean streamlines. Investigations by Wang et al. [52], Huang and Yang [56] also cite K-H instabilities as a fundamental mechanism for the formation of CS arising in swirling flowfields. A quantitative assessment of the observed structures was provided by a PSD of axial velocity fluctuations recorded within the inner shear-layer at the swirler exit although no comparison was given with experiment. For $S_{\mathrm{N}} \geq 0.7$, a dominate peak at $S_t = 0.24 - 0.28$ (based on the swirler exit radius) and associated higher harmonics appeared in the spectrum. The introduction of an un-swirled central jet at an annular jet $S_{\mathrm{N}} = 1.05$ had the effect of reducing the coherence of the inner and outer spiraling structures. It is interesting to note that this is in stark contrast to the experiments of Midgley [13] and Midgley et al. [14] who observed that the introduction of an un-swirled central jet in a confined swirl flow exerted a stabilising influence on structures emerging from within the swirler. However, it is difficult to make direct comparisons as the simulations reported in [54] are unconfined whilst the experiments in [13, 14] were conducted at a confinement ratio of $E = 3.72$. Furthermore, different S_{N} were investigated in both cases which also influence the stability of the structures. The addition of swirl to the central jet ($S_{\mathrm{N}} = 1$) had an even more dramatic impact on the flow, with the appearance of the structures becoming increasingly random and any regularity all but lost. Garcia-Villalba [57] further investigated the influence of the central jet by varying its location relative to the main annular duct for co-annular swirl flow. The swirl number of the main annular flow was set to $S_{\mathrm{N}} = 0.93$ and the central jet to $S_{\mathrm{N}} = 2$. When the central jet and main annulus exit planes were

coplanar at $x/D_s = 0$, no CS were observed which is consistent with that reported in [54]. The effects of retracting the central jet upstream of the main annulus exit plane to $x/D_s = -0.37$ had a dramatic influence, with the appearance of CS similar to those in [54] with the central jet was blocked. It is thought that with the central jet retracted it is only able to hit the upstream front of the CTRZ and cannot penetrate the inner shear-layer and impact on the CS.

Wegner et al. [58] investigated an LPP-type geometry based on a generic Turbomeca design using LES. Streamlines of time-mean velocity indicated that the furthest upstream point of the CTRZ due to the vortex breakdown phenomenon interacted with the main annular flow, resulting in separation from the inner wall upstream of the exit plane. A thorough assessment of first and second-order statistics yielded a good overall level of agreement with LDV. Using the λ_2 criterion of Jeong and Hussian [1] the presence of two helical vortices emerging from within the swirler were clearly visible. Spectral analysis based on time-traces of velocity and mixture fraction resulted in discrete spectral spikes directly related to the coherent motions at frequencies of approximately 1370Hz and 2900Hz respectively. A reasonable agreement with experimental LDV data was obtained (1280Hz and 2990Hz respectively) with discrepancies attributed to the boundary conditions specified at the domain inlet. Phase-averaging was used to provide insight into the influence of the observed helical structures on mixture fraction. In contrast to the more or less axisymmetric contours of time-mean mixture fraction, phase-averaged results exhibited a large degree of asymmetry, suggesting that the entrainment of air by the helical vortices allows them to impose their helical structure on the spreading fuel jet. Roux et al. [59] also investigated a similar configuration using a combination of compressible LES, acoustic analysis and LDA for both cold and premixed reacting flows. Under cold conditions, acoustic analysis using a Helmholtz solver found the first three longitudinal modes to be 172, 363 and 1409 Hz respectively. Of these, only the second acoustic mode was identified in experiments (around 340 Hz) and LES (around 360 Hz). Inside the combustion chamber, LES predictions and LDA measurements found the dominant instability mode to occur at 540Hz and 510Hz respectively. As this frequency did not appear as an acoustic eigenmode, the authors attributed it to hydrodynamic instability due to the presence of a PVC. Isosurfaces of pressure revealed the presence of a spiral structure in the vicinity of the swirler exit. Under reacting conditions at $\phi = 0.75$, the first three longitudinal acoustic eigen-modes shifted to 265, 588 and 1440Hz respectively. This time, both first and second acoustic modes where detected by LES (290 and 500Hz respectively) and experiment (300 and 570Hz respectively), whilst the third was suppressed. The major consequence of combustion is to damp the dominant hydrodynamic instability observed under cold-flow conditions and cause the pressure fluctuation in the chamber to lock onto the second acoustic mode of the device. The Turbomeca geometry was also investigated recently by Dunham et al. [50] under isothermal conditions using LES and has already been alluded to in the previous section.

Wang et al. [52] used LES to focus on the internal flow through a fuel injector at $S_N = 0.35$ and 0.49. The geometry consisted of three radial-entry slots used to generate counter-rotating inlet flow and resulted in an extremely complex flowfield. A PVC was present in both cases but its size and behaviour, particularly in regard to its interaction with other instabilities, varied. For $S_N = 0.35$, vortex shedding of highly organised hairpin-type structures was observed in the outer shear-layer from the trailing edge of the guide vanes. The authors attribute this occurance to K-H instabilities in axial and azimuthal directions and estimated a dominant frequency in the streamwise direction of approximately 10kHz. This was found to be comparable with that obtained from spectral analysis based on time-traces of pressure within the injector which indicated a dominant frequency at 13kHz. Further PSD plots, this time based on the time-varying coefficients of Proper Orthogonal Decomposition (POD) analysis, were also in excellent agreement; with the first two modes, accounting for 40% of the total streamwise turbulent kinetic energy, yielding discrete spikes at 13kHz. The effect of increasing S_N resulted in a growth of the CRZ in the radial direction, causing it to interact with the outer-shear layer. This, in addition to an increased dominance of helical instabilities, contributed to the eddy breakup and mixing process and the formation of streamwise CS was largely suppressed. POD analysis performed on a longitudinal plane showed a much more even distribution of turbulent kinetic energy; with the first two modes containing approximately 12% of the in-plane turbulent kinectic energy. For $S_N = 0.49$ spectral analysis revelaed the dominant mode to be assocciated with the PVC rather than highly organsied structures resulting from shear-driven instabilities. No comparison of time-mean flow statistics, spectra or the distribution of POD modes was made with experiment.

1.4 Thesis Objectives

The primary objectives of this thesis are driven by the industrial requirement for reliable computational methods that can aid the design and development of swirl-stabilised combustion systems. LES is well suited to the calculation of swirling flows, however very small timesteps used by explicit schemes are required for solution stability (CFL$<$ 1) and the computational cost may prove prohibitive for routine industrial applications. The alternative URANS approach is much more computationally affordable (one to two orders of magnitude [50]), but questions still exist as to whether the statistical turbulence models used in URANS (mainly calibrated against 2D, steady, near equilibrium shear flows) are capable of adequate performance in fundamentally unsteady and 3D swirl injector flowfields. The suitability of these methods to flowfields characteristics of swirl-stabilised combustion system is still a matter of fundamental debate and it is of current interest to continue to assess their relative merits.

Combustion systems utilising swirl injectors are often characterised by helical instability modes of varying frequencies. An essential requirement of URANS and LES is that the characteristic frequencies of *all* aerodynamic modes should be predicted with a high degree of fidelity. This

is because if any of these frequencies are consistent with prevalent acoustic modes within the combustor there is a potential for flow-acoustic coupling which may reinforce acoustic oscillations and drive combustion instabilities via the Rayleigh criterion (Equation 1.1). Clearly, this assessment can be made under isothermal conditions which avoids the complications that arise in reacting flows. Turbomeca has a low emissions industrial swirl injector (see Figure 1.6) which is well suited to these purposes as this exhibits similar unsteady behaviour under reacting and isothermal conditions [12].

The level of swirl (quantified via S_N) is known to exert a strong influence on the aerodynamic instability modes and characteristic frequencies of combustion systems. Therefore, another central aspect of this thesis is to explore a range of S_N by varying the inlet swirl vane angle, α_1, of a derivative of the Turbomeca design. PIV was selected as the most appropriate experimental measurement technique for this purpose as it provides a wealth of time-mean statistics and a suitable basis for CS analysis which are also both useful for CFD test case selection and validation. Although a vortex may elude a precise definition; Kline and Robertson [60] have stated that: *'A vortex exists when instantaneous streamlines mapped onto a plane normal to the core exhibit a roughly circular or spiral pattern, when viewed in a reference frame moving with the centre of the vortex core'*. This provides a valuable means of identifying and characterising CS, however it constitute a subjective approach which, as noted by Pope [7], can lead to controversy over their nature and significance. It is therefore essential that qualitative measures and eduction techniques are also used. The subject of CS eduction has received much attention (see, example, [61, 62]) and the techniques adopted in this thesis are detailed in Addendix A-2. In order to optimise key instrumentation setup parameters, such as inter-frame time, PIV measurements were performed in water under isothermal conditions. Once thoroughly validated, it is also of interest to utilise the available volumetric information from CFD to understand further the complex 3D behaviour of aerodynamic modes which cannot be extrapolated from planar PIV.

1.5 Thesis Structure

This thesis will be organised as follows:

- **Chapter 2** discusses the experimental aspects of this thesis. This includes a description of the water facility, the various swirl injector geometries investigated ('modular' swirler design) and a derivation of realistic test conditions. An overview of the PIV technique is given with a particular focus on measurement optimisation and how inherent sources of error can be minimised during acquisition. In order to utilise PIV data as a benchmark for validating CFD predictions presented in Chapters 5 and 6 the accuracy of derived statistics are quantified.

- **Chapter 3** discusses the numerical aspects of this thesis. A general discussion of the

mathematical background of CFD is given followed by specific details regarding URANS and LES methodologies and their implementation within the various CFD codes (in-house and commercial) utilised during this thesis. The generation of a suitable computational mesh and realistic boundary conditions is discussed.

- **Chapter 4** presents PIV results for the modular swirler with varying swirl vane angle. Particular attention is paid to the various CS arising in both the near and far-field using a range of eduction techniques which are described in Appendix A. Based on this analysis a suitable test case for CFD is selected.

- **Chapters 5 and 6** presents LES and URANS results of the selected test case respectively. A range of computational meshes are investigated and results validated against experiment. Following validation, available volumetric information is then utilised to gain an improved understanding of CS observed experimentally.

- **Chapter 7** provides a summary, conclusions and recommendations for further work.

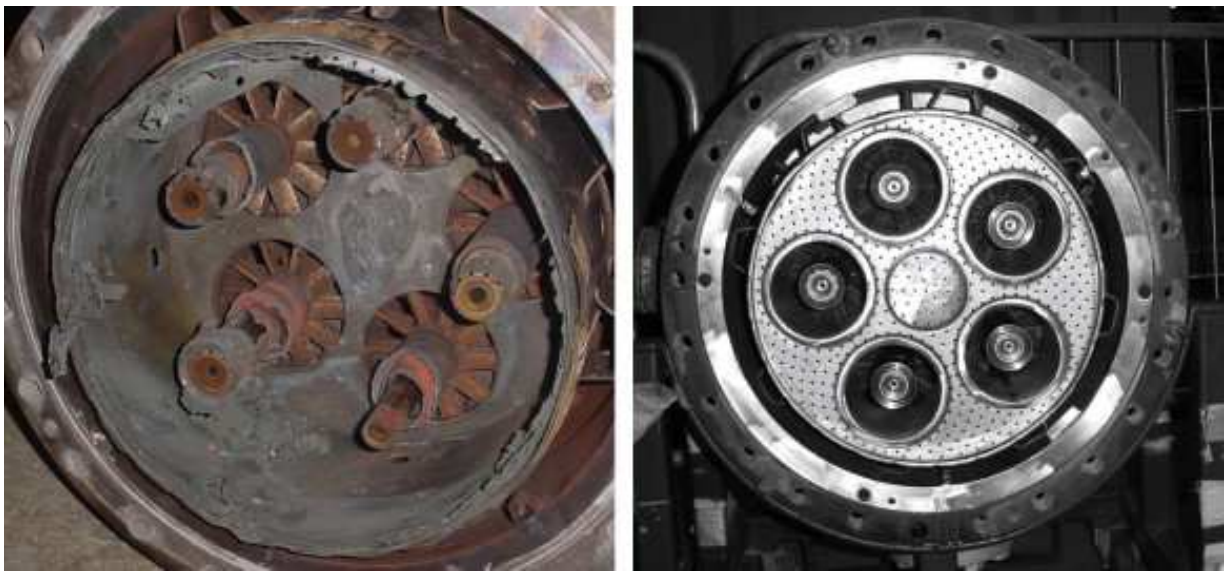

Figure 1.1: Burner assembly (left) damaged by combustion instability and new burner assembly (right) [63].

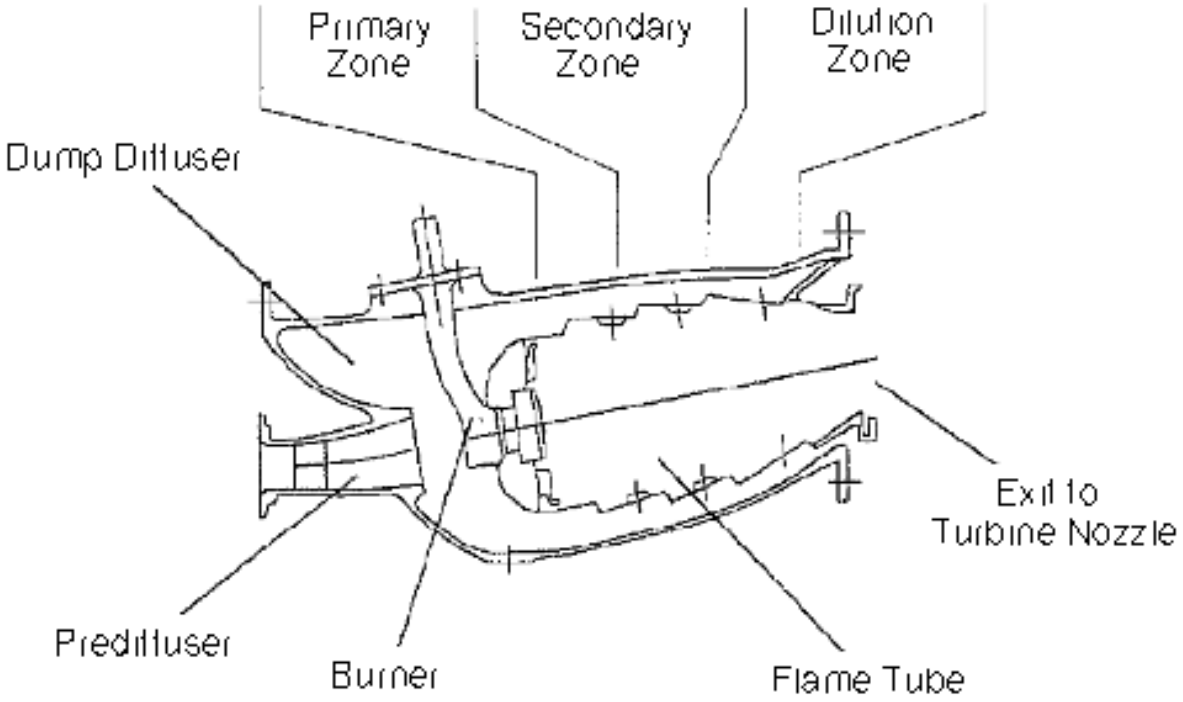

(a) Diffusion-flame - approximately 20% of delivery air from the HP compressor passes through swirl injector modules where it is mixed with fuel supplied via the burner arm and administered into the primary zone. Large quantities of NO_x are formed in the central hot region of the combustor due to oxidation of atmospheric nitrogen at temperatures over 1900K. The flame temperature, and thus NO_x production, can be reduced by the addition of more air into the primary zone, however this leads to a corresponding increase in CO and UHC due to low burning rates. As fuel preparation takes place in the hot environment of the primary zone, high level of NO_x may also result from buring at $\phi_{PZ} \approx 1$ in the presence of large droplets due to poor atomisation.

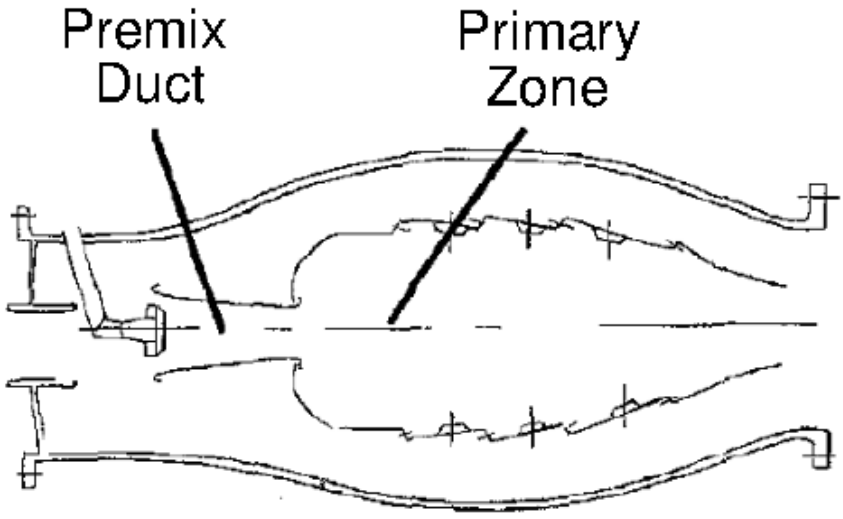

(b) LPP - fuel and air are premixed upstream of the primary zone to eliminate droplet combustion and supply the combustion zone with a low ϕ_{PZ} homogeneous mixture. This allows the combustion process to proceed at a uniformly low temperature, thus minimising NO_x formation. At reduced flame temperatures the amount of NO_x does not increase with residence time [64] and this can be taken advantage of to ensure that CO and UHC levels are minimised. In comparison to diffusion-flame systems which are relatively well understood, LPP systems suffer from more persistent instability problems.

Figure 1.2: Schematic of diffusion-flame and lean premixed prevaporised (LPP) combustors for aeronautical applications [65]

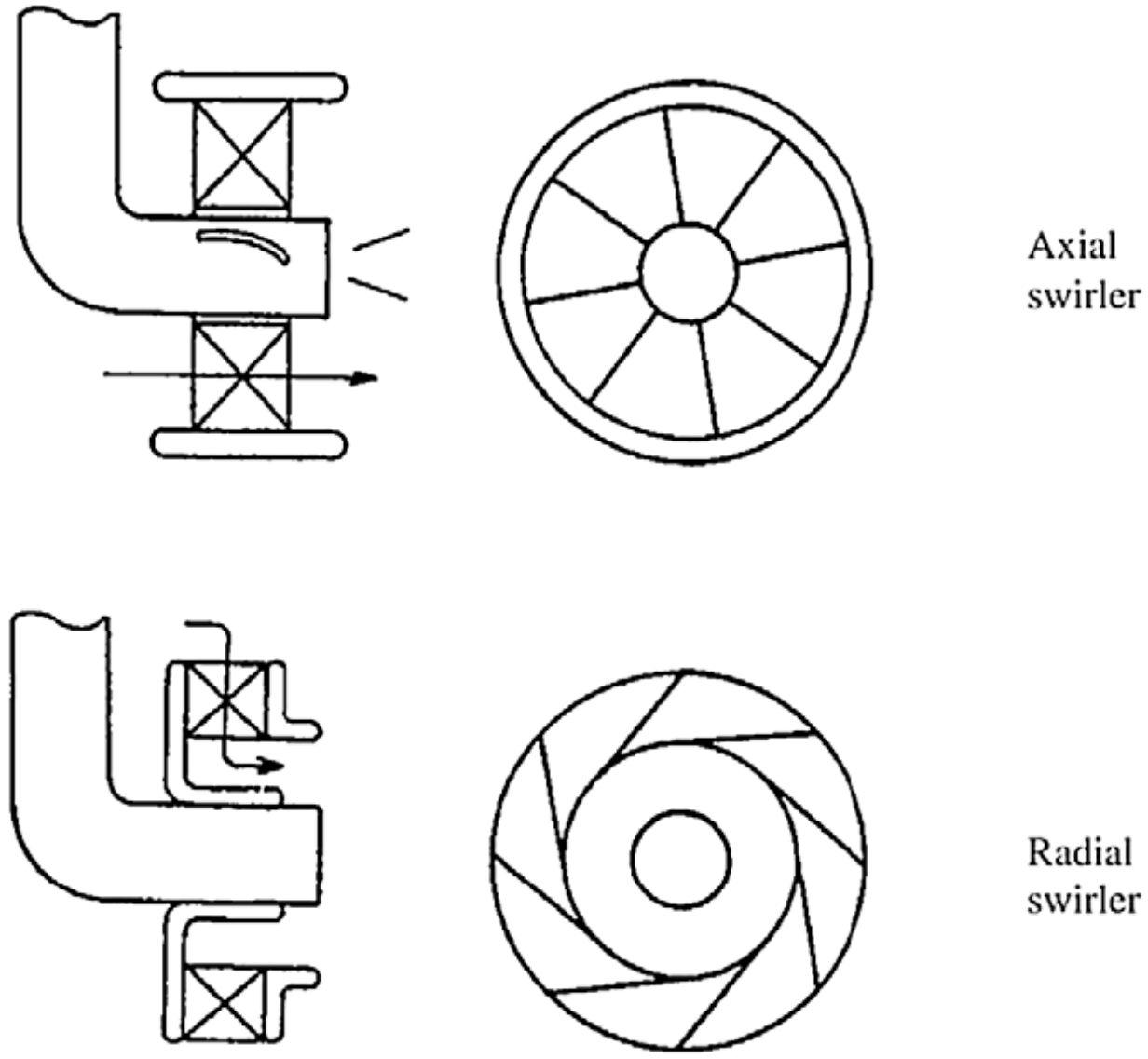

Figure 1.3: Schematic of axial and radial swirl injectors [64]

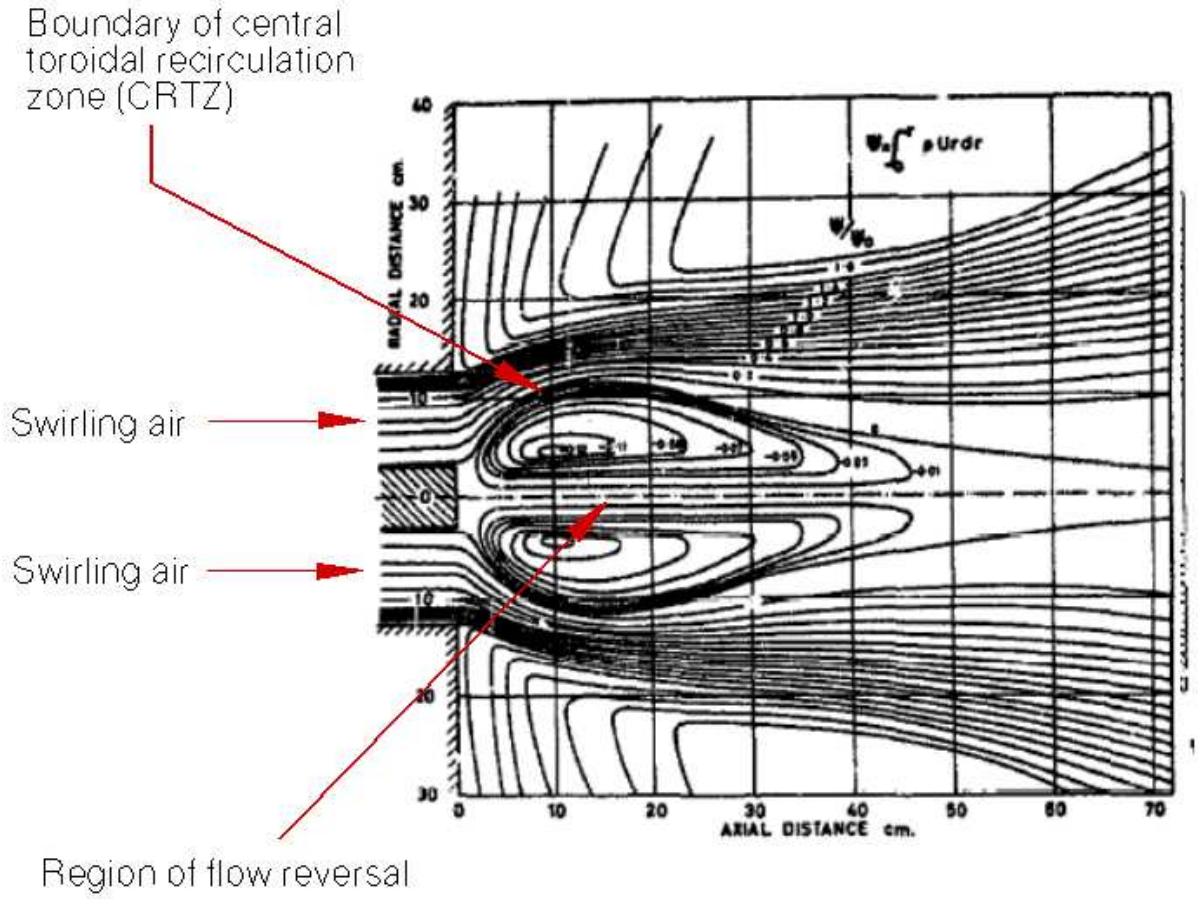

Figure 1.4: Streamlines of CTRZ in an unconfined swirling jet flow $S_N = 1.57$ [66]. When the level of swirl is sufficiently high ($S_N > 0.6$ for a round jet [16]), the forward momentum of the approach flow is insufficient to overcome the axial pressure gradient and reverse flow occurs. The resulting CTRZ causes the outer boundaries of the jet to expand rapidly soon after it emerges from the burner exit.

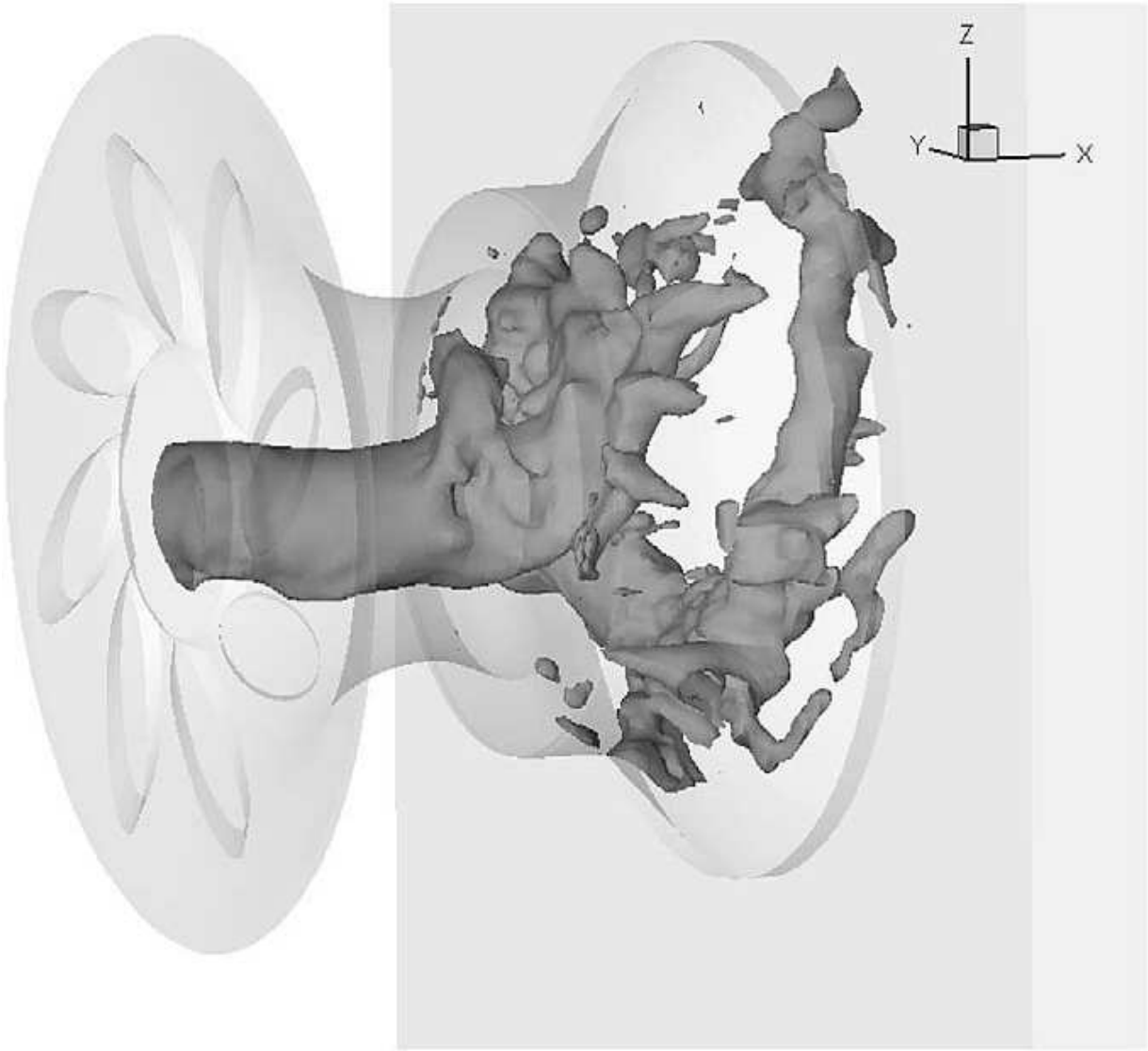

Figure 1.5: Typical swirl injector helical instability mode. Static pressure iso-surface at $p = 99,500$Pa [67]

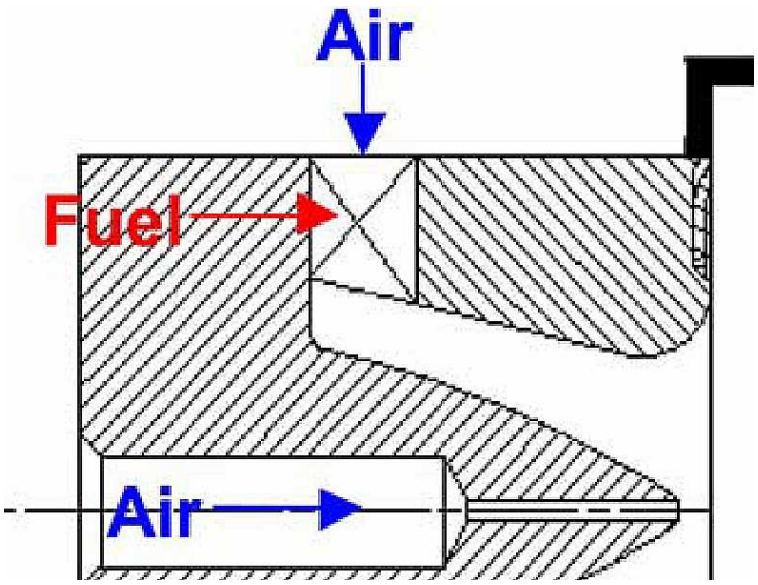

(a) Schematic of original Turbomeca design [68]

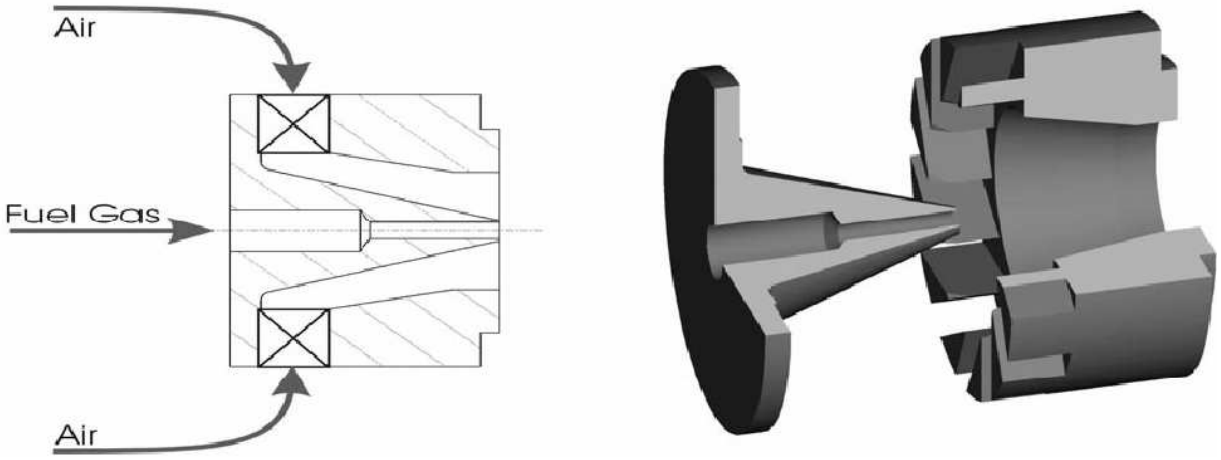

(b) Schematic and 3D view of modified design [12]. In an effort to reduce the complexity of generating block-structured computational meshes and to control separation points it was agreed by all MOLECULES [69] partners that the internal geometry in the swirl duct should be simplified. The curvature of the inner wall was replaced with a constant angle of 17° from the swirl vanes to the exit plane. The curvature of the outer wall was replaced with a constant angle of 12.5° until 10mm from the exit plane, after which the radius of the outer wall remained constant. This replaced the flare on the outer wall of the swirl duct, thus making it co-planar with the central jet at the exit plane

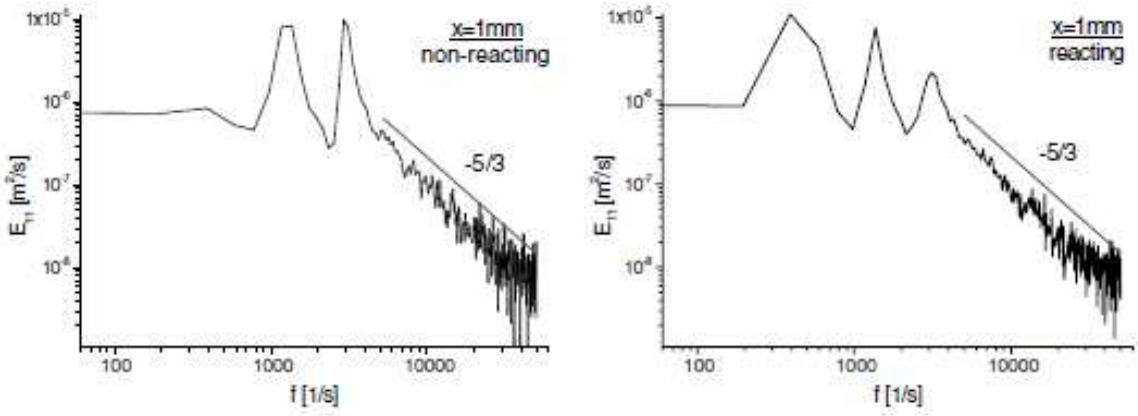

(c) Near-field PSD of velocity from isothermal (left) and reacting (right) test cases at 2 bar combustor pressure for modified design [12]. Monitor point in shear-layer between forward flow and CTRZ 1mm downstream of swirler exit

Figure 1.6: Geometry and spectral characteristics of industrial Turbomeca swirl injector

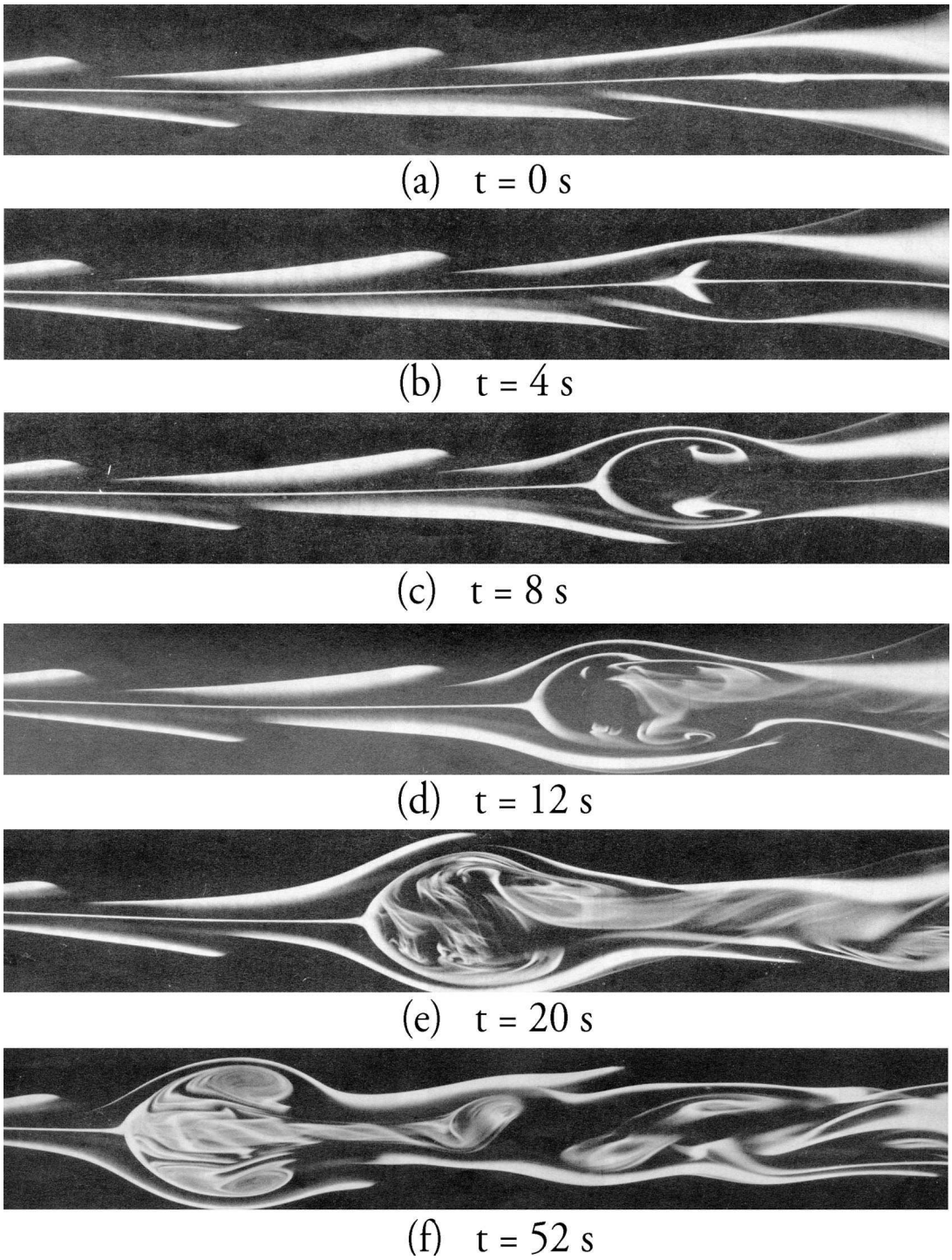

Figure 1.7: Formation of an axisymmetric bubble by core swelling [21].

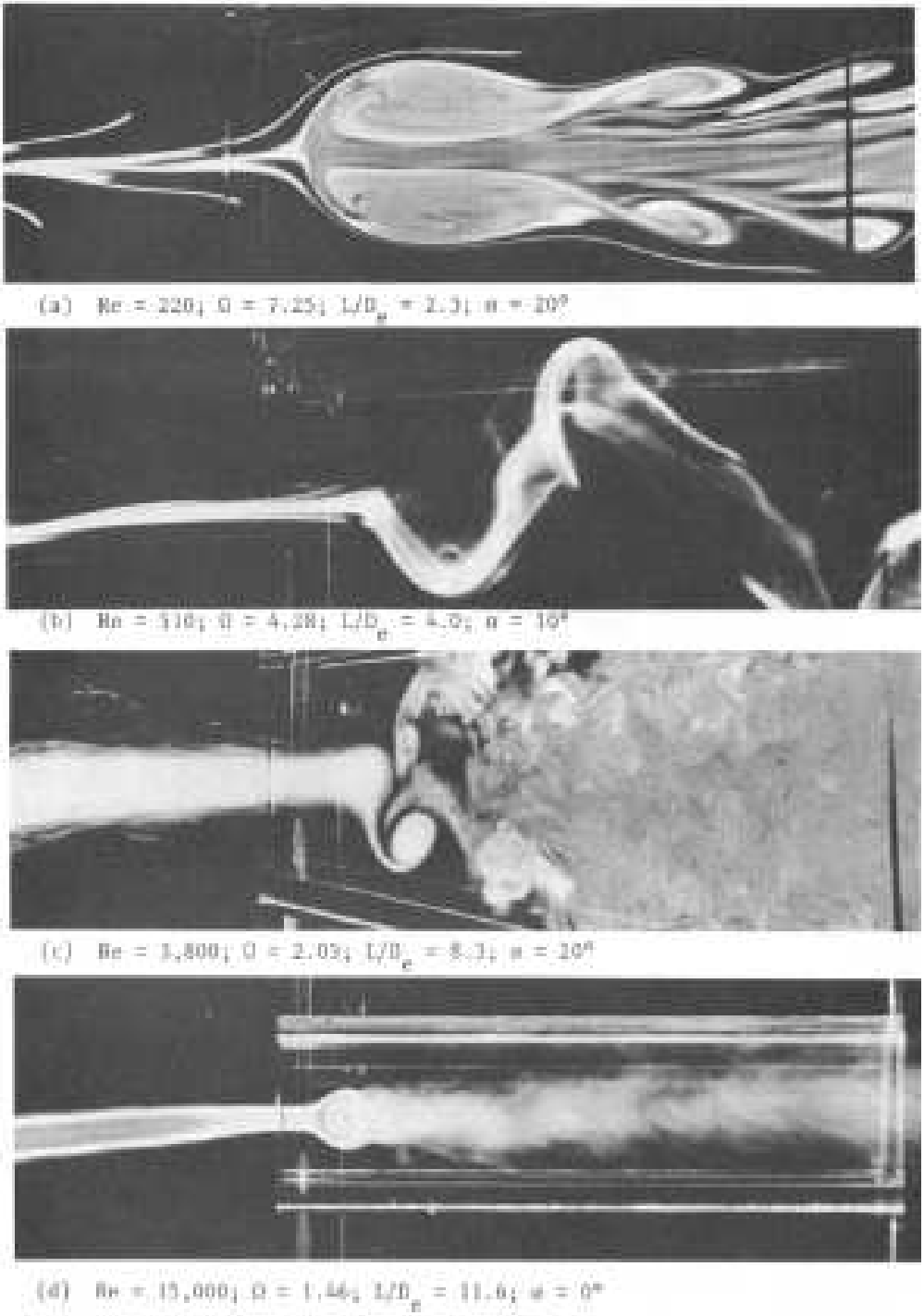

Figure 1.8: Various breakdown forms observed in a slit-tube arrangement [70].

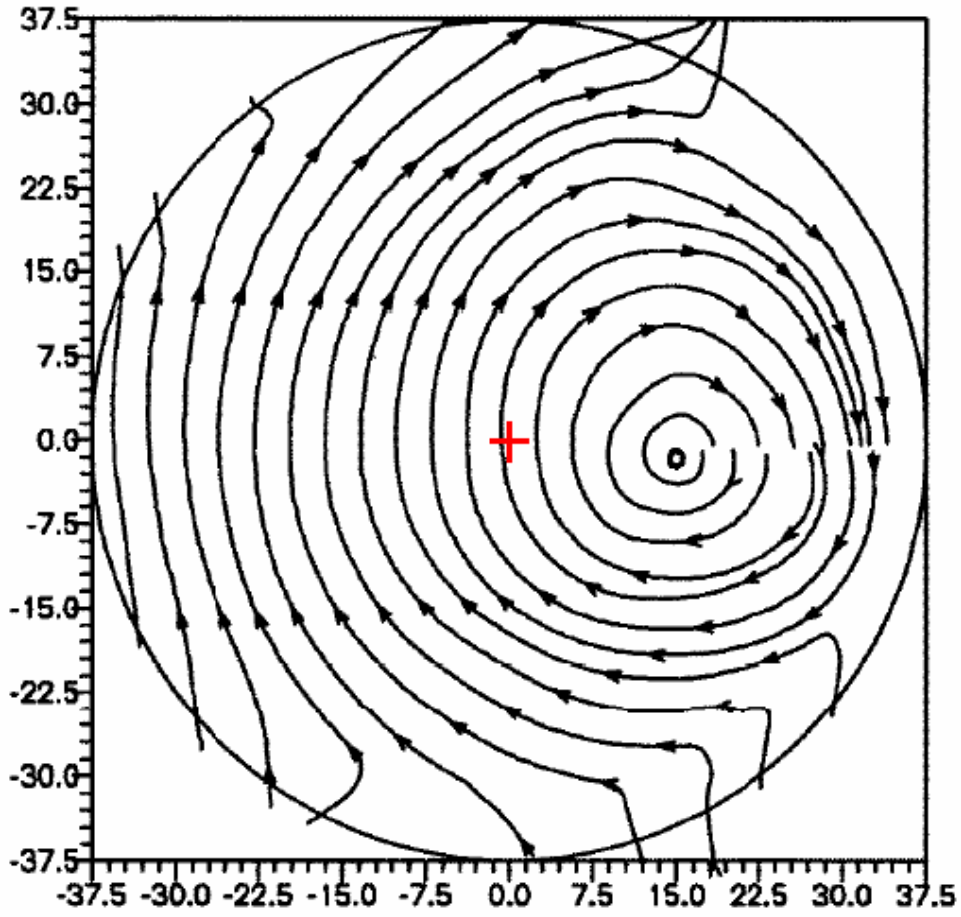

Figure 1.9: Instantaneous streamlines showing a precessing vortex core [36].

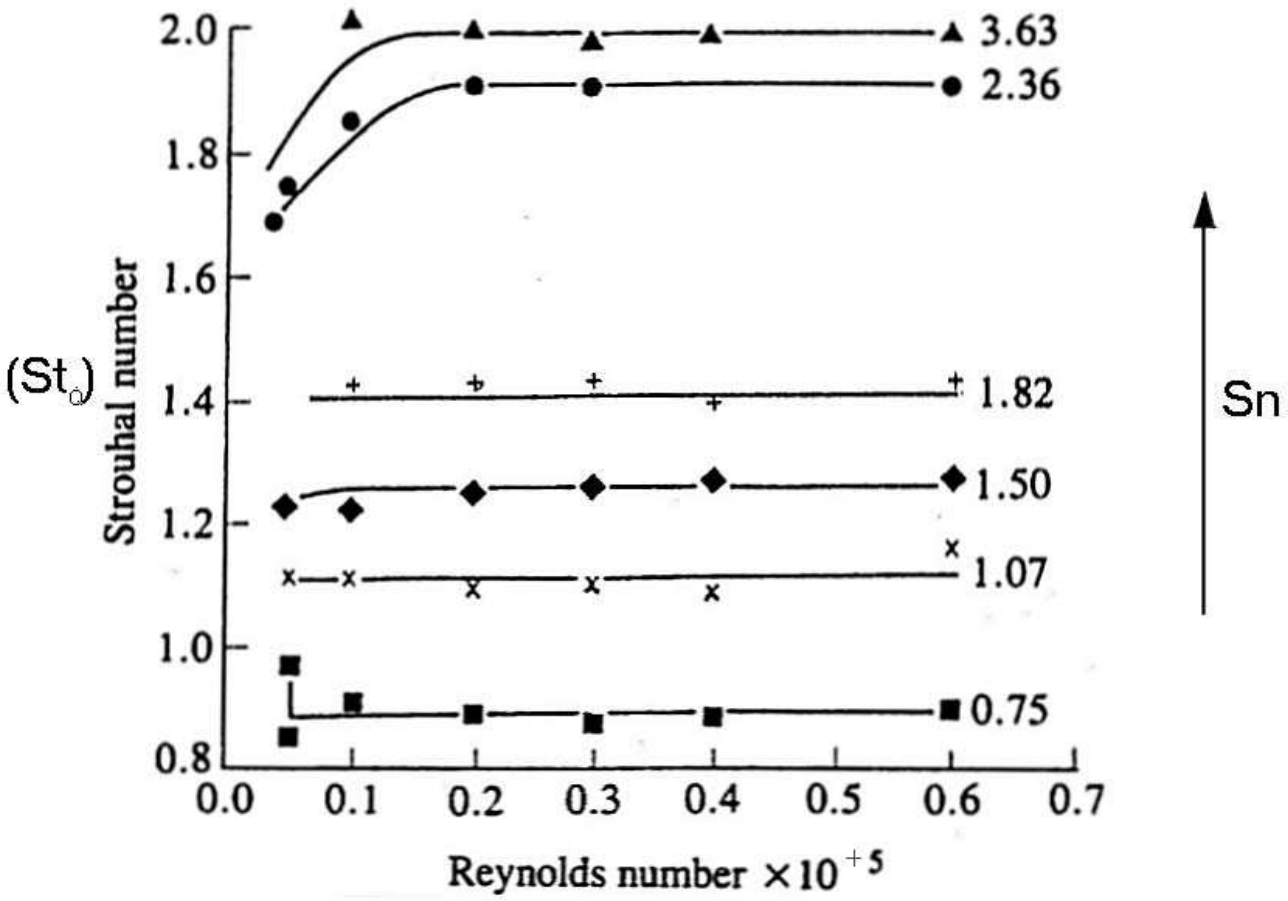

Figure 1.10: Variation of volumetric Strouhal number as a function of swirl number and Reynolds number [38].

Chapter 2

Experimental Facilities and Measurement Techniques

All measurements presented in this thesis were conducted in a water facility under isothermal conditions, utilising Particle Image Velocimetry (PIV) as the chosen measurement technique. No modifications to the existing facility were necessary during this project and a concise overview, particularly in regards to flow conditioning and optical access, is given in Section 2.1. Water was selected as the working medium as, for the same model size and Reynolds number, velocities are significantly reduced compared to equivalent airflow experiments due to the ratio of kinematic viscosities ($\nu_{\text{air}}/\nu_{\text{water}} \approx 14.6$). For dynamic similarity, testing was performed at $Re \approx 7.5 \times 10^4$ to ensure a stable CTRZ ($Re > 1.8 \times 10^4$ [16]) and for S_{N} independent of Re ($Re > 1.5 \times 10^4$ [38] Figure 1.10). The reduction in working velocities is well suited to PIV since key parameters, such as inter-frame time, are more readily optimised. Furthermore, errors associated with particle response time and velocity lag are significantly reduced using neutrally buoyant tracer particles, which can be achieved in water but not in air.

A slightly modified version of an industrial Turbomeca swirler (Figure 1.6(b)) was selected as a suitable test case as this exhibits similar unsteady behaviour under isothermal and combustion consditions [12] and its many complex aerodynamic characteristics make it a challenging test case for CFD methodologies. To explore the effect of S_{N} on CS development a modular version of the Turbomeca design which allows the inlet swirl vane angle, α_1, to be varied was utilised and is described in Section 2.2.

Although PIV is well suited to the class of flow studied in this thesis the technique in general can suffer from a number of error sources which can affect the quality of the resulting data. The vast majority of errors can be minimised by refining the experimental setup and user-defined parameters but in practice it is almost impossible to adhere to every required constraint and contamination of the recorded data is inevitable to some extent. Fortunately, certain 'types' of error,

such as those with a known bias, can be remedied through post-processing which can eliminate spurious data and apply suitable correction factors. The theoretical background of PIV and the optimisation of the technique in relation to the water facility is discussed in detail in Sections 2.3 and 2.4.

2.1 Water Flow Facility

The vertical water rig used during this investigation is a well-established test facility within the Aeronautical and Automotive department at Loughborough University that has contributed to three Ph.D. theses, namely Spencer [71], Hollis [72] and most recently Midgley [13]. The facility was originally designed to investigate multiple impinging jets in a confined cross-flow [71] but has since undergone a number of modifications to accommodate swirl injector geometries such as those studied in this thesis. For a detailed discussion of all the necessary modifications and their implementation the reader is referred to Midgley [13].

2.1.1 Flow Supply

The test facility, shown schematically in Figure 2.1, forms a closed-loop circuit and uses a pump to provide a continuous supply of water to an elevated header tank from a ground level sump tank. To maintain a constant level of water within the header tank, and therefore a steady driving force through the test section, it is housed within a larger overflow tank. This allows the pump to deliver a slightly higher mass flow than is required through the test section, ensuring a slight but continuous overflow that is returned to the sump tank in the manner illustrated. The mass flow rates through the test section are controlled by flow valves in the return pipes and measured using BS1042 orifice plates connected to manometers. Hollis [72] estimated the manometer calibration from test section inlet mass flow rates calculated from area integration of velocity profiles measured using the PIV technique. It was found that manometer based readings were repeatable and accurate to within $\pm 2\%$ of the desired values (to a confidence level of 95%).

Immediately downstream of the header tank the flow is split into two paths using concentrically mounted pipes which have inner diameters of 90mm and 140mm respectively and are manufactured from 5mm thick cast Acrylic. Flow within the inner pipe is referred to as the core flow and flow within the gap between the outer wall of the inner pipe and the inner wall of the outer pipe is referred to as the annular flow. The core flow develops over a distance of 18 core pipe diameters prior to the test section, and the annular flow over 53 annulus pipe heights. Flow straighteners are used to remove any residual tangential velocity components from both flows. As the swirl injectors studied in this thesis are fed only from the annular flow no further consideration will be given to the core flow. To ensure that the annular flow had reached a fully developed state before entering the test section Midgley [13] used PIV to measure the mass flow rate to peak velocity ratio ($\dot{m}/\langle\hat{u}_x\rangle$) 100mm ($x/D_s = -2.65$) upstream of the injector exit plane

for a range of Re based on an annular gap height of 20mm and a bulk average axial velocity which varied depending on mass flow rate. It was found that $\dot{m}/\langle\hat{u}_x\rangle$ becomes approximately constant and hence the flow fully developed at $Re > 3000$, which corresponds to a mass flow rate of $\dot{m} > 1.13$kg/s. To ensure measurement accuracy and repeatability, all measurements reported in this thesis were conducted using annulus mass flow rates above this value.

2.1.2 Test Section

After reaching a fully developed state the annular flow enters the test section, consisting of a model fuel injector, dump expansion chamber and a downstream blockage before passing through an exhaust manifold as shown in Figure 2.2. The purpose of the model injector, which is discussed in detail in Section 2.2, is to impart a tangential velocity component on to the annular flow. As discussed previously in Section 1.2.1 when a strongly swirling flow exhausts into a dump expansion chamber a long stable backflow region is produced and forward flow can only be re-established when the axial pressure gradient diminishes in strength sufficiently for it to be overcome by the forward momentum of the approach flow. In an engine gas turbine combustion system, the length of the CTRZ is controlled by radially impinging jets which are issued from primary ports that act as an aerodynamic blockage and reduce the level of swirl. Due to the impracticality of incorporating rows of impinging jets into the test facility, a blockage placed $x/D_s = 4.25$ downstream of the injector exit is used to physically impose the position of pressure recovery. For this purpose a cylindrical hollow tube with an outer diameter of 100mm is centrally mounted on the geometric centreline of the test section. By manufacturing the blockage from Perspex a convenient optical path allowing measurements to be acquired in planes parallel to the swirler exit is provided. The issue of optical access to the principle measurement planes investigated in this thesis is detailed further in Section 2.1.4. Midgley [13] found that placing the blockage $x/D_s < 3$ downstream of the exit plane had a tendency to damp the PVC. The final location was therefore chosen such that it imposed no significant influence on the upstream flow. A similar strategy was adopted by Khezzar [73] who placed a baffle plate 5.4 swirl passage diameters downstream of a radially fed swirler.

To assess the behaviour of the flow in the vicinity of the downstream blockage, Midgley [13] performed PIV measurements in the exhaust flow annular gap between the downstream blockage and test section wall. Time-mean velocity vectors in this region indicated a smooth channel flow, however high levels of axial r.m.s velocity (associated with an instantaneous separation of the flow in the annular exhaust duct) were detected close to the downstream blockage that persisted until $x/D_s \approx 5.25$. As the observed unsteadiness exerts an influence on the flow up to $x/D_s \approx 5.25$ it is clear that CFD boundary conditions should be set below this location.

2.1.3 Flow Exhaust

To exhaust the flow once it has passed the downstream blockage, a series of small circumferential gaps are used as shown in Figure 2.2. This arrangement ensures that the discrete pressure fields of the return pipes cannot influence what is designed to be an axisymmetric test section exit boundary plane.

2.1.4 Principle Measurement Planes

In strongly swirling flows, axial and tangential velocities are of similar magnitude and it is extremely important that both are measured accurately as they contain valuable information that can facilitate understanding of physical processes. In the 2C-PIV setup used during this project (see Figure 2.5), which is discussed in Section 2.3, it was not possible to capture both these velocities simultaneously. It was therefore necessary to conduct multiple PIV experiments in two principle measurements planes which were orthogonal with respect to each other. The first measurement plane was obtained by aligning the laser light sheet with the geometric centreline of the dump expansion chamber and a reference diameter of the injector which allowed the simultaneous capture of axial, u_x, and radial, u_r, velocities and as such is termed the $x-r$ plane. The second, referred to as the $r-\theta$ plane, was obtained by rotating the laser light sheet through 90° to be perpendicular to the geometric centreline, allowing illumination parallel to the swirler exit plane and the simultaneous capture of radial, u_r, and tangential, u_θ velocities. As PIV measures velocities on a Cartesian basis (see Section 2.3), the following transformation matrix was required in the $r-\theta$ plane:

$$\begin{bmatrix} u_r \\ u_\theta \end{bmatrix} = \begin{bmatrix} \cos\theta & \sin\theta \\ -\sin\theta & \cos\theta \end{bmatrix} \begin{bmatrix} u_i \\ u_j \end{bmatrix} \tag{2.1}$$

where $\theta = \arctan(z/y)$. Both principle measurement planes are shown in Figure 2.3 and further details regarding their optimisation are give in Section 2.4. With the camera positioned beneath the rig in the $r-\theta$ plane arrangement the flow is observed to rotate in a clockwise direction, i.e. when viewed from $x/D_s > 0$. Throughout this thesis a number of statistical quantities and CS eduction techniques are used and are detailed in Appendix A. The availability of mean velocity data and statistics from the principle measurement planes are summarised below in Table 2.1.

	x-r	**r-θ**	**Unavailable**
Mean velocity	$\langle u_x \rangle$, $\langle u_r \rangle$	$\langle u_r \rangle$, $\langle u_\theta \rangle$	-
Reynolds-stress	$\langle u'_x u'_x \rangle$, $\langle u'_x u'_r \rangle$, $\langle u'_r u'_r \rangle$	$\langle u'_r u'_r \rangle$, $\langle u'_r u'_\theta \rangle$, $\langle u'_\theta u'_\theta \rangle$	$\langle u'_x u'_\theta \rangle$
Spatial velocity correlation	R_{xx}, R_{xr}, R_{rr}	R_{rr}, $R_{r\theta}$, $R_{\theta\theta}$	$R_{x\theta}$
Integral lengthscale	${}^{x}L_{xx}$, ${}^{x}L_{rr}$, ${}^{r}L_{xx}$, ${}^{r}L_{rr}$	${}^{r}L_{rr}$, ${}^{r}L_{\theta\theta}$, ${}^{\theta}L_{rr}$, ${}^{\theta}L_{\theta\theta}$	${}^{x}L_{\theta\theta}$, ${}^{\theta}L_{xx}$
Vorticity	ω_θ	ω_x	ω_r

Table 2.1: Summary of available quantities from 2C-PIV

Although quantities such as swirl number, S_{N} (Equation 1.4), and total turbulent kinetic energy, k (Equation A-5), cannot be obtained directly from either measurement plane (this would require u_x, u_r and u_θ to be measured simultaneously) it is possible to do so by combining $x-r$ and $r-\theta$ data. Clearly, it is necessary for data points in both planes to be colocated. This was achieved by adopting a polar frame of reference in the $r-\theta$ plane whereby $\langle u_\theta \rangle$ and $\langle u'_\theta u'_\theta \rangle$ were interpolated from the original Cartesian PIV grid onto a polar-type mesh (see, for example, Figure 3.4(b)) with an identical radial resolution i.e. $\Delta r = \Delta x = \Delta y$ as the $x-r$ plane. As interpolation is not an error-free procedure, it was only performed once statistical quantities had been calculated in the original Cartesian basis rather than at each time-instant which would introduce a cumulative interpolation error. This was performed using the MATLAB function *interp2* and to assess the sensitivity to the grid resolution of the polar mesh the number of nodes in each direction were varied ($N_r = 40, 80, 160$ and $N_\theta = 40, 80, 160$) whilst maintaining a linear interpolation scheme. Inspection of circumferentially-averaged profiles (i.e. statistics averaged along lines of constant r from $0 \leq \theta \leq 2\pi$) indicated that first and second-order statistics were not influenced by the resolution of the polar mesh. The influence of the available interpolation schemes provided by Matlab (linear, nearest, cubic spline) were also investigated using a fixed grid resolution of $N_r = 42$ and $N_\theta = 80$ nodes and also found to have no significant influence on circumferentially averaged mean and r.m.s velocities. All combined data presented in this thesis uses a linear interpolation scheme with a grid resolution of $N_r = 42$ ($\Delta r = 0.45$mm) and $N_\theta = 80$.

2.2 Modular Swirler

The modular swirler has been investigated previously by Midgley [13] and Midgley et al. [15] and is shown schematically in Figure 2.4. It is based on the industrial Turbomeca design shown in Figure 1.6(b) and allows the effect of swirl vane angle ($\alpha_1 = 0°, 10°, 15°, 20°, 25°, 30°$) and swirl duct shape ($\alpha_2 = 0°, 13.5°, 17°, 20.5°$ and $\alpha_3 = 0°, 8.5°, 9.5°, 11.5°$) to be investigated. The most significant modification made to the modular swirler was the removal of the outer wall corner present in the Turbomeca design. However, through a combination of PIV and HWA this has been shown in [13] *not* to be responsible for the initiation of any large-scale unsteadiness, suggesting this source has a more fundamental fluid dynamic origin. The absence of the central jet

from the modular swirler has been shown [13, 14, 15] to result in the formation of a low-frequency PVC which presents a more challenging test case for CFD. During this thesis only the influence of swirl vane angle is investigated ($\alpha_1 = 10°, 15°, 20°, 30°$) with $\alpha_2 = 17°$ and $\alpha_3 = 9.5°$ selected to give a similar swirl duct definition as the Turbomeca design.

The isothermal test conditions used in this thesis, which are summarised below in Table 2.2 are based on those described by Midgley [13] which attempt to match as closely as possible the combusting conditions of Janus et al. [12]. For a detailed discussion of the derivation of these conditions the reader is referred to [13]. In order to maintain a similar expansion ratio as [12] ($E = 3.72$) in the water facility ($D_{ex} = 140$mm Figure 2.2), $D_{s,\text{outer}} = 37.63$mm and $D_{s,\text{outer}} = 6.76$mm leading to a scale factor of 1.35 relative to [12].

Swirl stream parameters	
Mass flow rate, $\dot{m}_s[kg/s]$	2.14
Temperature, T_s [K]	20
Density, ρ_s [kg/m^3]	998.2
Molecular viscosity, μ_s [Ns/m]	1.002×10^{-3}
Bulk average axial velocity, $U_{x,s}$ [m/s]	1.99
Reynolds number, Re_s	7.48×10^4

Table 2.2: Isothermal test conditions

Throughout this thesis $D_{s,\text{outer}}$ (D_s for brevity) and $U_{x,s}$ are selected as suitable length and velocity scales for normalisation.

2.3 Particle Image Velocimetry

Particle Image Velocimetry (PIV) is an optically-based [1] measurement technique that has the ability to provide spatially and temporally resolved velocity data. It has been previously categorised by Adrian [74] as a form of 'pulsed light velocimetry' that utilises the local displacement of a group of particle images to infer the components of a velocity vector. Unlike probe-based measurements, such as pitot tubes and hot wires, PIV is an non-intrusive technique, ensuring that local flow conditions are not influenced by potential blockage effects.

To facilitate discussion of the PIV process a generic experimental setup consisting of several

[1] During this thesis two-component (2C) planar PIV measurements were performed which use a single camera to capture in-plane velocity components parallel to a laser light sheet as shown in Figure 2.5. There are other 'forms' of PIV such as three-component (3C or stereoscopic) planar PIV which uses two cameras to capture both in-plane and out-of-plane velocity components and tomographic volumetric PIV which is able to measure all three velocity components within a 3D domain. In the present case only 2C-PIV was used and for the purposes of brevity will be simply referred to as PIV.

sub-systems (Figure 2.5), is considered. A light source, which is predominately provided by a monochromatic pulsed laser, together with suitable sheet optics, illuminates a plane of interest within the flow at least twice in quick succession. The interval between laser pulses, referred to as the inter-frame time, Δt, is a user-defined parameter and specification of a suitable value is absolutely crucial to ensuring that meaningful and accurate data is captured. The topic of PIV optimisation in relation to the water facility is covered in detail in Section 2.4. Incident light from each laser pulse is scattered by tracer particles seeded within the flow and focused through a lens onto the imaging plane of the recording device (digital CCD camera in the present case) which is arranged to view orthogonal to the lightsheet. If the shutter of the camera remains open for the duration of multiple laser pulses a single-frame multiple-exposure image is produced. If the shutter is quick enough to open and close to capture the incident light scattered by the first laser pulse and reopen to capture the incident light from the second laser pulse the result is two single-frame single-exposure images which form an image pair. During this thesis only single-frame single-exposure images are used.

In a manner analogous to CFD, the recorded digital images are divided up, or discretised, into a number of smaller regions known as interrogation cells which may either be contiguous or overlapping. In general, all interrogation cells are of equal size with dimensions $\Delta X = \Delta Y$ pixels (usually $\Delta X = 2^n$ as described in Section 2.3.2.1), thus forming a regular Cartesian grid. This allows the displacement, Δx, of a group of particle images within each interrogation cell to be determined on a statistical basis using either auto-correlation algorithms for single-frame multiple-exposure images or cross-correlation algorithms for single-frame single-exposure image pairs which is discussed in Section 2.3.2.1. An example illustration of the particle displacement within an individual interrogation cell of a discretised image pair is shown in Figure 2.6. Once the local displacement has been calculated, the inter-frame time, Δt, specified during the experiment can be used to determine the components of the local velocity vector in the following way:

$$u(x_i, t) = \frac{\Delta x}{\Delta t} \qquad\qquad v(x_i, t) = \frac{\Delta y}{\Delta t} \tag{2.2}$$

thus providing an Eulerian description of the flow. The implicit assumption in Equation 2.2 is that all particles move homogeneously within an interrogation cell but, as illustrated in Figure 2.6, this is not necessarily the case. Instantaneous velocity vectors calculated by the PIV technique are based on the displacement of a group of particles with the interrogation cell acting as a low pass spatial filter. This is known as sub-grid filtering (SGF) and can seriously affect higher-order statistics, such as r.m.s velocities, if it is not properly accounted for. The subject of sub-grid filtering is consider in detail in Section 2.3.4.

In general, a series of single-frame multiple-exposure images or single-frame single-exposure image pairs are captured over a period of time so statistical quantities such as mean and r.m.s can be computed. Each image pair is separated by a temporal interval, ΔT, know as the data acquisition rate and is another user-defined parameter. The following subsections consider image acquisition, image processing and vector validation in more detail.

2.3.1 Image Acquisition

The acquisition of high-quality images is arguably the most important aspect of the PIV process as they form the basis on which all subsequent analysis is performed. Assuming that the physical test rig and flow conditions in a particular area of interest (AoI) have been correctly defined prior to the PIV process, Hollis [72] identifies tracer particles, flow illumination, image recording parameters and timing parameters as being fundamental to successful image acquisition and these are the subjects of the following subsections.

2.3.1.1 Tracer Particles

As the PIV technique relies upon the displacement of a group of particle images within a single interrogation cell to infer the components of a local velocity vector, it is essential that they follow the flow faithfully in order to ensure a high level of measurement accuracy. The ability of tracer particles to follow the flow can be assessed in terms of two parameters: the particle response time, τ_p, which quantifies a particle's response to a step input, given as (Elghobashi [75]):

$$\tau_p = \frac{\rho_p}{\rho} \frac{d_p^2}{18\nu} \tag{2.3}$$

and velocity lag, U_p, which is a measure of the particle's ability to match the acceleration of a fluid particle when experiencing a constant acceleration, a, calculated from Stokes drag law, given as (Raffel et al. [76]):

$$U_p = d_p^2 \frac{\rho_p - \rho}{18\mu} a \tag{2.4}$$

Clearly, selection of neutrally buoyant ($\rho_p = \rho$) tracer particles eliminates U_p and reduces τ_p to a function of particle diameter, d_p, and the kinematic viscosity, ν, of the surrounding medium. In general, tracer particles typically used in water flow experiments, such as Polyamid spheres which are detailed in Table 2.3, are approximately neutrally buoyant, whereas those used in air flow experiments, such as oil particles, have densities greater than the surrounding fluid medium. For a particle to respond to all of the turbulent motions of a high Re flow, τ_p should be smaller than the smallest timescales of the flow, i.e. the Kolmolgorov scales. Midgley [13] has previously calculated $\tau_\eta \approx 40\mu$s in the vicinity of the swirler exit in flows similar to those studied in this

thesis. Whilst it is possible to minimise the τ_p by reducing d_p it should be borne in mind that another essential requirement of the tracer particle is that it scatters a sufficient amount of light to be detectable to the recording device and that its ability to do so is, amongst other things, proportional to its diameter. For spherical particles with diameters larger than the wavelength of the incident light ($\lambda = 532$nm in the present case), MIE's scattering theory [77] can be applied:

$$q = \left(\frac{\pi d_p}{\lambda}\right)^2 \tag{2.5}$$

From the above discussion it is clear that as there is a conflict of interest regarding d_p a compromise must be sought in practice as it is not possible to fulfill every theoretical ideal. Following Raffel et al. [76], Hollis [72] and Midgley [13], who performed PIV experiments under similar conditions to those considered in this thesis, Polyamid (polystyrene) particles of $d_p = 20\mu$m were selected as being the most suitable tracer particle, the properties of which in comparison to the surrounding medium are summarised in Table 2.3.

Parameter	
Particle diameter, d_p [μm]	20
Particle density, ρ_p [kg/m^3]	1003
Fluid density, ρ [kg/m^3]	998.2
Fluid molecular viscosity, μ [Nm/s^2]	8.904×10^{-7}
Fluid kinematic viscosity, ν [m^2/s]	8.920×10^{-4}
Particle velocity lag, U_p [m/s]	0
Particle response time, τ_p [μs]	24.9
Kolmolgorov time scale*, τ_η [μs]	40

Table 2.3: Flow properties and tracer particle characteristics. *In vicinity of swirler exit [13]

2.3.1.2 Flow Illumination

In the majority of PIV experiments, pulsed, rather than continuous wave (CW), lasers are preferable due to their ability to emit monochromatic light of high energy density at desired intervals with a very short pulse duration ($\approx$ 6ns [72]). Unlike CW, pulsed lasers allow energy to build up in the pump cavity before opening a device know as the Q-switch, discharging a very short burst of high intensity laser light. A typical 2.5W argon-ion CW laser has a power density of order 1×10^6W/m^2 whereas a 50mJ pulsed laser with a pulse length of 9ns has a power density of 5.7×10^{11}W/m^2, five orders of magnitude greater [78].

The beam emitted by the laser is shaped into a light sheet, which is necessary for illuminating an area of interest (AoI) within the flow, by sheet optics. Typically, this involves the use of

a spherical (diverging) lens to focus the beam and a cylindrical lens to form the light sheet. By adjusting the distance of the spherical and cylindrical lenses, the position of the cylindrical lens relative to the focal point of the beam is altered and thus the thickness of the light sheet too. In most scenarios it is desirable to keep the thickness of the light sheet to a minimum ($\approx$ 1mm) to reduce the chances of capturing any through plane particle motion.

2.3.1.3 Recording

The illuminated flowfield is recorded onto an electronic Charged Coupled Device (CCD) sensor within the camera housing. The CCD sensor is typically a rectangular array of individual CCD elements, referred to as pixels, which are able to register the intensity of the incident light in the form of charged electrons. The charge represents the digital intensity at each pixel, providing a digitised and rescaled version of the real object plane. The Imager Intense, which is detailed in Table 2.4, uses a full-frame interline transfer CCD sensor to allow the short inter-frame times required by the PIV technique. The operation of CCD devices can be found in Raffel et al. [76].

One of the first things to consider in any PIV experiment is the physical field of view (FoV) size. Whether or not the FoV can be accurately imaged on the CCD array depends on the particle image diameter, given as [76]:

$$d_\tau = \sqrt{M^2 d_p^2 + d_{\text{diff}}^2} \tag{2.6}$$

where M is the magnification of the image, defined as the ratio of the focal length, z_0, to the object distance, Z_0, or alternatively, the ratio of CCD sensor size, b_0, to the actual FoV size, B_0, d_p is the diameter of the tracer particle and d_{diff} is the diffraction limited image diameter, which is given as:

$$d_{\text{diff}} = 2.44\left(1 + M^2\right) f^{\#} \lambda \tag{2.7}$$

where $f^{\#}$ is the F-number given as the ratio of the focal length, z_0, to the aperture diameter and λ is the wavelength of the incident light, which is 523nm in the present case. As will be shown in Section 2.3.2, an optimum $d_\tau = 2.3$ pixels is required for accurate vector field calculation but this may not be possible if the FoV is too large as the magnification will be insufficient. A potential solution to this is to increase the physical size of the tracer particle, however, as discussed in Section 2.3.1.1, this has an effect on both τ_p and U_p and could be detrimental to results if the tracer particle can no longer follow the flow faithfully. In some instances d_τ is artificially increased by slightly defocussing and thus blurring the image. This, however, is not a particularly favorable

method as it leads to a degradation in image quality and may adversely affect results. A more suitable alternative is to decompose the overall target FoV into a series of smaller regions where experimental parameters may be more readily optimised and this is the method of choice for results presented in this thesis.

Another important parameter that depends on M and $f^{\#}$ is the depth of field, δz, which is given by the following equation [76]:

$$\delta z = 4\left(1 + M^{-1}\right)^2 f^{\#^2}\lambda \tag{2.8}$$

The depth of field is essentially the object focal depth and in practice should be slightly greater than the light sheet thickness (≈1mm) to ensure that all particles remain in focus in both frames of an image pair.

2.3.1.4 Timing

The 'quarter-rule' of Keane and Adrian [79] states that the spatial displacement of a particle image group within each interrogation cell should be less than one quarter of the cell dimensions ($\Delta x = \Delta X/4$). This reduces the chance of in-plane particle loss or gain. In practice an initial Δt is set by the user and then either increased or decreased depending on the resultant displacement. This process may go through several iterations until an optimum inter-frame time has been established. It is a mistake to interpret the quarter-rule as a freedom to set Δt to an extremely small value as it must be borne in mind that algorithms employed at the processing stage are typically able to detect the position of a particle only to within ±0.1 pixels [72]. Therefore, for small particle displacements, say 1 pixel, the relative positional error will be large, ±10% in this case, compared with a particle displcement of 8 pixels, which would have a relative error of ±1.25% in the example cited. Clearly, there are advantages to maximising Δt in order to maximise the particle group displacement.

Dynamic averaging is the extent to which the true motion of a particle is averaged as a result Δt. It is a direct result of using Eulerian velocities to approximate Lagrangian particle displacements and the effect, as shown in Figure 2.7, is to reduce the recorded levels of turbulence as all curvature information is lost between images and approximated by a linear displacement. In addition to setting Δt to satisfy the quarter-rule, consideration must also be given to the Kolmogorov timescale and Δt set less than or, at most, equal to it in order to minimise the effect of dynamic averaging. In highly turbulent flow, such as those studied in this thesis, it is likely that a given FoV will contain a wide range of velocities and it may not be possible to optimise every parameter. In such cases trade-offs must be made and compromises sought in order to obtain the most accurate measurements possible.

If there is significant through plane velocity, u_k, such as in the swirling flow studied in this thesis, Raffel [76] gives the following for determining an acceptable out of plane motion:

$$\frac{u_k \Delta t}{\delta z} \geq 0.3 \tag{2.9}$$

In other words, the maximum through plane displacement should be less than 30% of the depth of field, δz, which is typically $\approx$ 1mm. The presence of through plane motions can result in perspective projection errors which are considered in Seciton 2.4.3 and decreased Q-ratio or SNR as defined later.

2.3.2 Image Processing

The previous section has considered the practical aspects necessary for the acquisition of high quality PIV images. The next stage in the PIV process involves discretisation of these images into a number of smaller regions know as interrogation cells to allow the displacement of a group of particle images to be determined. The following subsections explain in more detail the basic methodologies for determining the displacement of a group of particle images and how additional algorithms are employed to improve accuracy.

2.3.2.1 Basic Vector Calculation

In practice, the displacement of a group of particle images between PIV frames is achieved by determining the best match between images provided by a local displacement between them in a statistical sense using auto-correlation in the case of single-frame multiple-exposure images and cross-correlation in the case of single-frame single-exposure image pair. Cross-correlation has been adopted during this thesis and is preferable to auto-correlation in nearly every instance for the following reasons [80]:

1. It produces only one correlation peak thus removing directional ambiguity.
2. It can measure zero displacements.
3. Relative to auto-correlation the signal to noise ratio (SNR) is increased, where the higher the SNR the higher the probability of the detection of the correct correlation peak.

In practice the cross-correlation is performed in Fourier space using an FFT algorithm (hence the reason individual interrogation cells typically have base-2 dimensions) and for details of this procedure the reader is referred to Raffel et al. [76]. The result is a correlation plane in each interrogation cell (Figure 2.8) with a maximum value, P_1, at the point where particle images from a single-exposure image pair align.

2.3.2.2 Practical Considerations

To determining the cross-correlation between image pairs a sufficient number of particle images, N_{PI}, are required within each interrogation cell at any given moment. The recommended minimum N_{PI} required to achieve a 95% valid detection probability varies quite significantly in the availiable literature. To ensure the accuracy of meausrements presented in this thesis it was ensured that $N_{\mathrm{PI}} \geq 5$ in each interrogation cell at all times which is in line with the recommendation 3 - 4 required by DaVis 7.2 [81]. The number of particle images within an individual interrogation cell is dependent on the cell size, the level of magnification and the volumetric seeding density of the flow.

Magnification has already been discussed in Section 2.3.1.3, and an optimum value is governed by the resulting d_τ, which should be approximately 2.3 pixels. This is due to the fact that for $d_\tau < 2.3$pixels the phenomena of peak locking can occur, whereby particle image displacements are biased towards integer values as shown in Figure 2.9. Selection of an appropriate ΔX is complicated by the fact that in addition to being large enough to contain a sufficient number of particle images, it should be small enough to result in the homogeneous movement of groups of particle images. This, in theory, requires ΔX to be less than, or at least equal to, the Kolmogorov lengthscale, η. Midgley [13] has previously calculated $\eta \approx 2\mu$m in the vicinity of the swirler exit in flows similar to those studied in this thesis. The ability to achieve this level of spatial resolution requires extremely small FoVs ($0.5\mathrm{mm}^2$) and high magnifications (4.6) which could not be realised using the available experimental apparatus detailed in Table 2.4. Although the non-resolution of the Kolmogorov scales leads to a smearing of the smallest eddies it will be seen in Section 2.3.4 that in order to capture the majority ($\approx 80\%$) of turbulent energy ΔX should be suitbaly small in relation to the integral lengthscale, ${}^{k}L_{ij}$ (see Equation A-13), suggesting that this, rather than the dissipative scale, is a more suitable measure for real engineering flows.

2.3.2.3 Advanced Methods

As cross-correlation methods used to determine the displacement of a group of particle images rely on discrete input data, correlation values exist only for integer pixel shifts. The highest value in the correlation plane then permits the displacement to be determined with an uncertainty of ± 0.5 pixel. It is possible to determine the position of the correlation peak to sub-pixel accuracy by fitting a continuous analytical function to the discrete correlation map. It has been shown that three-point estimators, such as a Gaussian peak fit, work best for rather narrow correlation peaks based on $d_\tau = 2.3$ pixels [82] and are typically able to determine pixel displacement with an accuracy of ± 0.1 pixel.

During discretisation it is common practice to create a regular grid of overlapping, rather than

contiguous, interrogation cells. Cell overlap is defined as the amount by which a given interrogation cell overlaps adjacent ones and is a way to increase the vector grid density and the perceived amount of flow information. For example, using a typical overlap of 50% increases the data yield fourfold. It should be stressed that such an approach does *not* increase the spatial resolution of the data as it is the final ΔX that determines which flow scales are resolved. By using a cell overlap the raw image data is used more than once at each location and this is very important to vector validation which is discussed in Section 2.3.3. The argument is that if a single vector, which is surrounded by valid vectors, is deemed to be spurious, replacement by linear interploation is justified on the basis that raw image information has already been utilised in producing the adjacent vectors.

Although a final interrogation cell size of $\Delta X = \Delta Y = 32$ pixels provides an optimum setup, for most practical levels of magnification [72] an initial pass using a larger interrogation cell of $\Delta X = \Delta Y = 64$ pixels is often performed on the particle images. This provides an estimate of the particle image displacement and allows subsequent smaller interrogation cells to be shifted by a given amount which helps to reduced the loss of in-plane particle pairs. This increases the likelihood that the correct particle pairs are correlated and allows smaller interrogation cells to be used than would otherwise be possible, thus increasing spatial resolution. All results presented in this thesis used an initial pass using a interrogation cell of 64×64 pixels followed by two subsequent passes using an interrogation cell of 32×32 pixels.

2.3.3 Vector Validation

Once high-quality images have been captured and processed using the techniques described in Section 2.3.2, calculated vectors fields are subjected to rigorous validation procedures that are able to detect, remove and replace spurious data points. Validation is an extremely important part of the PIV process as failure to account for questionable data at an early stage can have dire consequences on any subsequent results which are often statistical quantities, such as mean and r.m.s, and easily contaminated. There are a variety of methods available for the detection, removal and replacement of spurious data and are the subject of the following subsections.

2.3.3.1 Pre-Defined Limits

This approach essentially imposes hardwired limits on the flow and includes geometry masking and allowable velocity limits. Masking is used in regions where the user knows that no vectors appear, such as in the vicinity of near wall regions where vectors may be generated because of reflections. The definition of global limits on velocity should be used with extreme caution and requires extensive knowledge of the flowfield. If the experimental setup is well defined and FoVs optimised to local flow condition they should not be necessary and were not employed on data presented in this thesis.

2.3.3.2 Vector Quality

The quality of data calculated within an interrogation cell can be assessed in terms of the peak Q-ratio which is defined as the ratio of the strongest correlation peak, which is assumed to represent the true displacement, and the the next highest peak, which is assumed to be background noise. This measurement, referred to as the Q-ratio, is therefore a signal to noise ratio, given as [81]:

$$Q = \frac{P_1 - \min}{P_2 - \min} \tag{2.10}$$

where P_1 is the highest correlation peak and P_2 is the second highest correlation peak as shown in Figure 2.8. A Q-ratio of greater than 2 indicates a reasonably strong confidence that the vector is valid, whereas values closer to 1 indicate that the vector is probably false. By setting a lower limit on the Q-ratio it is possible to eliminate vectors that are more than likely a result of measurement noise. There is a risk that this method may result in the removal of valid vectors but if the quality of the data is high to begin with then this issue is largely negated. In this project a threshold value of (Q=1.5) was used.

2.3.3.3 Consideration of Local Flow Conditions

Consideration of a vector in relation to its neighbours is the most trusted method of validation as it is derived directly from physical reasoning. The method was first proposed by Westerweel [83], who stated that if a vector deviates substantially in direction or magnitude compared to its neighbouring vectors, flow continuity is not satisfied and the vector must be spurious. At each vector location, the average magnitude and standard deviation, σ, based on its 8 surrounding vectors, is calculated. If the vector differs from the average magnitude by some factor times by the standard deviation (a factor of 2 was used in this thesis as detailed in Table 2.9) it is deemed to be spurious and removed.

2.3.3.4 Replacing Removed Data

If a vector is deemed to be spurious through any of the methods discussed previously it is extremely important that it is replaced as this can affect the computed statistics in the event that zeros are included. Linear interpolation is a simple method that calculates the magnitude of the surrounding vectors and replaces the removed one with such a value. Although linear interpolation ensures continuity, if too many vectors are removed it can overly smooth the resultant flowfield.

Another method used by DaVis, which is preferable to linear interpolation, is to consider the next highest correlation peak if the vector associated with the first is deemed to be spurious. This process can also be repeated for the third and fourth highest peaks, but no further than this

as these are almost certainly due to measurement noise. If none of the peaks satisfy validation criteria then linear interpolation can be used.

2.3.4 Sub-grid Filtering

The issue of sub-grid filtering, SGF, was first introduced in Section 2.3 and is a direct result of the way in which instantaneous velocity vectors are calculated using the PIV technique. As the cross-correlation algorithm used to determine the displacement of groups of particles is performed over a finite area it is only possible to resolve the modal displacement as the interrogation cell acts as a low pass spatial filter. As a result measured r.m.s velocities, $\langle u'_{i,\text{meas}} \rangle$, can be lower than actual or 'true' values, $\langle u'_{i,\text{true}} \rangle$. The level of SGF depends on the size of ΔX relative to local turbulent lengthscales which, in real engineering flows, cover an extremely broad range. It is well know that the majority of turbulent motions contributing to flow statistics are contained within a relatively small wavenumber range of the energy spectrum, specifically, Pope [7] states that the energy containing scales which are responsible for approximately 80% of r.m.s velocities are in the range of motions $1/6 \geq \ell_0 < 6$ in size. In this case, ℓ_0, is taken as the integral lengthscale, ${}^kL_{ij}$, which is characterisitc of the larger eddies present within the flow. It is therefore logical that in order to record the majority of fluctuating velocities $\Delta X \leq^k L_{ij}$.

The method of accounting for SGF effects on PIV measurements used in this thesis is that proposed by Hollis [72] which is based on a theoretical examination of the phenomenon first presented by Hoest-Madsen and Nielsen [84] (to be referred to as HMN). This approach is based on an assumption of two-dimensional homogeneous isotropic turbulence (i.e. statistically invariant under translations, rotations and reflections of the coordinate system [7]) and attempts to relate the effect of SGF on r.m.s velocities (quatified via $\langle u'_{i,\text{meas}} \rangle / \langle u'_{i,\text{true}} \rangle$) to $\Delta X / {}^kL_{ij}$. For a detailed discussion of the theoretical background and implementation in respect to PIV applications the reader is referred to HMN [84] and Hollis [72] respectively, however, the most pertinent aspects are presented in the following.

Although exact isotropic turbulence does not exist in shear containing flows [85] isotropy is approached on a local (sub-grid) scale for many non-trivial flow problems and it is argued in HMN that the assumption of homogeneity and isotropy need only be true inside individual interrogation cells. The methodology proposed by HMN hinges on correlation functions which provide a statistical model relevant to the early and final stages of decay of homogeneous isotropic turbulence quoted by Hinze [85] which are given in terms of ${}^kL_{ij}$:

$$R_{ij} = e^{(-\Delta X_k / {}^kL_{ij})} \tag{2.11}$$

and Taylor micro-scale, ${}^k\lambda_{ij}$:

$$R_{ij} = e^{(-\Delta X_k^2/^k\lambda_{ij})} \tag{2.12}$$

These equations are then used in formulae representing the volume weighting and random errors in PIV measurements to derive the theoretical curves shown by the solid lines in Figure 2.10(a). To make an independent comparison with HMN, Hollis used a series of 'synthetically generated' velocity fields with prescribed ${}^kL_{ij}$ and correlation models (exponential and quadratic). Variation in the level of SGF was achieved by spatial averaging using an N×N box filter to imitate the influence of the interrogation cell. In order to fit trendlines to the discrete data points investigated, the following empirical laws were proposed [72] based on the exponential model:

$$\begin{aligned}\langle u'_{i,\text{meas}}\rangle/\langle u'_{i,\text{true}}\rangle|_{\Delta X/^kL_{ij,\text{true}}<1} &= e^{-0.3235(\Delta X/^kL_{ij,\text{true}})} \\ \langle u'_{i,\text{meas}}\rangle/\langle u'_{i,\text{true}}\rangle|_{\Delta X/^kL_{ij,\text{true}}\geq 1} &= -0.2181\ln(\Delta X/^kL_{ij,\text{true}}) + 0.7501\end{aligned} \tag{2.13}$$

and are shown by the dashed black line in Figure 2.10(a). From 2C-PIV measurements which are shown by the discrete points in Figure 2.10(a) it was confirmed [72] that trendlines based on the exponential model provided a reliable means of correcting for SGF effects. This is becuase high Re flows such as those considered in this thesis tends to exhibit exponential correlations, whilst the quadratic model is more appropriate for flow with homogeneous turbulence associated with low Re.

An important development by Hollis necessary for the proposed correction methodology to be applied to real PIV data is to account for the fact that ${}^kL_{ij}$ is not known a priori as has been the case thus far. In reality, ${}^kL_{ij}$ calculated directly from PIV data (${}^kL_{ij,\text{meas}}$) are also contaminated by SGF effects as the spatial correlations from which they are derived are based on measured fluctuating velocities which are, in most cases, lower than the actual 'true' value, (${}^kL_{ij,\text{true}}$). The result is to smooth the spatial correlation and ${}^kL_{ij,\text{meas}} > {}^kL_{ij,\text{true}}$. In a similar way to HMN, Hollis used synthetic velocity data with known statistical properties to provide a correlation that relates ${}^kL_{ij,\text{true}}/\Delta X$ to ${}^kL_{ij,\text{true}}/{}^kL_{ij,\text{meas}}$. Again, by fitting trendlines to the discrete data points investigated, Hollis was able to provide the following empirical laws based on an exponential model:

$$\begin{aligned}{}^kL_{ij,\text{true}}/{}^kL_{ij,\text{meas}}|_{\Delta X/^kL_{ij,\text{true}}<0.65} &= e^{-0.5151(\Delta X/^kL_{ij,\text{true}})} \\ {}^kL_{ij,\text{true}}/{}^kL_{ij,\text{meas}}|_{\Delta X/^kL_{ij,\text{true}}\geq 0.65} &= -0.23\ln(\Delta X/^kL_{ij,\text{true}}) + 0.623\end{aligned} \tag{2.14}$$

which are shown by the dashed black line in Figure 2.10(b). With ${}^kL_{ij,\text{true}}$ appearing on both sides of the equation an iterative approach is required with an initial estimation of ${}^kL_{ij,\text{true}} =^k L_{ij,\text{meas}}$. It has been found [72] that convergence is obtained (usually within 10 iterations) except in cases where $\Delta X/{}^kL_{ij}$ exceeds 1.5 and divergence may occur. As a result a lower correction limit of ${}^kL_{ij,\text{true}}/{}^kL_{ij,\text{meas}} = 0.3$ is recommended [72].

2.3.5 PIV System

The PIV hardware and software used during this thesis was purchased as a complete proprietary system from LaVison GmbH and are detailed below in Table 2.4. To allow the capture of multiple FoVs and expedite the data acquisition sequence a Dantec 3-axis traverse was implemented around the test facility and is also detailed below. Raw PIV images were processed using DaVis 7 [81] and the resulting vector fields analysed using in-house MATLAB (*Xact* [86]) and Fortran codes.

Illumination	Dual Head New Wave Solo Nd:YAG
Wavelength (λ)	532nm (green)
Pulse Length	9ns
Maximum Repetition Rate	18Hz
Maximum Energy	50mJ
Recording	Imager Intense
CCD	12-bit monochrome
CCD Size	8.88mm×6.71mm
Resolution	1376×1040 pixels
Pixel Width (d_r)	6.45μm
Maximum Frame Rate	10Hz
Minimum Inter-Frame Time	500ns
Lens	Nikon Nikkor Macro
Focal Lengths (z)	50mm, 105mm
F-Number f$^\#$	1.8 - 32
Traverse	3-axis Dantec
Resolution	6.25μm

Table 2.4: PIV system details

2.4 PIV Optimisation in Water Facility

For high *Re* flows the range of turbulent length and timescales is extremely broad and in order to ensure a high level of data quality and eliminate potential sources of error it is necessary to optimise experimental arrangements to suit local flow conditions. This requires a careful

selection of camera lenses in terms of focal length and operating parameters such as $f^{\#}$. For this thesis high-quality Nikon lenses with negligible aberrations were used with focal lengths of 50mm to 105mm and an $f^{\#}$ range of 1.8 to 32. Full details of the cameras and lenses used are provided in Table 2.4. Whether or not optimisation of all the various PIV operating parameters discussed in the preceding sections is realised is extremely dependent on the physical FoV size which is intimately linked to camera positioning and lens selection. These issues are considered in relation to the vertical water facility in the following subsections. The physical FoV size and positioning within the measurement domain were based on guidelines proposed by Midgley [13] designed to ensure the optimisation of PIV operating parameters and minimise the effects of SGF on recorded turbulence levels. The latter condition was verified by Midgley [13] who compared r.m.s velocities from optimised PIV experiments with LDA measured profiles which, due to the Lagrangian nature of the technique, do not suffer from SGF effects. Overall excellent agreement indicates that the experimental arrangement used in this thesis is suitable for capturing the majority of turbulent motions.

2.4.1 Axial-Radial Plane

As mentioned in Section 2.1.4, the $x-r$ plane was obtained by aligning the laser light sheet along the geometric centreline of the dump expansion chamber and illuminating a region that extended from the swirler exit plane, $x/D_s = 0.0$, to a downstream location of approximately $x/D_s = 2.76$. From the previous work of Midgley [13], it was known that many complex and diverse processes occur within this region that require varying levels of spatial resolution and optimisation of user-defined parameters to ensure a high level of measurement accuracy. For example, in the near-field, $x/D_s \leq 1.0$, the flow is dominated by complex shear-layers which exhibit relatively large characteristic velocities and require a high level of spatial resolution, whilst in the far field, $x/D_s > 1.0$, characteristic velocities associated with features such as the CTRZ are perhaps an order of magnitude less and clearly require quite different timing parameters if aspects such as the quarter-rule discussed in Section 2.3.2 are to be adhered to.

The FoVs size and position are shown schematically in Figure 2.11 and detailed in full in Tables 2.5 and 2.6.

FoV / D_s	z_0	M	Δx (mm)	$f^{\#}$
1.02×0.77	105	0.23	0.9	4.0

Table 2.5: x-r FoV details

Region	$r/D_{s,\min}$: $r/D_{s,\max}$	$x/D_{s,\min}$: $x/D_{s,\max}$
B_1	-0.07 : 0.95	0.0 : 0.77
B_2	0.78 : 1.8	0.0 : 0.77
B_3	-0.07 : 0.95	0.66 : 1.43
B_4	0.78 : 1.8	0.66 : 1.43
B_5	-0.07 : 0.95	1.32 : 2.1
B_6	0.78 : 1.8	1.32 : 2.1
B_7	-0.07 : 0.95	1.99 : 2.76
B_8	0.78 : 1.8	1.99 : 2.76

Table 2.6: x-r plane FoV size and arrangement

To assess the suitability of the FoV arrangement in the $x-r$ plane shown in Figure 2.11 the level of SGF was quantified by comparing the ratio of measured, $\langle u'_{i,\text{meas}} \rangle$, to 'true', $\langle u'_{i,\text{true}} \rangle$, r.m.s velocities in both axial and radial directions for $\alpha_1 = 30°$. The true r.m.s values are based on Equation 2.13 and the required 'true' integral lengthscale was determined iteratively using Equation 2.14. Figure 2.12 indicates that within the region considered the majority of turbulent energy has been captured as $\langle u'_{x,\text{meas}} \rangle / \langle u'_{x,\text{true}} \rangle$ and $\langle u'_{r,\text{meas}} \rangle / \langle u'_{r,\text{true}} \rangle \geq 0.9$ almost everywhere. In the axial direction the level of SGF filtering is highest in the vicinity of the inner body of the swirler and the end wall of the expansion chamber. These regions are located at $x/D_s \approx 0.0$ and extend from $0 \leq r/D_s \leq 0.09$ and $0.5 \leq r/D_s \leq 1.8$ respectively. In the radial direction the level of SGF is largely unaffected in these regions and reaches a maximum in the vicinity of the outer wall of the expansion chamber at $r/D_s = 1.8$. In a physical sense these observations are due to the fact that as the wall is approached the size of the eddies normal to it diminish and the corresponding integral lengthscale becomes small in relation to the interrogation cell. The increased levels of SGF in these flow regions are thus not an unexpected result and as they are not of immediate concern to the objectives of this thesis no further FoV refinement was deemed necessary.

2.4.2 Radial-Circumferential Plane

To capture the complex flow dynamics arising in the near-field of the dump expansion chamber PIV measurements were performed at four $r-\theta$ planes located at $x/D_s = 0.02, 0.27, 0.53, 1.06$. An additional $r-\theta$ plane was captured at $x/D_s = 2.39$ as the flowfield is known to be dominated by a PVC in this region [13]. These measurement locations are indicated by the numbered radial lines shown in Figure 2.11. It was mentioned in Section 2.1.4 that in order to gain access to the $r-\theta$ plane the camera was mounted beneath the test rig. Although the ability to manoeuvre the camera was largely restricted by the base of the exhaust manifold and test facility floor, it was possible to capture two FoV sizes by using 105mm and 50mm focal length lenses, further details of which are provided in Table 2.7. This was important for ensuring that PIV parameters could

be fully optimised in the central core of solid body rotation where large gradients in tangential velocity exist. Although the Imager Intense CCD camera itself was too large, the lens could be positioned within the downstream blockage as illustrated in Figure 2.3. This allowed the entire swirler exit plane to be captured with an optimum magnification using a 105mm focal length lens and also a large extent of the dump expansion chamber using a 50mm focal length lens as shown in Figure 2.13. The inner radius of the downstream blockage of $r/D_s \approx 1.2$ imposes a limit on the maximum FoV size that can be captured in the $r-\theta$ plane without experiencing major optical distortion.

FoV / D_s	z_0 (mm)	M	Δx (mm)	$f^{\#}$
1.51×1.07	105	0.16	1.25	4.0
3.15×2.35	50	0.07	2.76	5.6

Table 2.7: $r-\theta$ FoV details

In principle it is possible to assess the level of SGF on $\langle u'_{r,\text{true}} \rangle$ and $\langle u'_{\theta,\text{true}} \rangle$ in the $r-\theta$ plane in a similar way to the $x-r$ plane as shown in Figure 2.12, however, in practice this is not straightforward. The reason for this is that the correction methodology detailed in Equations 2.13 and 2.14 requires the longitudinal and lateral, or alternatively the streamwise and cross-streamwise, integral lengthscales, ${}^{i}L_{ii}$ and ${}^{j}L_{jj}$. In the $x-r$ plane this is trivial as the longitudinal and lateral lengthscales, ${}^{x}L_{xx}$ and ${}^{r}L_{rr}$, are naturally orientated along the Cartesian grid lines that result from the discretisation of the PIV domain. In the $r-\theta$ plane longitudinal and lateral lengthscales, ${}^{\theta}L_{\theta\theta}$ and ${}^{r}L_{rr}$, are orientated along circumferential and radial directions respectively and naturally require a cylindrical-polar bases for both velocities and coordinates. Whilst the conversion from Cartesian to cylindrical-polar velocities is error free the conversion from the original Cartesian PIV coordinate system to a polar-cylindrical one is not so. This is due to the fact that the method used to determine integral lengthscales in this thesis, which is detailed in Section A-1.2.1, requires instantaneous velocity components at all points directed along constant coordinate lines. As points along lines of constant r or θ within a cylindrical-polar coordinate system are unlikely to exactly coincide with ones with the original Cartesian system a procedure such as interpolation is required. Clearly, such a process is unsuitable as it essentially introduces an additional level of SGF on the same order of magnitude as that trying to be determined, thus raising questions as to the validity of any corrected values. An additional complication arises due the fact the original Cartesian spatial resolution, ΔX, is essentially 'lost' in the coordinate conversion and, as discussed in the proceeding sections, it is precisely this which determines the level of SGF in the first place and Equations 2.13 and 2.14 would require modifications to account for this. As it is felt that these issues would introduce too many unknowns into the correction methodology the level of SFG in the $r-\theta$ plane was not assessed globally as in Figure 2.12 but

rather by comparing radial profiles of measured radial r.m.s velocity, $\langle u'_{r,\text{meas}} \rangle$, obtained from the $r-\theta$ plane with corrected, or 'true', radial r.m.s velocity, $\langle u'_{r,\text{true}} \rangle$, taken from corresponding axial locations in the $x-r$ plane. This comparison is made in Section 2.4.3.

2.4.3 Field of View Alignment

To assess further the quality of the experimental setup shown in Figure 2.12, radial profiles of mean and r.m.s velocities were compared across adjacent FoVs in the $x-r$ plane at axial locations of $x/D_s = 0.27$, 0.53 and 1.06 for $\alpha_1 = 30°$. These particular axial locations were chosen as they coincide with the $r-\theta$ measurement planes shown in Figure 2.12. As $\langle u_r \rangle$ and $\langle u'_r \rangle$ are common to both $x-r$ and $r-\theta$ measurement planes further assessments could be made regarding the consistency of the experimental setup and the level of SGF in the $r-\theta$ plane as discussed in Section 2.4.2.

Figure 2.14 shows a very good overall agreement in both $\langle u_x \rangle$ and $\langle u'_x \rangle$ within the FoV overlap region which extends from $x/D_s \approx 0.8-1.0$ as shown in Figure 2.14(a). There is however a slight trend apparent in $\langle u_x \rangle$ whereby the left hand FoV (Regions B_1 at $x/D_s = 0.27$ and 0.53 and B_3 at $x/D_s = 1.06$) is marginally higher than the right hand FoV (Region B_2 at $x/D_s = 0.27$ and 0.53 and Region B_4 at $x/D_s = 0.27$ and 0.53). In Figure 2.15 the overall agreement of $\langle u_r \rangle$ in the $x-r$ plane across adjacent FoVs is reasonably good apart from at $x/D_s = 0.27$ where considerable discrepancies exist. Within this region the opposite to the trend noted in $\langle u_x \rangle$ occurs as $\langle u_r \rangle$ measured in the left hand FoV is lower than that in the right hand FoV. This is also the case at $x/D_s = 0.53$ and 1.06 although much less pronounced. The radial r.m.s velocity does not seem to suffer in the same way, exhibiting excellent agreement across the interface region.

As should be expected, $\langle u_r \rangle$ from both $x-r$ and $r-\theta$ measurement planes exhibits similar trends, however, the magnitude and position of the peak value differs notably at $x/D_s = 0.27$ and 0.53. At the furthest downstream location considered, $x/D_s = 1.06$, these discrepancies lessen to the extent that data from all FoVs and measurement planes collapse to form a more or less constant radial profile. Comparisons made between $\langle u'_r \rangle$ obtained from $x-r$ and $r-\theta$ measurement planes yield observations that are consistent with the discussions regarding SGF presented throughout this chapter. It can be seen that measured data using a 105mm focal length lens are at least equal to, or greater than, that obtained using a 50mm focal length lens and both are lower than $x-r$ plane measurements. The reason for this is due to the level of magnification (spatial resolution) at each measurement location, which is detailed in Tables 2.5 and 2.7. In the $x-r$ plane it was possible to achieve a higher level of spatial resolution and therefore recover a greater portion of the turbulent kinetic energy than in the $r-\theta$ plane and this is clearly reflected in Figure 2.15. It was shown in Figure 2.12 that in the $x-r$ plane $\langle u'_{r,\text{meas}} \rangle / \langle u'_{r,\text{true}} \rangle \geq 0.9$ across the majority of the measurement domain. As $x-r$ plane r.m.s

velocities presented in Figures 2.14 and 2.15 are corrected or 'true' values the level of SGF in the uncorrected (the reasons for this were given in Section 2.4.2) $r-\theta$ plane is not too severe as peak values are under-predicted by a maximum of approximately 10%. This illustrates that SGF is a second-order statistical error and a sufficient resolution has been adopted for first-order statistics.

Many of the differences discussed above regarding inconsistencies across adjacent FoVs and principle measurement planes can be attributed to perspective projection error which is a function of the camera viewing angle and the magnitude of the out-of-plane velocity component. The aim of the 2C-PIV setup used during this thesis is to recover the true in-plane velocity components, i.e. those parallel to the laser light sheet. This, however, is only realised in the case of truly 2D flows which are rarely found in engineering applications. If out-of-plane motions are present, Figure 2.16 shows that the measured displacement, $x_2 - x_1$, does not represent the 'true' real-world in-plane particle displacement, $X_2' - X_1$, but rather is some factor, Δx, either higher or lower than the actual value. The direction of the out-of-plane motion, which appears to move away from the camera is consistent with test conditions and the FoV arrangement used during this thesis. From Figure 2.16 it can be seen that Δx is completely defined by the magnitude and direction of the out-of-plane velocity component and the angle subtended by the particle position to the axis of the recording device, α, which will be referred to simply as the viewing angle. Raffel et al. [76] provide geometric expressions which relate the measured displacement and the true real-world in-plane particle displacement to the camera viewing angle and the out-of-plane particle displacement. Using the notation adopted in Figure 2.16 these are given as:

$$\begin{aligned} x_2 - x_1 &= -M\left[\left(X_2' - X_1\right) + \Delta z \tan\alpha\right] \\ y_2 - y_1 &= -M\left[\left(Y_2' - Y_1\right) + \Delta z \tan\beta\right] \end{aligned} \tag{2.15}$$

The second line of Equation 2.15 describes the effect of perspective projection on displacements orthogonal (i.e. out of the page) to that shown in Figure 2.16. If Equation 2.15 is divided through by Δt the following expressions are derived:

$$\begin{aligned} u_{i,\text{true}} &= u_{i,\text{meas}} - u_k \tan\alpha \\ u_{j,\text{true}} &= u_{i,\text{meas}} - u_k \tan\beta \end{aligned} \tag{2.16}$$

where $u_{i,\text{true}}$ and $u_{j,\text{true}}$ are the actual real-world in-plane velocities, $u_{i,\text{meas}}$ and $u_{j,\text{meas}}$ are the measured velocities which are contaminated by perspective projection error, u_k is the out-of-plane velocity component and α and β are the camera viewing angles. For a more concise description, the notation ϵ_i and ϵ_j is used to refer to the terms $u_k \tan\alpha$ and $u_k \tan\beta$. Although the above

discussion relates to perspective projection error on the in-plane Cartesian velocity components it is also possible to derive expressions which relate these to radial and tangential components as follows:

$$\begin{bmatrix} \epsilon_r \\ \epsilon_\theta \end{bmatrix} = \begin{bmatrix} \cos\theta & \sin\theta \\ -\sin\theta & \cos\theta \end{bmatrix} \begin{bmatrix} \epsilon_i \\ \epsilon_j \end{bmatrix} \tag{2.17}$$

To illustrate the effect of perspective projection error, Figure 2.17 shows ϵ_i, ϵ_j, ϵ_r and ϵ_θ for $Z_0 = 0.5$m, $u_k = 1$m/s (assumed to be uniform within the FoV) and a FoV of $y/D_s = z/D_s = 1$ which is fairly typical of test conditions. As would be expected, the perspective projection error based on Cartesian velocity components, ϵ_i and ϵ_j, increases towards the edge of the FoV with signs dependent on α and β respectively. It is interesting to note that whilst ϵ_r increases radially outwards, ϵ_θ is negligible everywhere suggesting that $u_{\theta,\text{meas}} = u_{\theta,\text{true}}$. From Equation 2.16, it is possible to recover $u_{i,\text{true}}$ and $u_{j,\text{true}}$ if u_k is known. In the 2C-PIV setup used during this thesis it is not possible to do this on an instantaneous basis as u_k remains unknown. However, if Equation 2.16 is applied to time-mean data, $\langle u_\theta \rangle$ from the $r-\theta$ plane can be used to obtain $\langle u_x \rangle_{\text{true}}$ and $\langle u_r \rangle_{\text{true}}$ from the $x-r$ plane. Furthermore, $\langle u_x \rangle_{\text{true}}$ can then be used to obtain $\langle u_r \rangle_{\text{true}}$ in the $r-\theta$ plane. From Figures 2.14 and 2.15 the largest discrepancies between adjacent FoVs and principle measurement planes were present in $\langle u_r \rangle$ at $x/D_s = 0.27$ and $x/D_s = 0.53$. After application of Equation 2.16 at these locations, Figure 2.18 shows that the agreement of the peak magnitude obtained from $x-r$ and $r-\theta$ planes and also values across adjacent FoVs in the $x-r$ plane is markedly improved. At $x/D_s = 0.53$ some discrepancies still persist, however, these can be partly attributed the experimental set-up. For example at $r/D_s = 0.0$, which coincides with the geometric centre of the dump expansion chamber, $\langle u_r \rangle$ should be zero such as at $x/D_s = 0.27$ and 1.06 in Figure 2.15. Whilst extreme care was taken to align the laser light sheet correctly, large tangential velocity gradients exist in the central core of solid body rotation and even very small positional errors can result in non-zero mean radial centreline velocities.

Figure 2.19 shows PDFs of instantaneous and fluctuating radial velocity from Regions B_1 and B_2 within the FoV overlap region at $x/D_s = 0.27$, $r/D_s = 0.9$. Although the shape of instantaneous PDFs (Figure 2.19(a)) are extremely similar they are shifted with respect to each other along the horizontal axis and centred about different mean values. This is consistent with Figure 2.15(a) which shows $\langle u_r \rangle$ in Region B_2 exceeds $\langle u_r \rangle$ in Region B_1 from $r/D_s \approx 0.8-1$ and is due to the fact that instantaneous velocities (and thus the resulting time-mean value) in each region will be either higher or lower than actual 'true' values depending on the camera viewing angle and direction and magnitude of u_k (Equation 2.15). Despite this shift, the good agreement of PDFs in Figure 2.19(b) suggests that the effect on instantaneous fluctuations (and thus the resulting r.m.s value) about the mean is negligible. This is consistent with evidence from Figures

2.14(b), (d) and (f) and 2.15(b), (d) and (f) in which $\langle u'_x \rangle$ and $\langle u'_r \rangle$ were in excellent agreement across adjacent FoVs. These observations explain why perspective projection appears only as a first-order biasing error.

Overall, it is felt that the agreement of mean and r.m.s velocities and minimal scatter across adjacent FoVs and between principle measurement planes suggests that a high degree of confidence can be placed in the consistency and repeatability of the experimental setup used here.

2.4.4 Statistical Convergence

As described in the preceding sections, it is possible to minimise errors associated with the PIV technique by careful selection and refinement of the experimental setup but this alone does not guarantee the acquisition of accurate and meaningful data. In common with point based measurement techniques, such as HWA or LDA, the effect of sample size on computed PIV statistics must be considered. It is well known that statistical quantities, such as mean and r.m.s velocities, are dependent on the number of statistically independent samples, N_{I}, and convergence is obtained given this is sufficiently large as long as the flow is statistically stationary. The likelihood that a particular sample is statistically independent is increased if the associated integral timescale, T_{ij}, (Equation A-17) is small compared to the sampling interval, ΔT. Midgley [13] has shown $T_{ij,max} \approx 60$ms for flows similar to those studied in this thesis which is approximately a factor of 4 smaller than the sampling interval of $\Delta T = 0.25$s. An increased confidence can therefore be placed on a given sample at any point within the flow being statistically independent.

Convergence of statistical quantities can be observed by plotting computed values against N_{I}. This, however, is only partly useful since, although convergence may be obtained in the limit of N_{I}, the result is only an estimate of the population, or 'true', parameter. If it is assumed that estimated values follow a normal distribution their reliability can be assessed using confidence intervals which produce a range of values likely to include a given population parameter. This requires the selection of a confidence level which specifies the proportion of estimates based on N_{I} likely to include the population parameter within the calculated confidence interval. Confidence intervals for mean and r.m.s quantities are gives as [87]:

$$\epsilon_{u,i} = \pm z\sigma\sqrt{\frac{1}{N_{\mathrm{I}}}} \tag{2.18}$$

$$\epsilon_{u',i} = \pm z\sigma\sqrt{\frac{1}{2N_{\mathrm{I}}}} \tag{2.19}$$

In practice a 95% or 99 % confidence level is commonly used which correspond to $z = 1.96$

and $z = 2.576$ respectively. The value of σ is by definition the population standard deviation which is usually unknown and in its absence is replaced by an estimation calculated from the finite sample. To demonstrate convergence of mean and r.m.s velocities, time-series acquired at $x/D_s = 0.02$, $r/D_s = 0.4$ and $x/D_s = 1.06$, $r/D_s = 0.0$ for $\alpha_1 = 30°$ were divided up into subsets consisting of 5, 10, 25, 50, 130 and 650 [2] independent samples and plotted against confidence intervals described in Equations 2.18 and 2.19 for confidence levels of 95% ($z = 1.96$) and 99% ($z = 2.576$). The results of this are shown in Figures 2.20 and 2.21 where $\langle u_i \rangle_{\mathrm{N}}$ and $\langle u_i' \rangle_{\mathrm{N}}$ are mean and r.m.s velocities based on the the number of members of the subset, whilst $\langle u_i \rangle_{\mathrm{P}}$ and $\langle u_i' \rangle_{\mathrm{P}}$ are the estimated population parameters based on 650 independent samples detailed below in Table 2.8.

x/D_s	r/D_s	$\langle u_x \rangle / U_{x,s}$	$\langle u_r \rangle / U_{x,s}$	$\langle u_\theta \rangle / U_{x,s}$	$\langle u_x' \rangle / U_{x,s}$	$\langle u_r' \rangle / U_{x,s}$	$\langle u_\theta' \rangle / U_{x,s}$
0.02	0.4	1.43	0.21	1.43	0.32	0.36	0.36
1.06	0.0	-0.1	-0.03	0.08	0.22	0.37	0.4

Table 2.8: Mean and r.m.s velocities at selected locations for $\alpha_1 = 30°$, $N_{\mathrm{I}} = 650$

At both locations considered, mean and r.m.s velocities are observed to converge within the specified confidence intervals as N_{I} is increased.

2.4.5 Measurement Accuracy

Throughout the preceding sections of this thesis a number of sources of experimental error that affect the accuracy of PIV measurements have been identified. These include pixel displacement uncertainties (Section 2.3.2.3), SGF (Section 2.3.4), perspective projection (Section 2.4.3) and statistical convergence (Section 2.4.4). Of these, SGF and perspective projection are essentially bias errors that can be accounted for after data acquisition and, in the case of the former, minimised through FoV refinement. SGF affects second-order statistics and is most severe in regions in which ${}^{k}L_{ij} < \Delta X$. In contrast, perspective projection error affects first-order statistics and is dependent on both the magnitude and direction of the out-of-plane velocity component and the camera viewing angle.

Throughout this thesis it has been customary to refer to statistical quantities in which bias errors have been accounted for as 'true' values. In reality, these remain estimates of unknown actual values and in order to quantify the accuracy of these, a number of factors must be considered. As it is only possible to determine instantaneous pixel displacements to within ± 0.1 pixels a degree of uncertainty always persists which can be expressed as:

$$\epsilon_{ds} = \pm 0.1 d_r \Delta t / M \tag{2.20}$$

[2] It has been shown previously by Midgley [13] that 650 independent samples yield sufficient accuracy for flows similar to those studied in this thesis.

where d_r is the pixel width. As ϵ_{ds} is a random error, the ensemble average should approach zero as $N_{\mathrm{I}} \rightarrow \infty$ and therefore the effect on time-mean statistics is negligible. This, however, is not the case for r.m.s quantities and the influence of ϵ_{ds} on this statistic must be accounted for. Figures 2.22(a) and (b) show $\epsilon_{u,i}/U_{x,s}$ (Equation 2.18) for $\langle u_x \rangle$ and $\langle u_r \rangle$ for all FoVs in the $x-r$ measurement plane based on a confidence level of 99% ($z = 2.576$) and $N_{\mathrm{I}} = 650$ for $\alpha_1 = 30°$. In the swirl stream $\epsilon_{u,i}/U_{x,s} \approx \pm 0.03 - 0.07$, whilst in the vicinity of the centreline $\epsilon_{u,i}/U_{x,s} \approx \pm 0.01 - 0.03$ and elsewhere $\epsilon_{u,i}/U_{x,s} \approx \pm 0.01$. In order to quantify the effect of ϵ_{ds} on the accuracy of r.m.s velocities it has been combined with $\epsilon_{u',i}$ (Equation 2.19) in a Pythagorean manner to arrive at a 'total' relative error, $\epsilon_{u',i,\mathrm{tot}}$:

$$\frac{\epsilon_{u',i,\mathrm{tot}}}{U_{x,s}} = \sqrt{\left(\frac{\epsilon_{u',i}}{U_{x,s}}\right)^2 + \left(\frac{\epsilon_{ds}}{U_{x,s}}\right)^2} \tag{2.21}$$

Figures 2.22(c) and (d) show $\epsilon_{u',i,\mathrm{tot}}/U_{x,s}$ for $\langle u'_x \rangle$ and $\langle u'_r \rangle$ for all FoV in the $x-r$ measurement plane based on a confidence level of 99% ($z = 2.576$) and $N_{\mathrm{I}} = 650$. It should be noted that the jumps in contour level observed in Figures 2.22(c) and (d) are a result of the varying Δt used in each FoV to optimise particle image displacement. In the swirl stream $\epsilon_{u,i,\mathrm{tot}}/U_{x,s} \approx \pm 0.03 - 0.06$, whilst in the vicinity of the centreline $\epsilon_{u,i,\mathrm{tot}}/U_{x,s} \approx \pm 0.01 - 0.03$ and elsewhere $\epsilon_{u,i,\mathrm{tot}}/U_{x,s} \approx \pm 0.01 - 0.02$.

The above comments regarding the accuracy of mean and r.m.s velocity estimates are perhaps rather pessimistic and should be treated as a worst case scenario. Strong evidence has already been presented in Figures 2.14 and 2.15 to suggest a high degree of consistency and repeatability with minimal data scatter in overlapping regions between adjacent FoVs in the $x-r$ plane and at locations at which $x-r$ and $r-\theta$ planes coincide with discrepancies attributed to biasing errors such as SGF and perspective projection. It is possible that the convergence of first and second-order statistics is aided by the inherent spatial averaging of the PIV technique. As cross-correlation algorithms determine the modal displacement of groups of particles within individual interrogation cells, it is less likely that extreme values are present in ensemble data. Furthermore, each instantaneous measurement is then validated using a range of methods to ensure that spurious data points are unable to contaminate derived statistics.

2.4.6 Summary of PIV Operating Parameters

Throughout the preceding sections of this chapter numerous statements have been made regarding the user-defined PIV processing parameters available within the DaVis 7 [81] software used during this thesis. For clarity these are presented below in Table 2.9.

Parameter	**Setting**
Processing	
Adaptive multi-pass Grids	Yes
Initial cell size [pixels]	64
Final cell size [number of iterations]	32 [2]
Cell overlap	50%
Validation	
Remove vectors with Q-ratio	<1.5
Remove vectors outside range	$> 2\sigma$
Replace removed vectors	With 2^{nd}, 3^{rd} or 4^{th} choice peaks or interpolated data where no peak fits surrounding fluid dynamic behaviour.

Table 2.9: Optimised PIV operating parameters

2.5 Closure

During this chapter an overview of the water facility has been given, particularly in regard to the operating ranges necessary for ensuring the accuracy and repeatability of flow measurements. A comprehensive overview of the PIV technique has been given, including its main sources of error and how these can be minimised through refinement of user-defined parameters and the experimental setup during the image acquisition stage. It was emphasised that in all but the most ideal scenarios it is unlikely that every theoretical ideal is achievable in the experimental setup and as a result various errors, such as those caused by SGF, may persist. In such cases it is possible to account for these errors through various post-processing operations. The final experimental setup and user-defined parameters adopted in this thesis have been shown to be capable of capturing the majority of turbulent kinetic energy in both principle measurement planes with only minimal levels SGF. The consistency of data within the overlap region of adjacent FoVs and between measurement planes is good and discrepancies are attributed to perspective projection error which are a function of viewing angle and the magnitude of the out-of-plane velocity component. A methodology has been developed to account for this which utilises time-mean data from both principle measurement planes to quantify the effect of out-of-plane motion on recorded in-plane velocities. Measured first and second order statistics have been shown to converge within theoretical confidence intervals for a given number of independent samples. This allows the level of precision of the measured quantities to be defined and thus facilitate the validation of computational predictions presented in Chapters 5 and 6.

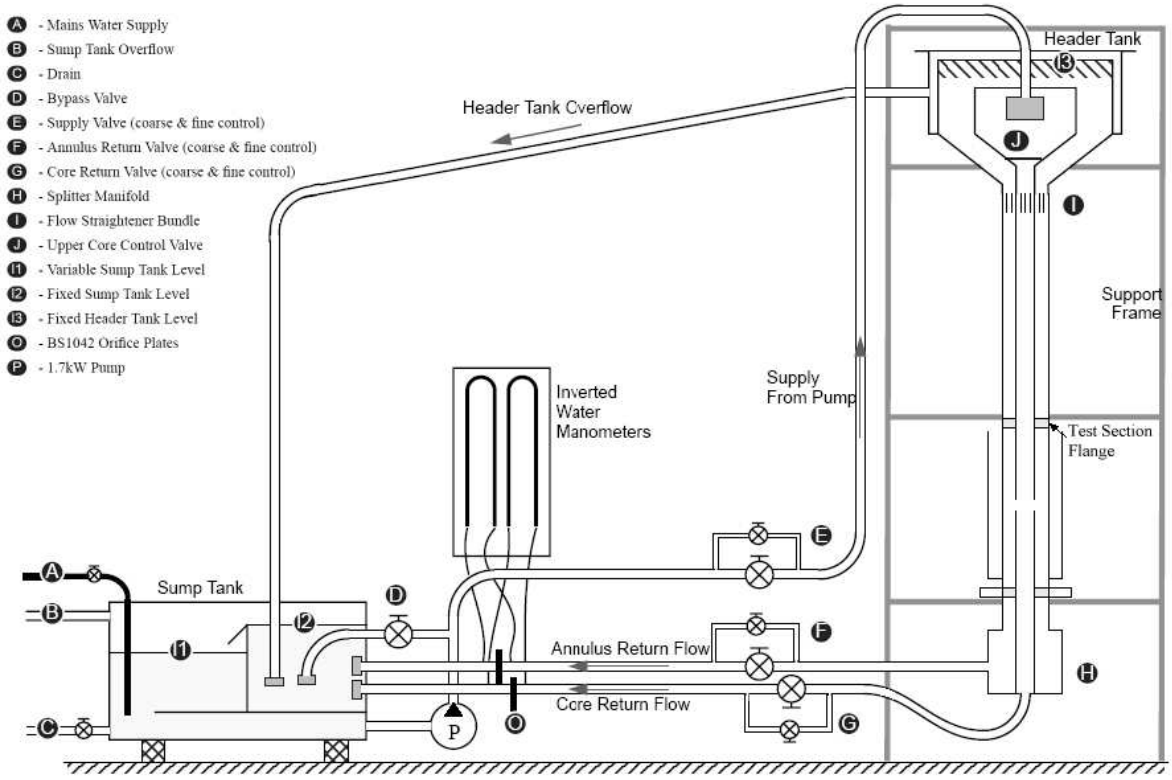

Figure 2.1: Schematic of vertical water facility [71]

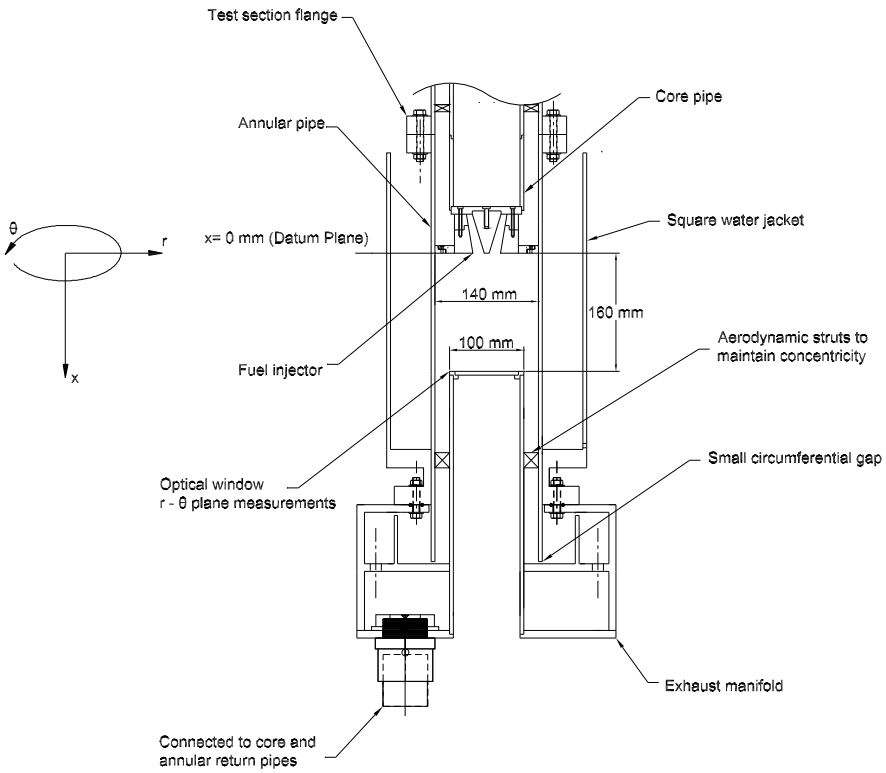

Figure 2.2: Schematic of test section [13]

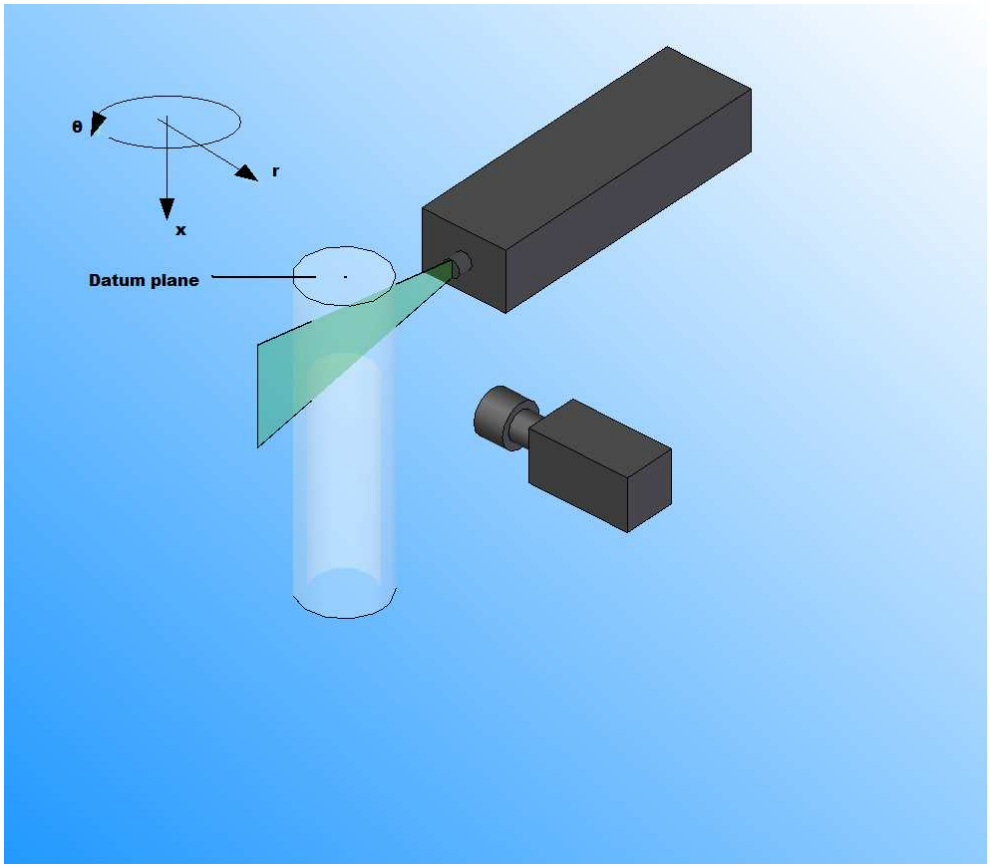

(a) $x - r$ plane

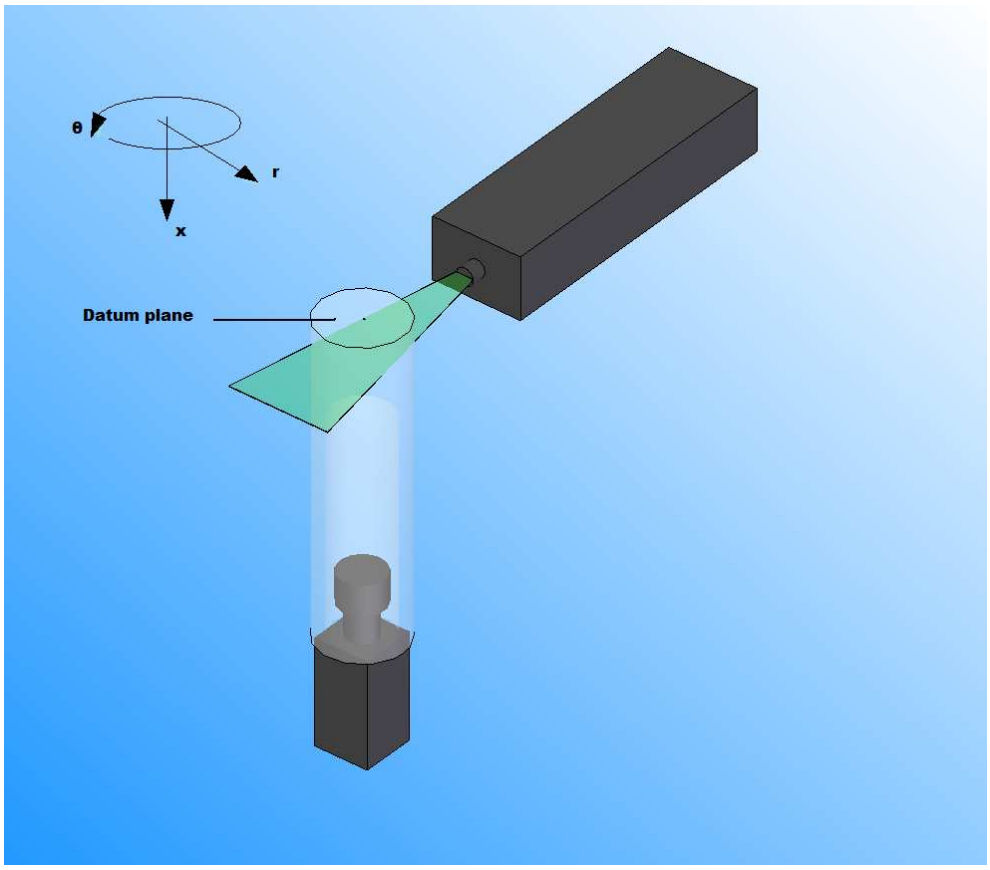

(b) $r - \theta$ plane

Figure 2.3: Component arrangement in principle measurement planes

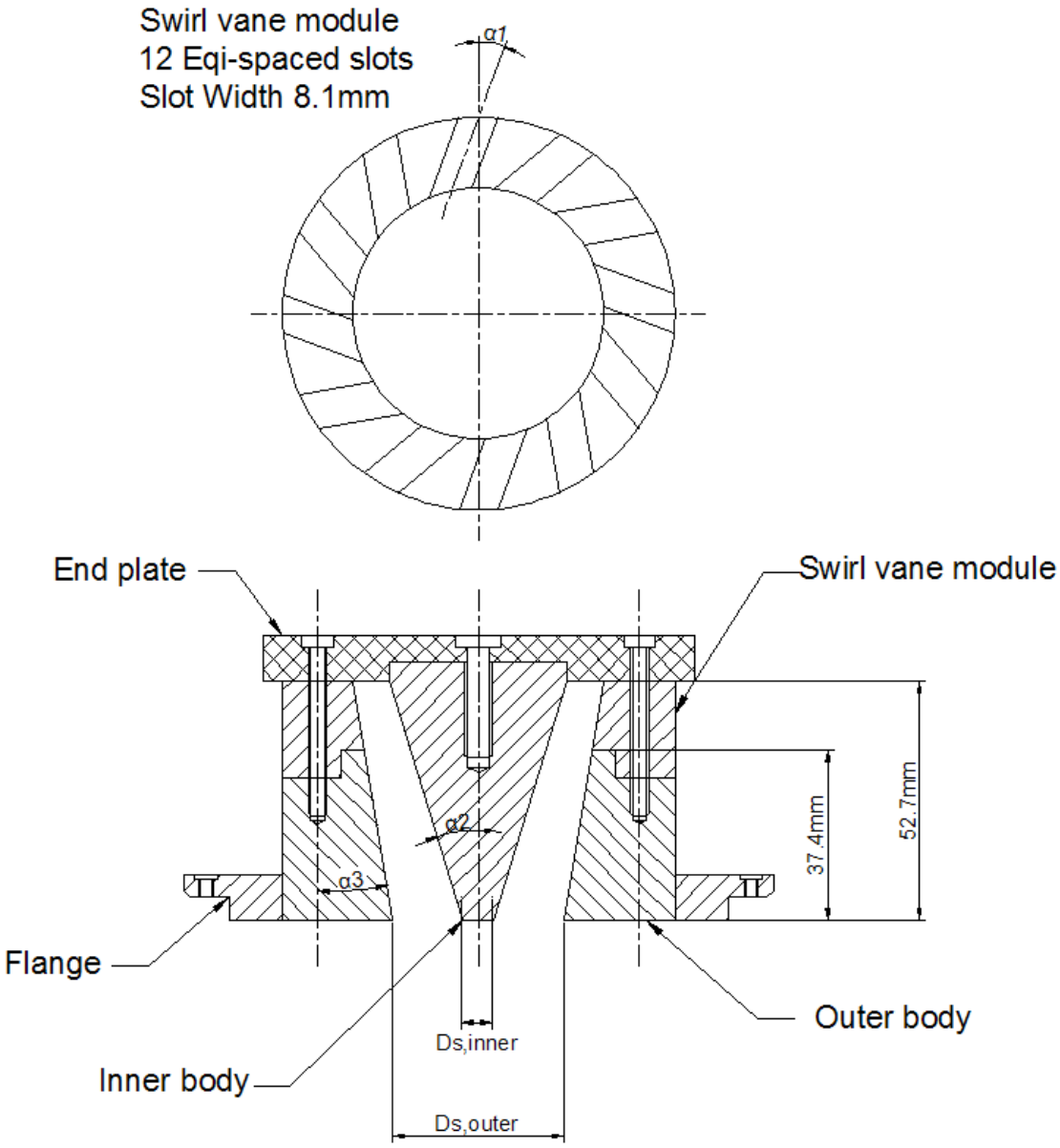

Figure 2.4: Exploded view of modular swirler [13]

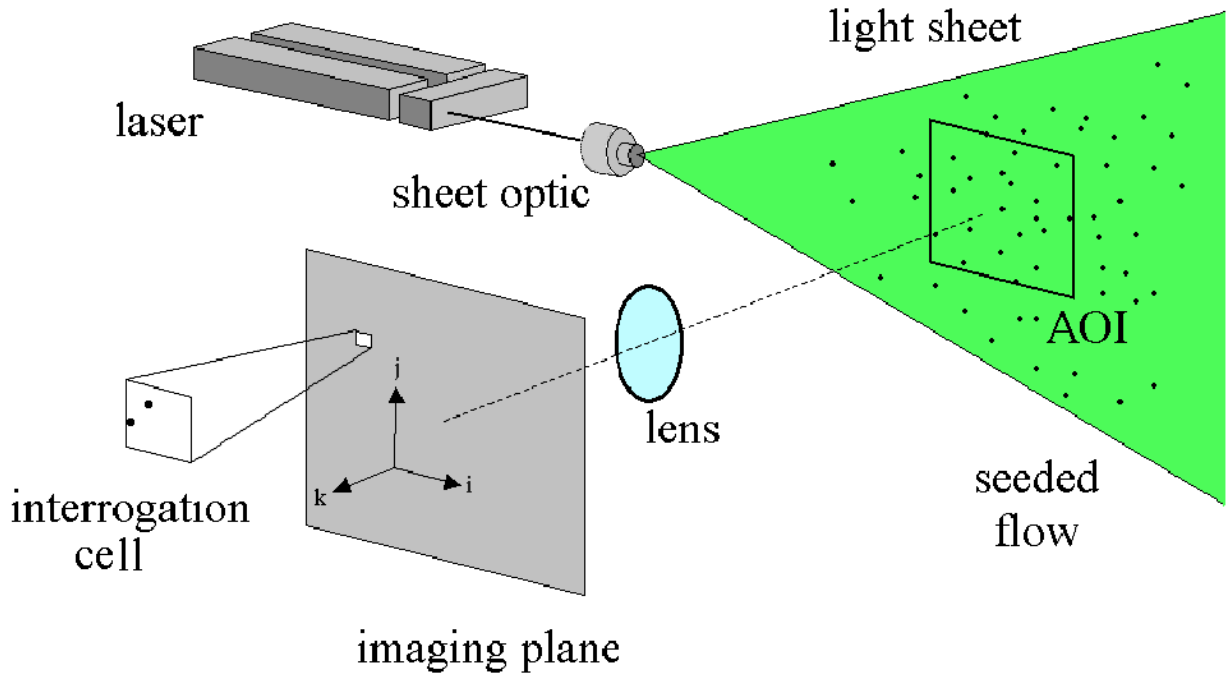

Figure 2.5: Typical arrangement of a 2C PIV experiment [81]

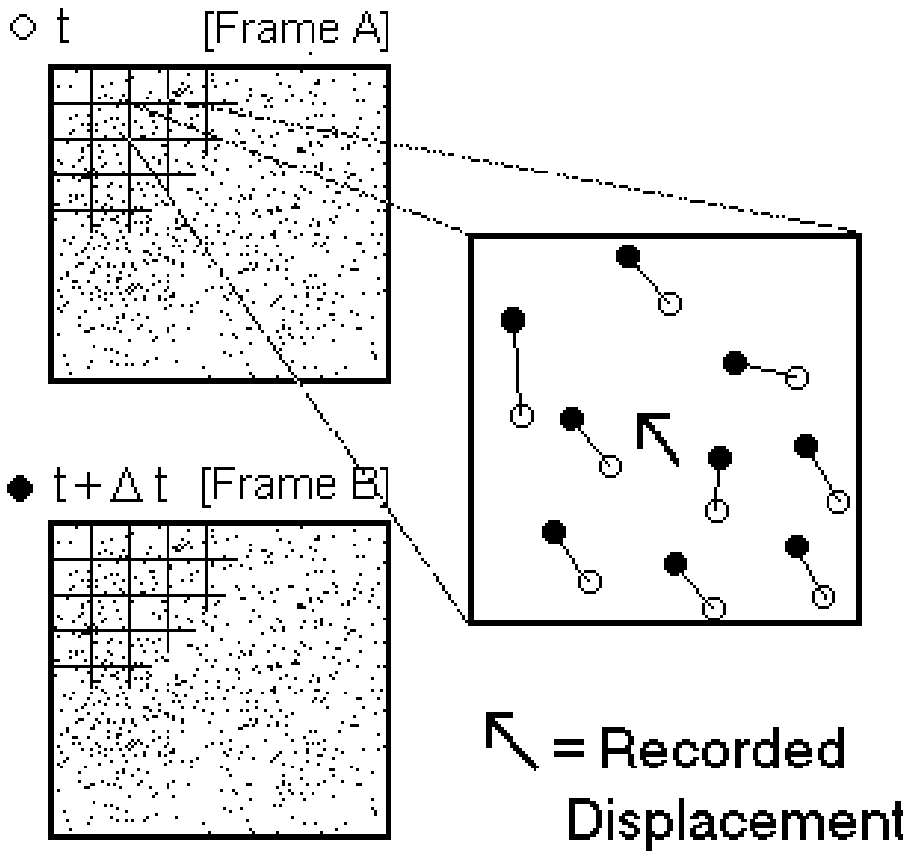

Figure 2.6: Image discretisation and individual cell illustration [72]

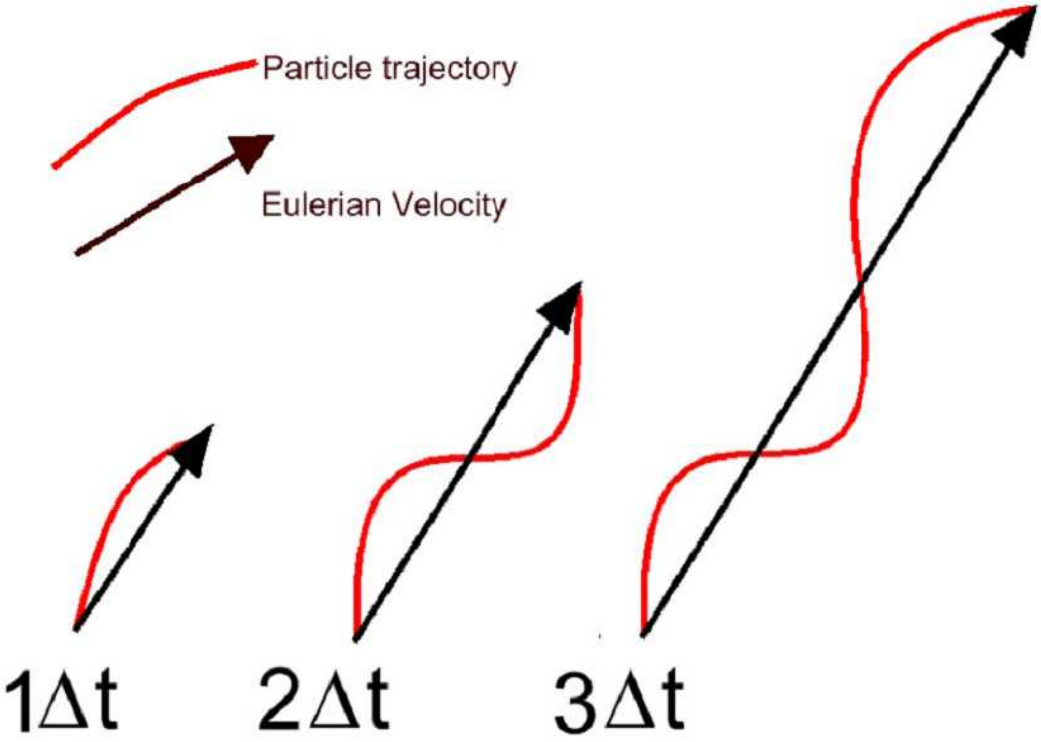

Figure 2.7: Effect of inter-frame time on dynamic averaging [13]

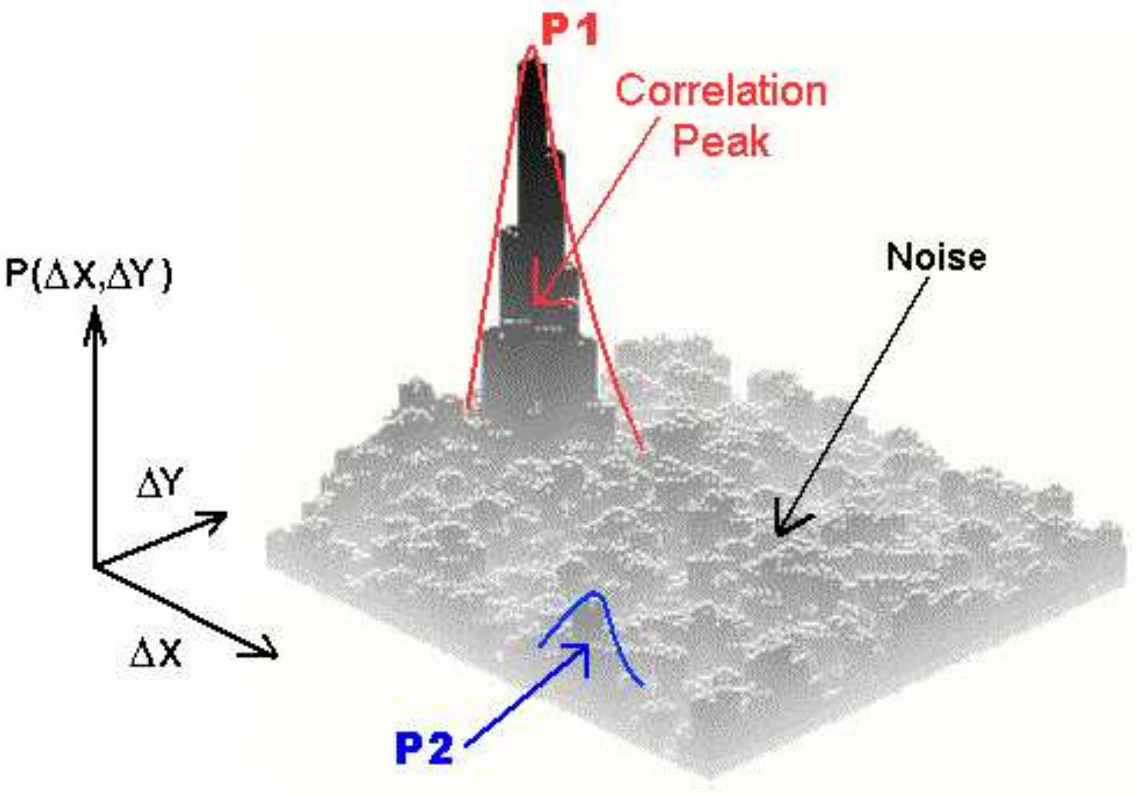

Figure 2.8: 3D visualisation of correlation map intensities [72]

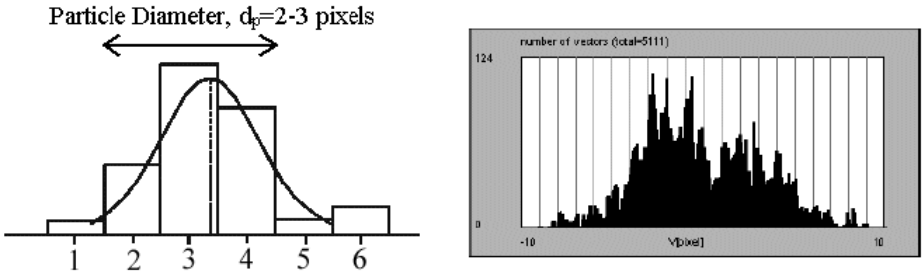

A particle image size of 2-3pixel guarantees only a slight bias to integral values in PIV evaluation.

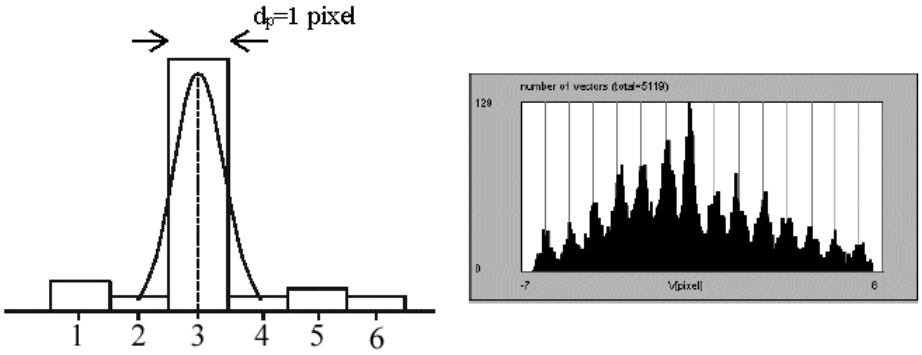

A particle image size smaller than 1pixel causes strong bias to integral values in the evaluation.

Figure 2.9: Examples of no peak locking (top) and strong peak locking (bottom) [72]

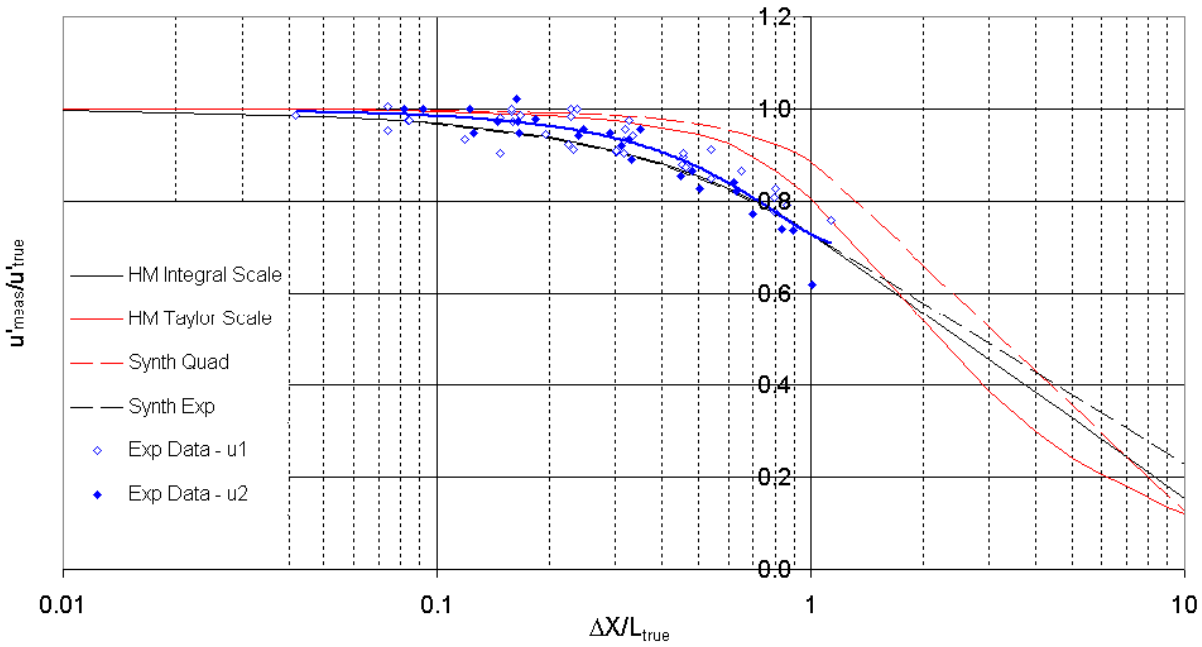

(a) $\langle u'_{i,\mathrm{meas}} \rangle / \langle u'_{i,\mathrm{true}} \rangle$

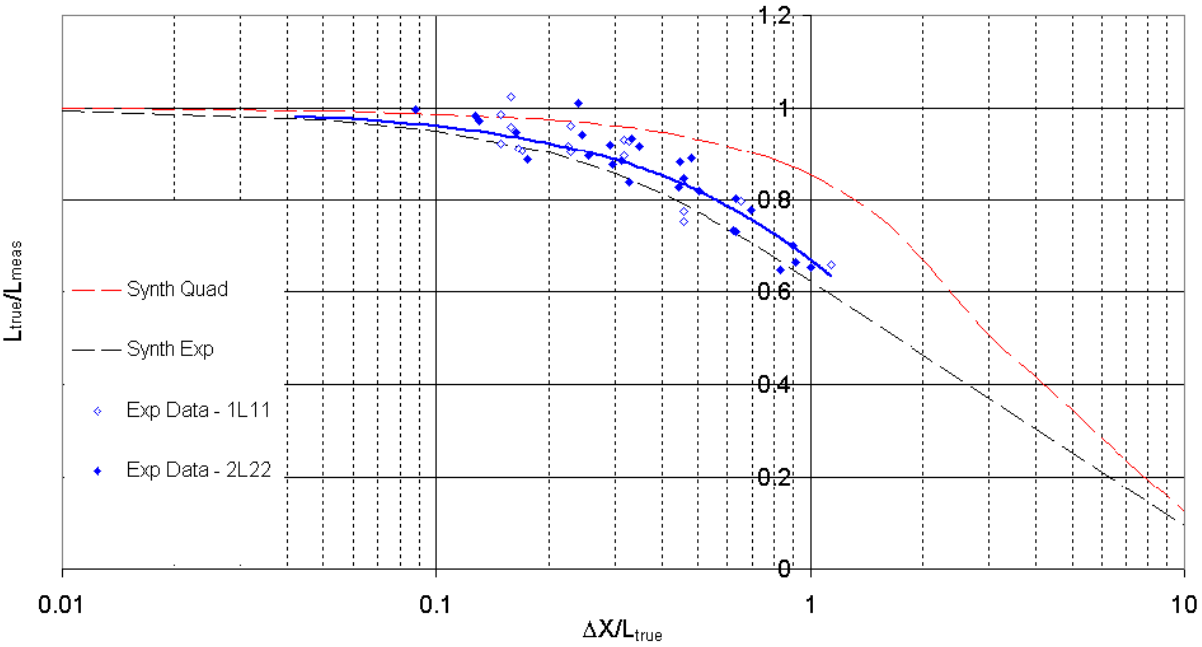

(b) $L_{\mathrm{meas}} / L_{\mathrm{true}}$

Figure 2.10: Theoretical [84] and measured (2C-PIV) [72] effect of sub-grid filtering on r.m.s quantities and integral lengthscales

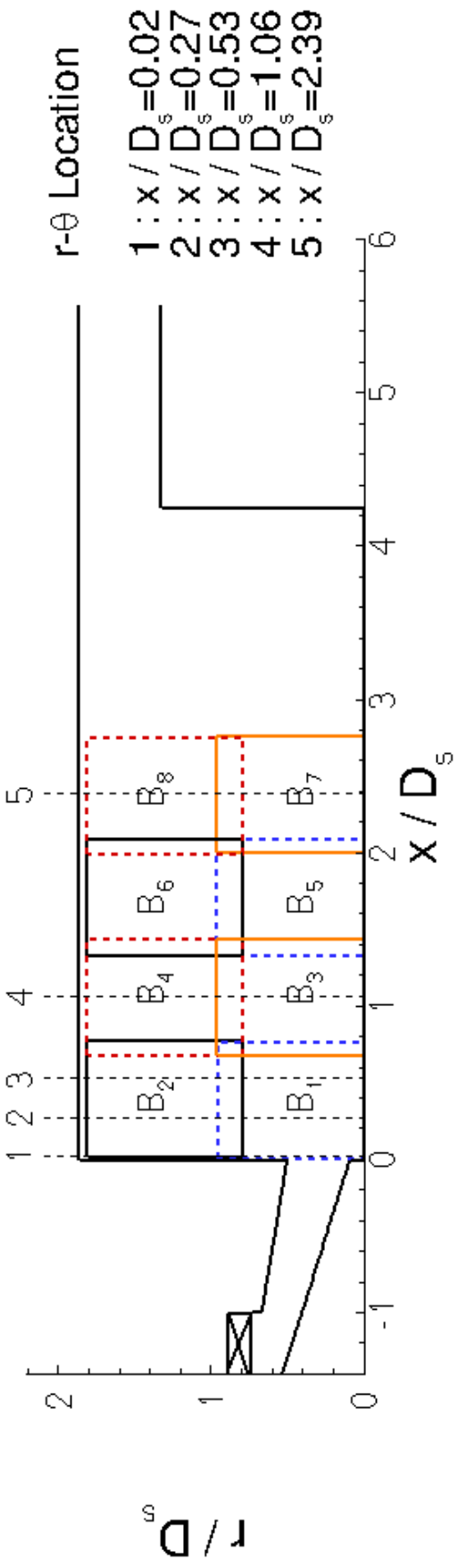

Figure 2.11: $x - r$ plane 40mm×30mm FoV arrangement

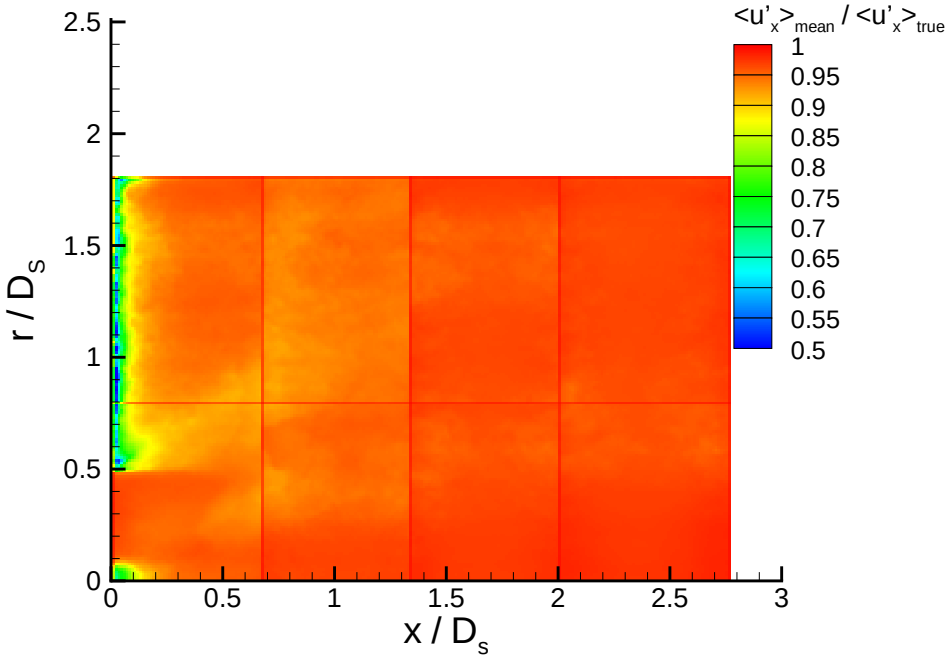

(a) $\langle u'_{x,\text{meas}} \rangle / \langle u'_{x,\text{true}} \rangle$

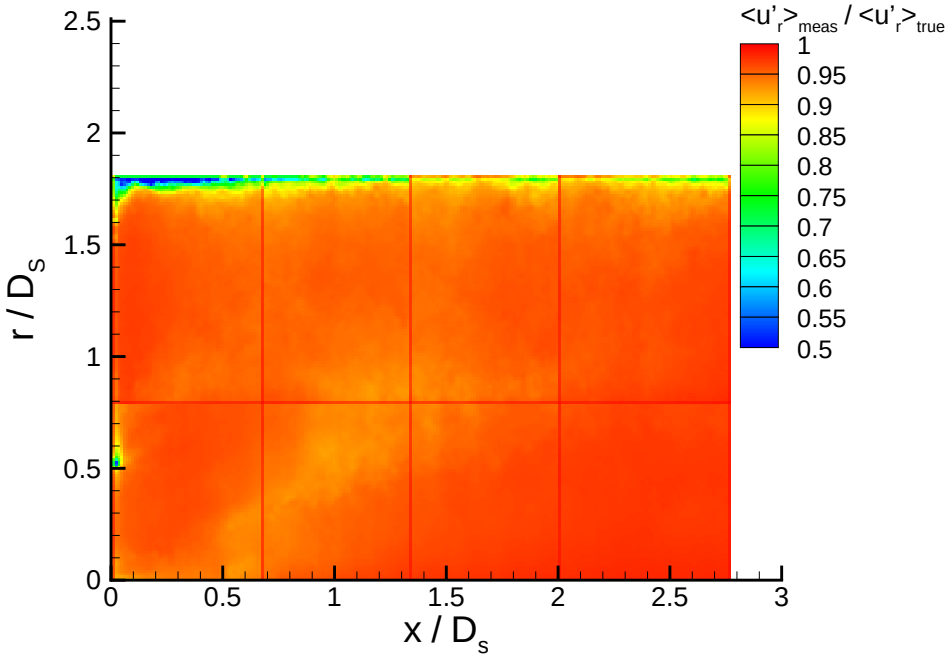

(b) $\langle u'_{r,\text{meas}} \rangle / \langle u'_{r,\text{true}} \rangle$

Figure 2.12: Ratio of measured to true axial and radial r.m.s velocities in $x-r$ plane for $\alpha_1 = 30°$

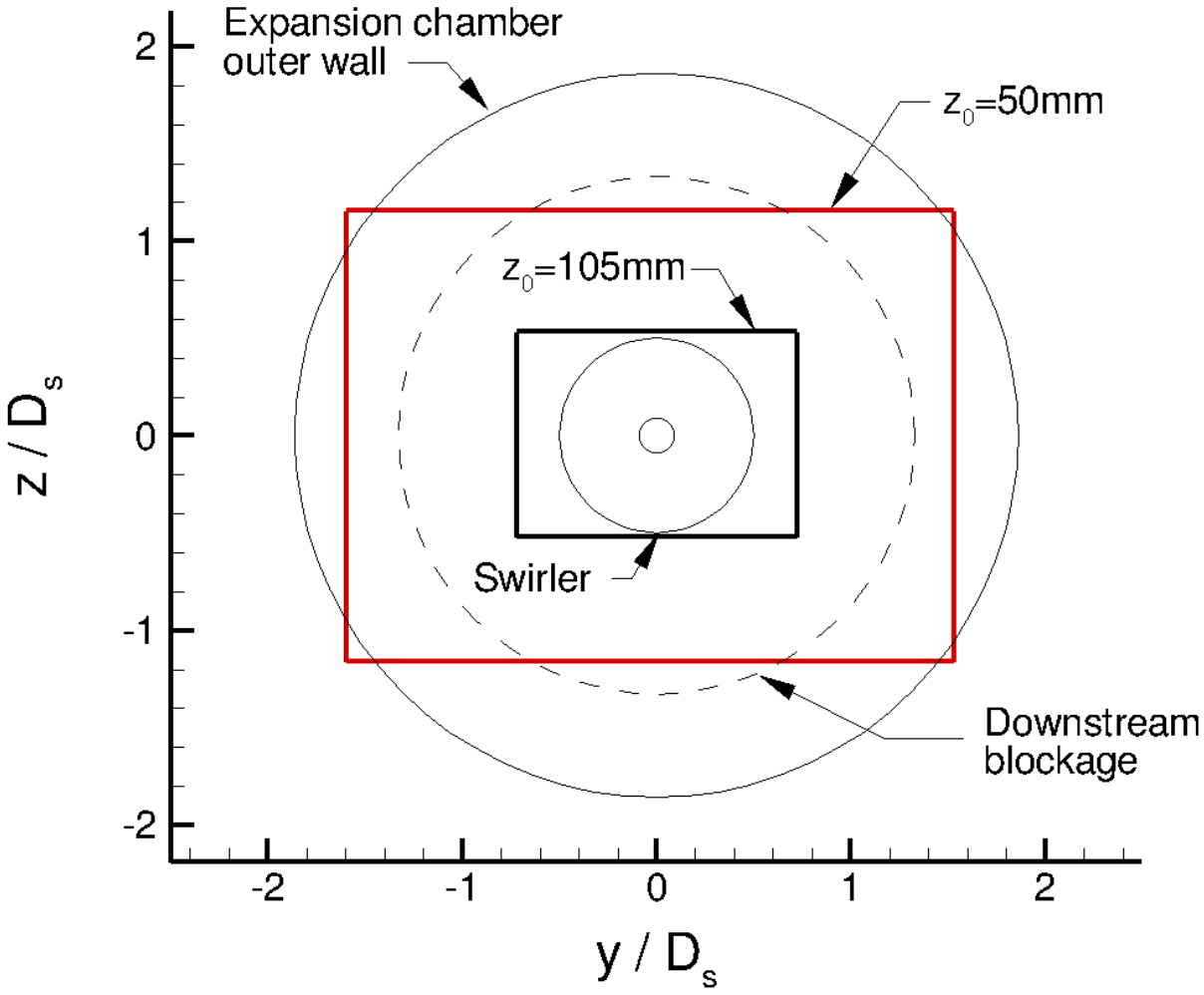

Figure 2.13: $r - \theta$ plane FoV arrangement

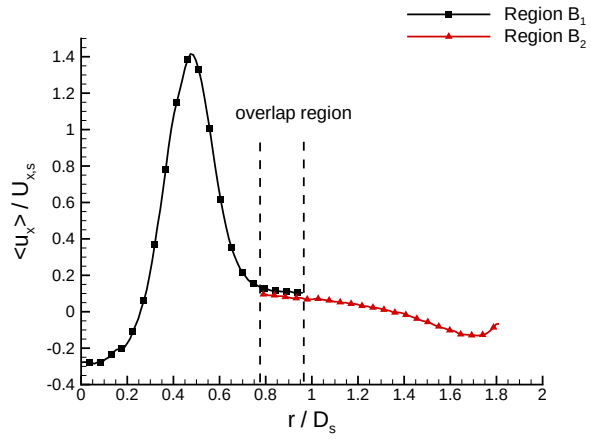

(a) Mean axial velocity $x/D_s = 0.27$

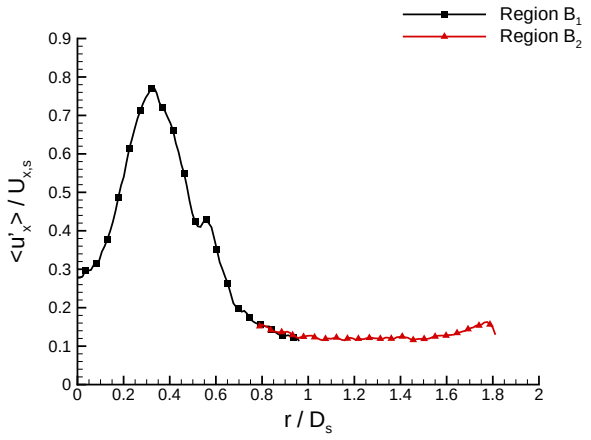

(b) r.m.s axial velocity $x/D_s = 0.27$

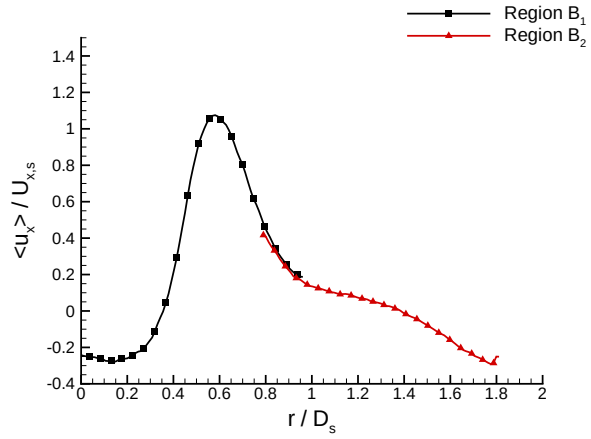

(c) Mean axial velocity $x/D_s = 0.53$

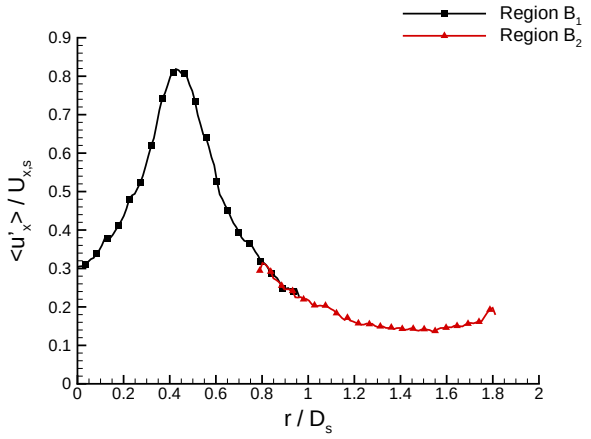

(d) r.m.s axial velocity $x/D_s = 0.53$

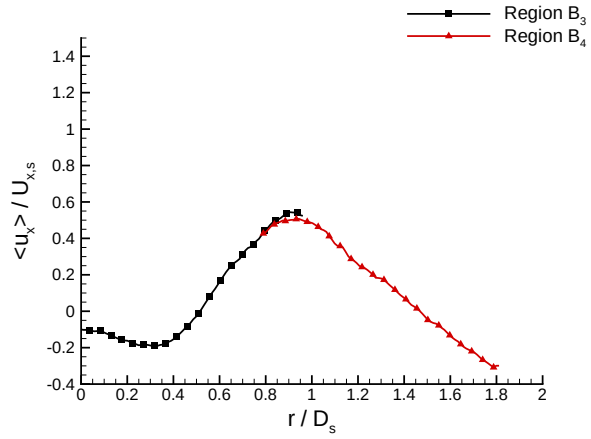

(e) Mean axial velocity $x/D_s = 1.06$

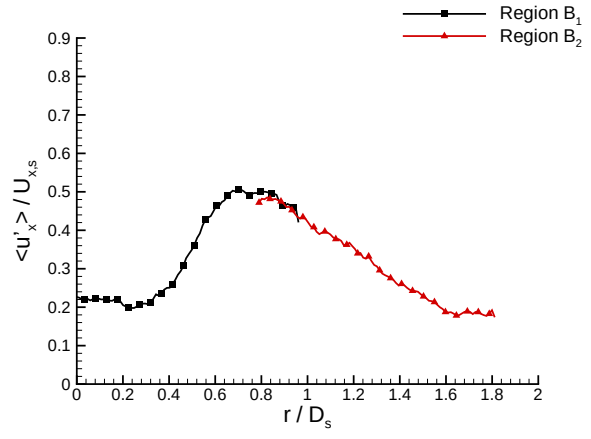

(f) r.m.s axial velocity $x/D_s = 1.06$

Figure 2.14: Comparison of $x - r$ plane mean and r.m.s axial velocities at various axial location for $\alpha_1 = 30°$

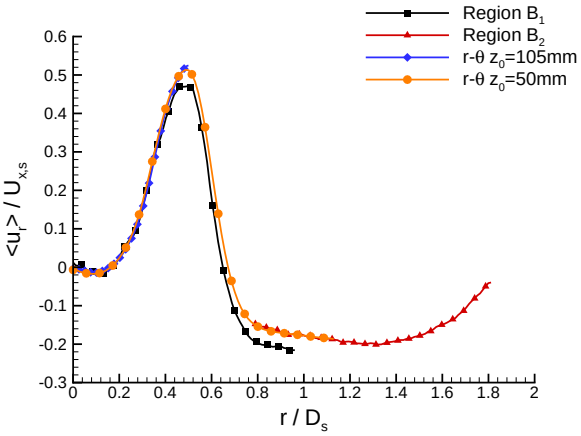

(a) Mean radial velocity $x/D_s = 0.27$

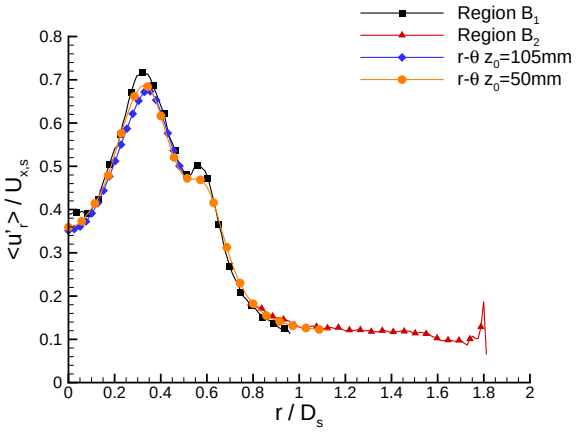

(b) r.m.s radial velocity $x/D_s = 0.27$

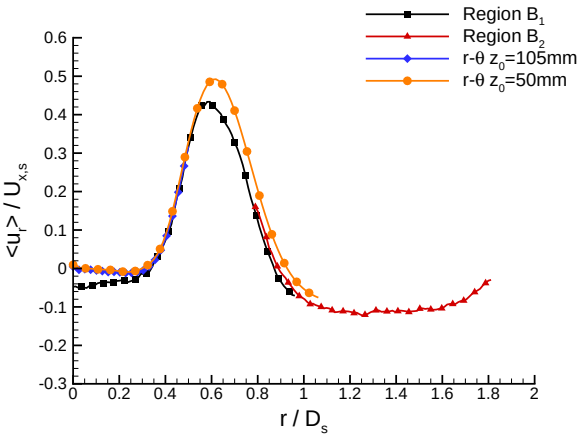

(c) Mean radial velocity $x/D_s = 0.53$

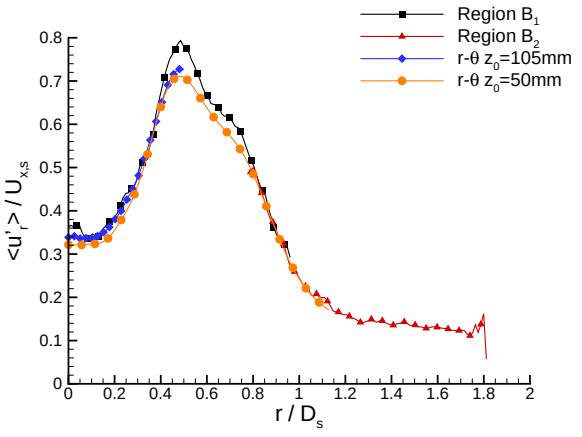

(d) r.m.s radial velocity $x/D_s = 0.53$

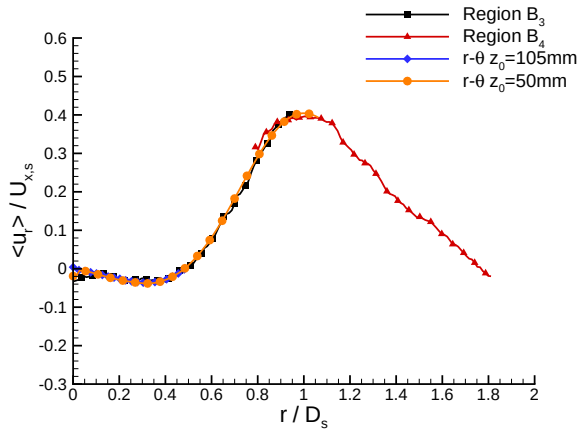

(e) Mean radial velocity $x/D_s = 1.06$

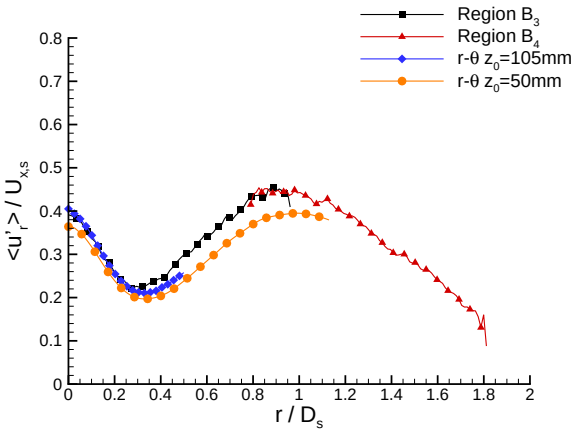

(f) r.m.s radial velocity $x/D_s = 1.06$

Figure 2.15: Comparison of $x - r$ and $r - \theta$ plane mean and r.m.s radial velocities at various axial location for $\alpha_1 = 30°$

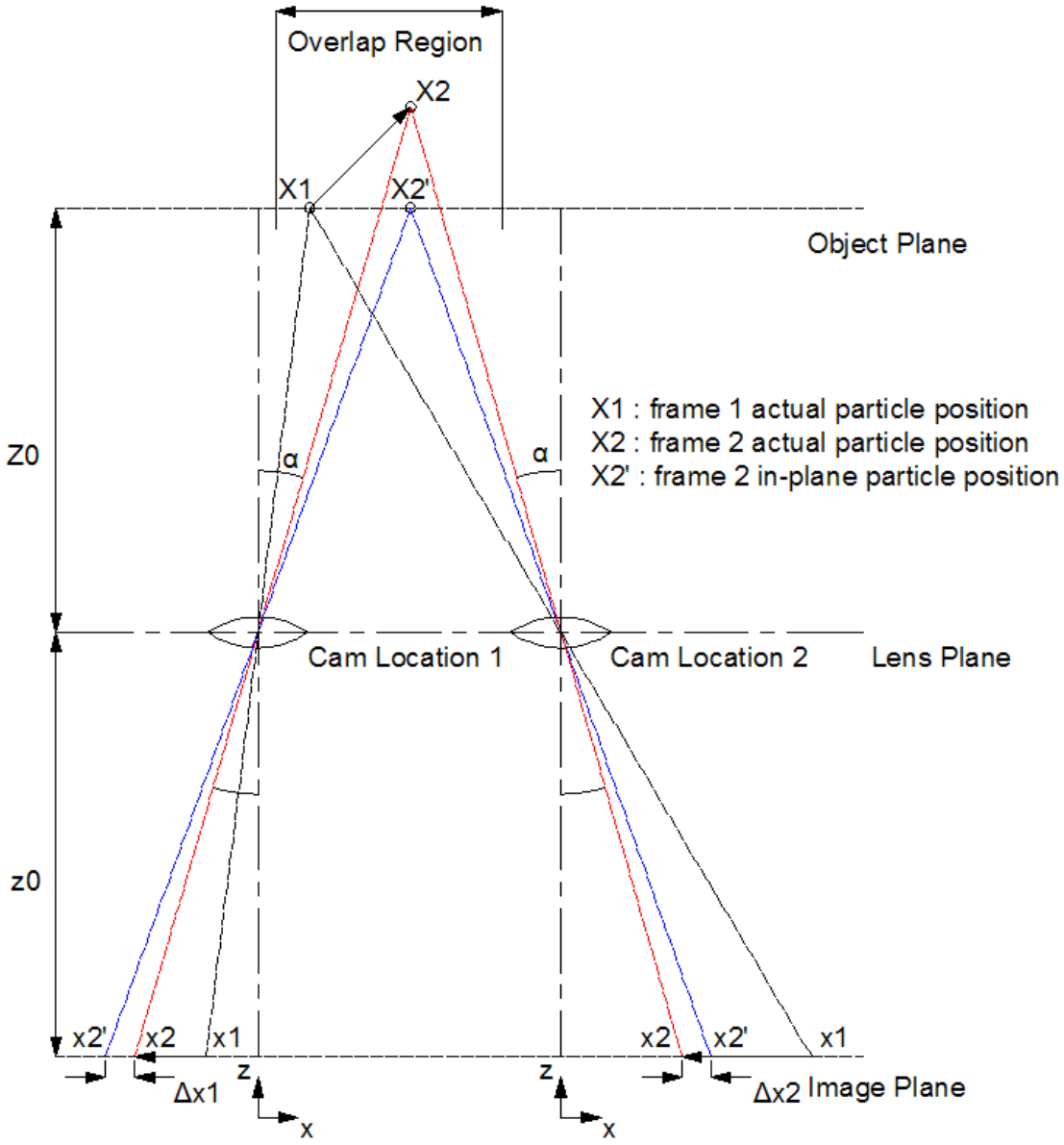

Figure 2.16: Schematic of perspective projection in 2C-PIV

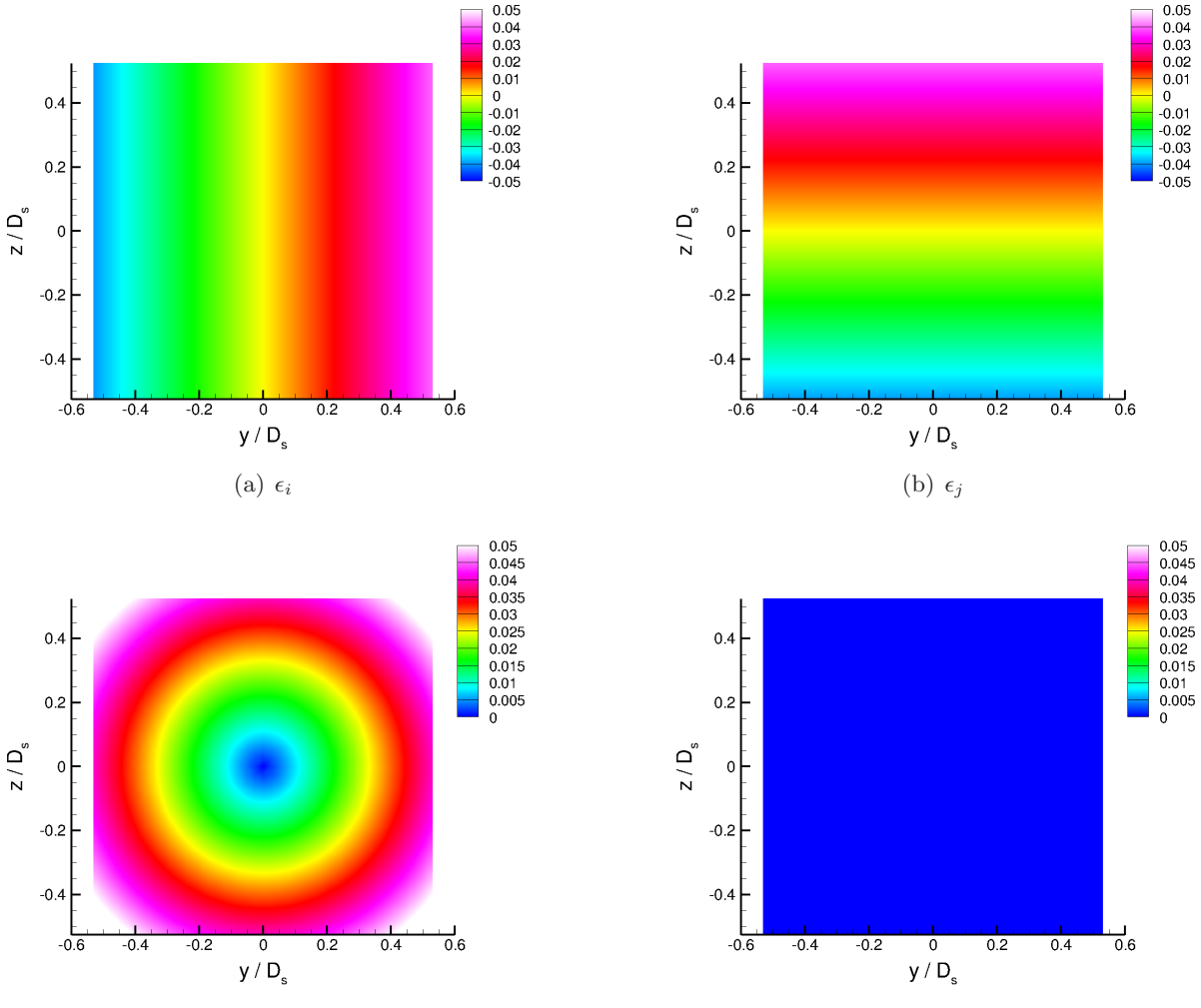

(a) ϵ_i

(b) ϵ_j

(c) ϵ_r

(d) ϵ_θ

Figure 2.17: Theoretical perspective projection error on Cartesian and polar velocity components

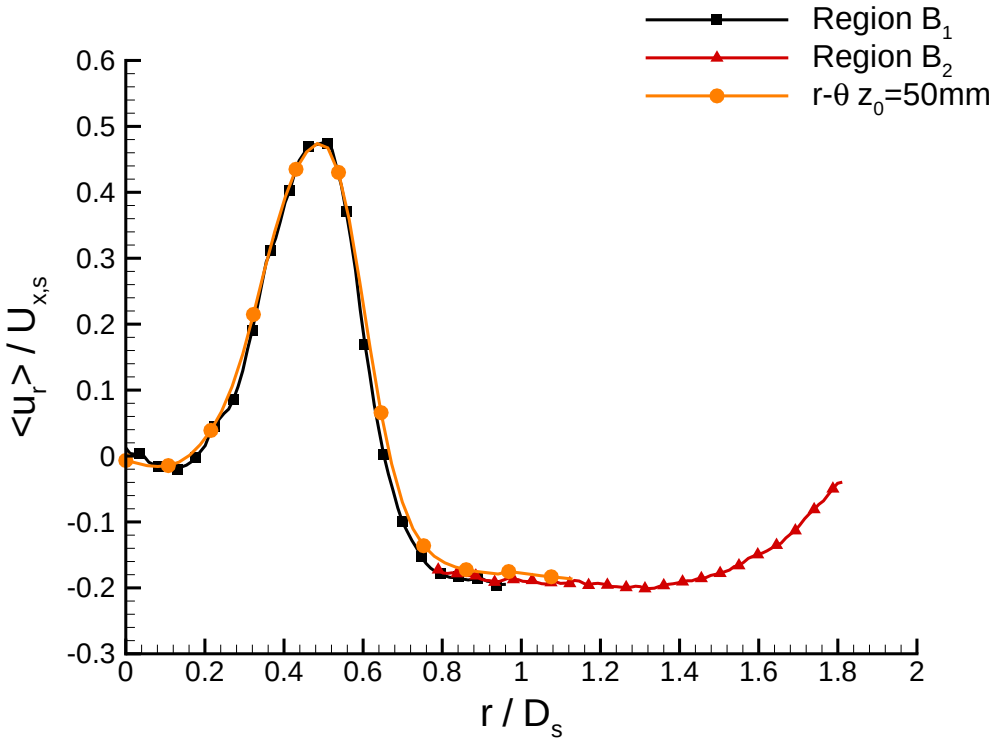

(a) $x/D_s = 0.27$

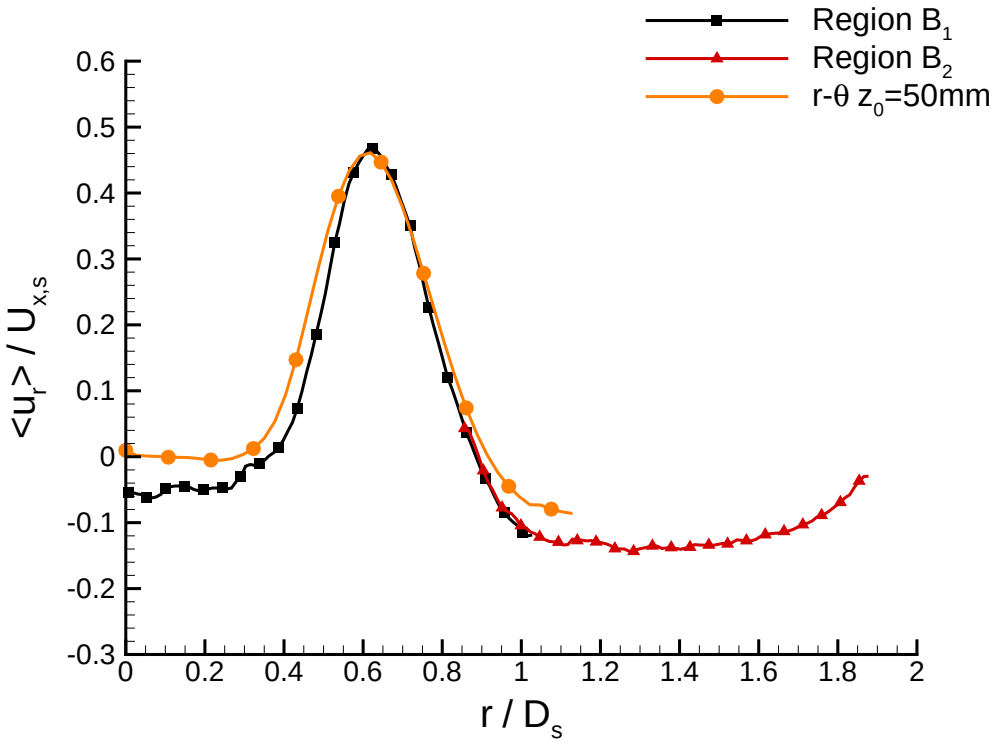

(b) $x/D_s = 0.53$

Figure 2.18: Corrected mean radial velocities in $x - r$ and $r - \theta$ plane at various axial locations for $\alpha_1 = 30°$

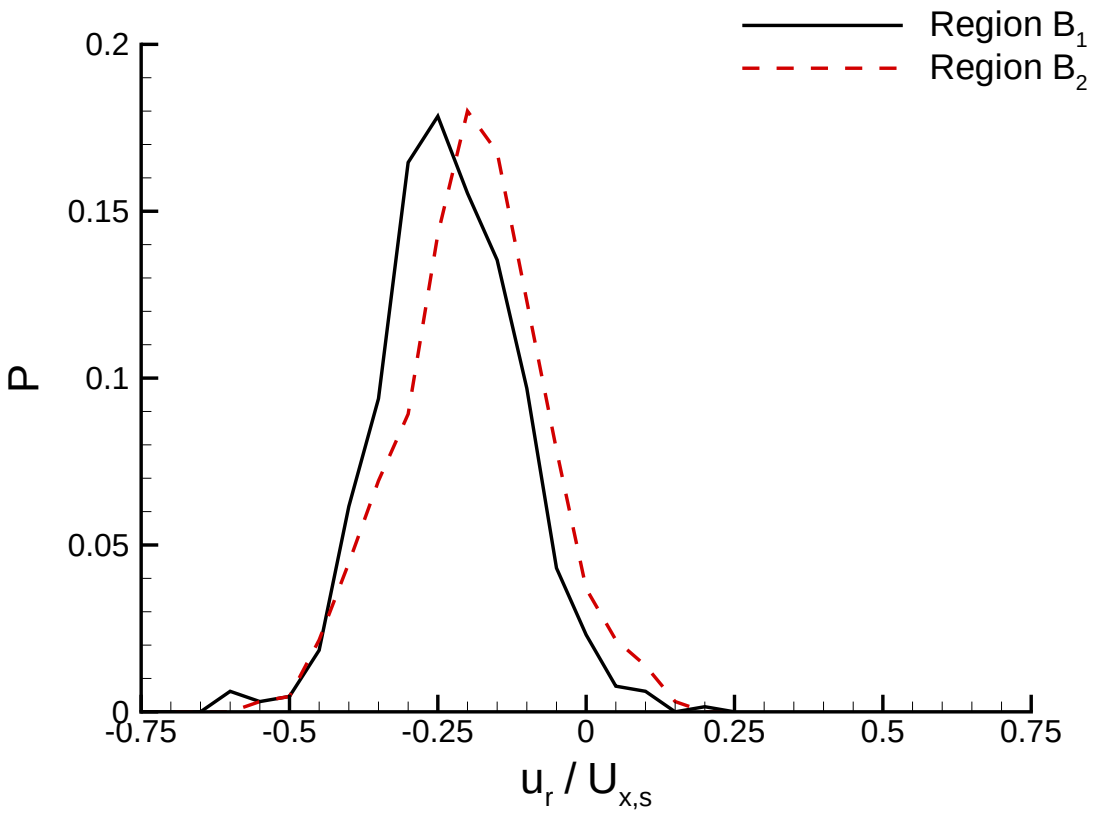

(a) Instantaneous

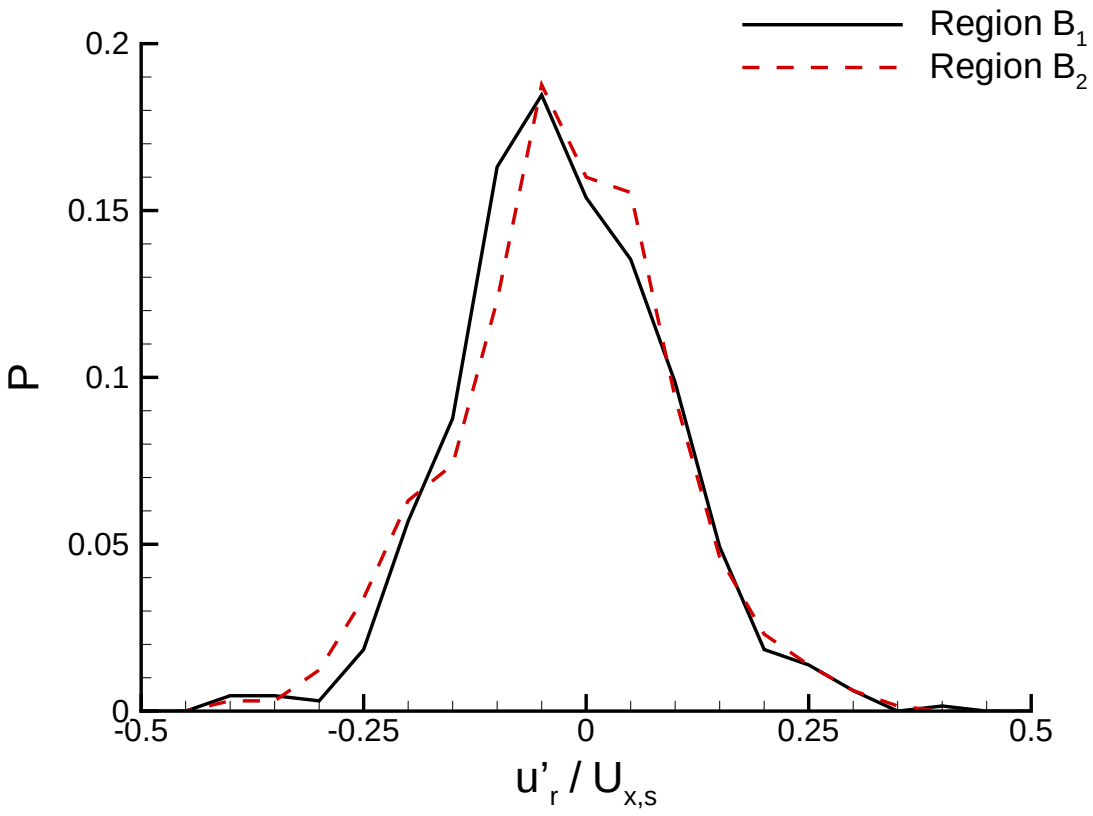

(b) Fluctuating

Figure 2.19: PDF of $x-r$ plane instantaneous and fluctuating radial velocities at $x/D_s = 0.27$, $r/D_s = 0.9$ for $\alpha_1 = 30°$

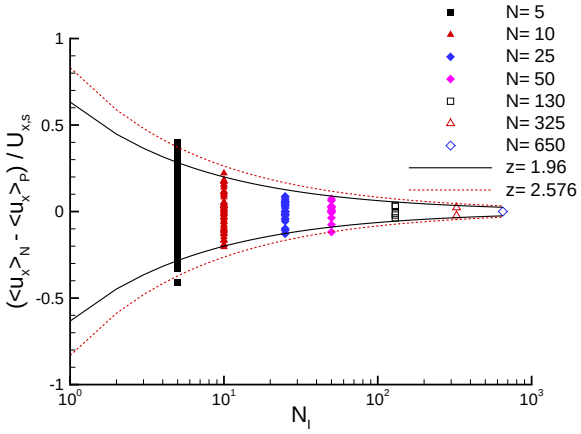

(a) Mean axial velocity

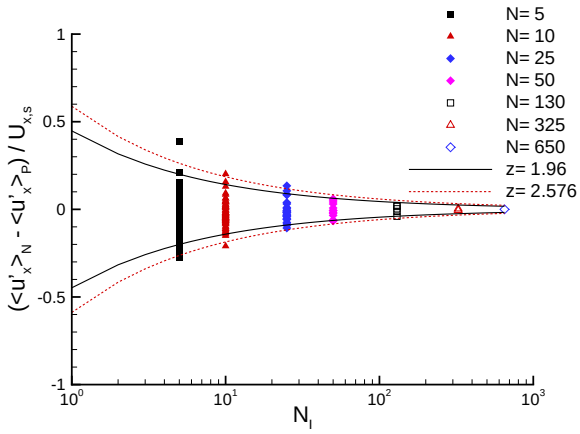

(b) r.m.s axial velocity

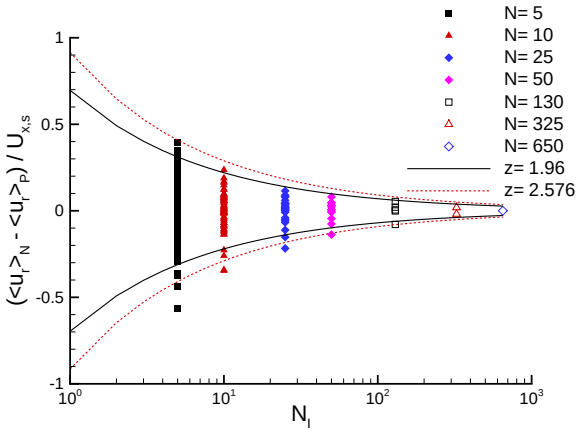

(c) Mean radial velocity

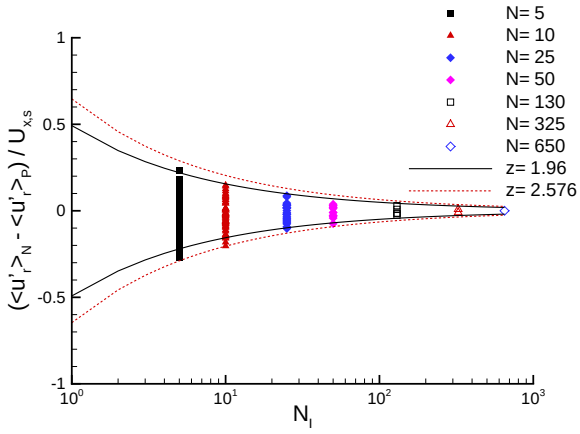

(d) r.m.s radial velocity

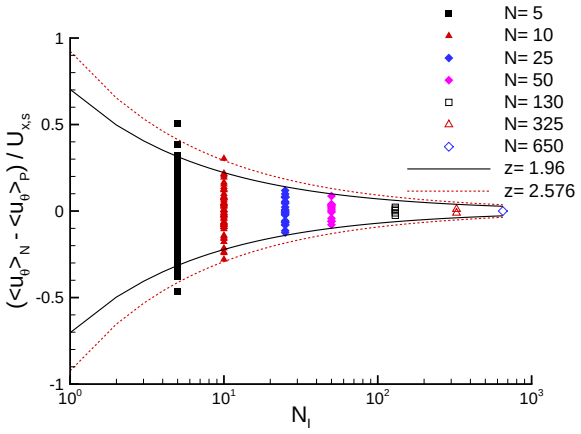

(e) Mean tangential velocity

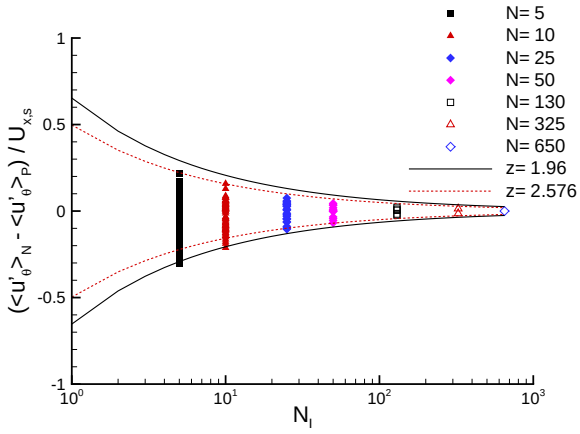

(f) r.m.s tangential velocity

Figure 2.20: Statistical convergence of mean and r.m.s velocities at $x/D_s = 0.02$, $r/D_s = 0.4$ for $\alpha_1 = 30°$

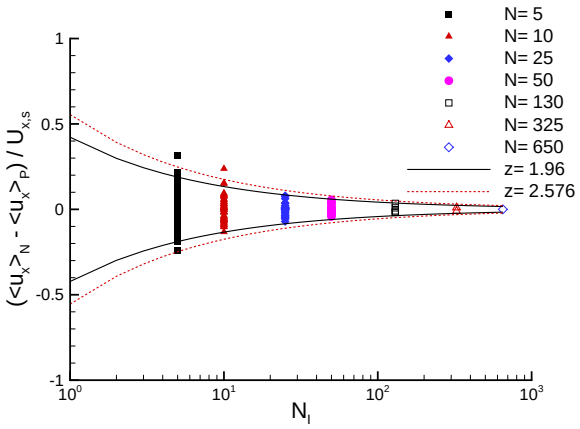

(a) Mean axial velocity

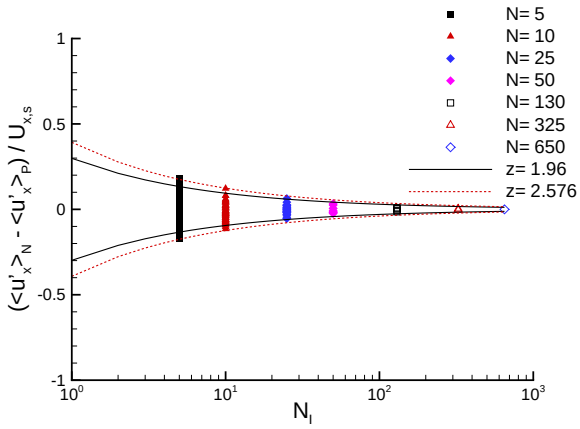

(b) r.m.s axial velocity

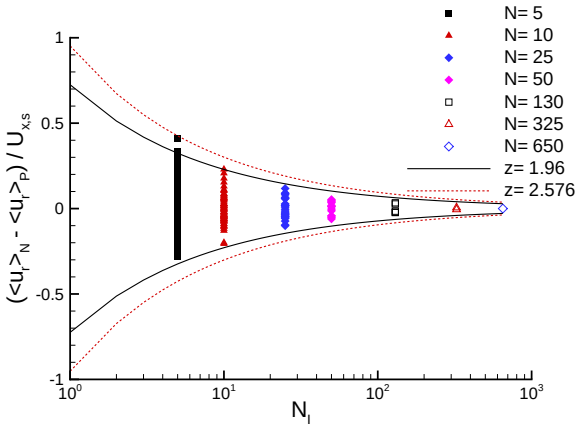

(c) Mean radial velocity

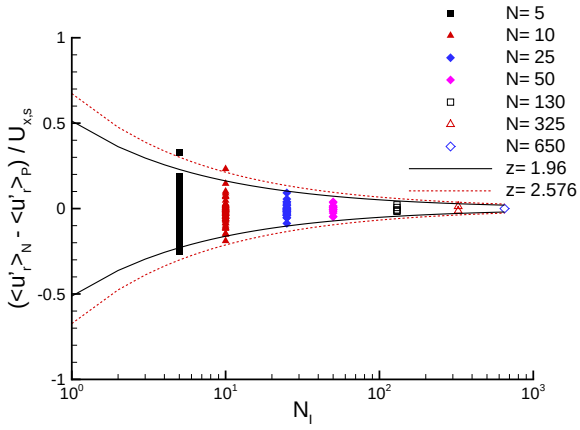

(d) r.m.s radial velocity

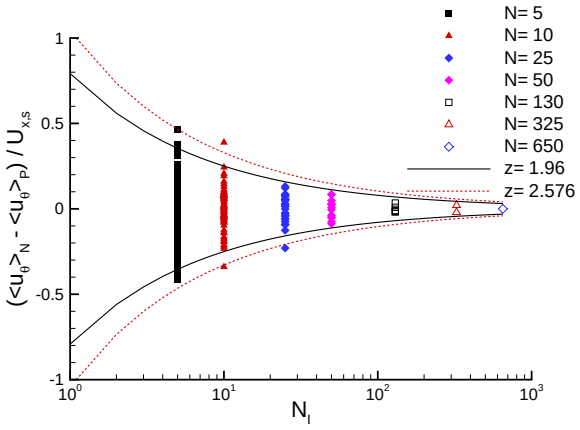

(e) Mean tangential velocity

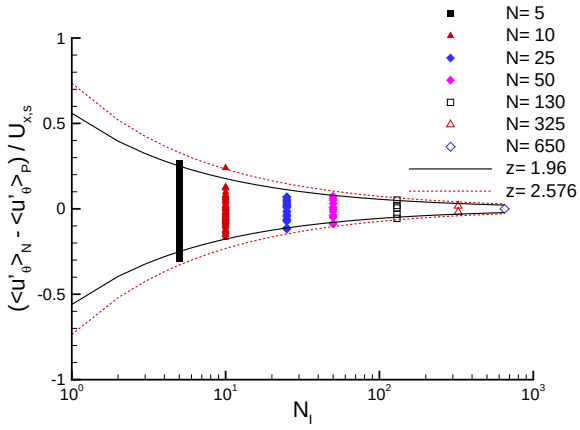

(f) r.m.s tangential velocity

Figure 2.21: Statistical convergence of mean and r.m.s velocities at $x/D_s = 1.06$, $r/D_s = 0.0$ for $\alpha_1 = 30°$

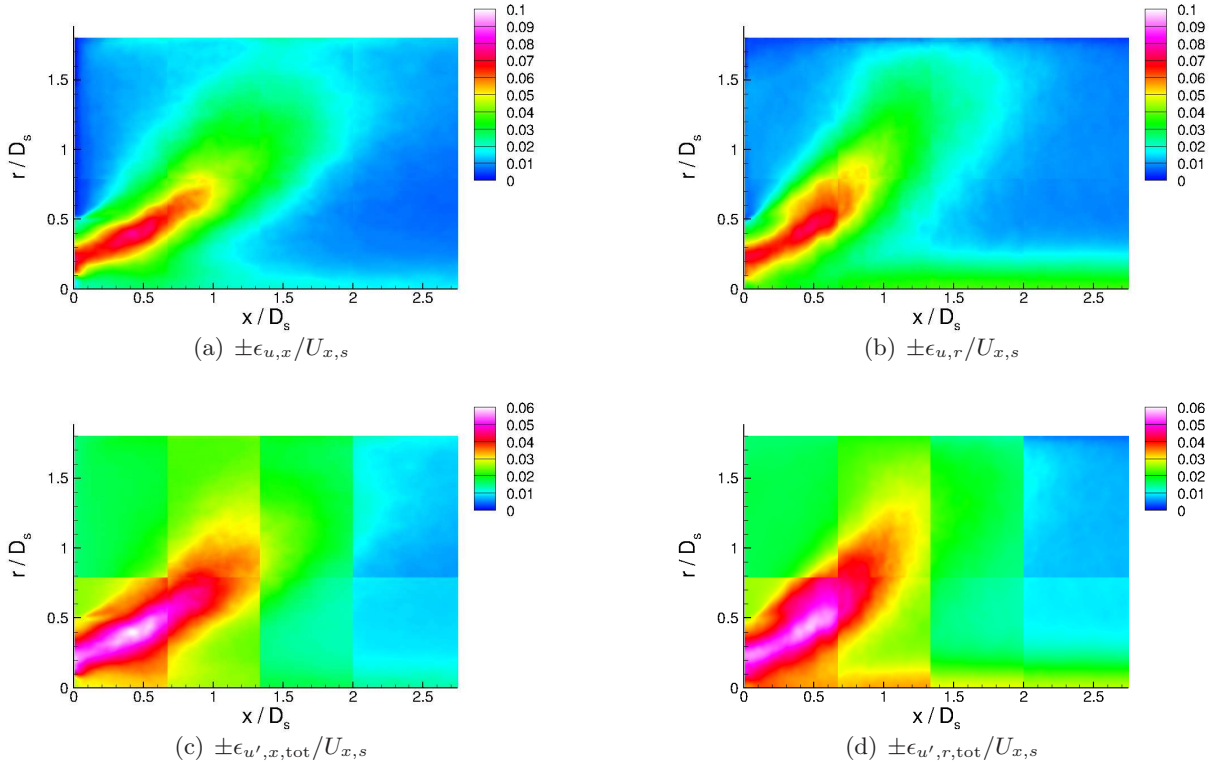

(a) $\pm\epsilon_{u,x}/U_{x,s}$ (b) $\pm\epsilon_{u,r}/U_{x,s}$

(c) $\pm\epsilon_{u',x,\mathrm{tot}}/U_{x,s}$ (d) $\pm\epsilon_{u',r,\mathrm{tot}}/U_{x,s}$

Figure 2.22: Total measurement error on $x-r$ plane first and second-order PIV statistics based on $N_\mathrm{I} = 650$ and $z = 2.576$ (99% confidence) for $\alpha_1 = 30°$

Chapter 3

Numerical Methods and Computational Implementation

Computational fluid dynamics (CFD) is a numerical approach that has the ability to predict complex flow behaviour on both an instantaneous and a time-mean basis. Given that all numerical and physical modelling components of the simulation are adequate, CFD predictions are an excellent companion to measured data and in many cases the combination leads to an improved understanding of the flow. An attractive property of CFD is that full volumetric information is available and issues regarding access do not arise. This allows analysis of regions of the flow not available from experimental data. It is in this complimentary spirit that CFD is used in the present work. An overview of the governing equations of CFD are given in Section 3.1 along with the particular methodologies adopted in this thesis, namely: Unsteady Reynolds-Averaged Navier-Stokes (RANS) and Large Eddy Simulation (LES). In order to solve the governing equations a suitable computer code is required. During this project both in-house (LULES and Delta) and commercial (Fluent) CFD codes were utilised, details of which are provided in Section 3.2. Other computational details, e.g. boundary conditions, are discussed in Section 3.4.1. The suitability and quality of the computational mesh used to approximate the governing equations exerts an important influence on the success of any CFD prediction, hence the topic of mesh generation is covered in Section 3.4.

3.1 CFD Methodology

The motion of all single phase, single species fluids is fully described by a set of coupled, non-linear, partial differential equations known as the Navier-Stokes equations, which are generalisations of the conservation laws of mass (continuity), momentum (Newtons 2^{nd} law) and energy. For the incompressible, isothermal flows (i.e. constant fluid property flow) studied in this thesis the continuity equation can be written using Cartesian tensor notation as follows:

$$\frac{\partial u_j}{\partial x_j} = 0 \tag{3.1}$$

and the momentum equations can be written as:

$$\frac{\partial u_i}{\partial t} + \frac{\partial}{\partial x_j}\left(u_i u_j\right) = -\frac{1}{\rho}\frac{\partial p}{\partial x_i} + \frac{\partial \tau_{ij}^{\nu}}{\partial x_j} \tag{3.2}$$

u_i and p are instantaneous values of velocity and static pressure respectively. For Newtonian fluids the constitutive relationship is chosen to assume a linear relationship between the viscous stress tensor, τ_{ij}^{ν}, and strain rate tensor, S_{ij}:

$$\tau_{ij}^{\nu} = 2\nu S_{ij} \tag{3.3}$$

where ν (μ/ρ) is the kinematic fluid viscosity. The strain rate tensor, S_{ij}, is given by:

$$S_{ij} = \frac{1}{2}\left(\frac{\partial u_i}{\partial x_j} + \frac{\partial u_j}{\partial x_i}\right) \tag{3.4}$$

In general the Navier-Stokes equations cannot be solved analytically and this must thus be accomplished numerically. This approach is known as Computational Fluid Dynamics (CFD), in which the continuous governing equations are discretised in both time (Δt) and space (Δx_i) to produce a system of linear algebraic equations which can then be solved numerically on a computer. In order to achieve a complete and accurate realisation of a turbulent flow the spatial and temporal discretisation employed must be sufficient to resolve the Kolmogorov length (η) and time (τ_η) scales respectively as these represent the smallest dynamically active scales [88]. This is known as Direct Numerical Simulation (DNS) and is, in principal, the most straightforward CFD methodology as no approximation, other than numerical discretisation, is involved. In practice, however, DNS is rarely a viable approach as high Re turbulent flows contain an extremely broad range of length and timescales that can only be fully resolved at considerable, and often prohibitive, computational expense. For example, the ratio of the most energetic lengthscale, ℓ_0, to that of the smallest dynamically active lengthscale, η, is [88]:

$$\frac{\ell_0}{\eta} = O(Re^{3/4}) \tag{3.5}$$

Since turbulent flow is always 3D, numerical mesh sizes will be proportional to $Re^{9/4}$. Clearly, for the engineering flows considered in this thesis with typical Re of $O[10^4 - 10^5]$ (see Table 2.2) DNS is not realistic given current and near future computing power.

In order to overcome the restrictions imposed by DNS it is necessary to reduce the number of computational operations such that the dynamics of all the scales of motion do not have to be calculated directly. This requires the introduction of a new (coarser) level of description of the flow and a decision as to which scales will represented directly (numerically resolved) and which will not. In practice, Reynolds-Averaged Navier-Stokes (RANS) and Large-Eddy Simulation (LES) methodologies are two widely used and well established means of providing a more economical alternative to DNS. They are the subject of the following subsections.

3.1.1 Unsteady Reynolds-Averaged Navier-Stokes Methods

The most straightforward method of reducing the number of computational operations required in a turbulent flow calculation is to compute only a few statistically averaged properties of the solution directly rather than attempt to resolve all details of the instantaneous flow. This is achieved by decomposing each instantaneous variable, $\phi(x_i, t)$, of the turbulent system into the sum of a statistical average, $\langle\phi(x_i, t)\rangle$, and a fluctuation, $\phi'(x_i, t)$, about that average. Such an operation is known as Reynolds decomposition and is expressed mathematically as:

$$\phi(x_i, t) = \langle\phi(x_i, t)\rangle + \phi'(x_i, t) \tag{3.6}$$

Note that at this stage the statistical average $\langle\ \rangle$ is allowed to depend on time. This implies the averaging is ensemble averaging over many repeated realisations of the same flow. In many instances, this average can be assumed to be independent of time (statistically stationary flow), or it may be further decomposed into a time independent part and a coherent time-dependent part not correlated with the fluctuating part. These represent traditional RANS and URANS formulations as described below.

The Reynolds-Averaged form of the governing equations is obtained by substituting Equation 3.6 for u_i and p into Equations 3.1 and 3.2 and averaging, which gives:

$$\frac{\partial\langle u_j\rangle}{\partial x_j} = 0 \tag{3.7}$$

$$\frac{\partial\langle u_i\rangle}{\partial t} + \frac{\partial}{\partial x_j}\left(\langle u_i\rangle\langle u_j\rangle\right) = -\frac{1}{\rho}\frac{\partial\langle p\rangle}{\partial x_i} + \frac{\partial}{\partial x_j}\left[\langle\tau_{ij}^{\nu_t}\rangle - \langle u_i' u_j'\rangle\right] \tag{3.8}$$

The additional terms appearing in Equation 3.8, $-\langle u_i' u_j' \rangle$, are known as the Reynolds stresses and are the components of a second-order, symmetric tensor containing in general 6 independent unknowns [7]. The elements along the leading diagonal are referred to as turbulent normal stresses, whilst the off-diagonal elements are turbulent shear stresses. The presence of the Reynolds stresses means that the conservation equations are not closed, i.e. they contain more variables than equations. To obtain closure the Reynolds stresses are determined from a turbulence model, either via the eddy-viscosity hypothesis or more directly from modelled Reynolds-stress transport (RST) equations. Both approaches are considered in Sections 3.1.1.1 and 3.1.1.2 respectively.

As noted above, the form of the governing equations in Equations 3.7 and 3.8 is relevant to both RANS and URANS formulations. As pointed out by Wegner et al. [45], the application of RANS-based methods to statistically unsteady flows is still a matter of fundamental debate. Durbin [89] has stated that one criterion allowing valid use of URANS decomposition is that the temporal spectrum should contain a very narrow spike, representing a periodical or coherent unsteadiness which is not correlated with the turbulent (broadband) unsteadiness at the same frequency. This then allows a form of triple decomposition to be used:

$$\phi(x_i,t) = \underbrace{\overline{\phi}(x_i) + \widehat{\phi}(x_i,t)}_{\langle \phi(x_i,t) \rangle} + \phi'(x_i,t) \tag{3.9}$$

where $\overline{\phi}(x_i)$ represents the long-time statistical average which is independent of time, $\widehat{\phi}(x_i,t)$ represents the coherent (perhaps periodic) unsteadiness and $\phi'(x_i,t)$ is the broadband (incoherent) turbulent unsteadiness. The source of the unsteadiness is unimportant and may be imposed externally, as in rotor-stator interactions; or it can be internally self-generated unsteadiness, as in vortex shedding. It is more important that the unsteadiness is of a deterministic nature (and not correlated with $\phi'(x_i,t)$) for URANS-based methods to be applied successfully. Flows which do not exhibit a spike in the temporal spectrum, are more likely to be statistically stationary and the ensemble average is not a function of time [89]. In this case, even if the URANS equations are solved, they should produce a steady solution despite the inclusion of a time-dependent term and an appropriate definition for the statistical mean, $\langle \phi(x_i,t) \rangle$, used in Equation 3.6 is then the temporal mean [90], $\overline{\phi}(x_i)$, given as:

$$\langle \phi(x_i,t) \rangle \Rightarrow \overline{\phi}(x_i) = \lim_{T \to \infty} \frac{1}{T} \int_t^{t+T} \phi(x_i,t) dt \tag{3.10}$$

where T is the averaging interval which should be large enough to eliminate the effects of the fluctuations. Clearly, where it is known that no coherent unsteady component exists, a steady RANS

formulation, in which the time-dependent term is omitted from the governing equations, is justified on the basis of avoiding unnecessary computational expense. For statistically unsteady flows Reynolds averaging is not synonymous with time-averaging [91] and a time dependent solution is required to ensure any potentially present coherent motions are resolved. This is highlighted in simulations over a wall-mounted cube performed by Iaccarino et al. [91] using both steady and unsteady RANS formulations. The URANS calculations were found to be in much better agreement with experiment, particularly in regard to the size of the recirculation area in the wake of the cube which was overpredicted by 100% in the RANS calculations. Durbin [89] attributes this difference due to the omission of the coherent spike from the mean flow (due to strong vortex shedding being present in the cube flow).

One contentious issue regarding the URANS approach is whether there should be a 'spectral gap' between any coherent unsteadiness spikes and the broadband turbulent contributions to the spectrum, or alternatively, an appropriately significant difference in time scales [48]. According to Durbin [89], this is not required because it is based on an insistence that Reynolds averaging equals temporal averaging which it does not. Wegner et al. [45] further point out that this insistence would require the averaging period, T, to be much smaller than the timescale of the coherent unsteady motion and at the same time orders of magnitude larger than the timescale range of all turbulent fluctuations. A better view of URANS validity is perhaps that it is appropriate when coherent and turbulent unsteady components are weakly correlated. Two motions will be well correlated if they share similar time *and* length scales. Hence even if there is no spectral gap (motions share similar timescales), if their dominant *spatial* scales are *not* closely comparable, the URANS approach should still be acceptable. Further, with weak correlation, the turbulence models which have been developed and calibrated in statistically stationary flows may well still perform adequately in the presence of uncorrelated coherent unsteadiness. Of course if the correlation is *not* weak, the inverse of these statements holds. For flows in which the coherent unsteadiness is due to internal instabilities the so-created vortical structures can sometimes share similar time and length scales to the energetic turbulent scales and a substantial amount of interaction may occur [90]. For example, the unresolved fluctuating term, $\phi'(x_i, t)$, in Equation 3.6 may contain a contribution due to a change in position and strength of a coherent vortical structure (i.e. correlated with $\widehat{\phi}_i(x_i, t)$) and exhibit significant energy at the coherent shedding frequency [89].

3.1.1.1 Turbulence Closure - $k-\epsilon$ Model

The $k-\epsilon$ turbulence model represents the most widely used RANS turbulent closure and is based on the eddy-viscosity hypothesis, first introduced by Boussinesq [92], which is mathematically analogous to the stress-strain relation for a Newtonian fluid given in Equation 3.3. The intrinsic assumption of the hypothesis is that the level of the anisotropy of the Reynolds stresses ($-\langle u_i' u_j' \rangle +$

$\frac{2}{3}\delta_{ij}k$) [7] is proportional to the mean strain rate. The specific assumption can be written:

$$-\langle u_i' u_j' \rangle = 2\nu_t \langle S_{ij} \rangle - \frac{2}{3}\delta_{ij}k = \langle \tau_{ij}^{\nu_t} \rangle - \frac{2}{3}\delta_{ij}k \tag{3.11}$$

where the constant of proportionality, ν_t, is referred to as the kinematic eddy-viscosity and k is the turbulent kinetic energy which is equal to half the trace of the Reynolds stress tensor, $k = \frac{1}{2}\langle u_i' u_i' \rangle$ [7]. Incorporating the eddy-viscosity hypothesis into the mean-momentum equations (i.e. substitution of Equation 3.11 into Equation 3.8) gives:

$$\frac{\partial \langle u_i \rangle}{\partial t} + \frac{\partial}{\partial x_j}\left(\langle u_i \rangle \langle u_j \rangle\right) = -\frac{1}{\rho}\frac{\partial \langle p^* \rangle}{\partial x_i} + \frac{\partial \langle \tau_{ij}^{\nu_{\text{eff}}} \rangle}{\partial x_j} \tag{3.12}$$

where ν_{eff} is the effective viscosity, equal to the sum of kinematic and eddy viscosities and $\langle p^* \rangle$ is a modified mean pressure term which includes the isotropic stress contribution.

$$\langle p^* \rangle = \langle p \rangle + \frac{2}{3}k \tag{3.13}$$

Note that Equation 3.12 has been written in a form suitable for both RANS and URANS. For RANS $\partial\langle u_i \rangle/\partial t = \partial \overline{u}_i/\partial t = 0$, for URANS $\partial\langle u_i \rangle/\partial t = \partial \widehat{u}_i/\partial t$. This practice is followed in all equations in Section 3.1.1.1. Unlike kinematic viscosity, ν, which is a fluid property and remains constant everywhere under isothermal conditions, ν_t is a flow property which varies from point to point and needs to be specified. Using dimensional analysis an appropriate form for ν_t is:

$$\nu_t = C_\mu \frac{k^2}{\epsilon} \tag{3.14}$$

where ϵ is the dissipation rate of turbulent kinetic energy and C_μ is an empirical constant defined in Table 3.1. Although it is possible to derive exact transport equations for k and ϵ (see, for example Smith et al. [17]) these include many additional unknowns that require further modelling assumptions. For high Re flow far removed from the near-wall region, two modelled equations for k and ϵ, which form the standard k-ϵ, are given by Launder and Spalding [93] as:

$$\frac{\partial k}{\partial t} + \frac{\partial}{\partial x_j}\left(\langle u_j \rangle k\right) = \frac{\partial}{\partial x_j}\left(\frac{\nu_t}{\sigma_k}\frac{\partial k}{\partial x_j}\right) + P_k - \epsilon \tag{3.15}$$

$$\frac{\partial \epsilon}{\partial t} + \frac{\partial}{\partial x_j}\left(\langle u_j \rangle \epsilon\right) = \frac{\partial}{\partial x_j}\left(\frac{\nu_t}{\sigma_\epsilon}\frac{\partial \epsilon}{\partial x_j}\right) + \frac{\epsilon}{k}\left(C_{\epsilon 1}P_k - C_{\epsilon 2}\epsilon\right) \tag{3.16}$$

where C_μ, $C_{\epsilon 1}$, $C_{\epsilon 2}$, σ_k and σ_ϵ are empirical constant identified by Launder and Spalding [93] and given in Table 3.1. The production of turbulent kinetic energy, P_k, is given by:

$$P_k = 2\nu_t \langle S_{ij} \rangle \langle S_{ij} \rangle \geq 0 \tag{3.17}$$

C_μ	$C_{\epsilon 1}$	$C_{\epsilon 2}$	σ_k	σ_ϵ
0.09	1.44	1.92	1.0	1.3

Table 3.1: Standard $k - \epsilon$ turbulence model coefficients [93]

In the presence of a wall the turbulent stresses fall rapidly to zero and the flow is strongly influenced by molecular viscous stresses. The standard $k - \epsilon$ model described above assumes a high turbulent Re ($\nu_t >> \nu$) and cannot capture these effects. Low Re variants of the $k-\epsilon$ model do exist (for example Jones and Launder [94]), however, they require a large number of near wall cells due to large gradients in both velocity and turbulence. An alternative to this is retention of the high Re model and the use of wall-functions which are a collection of semi-empirical formulae that link the solution variables at the wall-adjacent cells with relevant quantities on the wall (i.e. the wall shear stress). In order to apply wall-functions successfully it is necessary for the wall-adjacent cells to be located within the fully-turbulent region of the boundary layer. In the wall-function approach a transport equation for k (Equation 3.15) is solved throughout the entire computational domain including the wall-adjacent cells but the value of ϵ is fixed in these wall adjacent cells on the basis of the local equilibrium hypothesis [7].

$$\epsilon_{\mathrm{P}} = \frac{C_\mu^{3/4} k_{\mathrm{P}}^{3/2}}{\kappa y_{\mathrm{P}}} \tag{3.18}$$

where the subscript P refers to wall-adjacent values and κ is the von Karman constant (taken to be ≈ 0.41). A modification to the production of turbulent kinetic energy, P_k, in Equation 3.15 is required that is consistent with the log-law assumption and the local equilibrium hypothesis and an appropriate form is:

$$P_k = \frac{C_\mu^{1/2} k_{\mathrm{P}} \langle u_{\mathrm{P}} \rangle}{y_{\mathrm{P}} \ln\left(E y^*\right)} \tag{3.19}$$

where y^* is a non-dimensional near-wall distance given by:

$$y^* = \frac{C_\mu^{1/4} k_{\mathrm{P}}^{1/2} y_{\mathrm{P}}}{\nu} \tag{3.20}$$

Although the $k-\epsilon$ turbulence model is widely used, there are a number of deficiencies arising from both the intrinsic and specific assumptions in the eddy-viscosity hypothesis that have been identified by numerous authors (see, for example, Pope [7] and Smith et al. [17]). The majority of these stem from the use of an isotropic eddy viscosity and an invariant C_μ (same for all flows and all stress components) coefficient in Equation 3.14. This requires, in an analogous manner to the isotropic laminar viscosity, that the principal axes of the anisotropic Reynolds stress tensor and mean rate-of-strain tensor coincide. Pope [7] has shown that even in simple homogeneous turbulent shear flow the normal Reynolds stresses may be significantly different from each other despite the normal rates of strain being zero ($\langle S_{11}\rangle = \langle S_{22}\rangle = \langle S_{33}\rangle = 0$) and hence a considerable misalignment of principal axes exists. Moreover, the existence of non-zero Reynolds-stress anisotropies in the presence of zero local strain rates is also possible in real flows due to the prior history of straining to which the turbulence has been subjected. These anisotropies decay slowly on the turbulence timescale ($\tau = k/\epsilon$) and are not properly described by the eddy-viscosity hypothesis. A further requirement of alignment of principal axes and an algebraic stress/strain relation is that shear stresses respond immediately to changes in the mean rate of strain. In simple laminar flows the ratio of the molecular timescales to shear timescales is very small and molecular motions adjust rapidly to imposed straining. However, in turbulent shear flow the turbulence timescale and mean flow timescales are of the same order implying that Reynolds stresses take time to adjust to the imposed rates of strain. Finally, in complex flows, forces that act in preferred directions, for example the pressure gradients which balance the centripetal accelerations due to the streamline curvature present in the swirling flows studied in this thesis, exert a large influence on the turbulent structures. In such cases the fact that both shear and normal stresses should be calculated from the same eddy-viscosity is invalid as individual stress components may develop quite differently in the flowfield [17].

Despite the above shortcomings associated with the linear eddy-viscosity hypothesis the review of the available literature presented in Section 1.3.1 found that it has been utilised, exclusively with the $k-\epsilon$ turbulent model, in the limited number of URANS-based studies dedicated to investigating time-dependent swirling flows. Although there are numerous modelling alternatives, such as non-linear eddy-viscosity models, which attempt to eliminate the deficiencies associated with the linear eddy-viscosity model discussed above; none of these, as yet and to the knowledge of the author, have been applied to unsteady swirl flows (the alternative option of adopting Reynolds Stress Transport closure has in general been adopted, see below). Probably the most striking (and surprising) aspect of the studies reviewed in Section 1.3.1 was either the complete failure or remarkable success of the model in predicting CS such as the PVC. These findings highlight the uncertainty as to whether or not URANS-based approaches founded on the linear eddy-viscosity can be recommended for the types of flows characteristic of gas turbine swirl injectors. It is

for these reasons that it is felt that further investigation utilising both a linear eddy-viscosity hypothesis and the $k-\epsilon$ turbulence model is warranted.

3.1.1.2 Turbulence Closure - Reynolds-Stress Transport Model

A Reynolds Stress Transport (RST) closure provides a modelled transport equation for each of the non-zero Reynolds stresses, $\langle u_i' u_j' \rangle$, abandoning the isotropic eddy-viscosity hypothesis of Equation 3.11. Additional transport equations for k and ϵ, similar to those given in Equations 3.15 and 3.16, are also solved to implement boundary conditions and provide a timescale of the turbulence. The difference is that the transport equations for k and ϵ used in RST models calculate the production of turbulent kinetic energy, P_k, directly from the Reynolds-stresses ($P_k = \langle u_i' u_j' \rangle \partial \langle u_i \rangle / \partial x_j$) rather than from $2\nu_t \langle S_{ij} \rangle \langle S_{ij} \rangle$ as in Equation 3.17. The ϵ turbulent transport (diffusion) term may also involve an anisotropic diffusivity as opposed to the scalar diffusivity (ν_t/σ_k) used in Equation 3.16. Unlike models founded on the eddy-viscosity hypothesis, the RST model correctly reflects the fact that individual stresses are generated, dissipated and transported at different rates. It is able to predict anisotropy in the flow and is significantly more sensitive to streamline curvature than the standard $k-\epsilon$ model. The modelled Reynolds-stress transport equations, which are discussed in the following, provide simulations of the dissipative, diffusive and redistributive processes appearing in the exact equations for $\langle u_i' u_j' \rangle$. For high Re flows removed from the near-wall region these can be written as [7]:

$$\underbrace{\frac{\partial}{\partial t}(\langle u_i' u_j' \rangle)}_{\text{transient}} + \underbrace{\frac{\partial}{\partial x_k}(\langle u_k \rangle \langle u_i' u_j' \rangle)}_{C_{ij}} = \underbrace{-\left[\langle u_j' u_k' \rangle \frac{\partial \langle u_i \rangle}{\partial x_k} + \langle u_i' u_k' \rangle \frac{\partial \langle u_j \rangle}{\partial x_k}\right]}_{P_{ij}} - \epsilon_{ij} + \phi_{ij} - d_{ijk} \tag{3.21}$$

The transient term, mean flow convection, C_{ij}, and the production tensor, P_{ij}, are in closed form. However, models for the dissipation tensor, ϵ_{ij}, the pressure-rate-of-strain tensor, ϕ_{ij}, and the diffusion tensor, d_{ijk} are required. For high Re flows far removed from the near-wall region ϵ_{ij} is modelled assuming the dissipative motions to be isotropic [95].

$$\epsilon_{ij} = \frac{2}{3}\delta_{ij}\epsilon \tag{3.22}$$

The diffusion tensor, d_{ijk}, is generally modelled by the gradient-diffusion hypothesis proposed by Daly and Harlow [96] which uses the Reynolds-stress tensor to define an anisotropic diffusion coefficient:

$$d_{ijk} = C_s \frac{k}{\epsilon} \langle u_k' u_l' \rangle \frac{\partial \langle u_i' u_j' \rangle}{\partial x_l} \tag{3.23}$$

The classical approach to modelling the pressure-rate-of-strain tensor, ϕ_{ij}, uses the following decomposition [7]:

$$\phi_{ij} = \phi_{ij,1} + \phi_{ij,2} + \phi_{ij,w} \tag{3.24}$$

The first term in Equation 3.24, $\phi_{ij,1}$, is often referred to as the slow-pressure term and is usually modelled based on Rotta's proposal [97], which may be written as:

$$\phi_{ij,1} = -C_1 \left(\frac{\epsilon}{k}\right) \left(\langle u_i' u_j' \rangle - \frac{2}{3}\delta_{ij} k\right) \tag{3.25}$$

The sign of $\phi_{ij,1}$ is always such as to promote a change towards isotropy. The second term in Equation 3.24, $\phi_{ij,2}$, is often referred to as the rapid-pressure terms as it responds immediately to changes in the mean velocity gradient. According to Launder [98] $\phi_{ij,2}$ can be written as:

$$\phi_{ij,2} = -C_2 \left[\left(P_{ij} - \frac{1}{3}\delta_{ij} P_{kk}\right) - \left(C_{ij} - \frac{1}{3}\delta_{ij} C_{kk}\right)\right] \tag{3.26}$$

The last term in Equation 3.24, $\phi_{ij,w}$, is also know as the wall reflection term and is given as [98]:

$$\begin{aligned}\phi_{ij,w} = {} & C_1' \frac{\epsilon}{k} \left(\langle u_k' u_m' \rangle n_k n_m \delta_{ij} - \frac{3}{2}\langle u_i' u_k' \rangle n_j n_k - \frac{3}{2}\langle u_j' u_k' \rangle n_i n_k\right) \frac{k^{3/2}}{C_\ell \epsilon d} \\ & + C_2' \left(\phi_{\kappa m,2} n_k n_m \delta_{ij} - \frac{3}{2}\phi_{ik,2} n_j n_k - \frac{3}{2}\phi_{jk,2} n_i n_k\right) \frac{k^{3/2}}{C_\ell \epsilon d}\end{aligned} \tag{3.27}$$

where $C_\ell = C_\mu^{3/4}/\kappa$, n_k is the x_k component of the unit normal to the wall, d is the normal distance to the wall and $\kappa = 0.41$. The constants appearing above are summarised below in Table 3.2. For completeness, constants used in k and ϵ transport equations are also included.

C_1	C_2	C_1'	C_2'	C_s	C_μ	$C_{\epsilon 1}$	$C_{\epsilon 2}$	σ_k	σ_ϵ
1.8	0.6	0.5	0.3	0.09	0.22	1.44	1.92	1.0	1.3

Table 3.2: Reynolds-Stress Turbulence Model Coefficients

In general, when the turbulent kinetic energy is needed, it is obtained by taking the trace of the Reynolds stress tensor, i.e. $k = \frac{1}{2}\langle u_i' u_j' \rangle$. However, a transport equation for k (Equation 3.15) is sometimes solved in order to implement the wall boundary conditions for the individual Reynolds stresses. This approach has been adopted for RST calculations presented in Chapter 6 with the near-wall anisotropy of the Reynolds stress fixed at wall adjacent cells according to the following [99]:

$$\frac{\langle u_\tau'^2 \rangle}{k} = 1.098 \quad \frac{\langle u_\eta'^2 \rangle}{k} = 0.47 \quad \frac{\langle u_\lambda'^2 \rangle}{k} = 0.655 \quad \frac{\langle u_\tau'^2 u_\eta'^2 \rangle}{k} = 0.255 \tag{3.28}$$

The notation used above refers to a wall-local coordinate system where τ is the tangential coordinate, η is the normal coordinate and λ is the binomial coordinate as shown in Figure 3.1. In a similar way as described for the high-Re $k-\epsilon$ model in Section 3.1.1.1, in the vicinity of a wall a value of ϵ_{P} is specified for all wall-adjacent cells according to Equation 3.18.

3.1.2 Large Eddy Simulation (LES) Method

Unlike the RANS-based methods of Section 3.1.1 which are based on ensemble or time-averaging at a point, LES employs a low-pass spatial filter to reduce the number of computational operations required for turbulent flow calculations. The philosophy behind LES is founded on the observation that whilst large-scale turbulent motions are highly anisotropic and flow-dependent, small-scale ones are more universal, tending towards isotropy [7]. The purpose of the spatial filter is to separate instantaneous variables, $\phi(x_i, t)$, into filtered, $\widetilde{\phi}(x_i, t)$, and residual, $\phi'(x_i, t)$ components, which is expressed mathematically as:

$$\phi(x_i, t) = \widetilde{\phi}(x_i, t) + \phi'(x_i, t) \tag{3.29}$$

In order to perform the decomposition of the primitive variables in Equation 3.29 a filter must be used. For any space-time variable, $\phi(x_i, t)$, the filtering procedure is defined by:

$$\widetilde{\phi}(x_i, t) = \int_{-\infty}^{+\infty} \int_{-\infty}^{+\infty} \int_{-\infty}^{+\infty} \phi(\xi_i, t) G(x_i - \xi_i) d\xi_1 d\xi_2 d\xi_3 \tag{3.30}$$

where the convolution kernel, G, is characteristic of the filter employed. In practice the box or top-hat filter, the Gaussian filter and the spectral or sharp cutoff filter [7] are used. Filtering in LES can be explicit or implicit. When explicit, all primitive variables are convolved by G, according to Equation 3.30. In the latter case, the role of the filter is performed by the computational grid and the resulting filter has the form of the box filter:

$$G(x_i - \xi_i) = \begin{cases} \frac{1}{\Delta} & \text{for} \quad -\Delta/2 \leq x_i - \xi_i \leq \Delta/2 \\ 0 & \text{otherwise} \end{cases} \tag{3.31}$$

where Δ is related to the local mesh spacing at x_i. The box filter is described in physical space and the filtered variable is interpreted as a volume average, where Δ is, for example, the cube root of the cell volume $(\Delta_x \Delta_y \Delta_z)^{1/3}$. Eddies larger than Δ are thus the resolved scales which are computed directly and ones smaller than Δ are the residual, or sub-grid, scales and require modelling. Filtered versions of the governing equations (Equations 3.1 and 3.2) are:

$$\frac{\partial \widetilde{u}_i}{\partial x_i} = 0 \tag{3.32}$$

$$\frac{\partial \widetilde{u}_i}{\partial t} + \frac{\partial}{\partial x_j}\left(\widetilde{u}_i \widetilde{u}_j\right) = -\frac{1}{\rho}\frac{\partial \widetilde{p}}{\partial x_i} + \frac{\partial}{\partial x_j}\left[\widetilde{\tau}_{ij}^{\nu} - \widetilde{u_i' u_j'}\right] \tag{3.33}$$

The additional term $-(\widetilde{u_i u_j} - \widetilde{u}_i \widetilde{u}_j)$ appearing in Equation 3.33 is known as the residual-stress tensor and is a result of the nonlinear convective term in Equation 3.2. In a similar way to the RANS equations given in Section 3.1.1 its presence means that the filtered versions of the governing equations are not closed and some modelling approximations are required and are considered in the following section.

3.1.2.1 Sub-Grid Scale Modeling

In an analogous manner to the Boussinesq hypothesis give in Equation 3.11, the Smagorinsky model [100] relates the anisotropic residual-stress tensor to the filtered rate of strain in the following way:

$$-\widetilde{u_i' u_j'} = -(\widetilde{u_i u_j} - \widetilde{u}_i \widetilde{u}_j) = \widetilde{\tau}_{ij}^{\nu_{\text{sgs}}} \tag{3.34}$$

$$\widetilde{\tau}_{ij}^{\nu_{\text{sgs}}} = 2\nu_{\text{sgs}} \widetilde{S}_{ij} - \frac{2}{3}\delta_{ij} k_{\text{sgs}} \tag{3.35}$$

where ν_{sgs} and k_{sgs} $(= 1/2\langle \widetilde{u_i' u_i'} \rangle)$ are the eddy-viscosity and the kinetic energy of the residual motions respectively and $\widetilde{S}_{ij}$ is the filtered rate of strain defined as:

$$\widetilde{S}_{ij} = \frac{1}{2}\left(\frac{\partial \widetilde{u}_i}{\partial x_j} + \frac{\partial \widetilde{u}_j}{\partial x_i}\right) \tag{3.36}$$

By analogy to the mixing-length hypothesis, ν_{sgs} is modelled as:

$$\nu_{\text{sgs}} = (C_s\Delta)^2\widetilde{S} \tag{3.37}$$

where $\widetilde{S}$ is the characteristic filtered rate of strain given as:

$$\widetilde{S} = \sqrt{2\widetilde{S}_{ij}\widetilde{S}_{ij}} \tag{3.38}$$

The length scale in the ν_{sgs} is taken to be proportional to the filter width, $\Delta = (\Delta_x\Delta_y\Delta_z)^{1/3}$, where the constant of proportionality is the coefficient, C_s.

One difficulty or weakness of implementing the simple Smagorinsky model is that C_s remains constant throughout the entire computational domain. A theoretical value of C_s can be calculated from an assumption of local equilibrium as described by Sagaut [88], however, in practice it is highly flow dependent and is adjusted accordingly. For example, Clark et al. [101] used $C_s = 0.2$ for a case of isotropic homogeneous turbulence, while Deardorff [102] used $C_s = 0.1$ for a plane channel flow. The swirl flow simulation of Tang et al. [53], which is of more relevance to this thesis, used $C_s = 0.1$. This was based on previous observations by Yang and McGuirk [103] who found that the more advanced dynamic model of Germano et al. [104] did not provide any better representation of the swirl effects on turbulence. A similar conclusion was reached by Garcia-Villalba [105], also using $C_s = 0.1$ after comparing mean and turbulence statistics of swirling flows from both approaches. Based on these studies $C_s = 0.1$ is used throughout this thesis. An explanation of the good performance in general of such a simple model as the standard Smagorinsky model is provided by Pope [7], who has shown from work originated in Lilly [106] that, within inertial sub-range, in which the mean transfer of energy to the residual scales is balanced by dissipation, ℓ_s does in fact scale with Δ. If it is ensured that Δ lies in the inertial sub-range (this is determined mainly by the Re of the flow and the mesh density) then the Smagorinsky model should be sufficient to obtain satisfactory results. Further consideration is given to this topic in Section 5.1.3.

In the presence of a solid boundary, the SGS eddy viscosity should vanish to zero. Since the Smagorinsky model does not display this behaviour it is necessary to apply corrections such as the van Driest damping function:

$$C_s = C_{s_0}\left(1 - e^{\frac{-y^+}{A^+}}\right) \tag{3.39}$$

where y^+ is the non-dimensional distance from the wall and is defined as:

$$y^+ = \frac{u_\tau y_\mathrm{P}}{\nu} \tag{3.40}$$

and A^+ is a constant usually taken to be approximately 25. Incorporating the Smagorinsky model into the filtered momentum equations (i.e. substitution of Equation 3.37 into Equation 3.33) gives:

$$\frac{\partial \widetilde{u}_i}{\partial t} + \frac{\partial}{\partial x_j}\left(\widetilde{u}_i \widetilde{u}_j\right) = -\frac{1}{\rho}\frac{\partial \widetilde{p^*}}{\partial x_i} + \frac{\partial \widetilde{\tau}_{ij}^{\nu_\mathrm{eff}}}{\partial x_j} \tag{3.41}$$

where ν_eff is the sum of sub-grid and kinematic viscosities, i.e. $\nu_\mathrm{eff} = \nu + \nu_\mathrm{sgs}$ and $\widetilde{p^*}$ is the modified filtered pressure which includes the isotropic residual stress.

$$\widetilde{p^*} = \widetilde{p} + \frac{2}{3}k_\mathrm{sgs} \tag{3.42}$$

3.2 Numerical Implementation

The previous sections of this chapter has described in detail the mathematical background of CFD and in particular RANS and LES methodologies used in the work contained in this thesis. In order to apply these approaches to a particular flow problem a suitable computer code is required. During this project both in-house and commercial CFD codes were utilised: for URANS predictions the in-house code Delta and the commercial code Fluent were applied, for LES predictions, the in-house code LULES was applied. The following subsections describe the pertinent aspects of each code used.

3.2.1 LULES CFD Code

LULES is a structured multi-block LES code developed at Loughborough University which employs a finite volume discretisation to solve spatially filtered versions of the governing equations. The suitability of an incompressible, isothermal version of the code in respect to swirl flow applications has been demonstrated previously by Dunham et al. [50] and Tang et al. [107, 53]. Based on these previous successful applications it was used for all the LES calculations presented in this thesis. It should be noted that LULES does not included any grid generation capabilities or post-processing routines. In order to generate the computational domain the commercial software ICEMCFD was used and the output converted to the native format required by LULES. Post-processing routines were executed using an in-house Fortran computer code. In order to reduce the number of CPU hours required for numerical simulation a parallelised version of the

code was used during this thesis. Only a brief overview of the code will be provided here, a more detailed assessment can be found in Tang et al. [53, 108] and Wang [109].

The code is based on an orthogonal coordinate system formed by rotating or translating a 2D curvilinear orthogonal mesh in the 3^{rd} co-ordinate direction. The velocity vector is decomposed into grid-oriented (contravariant) physical components. In order to avoid pressure-velocity decoupling, a staggered gird arrangement is used which avoids the need for any pressure smoothing to prevent checkerboard oscillations and also ensures that velocities are stored at the exact locations required for the calculation of cell face flux terms. A schematic of the staggered grid arrangement used by LULES is shown in Figure 3.2 showing a computational (transformed) space view in 2D. Filtering is achieved implicitly through the spatial resolution of the computational domain and velocities at the corresponding grid points are interpreted as volume averages. The resulting filter has therefore the form of a top-hat filter described in Equation 3.31. The instantaneous filtered governing equations given in Cartesian tensor notation, x_j and $\widetilde{u}_j$, in Equations 3.32 and 3.33, are converted to general orthogonal coordinates using transformations as proposed by Pope [110]. Retaining the notation adopted by Pope [110], Tang et al. [108] give the continuity and momentum equations as:

$$\nabla_{(i)}\widetilde{u}_{(i)} = 0 \tag{3.43}$$

and:

$$\frac{\partial \widetilde{u}_{(j)}}{\partial t} + \nabla_{(i)}\left[\widetilde{u}_{(i)}\widetilde{u}_{(j)} + \widetilde{\tau}^{\nu_{\text{eff}}}_{(ij)}\right] = -\frac{1}{\rho}\frac{\partial \widetilde{p}}{\partial x_{(j)}} + H_i(j)\left[\widetilde{u}_{(i)}\widetilde{u}_{(j)} + \widetilde{\tau}^{\nu_{\text{eff}}}_{(ii)}\right] - H_j(i)\left[\widetilde{u}_{(i)}\widetilde{u}_{(j)} + \widetilde{\tau}^{\nu_{\text{eff}}}_{(ij)}\right] \tag{3.44}$$

where

$$\widetilde{\tau}^{\nu_{\text{eff}}}_{(ij)} = -\nu_{\text{eff}}\left(\frac{\partial \widetilde{u}_{(i)}}{\partial x_{(j)}} + \frac{\partial \widetilde{u}_{(j)}}{\partial x_{(i)}} - \widetilde{u}_{(i)}H_i(j) - \widetilde{u}_{(j)}H_j(i) + 2\delta_{ij}\widetilde{u}_{(l)}H_j(l)\right) \tag{3.45}$$

Definitions of the vector operators and the co-ordinate curvature terms, H_i, are given below for the particular orthogonal system used in LULES. The contribution of the sub-grid scale motions to the effective kinematic viscosity, ν_{eff}, is obtained from the Smagorinsky model detailed in Equation 3.37, however, the filtered rate of strain, $\widetilde{S}_{ij}$, now becomes:

$$\widetilde{S}_{ij} = \frac{1}{2}\left(\frac{\partial \widetilde{u}_{(i)}}{\partial x_{(j)}} + \frac{\partial \widetilde{u}_{(j)}}{\partial x_{(j)}} - \widetilde{u}_{(i)}H_i(j) - \widetilde{u}_{(j)}H_j(i) + 2\delta_{ij}\widetilde{u}_{(l)}H_i(l)\right) \tag{3.46}$$

In the notation used $x_{(i)}$ represents physical displacements measured along curvilinear coordinates lines and is related to a Cartesian displacements (dx_i) between the same two grid points via:

$$(dx_i)^2 = (h_i dx^i)^2 = (dx_{(i)})^2 \tag{3.47}$$

where dx^i represents the orthogonal coordinate system and h_i are scale factors obtained from the metric tensor, g_{ij}, which relates distances in the orthogonal coordinate system to the Cartesian system. Similarly, $\widetilde{u}_{(i)}$ represents the physical components of a filtered contravariant vector, $\widetilde{u}^i$, in the direction of the coordinate lines and is determined from:

$$\widetilde{u}_{(i)} = h_i \widetilde{u}^i \tag{3.48}$$

The divergence operator, $\nabla_{(i)}$, and the coordinate curvature terms, $H_i(j)$ are given as:

$$\nabla_{(i)} = \frac{h_i}{|h|} \frac{\partial}{\partial x_{(i)}} \left(\frac{|h|}{h_i} \right) \tag{3.49}$$

$$H_i(j) = \frac{1}{h_i h_j} \frac{\partial h_i}{\partial x_j} \tag{3.50}$$

where $|h|$ is the product of scale factors, representing the volume ratio between curvilinear and Cartesian coordinate systems. The coordinate variation terms, $H_i(j)$, represent the inverse of the radius of curvature of the j coordinate line and the suffix i is excluded from the summation convention. In the present code, the 3D computational domain is generated by either translating or rotating 2D (x_1, x_2) orthogonal grids. This results in fewer geometric quantities which only need to be calculated in the x_1/x_2 plane. The non-zero $H_i(j)$ terms in the present case are therefore $H_1(2)$, $H_2(1)$, $H_3(1)$ and $H_3(2)$, which can be computed numerically as follows:

$$H_1(2) = \frac{\Delta x_{j+1} - \Delta x_j}{\Delta x_{j+\frac{1}{2}} \Delta y_{j+\frac{1}{2}}} \tag{3.51}$$

$$H_2(1) = \frac{\Delta y_{i+1} - \Delta y_i}{\Delta x_{i+\frac{1}{2}} \Delta y_{i+\frac{1}{2}}} \tag{3.52}$$

$$H_3(1) = \frac{\Delta r_{i+1} - \Delta r_i}{\Delta x_{i+\frac{1}{2}} \Delta r_{i+\frac{1}{2}}} \tag{3.53}$$

$$H_3(2) = \frac{\Delta r_{j+1} - \Delta r_j}{\Delta y_{j+\frac{1}{2}} \Delta r_{j+\frac{1}{2}}} \tag{3.54}$$

where r denotes radius when the third dimension is rotated as is the present case.

An essential requirement of any numerical scheme used for LES is that it is both conservative and non-dissipative of mass, momentum and kinetic energy [108]. This is achieved in the present case using second-order central differencing for the spatial discretisation of all variables, which avoids difficulties associated with higher-order upwind or upwind-biased schemes which are difficult to implement and can produce too much numerical dissipation [111]. Temporal discretisation is also second-order accurate and uses an explicit Adams-Bashforth scheme which is described in Tang et al. [108] as:

$$\frac{\widehat{\widetilde{u}}_i - \widetilde{u}_i^n}{\Delta t} = \frac{3}{2}\psi_i^n - \frac{1}{2}\psi_i^{n-1} + \frac{1}{2\rho}\frac{\partial \widetilde{p}^{n-1}}{\partial x_i} \tag{3.55}$$

$$\nabla^2 \widetilde{p}^n = \frac{2\rho}{3\Delta t}\frac{\partial \widehat{\widetilde{u}}_j}{\partial x_j} \tag{3.56}$$

$$\frac{\widetilde{u}_i^{n+1} - \widehat{\widetilde{u}}_i}{\Delta t} = -\frac{3}{2\rho}\frac{\partial \widetilde{p}^n}{\partial x_i} \tag{3.57}$$

where $\widehat{\widetilde{u}}_i$ is the intermediate velocity and ψ_i denotes the contribution of convective and diffusive terms. Equation 3.55 is solved first to get the intermediate velocity, $\widehat{\widetilde{u}}_i$, then the Poisson equation for pressure (Equation 3.56), derived by imposing the divergence free condition for the new velocity field at $n+1$ time-level is solved to obtain pressures, finally the velocity field at the $n+1$ time-level is obtained from Equation 3.57. To ensure the numerical stability of the explicit Adams-Bashforth scheme the time step is restricted by the usual explicit method constraint that information propagates less than one cell spacing per time step. Both the CFL and DFS number should be less than unity and are:

$$\text{CFL} = \Delta t_{\max}\left(\frac{|u_x|}{\Delta x} + \frac{|u_y|}{\Delta y} + \frac{|u_z|}{\Delta z}\right) \tag{3.58}$$

$$\text{DFS} = \Delta t_{\max}\nu_{\text{eff}}\left(\frac{1}{\Delta x^2} + \frac{1}{\Delta y^2} + \frac{1}{\Delta z^2}\right) \tag{3.59}$$

The solution of the Poisson equation for pressure plays a vital role in computational efficiency, consuming up to 80% of the total CPU time [53]. To accelerate the solution of the pressure equation a multi-grid V-cycle is used which has been demonstrated by Tang et al. [108] to achieve a reduction of approximately 50% in computational effort in the calculation of a 180° bend square duct flow. The convergence criterion of the code is that based on the residual of the pressure equation defined as:

$$\phi = \sqrt{\sum_{ii} \left(b + \sum_{nb} A_{nb} P_{nb} - A_p P_p \right)_{ii}^2} \tag{3.60}$$

(where nb=E,W,N,S,R,L and ii runs over all of the computational nodes). This residual is iterated to be less than at the end of each time step.

The boundary conditions used in LULES are fairly standard and include inflow, outflow, centreline, periodic and solid wall types. In order to implement the boundary conditions an additional row of halo cells is automatically generated by the solver through a linear extrapolation.

Inflow Condition: At inflow planes, a specified velocity condition is used, which requires values of the three velocity components at each time step. In the present case this is achieved by specifying uniform profiles of velocity such that the conservation of mass and tangential momentum flow rate is ensured. A random perturbation, obtained from a normal distribution with zero mean and unit variance and then scaled by a specified level of turbulence intensity, is then superimposed on the uniform velocity components. Although such a method is not representative of real turbulence (the disturbances have no correlation in space or time, usually exhibit a flat spectrum similar to that of white noise and hence will decay rapidly as they pass through the solution domain) justification for this approach, along with further details regarding the calculation of appropriate boundary values, will be presented in Section 3.4.1.

Outflow Condition: At outlet boundaries a convective outflow condition is applied [109]:

$$\frac{\partial \widetilde{u}_i}{\partial t} + \widetilde{U} \frac{\partial \widetilde{u}_i}{\partial x} = 0 \tag{3.61}$$

where $\widetilde{U}$ is the bulk velocity defined at the outflow plane as:

$$\widetilde{U} = \frac{1}{A} \int \rho \widetilde{u}_i^n \cdot d\vec{A} \tag{3.62}$$

In practice the outflow boundary condition is applied at every timestep and carried out in two stages to be compatible with the Adams-Bashforth scheme (Equations 3.55 to 3.57):

$$\frac{\widehat{\widetilde{u}}_i - \widetilde{u}_i^n}{\Delta t} - \frac{3}{2}\widetilde{U}\frac{\partial \widetilde{u}_i^n}{\partial x} + \frac{1}{2}\widetilde{U}\frac{\partial \widetilde{u}_i^{n-1}}{\partial x} = 0 \tag{3.63}$$

$$\frac{\widetilde{u}_i^{n+1} - \widehat{\widetilde{u}}_i}{\Delta t} = 0 \tag{3.64}$$

To ensure overall mass conservation a velocity scaling is used which is applied after each stage of the above procedure:

$$\widetilde{u}_i = \widetilde{u}_i \frac{\dot{m}_{\text{in}}}{\dot{m}_{\text{out}}} \tag{3.65}$$

where $\dot{m}_{in}$ and $\dot{m}_{out}$ are inlet and outlet mass flow rates respectively.

Wall: In turbulent wall-bounded flow, as the Re increases and the viscous sub-layer shrinks, the number of grid points required in LES CFD to resolve the near-wall eddies increases dramatically and the mesh resolution for LES approaches that of DNS. In order to avoid this large computational penalty, it is necessary to apply approximations such as wall-functions. In LULES the simplest possible approach as proposed by Schumann [112] is implemented. This relies on a log-law relation between the wall stress and the velocity component at the first grid point in the near-wall region. The mean wall shear-stress is calculated in an iterative way from the logarithmic law of the wall and the mean velocity at the nearest mesh point to the wall. The non-dimensional near-wall distance $\langle y^+ \rangle$ is determined from Equation 3.40 using the currently available estimate for $\langle u_\tau \rangle$. The mean wall shear stress is updated using the current estimate of the mean near-wall velocity, $\langle u \rangle$, calculated from:

$$\langle u \rangle = \frac{\langle u_\tau \rangle}{\kappa} \ln(E y^+) \tag{3.66}$$

where $\kappa = 0.41$ and $E = 9$. The instantaneous wall shear-stress is then calculated by assuming it to be in phase with the instantaneous velocity, i.e.

$$\tau_w = \frac{u}{\langle u \rangle} \langle \tau_w \rangle \tag{3.67}$$

Periodic Conditions and Block Interfaces: The boundary condition treatment for block-to-block interfaces and periodic boundaries is very similar. With reference to Figure 3.2, the variables $\phi(1)$ and $\phi(\text{nip1})$ are not calculated directly but rather solution information is transferred according to:

$$\phi_1 = \phi_{\text{ni}}$$
$$\phi_2 = \phi_{\text{nip1}}$$

The same treatment is applied in the i and k directions.

Centreline Treatment: As mentioned above, 3D computational domains for use by LULES are generated by either rotating or translating 2D orthogonal grids. During this thesis rotation was employed in order to create geometries representative of swirl injectors. The result is a polar-type mesh such as that shown in Figure 3.4. At $r/D_s = 0$ the mesh collapses to a single point, resulting in a centreline which requires special treatment. All quantities except for the radial velocity component are staggered with respect to the centreline, whilst the radial component itself is collocated on the centerline. For axial velocity and pressure the centreline value ($j = 1$) is defined as the mean of the surrounding nodes stored at $j = 2$ and is computed in the following way:

$$\widetilde{\phi}_{\text{cl}} = \frac{1}{N_k} \sum_{k=1}^{N_k} \widetilde{\phi}_{k,j=2} \tag{3.68}$$

where N_k is the number of circumferential nodes and $\widetilde{\phi}_{\text{cl}}$ is the centreline value which is then used to set explicitly values for the boundary conditions:

$$\widetilde{\phi}_{k,j=1} = 2\widetilde{\phi}_{\text{cl}} - \widetilde{\phi}_{k,j=2} \tag{3.69}$$

The approach used to calculate the radial and tangential velocity component at the centreline makes use of the fact that there is only one vector at this location, which has to be identical in each k plane. In order to obtain this vector all neighbouring radial, $\widetilde{u}_r$, and tangential velocities, $\widetilde{u}_\theta$, stored at $j = 3$ and $j = 2$ respectively, are transformed into Cartesian components and averaged to define a single $\widetilde{u}_y$ and $\widetilde{u}_z$ at the centreline in the following way:

$$\widetilde{u}_{y,\mathrm{cl}} = \frac{1}{N_k}\sum_{k=1}^{N_k}(-\widetilde{u}_{\theta,k,j=2}\sin(\theta_k) + \widetilde{u}_{r,k,j=3}\cos(\theta'_k))$$
$$\widetilde{u}_{z,\mathrm{cl}} = \frac{1}{N_k}\sum_{k=1}^{N_k}(\widetilde{u}_{\theta,k,j=2}\cos(\theta_k) + \widetilde{u}_{r,k,j=3}\sin(\theta'_k)) \tag{3.70}$$

where $\theta_k = (2\pi/N_k)k$ and $\theta'_k = \theta_k + (\pi/N_k)$.

The radial and tangential components at the centreline are then obtained by transforming these components back into cylindrical components.

$$\begin{bmatrix} \widetilde{u}_{r,\mathrm{cl}} \\ \widetilde{u}_{\theta,\mathrm{cl}} \end{bmatrix} = \begin{bmatrix} \cos\theta & \sin\theta' \\ -\sin\theta & \cos\theta' \end{bmatrix} \begin{bmatrix} \widetilde{u}_{y,\mathrm{cl}} \\ \widetilde{u}_{z,\mathrm{cl}} \end{bmatrix} \tag{3.71}$$

Equation 3.69 is then used to define boundary values for $\widetilde{u}_{\theta,k,j=1}$.

3.2.2 Delta CFD Code

Like LULES, Delta is a finite volume CFD code developed at Loughborough University. It is based on a curvilinear non-orthogonal grid system that allows a wide range of complex geometries to be simulated using a multi-block structured mesh. In its original form, Delta was an Euler code but was later developed for the computation of compressible turbulent flows using the standard high-Re $k-\epsilon$ turbulence model as described in Page and McGuirk [113]. More recent developments include the addition of a low-Re turbulence model to investigate boundary layer relaminarisation [114] and an LES version of the code as described by Veloudis [115]. Since Delta was primarily written to simulate turbulent compressible flows, density-weighted ensemble-averaged conservation equations are solved for mass and momentum. However, for the incompressible flows considered in this thesis, the use of density-weighting, often referred to as Favre-averaging, reduces to conventional Reynolds-averaging [17] as described in Section 3.1.1. Furthermore, the Cartesian vector basis adopted by Delta results in forms of the governing equations and transport equation for k and ϵ as described in Sections 3.1.1 and 3.1.1.1 respectively.

The application of Delta to fully incompressible flows has been demonstrated by Salman et al. [116], who investigated vortical structures characteristic of lobed mixer devices. An important aspect of Delta relevant to the aims of this thesis is that it solves time-dependent forms of the governing equations. In the discussion regarding the application of URANS-based models to unsteady flows presented in Section 3.1.1 it was noted that the source of the unsteadiness may be imposed externally, as in rotor/stator interactions; or it can be spontaneous, self-generated unsteadiness, as in vortex shedding. Evidence of Delta's ability to capture self-excited unsteadiness using a standard $k-\epsilon$ turbulence model can be found in Birkby and Page [117]. This study

focused on underexpanded sonic jets and for Nozzle Pressure Ratios in excess of 6 unsteady solutions were observed (periodically repeating fluctuating pressure fields) with Strouhal numbers in reasonable agreement with experiment. From the studies mentioned above it is clear that Delta has previously been extremely successful in simulating a diverse range of flows. These include vortex dominated flows [116] and flows exhibiting strong unsteadiness [117], both of which are relevant to this thesis. Based on these previous successes Delta was selected as an suitable research code with which to investigate the application of URANS-based models to statistically unsteady swirl flows. A comprehensive overview of Delta is provided in an accompanying user's guide [118] and details of the numerical scheme can be found in Birkby and Page [117], however, a brief overview is provided in the following.

For grid generation and input Delta is able to read a number of common formats, for example Plot3d and a multi-block neutral format created by the commercial software ICEMCFD, and convert them to a native format. Post-processing facilities are included which allow full volumetric information of primary flow variables to be exported in Plot3d and Tecplot formats. A parallel version of Delta is available developed in order to accelerate computation, and full use of this was made during this project. As Delta adopts a colocated storage, Rhie-Chow [119] smoothing is used to avoid pressure-velocity decoupling. Delta follows a pressure-correction methodology, by default, the standard SIMPLE approximation of Patankar and Spalding [120] is used where a velocity / pressure linkage coefficient is constructed based upon the discretised momentum equations. In order to limit numerical diffusion errors a second-order accurate upwind spatial discretisation scheme is used for the convective fluxes in momentum, k and ϵ transport equations. The basic numerical scheme is first-order upwind, a higher-order discretisation using the total variation diminishing (TVD) principle is implemented as an explicit deferred correction to the basic upwind scheme. This essentially leads to a limited form of the Quadratic Upwind Interpolation Scheme for Convective Kinetics (QUICK) [121]. All diffusive terms are discretised using central differencing. A first-order backward Euler implicit method is used for temporal discretisation. For further details the reader is referred to Birkby et al. [117].

The boundary conditions used in Delta are implemented using two additional rows of halo cells which are automatically generated by the solver. The boundary conditions used during this thesis are described briefly in the following.

Fixed Velocity Inlet: As described in Section 3.2.1, the specification of all velocity components is required for this type of boundary condition. For URANS calculations where the inlet plane is some distance upstream from the region where significant turbulence production and / or unsteadiness takes place, the most straightforward way is to specify uniform distributions that ensure integral quantities such as the flow rates of mass and tangential momentum are

correctly represented and quantities like k and ϵ assume values reasonable for high Re duct flows.

Outflow Condition: The outflow condition used in Delta for RANS CFD specifies a zero gradient normal to the boundary for all flow variables, such that:

$$\frac{\partial \phi}{\partial n} = 0 \tag{3.72}$$

where n denotes the normal direction.

Symmetry (Centreline) Conditions: The symmetry boundary condition ensures no flow, convective or diffusive flux of any quantity across the boundary and can be described by:

$$u_n = 0 \tag{3.73}$$

and

$$\frac{\partial \phi}{\partial n} = 0 \tag{3.74}$$

where n is normal to the symmetry boundary or centreline.

Wall: For the high-Re $k-\epsilon$ model, Delta employs the near-wall treatment described in Section 3.1.1.1.

3.2.3 Fluent CFD Code

Fluent is a well-known finite volume commercial CFD code that provides an extremely broad range of modelling capabilities. This includes numerous turbulence modelling options, spatial and temporal discretisation schemes and the ability to simulate both steady and transient flows. Due to the sheer number of numerical options available within Fluent the interested reader is referred to the user manual which accompanies the software [99]. Although the version of Fluent (6.3.26) used during this project is a fully unstructured solver all computational grids were generated in a structured manner as described in Section 3.4.

One of the difficulties of using commercial CFD software for a research based project stems from the closed-source nature of the code. This can at times raise questions as to whether particular characteristics of a calculation are to be attributed to the fundamentals of a numerical

scheme or to the manner in which they are implemented in the commercial code. Despite the uncertainties arising from closed-source codes a number of the studies ([48, 41, 44]) reviewed in Section 1.3.1 have utilised commercial software (in these cases CFX) to simulate unsteady swirl flow using RANS-based approaches. To circumvent these uncertainties an approach was adopted whereby the numerical schemes and computational parameters of Fluent were configured such that they matched as closely as possible those used within Delta. Although Fluent was used primarily for the RST calculations presented in this thesis, predictions using the standard high-Re $k-\epsilon$ turbulence model were also performed. In this way a comparison could be made between Fluent and Delta results obtained using, in principle, identical turbulence models, boundary conditions, numerical schemes and computational parameters.

The standard high-Re $k-\epsilon$ model used by Fluent is identical to that described in Equations 3.15 and 3.16 of Section 3.1.1.1. The RST model used by Fluent is identical to that described in Equation 3.21 if the additional terms in Fluent describing production due to buoyancy and co-ordinate system rotation (which are absent in the present flow) are neglected. The pressure-rate-of-strain tensor, ϕ_{ij} is modelled according to Equations 3.25, 3.26 and 3.27 again ignoring terms relating to buoyancy and system rotation. To avoid numerical instabilities [99] associated with the gradient diffusion hypothesis proposed by Daly and Harlow [96] given in Equation 3.23 Fluent use the simplified scalar diffusivity of Lien and Leschziner [122]:

$$\langle u_i' u_j' u_k' \rangle = \frac{\nu_t}{\sigma_{rs}} \frac{\partial \langle u_i' u_j' \rangle}{\partial x_k} \tag{3.75}$$

where ν_t is computed from Equation 3.14 and $\sigma_{rs} = 0.82$, this differs slightly from the standard Daly Harlow model, but it is not believed to be significant of the flows of interest here.

Fixed velocity inlet, outflow and wall boundary conditions are all modelled in a similar fashion within Fluent as described in Section 3.2.2.

3.2.4 Summary of CFD Codes

The previous subsections have described the CFD codes used during this thesis and their particular numerical schemes. These details are summarised below in Table 3.3.

	LULES	Delta	FLUENT
Temporal discretisation	Second-order explicit Adams-Bashforth	First-order implicit Euler	First-order implicit Euler
Spatial discretisation	Central	QUICK	QUICK
Turbulence / sub-grid model	Smagorinsky	$k-\epsilon$	$k-\epsilon$ / RST
Pressure-velocity coupling	N / A	SIMPLE	SIMPLE

Table 3.3: Summary of Numerical Schemes

3.3 Computational Set-Up

Geometry definition, mesh generation and boundary condition specification are some of the most important aspects to consider during a CFD calculation. The following subsections consider each of these in more detail.

3.3.1 Geometry Considerations

Previous experimental work by Midgley [13] identified the presence of two families of coherent structures in radial swirler injectors similar to those considered here. These included a low-frequency precessing vortex core (PVC) oscillation about the centreline of the dump expansion chamber, and high-frequency shear-layer vortices which originated within the annular swirl duct and propagated downstream with the bulk flow. In Figure 2.2 the dump expansion chamber is the region that extends from the datum plane ($x = 0.0$mm, $x/D_s = 0.0$) to the downstream blockage ($x = 160$mm, $x/D_s = 4.25$). The exit plane of the annular swirl duct coincides with the datum plane and extends upstream to $x = -52.7$mm or $x/D_s = -1.4$ as shown in Figure 2.4. Clearly, in order to capture these features in CFD predictions the computational domain must include the annular swirl duct, the dump expansion chamber and a portion of the exhaust duct. As shown in Figure 2.4, the modular swirler used in the current experiments consists of 12 radial slots which impart a swirl component to the initially radial flow before entry to the annular swirl duct. Conceptually, the most straightforward way of simulating the modular swirler geometry would be to capture the entire geometry including swirl vanes. Previous computational studies, for example Lartigue et al. [68] and Wegner et al. [58], have adopted this approach to simulate a Turbomeca industrial swirl-driven fuel injector using LES (Figure 3.3). These studies also included a portion of the upstream feed pipe in order to provide realistic inlet conditions to the radial slots. This approach demands a complex mesh generation process requiring additional blocks and significantly increases the computational effort. In considering this problem at the start of the present work, it was realised that a computationally cheaper and sufficiently accurate alternative would be to begin the calculation at the exit plane of the radial slots. Midgley [13] has shown from $r-\theta$ plane PIV measurements inside the annular swirl duct of a Turbomeca fuel injector that, although the blockage effects are clearly visible at $x/D_s = -0.53$ they had

completely mixed out by $x/D_s = -0.43$. Further investigations [13] found that the high-frequency shear-layer vortices that originate in the annular swirl duct do so between $x/D_s = -0.43, x/D_s = -0.27$. This evidence suggests that the radial slots do not exert any significant influence on the formation of the large-scale periodic structures found downstream within the annular swirl duct. An alternative approach is considered below which is to specify computational domain inlet velocities (just downstream of the swirler vanes) such that quantities such as mass and tangential momentum flow rates (and hence the overall swirl number) derived from experimental measurements are fixed. A number of authors investigating swirl devices with radial entry, such as: Wang et al. [52], Tang et al. [53], Dunham et al. [50] and Garcia-Villalba et al. [55], have opted not to model the discrete effects of the radial slots. Despite this simplification the formation of large-scale unsteady structures within the swirl duct was not hindered, and hence this simpler approach is adopted here.

3.4 Mesh Generation

In addition to reducing the computational effort, neglecting the radial slots also simplifies the grid generation procedure. It was mentioned in Section 3.2.1 that the in-house LES code LULES used here is applicable to 3D geometries formed by rotating a 2D orthogonal grid formed in an $x - r$ plane. In the present case this imposes no restrictions as the annular swirl duct, dump expansion chamber and exhaust duct are all axisymmetric. The modular injector geometry is well described by generating a single $x - r$ plane mesh and rotating this about the geometric centreline ($r = 0$). To generate the $x - r$ plane mesh the commercial software ICEMCFD was used as it incorporates a wide range of meshing schemes that provide the user with the necessary control to ensure a high level of mesh quality. To define the computational domain completely, LULES requires three separate files specifying x, r and θ coordinates in a particular native format. To simplify the translation procedure, Plot3d was selected as the output format from ICEMCFD as it is broadly similar to that required by LULES. To facilitate comparison between LES and RANS-based methods it was convenient to use an identical computational mesh for all calculations. This was achieved by taking further advantage of the Plot3d format which can be read by both Delta and Fluent CFD codes described in Sections 3.2.2 and 3.2.3 respectively. It was then possible to utilise the coordinates obtained from the $x - r$ plane together with an in-house Fortran code to complete the geometry definition. For LULES this simply involved generating θ coordinates, where the k^{th} coordinate was obtained from $\theta_k = (2\pi/n_k)(k-1)$. A different routine was required for Delta and Fluent as 3D geometries are specified in terms of x, y and z coordinates, rather then x, r and θ. Using single index notation to relate locations in 3D Cartesian space (ijk) to locations in the 2D $x - r$ plane (ij), together with the k^{th} θ coordinate, the following relationships were used: $x(ijk) = x(ij)$, $y(ijk) = r(ij)\cos\theta(k)$ and $z(ijk) = r(ij)\sin\theta(k)$. The result is a polar-type structured mesh such as that shown in Figure 3.4. This consists of 25 individual blocks which help to ensure that mesh quality is maintained

and are necessary for utilising the parallel capability of the CFD code. In Section 2.1.2 it was mentioned that previous experimental work by Midgley [13] indicated that vortex shedding from the corner of the downstream blockage exerted an influence on the flow up to $x/D_s \approx 5.25$. As a result the computational outlet plane was positioned downstream of the this location at $x/D_s = 5.58$. During the course of this study a number of grid densities were investigated. It was found that the nodal distribution in the near-wall region was critical to the formation of coherent structures. As a result any further discussion regarding the computational mesh is left until Chapter 5 following a fuller discussion of experimental observations presented in Chapter 4.

3.4.1 Inlet Boundary Conditions

It was emphasised in Section 3.2 that the boundary conditions required by LES and RANS CFD codes differ. LES predictions require the specification of all three instantaneous velocity components (u_x, u_r, u_θ) at each time step whilst URANS-based methods use ensemble (time) averaged velocity components $(\langle u_x \rangle, \langle u_r \rangle, \langle u_\theta \rangle)$ in addition to statistical quantities, such as k and ϵ, representative of the turbulence. For LES calculations, although more refined methods are available, and much research is underway to develop these (see, for example Robinson [86]), a simple random noise superposition approach was used. Any instantaneous quantity is obtained by the addition of a disturbance to its statistically averaged time-mean value in the following way:

$$\phi(x_i, t) = \langle \phi(t) \rangle + \phi'(x_i, t) \tag{3.76}$$

In the present case, time-averaged quantities, $\overline{\phi}(x_i)$, were calculated based on a knowledge of mass and tangential momentum flow rate, $\dot{m}$ and $\dot{G}_\theta$ respectively, derived from PIV data at the swirler exit, $x/D_s = 0.02$. Since mass flow rate is a conserved quantity and tangential momentum flow rate decays only as a result of wall friction [123], these are suitable system properties with which to specify physically realistic velocity components at the inlet plane. Both $\dot{m}$ and $\dot{G}_\theta$ can be expressed as generalised surface integrals in the following way:

$$\int \rho\phi\vec{u} \cdot d\vec{A}\Big|_{in} = \int \rho\phi\vec{u} \cdot d\vec{A}\Big|_{x/D_s=0.02} \tag{3.77}$$

In order to provide the three instantaneous velocity components required by LES a random disturbance was added at each time step. A library routine was used to generated a random number from a distribution with zero mean and unit variance. This was then scaled by an r.m.s velocity magnitude, $\langle u'_{\mathrm{tot,in}} \rangle$, obtained from an assumed turbulence intensity, TI, of 5%. It should be

noted that although a number of simplifications have been made leading to a highly ideaised scenario there is sufficient evidence in the avaliable literature [52, 50, 53, 55] to suggest that precise details, such as modelling the discrete blockage effects of the radial slots or specifying turbulence with particular spatial / temporal correlations at the inlet plane, do not influence the development of coherent structures within the swirl duct provided the computational inlet plane is sufficiently far upstream of the important region of the flow as in the present case. As reasoned by Wang et al. [52] this is most likely due to the fact that the incoming turbulence is overshadowed by the strong shear-layer and high turbulent intesnity generated by swirling flowfields.

For RANS calculations identical values of $\langle u_r \rangle_{\text{in}}$ and $\langle u_\theta \rangle_{\text{in}}$ were used. Values of k_{in} and ϵ_{in} were prescribed at the inlet plane in order to provide a statistical representation of the turbulence using the following:

$$k_{in} = \frac{3}{2}\left(\sqrt{\langle u_r \rangle_{\text{in}}^2 + \langle u_\theta \rangle_{\text{in}}^2} I\right)^2 \tag{3.78}$$

$$\epsilon_{in} = C_\mu^{3/4} \frac{k_{\text{in}}^{3/2}}{\ell} \tag{3.79}$$

where $\ell = 0.07 x_{\text{in}}$ and $C_\mu = 0.09$

3.5 Closure

This chapter has described the mathematical background of LES and URANS ($k-\epsilon$ and RST) CFD methodologies along with the implementation of these within the in-house and commercial CFD codes utilised during this thesis. The topics of mesh generation, assumptions made regarding the modular swirler geometry and the calculation of appropriate boundary conditions were also discussed.

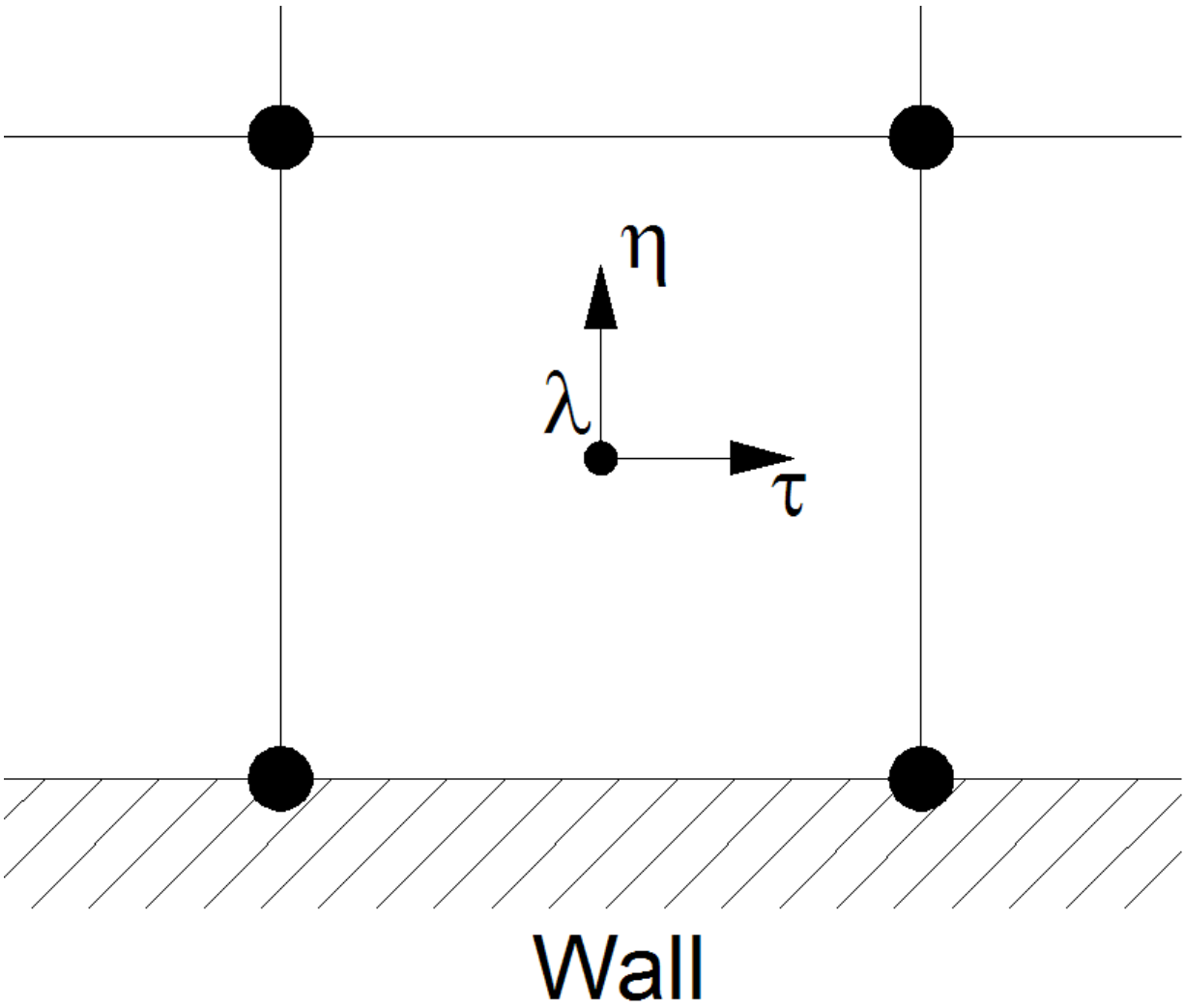

Figure 3.1: Local wall coordinate system of Fluent

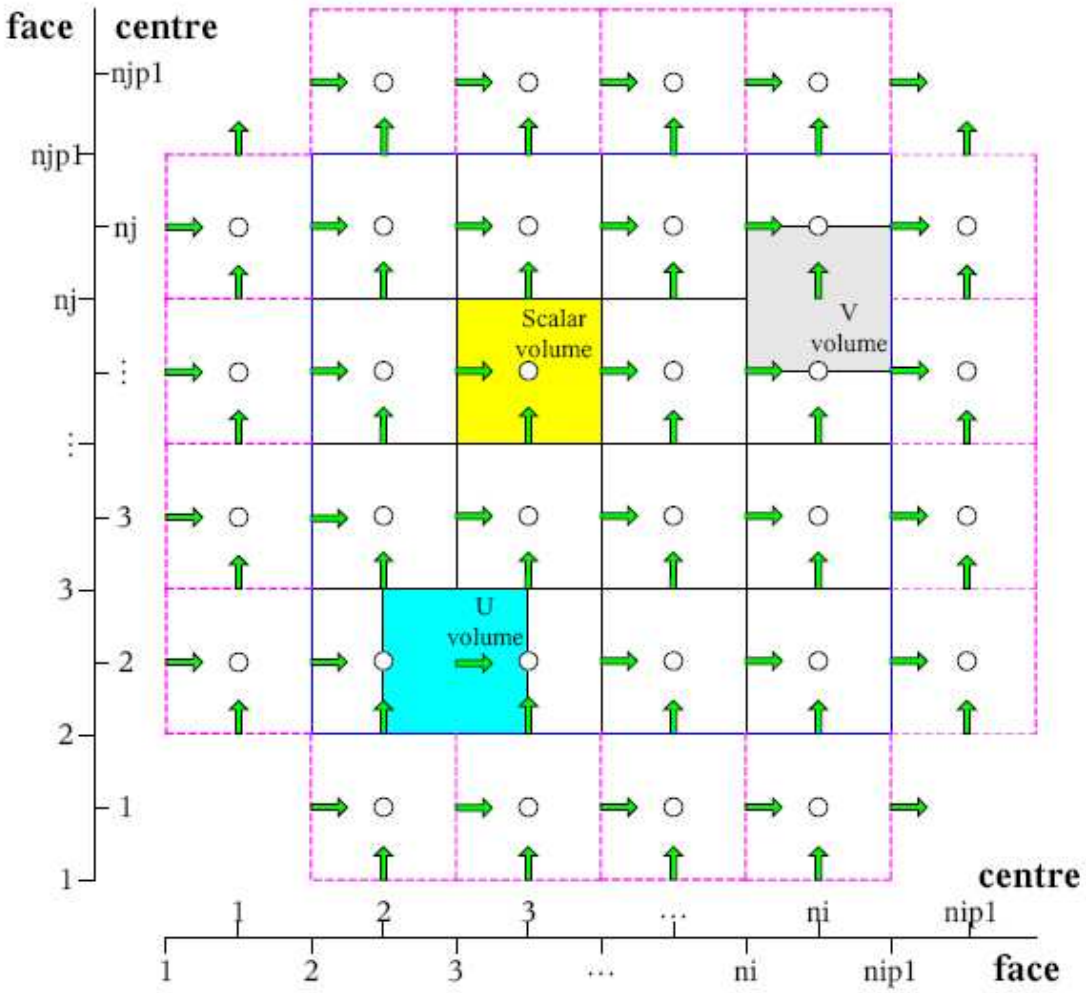

Figure 3.2: LULES staggered grid arrangement [109]

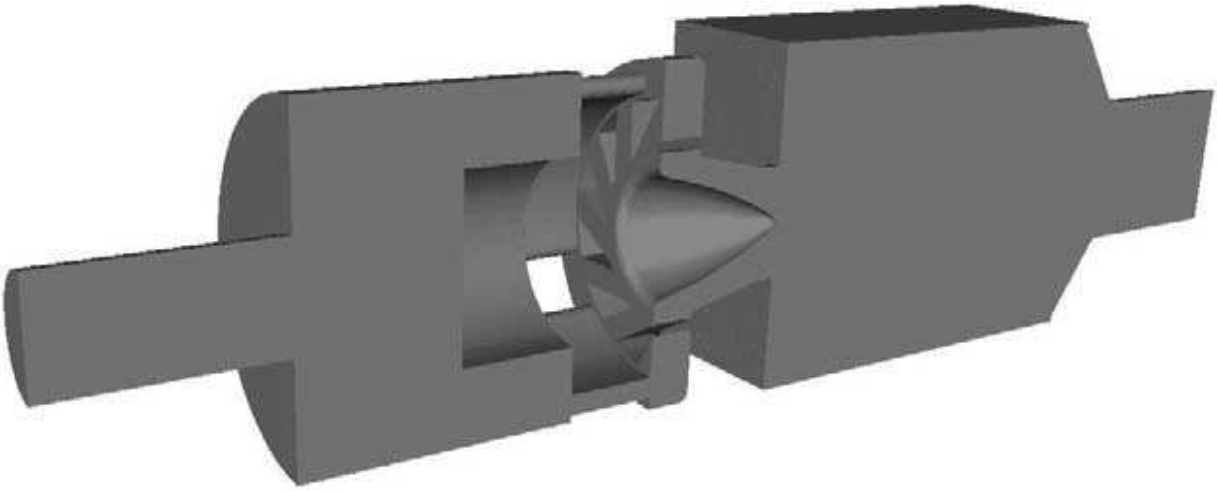

(a) Cross-section of computational domain with Turbomeca swirl injector

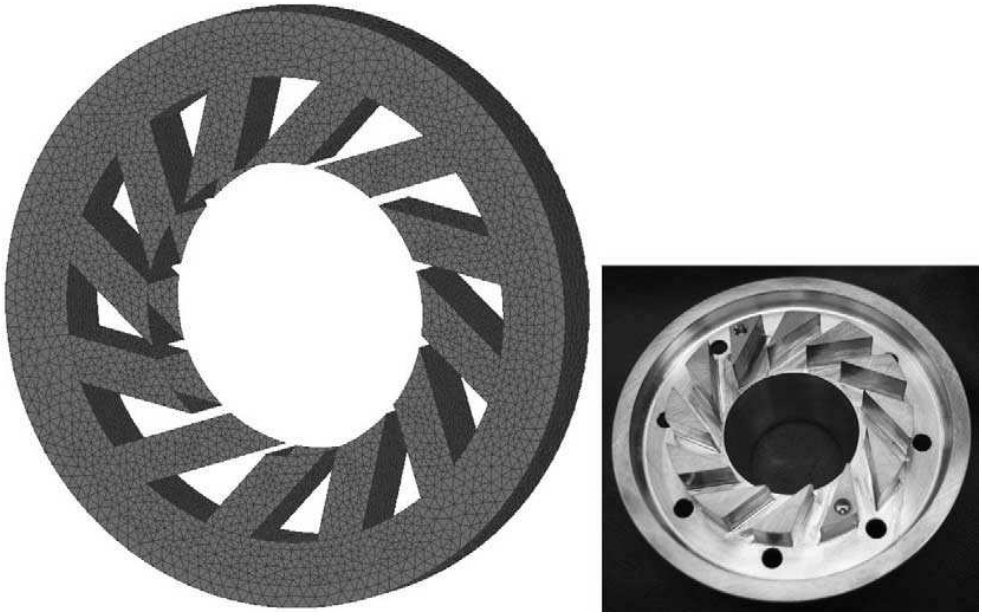

(b) Detail of Turbomeca swirl vanes

Figure 3.3: Computational domain of Lartigue et al. [68]

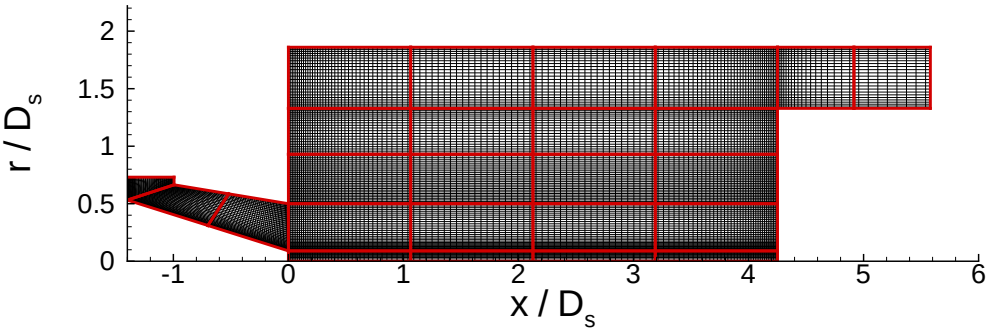

(a) $x - r$ Plane

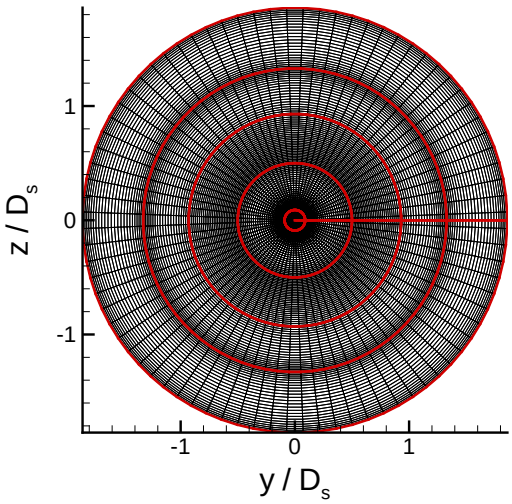

(b) $r - \theta$ Plane at Swirler Exit $x/D_s = 0.02$

Figure 3.4: Typical LPP swirler computational mesh

Chapter 4

Experimental Results

The modular swirler with varying swirl vane angle, α_1, has been investigated previously and reported in Midgley [13] and Midgley et al. [15] utilising a combination of PIV and HWA. In order to optimise key instrumentation setup parameters, such as Δt, PIV measurements were performed in water and were used primarily to acquire statistical information and provided the basis for CS eduction methods. As PIV measurements were performed at a relatively low sampling frequency of 15Hz, companion HWA data with a temporal resolution of 25kHz were used to deduce spectral information from velocity time-histories acquired in the vicinity of the CS. Although these complementary measurements provide a valuable insight into the influence of S_{N} on CS development, there are a number of limitations of the Midgley data with regard to CFD validation. For example, PIV measurements in $x-r$ and $r-\theta$ planes were performed with relatively large FoVs (approximately 80×80mm in size). As already highlighted in Section 2.3.4, this can lead to significant levels of SGF which contaminates second-order statistics such as r.m.s velocities and shear-stresses. In order to validate the computational predictions to be presented in Chapters 5 and 6 it was argued it is necessary to refine the FoV size (in Section 2.4.1 it was shown that a FoV of approximately 40×30mm yielded $\langle u'_{x,\mathrm{meas}}\rangle/\langle u'_{x,\mathrm{true}}\rangle$ and $\langle u'_{r,\mathrm{meas}}\rangle/\langle u'_{r,\mathrm{true}}\rangle \geq 0.9$ remote from the walls of the test section) such that the influence SGF on reported second-order statistics was minimised. In the $r-\theta$ plane, the Midgley PIV measurements were only performed at the swirler exit ($x/D_s = 0.02$), therefore additional measurements were acquired in the present study at $x/D_s = 0.27, 0.53, 1.06$ and 2.39 with the latter being useful for understanding far-field behaviour, which is often characterised by the presence of a PVC. From HWA spectra presented in [15] characteristic frequencies, and thus dominant instability modes, were seen to be a strongly dependent on swirl vane angle. No PIV measurements were performed for $\alpha_1 = 15^\circ$ and therefore gaining an insight into this flowfield through CS eduction techniques is of current interest.

In order to establish a complete understanding of the influence of S_{N}, Section 4.1 utilises first and second order statistics to explore global flow features such as central and corner recirculation zones and identify regions of high turbulence which may be indicative of the presence of

CS. Subsequent analysis in Section 4.2 then uses a combination of instantaneous PIV measurements, HWA measurements presented in [13] and CS eduction techniques, such as conditional and rotational-averaging, to investigate further their nature and significance. Finally, based on this analysis, a suitable test case is selected with which to assess the ability of Large Eddy Simulation (LES) and Unsteady Reynolds-Averaged Navier-Stokes (URANS) CFD methodologies (Chapters 5 and 6 respectively) to capture the observed physics.

4.1 Time-Averaged Velocity Field

First and second-order statistics presented in this section were acquired from two orthogonal PIV measurement planes ($x-r$ and $r-\theta$) as detailed in Table 2.1. Comparisons between $\langle u_r \rangle$ and $\langle u'_r \rangle$ which are common to both measurement planes have already been made at various axial locations (see Section 2.4.3) and have been shown to be in good agreement. For information regarding the convergence and accuracy of statistics presented here the reader is referred to Sections 2.4.4 and 2.4.5. All $r-\theta$ plane statistics ($\langle u_\theta \rangle$, $\langle u'_\theta \rangle$ and $\langle u'_r u'_\theta \rangle$) have been circumferentially-averaged as described in Section 2.1.4.

Figure 4.1 shows time-mean streamtraces in the expansion chamber superimposed on contours of time-mean axial velocity for varying swirl vane angle, α_1. There are many similarities between Figures 4.1(a)-(d) which are characteristic of confined swirl flows, such as the CRZ and CTRZ. Clearly, α_1 exerts a notable influence on the swirl cone deflection angle and the size and shape of the CRZ which is defined by the reattachment location of the outer swirler shear-layer on the outer wall of the expansion chamber, x_{L}/D_s. For $\alpha_1 = 30^\circ$, this is located at $x_{\mathrm{L}}/D_s \approx 1.45$ whilst reducing the swirl vane angle to $\alpha_1 = 10^\circ$ results in a downstream movement to $x_{\mathrm{L}}/D_s \approx 2.5$. These observations are due to a reduced radial pressure gradient ($\partial p/\partial r$) which balances centripetal accelerations ($\rho u_\theta^2/r$) as defined in Equation 1.3. Despite this reduction in radial pressure gradient at $\alpha_1 = 10^\circ$, the corresponding axial pressure gradient to which it gives rise is still sufficient for vortex breakdown within the expansion chamber which is characterised by strong negative velocities in the vicinity of the centreline, indicated by blue contour values.

Figures 4.2 to 4.4 show radial profiles of time-mean axial, radial and tangential velocity obtained at $x/D_s = 0.02, 0.27, 0.53$ and 1.06 for varying α_1. Axial and radial velocities have been corrected for perspective projection error using the procedure outlined in Section 2.4.3. In order to quantify levels of swirl intensity, the non-dimensional swirl number, S_{N} (Equation 1.4), was computed based on axial and tangential velocity profiles at the swirler exit ($x/D_s = 0.02$) as detailed below in Table 4.1.

α_1	$\dot{m}$	$\dot{G}_x$	$\dot{G}_\theta$	S_N	$U_{x,s}$	T_s
30	2.15	5.26	7.82×10^{-2}	0.80	2.0	0.02
20	2.15	4.77	6.39×10^{-2}	0.71	2.0	0.03
15	2.15	4.47	5.22×10^{-2}	0.62	2.0	0.04
10	2.15	4.27	4.12×10^{-2}	0.51	2.0	0.05

Table 4.1: Swirler exit flow rates calculated at $x/D_s = 0.02$

To ensure the best possible estimate of the swirl duct conservative quantities, integration was performed from $0.09 \geq r/D_s \leq 0.5$. Furthermore, axial velocities of less than zero were not included in the integral as these are associated with reverse flow due to vortex breakdown in the expansion chamber and not the forward flow from the swirl duct. It was found that exclusion of these points had a negligible effect ($\approx 2\%$) as they are located at small radii. In Table 4.1, T_s is a timescale based on tangential momentum flow rate, $\dot{G}_\theta$ (from Equation 1.4), which is useful for characterising the rotation rate of the flowfield in the vicinity of the swirler exit. It has been derived from the following relationship:

$$T_s = \frac{\pi D_{s,\mathrm{mid}}}{U_{\theta,s}} = \frac{\pi D_{s,\mathrm{mid}} U_{x,s}}{G_\theta} \int_{r_1}^{r_2} r^2 dr = \frac{\pi D_{s,\mathrm{mid}} U_{x,s}}{3G_\theta} \left(r_{\mathrm{outer}}^3 - r_{\mathrm{inner}}^3\right) \tag{4.1}$$

At $x/D_s = 0.02$ increasing α_1 from 10° to 30° results in the axial velocity distribution moving from a close to uniform profile to a heavy outer wall bias as shown in Figure 4.2(a). The negative axial velocities observed at $r/D_s > 0.09$ for $\alpha_1 = 20°$ and 30° indicate a time-mean penetration of the CRTZ into the swirl duct which extends from $0.09 \geq r/D_s \leq 0.5$. The corresponding radial velocities shown in Figure 4.3(a) exhibit a peak value that increases in magnitude and moves further inboard as a function of α_1. For $\alpha_1 = 15°, 20°$ and 30° positive radial velocities at $x/D_s = 0.02$ indicate that the radial pressure gradient experienced by the swirl duct exit flow is sufficient to deflect it outwards away from the centreline. This is in contrast to $\alpha_1 = 10°$ in which negative radial velocities suggest a significant decrease in radial pressure gradient and the flow continues on a path defined by the inner wall of the swirl duct. The combination of negative axial velocity and positive radial velocity at $x/D_s = 0.02$, $r/D_s > 0.09$ is indicative of flow separation from the inner wall of the swirl duct. This is shown more clearly in Figure 4.5 which displays time-mean velocity vectors superimposed on contours of time-mean axial velocity in the near-field of the swirler exit ($x/D_s < 1$). Profiles of tangential velocity at $x/D_s = 0.02$ shown in Figure 4.4(a) are of a Rankine-type distribution for all α_1. Further downstream in the expansion chamber at $x/D_s = 0.27, 0.53$ and 1.06, Figures 4.2(b)-(d) and 4.3(b)-(d) show that the location of peak axial and radial velocity moves radially outwards as a function of α_1. This is consistent with Figure 4.1 in which the swirl cone deflection angle was observed to increase with α_1. Negative axial velocities are observed at the geometric centre of the expansion chamber

($r/D_s = 0$) for all axial stations investigated. Again, this is a result of the vortex breakdown phenomena described in Section 1.2.1 caused by a strong coupling between axial and radial pressure gradients. It should be noted that downstream tangential velocities presented in Figures 4.3(b)-(d) do not extend to the outer wall of the expansion chamber and terminate at $r/D_s \approx 1.2$. This is a result of limited optical access in the $r-\theta$ measurement plane as discussed in Section 2.4.2. The overall agreement of $\langle u_x \rangle$ and $\langle u_r \rangle$ in the FoV overlap region ($r/D_s \approx 0.8-1.0$) is good apart from at $x/D_s = 1.06$ for $\alpha_1 = 20°$ and 30°. The reason for these discrepancies is not immediately clear, however they could be related to the fact that, in comparison to $x/D_s = 0.27$ and 0.53, all time-mean and r.m.s (Figures 4.6(d), 4.7(d) and 4.8(d)) velocity components are of considerable magnitude and approach a local maximum in this region which may have some cumulative influence.

Figures 4.6 to 4.8 show radial profiles of axial, radial and tangential r.m.s velocities for varying α_1. It should be noted that axial and radial r.m.s velocities shown in Figure 4.6 and 4.7 respectively were obtained from the $x-r$ measurement plane and have been corrected for SGF effects using the correction methodology presented in Section 2.3.4 and are therefore taken as a best estimate of the 'true' values. The difficulties associated with implementing this correction methodology in the $r-\theta$ plane were discussed in Section 2.4.2 and, as a result, r.m.s tangential velocities shown in Figure 4.8 remain uncorrected. As flow from the swirl duct enters the expansion chamber, inner and outer shear-layers are formed as a result of the velocity difference between it and the CTRZ and CRZ respectively. The inner shear layer is characterised by peak axial and radial r.m.s velocities (Figures 4.6 and 4.7) which are observed to move radially outwards as a function of α_1 and downstream distance from the swirler exit. The outer shear layer is identified as the secondary peak located at relatively large radii which is observed most clearly at $x/D_s = 0.27$, $r/D_s \approx 0.6$ in Figures 4.6(b) and 4.7(b). In general, the magnitude of peak axial and radial r.m.s velocities associated with the inner shear layer increases as a function of α_1, however, at $x/D_s = 0.02$ Figures 4.6(a) and 4.7(a) indicate that $\alpha_1 = 15°$ exceeds $\alpha_1 = 20°$. At $x/D_s = 0.02$, a distinct peak in tangential r.m.s velocity is only observed away from the centreline for $\alpha_1 = 20°$ and 30° which suggests that the strength of the inner azimuthal shear layer is diminished for $\alpha_1 = 10°$ and 15°. Further downstream at $x/D_s = 0.27$, 0.53 and 1.06, the distribution of tangential r.m.s velocity is also quite different to axial and radial counterparts in the sense that distinct peaks indicative of inner and outer shear layers are not such a prominent feature. Although axial, radial and tangential r.m.s velocity levels are broadly similar at $x/D_s = 0.02$, comparison of Figures 4.6(b)-(d) and 4.7(b)-(d) with Figure 4.8(b)-(d) shows that the tangential component decays more rapidly than axial and radial counterparts. In the vicinity of the centreline ($r/D_s \approx 0$) at $x/D_s = 1.06$, similar levels of axial r.m.s velocity are observed for all α_1, however, there is a notable increase in both radial and tangential r.m.s components at this location for $\alpha_1 = 30°$. This is evidence of a highly turbulent flow structure with a strong dependence on the level of swirl. In a similar way

to $\langle u_x \rangle$ and $\langle u_r \rangle$, the overall agreement of $\langle u'_x \rangle$ and $\langle u'_r \rangle$ in the FoV overlap region is good with the exception of at $x/D_s = 1.06$ for $\alpha_1 = 20°$ and 30°. This may be attributed to the fact that all three time-mean and r.m.s velocity components approach a local maximum in this region as discussed above.

Figures 4.9 and 4.10 show radial profiles of $\langle u'_x u'_r \rangle$ and $\langle u'_r u'_\theta \rangle$ for varying α_1 ($\langle u'_x u'_\theta \rangle$ cannot be obtained from 2C-PIV applied in two orthogonal planes as detailed in Table 2.1). At $x/D_s = 0.02$, a strong coupling exists between u'_x and u'_r which produces a region of negative $\langle u'_x u'_r \rangle$ across the extent of the swirler exit. In a similar way to peak r.m.s levels (Figures 4.6 to 4.8), the location of maximum $\langle u'_x u'_r \rangle$ moves radially outwards as a function α_1. Regions of negative $\langle u'_x u'_r \rangle$ persist further downstream at $x/D_s = 0.27$, 0.53 and 1.06, however, in the vicinity of the outer shear layer an area of positive correlation can be observed. In comparison to $\langle u'_x u'_r \rangle$, peak levels of $\langle u'_r u'_\theta \rangle$ (Figure 4.10) are reduced by between one-half ($\alpha_1 = 15°$) and one-sixth ($\alpha_1 = 30°$) at the swirler exit. At $x/D_s = 0.02$, reducing α_1 results in the appearance of a region of positive $\langle u'_r u'_\theta \rangle$ across the swirler exit ($0.09 \leq r/D_s \leq 0.5$) indicating a fundamental change in the spatial structure of turbulence. It is interesting to observe that, despite notable levels of r.m.s velocity in the vicinity of the centreline, $\langle u'_x u'_r \rangle$ and $\langle u'_r u'_\theta \rangle$ are negligible. This is particularly notable at $x/D_s = 1.06$ and is consistent with the Rankine-type distribution of time-mean tangential velocity (Figure 4.4(d)) in which the inner forced region is expected to be shear or strain free [17].

Observed differences in Reynolds-stress distribution and magnitude indicate a high level of anisotropy in the flows currently under consideration. In order to characterise the local state of Reynolds-stress anisotropy the 'flatness parameter' or 'anisotropy index' introduced by Lumley [124] is often used. To compute this $\langle u'_x u'_\theta \rangle$ is required which is unavailable in the present case as discussed above. As an alternative, the anisotropy of the normal Reynolds-stresses is assessed in the swirl cone at $x/D_s = 0.27$ and in the CTRZ at $x/D_s = 1.06$ for varying α_1 from the ratio $\langle u'_i u'_i \rangle / k$. The swirl cone is bounded by the CRTZ and CRZ with inner and outer radii ($r_{\mathrm{SC,inner}}$ and $r_{\mathrm{SC,outer}}$) which are defined here as the peaks observed in u'_x and u'_r in Figures 4.6(b) and 4.7(b). The mid-radius of the swirl cone is thus defined as $r_{\mathrm{SC,mid}} = r_{\mathrm{SC,inner}} + 1/2(r_{\mathrm{SC,outer}} - r_{\mathrm{SC,inner}})$. The radius of the CTRZ (r_{CRTZ}) is defined as the first radial point from the centreline at which $\langle u_x \rangle = 0$ at $x/D_s = 1.06$. Figure 4.11 shows $r_{\mathrm{SC,inner}}$, $r_{\mathrm{SC,outer}}$, $r_{\mathrm{SC,mid}}$ and r_{CRTZ} for $\alpha_1 = 30°$. In order to compare varying α_1 across the swirl cone at $x/D_s = 0.27$ radial distances in Figure 4.12 have been normalised by $(r - r_{\mathrm{SC,mid}})/(r_{\mathrm{SC,outer}} - r_{\mathrm{SC,inner}})$. Similarly, for comparisons across the CTRZ at $x/D_s = 1.06$ radial distances in Figure 4.13 have been normalised by r/r_{CRTZ}. The horizontal dashed line in Figures 4.12 and 4.13 corresponds to isotropic turbulence in which $\langle u'_x u'_x \rangle / k = \langle u'_r u'_r \rangle / k = \langle u'_\theta u'_\theta \rangle / k = 2/3$. From Figure 4.12 $\langle u'_x u'_x \rangle / k$ and $\langle u'_r u'_r \rangle / k$ follow a similar trend across the majority of the swirl cone ($-0.5 \leq r - r_{\mathrm{SC,mid}}/r_{\mathrm{SC,outer}} - r_{\mathrm{SC,inner}} \leq 0.25$)

for $\alpha_1 = 30°$, $20°$ and $15°$ and deviate quite significantly from the line of isotropic turbulence. Although $\langle u'_\theta u'_\theta \rangle / k$ is similar for all α_1, $\langle u'_x u'_x \rangle / k$ and $\langle u'_r u'_r \rangle / k$ are quite different for $\alpha_1 = 10°$ with the former tending towards the line of isotropic turbulence at $r_{\mathrm{SC,mid}}$ and the latter away from it at this location. From Figure 4.13 $\langle u'_x u'_x \rangle / k$, $\langle u'_r u'_r \rangle / k$ and $\langle u'_\theta u'_\theta \rangle / k$ follow a similar trend across the CTRZ for $\alpha_1 = 20°$, $15°$ and $10°$ and are closely distributed around the line of isotropic turbulence. This is in contrast to $30°$ which deviates more significantly from isotropy. Figures 4.12 and 4.13 imply significant levels of normal Reynolds-stress anisotropy for all α_1 in the swirl cone, whilst in the vicinity of the CRTZ these levels are largest for $\alpha_1 = 30°$ and lower levels of swirl ($\alpha_1 = 20°$, $15°$ and $10°$) display a more isotropic behaviour. These observations will have implications for companion computational predictions presented in Chapters 5 and 6 particularly the $k - \epsilon$ model in which each of the turbulent normal and shear stresses should be calculated from the same (isotropic) eddy-viscosity.

In order to make a global assessment of regions of peak turbulence, Figure 4.14 shows contours of time-mean turbulent kinetic energy (based on u'_x and u'_r) for varying α_1. In each case, peak levels of turbulence are observed in the near-field of the swirler exit ($x/D_s < 1$) at the interface of the swirl stream and CTRZ. The decay of peak turbulence with α_1 is consistent with trends identified in profiles of r.m.s velocity components (Figures 4.6 to 4.8). For $\alpha_1 = 30°$, considerable levels of turbulence ($k/U^2_{x,s} \approx 0.1$) are present along the centreline of the expansion chamber. This is in contrast to $\alpha_1 = 10°$, $15°$ and $20°$ in which negligible turbulence is observed at this location at downstream distances of $x/D_s > 0.5$. To complement Figure 4.14, Figures 4.15 and 4.16 show the distribution of time-mean turbulent kinetic energy (based on u'_r and u'_θ) in $r - \theta$ planes at $x/D_s = 0.02$ and 2.39 respectively. At $x/D_s = 0.02$, there is a close to axisymmetric distribution of turbulence with peak magnitudes comparable to those in the $x - r$ plane shown in Figure 4.14. For $\alpha_1 = 30°$, Figure 4.16 reveals an axisymmetric distribution of turbulence in the far-field with peak maxima concentrated at the geometric centre of the expansion chamber. A similar axisymmetric distribution is also observed for $\alpha_1 = 20°$ although levels are much reduced relative to $\alpha_1 = 30°$. For $\alpha_1 = 10°$ and $15°$ the situation is quite different with a more or less uniform distribution of turbulence of comparatively negligible magnitude.

The first and second-order single-point statistics presented above provide a valuable insight into the influence of α_1 on many fundamental aspects of flowfields typical of swirl injectors. The regions of high turbulence and shear identified through this analysis are of particular interest as these are often indicative of the presence of CS. In order to gain an improved understanding of these regions, the following section utilises a combination of instantaneous PIV velocity fields, CS eduction techniques and spectral information deduced from HWA presented in Midgley [15].

4.2 Coherent Structure Analysis

Within Figures 4.14 to 4.16, high levels of time-mean turbulent kinetic energy were observed at the interface of the swirl stream and CTRZ and, for $\alpha_1 = 20°$ and 30°, in the vicinity of the expansion chamber centreline. These regions are investigated further in Sections 4.2.1 and 4.2.2 respectively.

4.2.1 Near-Field

An important point raised by Adrian et al. [61] with regard to the analysis of instantaneous velocity fields is the influence of convection velocity. This is intimately linked to the definition of a vortex proposed by Kline and Robertson [60] which states that: *"A vortex exists when instantaneous streamlines mapped onto a plane normal to the core exhibit a roughly circular or spiral pattern, when viewed in a reference frame moving with the centre of the vortex core"*. This implies that a velocity field must be viewed in a frame of reference that moves at the same speed as the core of the vortex, i.e. at the local convection velocity. For flows similar to those considered here Midgley [13] has shown that a classical Reynolds-decomposition (i.e. subtraction of the time-mean flow from each instantaneous realisation) is suitable for these purposes. A second key condition proposed in [61] is that the vorticity is concentrated in a 'core'. Based on these considerations, Figure 4.17 shows instantaneous (Figures 4.17(a), (c) and (e)) and Reynolds-decomposed (Figures 4.17(b),(d) and (f)) streamtraces on contours of azimuthal vorticity, ω_θ, (Equation A-19) for $\alpha_1 = 30°$ at three arbitrary time-instants (I, II and III) in an $x-r$ measurement plane within the near-field of the swirler exit (region B_1 in Table 2.6). Similarly, Figure 4.18 shows instantaneous (Figures 4.18(a), (c) and (e)) and Reynolds-decomposed (Figure 4.18(b), (d) and (f)) streamtraces on contours of axial vorticity, ω_x, in an $r-\theta$ plane at $x/D_s = 0.02$ at arbitrary time-instants for $\alpha_1 = 30°$. It should be noted that the time-instants shown in Figure 4.17 do not correspond to those in Figure 4.18 as these were acquired during separate tests in different measurement planes. From Figure 4.17, the presence of CS in both inner and outer shear-layers shed from the swirler exit are clearly visible and coincide with regions of peak ω_θ. It is reasonable to assume that these are responsible for the regions of high time-mean turbulent kinetic energy (Figure 4.14(a)), particularly in the vicinity of the inner shear-layer. Although removal of the time-mean velocity field alters the observed $x-r$ plane vortical structures to some extent, the influence is much more pronounced in the $r-\theta$ plane as shown in Figure 4.18. In general, the instantaneous velocity field (Figures 4.18(a), (c) and (e)) is characterised by a turbulent structure consisting of two large vortices separated by approximately π radians which rotate about their own axes in the direction of the bulk flow, i.e. counter-clockwise with positive ω_x when viewed from $x/D_s > 0$. Following a thorough qualitative analysis of all 650 instantaneous velocity fields, this mode shape appeared in the majority of cases, however, there was some degree of variability such as that shown in Figure 4.18(e) in which no CS were detected. This suggests a bimodal switching between flow states, however the PIV measurements presented in

this thesis do not have the necessary temporal resolution to further investigate this transition. In addition to the vortex pair deduced from instantaneous streamtraces in a laboratory frame of reference, the Reynolds-decomposition (Figures 4.18(b), (d) and (f)) reveals the presence of a secondary vortex pair also separated by π radians and $\pi/2$ out of phase with the primary pair. In contrast to the primary pair which rotate about their axes in the same direction as the bulk flow, the secondary pair rotate about their respective axes in a clockwise direction with negative ω_x which is opposed to the bulk flow. It is suggested that these could not be detected from instantaneous streamtraces due to high levels of distortion caused by the presence of the mean flow, therefore, for the remainder of this thesis the majority of CS analysis will be performed on a Reynolds-decomposed, rather than instantaneous, basis.

Figures 4.19 and 4.20 show Reynolds-decomposed streamtraces in $x-r$ and $r-\theta$ measurement planes ($x/D_s = 0.02$) respectively at two arbitrary time-instants (I and II) for $\alpha_1 = 10°$, 15° and 20°. Although there is clear evidence of the presence of CS, the spatial coherence of the resulting vortex structure was found to decrease (relative to $\alpha_1 = 30°$) as a function of α_1 which is consistent with the reduced levels of time-mean turbulent kinetic energy (Figure 4.15). Although a qualitative assessment of instantaneous and Reynolds-decomposed velocity fields provides a means of identifying and characterising CS it constitutes a subjective approach which, as noted by Pope [7], can lead to controversy over their nature and significance. It is therefore essential that they are combined with qualitative measures and eduction techniques which are considered in the following.

The HWA measurements presented in Midgley [15] used a 5μm Dantec 55P11 miniature single hotwire with a maximum sampling frequency of 25kHz and frequency resolution of 6.1Hz. These measurements were performed in air and the reference scales of $D_s = 0.03763$m and $U_{x,s} = 27.19$m/s [13] give a Strouhal number range of $S_{t,\min} = 8.4 \times 10^{-3}$ to $S_{t,\max} = 34.6$. Instantaneous velocities measured with a single hotwire are sensitive to *all* flowfield velocity components normal to it, i.e. $u = \sqrt{(u_{n,1}^2 + u_{n,2}^2)}$. As a result it is not possible to recover individual velocity components from this arrangement; however, spectral analysis still allows any characteristic (tonal) frequencies of the velocity field to be identified. Figure 4.21 shows the PSDs of velocity presented in [13] for varying α_1 at $x/D_s = 0.27$ for various radial locations. It should be noted that the amplitude normalisation used in [13] is not clear and the following discussion focuses on the frequency content of the PSDs. The issue of PSD amplitude is addressed in Section 5.4.1. The majority of spectra for $\alpha_1 = 30°$ are characterised by primary and secondary peaks occurring at $S_t \approx 0.62$ and 1.24 respectively. Similar trends are also observed for $\alpha_1 = 20°$ although the secondary peak is not such a prominent feature and can only be identified at $r/D_s = 0.24$, 0.32 and 0.4. The prominence of the secondary peak continues to decrease as a function of α_1 and does not appear at all in spectra derived from $\alpha_1 = 15°$. For

this particular level of swirl, a primary peak at $S_t \approx 0.62$ is clearly visible at all radii with an amplitude comparable to spectra derived from $\alpha_1 = 20°$ and 30°. The most dramatic change in spectral characteristics is observed for $\alpha_1 = 10°$. For this level of swirl distinct peaks occurring at $S_t \approx 0.62$ and 1.24 are not a dominant feature and spectra are more reminiscent of high Re broadband turbulence.

The link between CS observed in the inner shear-layer of the swirl stream and the strongly periodic events observed in the spectra is clarified via spatial velocity correlations in $x-r$ (R_{uu} and R_{rr}) and $r-\theta$ (R_{rr} and $R_{\theta\theta}$) measurement planes for $\alpha_1 = 30°$ shown in Figures 4.22 and 4.23. In order to gain further insight into flow behaviour across the swirler exit, a number of reference points were selected at $r/D_s = 0.15$, 0.25 and 0.38 and are indicated by the yellow dot. To identify only the high energy turbulent events, a conditionally-averaged sub-set of data (Section A-2.3) was created by selecting only instantaneous velocity fields that exhibited fluctuating velocities greater than 1.5 standard deviations at each reference point (e.g. $u_i' > 1.5\langle u_i' \rangle$). In all cases, the number of samples, N_c, of the ensemble-averaged sub-set has been indicated. In the $x-r$ plane (Figure 4.22), both R_{uu} and R_{rr} exhibit sequential regions of positive and negative correlation indicating highly coherent events in this region. Conditionally-averaged velocity fields based on u_x' clearly reveal the presence of multiple CS, however, these appear disordered in comparison to those conditioned by u_r' which are characterised by three counter-rotating vorticies with an axial separation wavelength of $d/D_s \approx 0.32$ (see Figure 4.22(d)). In the $r-\theta$ plane (Figure 4.23), R_{rr} and $R_{\theta\theta}$ also exhibit distinct regions of positive and negative correlations and the conditionally-averaged velocity fields confirm the vortex structure previously identified in Figure 4.18. From Figure 4.23, the conditionally-averaged radial location of the vortex 'eyes' is at $r/D_s \approx 0.25$. At this location, Figure 4.4(a) shows that $\langle u_\theta \rangle / U_{x,s} \approx 1.1$. If it is assumed that a *single* vortex is convected at this velocity along a circular path of radius $r/D_s = 0.25$, this gives an angular velocity of $\omega = \langle u_\theta \rangle / r = 230$r/s and a corresponding $S_t = \omega D_s / 2\pi U_{x,s} = 0.7$ which is close to the primary peak of $S_t = 0.62$ presented in Figure 4.21. From this evidence the secondary peak of $S_t = 1.24$ must be associated with a vortex *pair* passing a fixed point and the appearance of higher harmonics at $S_t = 1.86$ and 2.48 are a result of the secondary pairing.

Based on Figures 4.22 and 4.23 u_r' appears to be a more suitable conditioning signal than u_x' in the $x-r$ plane and yields very similar results to u_θ' in the $r-\theta$ plane. Furthermore, as u_r' is common to both measurement planes and the location of the reference point exerts only a negligible influence on spatial correlations and CS; analysis for $\alpha_1 = 20°, 15°$ and 10° presented in Figures 4.24 and 4.25 is based only on $r/D_s = 0.25$ and u_r'. For $\alpha_1 = 20°$ and 15° in the $x-r$ plane, R_{rr} exhibits similar trends to $\alpha_1 = 30°$ and conditioned velocity fields are also characterised by counter-rotating vortices. However, the level of correlation between these is reduced relative to $\alpha_1 = 30°$ and the separation wavelength is increased ($d/D_s \approx 0.47$ for $\alpha_1 = 15°$ in Figure 4.24(b))

with only two visible within the experimental FoV. In the $r-\theta$ plane the conditionally-averaged velocity field reveals the presence of two vortical structures for $\alpha_1 = 20°$, however for $\alpha_1 = 15°$ it is increasingly difficult to identify any coherent motion. In a similar way to the $x-r$ plane, levels of R_{rr} for $\alpha_1 = 20°$ and $15°$ are reduced relative to $\alpha_1 = 30°$. From Figures 4.24(c) and 4.25(c) spatial correlations and conditional-averages suggest that no dominant CS exist for $\alpha_1 = 10°$. This is consistent with qualitative analysis presented in Figures 4.19(e)-(f) and 4.20(e)-(f) and velocity spectra in Figure 4.21.

Although conditional-averaging provides a valuable insight into CS the number of samples within each sub-set is relatively low ($N_c \leq 54$). In order to avoid this issue a rotational-averaging procedure (see Section A-2.2) was applied for varying α_1 at $x/D_s = 0.02$ in the $r-\theta$ plane. In keeping with analysis presented above, a Reynolds-decomposition was performed on each instantaneous velocity field to isolate turbulent motions. In order to track the motion of a single reference vortex (see Figure A-2) from low-speed PIV ($\Delta T = 0.25$s) its initial angular location ($\theta(t_0)$) was determined by applying Equation A-24 to the entire FoV, i.e. from $\theta = 0 - 2\pi$. At subsequent times its location was first estimated based on $\theta(t_n) \approx \theta(t_{n-1}) + \omega\Delta T$ (where t_{n-1} is its previous location, ω is the angular velocity of a single vortex defined above and ΔT is the PIV sampling interval) and then Equation A-24 applied to *either* $0 \leq \theta \leq \pi$ *or* $\pi < \theta < 2\pi$ depending on the estimated location within the FoV. The instantaneous velocity field from the original Cartesian PIV was then interpolated onto a polar-type mesh (see, for example, Figure 3.4(b)) and rotated by θ radians.

Figure 4.26 shows rotationally-averaged Reynolds-decomposed streamtraces at $x/D_s = 0.02$ superimposed on contours of $\langle u'_r \rangle_{\text{rot}}$ and $\langle u'_\theta \rangle_{\text{rot}}$ for $\alpha_1 = 30°$. The vortex pattern identified through qualitative analysis and conditional-averaging (Figures 4.18 and 4.23 respectively) consisting of two pairs of counter-rotating vortices is clearly visible. These are centred on regions defined by $\langle u'_r \rangle_{\text{rot}} = \langle u'_\theta \rangle_{\text{rot}} = 0$ and the large circumferential gradients of $\langle u'_r \rangle_{\text{rot}}$ and large radial gradients of $\langle u'_\theta \rangle_{\text{rot}}$ in the vicinity of the vortices gives rise to a component of rotationally-averaged axial vorticity, $\langle \omega_x \rangle_{\text{rot}}$ (calculated from Equation A-20 due to the polar-cylindrical coordinate basis used for rotational-averaging), as shown in Figure 4.27(a). The regions of positive and negative $\langle \omega_x \rangle_{\text{rot}}$ result from the clockwise or counter-clockwise rotation of each vortex about its centre as discussed above. It is interesting to note that for $\alpha_1 = 20°$ (Figure 4.27(b)) rotational-averaging reveals an instability mode similar to $\alpha_1 = 30°$ which was not identified using the conditional-averaging technique. It is possible that this is due to the limited number of samples of the ensemble-averaged sub-set in the case of the latter. In comparison to $\alpha_1 = 30°$, the streamtrace distribution for $\alpha_1 = 20°$ is less smooth which suggests an increasing degree of incoherent motions and a reduced spatial coherence which has already been observed in R_{rr}. This is consistent with spectral analysis presented in Figure 4.21 in the sense that although $\alpha_1 = 30°$ and $20°$ both

exhibit broadly similar frequency characteristics the appearance of higher-order spikes associated with vortex parings is diminished in the case of the latter. For $\alpha_1 = 15°$ (Figure 4.27(c)) a quite different instability mode is apparent which is dominated by two vortex-like structures. Unlike for $\alpha_1 = 30°$ and $20°$ in which each vortex is defined by an approximately circular streamline distribution, these appear significantly more distorted and are consistent with those educed from conditional-averaging in Figure 4.25(b). The variation in the characteristic instability mode for $\alpha_1 = 15°$ relative to $\alpha_1 = 30°$ and $20°$ is again in accordance with the spectral analysis of Figure 4.21 in which only a single dominant spike appeared at $S_t \approx 0.62$. Although a number of vortical structure result from the application of rotational-averaging to $\alpha_1 = 10°$ (Figure 4.27(d)) this can not be classified as constituting a global instability mode.

Figure 4.28 shows rotationally-averaged Reynolds-decomposed streamtraces on contours of the ratio of rotationally-averaged to time-averaged (i.e. in a laboratory frame of reference) turbulent kinetic energy, $\langle k \rangle_{\mathrm{rot}}/k$, for varying α_1. In a laboratory frame of reference at a particular spatial location k is a function of coherent and incoherent velocity fluctuations of varying magnitude. In a rotating frame of reference there is a bias to both the magnitude and nature of the velocity fluctuations (i.e. whether they are coherent or incoherent) at a particular spatial location as the averaging procedure is necessarily 'locked' to a particular flow feature. This is highlighted in Figure 4.29 which shows a PDF of u'_r and u'_θ extracted at $x/D_s = 0.02$, $r/D_s = 0.25$, $\theta = \pi$ from laboratory and rotating frames of reference for $\alpha_1 = 30°$. In both cases, the distribution of u'_r is extremely similar. However, in the rotating frame reference, the distribution of u'_θ is much broader with the probability of encountering extreme values significantly increased relative to the laboratory frame of reference. For $\alpha_1 = 30°$, $\langle k \rangle_{\mathrm{rot}}$ exceeds k in the vicinity of the clockwise vortex pair located at $\theta = 0$ and π which indicates that this localised feature will contribute significantly to the regions of high time-averaged turbulence levels observed in Figure 4.15. Similar trends are also observed for $\alpha_1 = 20°$, however $\langle k \rangle_{\mathrm{rot}}/k$ is diminished across the majority of swirler exit plane and continues to reduce for $\alpha_1 = 15°$ before reaching an approximately uniform distribution for $\alpha_1 = 10°$.

4.2.2 Far-Field

In a similar way to the analysis of near-field CS presented in the previous section, a valuable insight into far-field behaviour is gained through a qualitative analysis of instantaneous and Reynolds-decomposed streamtraces. Figure 4.30 shows instantaneous streamtraces at $x/D_s = 2.39$ at three arbitrary time-instants (I, II and III) for varying α_1. For $\alpha_1 = 30°$, a significant displacement of the aerodynamic centre from the geometric centre (highlighted by a red dot) is observed which is indicative of a PVC. This rotates counter-clockwise about its own axis and has a time-dependent counter-clockwise rotation in the direction of the time-mean flow. For $S_{\mathrm{N}} = 0.75$, Syred et al. [38] measured a volumetric flow rate Strouhal number based on duct

diameter of $S_{t_{\dot{Q}}} \approx 0.9$ (Figure 1.10) for a tangential entry swirl burner. A similar broadband frequency spike of $S_t = 0.66 - 0.78$ has also been confirmed for the Turbomeca swirler with $\alpha_1 = 30°$ by Midgley [13] using HWA. This corresponds to $S_{t_{\dot{Q}}} = 0.84 - 0.99$ based on Equation 1.6 and $S_t = 1.24 \times 10^{-2} - 1.47 \times 10^{-2}$ based on D_s and $U_{x,s} = 1.99$m/s as given in Table 2.2. Similar behaviour is also observed for $\alpha_1 = 20°$ and $\alpha_1 = 15°$, however for $\alpha_1 = 10°$ it is increasingly difficult to identify a clear aerodynamic centre. In order to further quantify the behaviour of the PVC, Equation A-24 was used to determine its radial (r_{PVC}) and angular (θ_{PVC}) location at each time-instant. The computed location of the PVC is indicated by the blue dot in Figure 4.30 and is in excellent agreement with streamtraces from $\alpha_1 = 30°$, 20° and 15°. Although Equation A-24 clearly locates a vortex centre for $\alpha_1 = 10°$ these structures cannot be classified as a PVC and no further analysis is performed for this swirl vane angle. Figure 4.31 shows a PDF of the radial displacement of the PVC from the geometric centreline for $\alpha_1 = 30°$, 20° and 15°. It should be noted that the expansion chamber diameter, D_{ex}, has been used for normalisation rather than the swirler exit diameter, D_s, as in preceding sections. Interestingly, the mean radial displacement of the PVC, $\langle r_{\text{PVC}} \rangle / D_{ex}$, is inversely proportional to α_1 as detailed below in Table 4.2. It is possible that this is due to the influence of features such as the CRTZ (see Figure 4.1) which surround the PVC and may interact with it on an instantaneous basis.

α_1	$\langle r_{\text{PVC}} \rangle / D_{ex}$
30	3.49×10^{-2}
20	5.17×10^{-2}
15	6.47×10^{-2}

Table 4.2: Mean radial displacement of PVC at $x/D_s = 2.39$ for varying swirl vane angle

Figure 4.32 shows Reynolds-decomposed streamtraces at $x/D_s = 2.39$ at identical time-instants as Figure 4.30 for varying α_1. For $\alpha_1 = 30°$ and 20° the turbulent field forms two counter-rotating vortices which have been previously observed by Midgley [13] and Graftieux et al. [125]. It is these large fluctuations in the centreline region which contribute to the axisymmetric distribution of turbulence identified previously in Figure 4.16 for $\alpha_1 = 30°$ and 20°. Clearly, for $\alpha_1 = 15°$ and 10° a similar level of coherence is not observed and explains the relatively negligible levels of turbulence observed in Figures 4.16(c) and (d).

4.3 Closure

From the analysis presented in this chapter, the influence of swirl number on both near and far-field instability modes has been clearly established. For $\alpha_1 = 30°$, 20° and 15° CS were identified in the vicinity of the swirler exit whose spectral characteristics have a strong dependence on the level of swirl. In the case of $\alpha_1 = 10°$, no distinct peaks indicative of coherent vortex motion were identified in velocity spectra and these observations were confirmed through a combination

of spatial correlations and conditional-averaging techniques. In the far-field, turbulence levels at $x/D_s = 2.39$ were only notable for $\alpha_1 = 30^\circ$ and have been shown to be due to the presence of a PVC. If computational methods, such as URANS and LES, are to become integral to the design and development of swirl combustors it is of paramount importance that frequency components associated with CS are predicted with a high degree of fidelity. The most challenging test case with which to assess the suitability of these approaches is therefore $\alpha_1 = 30^\circ$ as this features both near and far-field instability modes exhibiting a wide range of characteristic frequencies and the highest levels of normal Reynolds-stress anisotropy. Large Eddy Simulation (LES) and Unsteady Reynolds-Averaged Navier-Stokes (URANS) calculations for $\alpha_1 = 30^\circ$ are presented in Chapters 5 and 6 respectively. When making comparisons it is informative to remember the experimental accuracy presented in Figure 2.22.

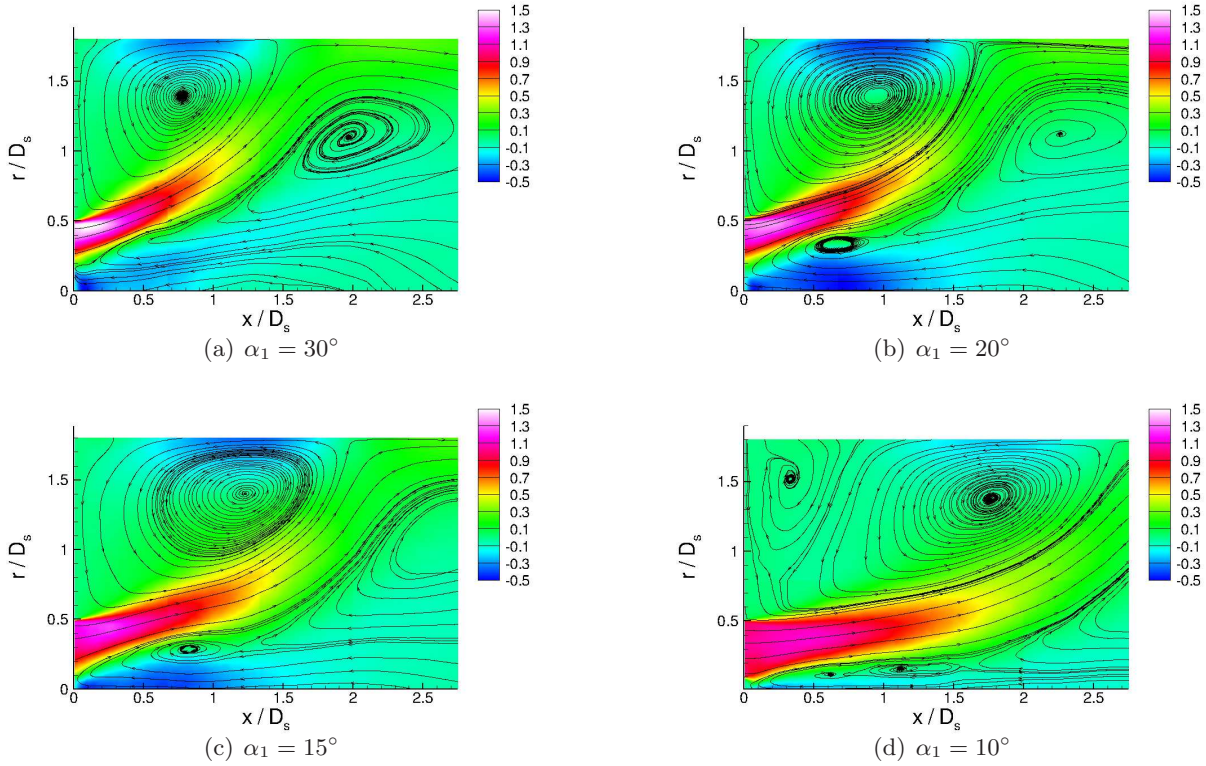

(a) $\alpha_1 = 30°$ (b) $\alpha_1 = 20°$

(c) $\alpha_1 = 15°$ (d) $\alpha_1 = 10°$

Figure 4.1: Time-mean streamtraces on contours of time-mean axial velocity, $\langle u_x \rangle / U_{x,s}$, in dump expansion chamber for varying swirl vane angle.

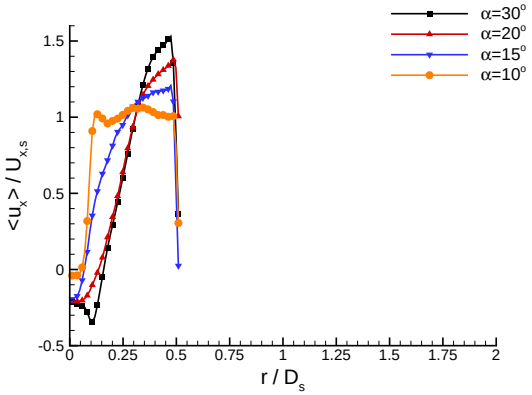

(a) $x/D_s = 0.02$

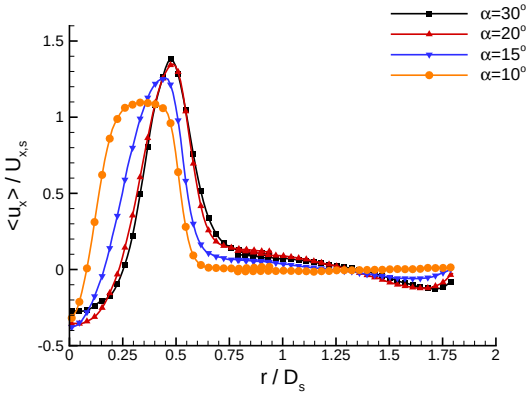

(b) $x/D_s = 0.27$

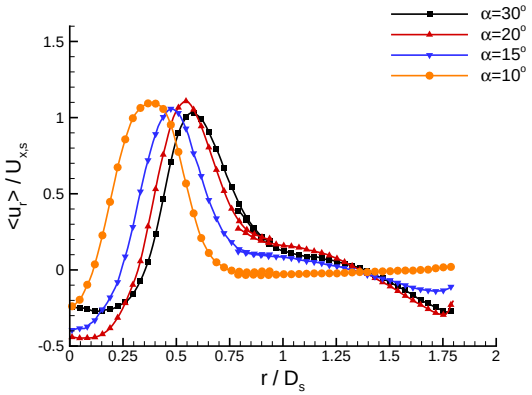

(c) $x/D_s = 0.53$

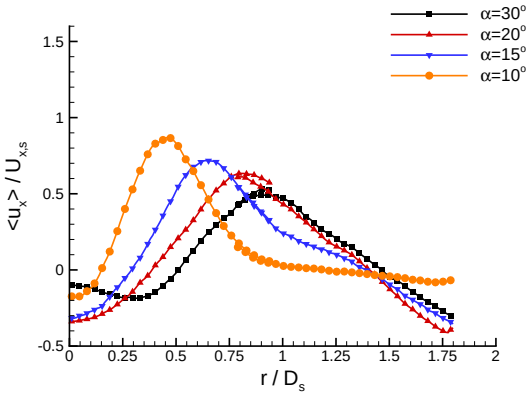

(d) $x/D_s = 1.06$

Figure 4.2: Radial profiles of time-mean axial velocity for varying swirl vane angle at various axial locations in expansion chamber.

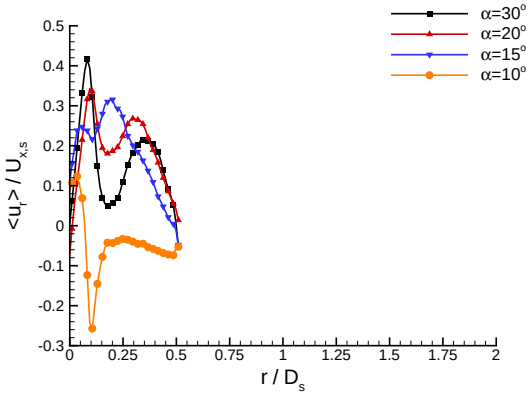

(a) $x/D_s = 0.02$

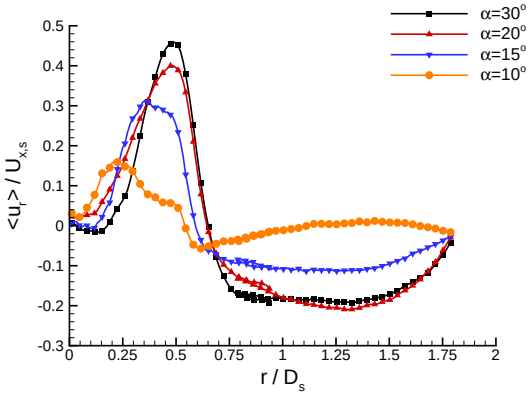

(b) $x/D_s = 0.27$

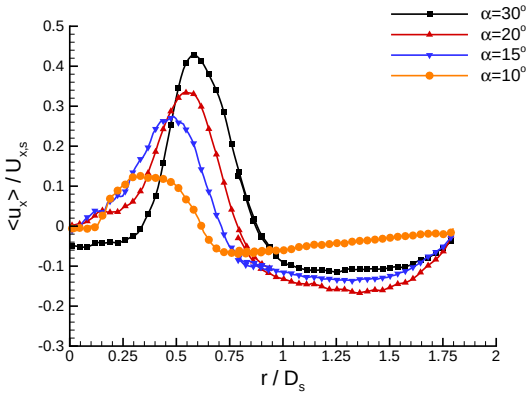

(c) $x/D_s = 0.53$

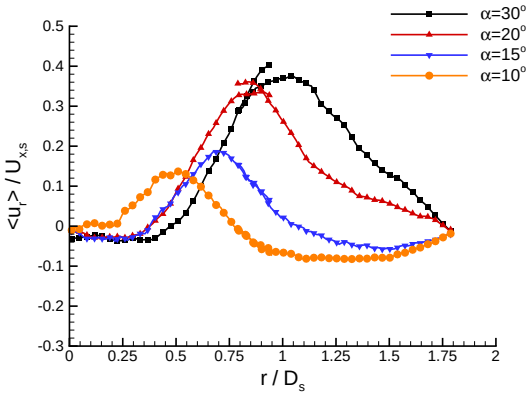

(d) $x/D_s = 1.06$

Figure 4.3: Radial profiles of time-mean radial velocity for varying swirl vane angle at various axial locations in expansion chamber.

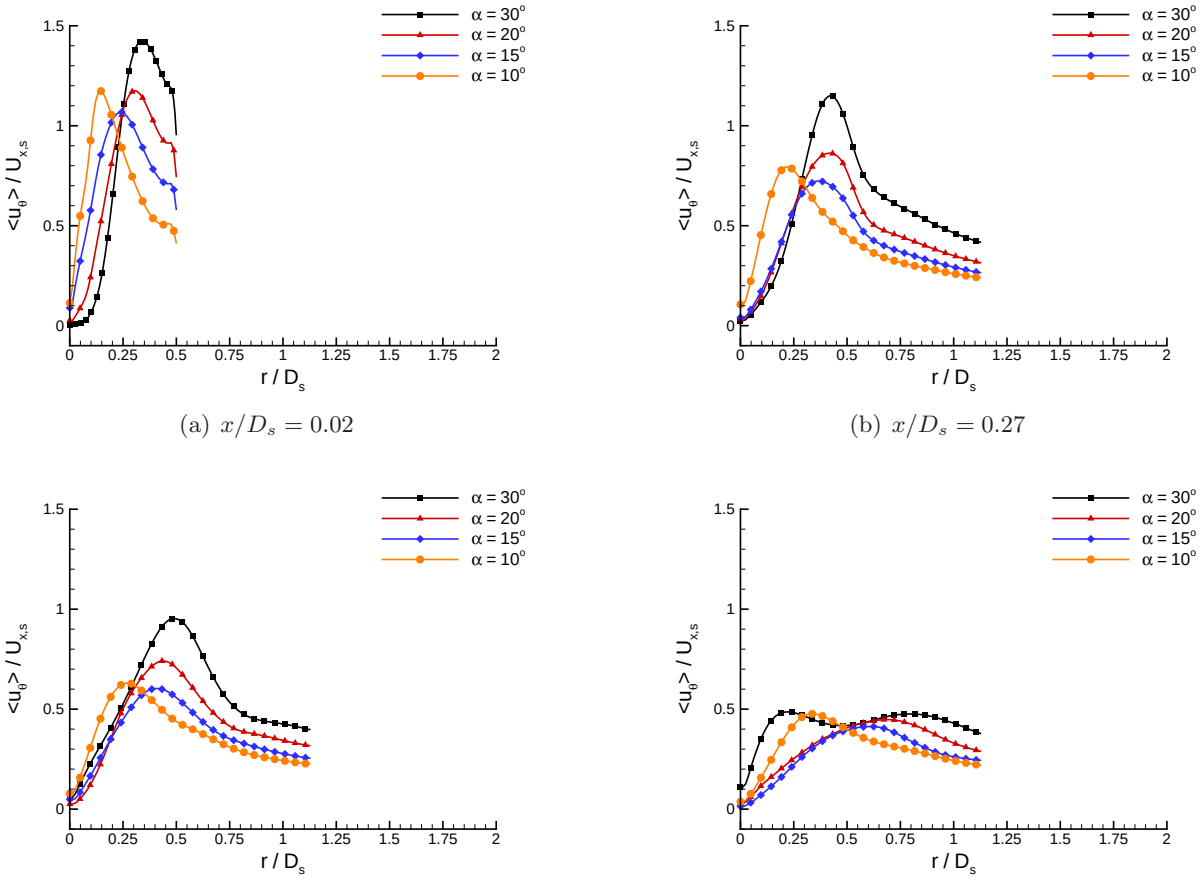

(a) $x/D_s = 0.02$

(b) $x/D_s = 0.27$

(c) $x/D_s = 0.53$

(d) $x/D_s = 1.06$

Figure 4.4: Radial profiles of time-mean tangential velocity for varying swirl vane angle at various axial locations in expansion chamber.

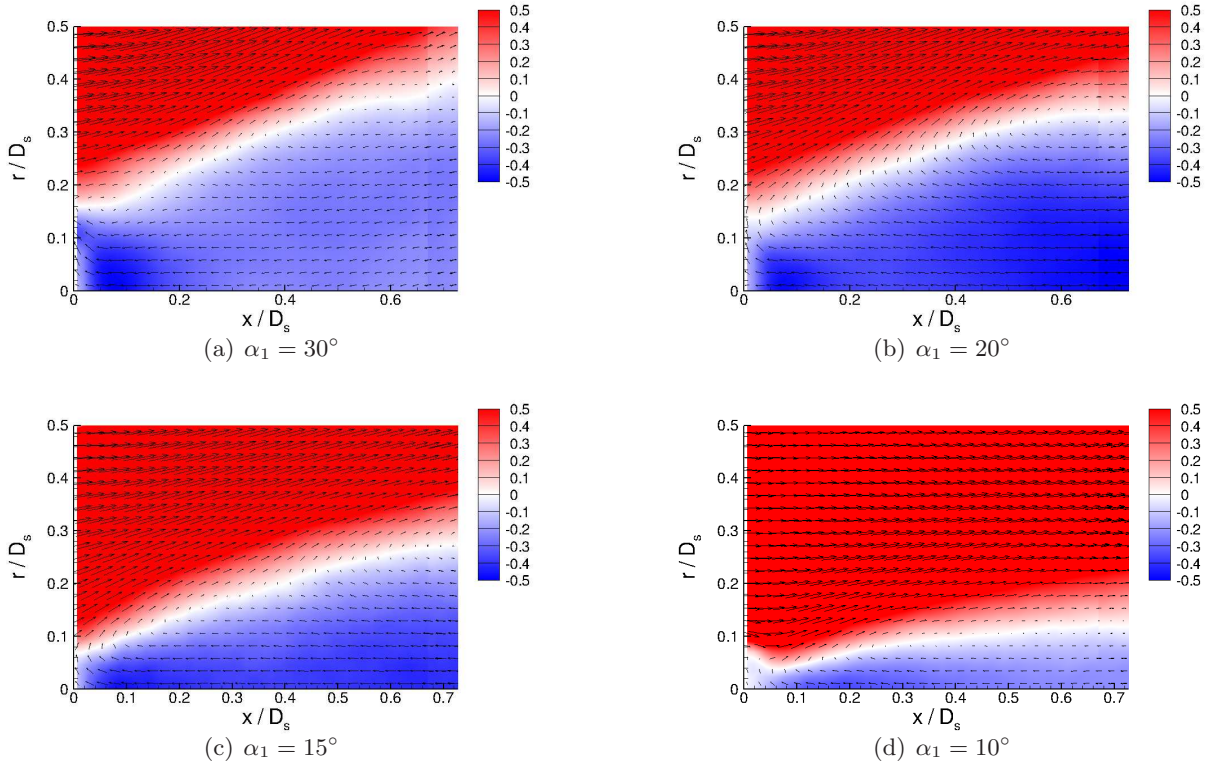

(a) $\alpha_1 = 30°$ (b) $\alpha_1 = 20°$

(c) $\alpha_1 = 15°$ (d) $\alpha_1 = 10°$

Figure 4.5: Time-mean velocity vectors on contours of time-mean axial velocity, $\langle u_x \rangle / U_{x,s}$, in near-field of expansion chamber for varying swirl vane angle.

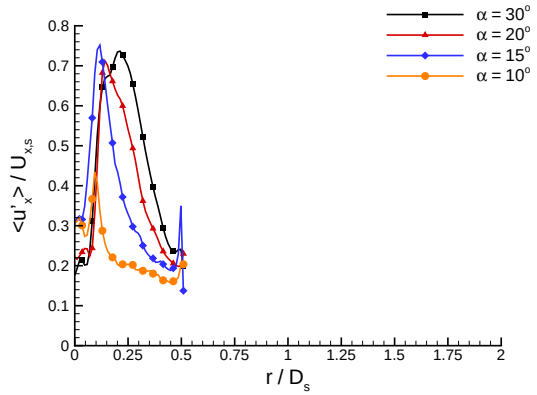

(a) $x/D_s = 0.02$

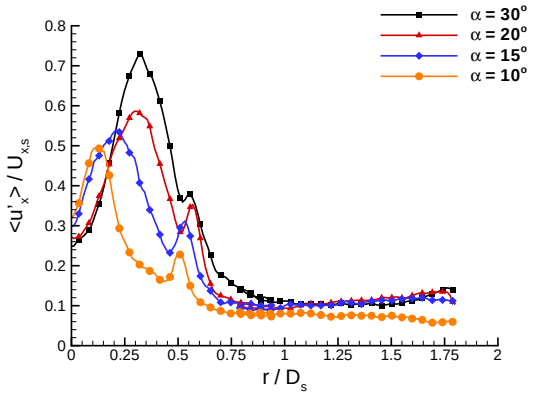

(b) $x/D_s = 0.27$

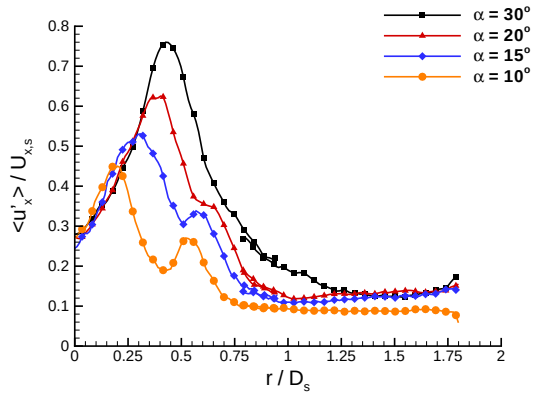

(c) $x/D_s = 0.53$

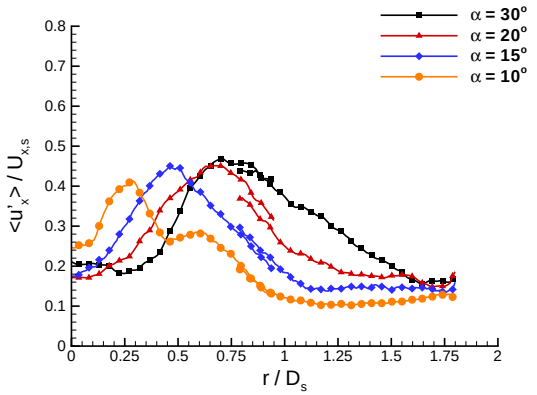

(d) $x/D_s = 1.06$

Figure 4.6: Radial profiles of r.m.s axial velocity for varying swirl vane angle at various axial locations in expansion chamber.

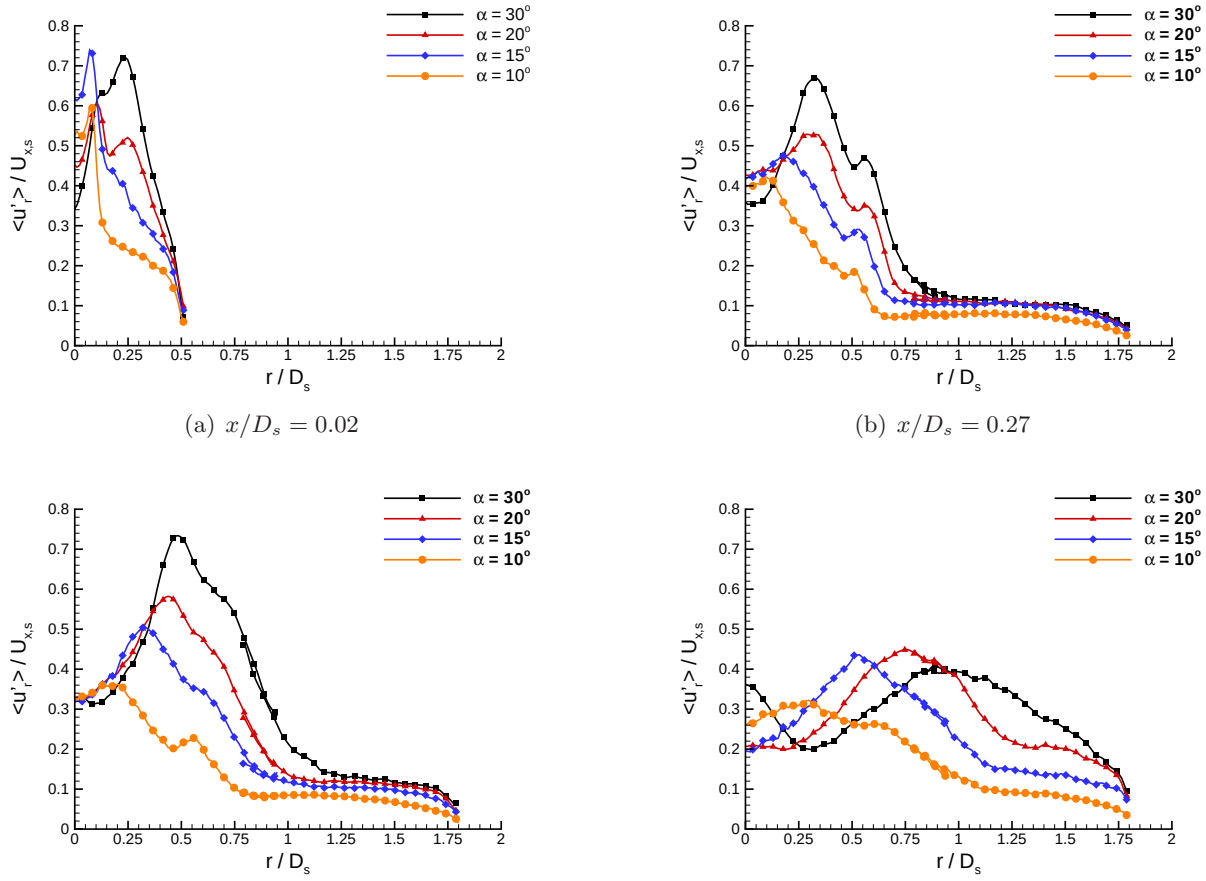

(a) $x/D_s = 0.02$

(b) $x/D_s = 0.27$

(c) $x/D_s = 0.53$

(d) $x/D_s = 1.06$

Figure 4.7: Radial profiles of r.m.s radial velocity for varying swirl vane angle at various axial locations in expansion chamber.

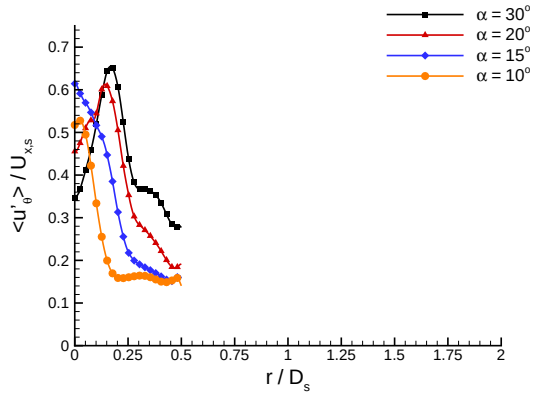

(a) $x/D_s = 0.02$

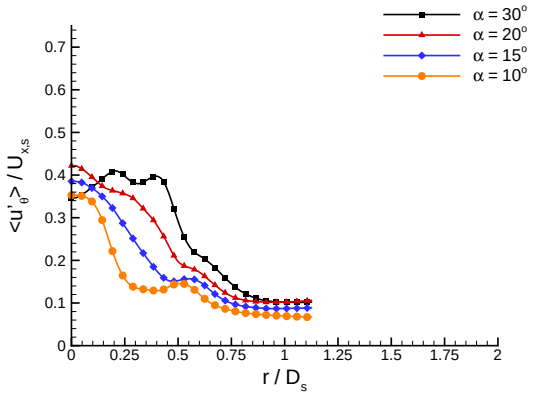

(b) $x/D_s = 0.27$

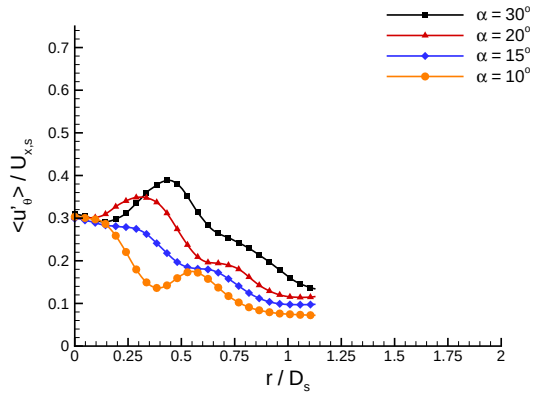

(c) $x/D_s = 0.53$

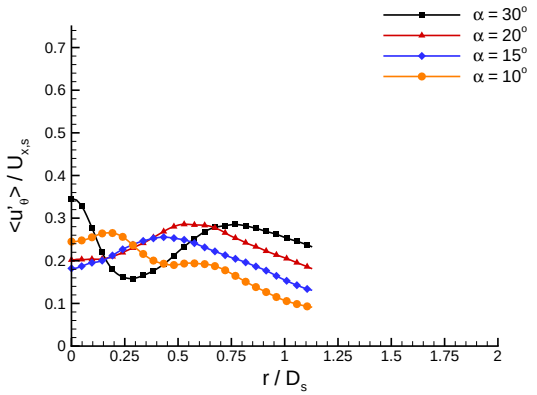

(d) $x/D_s = 1.06$

Figure 4.8: Radial profiles of r.m.s tangential velocity for varying swirl vane angle at various axial locations in expansion chamber.

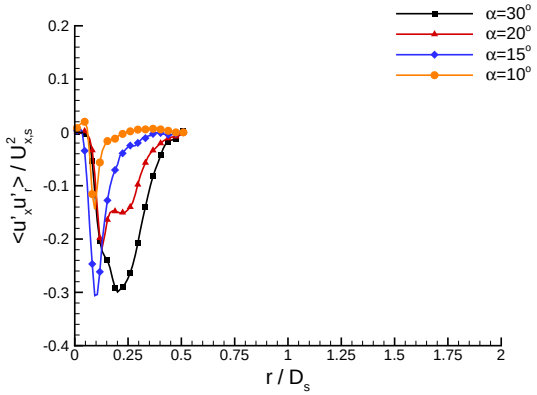

(a) $x/D_s = 0.02$

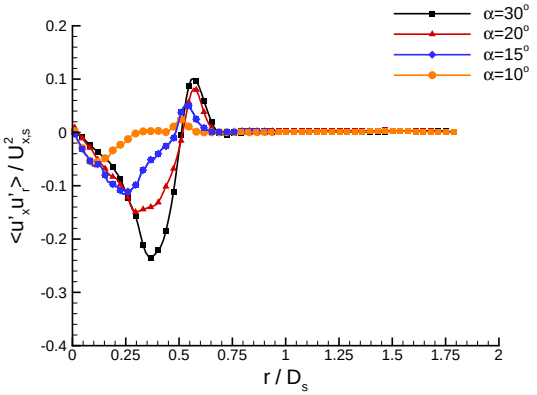

(b) $x/D_s = 0.27$

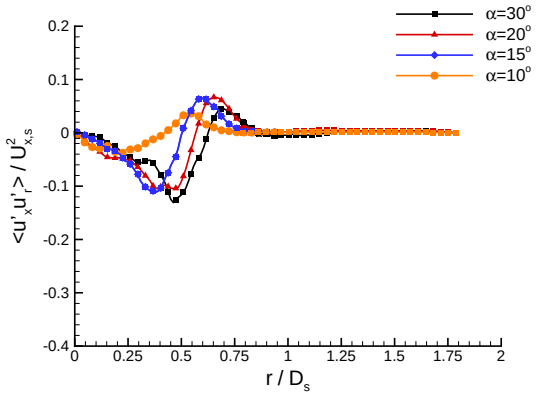

(c) $x/D_s = 0.53$

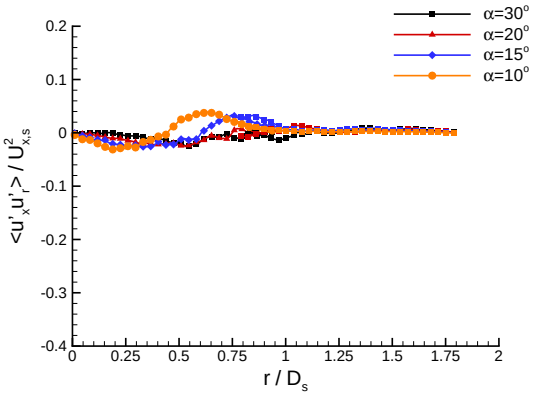

(d) $x/D_s = 1.06$

Figure 4.9: Radial profiles of axial-radial shear stress for varying swirl vane angle at various axial locations in expansion chamber.

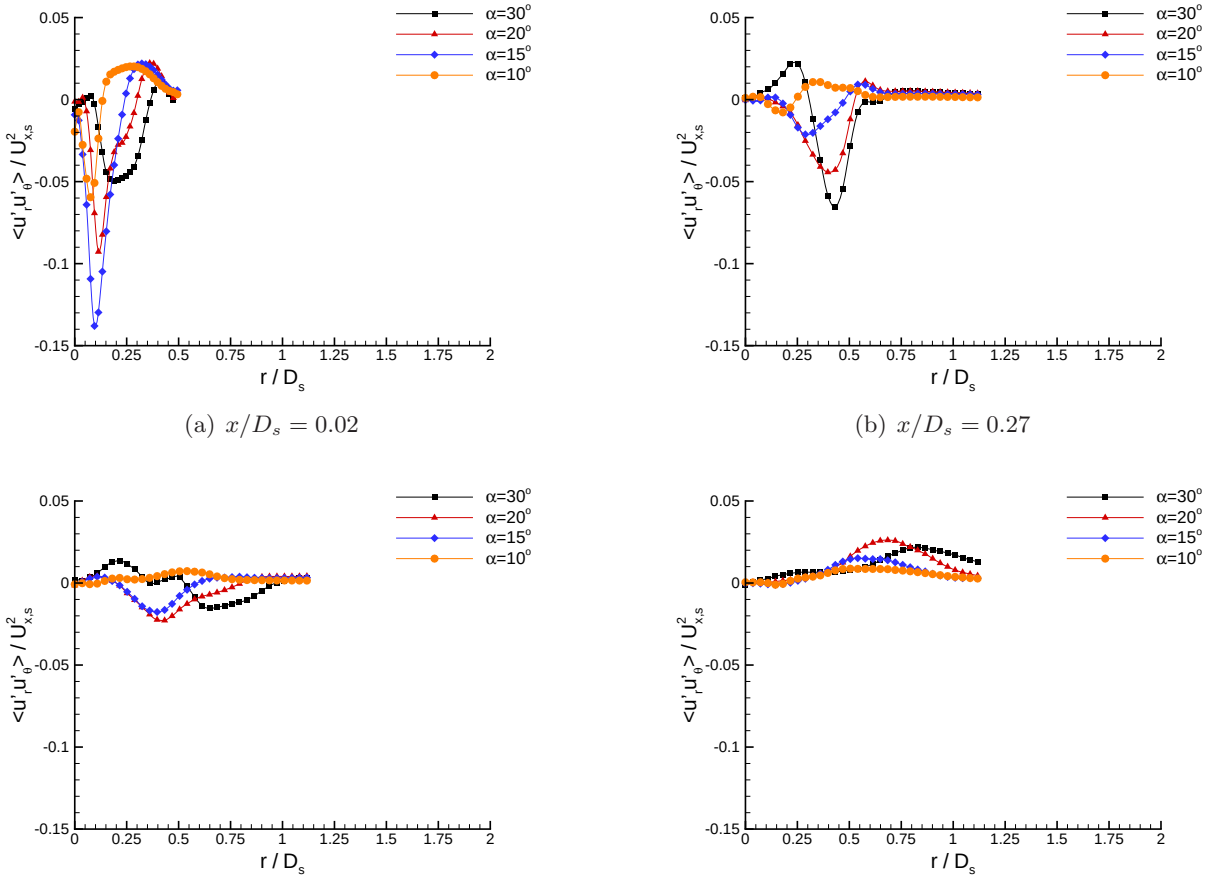

(a) $x/D_s = 0.02$

(b) $x/D_s = 0.27$

(c) $x/D_s = 0.53$

(d) $x/D_s = 1.06$

Figure 4.10: Radial profiles of radial-tangential shear stress for varying swirl vane angle at various axial locations in expansion chamber.

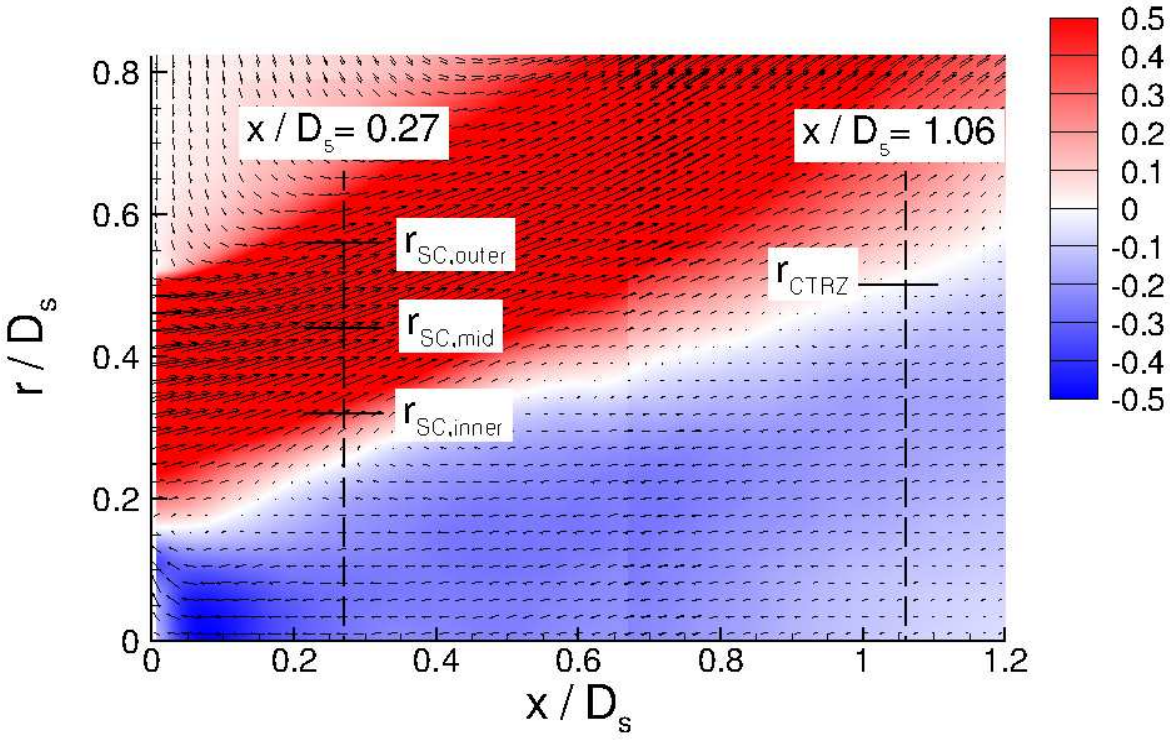

Figure 4.11: Swirl cone and CTRZ locations for $\alpha_1 = 30°$. Mean velocity vectors on contours of $\langle u_x \rangle / U_{x,s}$

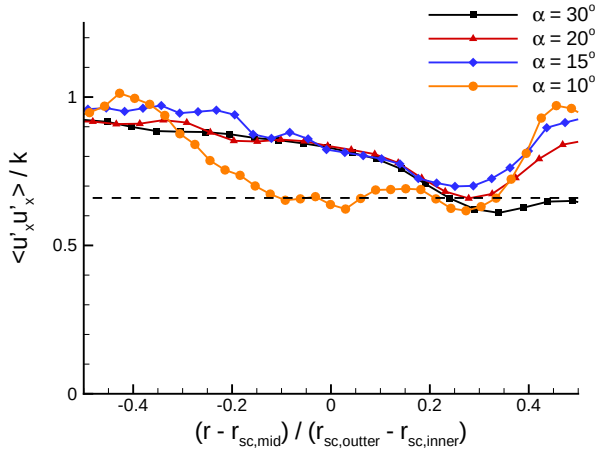

(a) $\langle u'_x u'_x \rangle / k$

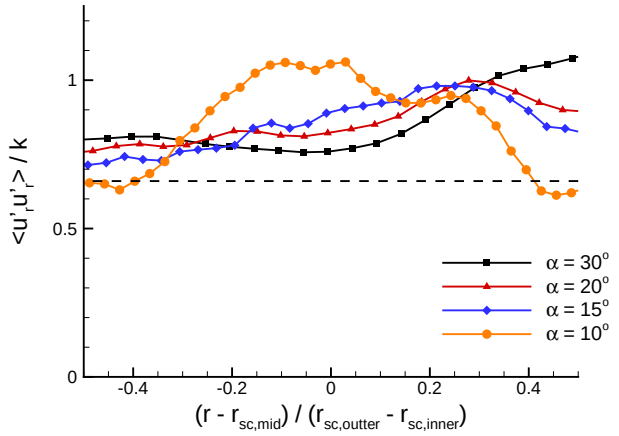

(b) $\langle u'_r u'_r \rangle / k$

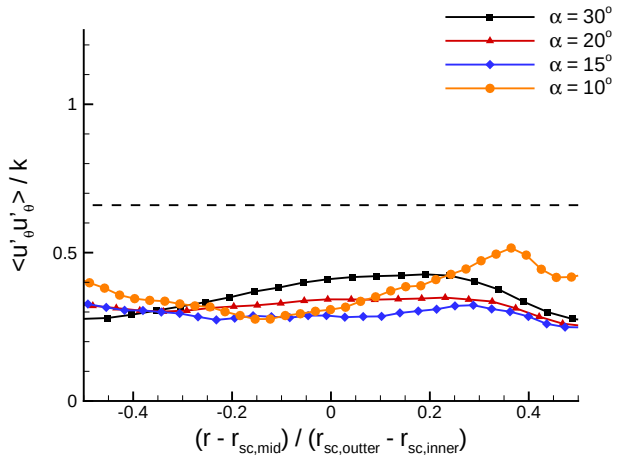

(c) $\langle u'_\theta u'_\theta \rangle / k$

Figure 4.12: Radial profiles of $\langle u'_x u'_x \rangle / k$, $\langle u'_r u'_r \rangle / k$ and $\langle u'_\theta u'_\theta \rangle / k$ across swirl cone at $x/D_s = 0.27$ for varying swirl vane angle. Horizontal dashed line indicates isotropic turbulence in which $\langle u'_x u'_x \rangle / k = \langle u'_r u'_r \rangle / k = \langle u'_\theta u'_\theta \rangle / k = 2/3$

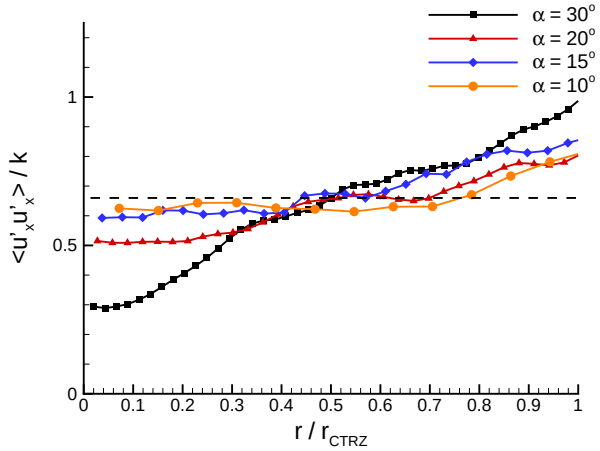

(a) $\langle u'_x u'_x \rangle / k$

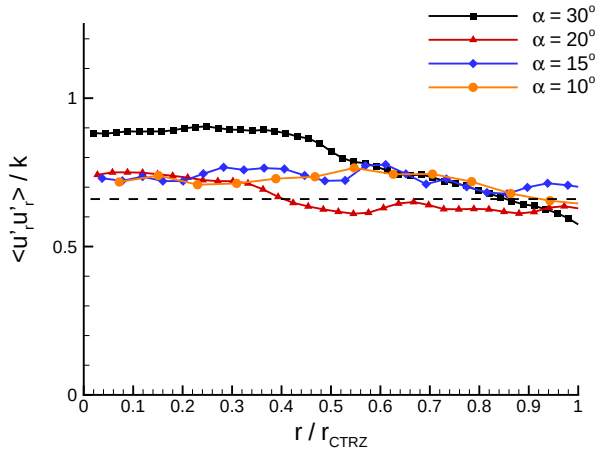

(b) $\langle u'_r u'_r \rangle / k$

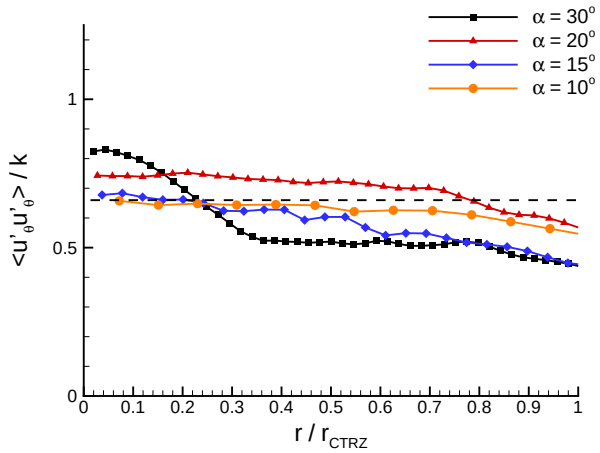

(c) $\langle u'_\theta u'_\theta \rangle / k$

Figure 4.13: Radial profiles of $\langle u'_x u'_x \rangle / k$, $\langle u'_r u'_r \rangle / k$ and $\langle u'_\theta u'_\theta \rangle / k$ across CTRZ at $x/D_s = 1.06$ for varying swirl vane angle. Horizontal dashed line indicates isotropic turbulence in which $\langle u'_x u'_x \rangle / k = \langle u'_r u'_r \rangle / k = \langle u'_\theta u'_\theta \rangle / k = 2/3$

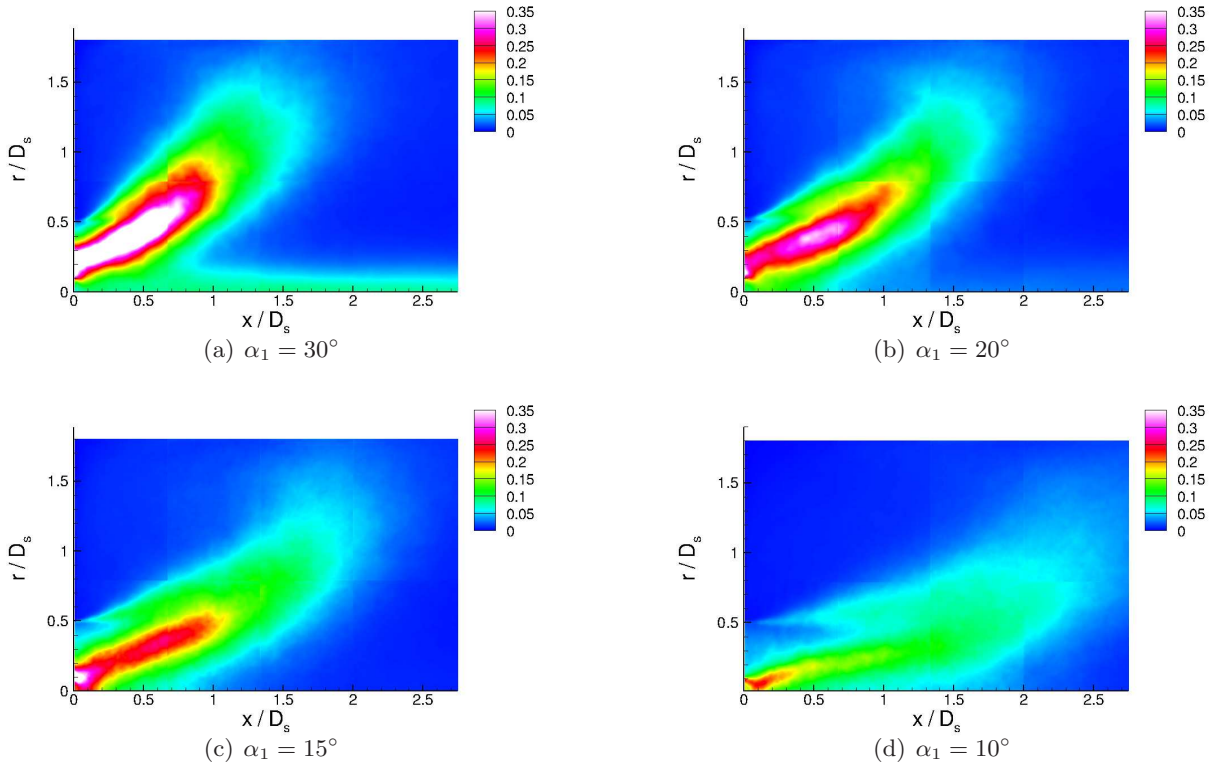

(a) $\alpha_1 = 30°$ (b) $\alpha_1 = 20°$

(c) $\alpha_1 = 15°$ (d) $\alpha_1 = 10°$

Figure 4.14: Contours of time-mean in-plane turbulent kinetic energy, $k/U_{x,s}^2$ (based on u_x' and u_r'), in dump expansion chamber for varying swirl vane angle.

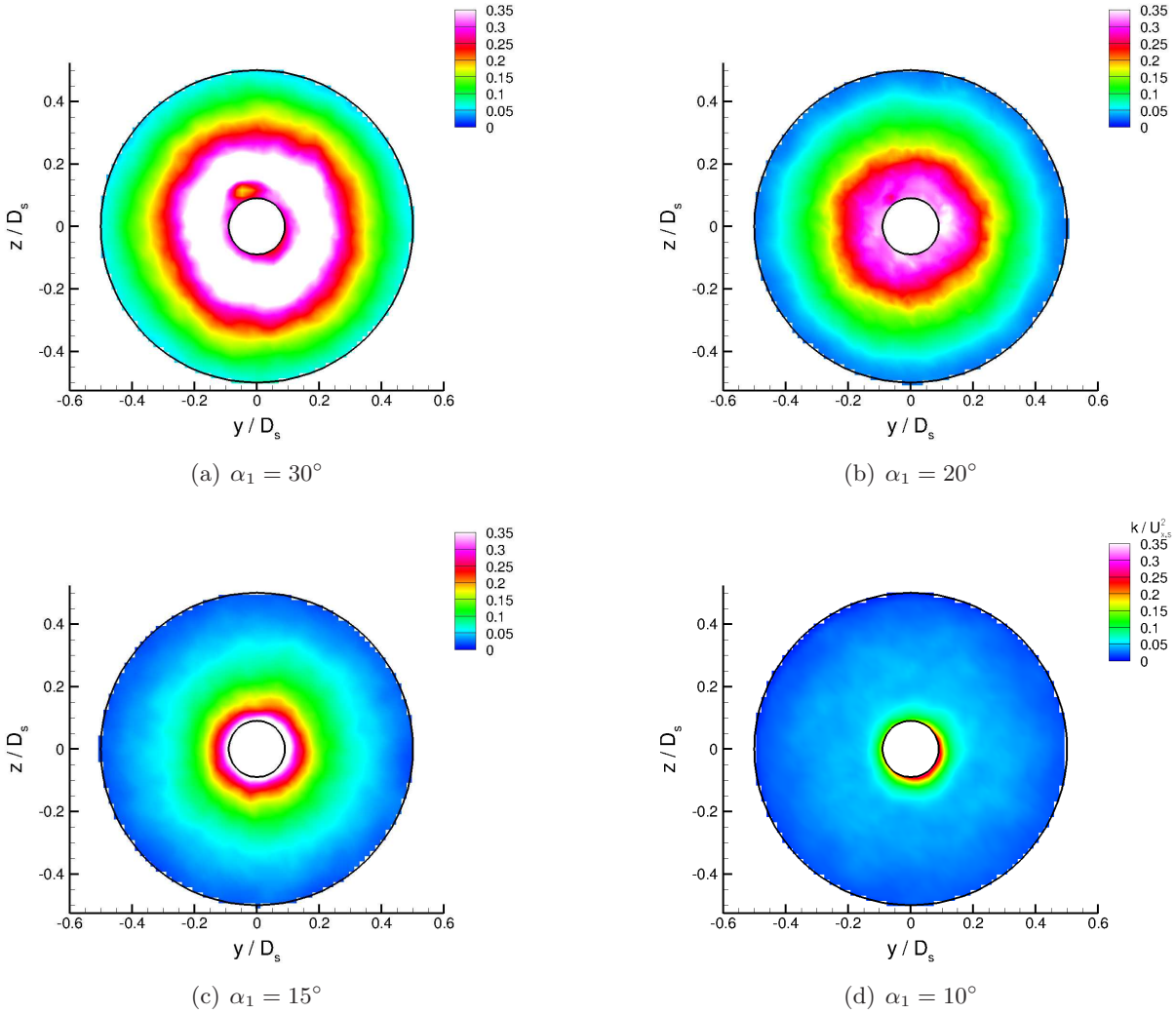

(a) $\alpha_1 = 30°$

(b) $\alpha_1 = 20°$

(c) $\alpha_1 = 15°$

(d) $\alpha_1 = 10°$

Figure 4.15: Contours of time-mean in-plane turbulent kinetic energy, $k/U_{x,s}^2$ (based on u_r' and u_θ'), at $x/D_s = 0.02$ for varying swirl vane angle.

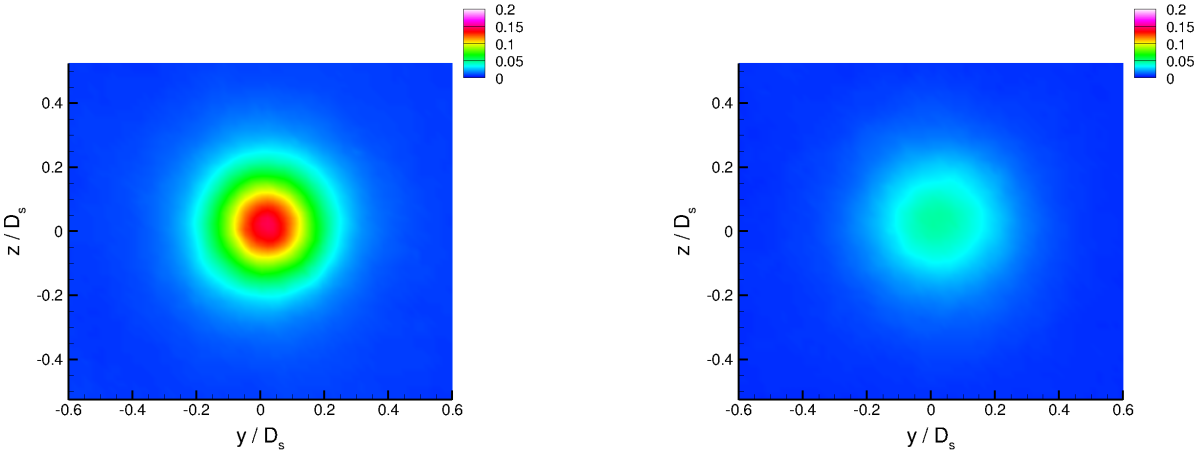

(a) $\alpha_1 = 30°$

(b) $\alpha_1 = 20°$

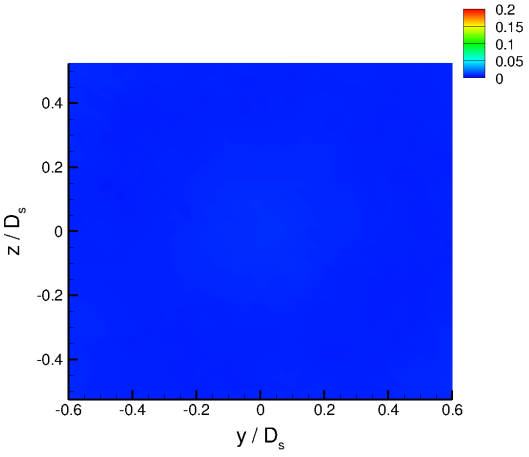

(c) $\alpha_1 = 15°$

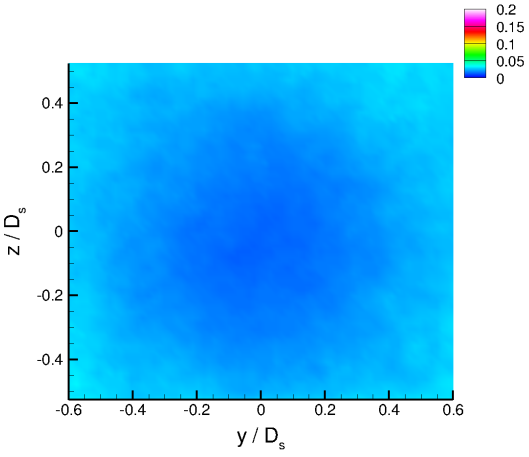

(d) $\alpha_1 = 10°$

Figure 4.16: Contours of in-plane turbulent kinetic energy, $k/U_{x,s}^2$ (based on u_r' and u_θ'), at $x/D_s = 2.39$ for varying swirl vane angle.

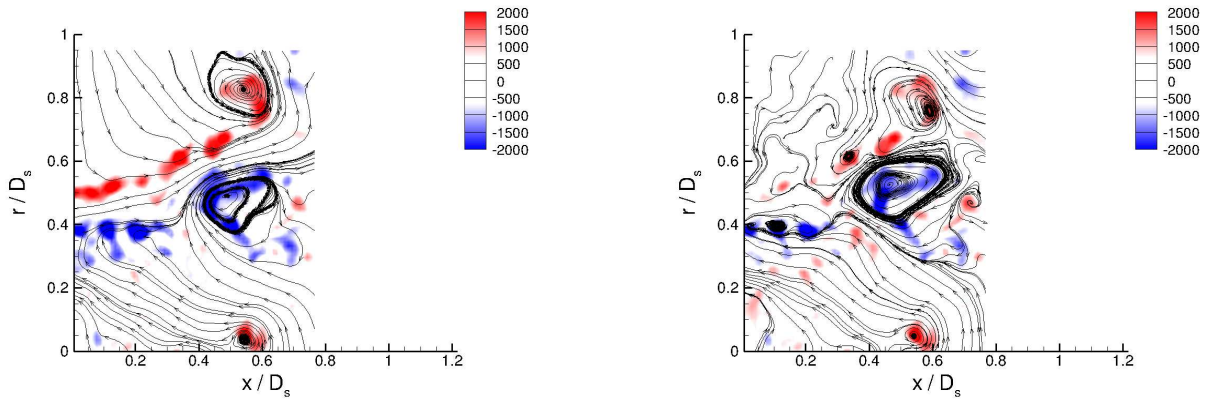

(a) Instantaneous - time I

(b) Reynolds-decomposed - time I

(c) Instantaneous - time II

(d) Reynolds-decomposed - time II

(e) Instantaneous - time III

(f) Reynolds-decomposed - time III

Figure 4.17: Instantaneous and Reynolds-decomposed streamtraces on contours of azimuthal vorticity, ω_θ, in Region B_1 at arbitrary time-instants for $\alpha_1 = 30°$.

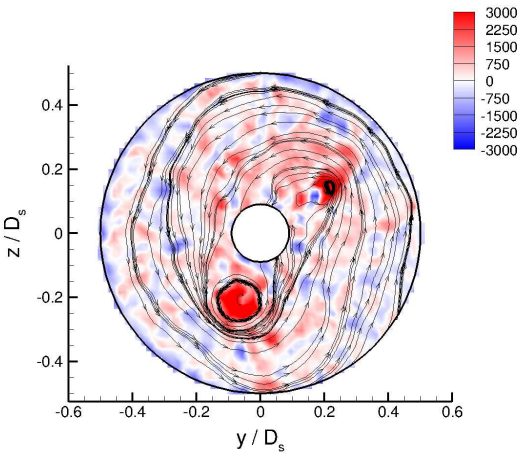

(a) Instantaneous - time I

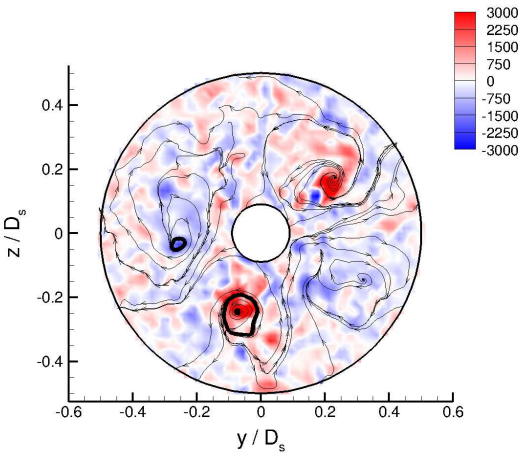

(b) Reynolds-decomposed - time I

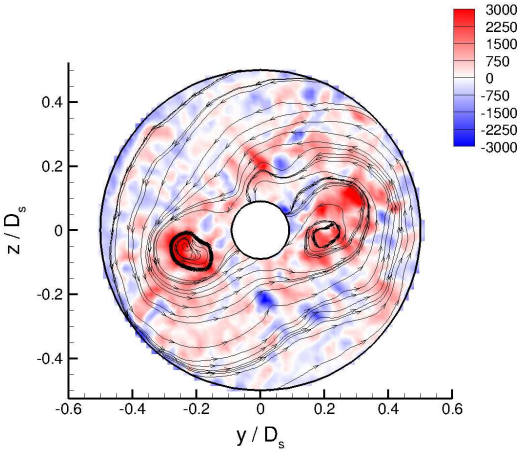

(c) Instantaneous - time II

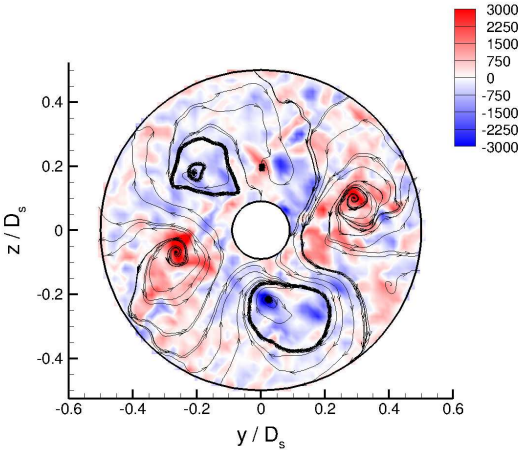

(d) Reynolds-decomposed - time II

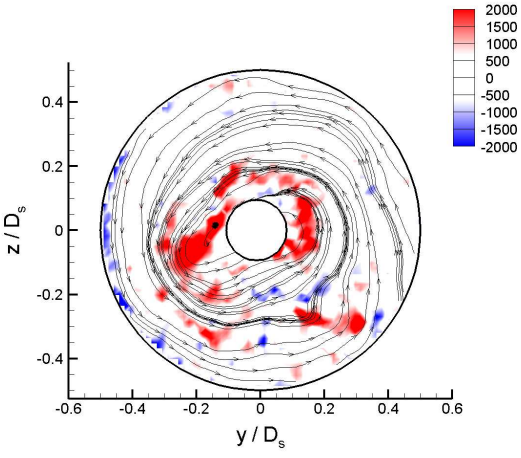

(e) Instantaneous - time III

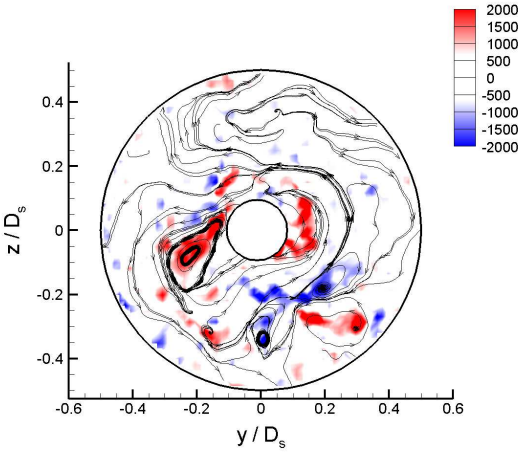

(f) Reynolds-decomposed - time III

Figure 4.18: Instantaneous and Reynolds-decomposed streamtraces on contours of axial vorticity, ω_x, at $x/D_s = 0.02$ at arbitrary time-instants for $\alpha_1 = 30°$.

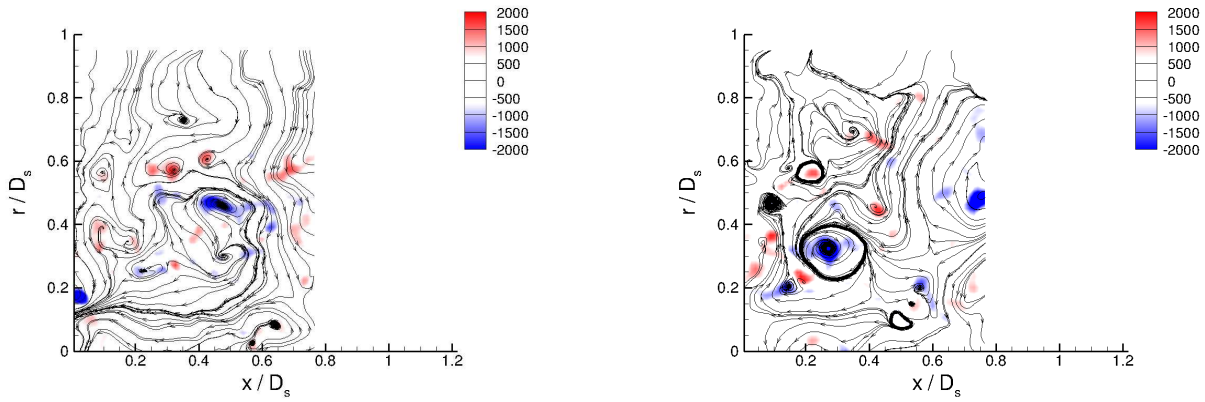

(a) $\alpha_1 = 20°$ - time I

(b) $\alpha_1 = 20°$ - time II

(c) $\alpha_1 = 15°$ - time I

(d) $\alpha_1 = 15°$ - time II

(e) $\alpha_1 = 10°$ - time I

(f) $\alpha_1 = 10°$ - time II

Figure 4.19: Reynolds-decomposed streamtraces on contours of azimuthal vorticity, ω_θ, in Region B_1 at arbitrary time-instants for $\alpha_1 = 20°$, $\alpha_1 = 15°$ and $\alpha_1 = 10°$.

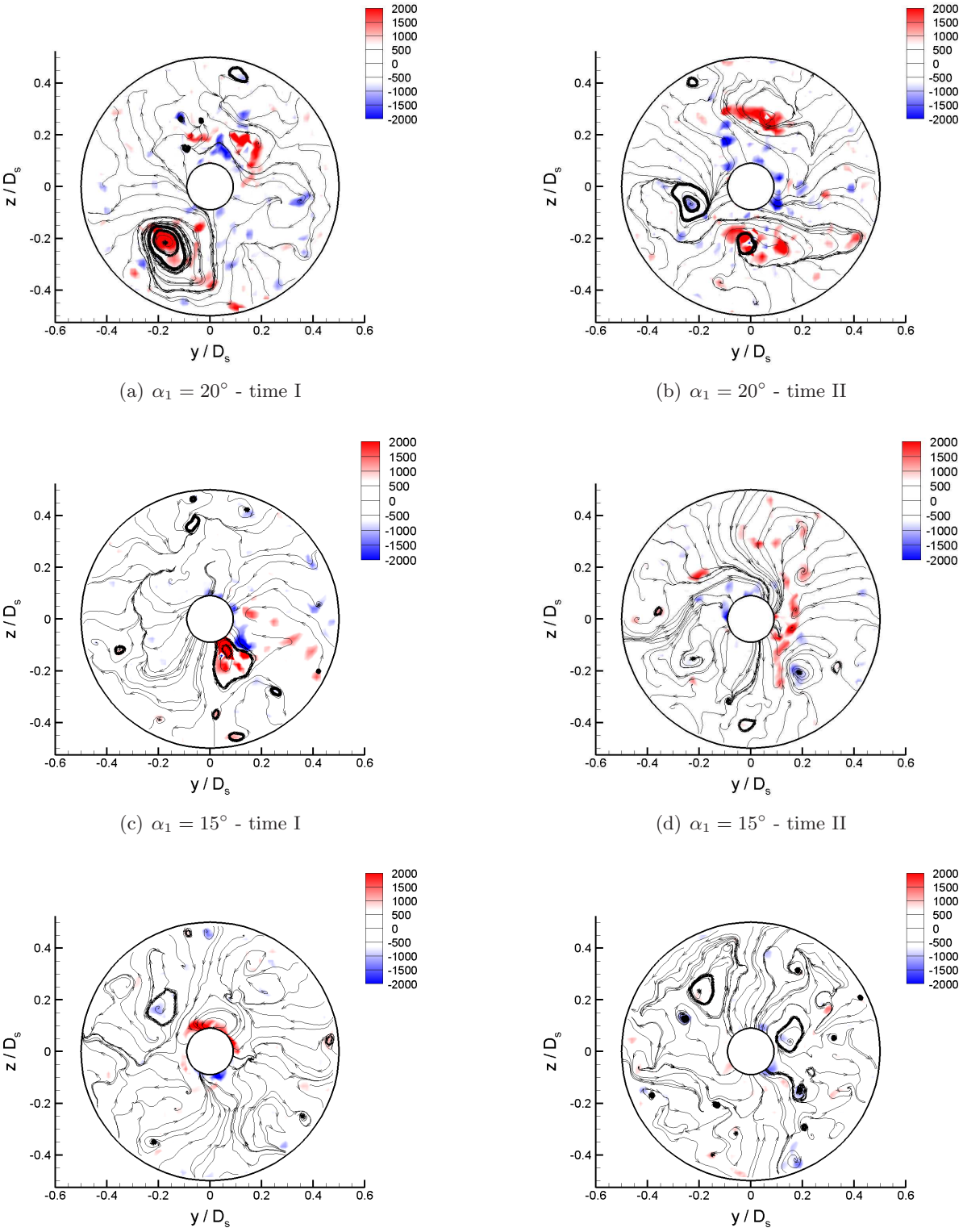

(a) $\alpha_1 = 20°$ - time I

(b) $\alpha_1 = 20°$ - time II

(c) $\alpha_1 = 15°$ - time I

(d) $\alpha_1 = 15°$ - time II

(e) $\alpha_1 = 10°$ - time I

(f) $\alpha_1 = 10°$ - time II

Figure 4.20: Reynolds-decomposed streamtraces at on contours of axial vorticity, ω_x, $x/D_s = 0.02$ at arbitrary time-instants for $\alpha_1 = 20°$, $\alpha_1 = 15°$ and $\alpha_1 = 10°$.

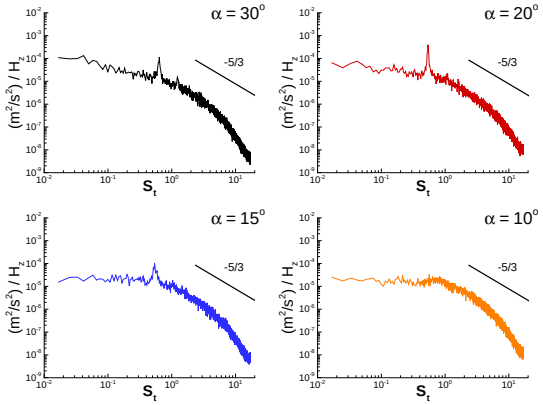

(a) $r/D_s = 0.08$

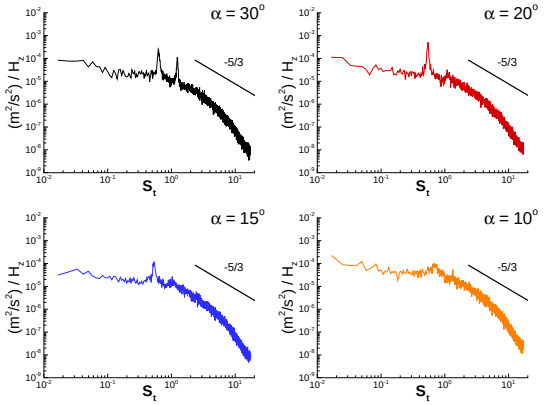

(b) $r/D_s = 0.16$

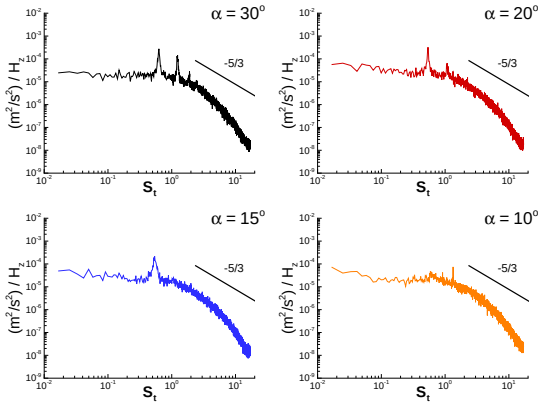

(c) $r/D_s = 0.24$

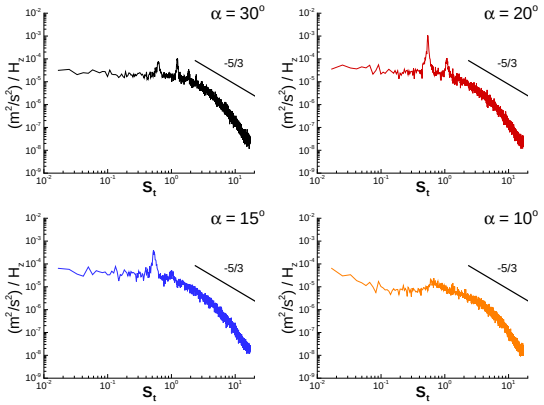

(d) $r/D_s = 0.32$

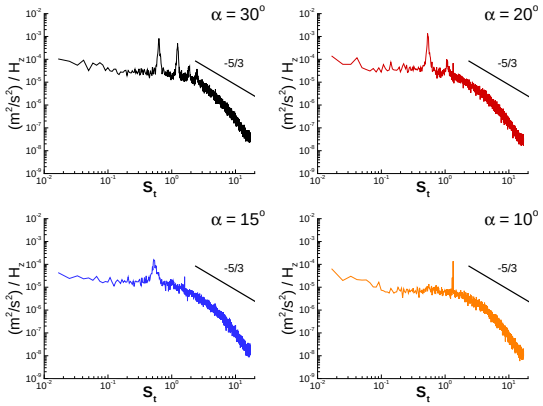

(e) $r/D_s = 0.40$

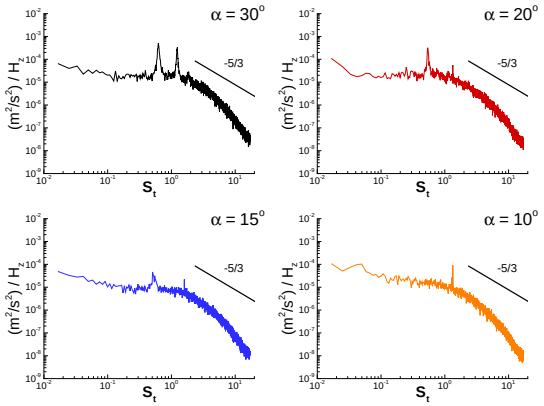

(f) $r/D_s = 0.42$

Figure 4.21: PSDs of velocity at $x/D_s = 0.27$ for varying swirl vane angle at various radial locations [13].

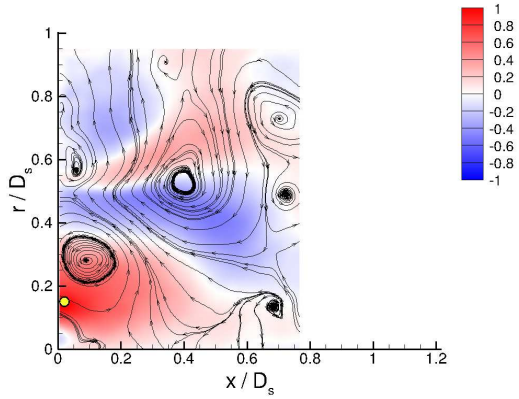

(a) R_{xx} and $u'_x > 1.5\langle u'_x \rangle$ at reference point $x/D_s = 0.02$, $r/D_s = 0.15$ based on $N_c = 8$

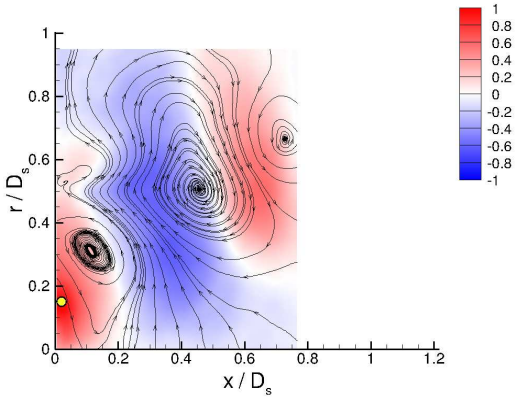

(b) R_{rr} and $u'_r > 1.5\langle u'_r \rangle$ at reference point $x/D_s = 0.02$, $r/D_s = 0.15$ based on $N_c = 41$

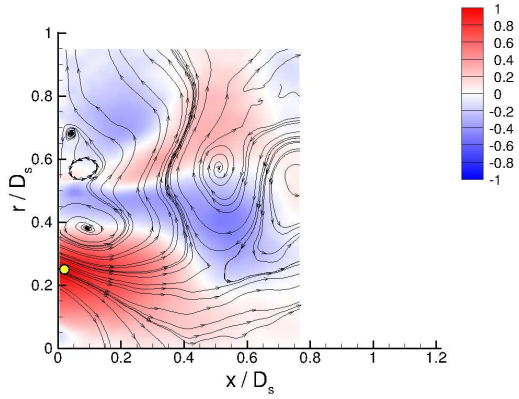

(c) R_{xx} and $u'_x > 1.5\langle u'_x \rangle$ at reference point $x/D_s = 0.02$, $r/D_s = 0.25$ based on $N_c = 47$

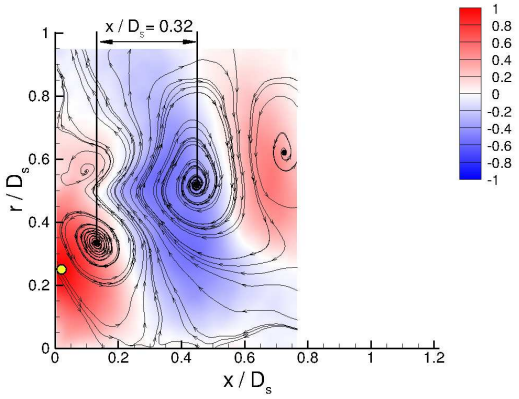

(d) R_{rr} and $u'_r > 1.5\langle u'_r \rangle$ at reference point $x/D_s = 0.02$, $r/D_s = 0.25$ based on $N_c = 34$

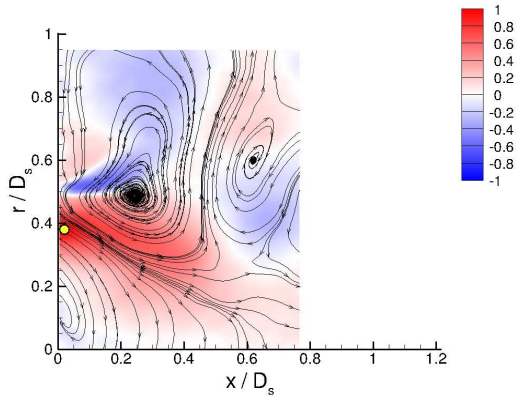

(e) R_{xx} and $u'_x > 1.5\langle u'_x \rangle$ at reference point $x/D_s = 0.02$, $r/D_s = 0.38$ based on $N_c = 41$

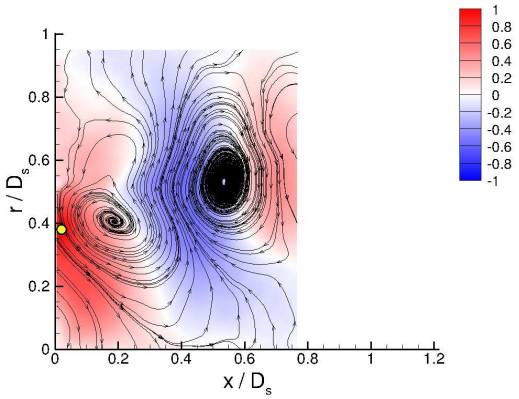

(f) R_{rr} and $u'_r > 1.5\langle u'_r \rangle$ at reference point $x/D_s = 0.02$, $r/D_s = 0.38$ based on $N_c = 45$

Figure 4.22: Conditionally-averaged velocity fields on contours of spatial velocity correlations for $\alpha_1 = 30°$ at various reference points indicated by yellow circle.

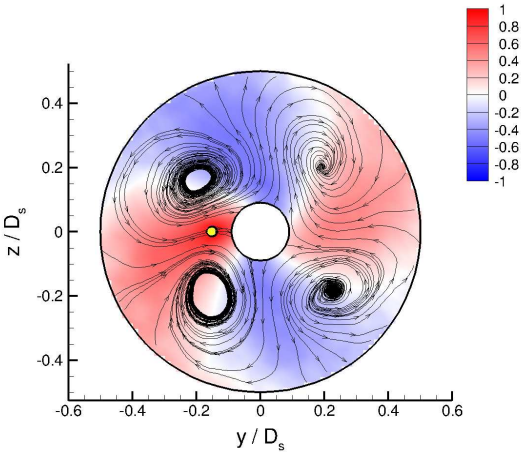

(a) R_{rr} and $u'_r > 1.5\langle u'_r \rangle$ at reference point $r/D_s = 0.15$, $\theta = \pi$ based on $N_c = 44$

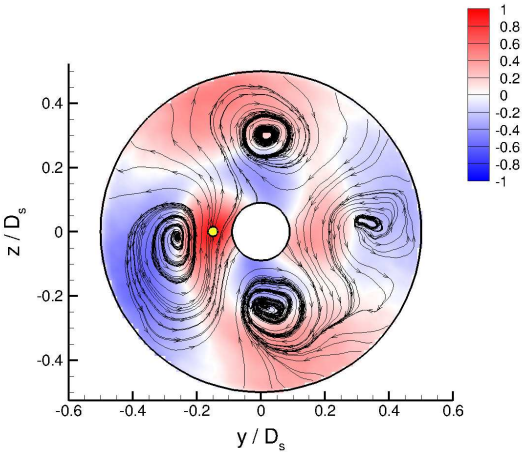

(b) $R_{\theta\theta}$ and $u'_\theta > 1.5\langle u'_\theta \rangle$ at reference point $r/D_s = 0.15$, $\theta = \pi$ based on $N_c = 41$

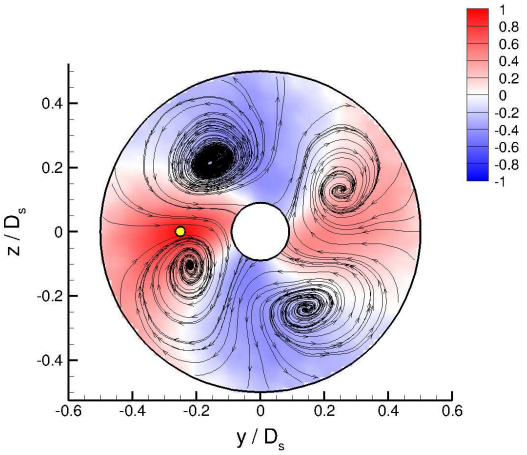

(c) R_{rr} and $u'_r > 1.5\langle u'_r \rangle$ at reference point $r/D_s = 0.25$, $\theta = \pi$ based on $N_c = 54$

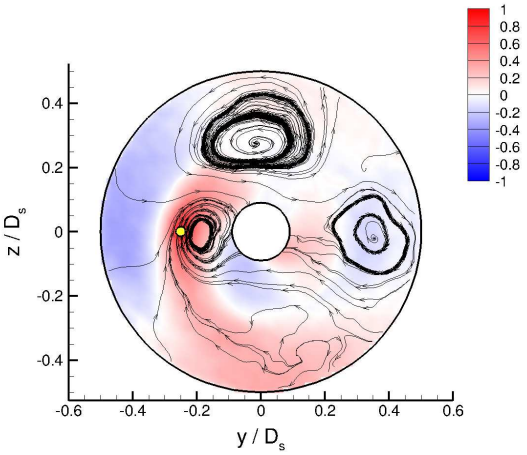

(d) $R_{\theta\theta}$ and $u'_\theta > 1.5\langle u'_\theta \rangle$ at reference point $r/D_s = 0.25$, $\theta = \pi$ based on $N_c = 31$

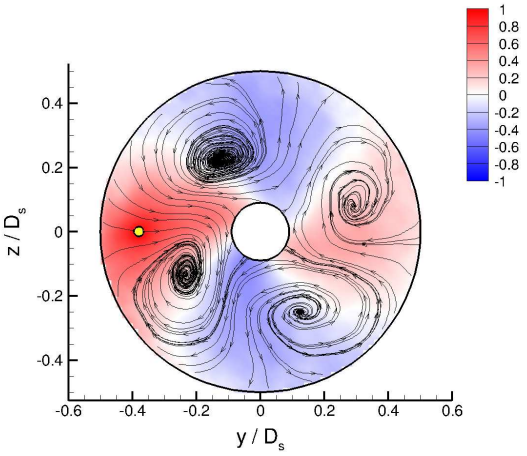

(e) R_{rr} and $u'_r > 1.5\langle u'_r \rangle$ at reference point $r/D_s = 0.38$, $\theta = \pi$ based on $N_c = 43$

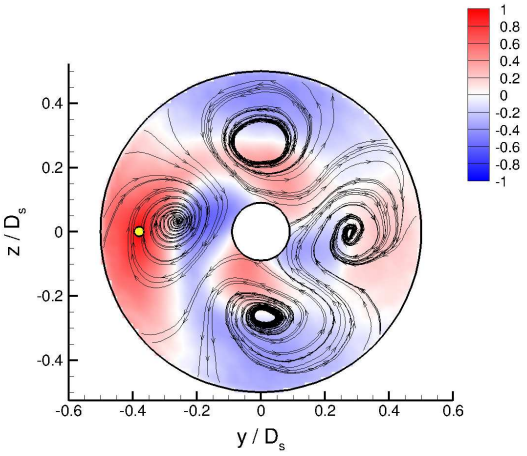

(f) $R_{\theta\theta}$ and $u'_\theta > 1.5\langle u'_\theta \rangle$ at reference point $r/D_s = 0.38$, $\theta = \pi$ based on $N_c = 55$

Figure 4.23: Conditionally-averaged velocity fields on contours of spatial velocity correlations at $x/D_s = 0.02$ for $\alpha_1 = 30°$ at various reference points indicated by yellow circle.

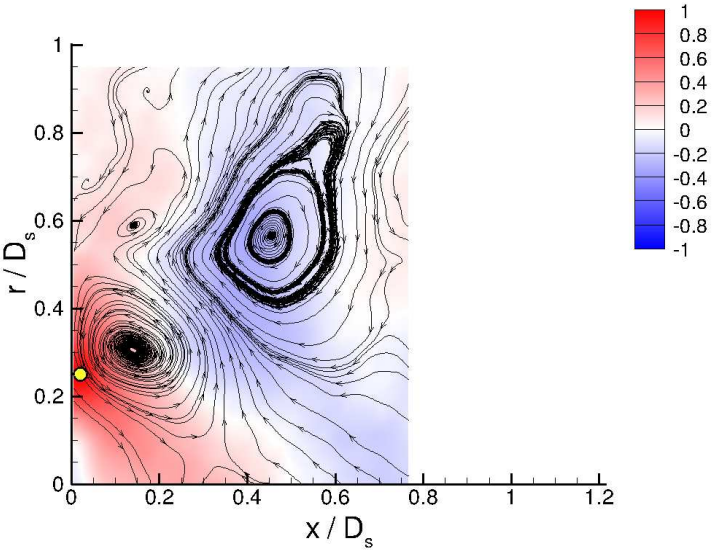

(a) $\alpha_1 = 20°$ based on $N_c = 39$

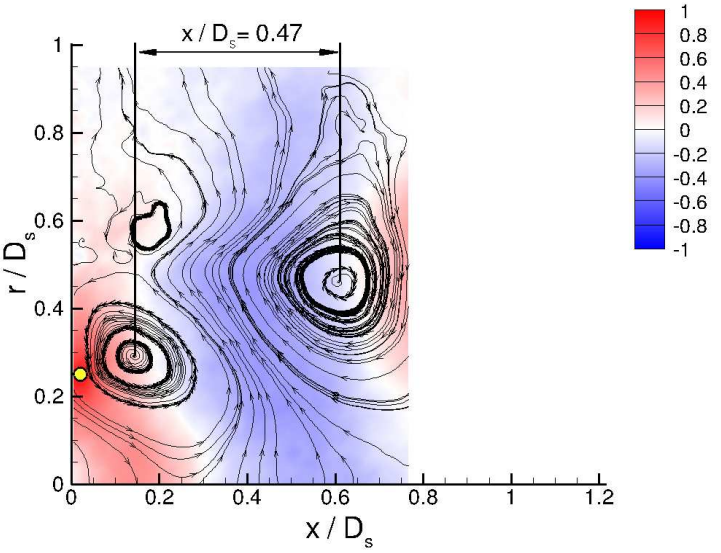

(b) $\alpha_1 = 15°$ based on $N_c = 48$

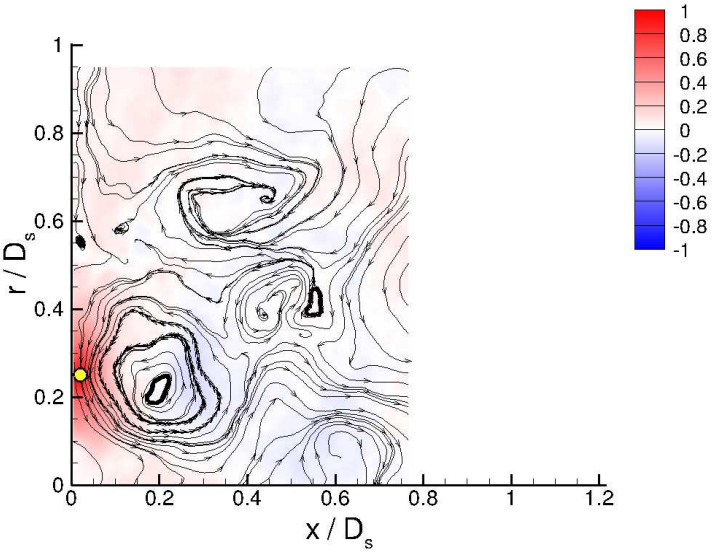

(c) $\alpha_1 = 10°$ based on $N_c = 32$

Figure 4.24: Conditionally-averaged velocity fields ($u_r' > 1.5\langle u_r' \rangle$) on contours of R_{rr} at a reference point of $x/D_s = 0.02$, $r/D_s = 0.25$ for varying swirl vane angle

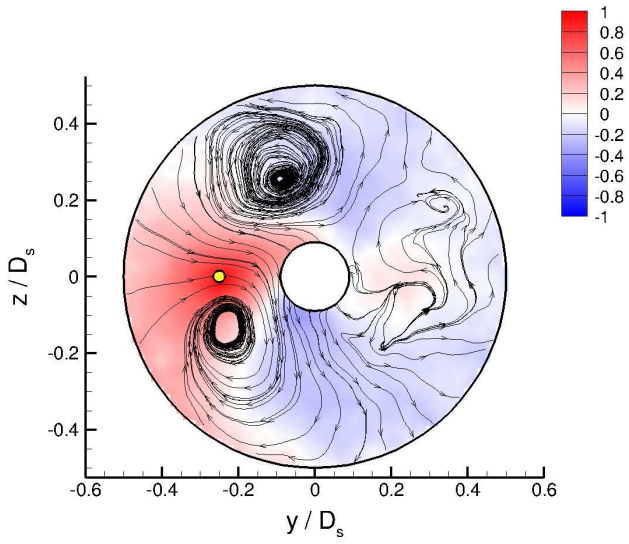

(a) $\alpha_1 = 20°$ based on $N_c = 44$

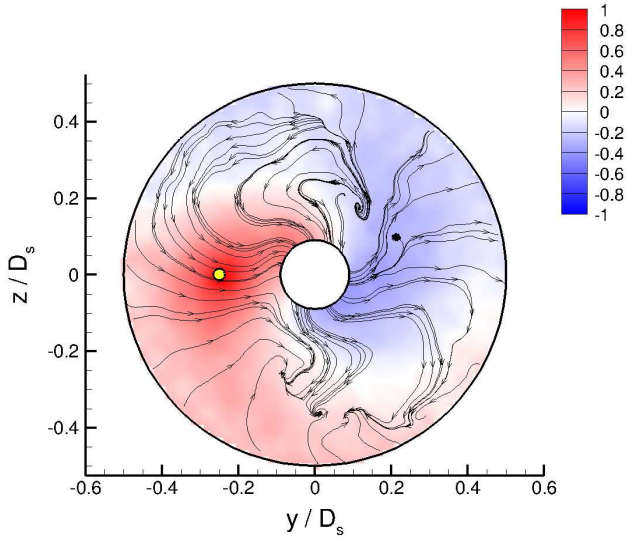

(b) $\alpha_1 = 15°$ based on $N_c = 36$

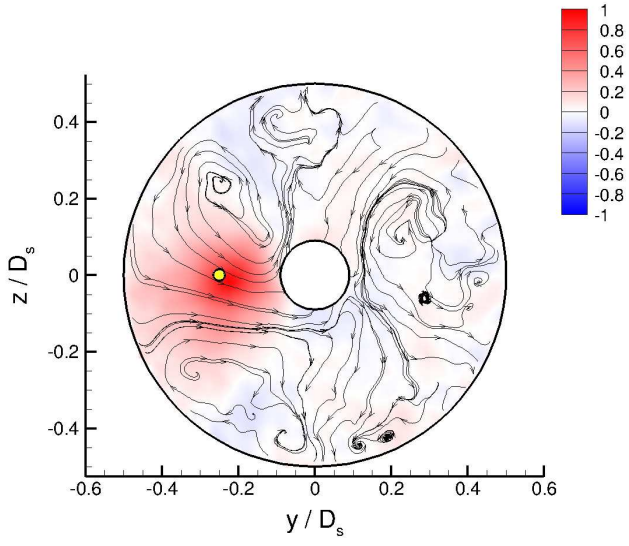

(c) $\alpha_1 = 10°$ based on $N_c = 51$

Figure 4.25: Conditionally-averaged velocity fields ($u'_r > 1.5\langle u'_r \rangle$) on contours of R_{rr} at $x/D_s = 0.02$ at a reference point of $x/D_s = 0.02$, $r/D_s = 0.25$ for varying swirl vane angle

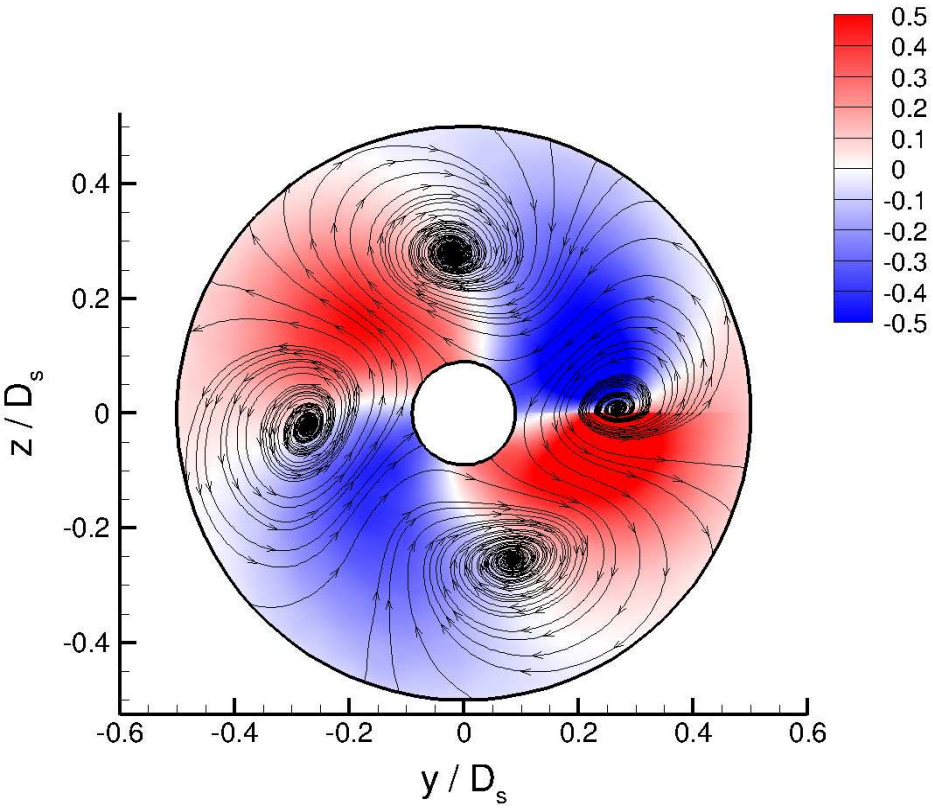

(a) $\langle u_r' \rangle_{\text{rot}}$

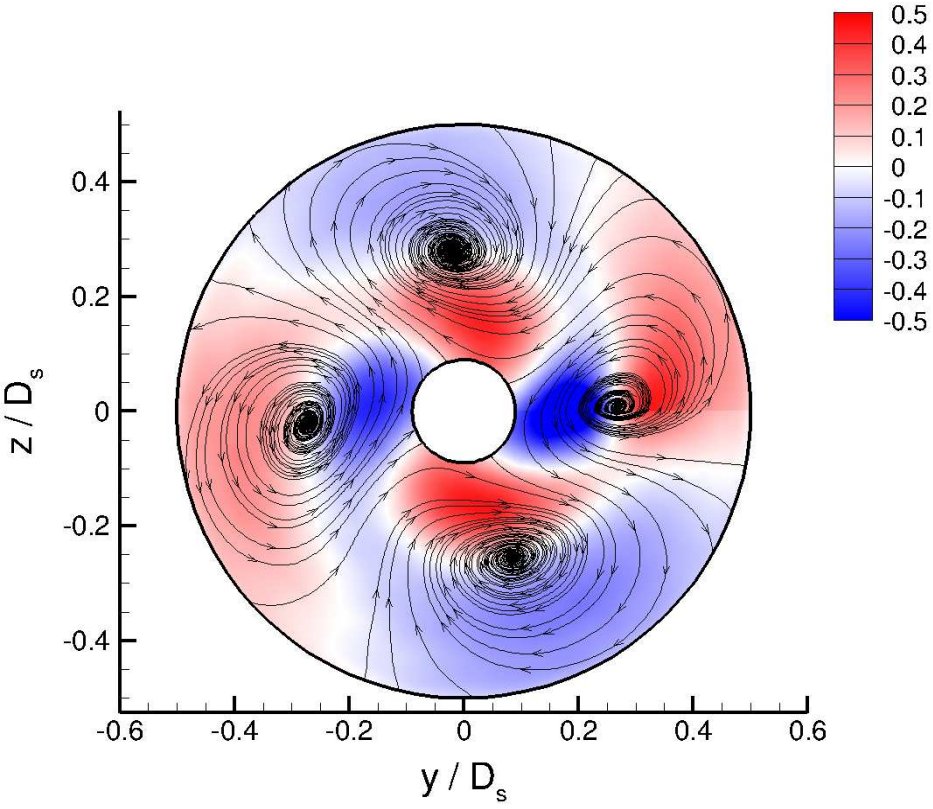

(b) $\langle u_\theta' \rangle_{\text{rot}}$

Figure 4.26: Rotationally-averaged Reynolds-decomposed streamtraces on contours of rotationally-averaged velocities at $x/D_s = 0.02$ for $\alpha_1 = 30°$.

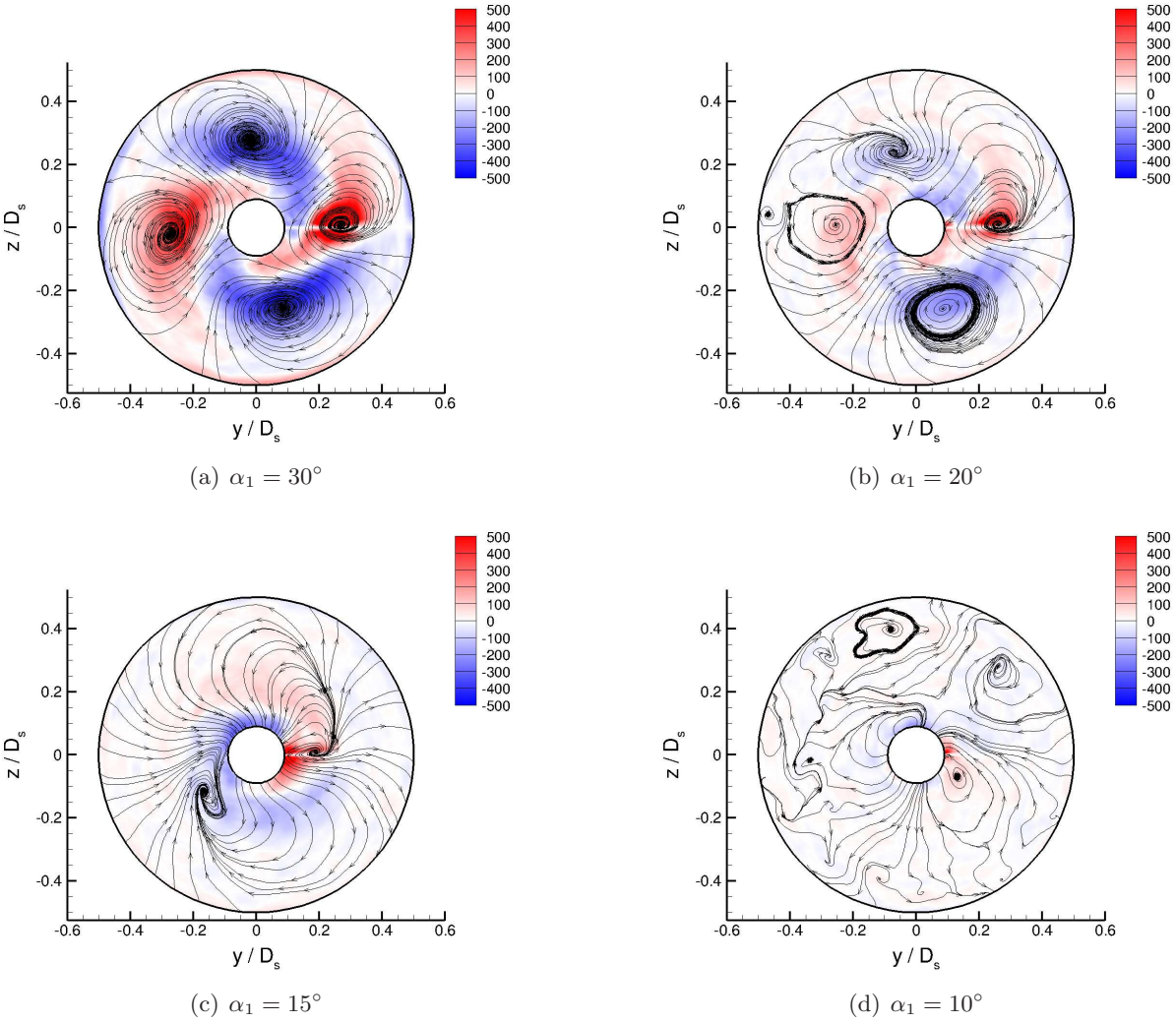

(a) $\alpha_1 = 30°$

(b) $\alpha_1 = 20°$

(c) $\alpha_1 = 15°$

(d) $\alpha_1 = 10°$

Figure 4.27: Rotationally-averaged streamtraces on contours of rotationally-averaged axial vorticity at $x/D_s = 0.02$ for varying swirl vane angle.

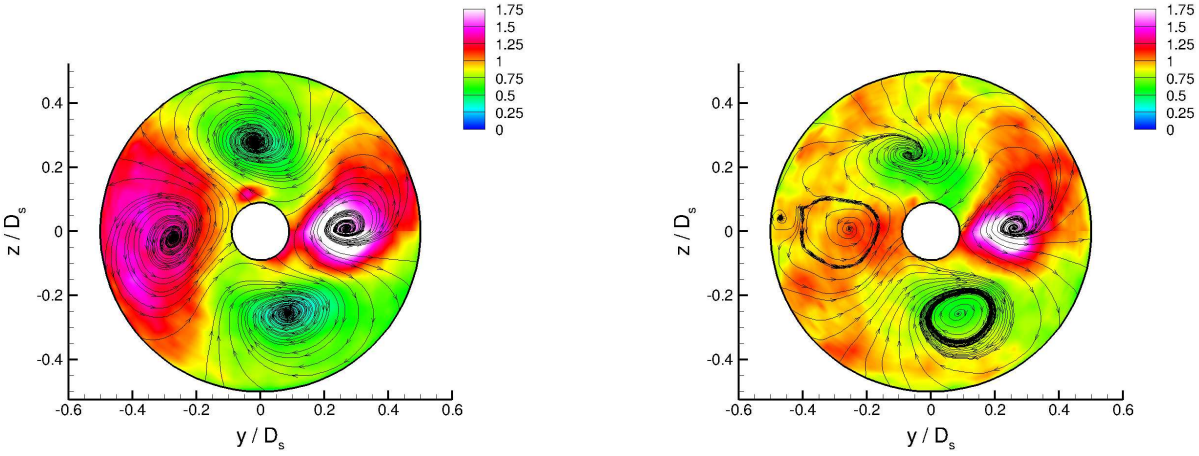

(a) $\alpha_1 = 30°$

(b) $\alpha_1 = 20°$

(c) $\alpha_1 = 15°$

(d) $\alpha_1 = 10°$

Figure 4.28: Rotationally-averaged streamtraces on contours of rotationally-averaged to time-averaged turbulent kinetic energy ratio at $x/D_s = 0.02$ for varying swirl vane angle.

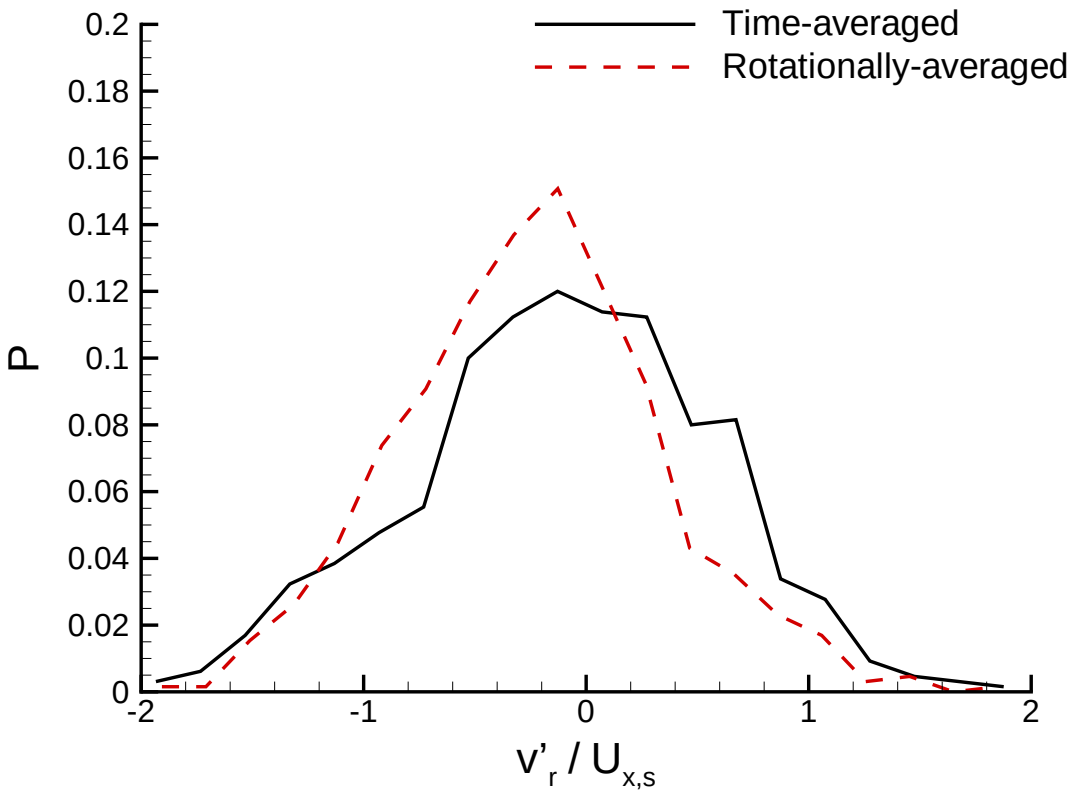

(a) Radial velocity

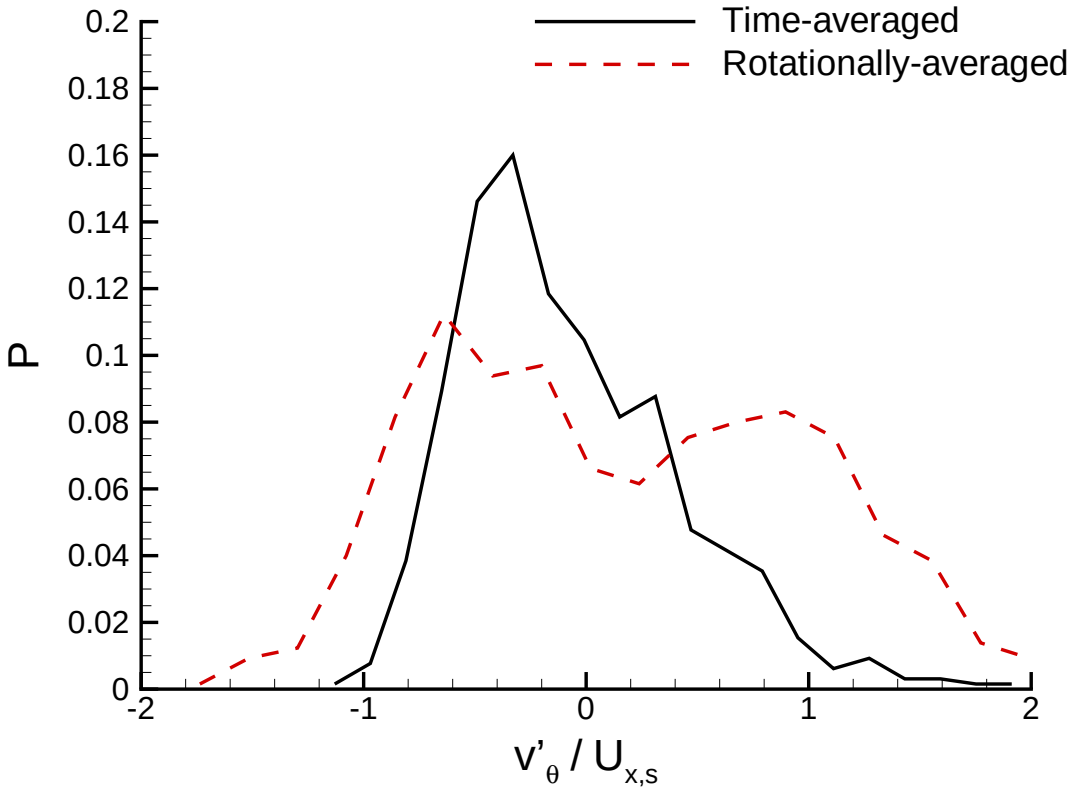

(b) Tangential velocity

Figure 4.29: PDF of fluctuating velocity components in laboratory and rotating frame of reference at $x/D_s = 0.02$, $r/D_s = 0.25$, $\theta = \pi$ for $\alpha_1 = 30°$

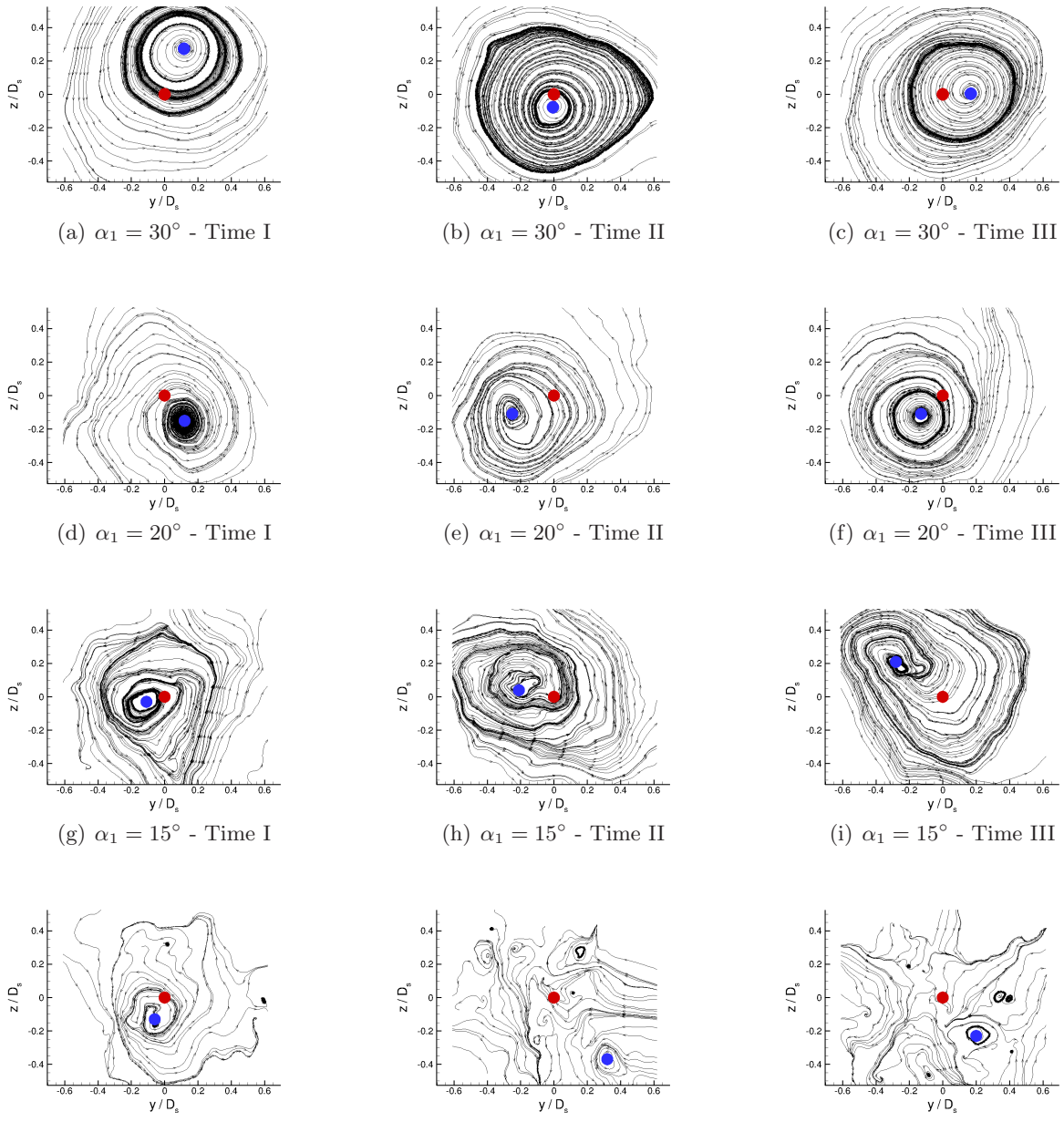

(a) $\alpha_1 = 30°$ - Time I (b) $\alpha_1 = 30°$ - Time II (c) $\alpha_1 = 30°$ - Time III

(d) $\alpha_1 = 20°$ - Time I (e) $\alpha_1 = 20°$ - Time II (f) $\alpha_1 = 20°$ - Time III

(g) $\alpha_1 = 15°$ - Time I (h) $\alpha_1 = 15°$ - Time II (i) $\alpha_1 = 15°$ - Time III

(j) $\alpha_1 = 10°$ - Time I (k) $\alpha_1 = 10°$ - Time II (l) $\alpha_1 = 10°$ - Time III

Figure 4.30: Instantaneous streamtraces at $x/D_s = 2.39$ at arbitrary time-instants for varying swirl vane angle •- geometric centre •- aerodynamic centre from Equation A-24

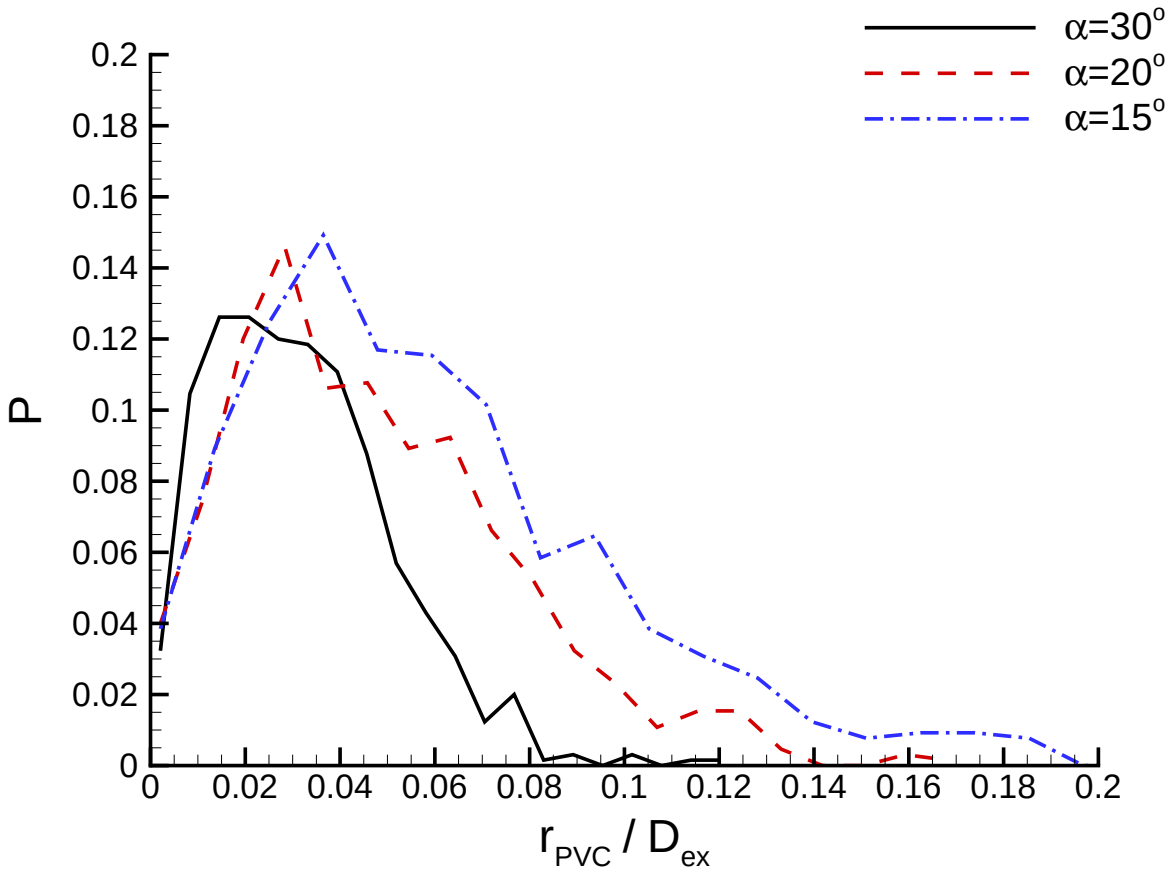

Figure 4.31: Probability density function of radial displacement of PVC for varying swirl vane angle.

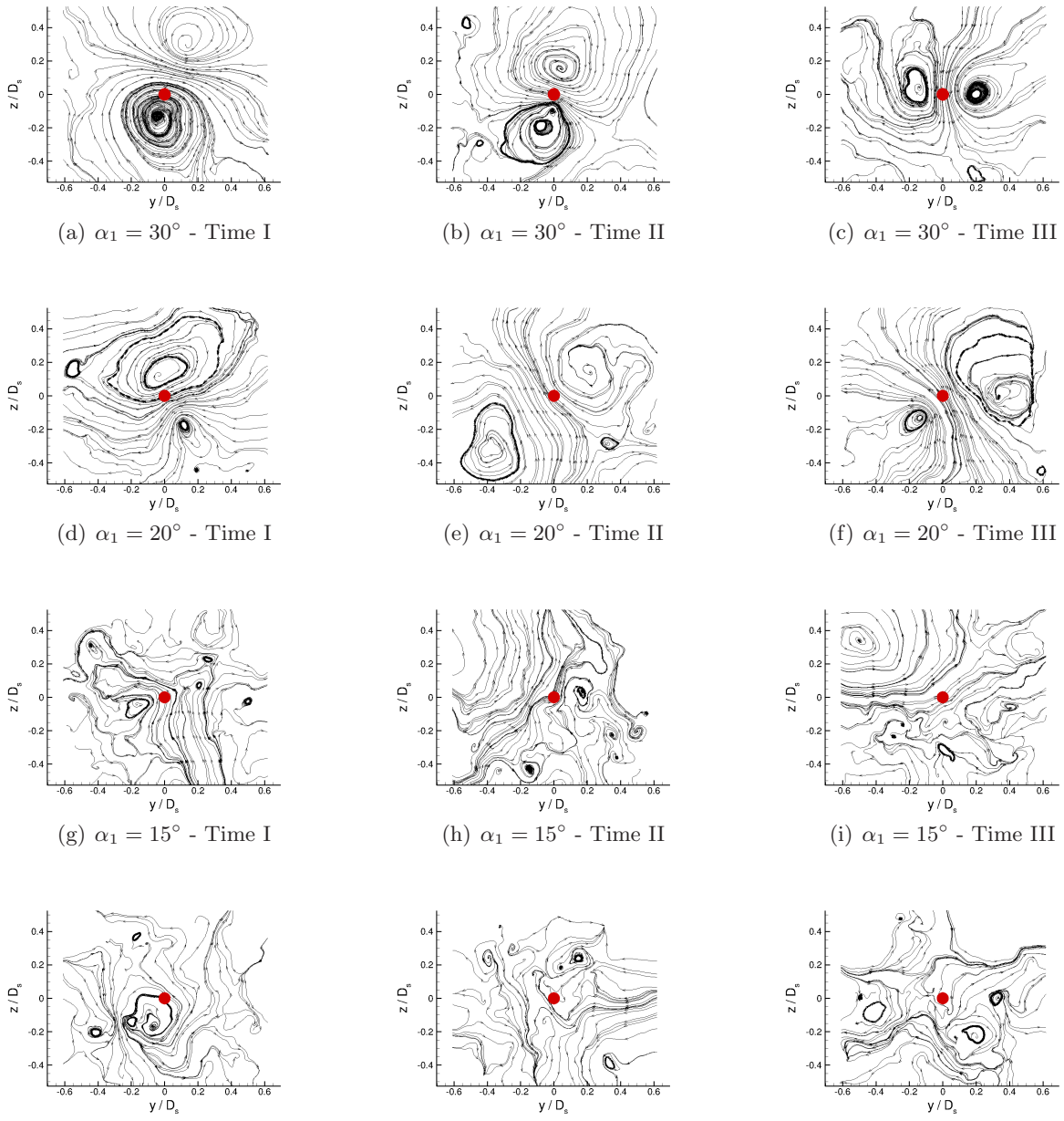

(a) $\alpha_1 = 30°$ - Time I (b) $\alpha_1 = 30°$ - Time II (c) $\alpha_1 = 30°$ - Time III

(d) $\alpha_1 = 20°$ - Time I (e) $\alpha_1 = 20°$ - Time II (f) $\alpha_1 = 20°$ - Time III

(g) $\alpha_1 = 15°$ - Time I (h) $\alpha_1 = 15°$ - Time II (i) $\alpha_1 = 15°$ - Time III

(j) $\alpha_1 = 10°$ - Time I (k) $\alpha_1 = 10°$ - Time II (l) $\alpha_1 = 10°$ - Time III

Figure 4.32: Reynolds-decomposed streamtraces at $x/D_s = 2.39$ at arbitrary time-instants for varying swirl vane angle ●- geometric centre.

Chapter 5

Large Eddy Simulation Results

This chapter presents Large Eddy Simulation (LES) calculations of the modular swirler with $\alpha_1 = 30°$. This has been shown experimentally to exhibit both near and far-field instability modes with a broad range of characteristic frequencies that differ by approximately two orders of magnitude ($S_t \approx 0.01 - 1.2$). In order to capture these features the grid, or spatial filter (Δ), required by LES must be sufficiently fine and is considered in Sections 5.1 and 5.2. Since LES provides a spatially-averaged representation of the instantaneous flowfield long integration times are necessary to obtain statistically-converged ensemble-averaged statistics. Furthermore, since the far-field of the current flow is characterised by a low-frequency PVC ($S_t \approx 0.01$) an adequate number of samples in relevant regions must be captured for spectral analysis. The acquisition of a suitable LES ensemble dataset and a comparison with first and second-order PIV statistics are detailed in Section 5.3. If LES-based methods are to become integral to the design and development of swirl-stabilised combustors it is of paramount importance that frequency components associated with *both* near and far-field CS are predicted with a high degree of fidelity. In order to validate the frequencies predicted by LES, comparison are made with expected frequencies derived from experiment [13, 38] in Section 5.4. An attractive property of CFD is that full volumetric information is available which can be utilised to explore regions unavailable experimentally. Conditional-averaging techniques, such as rotational-averaging, that were applied to 2C-PIV in the previous chapter can also be extended to explain complex 3D flow behaviour. A volumetric analysis of near and far-field CS is performed in Section 5.5.

5.1 Computational Domain

In Section 3.3.1 it was argued that in order to capture the unsteady dynamics of the modular swirler, the computational domain must include the swirl duct, expansion chamber and a portion of the exhaust. To simplify the mesh generation procedure and reduce the computational effort, it was decided to begin the calculation just downstream of the radial vanes rather than model them explicitly. This decision was based on previous experimental [14] and computational studies [52, 50, 53, 55] which have shown that to include the vanes in the swirler does not exert any

significant influence on the formation of any unsteady periodic structures. Hence, the computational geometry and domain used here for LES calculations is axisymmetric with respect to the geometric centreline, allowing a polar-type mesh (Figure 3.4) to be used. To ensure the quality and suitability of the meshes used in this thesis a number of factors considered are covered in the following subsections.

5.1.1 Near-Wall Resolution

Initially, consideration had to be given to the appropriate resolution requirements of the high Re wall-bounded flow within the swirl duct. As already discussed in Section 3.2.1, wall-dominated flows require extensive mesh refinement to resolve energy-containing near-wall eddies and the associated computational cost is often considerable. Furthermore, as LULES adopts a structured multi-block approach requiring conformal mapping between connecting blocks, it is clear from Figure 3.4 that high levels of local mesh refinement within the swirl duct would then be imposed throughout the expansion chamber. In order to avoid this large computational penalty, it was decided to adopt the wall-function approach. (Equation 3.66). For this to be implemented correctly, Sagaut [88] recommends that the near-wall radial spacing should be such that $y^+ \approx 20 - 200$. The procedure adopted to achieve this is considered in the following subsection along with considerations regarding an adequate mesh density.

5.1.2 Mesh Density

Previous LES calculations of swirl injector flows reviewed in Section 1.3.2 have utilised a range of grid densities on both structured and unstructured meshes. Wegner et al. used a $0.8{\times}10^6$ node structured mesh to investigate a non-premixed swirl-burner previously studied in the TECFLAM-project (Schneider et al. [46]). The entire swirler, including radial vanes, was included in the calculation and 16 radial nodes were used across the swirl duct. Studies by Tang et al. [51, 108] used a polar-type grid to investigate a multi-stream swirler consisting of $\approx 0.5 \times 10^6$ nodes with 66 in the azimuthal direction. For these simulations 52 radial nodes were used from the centreline to the outer wall of the expansion chamber, however, it is not clear how many of these were used across the swirl duct. Polar-type meshes have also been employed by Lu et al. [126], Dunham et al. [50] and Wang et al. [52]. The studies of Lu et al. [126] investigated turbulent swirling flows in a dump chamber ($E = 1.5$), whilst Dunham et al. [50] simulated the current Turbomeca swirler geometry ($E = 3.72$) under various conditions. Both used $\approx 0.9 \times 10^6$ nodes with 81 in the azimuthal direction. In Lu et al. [126] 75 radial nodes were used from the centreline to the outer wall of the expansion chamber, however, it is not clear how many of these were used across the swirler exit. In Dunham et al. [50], a total of 180 radial nodes were used with 39 across the swirl duct. The flows considered in Wang et al. [52] were extremely complex, featuring three sets of counter-rotating swirl vanes requiring a somewhat denser mesh consisting of $\approx 2 \times 10^6$ nodes with around half situated within the swirler. The major disadvantage of polar-type meshes, as noted by Tang et al. [51], is the time-step restriction imposed on explicit LES methods by the

small cell size in the vicinity of the centreline. To overcome this restriction, a number of authors have utilised structured O-grids which also avoid the necessity of specifying centreline boundary conditions. For example, Wegner et al. [58] used this approach to perform a calculation of the Turbomeca injector geometry, including the radial vanes, consisting of 3.5×10^6 nodes. Although the overall mesh density of Wegner et al. [58] is considerably higher than Dunham et al. [50], a similar radial resolution was used within the swirl duct (30 and 39 nodes respectively). Garcia-Villalba et al. [55] used an O-grid mesh consisting of around 6×10^6 hexahedral cells with 160 nodes in the azimuthal direction to investigate an annular swirling jet issuing into an unconfined ambient fluid. Roux et al. [59] also investigated the Turbomeca swirler using a similar grid density as Wegner et at. [58] with an unstructured mesh consisting of 3×10^6 elements. Of these, 20% (0.6×10^6) of the elements were located in the upstream plenum and swirler and 50% (1.5×10^6) in the upstream half of the combustion chamber.

To assess the sensitivity of the solution to the selected numerical grid, a refinement study was undertaken. An initial mesh was designed with 81 azimuthal nodes. For clarity this will be referred to as the datum mesh and is shown in Figure 5.1. Since y^+ includes u_τ it was necessary to perform a number of preliminary simulations (based on 35 radial nodes across the swirl duct similar to Dunham et al. [50] and Wegner et al. [58]) with varying near-wall spacing, y_P. The final $y_\mathrm{P} = 0.3 \times 10^{-3}$m gave $y^+ \approx 20$ along the inner wall of the swirl duct which is consistent with the recommendation [88] given above. To limit discretisation errors, great care was taken to ensure that the grid expansion ratio did not exceed 5% in any direction. To investigate the effect of axial refinement on the datum mesh, the nodal distribution in the radial and circumferential directions was fixed and the number of nodes doubled in the axial direction throughout the swirl duct and the near-field of the expansion chamber ($0 \geq x/D_s \leq 1.0$). To investigate the effect of circumferential refinement on the datum mesh the nodal distribution in the axial and radial directions was fixed and the number of nodes doubled in the circumferential direction. The resulting meshes will be referred to as the datum mesh with axial refinement (w.a.r) and the datum mesh with circumferential refinement (w.c.r) respectively (see Figure 5.2). Further details regarding the computational meshes used in the refinement study are provided below in Table 5.1.

	Swirl Duct				Expansion Chamber				Exhaust Duct				Domain Total
	ni	nj	nk	Total	ni	nj	nk	Total	ni	nj	nk	Total	ni×nj×nk
Datum	89	35	81	0.25×10^6	116	123	81	1.16×10^6	28	25	81	56.7×10^3	1.46×10^6
Datum w.c.r	89	35	161	0.5×10^6	116	123	161	2.3×10^6	28	25	161	112.7×10^3	2.91×10^6
Datum w.a.r	175	35	81	0.5×10^6	166	123	81	1.65×10^6	28	25	81	56.7×10^3	2.2×10^6

Table 5.1: Details of computational grids used in refinement study (ni: axial direction, nj: radial direction, nk: circumferential direction)

5.1.3 Filter Width

The concept and mathematical background of LES was introduced in Section 3.1.2, however, to make a distinction between its variants Pope [7] suggests the following definitions:

- LES with full near-wall resolution - the filter (usually the grid) are sufficiently fine to resolve 80% of the energy everywhere.
- LES with near-wall modelling - the filter and grid are sufficiently fine to resolve 80% of the energy remote from the wall, but not in the near-wall region.
- VLES - the filter and grid are too coarse to resolve 80% of the energy in any region of the flow.

Pope [7] has shown that for high-Re homogeneous isotropic turbulence and an isotropic filter of width $\Delta = 1/6{}^{i}L_{ii}$, where ${}^{i}L_{ii}$ is the integral lengthscale, the filtered field contains 80% of the energy. Clearly, ${}^{i}L_{ii}$, which is readily availiable from the PIV data presented in Chapter 4 for the current flow, can be utilised to assess the adequacy of the numerical grids detailed above. For the inhomogeneous flows considered in this thesis, the LES transport equations are solved on anisotropic grids with spacings Δx, Δr and $r\Delta\theta$ in the three coordinate directions. The filter is then anisotropic and the characteristic width is generally taken as $\Delta = (\Delta x \Delta\theta r \Delta r)^{1/3}$ as suggested by Deardorff [102]. In practical LES applications, ${}^{i}L_{ii}$ is likely to vary over an extremely broad range and a strict adherence to Pope's criterion may result in excessively large numerical grids. Moreover, if characteristic timescales of the flow are large in comparison to the timestep required for numerical stability (see Section 5.1.4) the associated computational cost may prove prohibitive. Since the current aim of this thesis is to assess the fidelity with which LES captures important quantitative details of the near-field and far-field CS reported in Chapter 4, it was decided that the most suitable approach would be to choose grids that enforce Pope's criterion in these critical regions and introduce a degree of relaxation elsewhere. In this way, overall computational requirements could be minimised, thus allowing calculations to proceed for a duration sufficient to provide a frequency resolution ($f_{\text{res}} = 1/N_{\text{T}}\Delta t$) suitable for making a quantitative assessment of near-field (high frequency) and far-field (low frequency) CS with the available computational resources. From the $x - r$ plane PIV measurements for $\alpha_1 = 30°$ shown in Figure 4.14(a), near-field CS may be identified from maxima of in-plane turbulent kinetic energy in the region defined approximately as $0 \geq x/D_s \leq 0.7$, $0.1 \geq r/D_s \leq 0.6$. Far-field CS are located in the vicinity of the expansion chamber centreline, say $r/D_s \leq 0.1$, which can also be observed in Figure 4.14(a). Figure 5.3 shows the characteristic filter width ($\Delta = (\Delta x \Delta\theta r \Delta r)^{1/3}$) for various meshes compared with one-sixth axial, radial and circumferential lengthscales ($1/6\ {}^{x}L_{xx}$, $1/6\ {}^{r}L_{rr}$ and $1/6\ {}^{\theta}L_{\theta\theta}$ respectively) derived from PIV at various axial locations. At $x/D_s = 0.02$, all grids are fine enough to resolve the majority of energy containing scales across the majority of the swirl duct. The grids are not sufficiently fine to resolve 80% of the energy in the outer region, however,

it is argued that this is not so important as this is outside of the region containing the near-field CS emerging from the swirl duct. Further downstream at $x/D_s = 0.27$ and $x/D_s = 0.53$, the datum w.c.r and the datum w.a.r meshes are finer than, or at worst equal to, all the one-sixth lengthscales in the region $0 \geq r/D_s \leq 0.5$ which includes the area directly influenced by near-field CS identifed above. Although the datum mesh slightly exceeds one-sixth lengthscales at $x/D_s = 0.53$, $r/D_s \approx 0.32$, it is at least comparable and should not prove detrimental to the fidelity of the simulation. At larger radii ($r/D_s \geq 0.5$), decreases in one-sixth lengthscale are observed at $x/D_s = 0.27$ and $x/D_s = 0.53$, partially attributable to the presence of solid boundaries such as the end wall of the expansion chamber. From Figure 4.1(a), which shows time-mean streamtraces from $x - r$ plane PIV measurements in the expansion chamber for $\alpha_1 = 30°$, this region is characterised by a CRZ and the levels of grid refinement required to resolve 80% of the energy associated with this feature are considered not crucial to the present aim. The fact that all grids are sufficiently fine in comparison to one-sixth lengthscales downstream of the swirl exit in the vicinity of the expansion chamber centreline suggests that far-field CS should be well resolved.

To assess further the adequacy of the meshes used it is informative to examine the ratio of sub-grid to molecular viscosity, ν_{sgs}/ν (ν_{sgs} from Equation 3.37). Figure 5.4 shows time-averaged contours of ν_{sgs}/ν for the various meshes. According to Durbin and Medic [127], values of ν_{sgs}/ν up to around 20 are in the well-resolved LES regime. A maximum of $\nu_{\text{sgs}}/\nu \approx 20$ is reported in Garcia-Villalba [105] in the near-field of the swirler exit using the Smagorinsky model. Inside the swirl duct ($x/D_s \leq 0$) and in the vicinity of the swirler exit ($x/D_s = 0.0$, $0 < r/D_s < 0.5$), $\nu_{\text{sgs}}/\nu \leq 10$ for all grids. Further downstream in the expansion chamber, a similar ratio of ν_{sgs}/ν is also observed close to the centreline. At larger radii, increased levels of sub-grid scale viscosity persist in regions of the flow characterised by the presence of the CRZ with $\nu_{\text{sgs,max}}/\nu \approx 20$ in the case of the datum mesh. It can be concluded that, based on the criterion of Durbin and Medic [127], regions identified as being critical to the fidelity of near-field and far-field CS analysis are adequately well resolved.

5.1.4 Computational Requirements

Due to the explicit Adams-Bashforth scheme used by LULES the maximum timestep, Δt_{max}, is restricted by the CFL and DFS numbers defined in Equations 3.58 and 3.59. For the datum mesh it was found that $\Delta t_{\text{max}} = 2.0 \times 10^{-6}$ gave a maximum average CFL number of approximately 0.25 and an maximum average DFS number of approximately 0.055. Although the axial and circumferential location of the maximum CFL and DFS numbers varied during the simulation the radial location always coincided with the centreline ($j = 2$) node. For the datum mesh with axial refinement $\Delta t_{\text{max}} = 2.0 \times 10^{-6}$ was also suitable for solution stability, however, for the datum mesh with circumferential refinement it was necessary to reduce the time step to $\Delta t_{\text{max}} = 1.0 \times 10^{-6}$ to achieve stability.

To improve the computational efficiency of the code, the solution of the Possion equation for pressure is accelerated using a multi-grid V-cycle as described in Section 3.2.1. An appropriate number of multi-grid cycles was determined by examining the residual of the pressure equation (defined in Equation 3.60). By comparing the ratio of the residual at cycle i, ϕ^i, to that of the previous cycle, ϕ^{i-1}, it was found that ϕ^i/ϕ^{i-1} asymptotes to approximately unity after 15 cycles and this was taken as a sufficient indication of solution convergence. This was also found to be the case for meshes with axial and circumferential refinement. All calculations were performed on a PC cluster comprising 16 64-bit Itanium processors. Since some processors treated more than one block, a weight function was used to obtain an appropriate load balance to achieve optimum computational efficiency. This is an important feature for a numerical solver dealing with block-based structured grids in a distributed computing environment.

To assess the impact of the numerical settings required for solution stability and convergence on the number of CPU hours required for a simulation it is instructive to use characteristic timescales of the flow being simulated. The timescale, T_s (Equation 4.1), is characteristic of bulk flowfield rotation in the vicinity of the swirler exit. Another important timescale, particularly for ensuring initial transients of the solution have propagated through the computational domain, is the residence or flow-through time which will be denoted T_r. In the present case since fluid elements follow helical paths the following practice was adopted to compute T_r. An estimate for T_r was obtained (using Tecplot) from the length of a streamtrace released from the inlet plane of a time-mean dataset and the average velocity magnitude along it (see Figure 5.5). This gave a characteristic length and velocity of 0.88m and 1.31m/s respectively, and thus, $T_r \approx 0.67$s. Table 5.2 compares the ratio of T_s and T_r relative to $\Delta t_{\max}$ for all computational meshes based on 15 multi-grid pressure cycles and 16 64-bit Itanium processors.

	$\Delta t_{\max}$	$T_s/\Delta t_{\max}$	CPU Hrs. / T_s	$T_r/\Delta t_{\max}$	CPU Hrs. / T_r	% Increase CPU Hrs. (approx)
Datum	2.0×10^{-6}	10×10^{3}	5.9	670×10^{3}	195	-
Datum w.c.r	1.0×10^{-6}	20×10^{3}	23.4	1.34×10^{6}	782	300
Datum w.a.r	0.5×10^{-6}	10×10^{3}	8.9	670×10^{3}	298	50

Table 5.2: LES computational requirements - calculations performed on 16 64-bit Itanium processors with 15 multi-grid pressure cycles

This highlights the increase in computational expense resulting from finer numerical grids. The increase associated with axial refinement relative to the datum mesh ($\approx 50\%$) is relatively modest in comparison with that associated with circumferental refinement ($\approx 300\%$). There are two reasons for this. Firstly, in the former case it was possible to maintain soultion stability with a computational timestep identical to that of the datum mesh, whilst in the latter case this had to be halved. Secondly, axial refinement could be undertaken locally in regions of high spatial

gradients, i.e. inside the swirler and the near-field of the expansion chamber, resulting in $\approx 50\%$ more nodes relative to the datum mesh. Circumferential refinement is performed on a global basis and the required number of nodes is double that of the datum mesh. Careful consideration must be given as to whether or not the additional levels of refinement are necessary. In the present case this is achieved through a qualitative assessment of near and far-field CS development and is considered in the following seciton.

5.2 Coherent Structure Development

An essential requirement of the numerical grids detailed in Table 5.1 is that they are capable of capturing the main flow features and unsteady dynamics of the modular swirler observed experimentally in Chapter 4. The importance of S_{N} on the flow has already been demonstrated and, thus, in order to perform a comparable analysis between simulation and experiment it was essential to match this parameter as closely as possible. Appropriate inlet conditions were calculated using Equation 3.77 together with measured $\dot{m}$ and $\dot{G}_\theta$ from Table 4.1 applicable to $\alpha_1 = 30°$. This lead to mean radial and tangential swirl duct inlet velocities of $\langle u_r \rangle_{\mathrm{in}} = 0.78\mathrm{m/s}$ and $\langle u_\theta \rangle_{\mathrm{in}} = 1.38\mathrm{m/s}$ respectively. It was found that in order to match $G_\theta = 0.078\mathrm{kgm/s^2}$ at $x/D_s = 0.02$ it was necessary to increase $\langle u_\theta \rangle_{\mathrm{in}}$ by $\approx 7\%$ to 1.484m/s. Due to the action of wall-shear within the swirl duct $\dot{G}_\theta$ decays and hence the need for this adjustment. Table 5.3 details flow rates at swirler exit obtained through direct integration of mean profiles of axial and tangential velocity at $x/D_s = 0.02$. In keeping with the approach adopted for experimental data presented in Chapter 4, to ensure these were representative of only the swirl stream, integration was performed from $0.09 \geq r/D_s \leq 0.5$ and negative axial velocities associated with the CTRZ excluded from the summation.

	$\dot{m}$	$\dot{G}_x$	$\dot{G}_\theta$	S_{N}	$U_{x,s}$
PIV	2.15	5.26	7.82×10^{-2}	0.80	2.0
LES	2.11	5.28	7.87×10^{-2}	0.79	1.96

Table 5.3: Swirler exit flow rates $x/D_s = 0.02$ for $\alpha_1 = 30°$

Following Tang et al. [108], each simulation was run for approximately $3T_r$ to allow initial transients to propagate through the computational domain and for the flow to reach a statistically-stationary state. As already shown in Chapter 4, the presence of CS can be determined qualitatively by examining instantaneous velocity vectors or streamtraces in $x-r$ and $r-\theta$ measurement planes. Figure 5.6 shows instantaneous streamtraces for the three computational grids investigated at an arbitrary time instant after the initial transient period ($t > 3T_r$). It should be noted that, in order to provide a clearer picture of the flowfield, azimuthal averaging has been applied to Figure 5.6. After a period of $3T_r$ the flow is well developed and large-scale features such as CRZ and CTRZ are well established. These features dominate the expansion chamber and the

strong shear-layers they form with the swirl cone issuing from the swirl duct are clearly visible. In Chapter 4 it was shown that the near-field of the expansion chamber ($0 \geq x/D_s \leq 1$) is dominated by a pair of high-frequency vortical structures, whilst in the far-field ($x/D_s > 1$) a low-frequency PVC exists. To examine the ability of the various computational grids to capture these important unsteady features, the instantaneous flow was examined at two $r - \theta$ planes extracted from the computational volume located at $x/D_s = 0.02$ (Figure 5.7) and $x/D_s = 2.39$ (Figure 5.8). It should be noted that although these Figures were obtained at arbitrary time instants, computational predictions were constantly monitored before ($t < 3T_r$) and after ($t > 3T_r$) the initial transient period to ensure that the examples presented here are representative of the statistically stationary flowfield. Clearly, evidence from Figure 5.7 suggests that none of the computational grids are able to adequately capture the expected CS in the vicinity of the swirler exit. Further downstream, Figure 5.8 shows a significant displacement of the aerodynamic centre of the flow from the geometric centre as highlighted by the red dot. As noted previously, this behaviour is strongly associated with a PVC phenomenon thus demonstrating the suitability of all computational grids in this region of expansion chamber.

From the discussion presented above it can be concluded that axial or circumferential refinement on the datum mesh does not exert a significant influence on the formation (or not) of CS in the vicinity of the swirler exit. Previously, Midgley [13] has suggested that these are formed as a result of flow separation from the inner wall of the swirl duct. To avoid the large computational penalty associated with resolving the near-wall dynamics of high-Reynolds turbulent flow it should be recalled from Section 5.1.1 that all computational grids detailed in Table 5.1 were designed with a near-wall resolution such that the wall-function approach described in Equation 3.66 could be implemented. It is likely that this approach, developed within the ideal framework of attached equilibrium turbulent boundary layers without pressure gradient, is not immediately relevant to the complex near-wall dynamics associated with the types of flows considered here. A number of studies reviewed in Section 5.1.2 have reported near-wall resolutions that fall in both the viscous sublayer ($y^+ < 5$) and buffer layer ($5 < y^+ < 30$). For example, Lu et al. [126] used $y^+ \approx 2 - 6$, Wegner et al. [58] and Wang et al. [52] both used $y^+ \approx 3 - 10$ without a near-wall model, whilst Tang et al. [108] used $y^+ \approx 1.5 - 50$. Although these do not have sufficient mesh densities to faithfully represent *all* of the near-wall dynamics (such as boundary-layer streaks), they do however suggest that increased resolution and, in particular use of the no-slip condition rather than a near-wall model, may be more suitable in the present situation. In order to minimise computational expense, it was decided therefore to investigate the effect of radial refinement on the datum mesh in the near-wall region of the swirl duct since increased axial or circumferential refinement have been shown not to be significant. In keeping with the conventions adopted in Section 5.1.2, this will be referred to as the datum mesh with radial refinement (w.r.r) and was generated with an identical number of axial, radial and circumferential nodes

as the datum mesh detailed in Table 5.1. The axial and circumferential nodal distribution was kept constant whilst the radial distribution was clustered towards the inner wall of the swirl duct with a near-wall spacing of 0.1×10^{-3}m ($y^+ = 2 - 11$) as shown in Figure 5.9. By employing an identical number of nodes, the solution from the datum mesh could be utilised as a starting solution to avoid the considerable computational effort if starting from a basic level of initial conditions. To allow the flowfield to adjust to the imposed changes, the simulation was run for one additional flow-through time.

Figure 5.10 shows instantaneous and Reynolds-decomposed streamtraces in an $r - \theta$ plane at the swirler exit ($x/D_s = 0.02$) for the datum mesh with radial refinement. The turbulent structures identified in Figure 5.10 are in good agreement with experimental observations (Figure 4.18), indicating the importance of an increased near-wall resolution within the swirl duct. The ability of LES to capture the unsteady dynamics of the modular swirler are presented in Sections 5.4 and 5.5 following a statistical analysis of the predictions considered in the next section.

5.3 Large-Eddy Simulation Ensemble Data

LES simulations were performed for approximately $4T_r$ to allow initial transients to propagate through the computational domain. At this point the flowfield is statistically stationary as shown in Figure 5.6 and data sampling can begin. In order to validate LES calculations against the PIV data presented in Chapter 4, consideration had to be given to the total number of samples, N_{T}, and sampling frequency, f_s (or sampling interval $\Delta T = 1/f_s$), required. To investigate the spectral characteristics of the Turbomeca injector considered here, Midgley [13] used a 5μm Dantec 55P11 miniature single hotwire with a maximum sampling frequency of 25kHz. These measurements were performed in air and the reference scales of $D_s = 0.03763$m and $U_{x,s} = 27.19$m/s [13] therefore give a maximum Strouhal number of $S_{t,\max} = 34.6$. At $x/D_s = 2.65$, $r/D_s = 0.19$ a PVC frequency of $S_t \approx 13.2 \times 10^{-3}$ was measured [13]. For the LES calculations presented here which utilise water as the working medium, a sampling frequency of 2kHz ($\Delta T = 0.5$ms) leads to $S_{t,\max} = 38.4$ based on the reference scales in Table 5.3. To capture $O[5]$ PVC cycles for spectral analysis, a total of 16384 (2^{14}) samples were collected at 2kHz giving a frequency resolution of 0.12Hz and a corresponding minimum Strouhal number of $S_{t,\min} = 2.3 \times 10^{-3}$. In order to utilise fully the available volumetric information from LES, complete 3D velocity and pressure fields were exported at each sampling interval, requiring a total storage capacity of 439GB. Details of the LES ensemble are summarised in Table 5.4.

N_T	ΔT	$N_T \Delta T$	$(N_T \Delta T)/T_s$	$(N_T \Delta T)/T_r$	$S_{t,\min}$	$S_{t,\max}$	CPU Hrs.
16384	0.5ms	8.192s	409.6	12.2	2.3×10^{-3}	38.4	2379*

Table 5.4: Summary of LES ensemble data - calculations performed on 16 64-bit Itanium processors with 15 multi-grid pressure cycles. *It should be noted that an additional 4 flow through times were required prior to sampling to obtain a fully-developed flowfield (see Section 5.2) increasing the overall walltime to approximately 3160 CPU hours.

As already highlighted in Section 2.4.5, the accuracy of estimates for statistical quantities, such as mean and r.m.s velocities, is dependent on the number of (statistically) independent samples, N_I and is considered in the following subsection.

5.3.1 Statistical Convergence

In Section 2.4.4, two points were selected, $x/D_s = 0.02$, $r/D_s = 0.4$ and $x/D_s = 1.06$, $r/D_s = 0.0$ to investigate the statistical convergence of PIV data based on 650 independent samples. In order to determine the number of statistically independent samples available from the total LES ensemble of $N_T = 16384$ samples it was necessary to determine local integral timescales at these locations. The integral timescale, T_{ij}, is defined in Equation A-17 and is taken as the integral of the autocorrelation function (ACF) from zero temporal offset ($\tau = 0$) to the first zero crossing (FZC) of the time axis. At this point, a property at $t = t_0 + \tau$ is statistically independent, or uncorrelated, with that at t_0. Figure 5.11 shows ACFs obtained at $x/D_s = 0.02$, $r/D_s = 0.4$, $\theta = \pi$ and $x/D_s = 1.06$, $r/D_s = 0.0$, $\theta = \pi$ based on the above selected sample rate (2kHz, $\Delta T = 0.5$ms). In Figure 5.11, the range of the temporal offset axis has been adjusted from $t/T_s = 0 - 10$ at $x/D_s = 0.02$ to $t/T_s = 0 - 100$ at $x/D_s = 1.06$ in order to account for the large variation in local timescale. Figure 5.11 was obtained at $\theta = \pi$ but subsequent analysis performed at all circumferential nodes from $\theta = 0 - 2\pi$ revealed some degree of variation in the ACF and corresponding integral timescale. To account for this, integral timescales were computed from $\theta = 0 - 2\pi$ and then circumferentially averaged. These are detailed below in 5.5 relative to the sampling interval, ΔT, and total duration of the LES ensemble, $N_T \Delta T$.

x/D_s	r/D_s	$\langle T_{xx} \rangle/\Delta T$	$\langle T_{rr} \rangle/\Delta T$	$\langle T_{\theta\theta} \rangle/\Delta T$	$N_T \Delta T/\langle T_{xx} \rangle$	$N_T \Delta T/\langle T_{rr} \rangle$	$N_T \Delta T/\langle T_{\theta\theta} \rangle$
0.02	0.4	4	3	4	4602	5980	4428
1.06	0.0	79	90	88	207	182	186

Table 5.5: Integral timescale relative to ΔT and $N_T \Delta T$ at selected locations

At the first point approximately 1 in 4 samples are statistically independent, whilst at the second point only 1 in every 90 samples is uncorrelated since the integral timescale is approximately one order of magnitude larger. In Section 2.4.5, statistical convergence of PIV data was demonstrated

by dividing datasets at each location into subsets and plotting against confidence interval curves (Equations 2.18 and 2.19) for confidence levels of 95% and 99%. A similar analysis was performed on the LES data and is shown in Figures 5.12 and 5.13. In the notation used, $\langle u_{i,\mathrm{N}} \rangle$ and $\langle u'_{i,\mathrm{N}} \rangle$ are the mean and r.m.s velocities based on the number of members of the subset, whilst $\langle u_{i,\mathrm{P}} \rangle$ and $\langle u'_{i,\mathrm{P}} \rangle$ are the estimated population parameters based on the maximum number of samples. In the vicinity of the swirler exit (Figure 5.12), all statistical quantities are observed to converge within the specified confidence intervals as N_I is increased. Due to the integral timescale at $x/D_s = 1.06, r/D_s = 0.0$, it was only possible to obtain ≈ 180 statistically independent samples. To increase N_I and fully utilise the volumetric information provided by CFD, spatial averaging in a statistically homogeneous direction is often used. The polar-type computational grids used here are well suited to this form of averaging in the azimuthal direction and this has been adopted throughout this thesis. The increase in independent samples depends on the integral lengthscale defined in Equation A-13 which is a measure of the distance over which two points are correlated in space. In direct analogy to the integral timescale, only one statistically independent sample exists per integral lengthscale. Unfortunately, this approach does not significantly increase N_I in the vicinity of the geometric centreline as phenomena here are hightly correlated and the spatial separation between grid points is small.

5.3.2 Single Point Statistics

In this subsection direction comparison between mean, rms and shear stresses extracted from LES at axial stations of $x/D_s = 0.02, 0.27, 0.53$ and 1.06 are made with PIV. From Figure 4.1(a), the outer shear-layer shed from the swirler has a time-mean reattachment location on the outer wall of the expansion chamber of $x_\mathrm{L}/D_s \approx 1.45$. Regular monitoring of LES revealed a large variation in the instantaneous reattachment location as shown for various time instants in Figure 5.14. It should be noted that in Figure 5.14, and for the remainder of this Chapter, $t/T_s = 0$ refers to the beginning of the sampling period *after* the flow had reached a statistically stationary (i.e. after $4T_r$) state *not* the beginning of the simulation at initial conditions. Figure 5.15 shows the instantaneous reattachment location of the outer shear-layer on the outer wall of the expansion chamber as a function of non-dimensional time, t/T_s. This fluctuates around $x_\mathrm{L}/D_s \approx 1.4$ from $t/T_s \approx 0 - 100$ and $x_\mathrm{L}/D_s \approx 1.8$ from $t/T_s \approx 100$ onwards. Throughout this period the instantaneous flowfield was continuously monitored at $x/D_s = 0.02$ as shown in Figure 5.16. The vortex pattern identified in Figure 5.10 is clearly visible from $t/T_s \approx 0 - 125$ (Figures 5.16(a)-(f)) and $t/T_s \approx 300 - 325$ (Figures 5.16(j) and (k)) whilst at other times no CS are detected. Similar behaviour has already been observed experimentally (Figure 4.18) suggesting a similar bimodal switching between flow states has been captured by LES. It is interesting to note that the reattachment location appears to be intimately linked to the presence of CS at the swirler exit. For example, when these are observed from $t/T_s \approx 0 - 100$ the reattachment point is located significantly further upstream than when no CS were detected. To ensure a statistical

analysis of LES comparable with experiment some consideration had to be given to these issues. From the available LES ensemble data, two sets of single point statistics were created. The first used only samples from $t/T_s = 0 - 125$ which corresponds to the period during which LES captures the experimentally observed vortex structure at the swirler exit. This will be referred to as the conditioned set and has a time-mean reattachment location identical to experiment, i.e. $x_{\mathrm{L}}/D_s = 1.45$. The second utilised all members of the ensemble from $t/T_s = 0 - 409.6$ which gives a time-mean reattachment location of $x_{\mathrm{L}}/D_s = 1.72$ (19% larger than PIV) and will be referred to as the complete set.

Figure 5.17 shows axial velocity profiles from both sample sets are in reasonable agreement with experiment, however the conditioned set reproduces overall measured trends more faithfully. At $x/D_s = 0.02$, the complete set deviates slightly from experiment between $0 \geq r/D_s \geq 0.15$ and discrepancies in this region remain with increased downstream distance. This is most notable at $x/D_s = 1.06$ in which the peak axial velocity within the swirl stream is located further inboard ($r/D_s = 0.72$) relative to PIV ($r/D_s = 0.92$). Broadly, these disparities can be attributed to differences in gross flow features such as the size and shape of the CRZ and trajectory of the swirl cone which have already been discussed above. It is interesting to note the variation in centreline ($r/D_s = 0$) axial velocity between the two sample sets at $x/D_s = 0.53$ and $x/D_s = 1.06$. It is reasonable to assume that this is the result of the limited number of statistically independent samples available in this region as characteristic timescales are large in comparison to the sampling interval.

Examination of predicted radial velocity distributions presented in Figure 5.18 reveals the conditioned set is again in overall better agreement with experiment in comparison to the complete set. At $x/D_s = 0.02$, both sets are in reasonable qualitative agreement with experiment, however, neither capture the lower radial velocities measured by PIV which begin at $r/D_s = 0.08$ and results in a minimum at $r/D_s \approx 0.17$. In the vicinity of the experimental minimum, LES predicts a more constant distribution of radial velocity of $\langle u_r \rangle / U_{x,s} \approx 0.2$ which, given the good agreement of axial velocity at this location shown in Figure 5.17(a), suggests that the computed flow angle is too steep in comparison to experiment. It is reasonable to assume that these difference are due to the time-mean location of flow separation from the inner wall of the swirl duct. The location of peak radial velocity obtained from the conditioned set is in excellent agreement with experiment at all locations within the expansion chamber. Apart from a slight underprediction at $x/D_s = 0.27$, the peak magnitude is also well represented. This is contrast to the complete set in which the peak is underpredicted at all axial stations. In a similar way to axial velocity trends discussed above, the location of peak radial velocity deviates furthest from experiment at $x/D_s = 1.06$ which is again attributed to differences in gross flow features.

Although axial and radial velocity distributions differ only slightly between sample sets at $x/D_s = 0.02$, Figure 5.19(a) indicates that greater discrepancies exist in the predicted tangential velocity component. In comparison to experiment and the conditioned set (which exhibit good agreement), the complete set predicts a consistently higher tangential velocity in the region $0 \geq r/D_s \geq 0.25$. Further downstream at $x/D_s = 0.27$ and $x/D_s = 0.53$, both sample sets predict a similar Rankine-like distribution of tangential velocity in accordance with measured trends. At these locations, the predicted position of peak tangential velocity, which is the demarcation between forced and free vortex regions, is in reasonable agreement with PIV. However, at $x/D_s = 0.53$ the predicted magnitude is approximately 10% higher and located slightly inboard. Furthmore, at this location the gradient of tangential velocity across the forced vortex region predicted by both conditioned and complete sets is steeper than that obtained from PIV. At $x/D_s = 1.06$, notable differences exist between simulation and experiement which include an overprediction in peak tangential velocity at $r/D_s \approx 0.2$ by LES and a steeper gradient across the inner forced vortex region. In a similar way to axial and radial velocities, it is suggested that discrepancies between LES sample sets close to the centreline are attributed to variations in the number of statistically independent samples, whilst those at larger radii, for example at $r/D_s \approx 0.6$, are a result of differences associated with gross flow features.

Figures 5.20 to 5.22 show radial profiles of all 3 r.m.s components. As r.m.s velocities measured by PIV are contaminated by sub-grid filtering effects (see Section 2.3.4), Equation 2.13 has been employed to recover actual or 'true' values for axial and radial components in the $x-r$ plane. The difficulties associated with implementing this correction methodology in the $r-\theta$ plane were discussed in Section 2.4.2 and, as a result, r.m.s tangential velocities remain uncorrected. Overall, measured trends of r.m.s axial velocity are faithfully reproduced by the conditioned set as shown in Figure 5.20. This includes the location and magnitude of peak values arising at the interface of the CTRZ and swirl stream, suggesting that the inner axial shear-layer is well resolved. Similarly, conditioned r.m.s radial velocities shown in Figure 5.21 are in good agreement with experimental observations. The radial location of peak values is well represented at all axial stations, however at $x/D_s = 1.06$ the corresponding magnitude is underpredicted relative to PIV. Despite the limited number of statistically independent samples, profiles of conditioned axial and radial r.m.s velocity exhibits a good agreement with experiment in the vicinity of the centreline. Although profiles of conditioned r.m.s tangential velocity shown in Figure 5.22 do not compare as favourably with experiment, the overall agreement is adequate. At $x/D_s = 0.02$, the location of the peak value is inboard of experiment, however the corresponding magnitude is comparable. In a similar way to r.m.s radial velocities at $x/D_s = 1.06$ shown in Figure 5.21(d), the magnitude of the peak tangential components is less than that derived from PIV. Note the peak in $\langle u'_\theta \rangle$ at $x/D_s = 1.06$, which is typical of a PVC. Clearly, there are pronounced differences between samples sets and the agreement of the complete set with experiment is not as

favourable. This is highlighted by notable discrepancies in the location and magnitude of peak quantities in all 3 components at the majority of axial stations. Although this can be partially attributed to differences in the time-mean velocity field discussed above, it is more likely that this is due to the details of CS from within the swirler. Experimentally, these are observed to contribute significantly to turbulence levels and exhibit some bimodal behaviour (Figure 4.18) over a duration ≈ 20 times larger than that captured by LES. Although PIV data presented in Chapter 4 does not have the necessary temporal resolution to investigate the transition between flow states, inspection of instantaneous flowfields revealed that the turbulent structure observed in Figures 4.18(a) and (b) appeared in the majority of cases. Evidence presented in Figure 5.16 suggests that this transition takes place over a timescale which is perhaps up to four order of magnitude larger than the LES sampling interval, or six orders of magnitude larger than Δt. As this places severe restrictions on the number of transition cycles that can be captured computationally, the conditioning of statistics undertaken here is justified on the basis that this provides the most representative comparison with experiment. Further analysis presented in this subsection is therefore based on the conditioned LES set.

From the literature reviewed in Chapter 1 it was found that Reynolds shear-stresses are a largely unreported LES statistic, even in validation calculations. Given that momentum mixing is strongly influenced by cross correlations, this is quite surprising. It was therefore of great interest to assess the performance of LES in this regard and Figures 5.23 to 5.25 show radial profiles of all 3 shear-stress components. Regions of positive and negative correlation between fluctuating axial and radial velocity components at $x/D_s = 0.02, 0.27$ and 0.53, including the location and magnitude of peak values, are faithfully reproduced by LES at all axial stations (Figures 5.23(a)-(c)). Since the shear-stress distribution at these locations is firmly linked to CS emerging from within the swirl duct, the favourable agreement between simulation and experiment suggests that the former is able to capture the essential details of their spatial characteristics. Further downstream at $x/D_s = 1.06$, the expected region of zero shear in the forced vortex region ($0 \geq r/D_s \geq 0.2$ from Figure 5.19) is also predicted by LES. In terms of radial-tangential stresses (Figure 5.24), the overall level of agreement between LES and PIV is satisfactory. At $x/D_s = 0.02$, there are notable discrepancies in terms of the location and magnitude of peak values, however, it should be noted that these are somewhat magnified due to the fact that the vertical scale resolution of Figure 5.24 is approximately one-quarter of that used in Figures 5.23. From 2C-PIV it is only possible to obtain 5 out of 6 independent Reynolds-stress as u_x and u_θ cannot be measured simultaneously. As a result, no comparison of $\langle u'_x u'_\theta \rangle$ with experiment is made in Figure 5.25.

In Figure 5.3, LES filter widths ($\Delta = (\Delta x \Delta\theta r \Delta r)^{1/3}$) for various numerical grids were compared with one-sixth integral lengthscales ($1/6\ {}^{i}L_{ii}$) obtained from PIV measurements to assess the expected level of resolved turbulent kinetic energy from LES predictions prior to computa-

tion. From Figure 5.3 it was concluded that Δ for the datum mesh with radial refinement used in the present simulation should be adequate. To provide a definitive answer to this question, it is necessary to evaluate resolved and SGS energy. k_{res} can be obtained from 2C-PIV by combining data obtained from both $x-r$ ($\langle u'_x u'_x \rangle$ and $\langle u'_r u'_r \rangle$) and $r-\theta$ ($\langle u'_\theta u'_\theta \rangle$) measurement planes. Figure 5.26 shows resolved levels of turbulent kinetic energy obtained from LES are comparable to values from experiment at $x/D_s = 0.02$ and further downstream in the expansion chamber. It is interesting that resolved levels of turbulent kinetic energy from LES agree well with measured values even in regions where the filter width exceeded $1/6\ {}^{i}L_{ii}$. As a final comparison, ratios of peak resolved turbulent kinetic energy from LES and measured turbulent kinetic energy from PIV, denoted $(\hat{k}_{\text{LES}})_{\text{RES}}$ and $(\hat{k}_{\text{PIV}})_{\text{TRUE}}$ respectively, at each axial station are presented in Table 5.6.

x/D_s	$(\hat{k}_{\text{PIV}})_{\text{TRUE}}/U^2_{x,s}$	$(\hat{k}_{\text{LES}})_{\text{RES}}/U^2_{x,s}$	$(\hat{k}_{\text{LES}})_{\text{RES}}$ / $(\hat{k}_{\text{PIV}})_{\text{TRUE}}$
0.02	0.68	0.56	0.82
0.27	0.58	0.52	0.93
0.53	0.62	0.54	0.87
1.06	0.22	0.17	0.77

Table 5.6: Comparison of peak turbulent kinetic energy magnitudes from PIV and LES

This evidence suggests the choice of grid appears adequate in terms of resolved levels of turbulent kinetic energy.

5.4 Spectral Analysis

In Section 1.1, it was reported that numerous authors attribute CS structures related to flow instabilities, excited via acoustic resonant modes in the combustion chamber and the heat release process as a source of combustion instability. If frequencies associated with the most unstable aerodynamic modes are consistent with prevalent acoustic modes there is a potential for flow-acoustic coupling which may reinforce acoustic oscillations and drive combustion instabilities via the Rayleigh criterion defined in Equation 1.1. If LES-based methods are to become integral to the design and development of swirl combustors it is of paramount importance that frequency components associated with CS are predicted with a high degree of fidelity. Spectral analysis of the LES ensemble data detailed in Table 5.4, was therefore performed through direct application of the fast Fourier transform (FFT) algorithm of Danielson and Lanczos as described by Press et al. [128].

5.4.1 Near Field

Near-field velocity spectra deduced from HWA measurements performed in air by Midgley [13] were extremely similar across the radial extent of the swirler and characterised by dominant frequencies of $S_t = 0.62$ and 1.24 (Figure 4.21). As these measurements were obtained using a single

hotwire, the resulting PSDs do not correspond to individual velocity components (see Section 4.2.1). As a result, the expected tonal frequencies of $S_t = 0.62$ and 1.24 are indicated only by vertical dashed lines in Figure 5.27 which shows PSDs of all 3 velocity components obtained from LES at $x/D_s = 0.27$, $r/D_s = 0.24$. The details of CS from within the swirler have been shown above to influence first and second-order single-point statistics. To assess the effect on frequency characteristics, PSDs in Figures 5.27(a),(c) and (e) are based on 4096 ($t/T_s = 0 - 102.4$) samples and Figures 5.27(b),(d) and (f) are based on 16384 ($t/T_s = 0 - 409.6$) samples. In keeping with the previous section these will be referred to as conditioned and complete sample sets. In both cases, distinct peaks are predicted within the range of turbulent broadband frequencies which line up well with HWA.

There are a number of differences between sample sets with the most notable being the amplitude relationship between primary and secondary peaks. From HWA (Figure 4.21) the primary peak is observed to dominate the secondary peak at the majority of radial locations including $r/D_s = 0.24$ which is considered here. For the complete set the primary peak is greater than, or at least equal to, the secondary peak whilst for the conditioned set the secondary peak dominates the primary peak for all velocity components. These differences are clearly linked to the the temporal variation of CS from within the swirler shown in Figure 5.16. From $t/T_s = 0 - 100$ (Figures 5.16(a)-(e)) there is evidence of a strong pairing between vortices and hence the prominence of the secondary peak in the conditioned set which is derived from samples between $t/T_s = 0 - 102.4$. For the complete set, spectral characteristics are altered by the bimodal behaviour of the flow-field which, in addition to the vortex pair, is characterised by the appearance of a single vortex (Figure 5.16(f)) and the absence of any CS (Figures 5.16(g)-(i) and (l)). Although the presence of higher harmonics are observed in both cases, they are a much more prominent feature of the conditioned set. It is reasonable to assume that this a result of an increased spatial coherence of the vortical structure from $t/T_s = 0 - 100$ in comparison to other time-instants. PSDs deduced from tangential velocity are broadly similar to those based on axial and radial velocities, however examination of the lower end of the spectra ($0.02 < S_t < 0.1$) from both sample sets reveals notable differences. In this region PSD amplitudes obtained from axial and radial velocity remain relatively constant. This is in contrast to PSDs of tangential velocity which show a notable rise in energy; reaching an amplitude approximately an order of magnitude greater than the axial and radial velocity counterparts at $S_t = 0.01$. Similar spectral characteristics were observed in Dunham et al. [50] in which it was suggested that this behaviour is a consequence of additional unsteadiness due to the presence of a PVC. As this feature has a relatively low characteristic frequency ($S_t \approx 13.2 \times 10^{-3}$ [13]) only $O[1]$ PVC cycles are captured by the conditioned set in comparison to $O[5]$ for the complete set. This explains the differences in amplitude at $S_t = 0.01$ in Figures 5.27(e) and (f).

In Section 4.2.1 it was noted that the PSD amplitude normalisation used in Midgley [13] was uncertain. To address this issue, high-speed 2C-PIV (HS 2C-PIV) data acquired in water for the Turbomeca injector in a 'no-jet' configuration (also presented in [13]) was utilised as this has identical spectral characteristic to the modular injector studied here. These measurements were acquired in an $x-r$ plane (FoV$\approx 40 \times 40$mm, $\Delta X \approx 1.4$mm) at a sampling frequency of 500Hz with a frequency resolution of 0.24Hz and, based on the reference scales of $D_s = 0.03763$m and $U_{x,s} = 1.99$m/s [13], give a Strouhal number range of $S_{t,\min} = 4.6 \times 10^{-3}$ to $S_{t,\max} = 9.5$. Figure 5.28 shows PSDs of axial and radial velocity obtained from both conditioned and complete LES sets against high-speed PIV at $x/D_s = 0.27$, $r/D_s = 0.27$. Aside from the differences in the frequency relationship between primary and secondary peaks discussed above, the overall agreement in PSD amplitude between PIV and both sample sets across the entire frequency range is reasonable.

5.4.2 Far Field

In order to capture $O[5]$ PVC cycles (see Section 5.3), far-field spectral analysis presented in this subsection is based on the complete LES sample set ($t/T_s = 409$). For $S_{\mathrm{N}} = 0.75$, Syred et al. [38] measured a volumetric flow rate based Strouhal number of $S_{t\dot{\mathrm{Q}}} \approx 0.9$ for a tangential entry swirl burner as an indication of the PVC frequency. From Equation 1.6 and based on D_s and $U_{x,s}$ from Table 5.3 this becomes $S_t = 1.35 \times 10^{-2}$. This is indicated on Figures 5.29 to 5.31 which show PSDs of axial, radial and tangential velocity components at $x/D_s = 2.65$ for various radial locations. From PSDs of axial velocity shown in Figure 5.29 there is no evidence to suggest coherent motion occurring at $S_t = 1.35 \times 10^{-2}$ at any of the radial locations considered. This is in contrast to PSDs deduced from radial velocity shown in Figure 5.30 in which a significant increase in amplitude localised around $S_t = 1.35 \times 10^{-2}$ is observed at all radii. A similar increase is apparent in a PSD obtained from tangential velocity at $r/D_s = 0.08$ shown in Figure 5.31(a). Given that the PVC is aligned predominantly in the streamwise direction, it is not surprising that the expected frequency is only exhibited in radial and tangential PSDs. Additionally, the average amplitude in the region $S_t < 0.05$ in PSDs deduced from radial and tangential velocities ($O[10^{-1}]$) is approximately two orders of magnitude greater than those from axial velocity ($O[10^{-3}]$). Unlike near-field spectra presented in Section 5.4.1 in which characteristic frequencies linked to coherent vortex motion could be readily identified, the relatively coarse frequency resolution and limited number of PVC cycles included in the LES ensemble negates a more precise definition of its characteristic frequency. Despite these limitations, the localisation of significant energy at $S_t = 1.35 \times 10^{-2}$ suggests that important qualitative details of the PVC phenomena predicted by LES is consistent with previous experimental observations [38].

In addition to the presence of the expected PVC frequency of $S_t = 1.35 \times 10^{-2}$, prominent peaks occurring at $S_t = 3.5 \times 10^{-2}$ and 4.9 are observed in Figures 5.29 to 5.31. As these fre-

quencies do not appear to be harmonics associated with the PVC (within the limits of accuracy imposed by the frequency resolution), further time-dependent analysis was undertaken using the vortex detection algorithm of Grosjean et al. [36]. For validation purposes, the computed location of the PVC using this methods was compared with its location deduced from instantaneous streamtraces at various time-instants. In all cases considered, both approaches were in excellent agreement as shown from the examples presented in Figure 5.32. At a given axial station, the location of the PVC is defined by its radial distance, r_{PVC} and angular displacement measured relative to some datum plane, θ_{PVC}. In this case, $\theta_{\mathrm{PVC}} = 0$ is taken along the line $z/D_s = 0$, $y/D_s \geq 0$ and is positive in an anti-clockwise direction. Figures 5.33 and 5.34 show the PVC location as a function of θ_{PVC}, r_{PVC}/D_{ex} and non-dimensional time, t/T_s, at $x/D_s = 2.39$. For clarity, the total record length of the LES ensemble has been divided into two segments from $t/T_s = 0-205$ and $t/T_s = 205-409$ respectively. Large portions of Figure 5.33 are dominated by a well defined sawtooth waveform indicative of precessional motion. In general, θ_{PVC}, increases as a function of time, and, therefore, the PVC precesses in an anti-clockwise direction with the bulk flow. Interestingly, there is a considerable degree of variability in the waveform period, defined here as the temporal interval between $\theta_{\mathrm{PVC}} = 0 - 2\pi$, throughout the time series. It is reasonable to assume that it is this variation that is responsible for the various frequency components noted in PSDs above. For example, the expected PVC frequency of $S_t = 1.35 \times 10^{-2}$ has a corresponding non-dimensional timescale of $t/T_s \approx 71$, whilst, for example, the higher frequency peak occurring at $S_t = 4.9 \times 10^{-2}$ has an associated non-dimensional timescale of $t/T_s \approx 20$. Both these timescales are clearly distinguishable in Figures 5.33(a) and (b) as indicated by the dashed lines. An explanation for the variation in waveform period is provided in Figure 5.34 which shows the radial displacement of the PVC. The average radial displacement of the PVC, $\langle r_{\mathrm{PVC}} \rangle / D_{ex} = 2.3e^{-2}$, is indicated by the horizontal dashed line. Given the limited number of PVC cycles included in the LES ensemble, this agrees favourably with PIV measurements (Table 4.2) at 3.5% of the duct diameter. Between $t/T_s = 0 - 205$ each instantaneous radial displacement of the PVC is, in general, less than the average displacement, whilst between $t/T_s = 205 - 409$ the majority of instantaneous displacements exceed this value. Thus, between $t/T_s = 205 - 409$ the characteristic in-plane path length of the PVC is increased relative to that between $t/T_s = 0 - 205$ which, assuming a similar convection velocity throughout, results in a corresponding increase or decrease in waveform period and hence the appearance of various frequency components in Figures 5.29 to 5.31.

5.4.3 Frequency Contours

Spectra presented above have demonstrated the ability of LES to capture the broad range of frequencies present in the current flow and shown excellent agreement with experiment. Volumetric information available from LES can then be utilised to gain an improved understanding of how the instability modes identified as strong peaks in the spectra are distributed and develop

throughout the swirl duct and expansion chamber. Figure 5.35 shows contours of peak S_t for all three velocity components extracted from an $x-r$ plane at $\theta = \pi$ based on the conditional LES sample set ($t/T_s = 102$). In order to distinguish more clearly between the broad range of frequencies within the domain, a log-scale ($\log_{10}(S_t)$) has been adopted. Although not shown here, a similar analysis was performed based on the complete LES sample set ($t/T_s = 409$). It was found that the general trends were in accordance with Figure 5.35 in that high frequency modes are most prevalent in the fuel injector near-field whilst low frequency ones dominate the far-field. The predominant Strouhal numbers of $S_t \approx 0.7$ and 1.4 noted above become $\log_{10}(0.7) = -0.15$ and $\log_{10}(1.4) = 0.15$ respectively on the scale used in Figure 5.35 and are observed clearly for all velocity components. It is interesting to note the prevalence of these frequencies throughout the entire swirl duct. Previously, Midgley [13] postulated that vortices responsible for these frequencies are generated as a result of flow separation from the inner wall of the swirl duct ($-0.43 \geq x/D_s \leq -0.27$). The fact that associated frequencies are observed upstream of this point suggests that flow within the swirl duct exists in a sub-critical state allowing disturbances to propagate downstream *and* upstream.

To complement Figure 5.35 and further understand the dominant near-field frequencies, Figures 5.36 and 5.37 show PSD amplitudes ($[m^2/s^2]$/Hz) associated with $S_t = 0.72$ and 1.44 for the conditioned LES sample set. Despite the presence of these frequencies throughout the swirl duct they are only of significant amplitude in the region $0.25 < x/D_s < 0.75$ which encompasses the majority of the injector near-field. In general, amplitudes of $S_t = 1.44$ exceed those of $S_t = 0.72$ which is consistent with PSDs of the conditioned LES sample set (Figures 5.27(a),(c) and (e)). Figure 5.38 shows PSD amplitudes of the expected PVC frequency ($S_{t\dot{Q}} = 0.9$) for all three velocity components. Due to the relatively low characteristic frequency of this feature it was necessary to utilise the complete LES sample set. Maximum amplitudes of $S_t = 1.35 \times 10^{-2}$ based on u_r and u_θ are observed close to the centreline ($r/D_s < 0.2$). The fact that these frequencies have significant amplitude as far upstream as $x/D_s \approx 1.2$ (Figure 5.38(c)) supports the hypothesis of Midgley [13] that it is the presence of the PVC that is responsible to disrupting the coherence near-field vortices.

5.5 Coherent Structure Analysis

In order to gain further insight into near and far-field CS, the rotational averaging procedure described in Section A-2.2 was applied to the conditional LES sample set. In the near-field an $r-\theta$ plane extracted at $x/D_s = 0.02$ at each time-instant was used to located the centre of the reference vortex (see Figure A-2) and in the far-field an $r-\theta$ plane extracted at $x/D_s = 2.39$ was used. In keeping with the analysis of PIV data presented in Section 4.2.1, the long-time mean was subtracted from each instantaneous velocity field to isolate the turbulent motions. In the following, vorticity derived from the rotationally averaged Reynolds-decomposed velocity field

($\langle u'_x \rangle_{\text{rot}}$, $\langle u'_r \rangle_{\text{rot}}$, and $\langle u'_\theta \rangle_{\text{rot}}$) will be referred to as rotationally-averaged vorticity with individual components $\langle \omega_x \rangle_{\text{rot}}$, $\langle \omega_r \rangle_{\text{rot}}$ and $\langle \omega_\theta \rangle_{\text{rot}}$ and magnitude $\langle |\omega| \rangle_{\text{rot}}$ and obtained from Equation A-20. Similarly, the Q-criterion (Equation A-21) will be denoted $\langle Q \rangle_{\text{rot}}$.

5.5.1 Near-Field

Figure 5.39 shows rotationally averaged Reynolds-decomposed streamtraces at $x/D_s = 0.02$ superimposed on contours of $\langle u'_x \rangle_{\text{rot}}$, $\langle u'_r \rangle_{\text{rot}}$, and $\langle u'_\theta \rangle_{\text{rot}}$. These exhibit many similarities with instantaneous fluctuating streamtraces shown in Figure 5.10(b) but allow a clearer interpretation of the four vortical structures. From Figure 5.39, each vortex is centred on regions defined by $\langle u'_x \rangle_{\text{rot}} = \langle u'_r \rangle_{\text{rot}} = \langle u'_\theta \rangle_{\text{rot}} = 0$. The large circumferential gradients of $\langle u'_x \rangle_{\text{rot}}$ and $\langle u'_r \rangle_{\text{rot}}$ and large radial gradients of $\langle u'_\theta \rangle_{\text{rot}}$ in the vicinity of the vortices gives rise to rotationally-averaged vorticity in the three principle directions as shown in Figure 5.40. The regions of positive and negative $\langle \omega_x \rangle_{\text{rot}}$ shown in Figure 5.40(a) result from the clockwise or counter-clockwise rotation of each vortex about its centre. Comparable values in $\langle \omega_x \rangle_{\text{rot}}$, $\langle \omega_r \rangle_{\text{rot}}$ and $\langle \omega_\theta \rangle_{\text{rot}}$ shown in Figures 5.40(a)-(c) indicate the strong three-dimensionality of the vortices. From Figure 5.40(d), maxima of $\langle |\omega| \rangle_{\text{rot}}$ are observed at the 'eyes' of the counter-rotating vortex pair located at $\theta = 0$ and π. Although significant levels of $\langle |\omega| \rangle_{\text{rot}}$ exist in the vicinity of the clockwise vortex pair located at $\theta = \pi/2$ and $3\pi/2$, this is not sufficient to distinguish vortical motions from background shear due to large gradients in $\langle u'_x \rangle_{\text{rot}}$, $\langle u'_r \rangle_{\text{rot}}$ and $\langle u'_\theta \rangle_{\text{rot}} = 0$. As an alternative, $\langle Q \rangle_{\text{rot}}$ (Equation A-21) avoids this issue by identifying vortices as regions where vorticity magnitude prevails over strain-rate magnitude as shown in Figure 5.40(e). Figure 5.41 shows rotationally averaged Reynolds-decomposed streamtraces superimposed on contours of $\langle \omega_x \rangle_{\text{rot}}$ and $\langle \omega_\theta \rangle_{\text{rot}}$ on a meridional slice extracted at $z/D_s = 0$. The dashed lines shown in Figure 5.41 indicate time-mean inner and outer shear layers. In the upper portion of Figure 5.41(b) ($z/D_s > 0$), $\langle \omega_\theta \rangle_{\text{rot}}$ is defined as positive out of the page whilst in the lower portion it is positive into the page. The streamtraces clearly identify a series of vortical structures with alternating signs of of $\langle \omega_x \rangle_{\text{rot}}$ and $\langle \omega_\theta \rangle_{\text{rot}}$. These are located approximately within the swirl cone bounded the by time-mean inner and outer shear layer. The separation wavelength between these is $x/D_s \approx 0.36$ as indicated in Figure 5.41(a) which is close to $x/D_s \approx 0.32$ from conditionally-averaged PIV in Figure 4.22(d).

In order to gain further insight into the three-dimensional spatial structure of the vortices shown in Figures 5.39 to 5.41, iso-surfaces of $\langle Q \rangle_{\text{rot}} = 40 \times 10^3$ are shown in Figure 5.42. To make clear the rotation of each vortex about its centre, iso-surfaces of $\langle Q \rangle_{\text{rot}}$ are coloured by $\langle \omega_x \rangle_{\text{rot}}$. From Figure 5.42, each vortex is clearly visible and follows a helical path which originates inside the swirl duct and terminates at $x/D_s \approx 0.8$ for the selected value of $\langle Q \rangle_{\text{rot}}$. This is consistent with frequency contour maps presented in Section 5.4.3 which indicated that frequencies associated with this vortex structure decayed by $x/D_s = 1$. Interestingly, Figure 5.42(b) clearly shows that the helical paths followed by the vorticies are wound clockwise which is opposed to the counter-

clockwise motion of the mean flow. Although not stated explicitly, iso-surfaces of λ_2 presented in Wegner et al. [58] (presumable derived from an instantaneous velocity field) also indicate a double-helix wound opposed to the bulk flow for a derivative of a Turbomeca injector similar to that investigated here. In the case of a plug flow axial jet/wake velocity profile with a purely swirling cylindrical vortex sheet, Martin and Meiburg [129] have determined that for centrifugally stabilising flows ($\Gamma_c - \Gamma_\infty < 0$, where Γ_c is the circulation of a straight vortex filament and Γ_∞ is the external circulation), dominant instabilities are of a Kelvin-Helmholtz (K-H) type, feeding on both axial and azimuthal vorticity, and counter-rotating helical waves are the most unstable. When the flow is centrifugally destabilising ($\Gamma_c - \Gamma_\infty > 0$), the most unstable modes consist of co-rotating helical waves. Figure 5.43(a) shows contours of time-mean streamwise circulation, $\langle \Gamma_x \rangle$, calculated as:

$$\Gamma_x = \oint \vec{u} \cdot \vec{dl} \tag{5.1}$$

To classify regions of the current flow as either centrifugally stable or unstable Figure 5.43(b) shows contours of $\partial\Gamma/\partial r$ coloured as red if $\partial\Gamma/\partial r > 0$, blue if $\partial\Gamma/\partial r < 0$ and black if $\partial\Gamma/\partial r = 0$. Evidence from Figures 5.42 and 5.43 suggests that in the centrifugally stable regions of the mean flow ($\partial\Gamma_x/\partial r > 0$) helices wound opposed to the mean flow are the dominant instability mechanism which is consistent with [129].

In order to quantify the relationship between the helices identified by the Q-criterion and the time-mean streamtraces shown in 5.42(a), the angle between the rotationally-averaged vorticity vector, $\langle \vec{\omega} \rangle_{\text{rot}}$, and time-mean velocity vector, $\langle \vec{u} \rangle$, was calculated from:

$$\theta_{\text{rot}} = \arccos \frac{\langle \vec{\omega} \rangle_{\text{rot}} \cdot \langle \vec{u} \rangle}{|\langle \vec{\omega} \rangle_{rot}| \, |\langle \vec{u} \rangle|} \tag{5.2}$$

Figure 5.44 shows a PDF of θ_{rot} calculated from $\langle \vec{\omega} \rangle_{\text{rot}}$ and $\langle \vec{u} \rangle$ extracted from iso-surfaces of $\langle Q \rangle_{\text{rot}}$ (Figure 5.42) using a bin-width of $5\pi/180$. The most probable angle between $\langle \vec{\omega} \rangle_{\text{rot}}$ and $\langle \vec{u} \rangle$ is close to $\pi/2$, suggesting that the helices shown in Figure 5.42 are a result shear dependent K-H-like instabilities. Similar conclusions were reached by Garcia-Villalba et al. [55] although this was based on a purely qualitative assessment.

5.5.2 Far Field

Figure 5.45 shows rotationally averaged Reynolds-decomposed streamtraces at $x/D_s = 2.39$ superimposed on contours of $\langle u'_x \rangle_{\text{rot}}$, $\langle u'_r \rangle_{\text{rot}}$, and $\langle u'_\theta \rangle_{\text{rot}}$ from which the presence of two counter-rotating vorticies are clearly visible. The vortex located in the region of positive axial velocity

shown in Figure 5.45(a) was used as a reference for rotational averaging and rotates about its centre counter-clockwise in the direction of the bulk flow. Unlike in the near-field, gradients of $\langle u'_x \rangle_{\text{rot}}$, $\langle u'_r \rangle_{\text{rot}}$, and $\langle u'_\theta \rangle_{\text{rot}}$ in the far-field only give rise to an axial component of rotationally-averaged vorticity, $\langle \omega_x \rangle_{\text{rot}}$, as shown in Figure 5.46(a). This suggest that the PVC is aligned predominantly in the streamwise direction confirmed via iso-surfaces of $\langle Q \rangle_{\text{rot}} = 1500$ shown in Figure 5.47. As in Figure 5.42, iso-surfaces of $\langle Q \rangle_{\text{rot}}$ are coloured by $\langle \omega_x \rangle_{\text{rot}}$ in order to illustrate the clockwise or counter-clockwise rotation of each vortex about its centre. The path of the vortical structures identified at $x/D_s = 2.39$ in Figure 5.45 are displaced slightly from the geometric centre which is indicated by the horizontal dashed line. These are approximately parallel at $x/D_s \geq 2$ and begin to converge as they approach the near-field. This is consistent with the contours of PSD amplitude corresponding to $S_{t_{\dot{Q}}} \approx 1.35 \times 10^{-2}$ shown in Figure 5.38. The predominant streamwise alignment of the vortices makes it difficult to determine the direction of their winding relative to the time-mean flow from a downstream view of $\langle Q \rangle_{\text{rot}}$ as used above. As an alternative, Figure 5.48 shows rotationally averaged Reynolds-decomposed streamtraces extracted at various $r-\theta$ planes downstream of the swirler exit. From this sequence, the counter-rotating vortex pair are observed to twist in a clockwise direction i.e. also opposed to the base flow as the near-field CS.

5.6 Closure

From calculations presented in this chapter it has been shown that LES is capable of capturing the unsteady dynamics and instability modes characteristic of swirl injectors in excellent agreement with experiment. Using lengthscale information derived from PIV it was possible to ensure that the spatial filter (Δ) of all computational grids investigated was adequate to resolve the majority ($\approx 80\%$) of turbulent kinetic energy in 'critical' regions of the flow, such as in the vicinity of the swirler exit. Following a preliminary investigation with these grids it was found that the wall-function approach within the swirl duct was not suitable for capturing the near-field CS observed experimentally, however, a further calculation performed with an increased near-wall resolution and the no-slip condition resulted in the appearance of this feature. In order to validate predictions against experiment, an ensemble LES dataset was collected that included a sufficient number of independent samples for converged first and second-order statistics and an adequate number of PVC cycles for a detailed frequency analysis. Regular monitoring of this revealed a bimodal behaviour at the swirler exit similar to that observed experimentally which was characterised by the presence or absence of CS. It was found that first-order statistics based on all members of ensemble were in reasonable agreement with experiment, however second-order r.m.s quantities were not well represented. It was argued that the most notable discrepancies could be attributed to the details of CS from within the swirler as these contribute significantly to turbulence levels. Since vortex transition occurred on a timescale several orders of magnitude larger than the LES sampling interval this placed severe restrictions on the number of cycles

that could be captured. To provide a more representative comparison with experiment a second 'conditioned' dataset was created corresponding to the period during which CS were observed at the swirler exit. The agreement of first and second-order statistics (including turbulent shear-stresses which were found to be largely unreported in the available literature) of the conditioned set with experiment were found to be much improved. Velocity spectra derived from LES found that the all-important frequency content of near and far-field instability modes was predicted in accordance with experiment. Utilising volumetric information available from LES the near-field vortex structure observed experimentally was shown to consists of four helices which rotated about their respective axes in the same direction as the bulk flow but with a filament winding opposed to it. Given that the angle formed between each helix and the bulk flow was close to $\pi/2$ radians it was postulated that these structures were a result of a Kelvin-Helmholtz (K-H) shear instability. Although LES is clearly well suited to swirl injector flows the computational expense (3160 CPU hours) is considerable. It is therefore of current interest to assess the suitability of the computational cheaper alternative of the Unsteady Reynolds-Averaged Navier-Stokes (URANS) CFD methodology which is considered in the following chapter based on both $k - \epsilon$ and RST turbulence models.

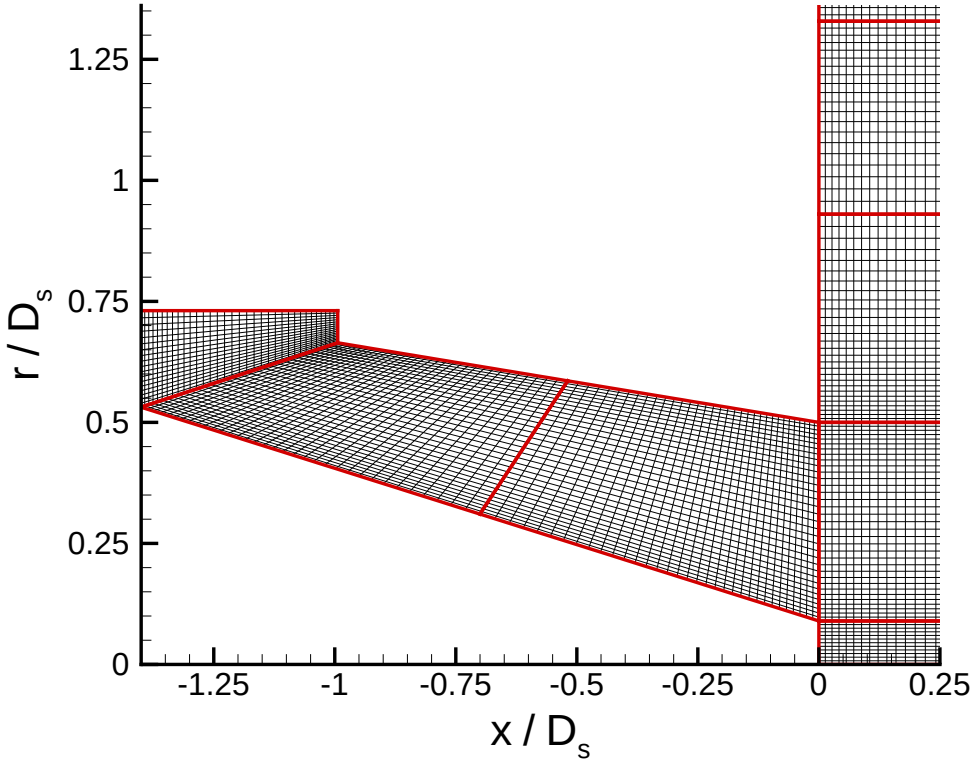

(a) $x - r$ plane within swirl duct

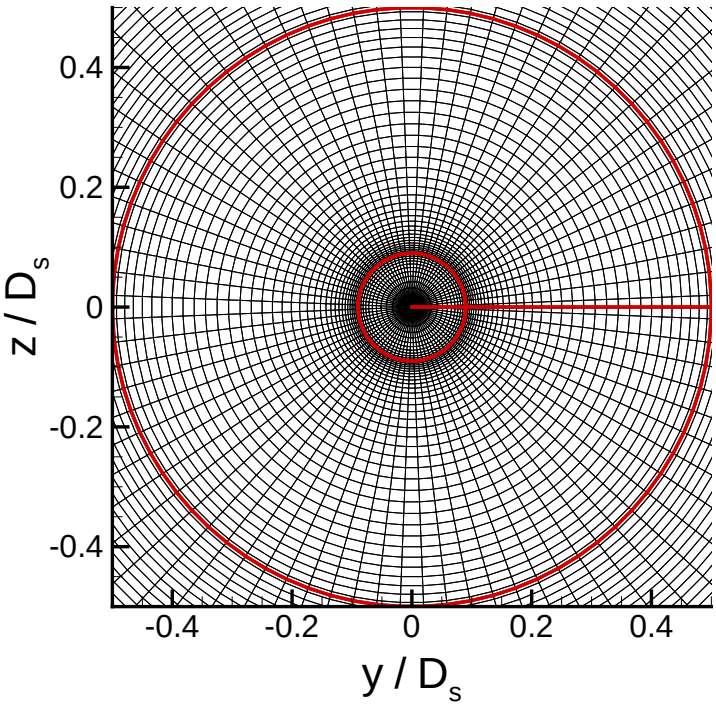

(b) $r - \theta$ plane at swirler exit ($x/D_s = 0.02$)

Figure 5.1: Datum mesh detail

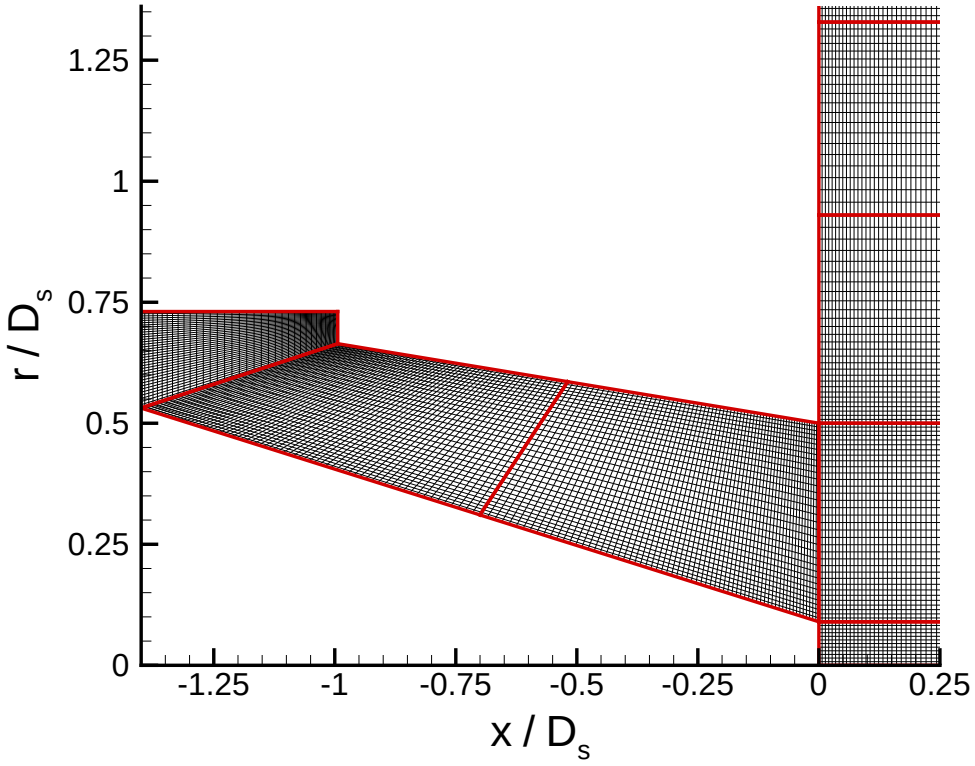

(a) $x - r$ plane within swirl duct - datum mesh with axial refinement

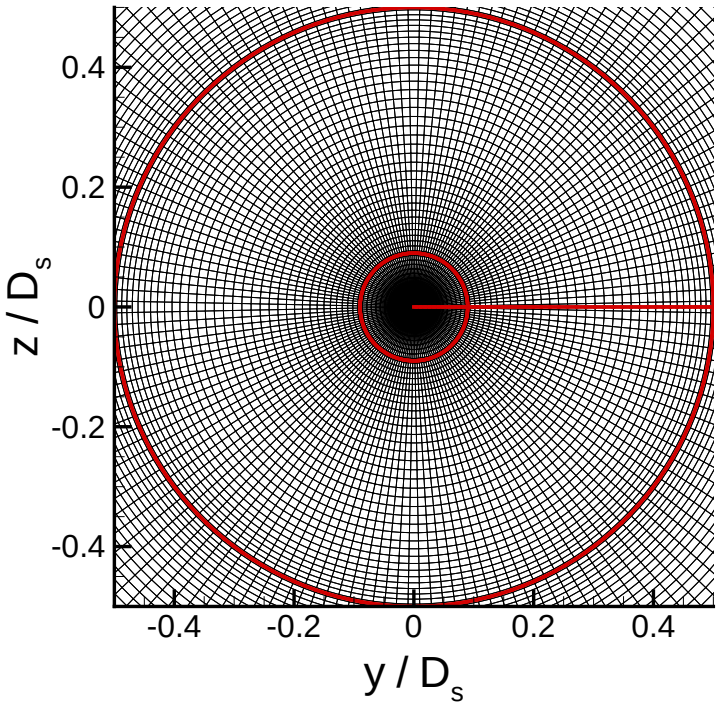

(b) $r - \theta$ plane at swirler exit ($x/D_s = 0.02$) - datum mesh with circumferential refinement

Figure 5.2: Mesh refinement detail

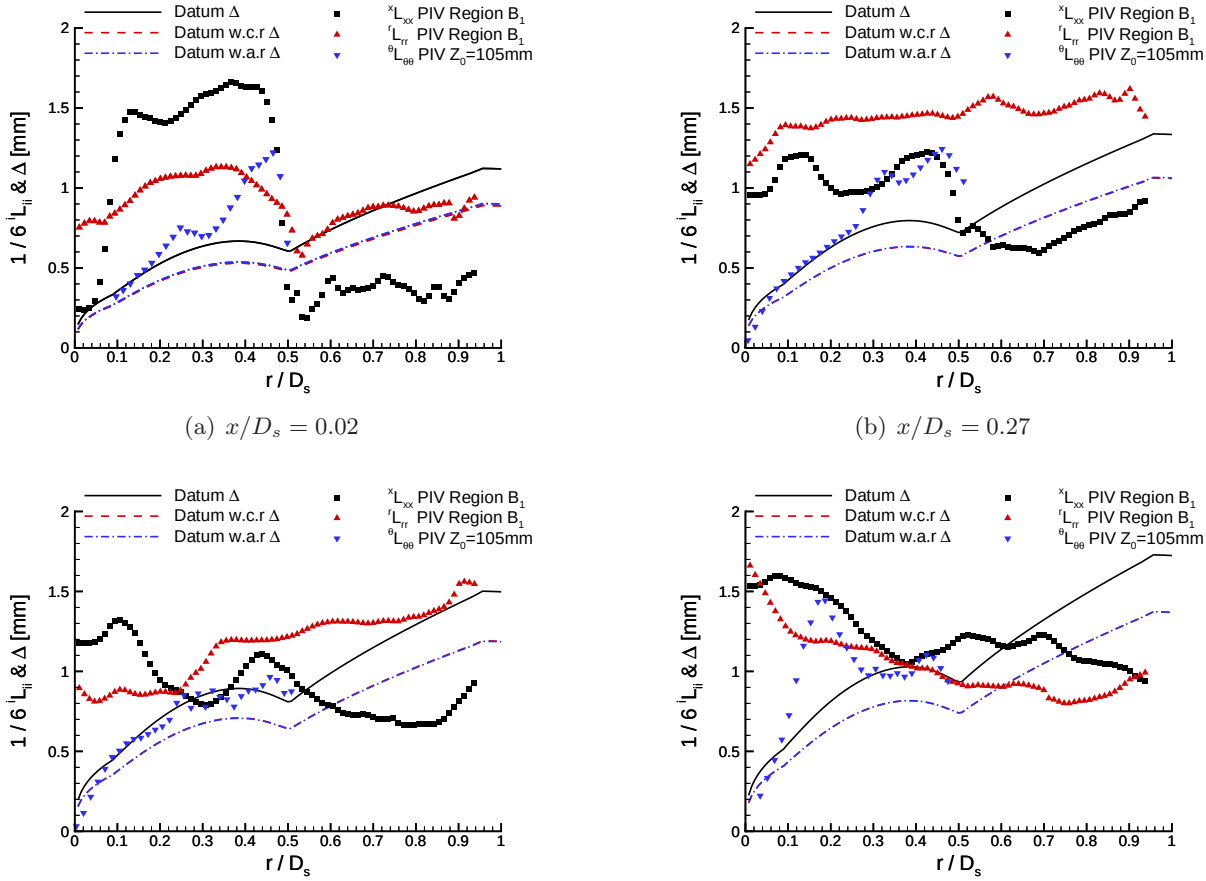

(a) $x/D_s = 0.02$

(b) $x/D_s = 0.27$

(c) $x/D_s = 0.53$

(d) $x/D_s = 1.06$

Figure 5.3: Comparison of characteristic LES filter width Δ ($\Delta = (\Delta x \Delta\theta r \Delta r)^{1/3}$) against $1/6^{i}L_{ii}$ from PIV data.

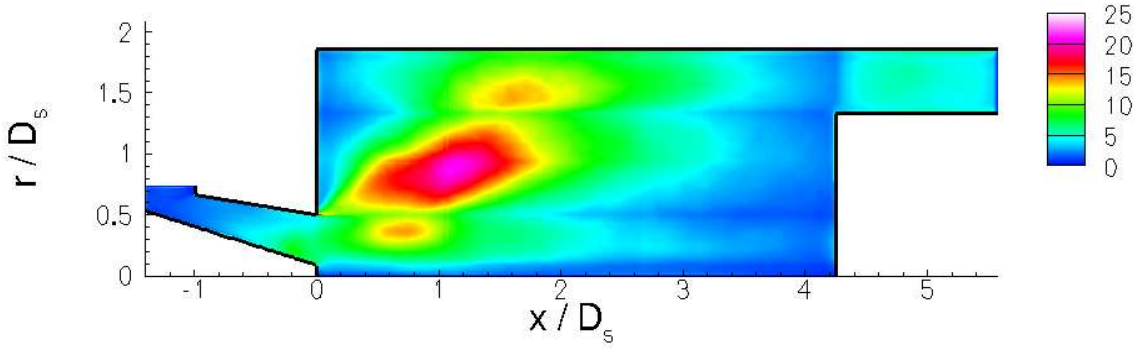

(a) Datum mesh

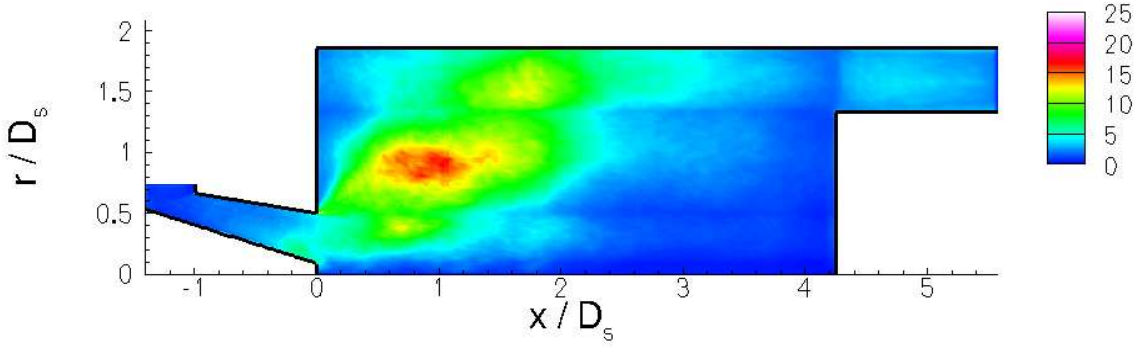

(b) Datum mesh with circumferential refinement

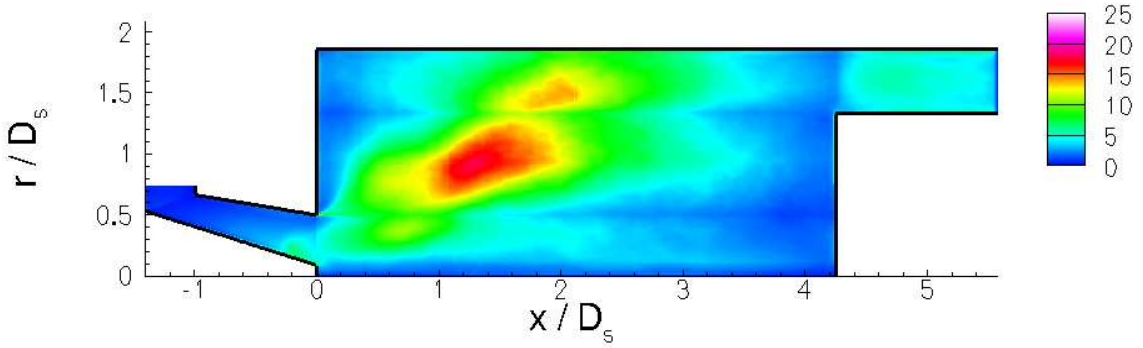

(c) Datum mesh with axial refinement

Figure 5.4: Time-averaged contours of ν_{sgs}/ν for various mesh densities

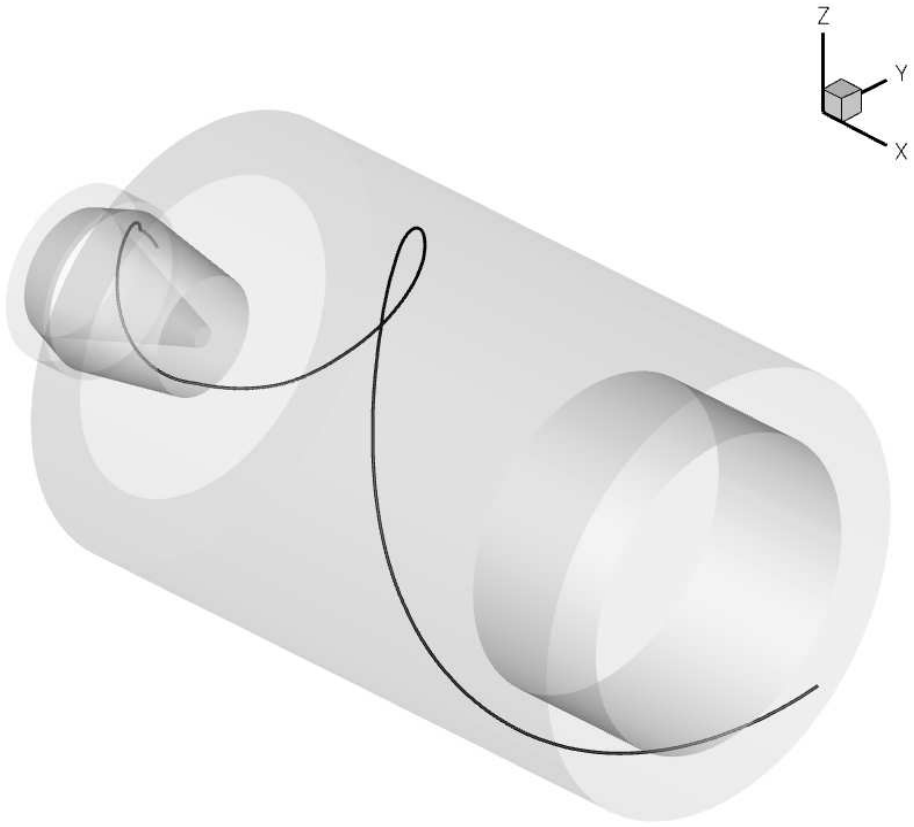

Figure 5.5: Streamtrace released from inlet plane of time-averaged dataset used to calculate T_r

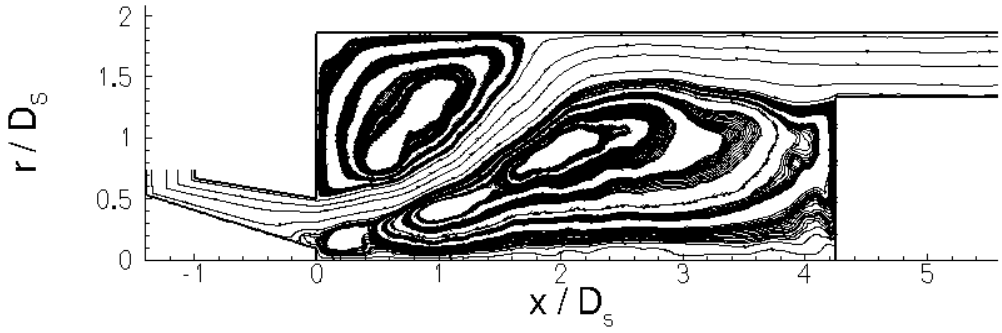

(a) Datum mesh

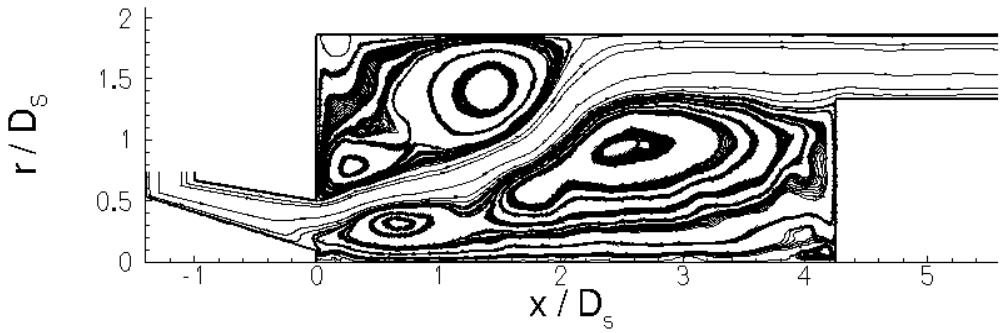

(b) Datum mesh with circumferential refinement

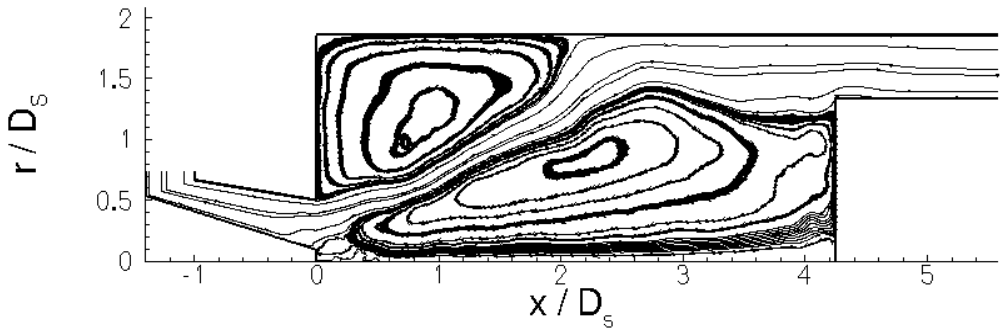

(c) Datum mesh with axial refinement

Figure 5.6: Instantaneous streamtraces in $x - r$ plane at arbitrary time-instant for varying mesh densities

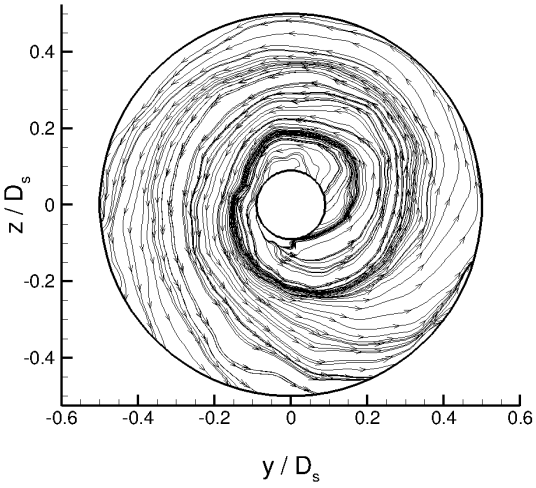

(a) Datum mesh

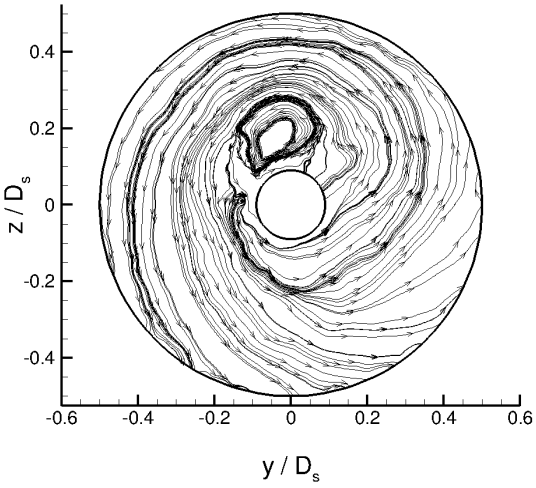

(b) Datum mesh with circumferential refinement

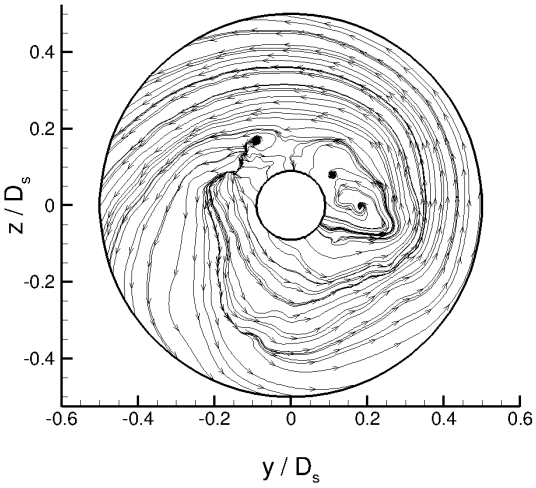

(c) Datum mesh with axial refinement

Figure 5.7: Instantaneous streamtraces at swirler exit ($x/D_s = 0.02$) at arbitrary time-instant for varying mesh densities

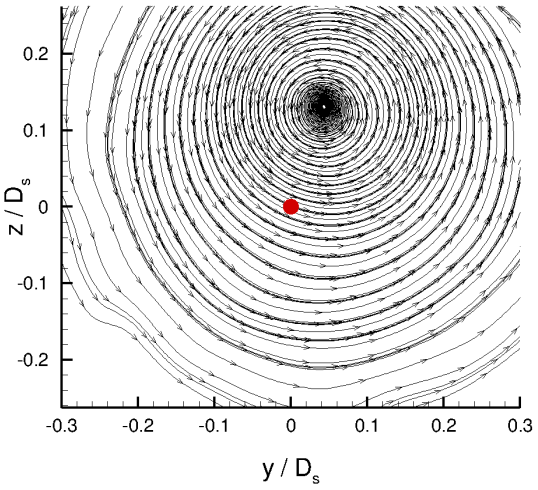

(a) Datum mesh

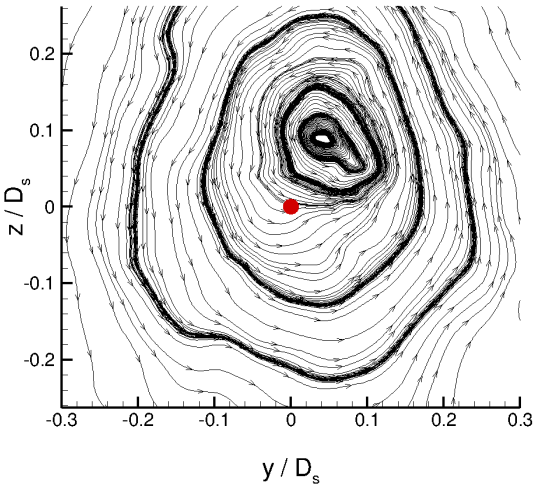

(b) Datum mesh with circumferential refinement

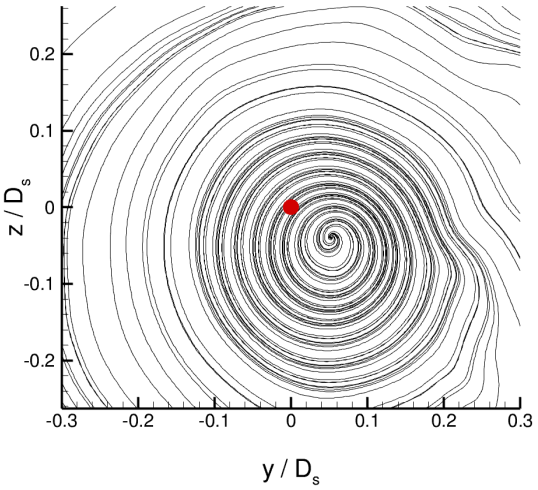

(c) Datum mesh with axial refinement

Figure 5.8: Instantaneous streamtraces at $x/D_s = 2.39$ at arbitrary time-instant for varying mesh densities

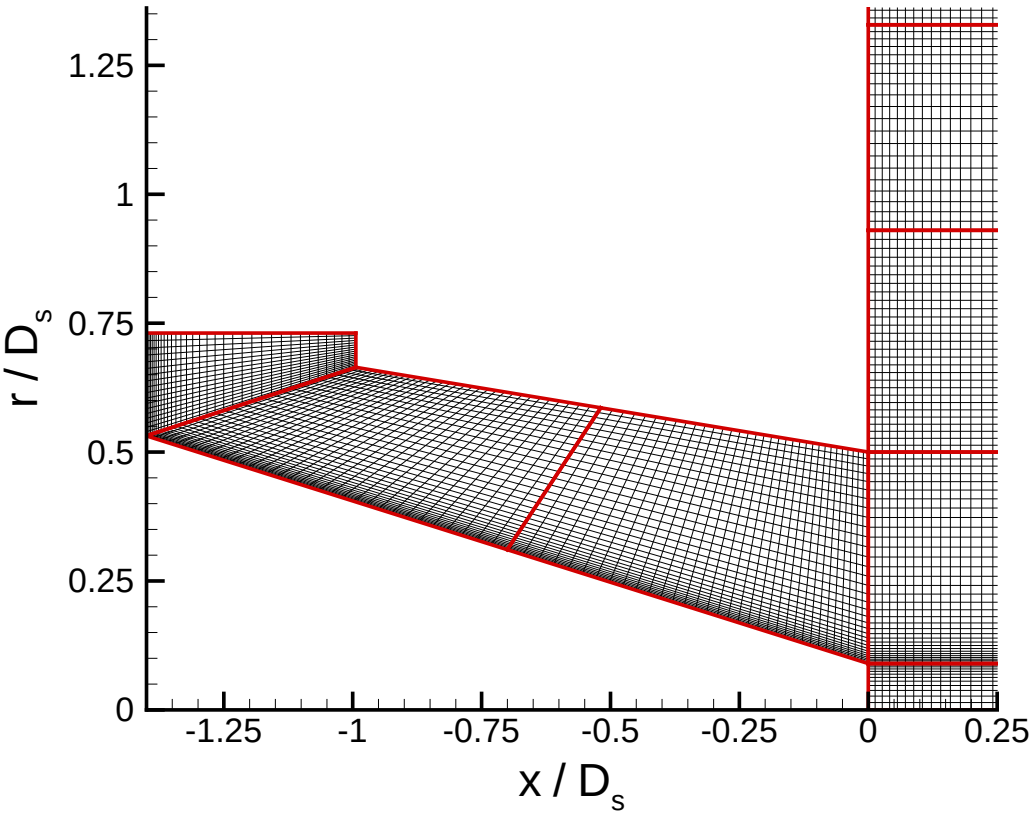

Figure 5.9: $x - r$ plane within swirl duct - datum mesh with radial refinement

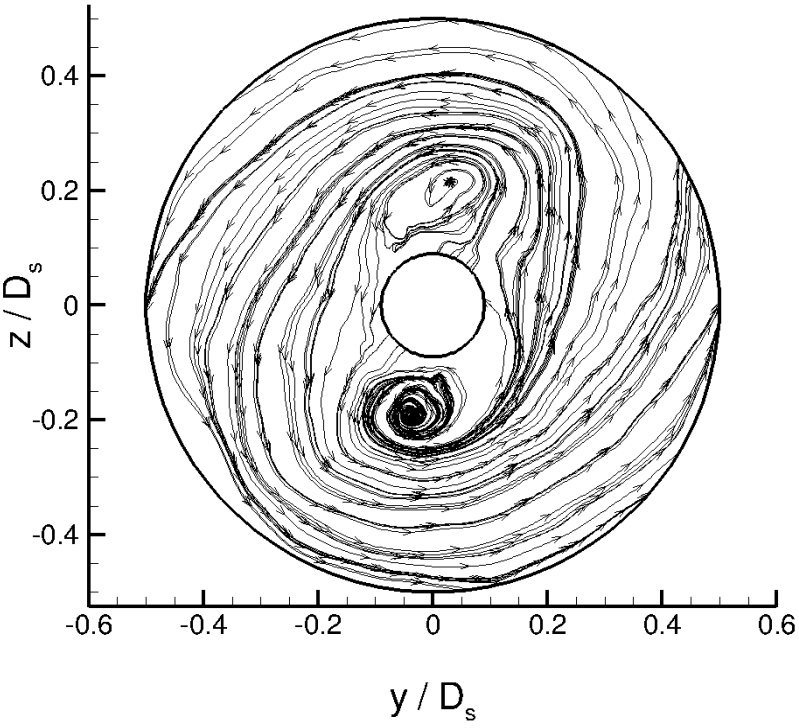

(a) Instantaneous

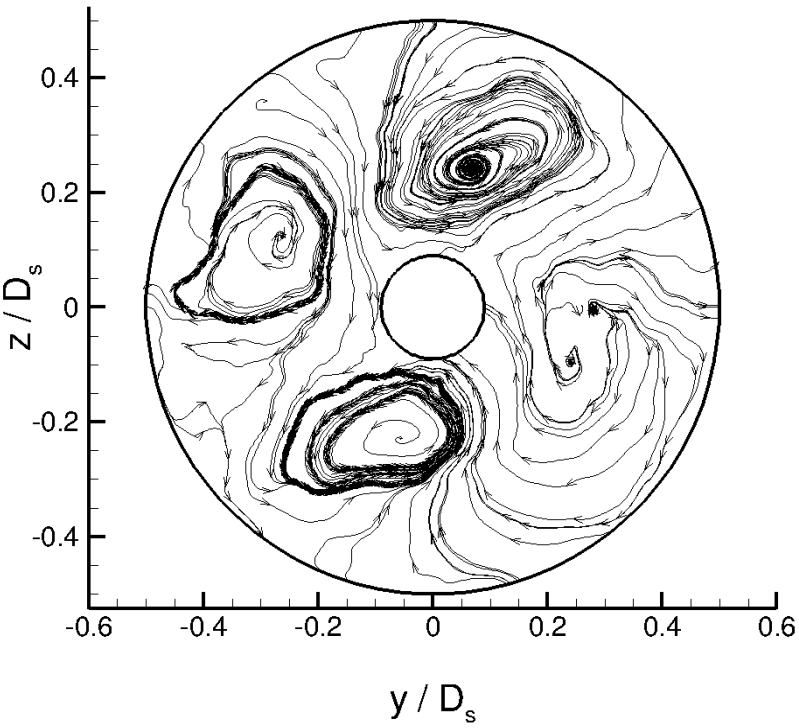

(b) Reynolds-decomposed

Figure 5.10: Instantaneous and Reynolds-decomposed streamtraces at $x/D_s = 0.02$ at arbitrary time-instant for datum mesh with radial refinement

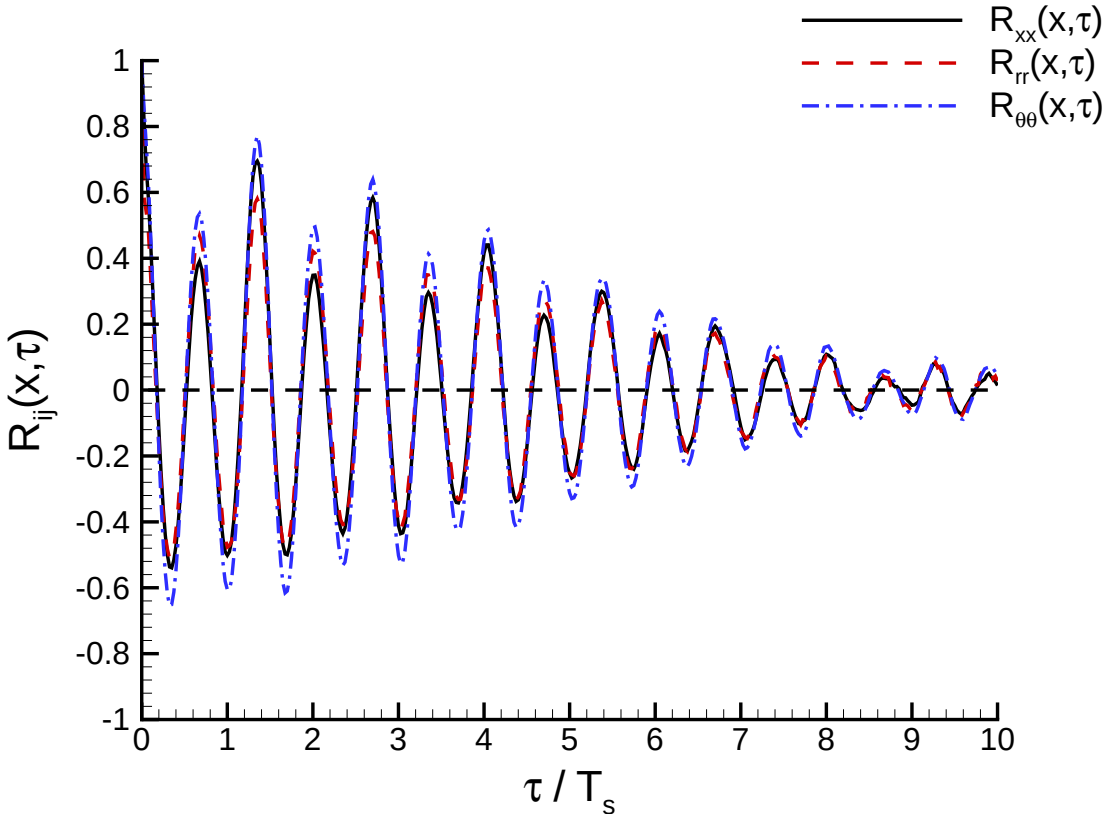

(a) $x/D_s = 0.02$, $r/D_s = 0.4$, $\theta = \pi$

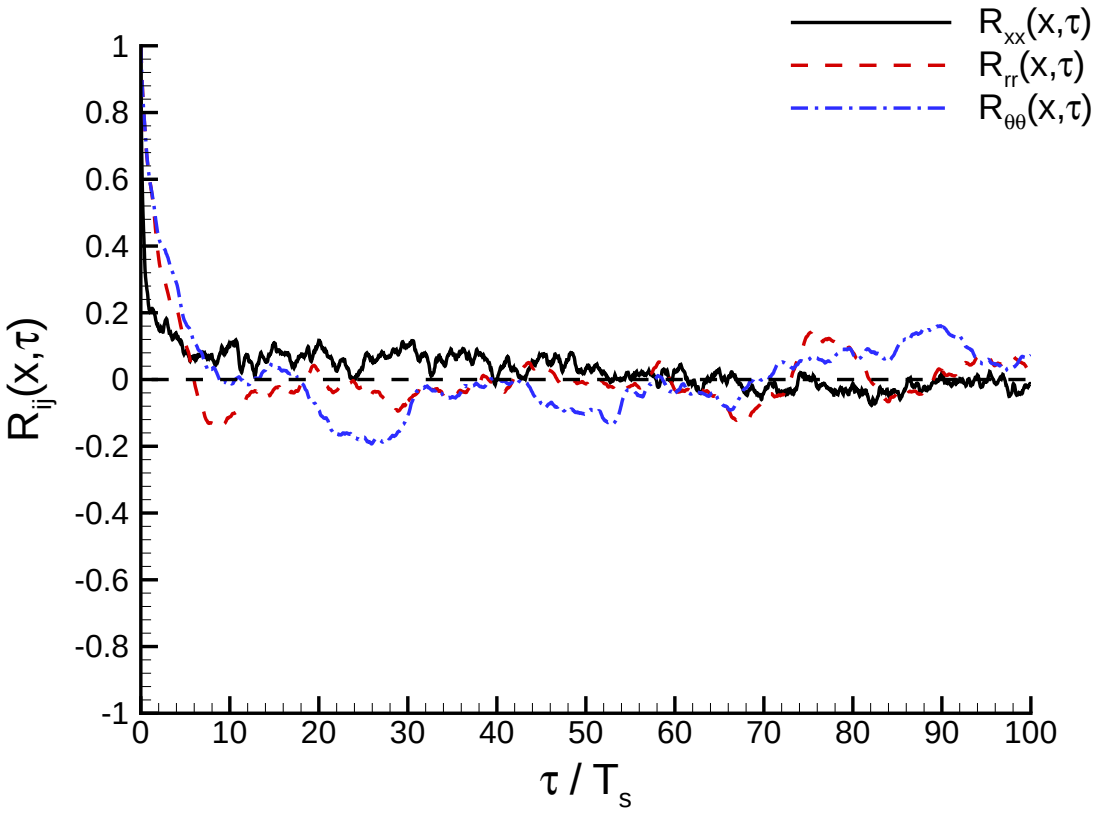

(b) $x/D_s = 1.06$, $r/D_s = 0.0$, $\theta - \pi$

Figure 5.11: Autocorrelation function, $R_{ij}(\vec{x}, \tau)$, at various locations

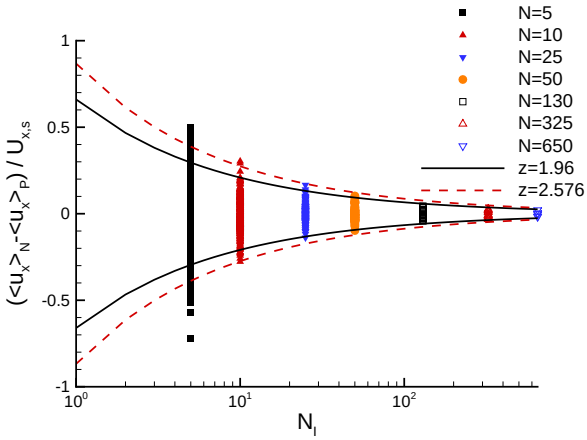

(a) Mean axial velocity

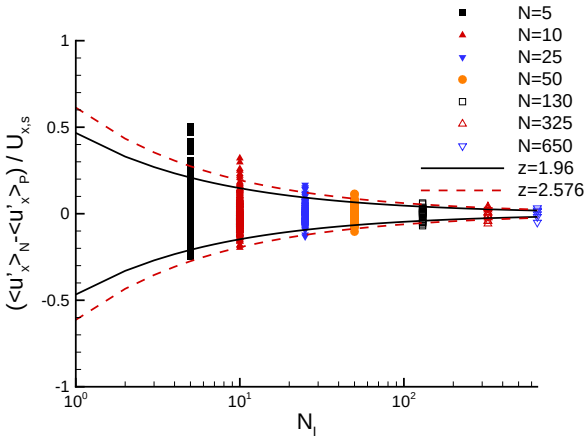

(b) r.m.s axial velocity

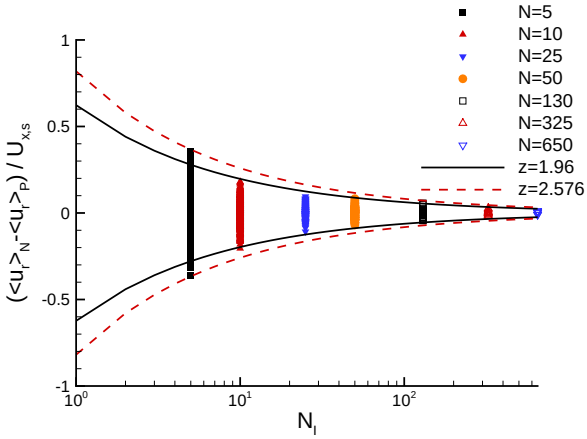

(c) Mean radial velocity

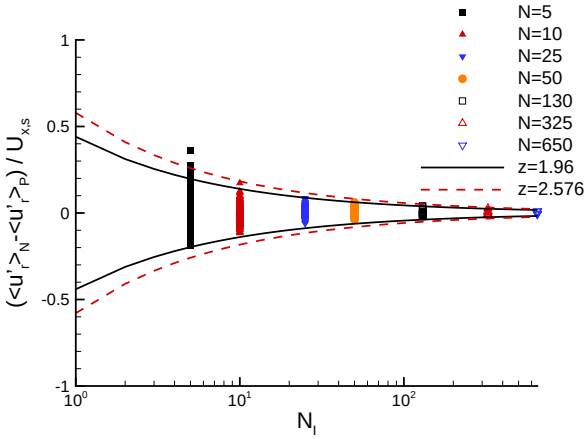

(d) r.m.s radial velocity

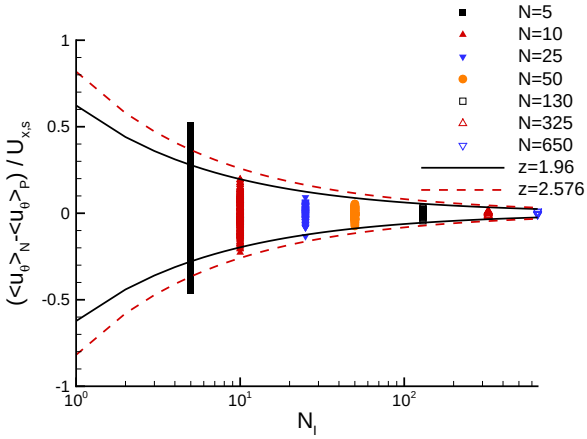

(e) Mean tangential velocity

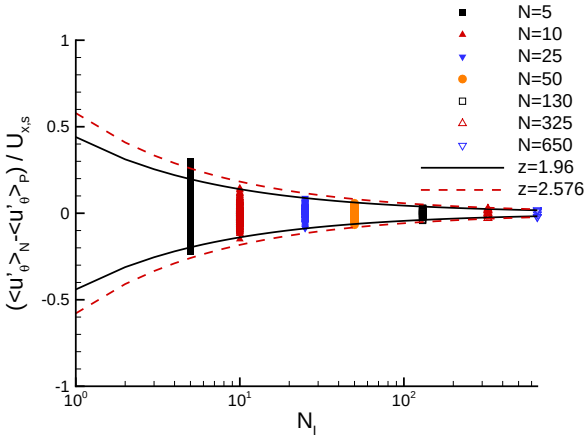

(f) r.m.s tangential velocity

Figure 5.12: Statistical convergence of mean and r.m.s velocities at $x/D_s = 0.02$, $r/D_s = 0.4$, $\theta = \pi$

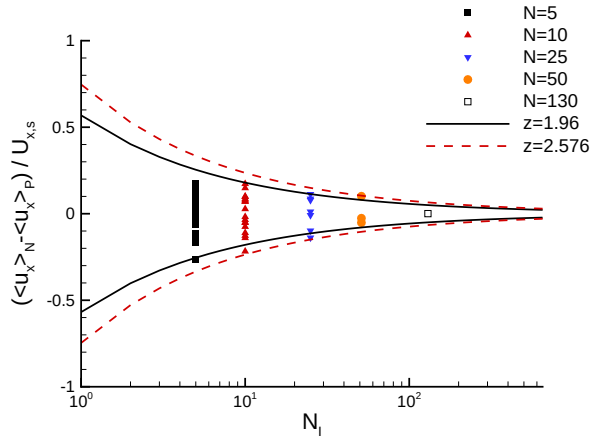

(a) Mean axial velocity

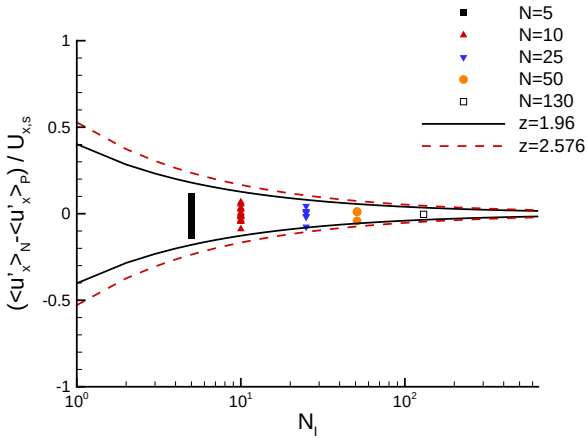

(b) r.m.s axial velocity

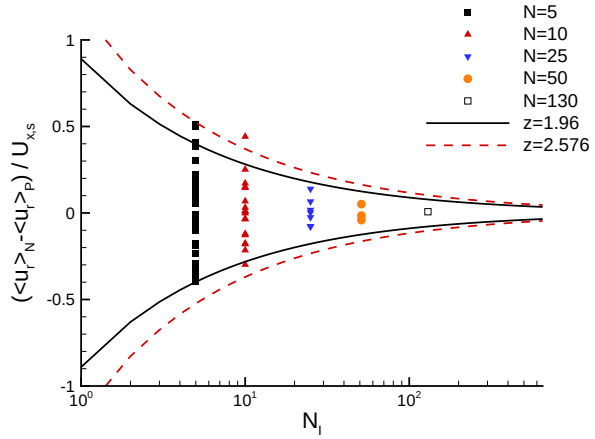

(c) Mean radial velocity

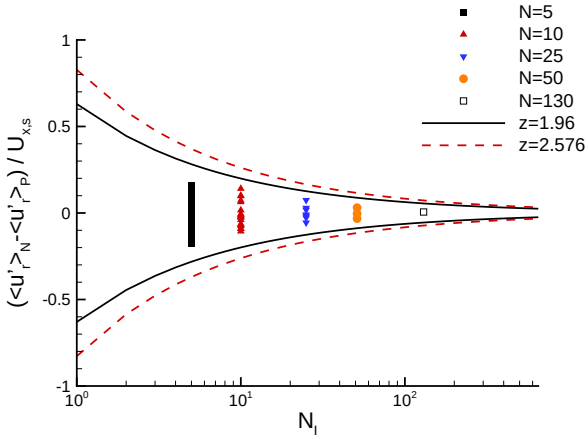

(d) r.m.s radial velocity

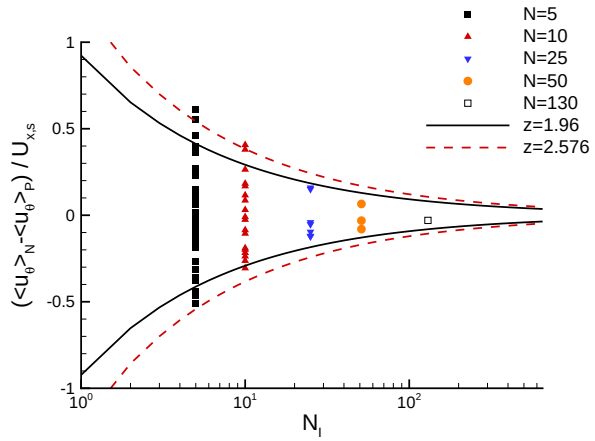

(e) Mean tangential velocity

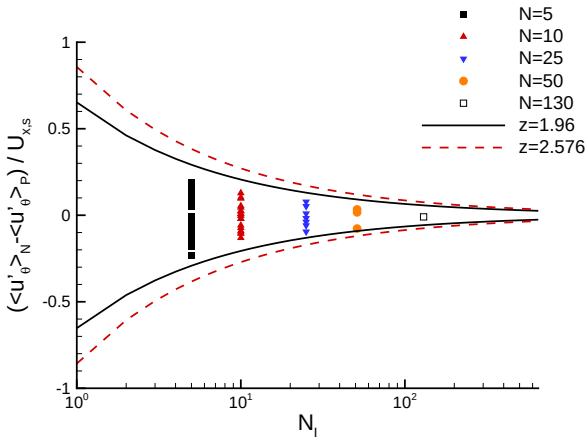

(f) r.m.s tangential velocity

Figure 5.13: Statistical convergence of mean and r.m.s velocities at $x/D_s = 1.06$, $r/D_s = 0.0$, $\theta = \pi$

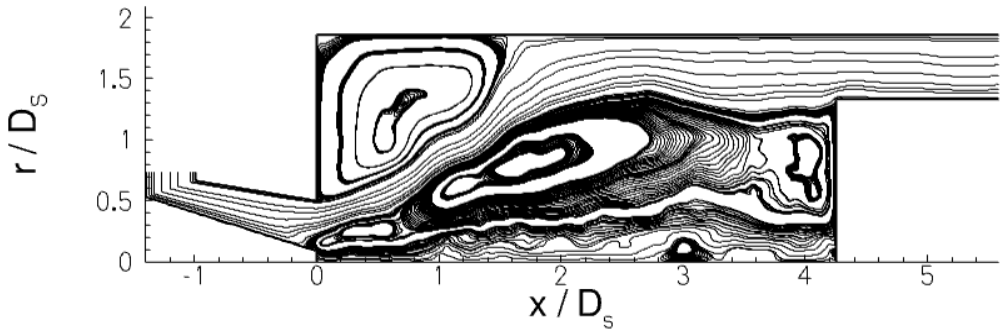

(a) $t/T_s = 0$, $x_{\mathrm{L}}/D_s \approx 1.6$

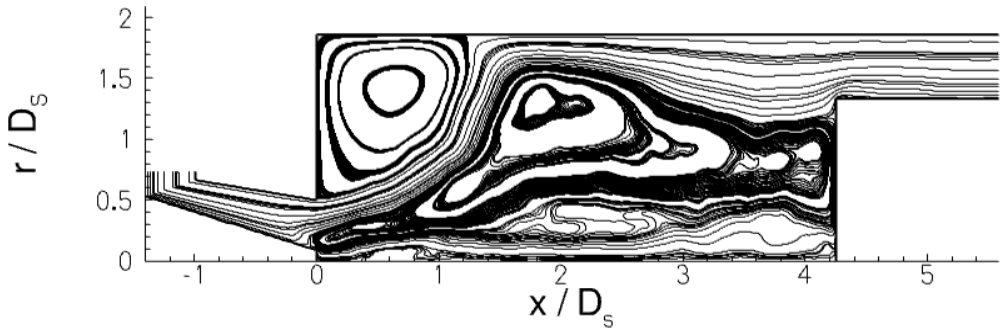

(b) $t/T_s = 50$, $x_{\mathrm{L}}/D_s \approx 1.26$

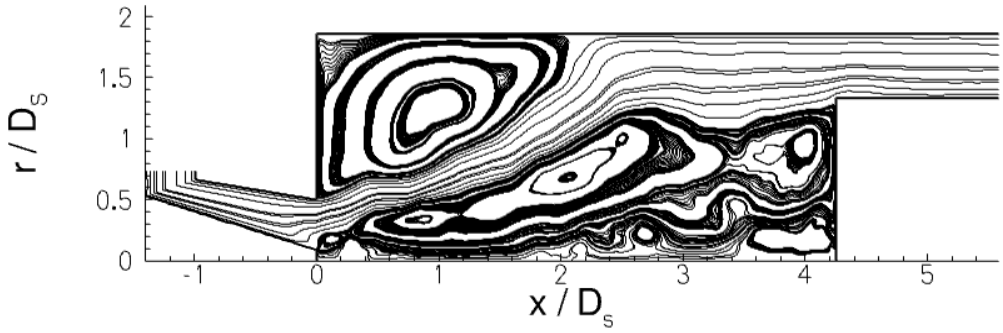

(c) $t/T_s = 250$, $x_{\mathrm{L}}/D_s \approx 2.17$

Figure 5.14: Instantaneous streamtraces in $x - r$ plane at various time-instants

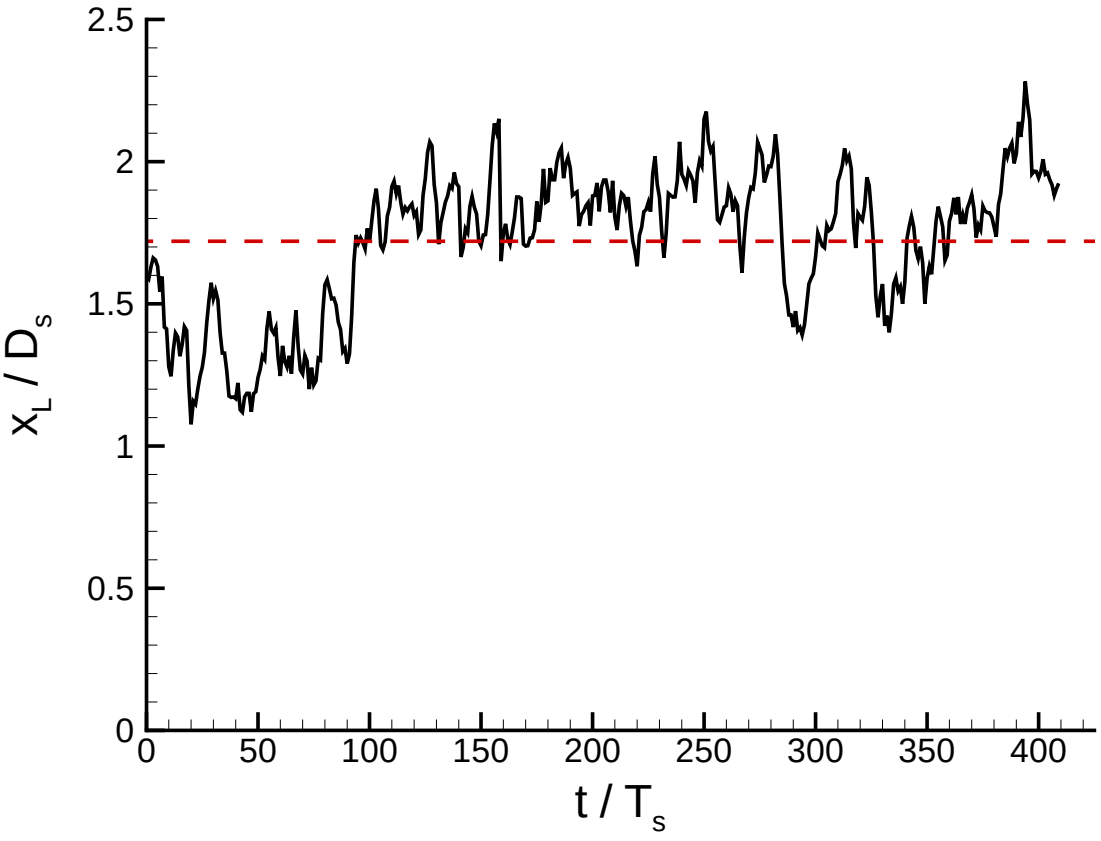

Figure 5.15: Instantaneous reattachment location of outer shear-layer at $r/D_s = 1.86$. Horizontal dashed line indicates time-mean location

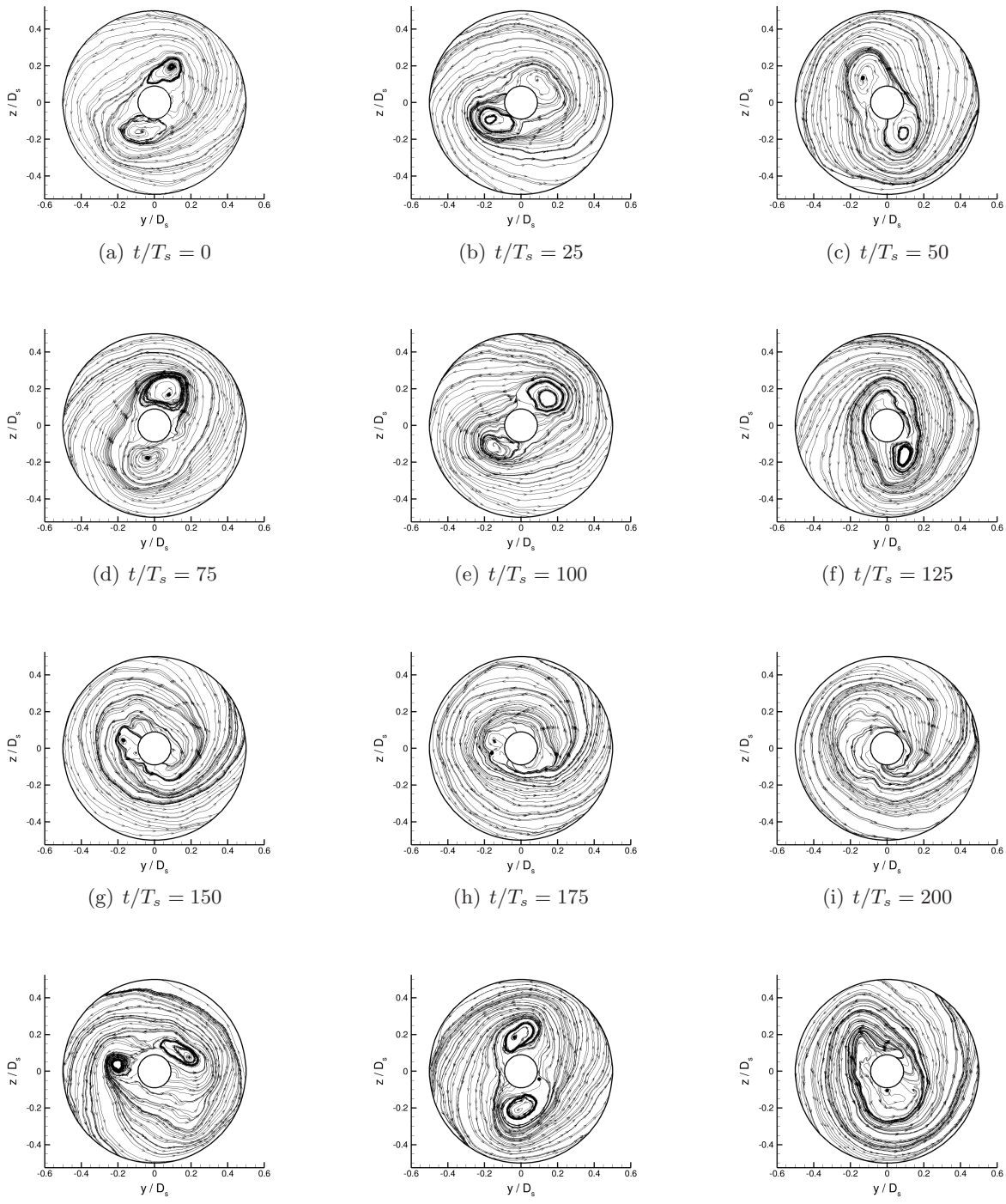

(a) $t/T_s = 0$ (b) $t/T_s = 25$ (c) $t/T_s = 50$

(d) $t/T_s = 75$ (e) $t/T_s = 100$ (f) $t/T_s = 125$

(g) $t/T_s = 150$ (h) $t/T_s = 175$ (i) $t/T_s = 200$

(j) $t/T_s = 300$ (k) $t/T_s = 325$ (l) $t/T_s = 350$

Figure 5.16: Instantaneous streamlines at various time-instants at swirler exit ($x/D_s = 0.02$)

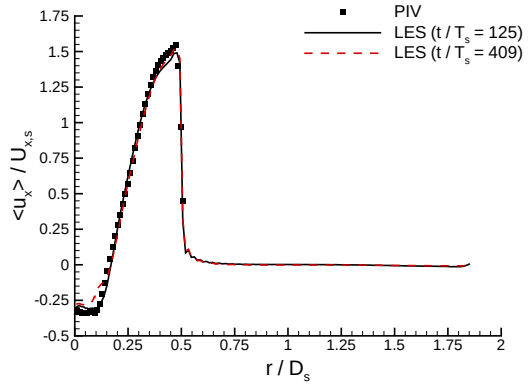

(a) $x/D_s = 0.02$

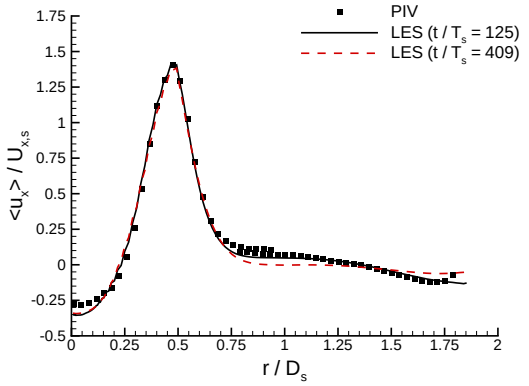

(b) $x/D_s = 0.27$

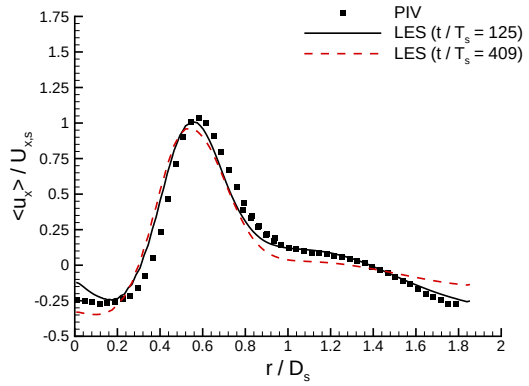

(c) $x/D_s = 0.53$

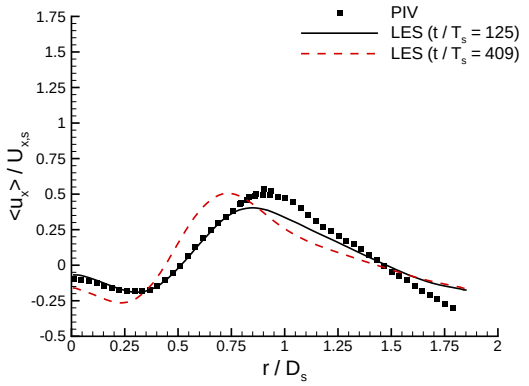

(d) $x/D_s = 1.06$

Figure 5.17: Comparison of mean axial velocity for conditioned ($t/T_s = 125$) and complete ($t/T_s = 409$) LES sample sets against PIV at various axial locations in expansion chamber

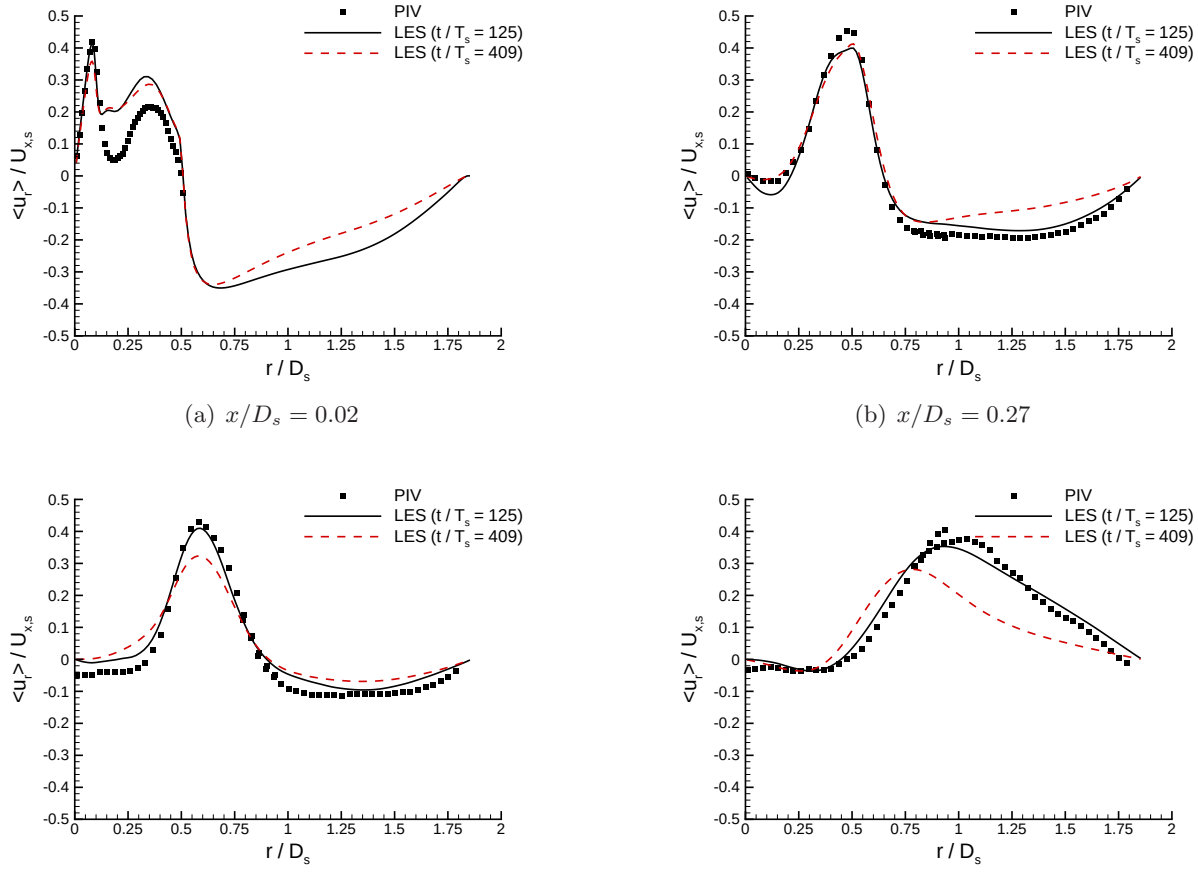

(a) $x/D_s = 0.02$

(b) $x/D_s = 0.27$

(c) $x/D_s = 0.53$

(d) $x/D_s = 1.06$

Figure 5.18: Comparison of mean radial velocity for conditioned ($t/T_s = 125$) and complete ($t/T_s = 409$) LES sample sets against PIV at various axial locations in expansion chamber

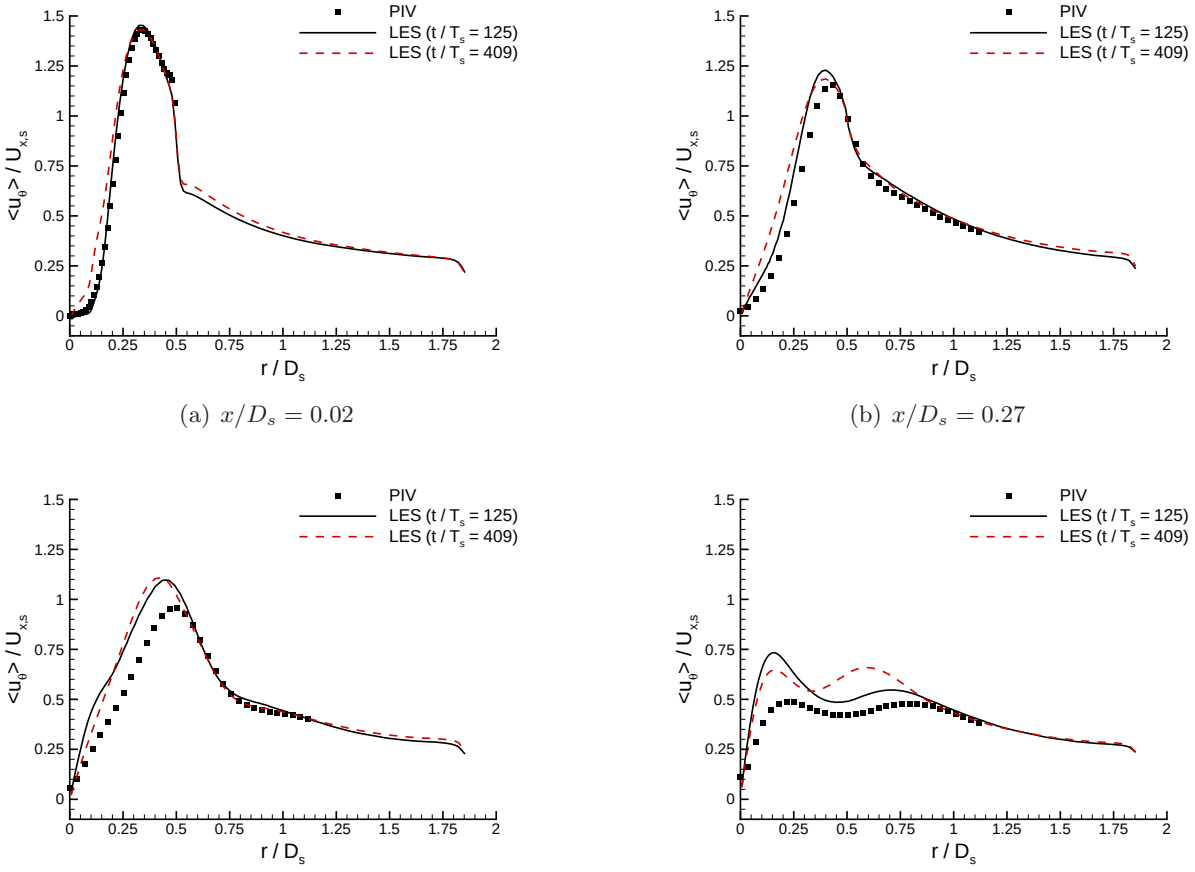

(a) $x/D_s = 0.02$

(b) $x/D_s = 0.27$

(c) $x/D_s = 0.53$

(d) $x/D_s = 1.06$

Figure 5.19: Comparison of mean tangential velocity for conditioned ($t/T_s = 125$) and complete ($t/T_s = 409$) LES sample sets against PIV at various axial locations in expansion chamber

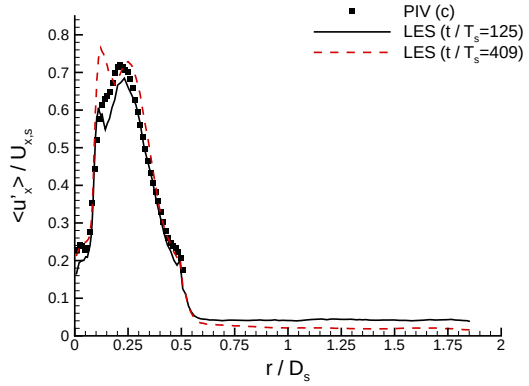

(a) $x/D_s = 0.02$

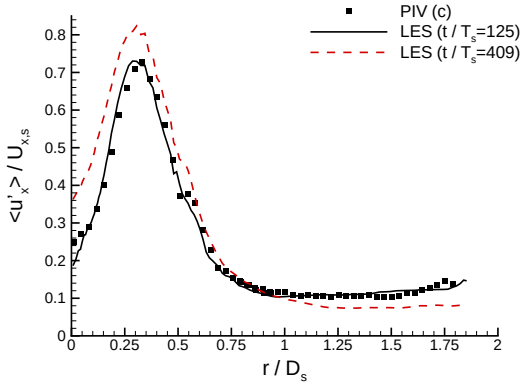

(b) $x/D_s = 0.27$

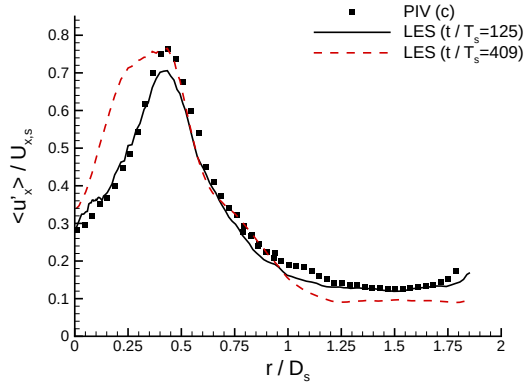

(c) $x/D_s = 0.53$

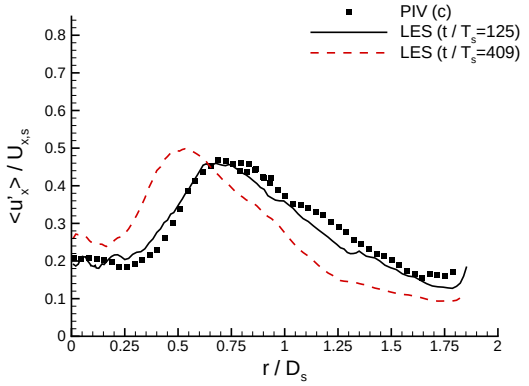

(d) $x/D_s = 1.06$

Figure 5.20: Comparison of r.m.s axial velocity for conditioned ($t/T_s = 125$) and complete ($t/T_s = 409$) LES sample sets against PIV at various axial locations in expansion chamber

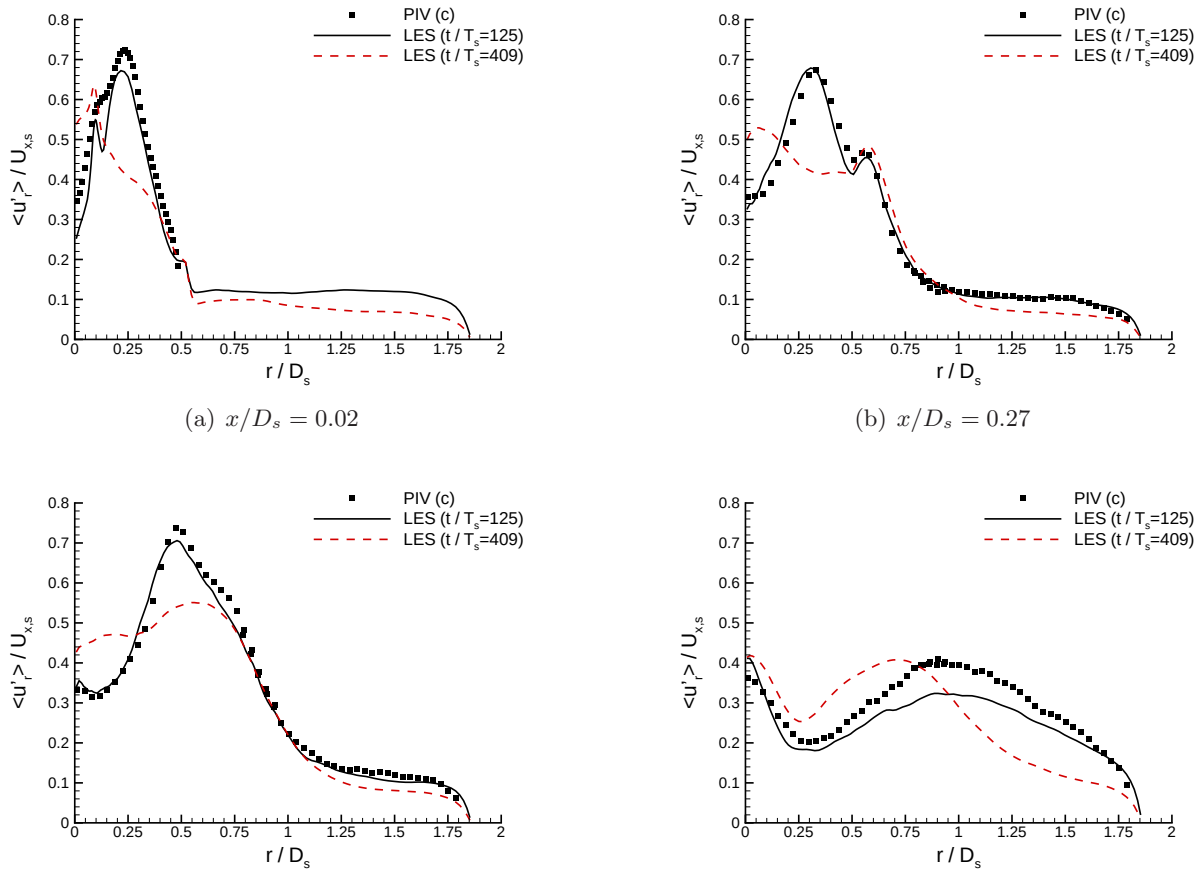

(a) $x/D_s = 0.02$

(b) $x/D_s = 0.27$

(c) $x/D_s = 0.53$

(d) $x/D_s = 1.06$

Figure 5.21: Comparison of r.m.s radial velocity for conditioned ($t/T_s = 125$) and complete ($t/T_s = 409$) LES sample sets against corrected PIV at various axial locations in expansion chamber

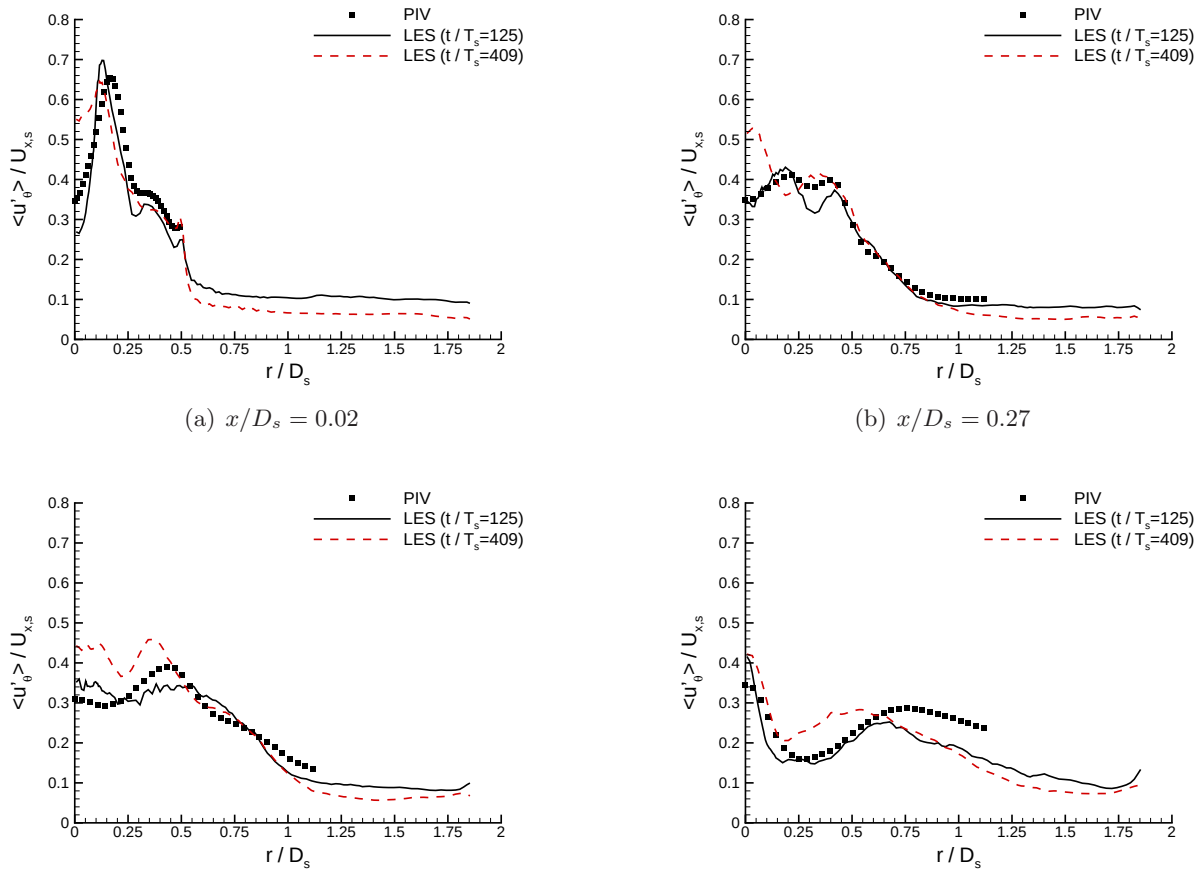

(a) $x/D_s = 0.02$

(b) $x/D_s = 0.27$

(c) $x/D_s = 0.53$

(d) $x/D_s = 1.06$

Figure 5.22: Comparison of r.m.s tangential velocity for conditioned ($t/T_s = 125$) and complete ($t/T_s = 409$) LES sample sets against corrected PIV at various axial locations in expansion chamber

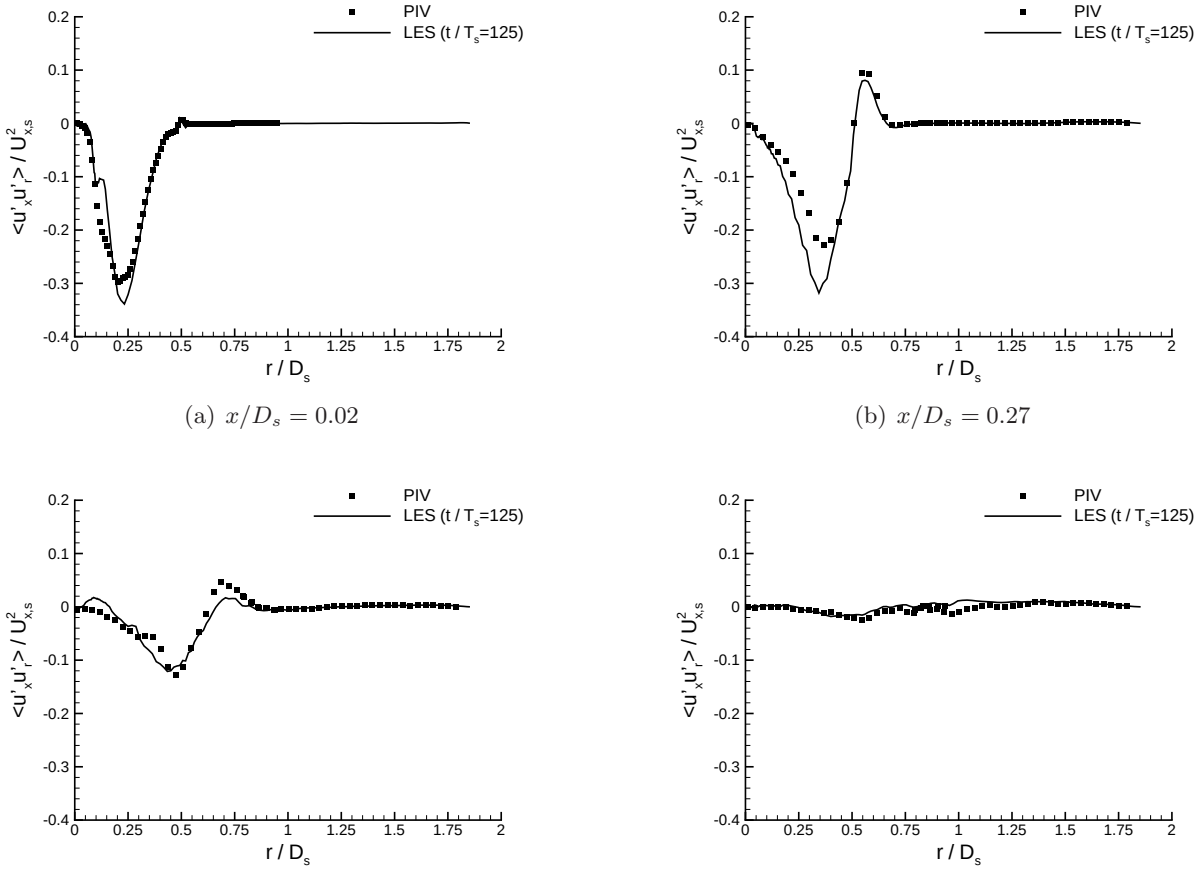

(a) $x/D_s = 0.02$

(b) $x/D_s = 0.27$

(c) $x/D_s = 0.53$

(d) $x/D_s = 1.06$

Figure 5.23: Comparison of axial-radial shear-stress for conditioned ($t/T_s = 125$) LES sample set against PIV at various axial locations in expansion chamber

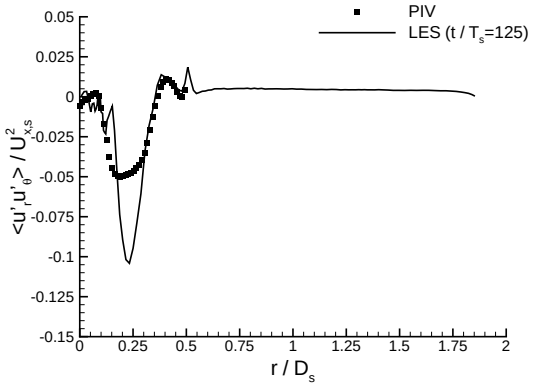

(a) $x/D_s = 0.02$

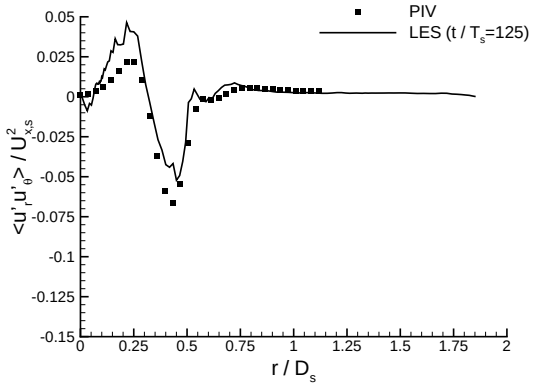

(b) $x/D_s = 0.27$

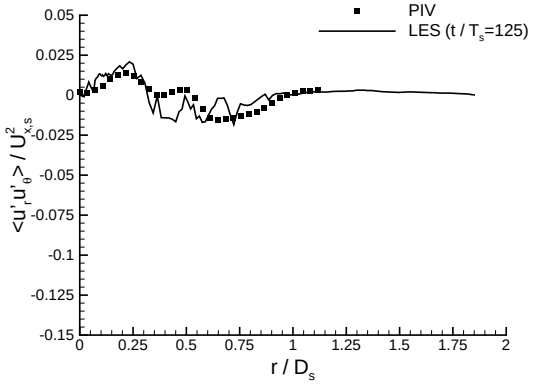

(c) $x/D_s = 0.53$

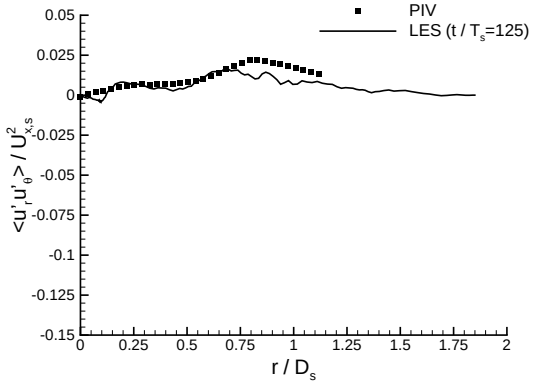

(d) $x/D_s = 1.06$

Figure 5.24: Comparison of radial-tangential shear-stress for conditioned ($t/T_s = 125$) LES sample set against PIV at various axial locations in expansion chamber

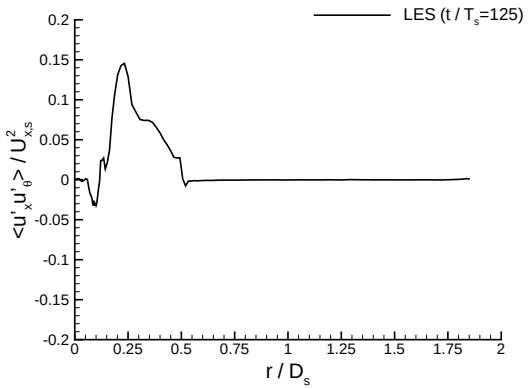

(a) $x/D_s = 0.02$

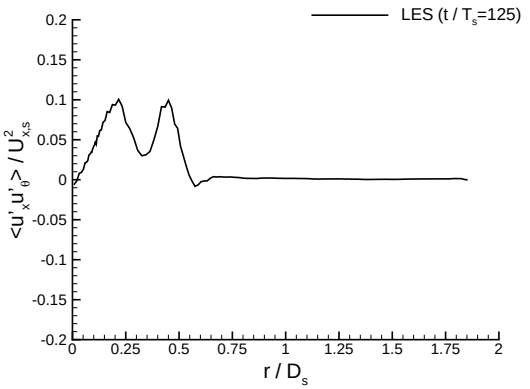

(b) $x/D_s = 0.27$

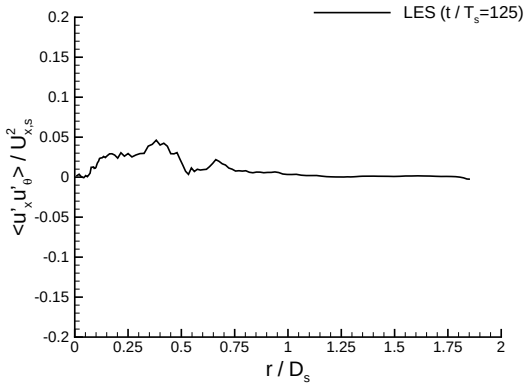

(c) $x/D_s = 0.53$

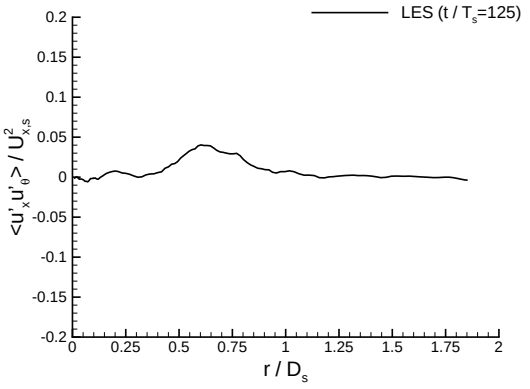

(d) $x/D_s = 1.06$

Figure 5.25: Axial-tangential shear-stress for conditioned ($t/T_s = 125$) LES sample set at various axial locations in expansion chamber

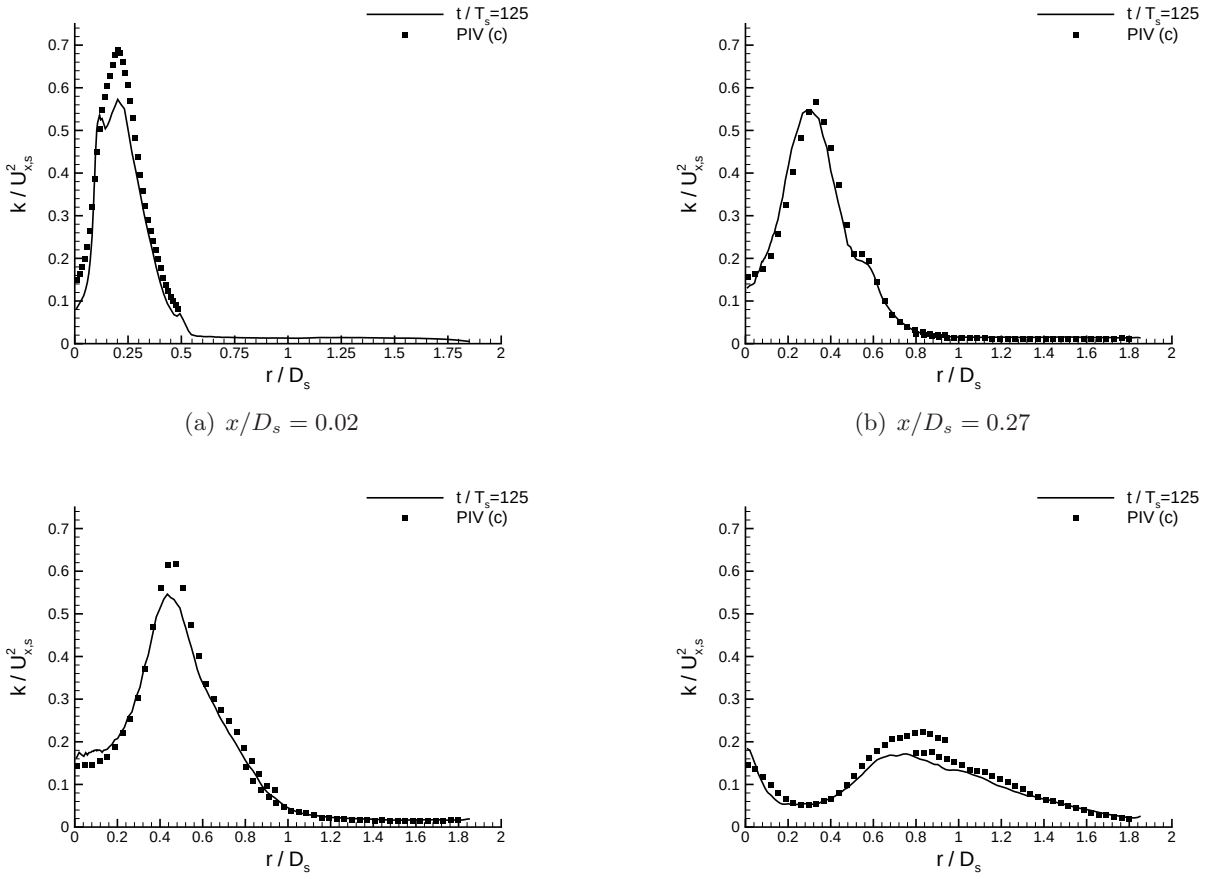

(a) $x/D_s = 0.02$

(b) $x/D_s = 0.27$

(c) $x/D_s = 0.53$

(d) $x/D_s = 1.06$

Figure 5.26: Comparison of turbulent kinetic energy for conditioned ($t/T_s = 125$) LES sample set against corrected PIV at various axial locations in expansion chamber

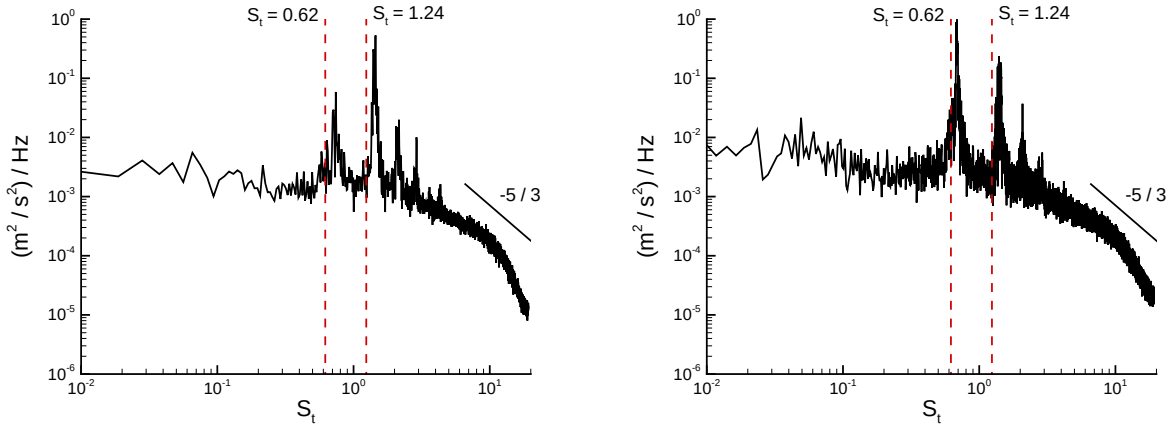

(a) Axial velocity ($t/T_s = 102$)

(b) Axial velocity ($t/T_s = 409$)

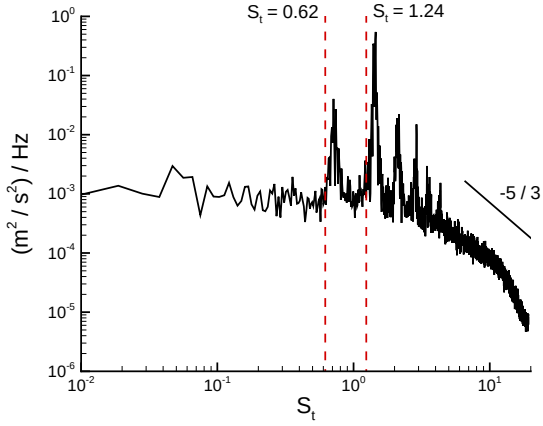

(c) Radial velocity ($t/T_s = 102$)

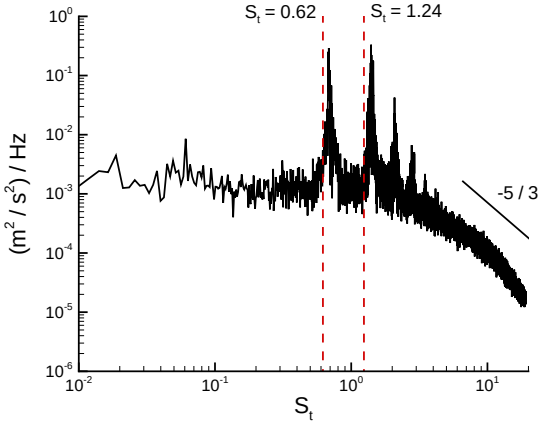

(d) Radial velocity ($t/T_s = 409$)

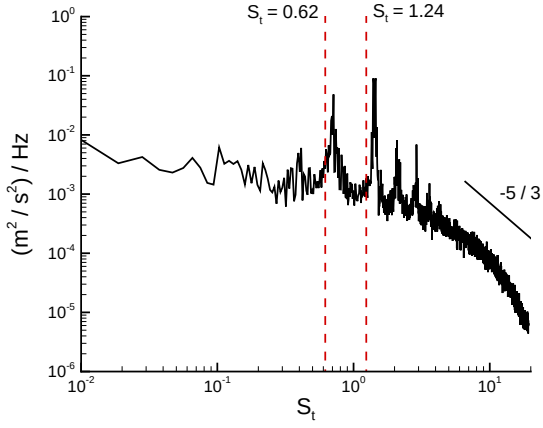

(e) Tangential velocity ($t/T_s = 102$)

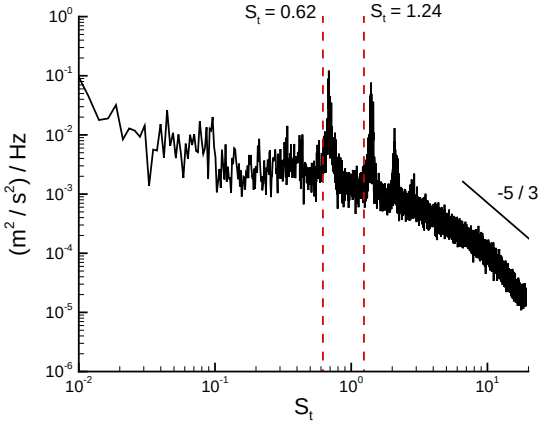

(f) Tangential velocity ($t/T_s = 409$)

Figure 5.27: PSDs of axial, radial and tangential velocity at $x/D_s = 0.27$, $r/D_s = 0.24$ for conditioned ($t/T_s = 102$) and complete ($t/T_s = 409$) LES sample sets. Vertical dashed lines indicated expected frequencies of Midgley [13].

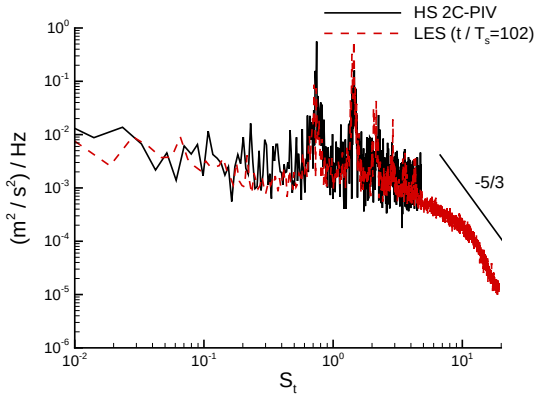

(a) Axial velocity ($t/T_s = 102$)

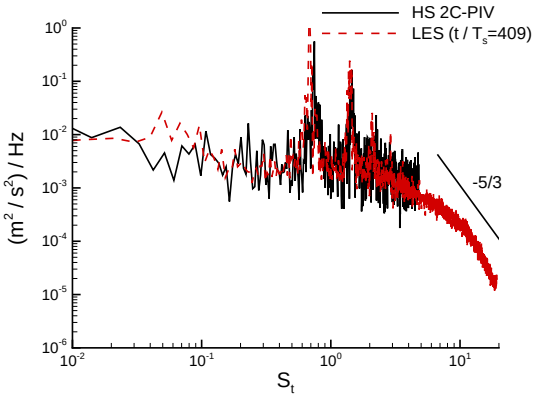

(b) Axial velocity ($t/T_s = 409$)

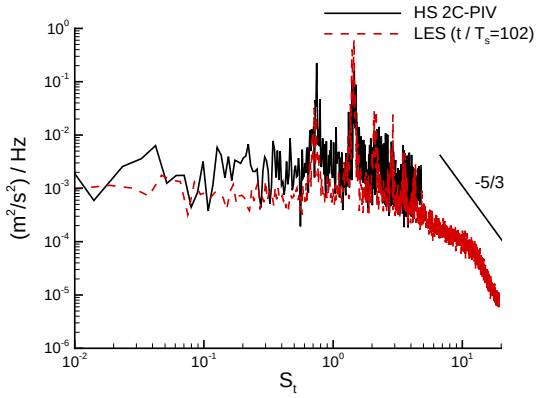

(c) Radial velocity ($t/T_s = 102$)

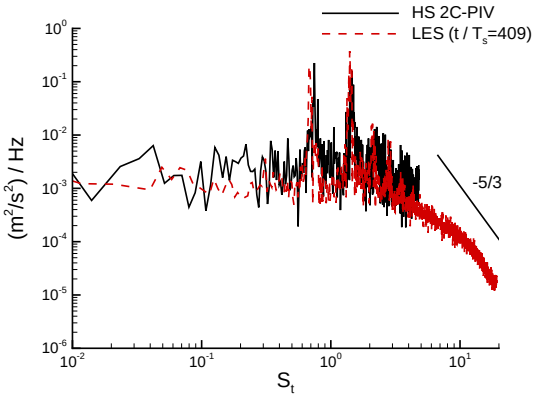

(d) Radial velocity ($t/T_s = 409$)

Figure 5.28: PSDs of axial and radial velocity at $x/D_s = 0.27$, $r/D_s = 0.27$ for conditioned ($t/T_s = 102$) and complete ($t/T_s = 409$) LES samples sets against high-speed PIV [13].

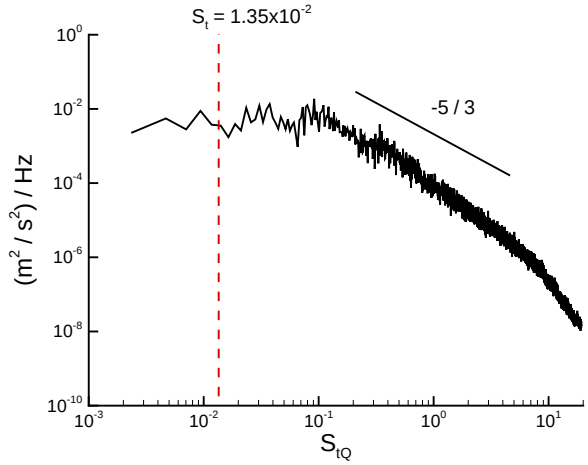

(a) $r/D_s = 0.08$

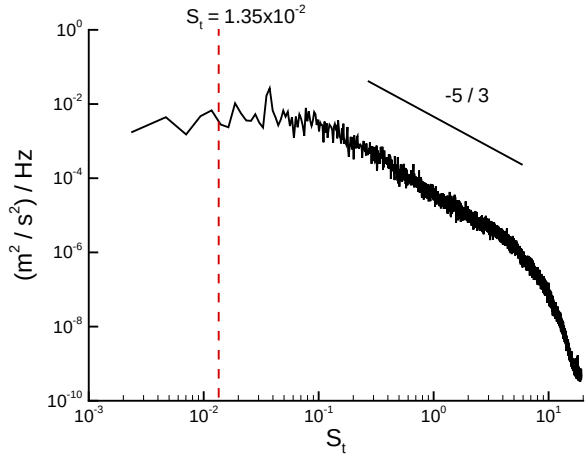

(b) $r/D_s = 0.16$

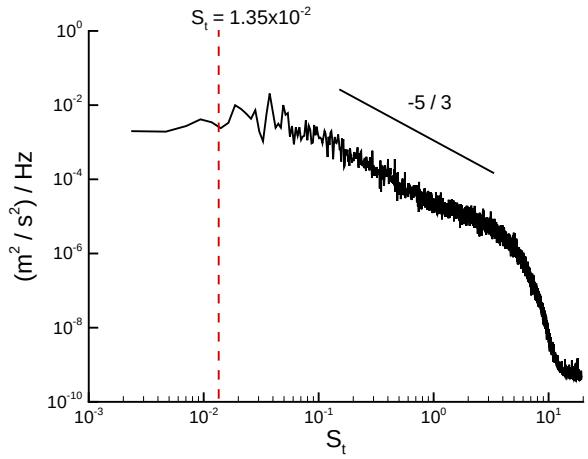

(c) $r/D_s = 0.24$

Figure 5.29: PSD of axial velocity at $x/D_s = 2.65$ for various radial locations. Vertical dashed line indicates expected PVC frequency of Syred et al. [38]

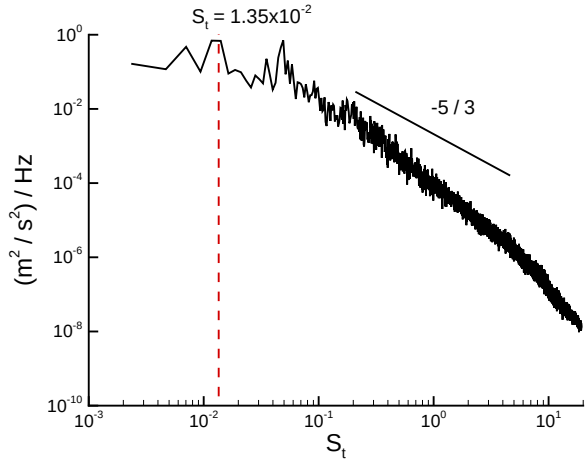

(a) $r/D_s = 0.08$

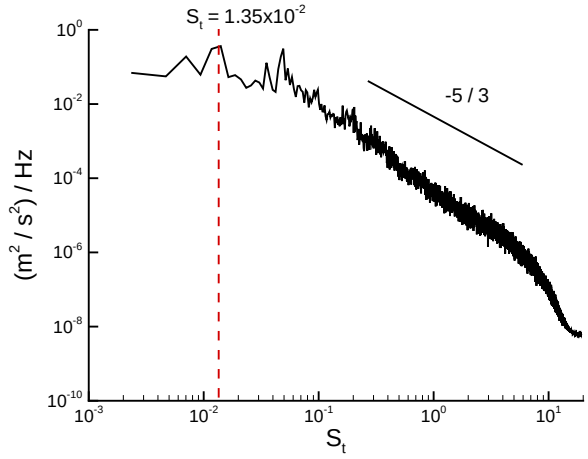

(b) $r/D_s = 0.16$

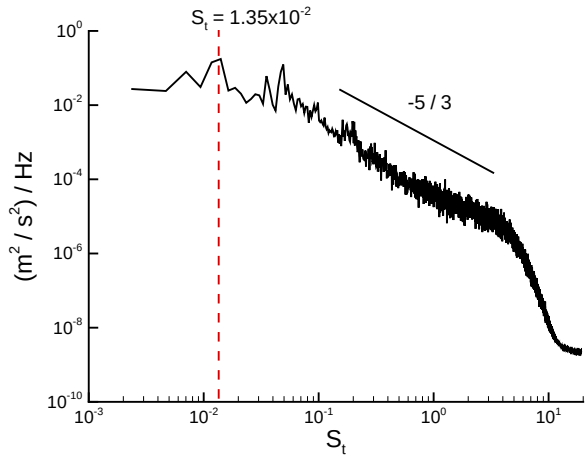

(c) $r/D_s = 0.24$

Figure 5.30: PSD of radial velocity at $x/D_s = 2.65$ for various radial locations. Vertical dashed line indicates expected PVC frequency of Syred et al. [38]

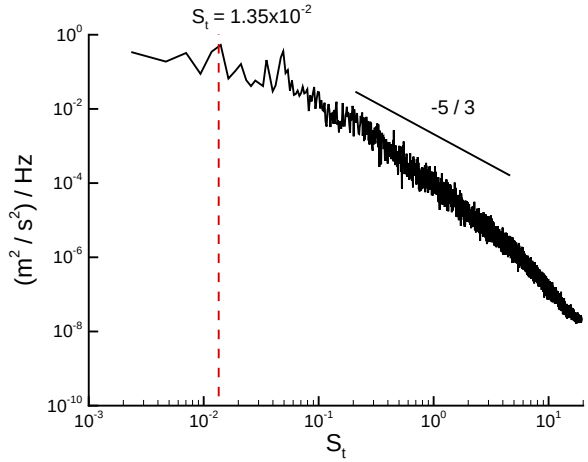

(a) $r/D_s = 0.08$

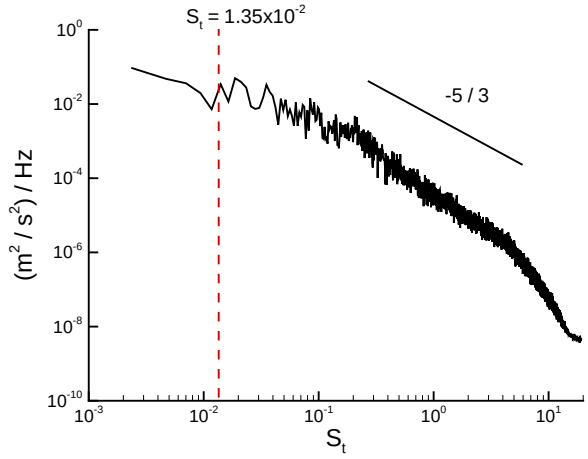

(b) $r/D_s = 0.16$

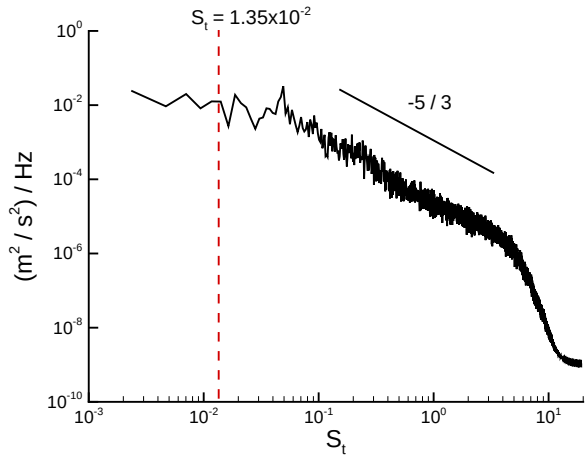

(c) $r/D_s = 0.24$

Figure 5.31: PSD of tangential velocity at $x/D_s = 2.65$ for various radial locations. Vertical dashed line indicates expected PVC frequency of Syred et al. [38]

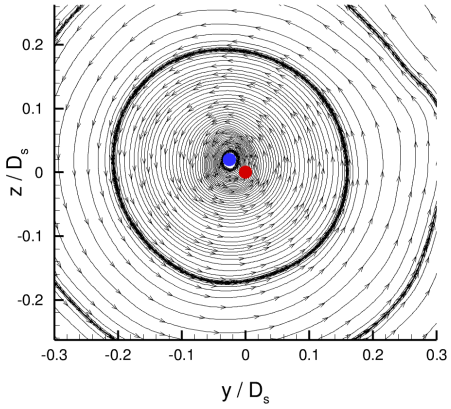

(a) $t/T_s = 0$

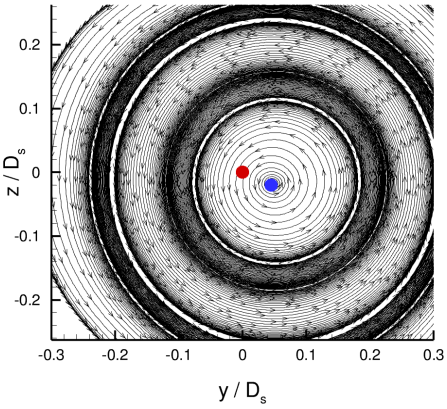

(b) $t/T_s = 50$

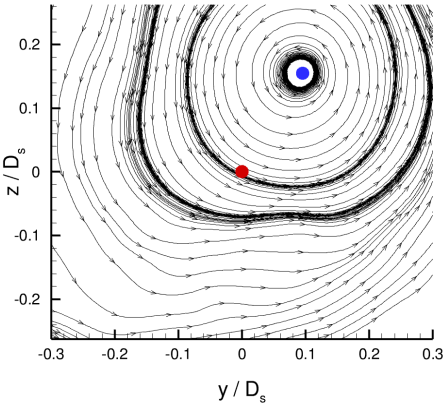

(c) $t/T_s = 250$

Figure 5.32: Instantaneous streamtraces at $x/D_s = 2.39$ at various time-instants ●- geometric centre ●aerodynamic centre from Equation A-24

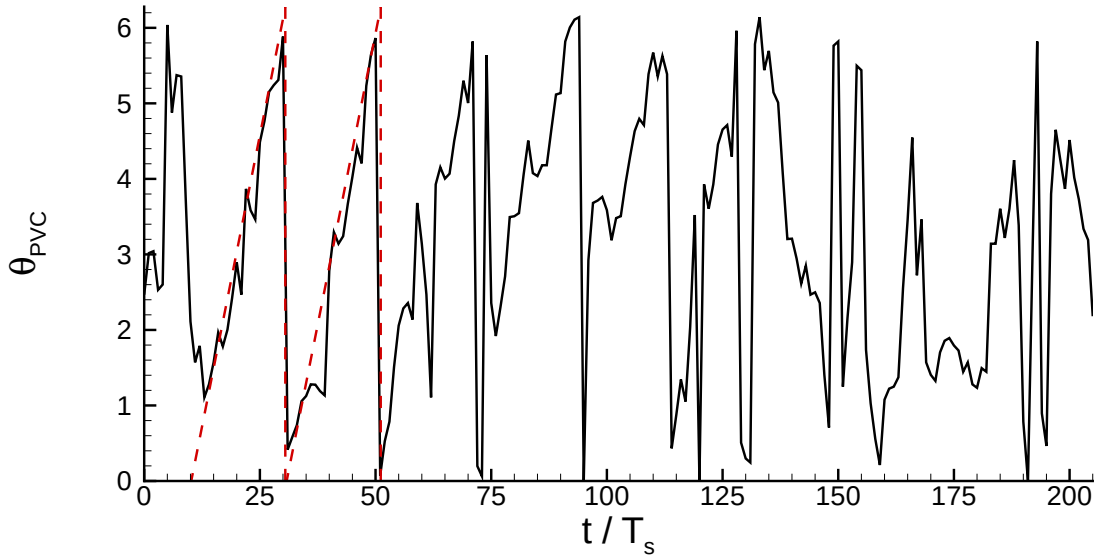

(a) $t/T_s = 0 - 205$. Dashed line indicates characteristic timescale of $t/T_s = 20$

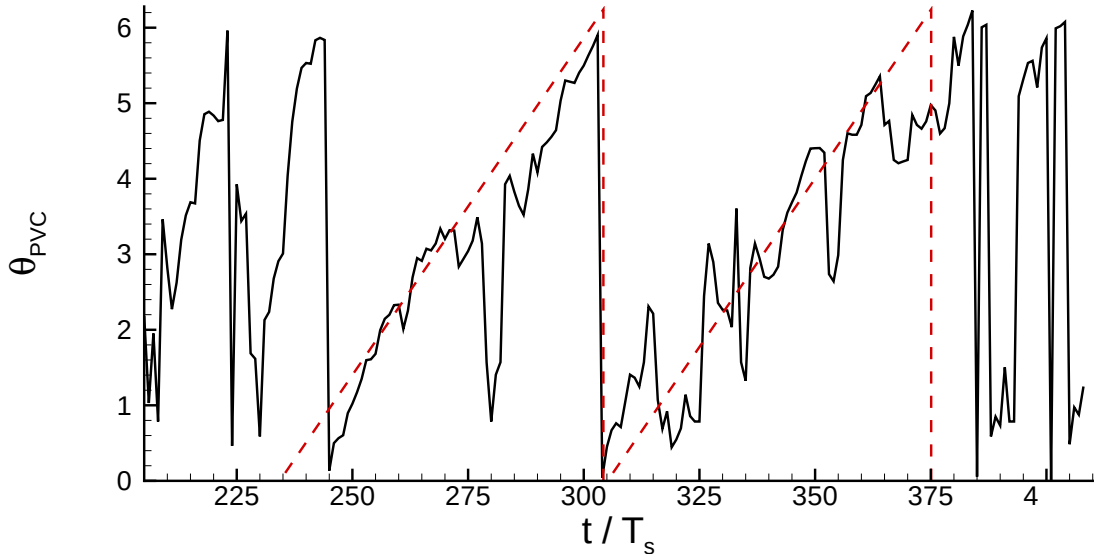

(b) $t/T_s = 205 - 409$. Dashed line indicates characteristic timescale of $t/T_s = 72$

Figure 5.33: Angular location of PVC at $x/D_s = 2.39$

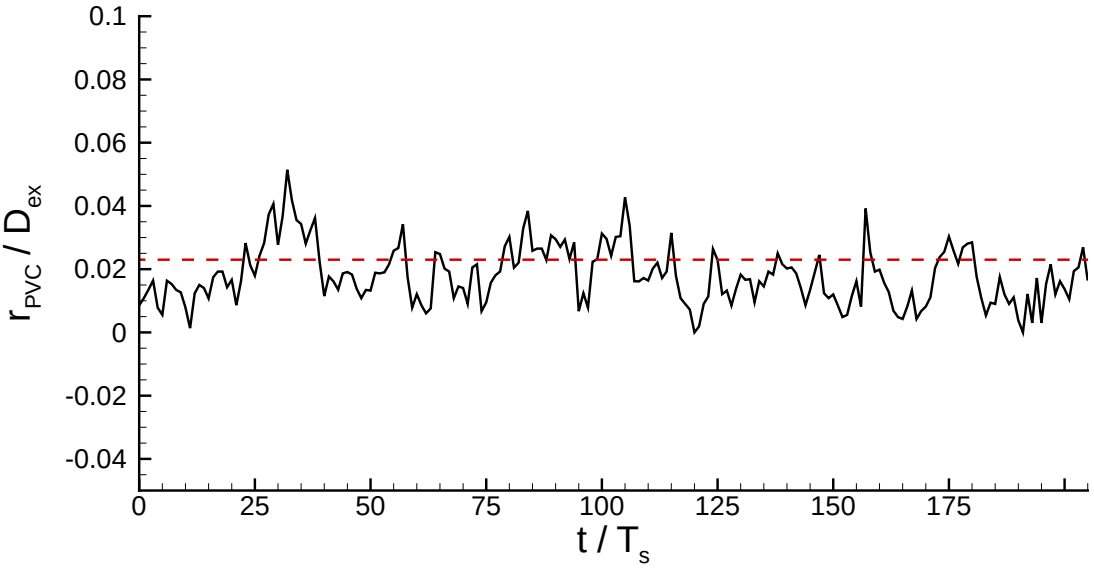

(a) $t/T_s = 0 - 205$

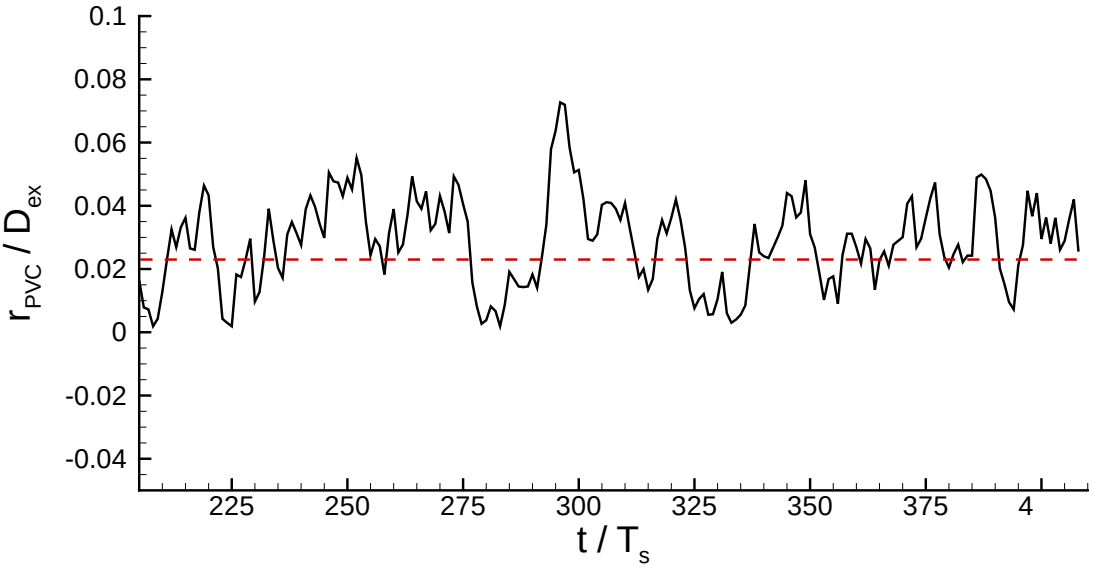

(b) $t/T_s = 205 - 409$

Figure 5.34: Radial displacement of PVC at $x/D_s = 2.39$. Horizontal dashed line indicates mean radial displacement of PVC.

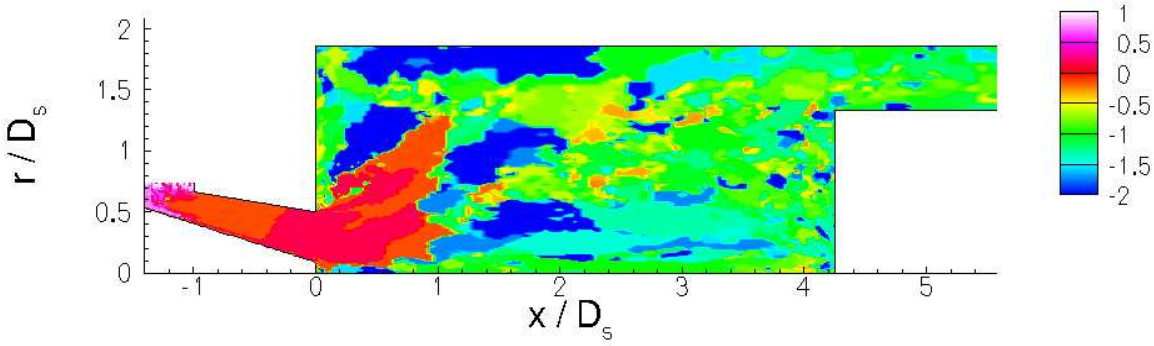

(a) Axial Velocity

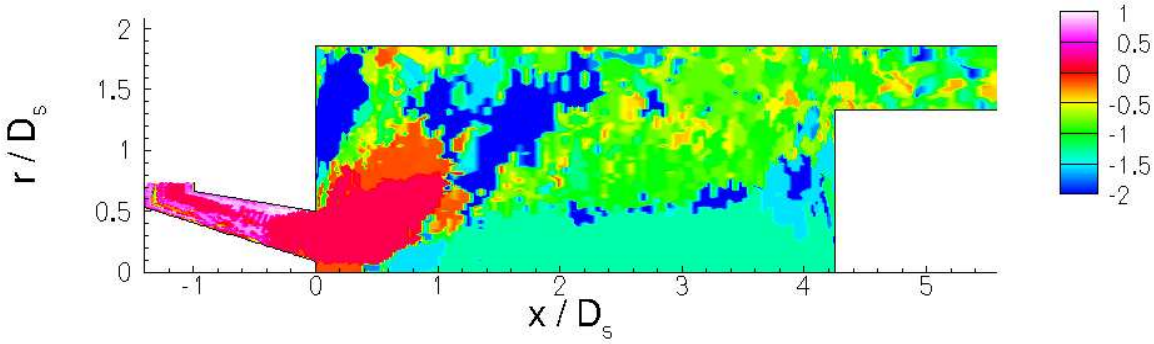

(b) Radial Velocity

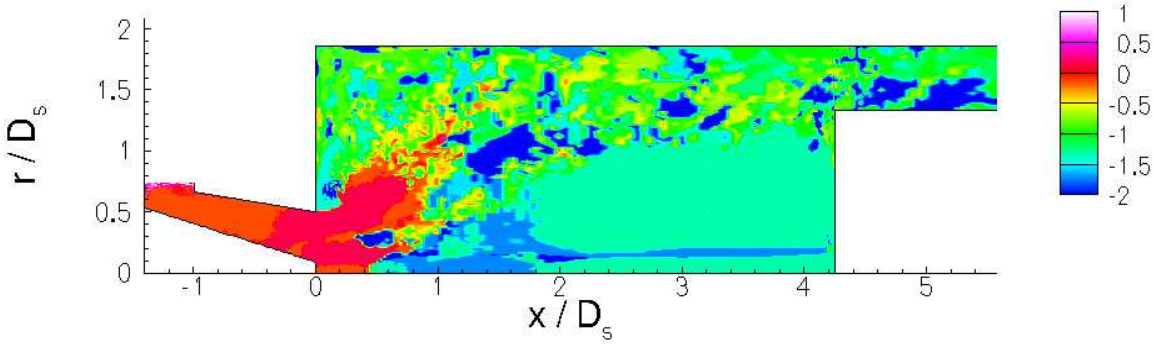

(c) Tangential Velocity

Figure 5.35: Contours of peak $\log_{10} S_t$ for conditioned ($t/T_s = 102$) LES sample set.

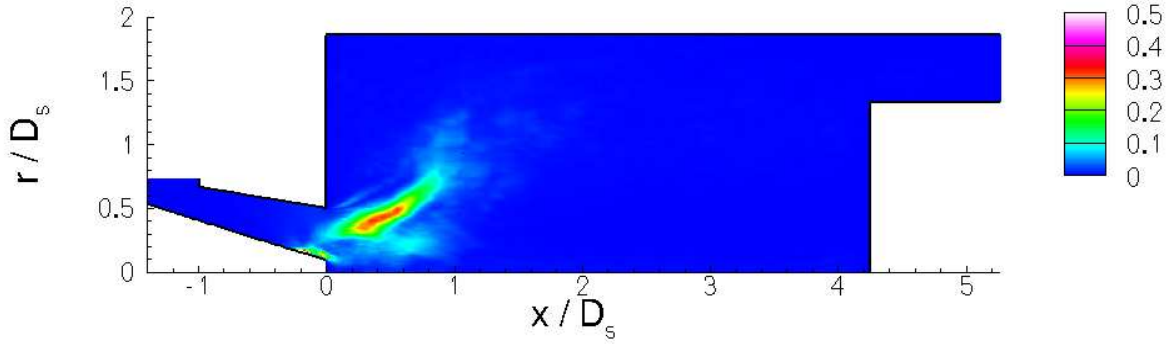

(a) Axial velocity

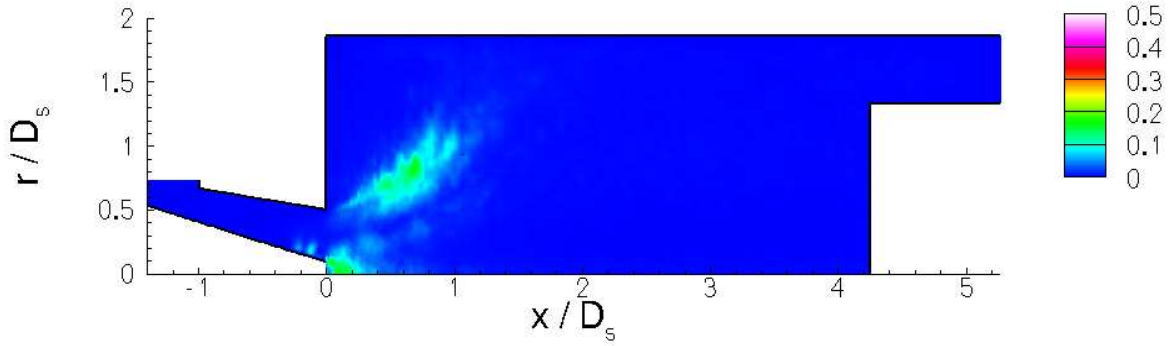

(b) Radial velocity

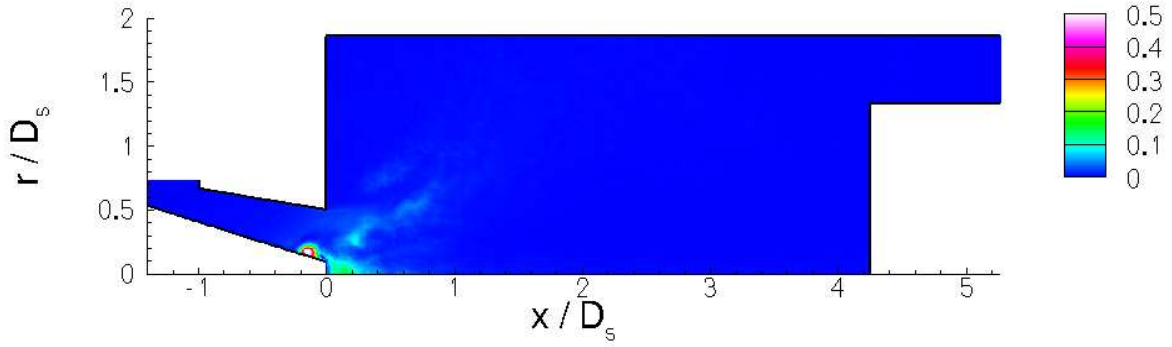

(c) Tangential velocity

Figure 5.36: Amplitude of PSD (m^2/s^2/Hz) at $S_t = 0.72$ for axial, radial and tangential velocities for conditioned ($t/T_s = 102$) LES sample set.

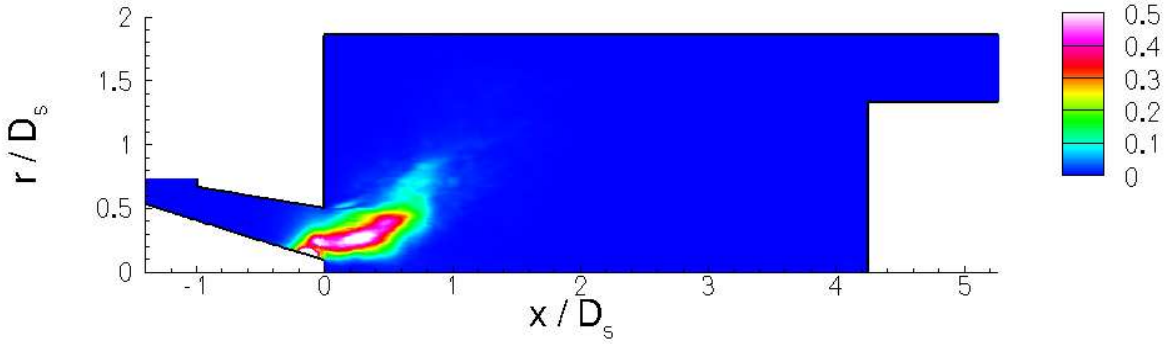

(a) Axial velocity

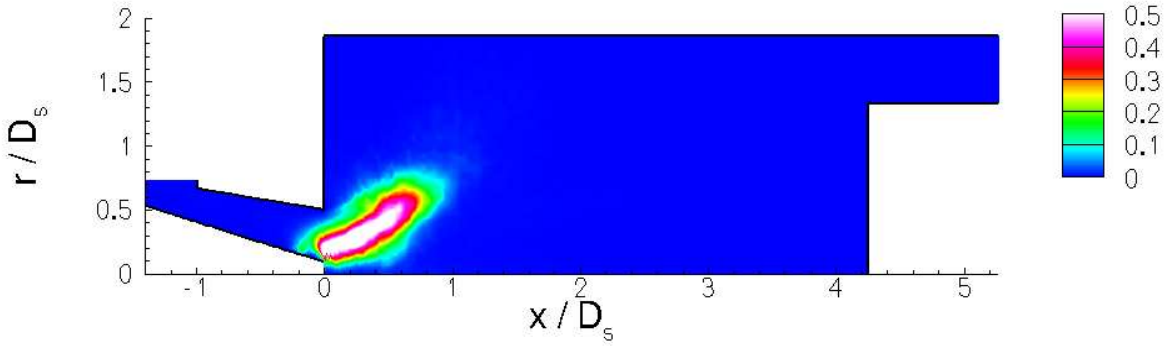

(b) Radial velocity

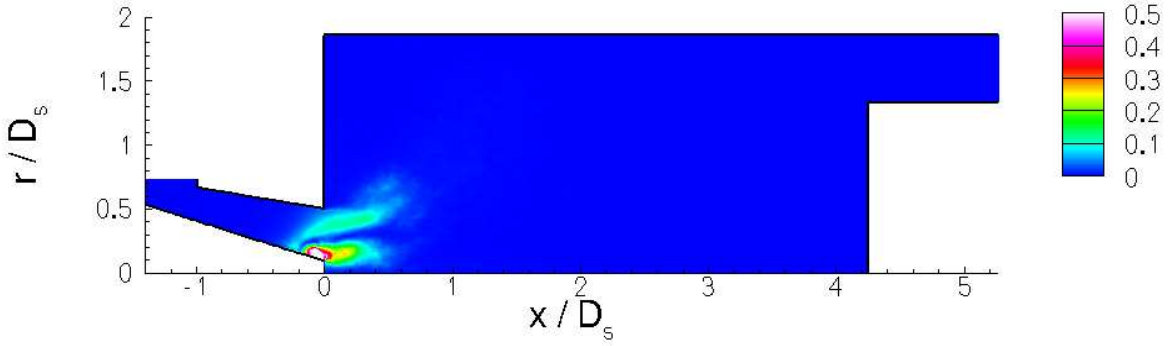

(c) Tangential velocity

Figure 5.37: Amplitude of PSD (m^2/s^2/Hz) at $S_t = 1.44$ for axial, radial and tangential velocities for conditioned ($t/T_s = 102$) LES sample set.

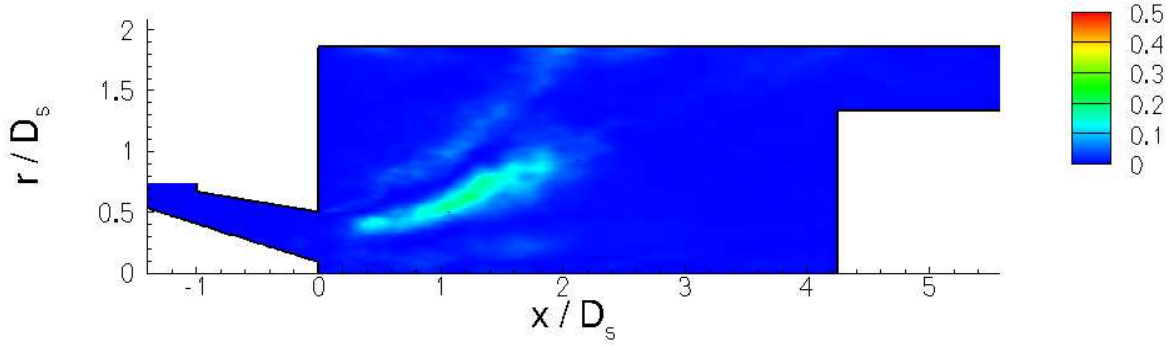

(a) Axial Velocity

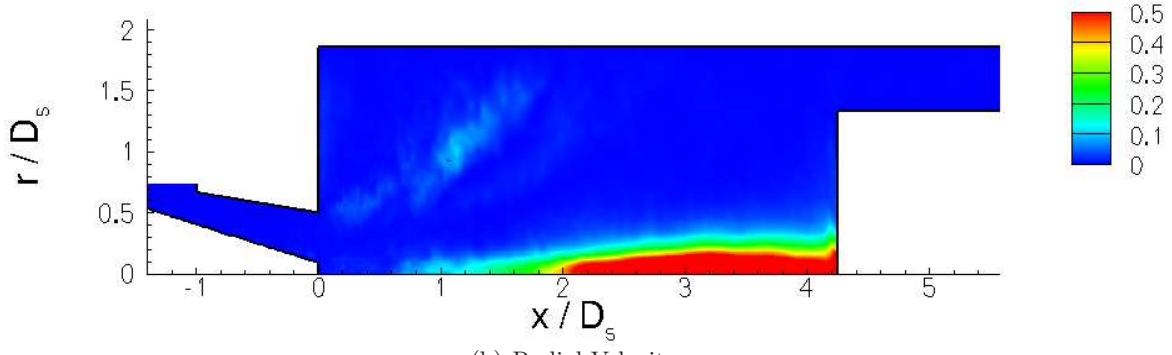

(b) Radial Velocity

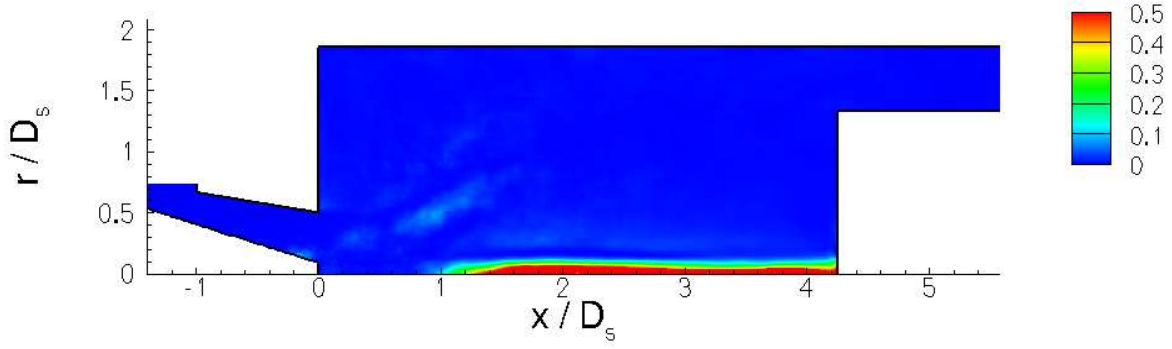

(c) Tangential Velocity

Figure 5.38: Amplitude of PSD (m^2/s^2/Hz) at $S_t = 1.35 \times 10^{-2}$ for axial, radial and tangential velocities for complete LES sample set ($t/T_s = 409$).

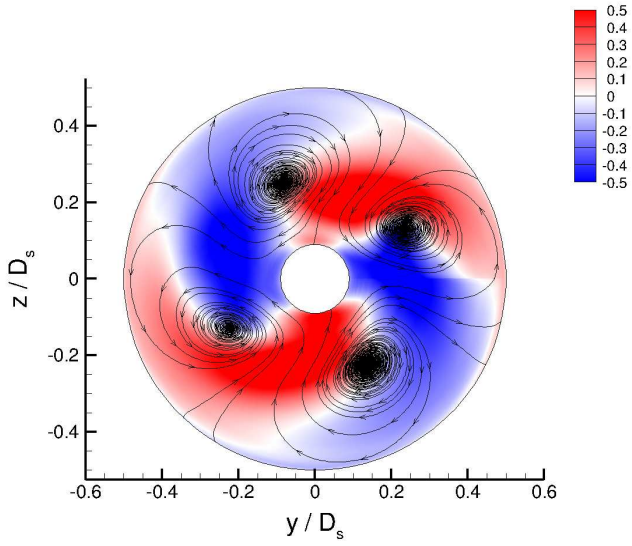

(a) $\langle u_x' \rangle_{\mathrm{rot}} / U_{x,s}$

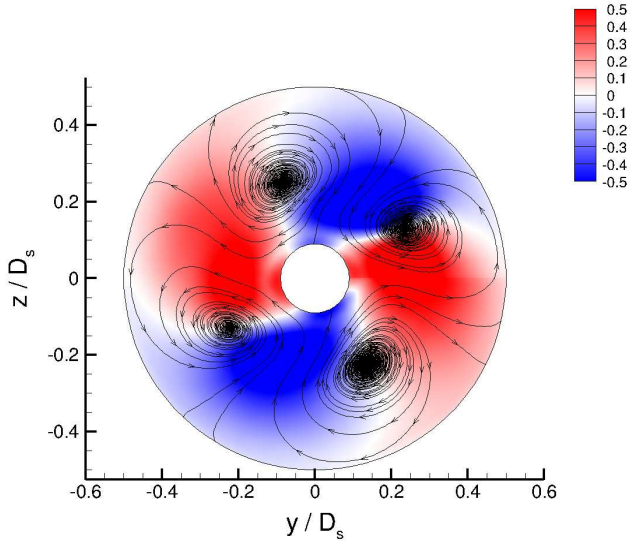

(b) $\langle u_r' \rangle_{\mathrm{rot}} / U_{x,s}$

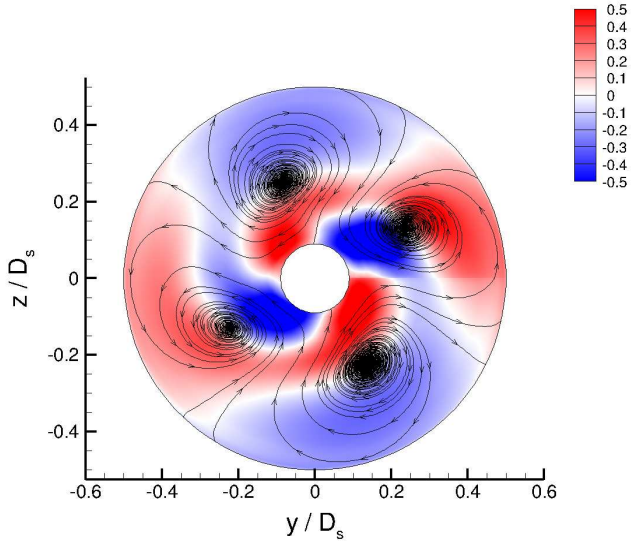

(c) $\langle u_\theta' \rangle_{\mathrm{rot}} / U_{x,s}$

Figure 5.39: Rotationally averaged Reynolds-decomposed streamtraces superimposed on contours of rotationally averaged velocities at $x/D_s = 0.02$

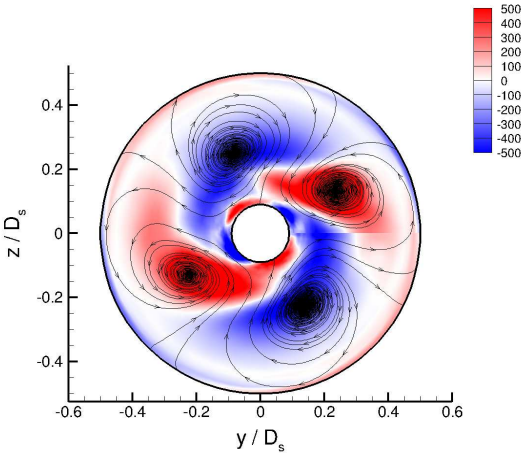

(a) $\langle \omega_x \rangle_{\text{rot}}$

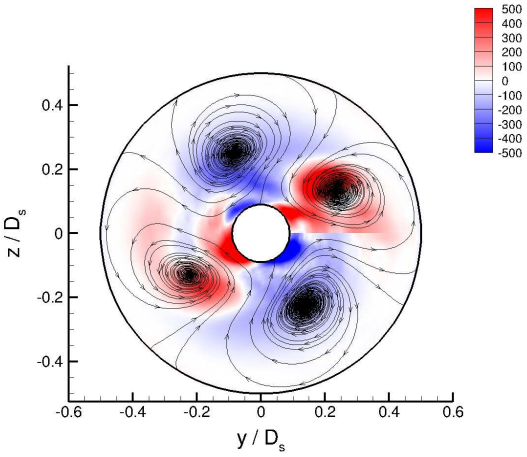

(b) $\langle \omega_r \rangle_{\text{rot}}$

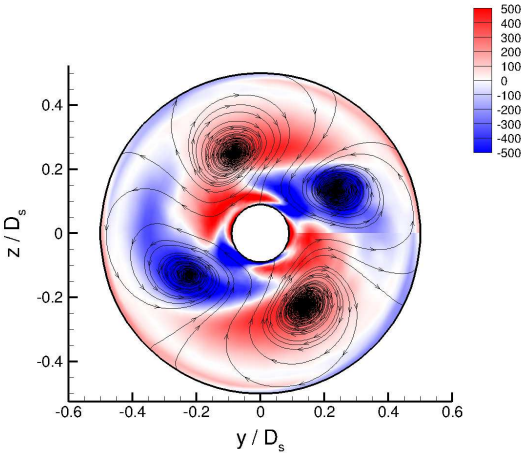

(c) $\langle \omega_\theta \rangle_{\text{rot}}$

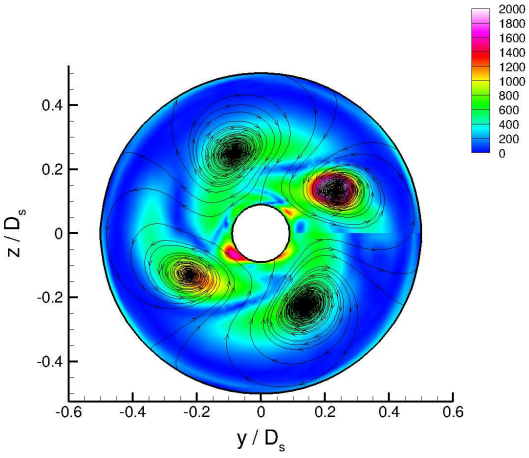

(d) $\langle |\omega| \rangle_{\text{rot}}$

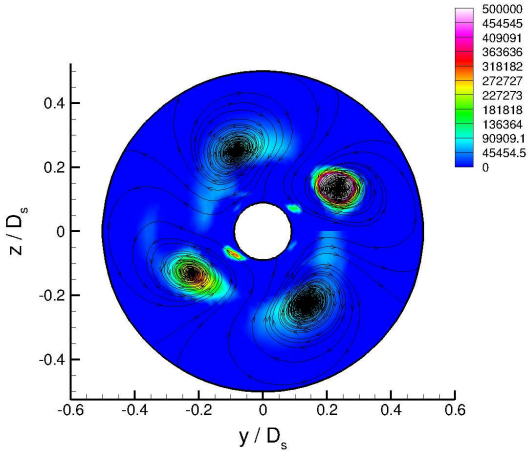

(e) $\langle Q \rangle_{\text{rot}}$

Figure 5.40: Rotationally averaged Reynolds-decomposed streamtraces superimposed on contours of rotationally-averaged vorticity and Q-criterion at $x/D_s = 0.02$

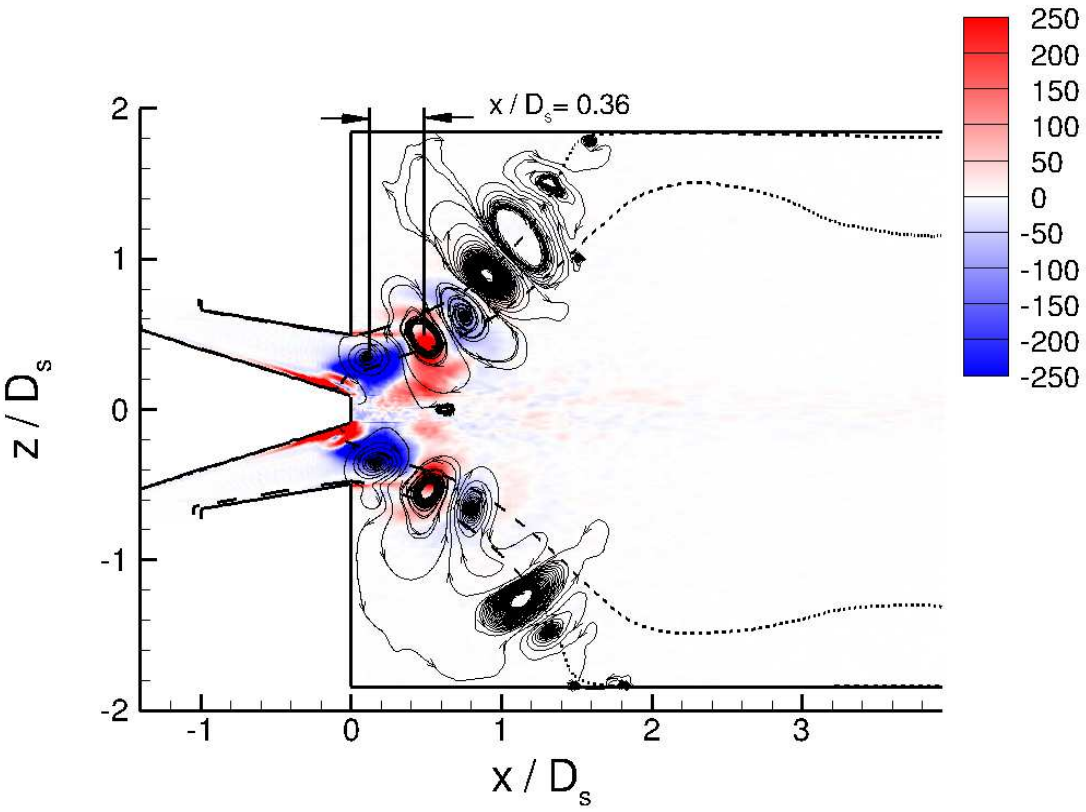

(a) $\langle \omega_x \rangle_{\text{rot}}$

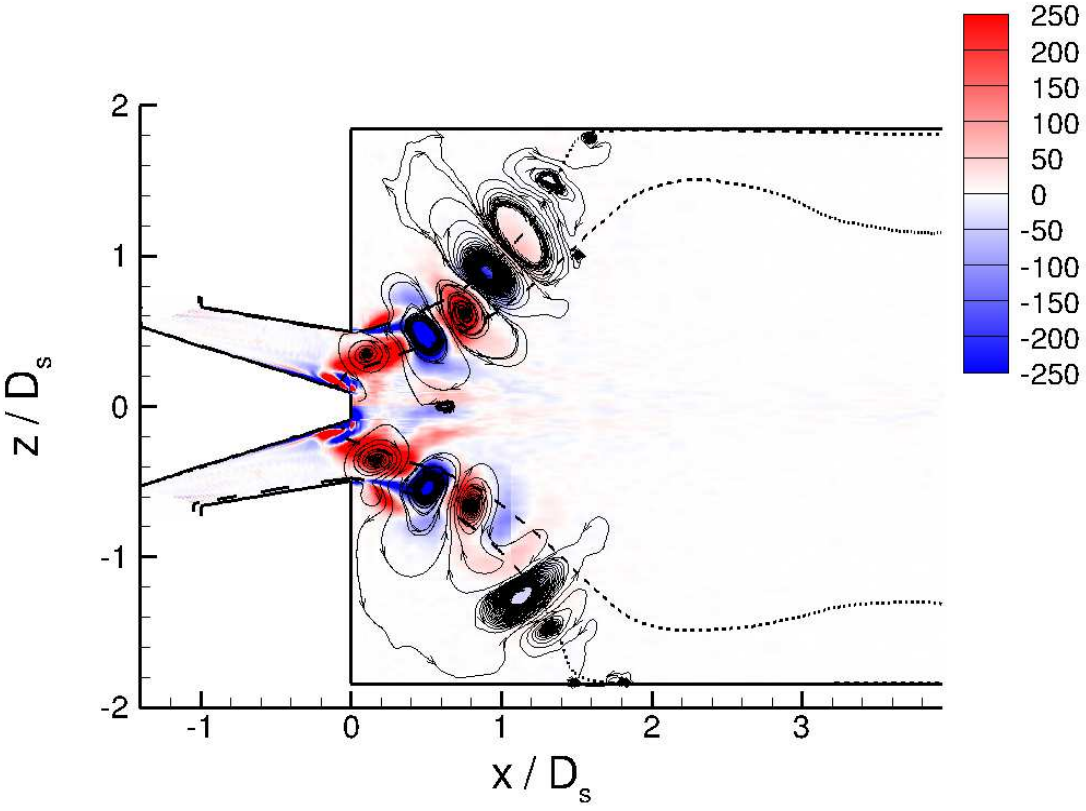

(b) $\langle \omega_\theta \rangle_{\text{rot}}$

Figure 5.41: Rotationally averaged Reynolds-decomposed streamtraces superimposed on contours of rotationally-averaged axial and azimuthal vorticity. Dashed line indicates time-mean inner and outer shear layer.

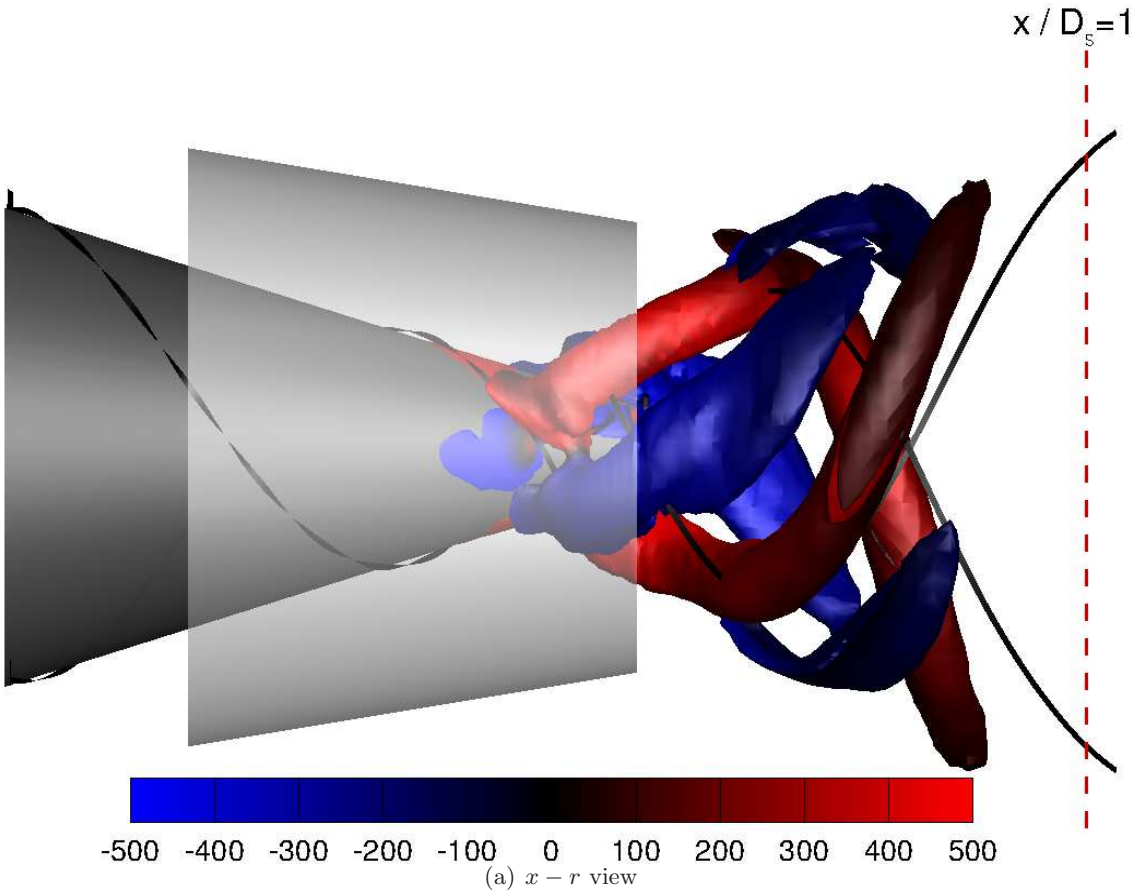

(a) $x - r$ view

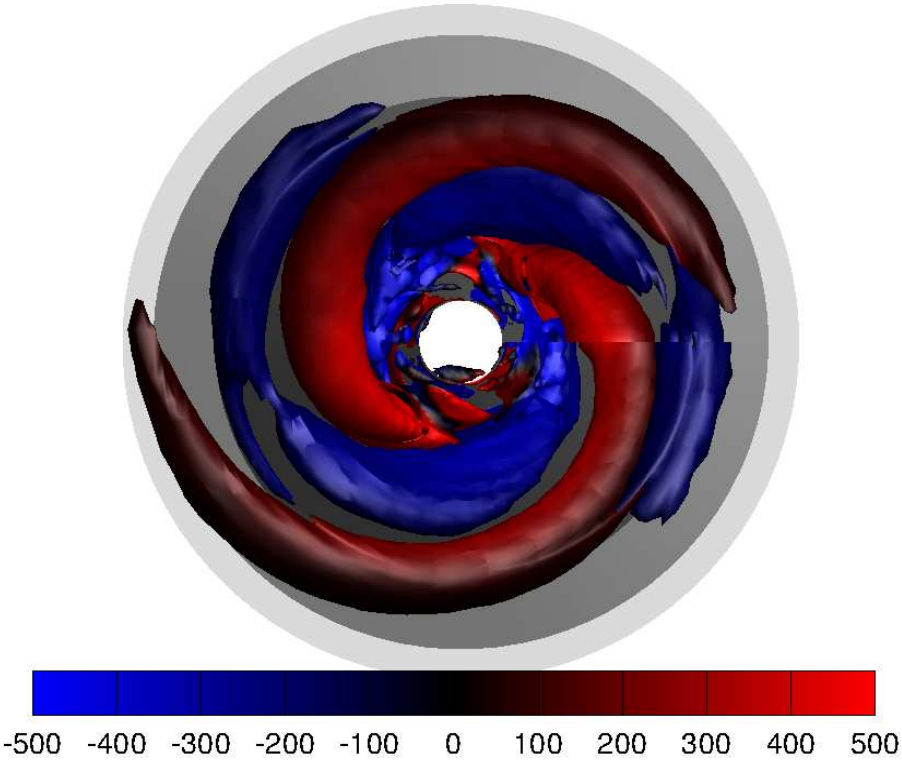

(b) $r - \theta$ view

Figure 5.42: Iso-surface of rotationally-averaged Q-criterion $\langle Q \rangle_{\text{rot}} = 40 \times 10^3$ coloured by $\langle \omega_x \rangle_{\text{rot}}$ with time-mean streamtraces ($r - \theta$ plane at $x/D_s = 0.02$ used as reference for rotational averaging)

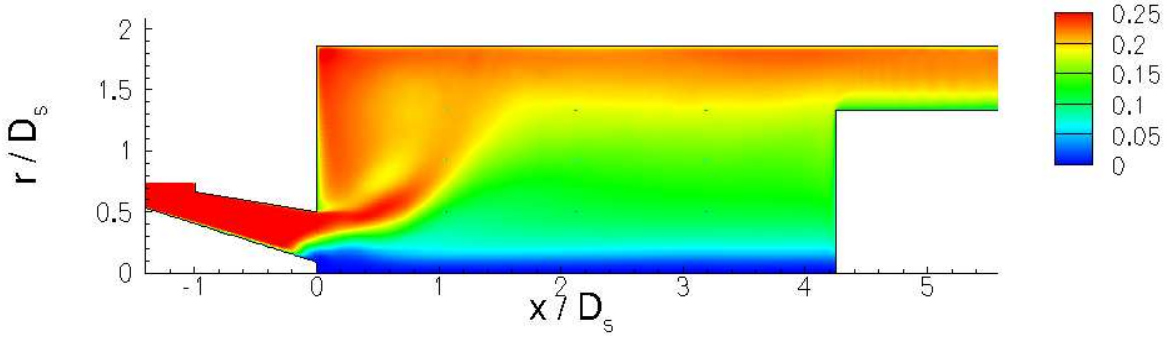

(a) Contours of time-mean streamwise circulation, $\langle \Gamma_x \rangle$

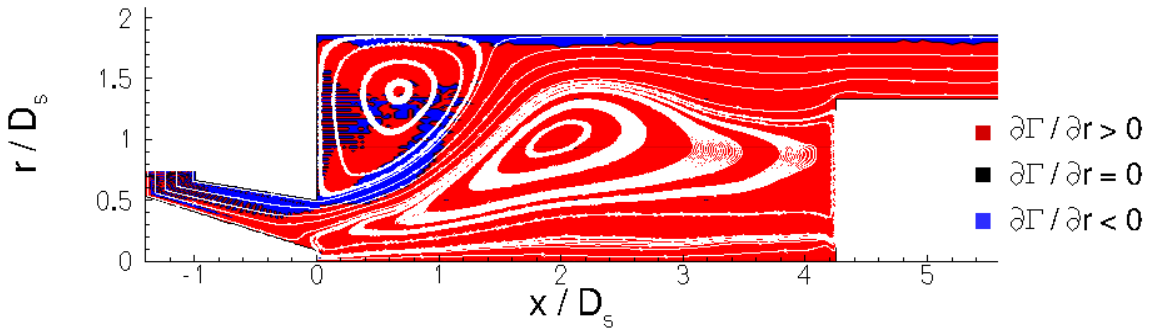

(b) Contours of Rayleigh's inviscid criterion, $\partial\Gamma/\partial r$

Figure 5.43: Classification of centrifugal stability

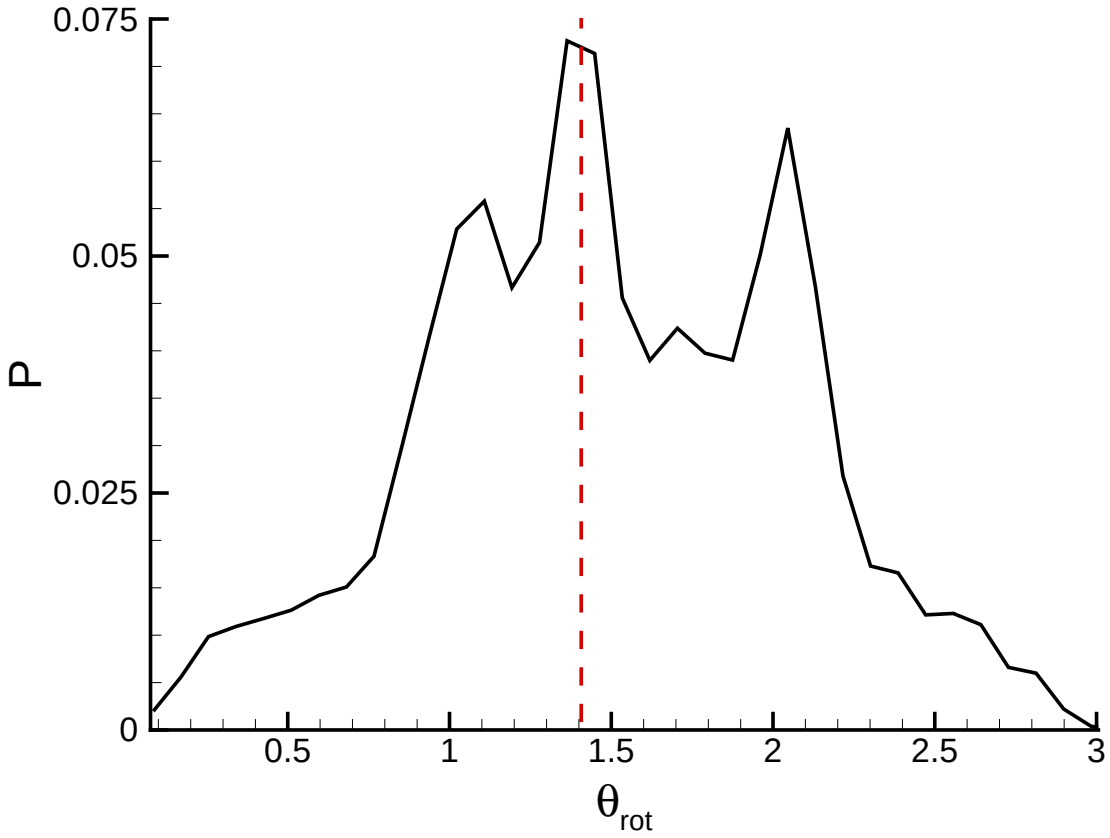

Figure 5.44: PDF of θ_{rot}

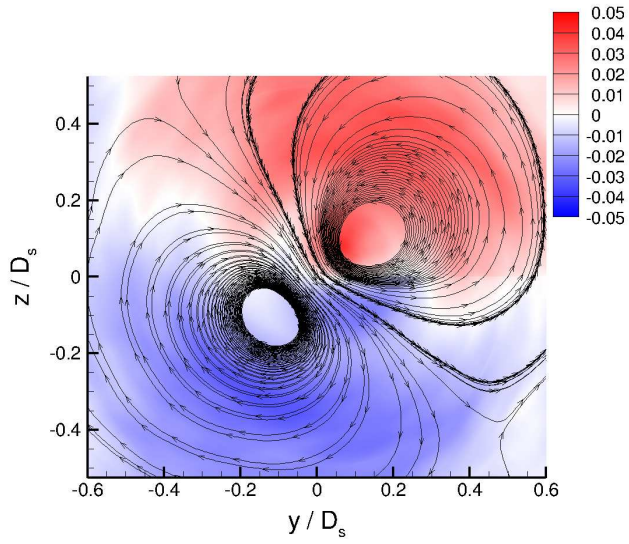

(a) $\langle u_x' \rangle_{\mathrm{rot}} / U_{x,s}$

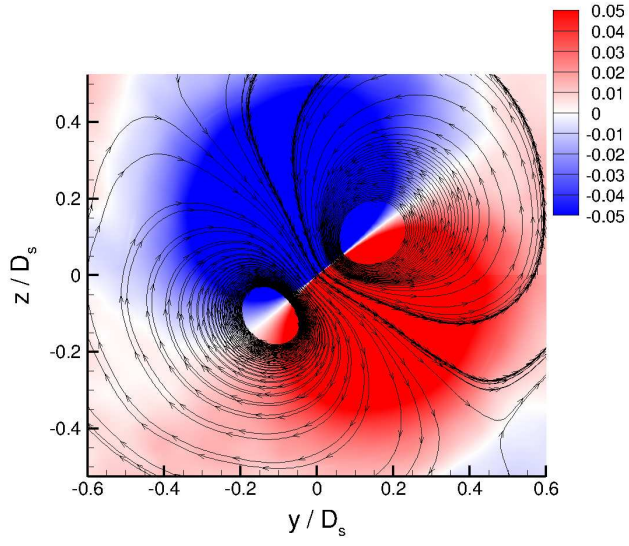

(b) $\langle u_r' \rangle_{\mathrm{rot}} / U_{x,s}$

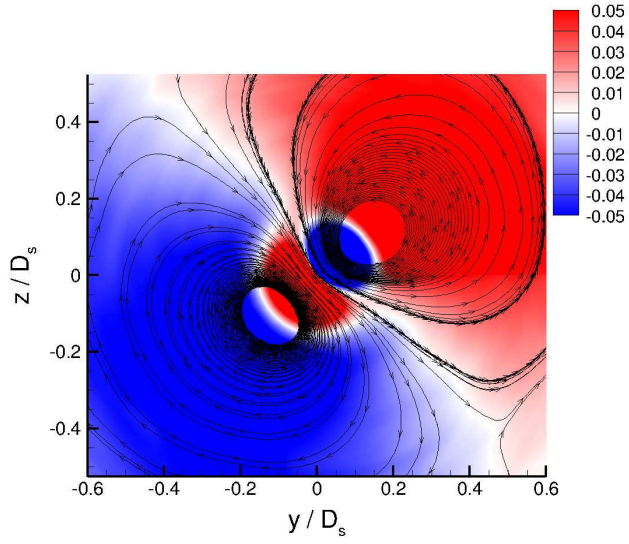

(c) $\langle u_\theta' \rangle_{\mathrm{rot}} / U_{x,s}$

Figure 5.45: Rotationally averaged Reynolds-decomposed streamtraces superimposed on contours of rotationally averaged velocities at $x/D_s = 2.39$

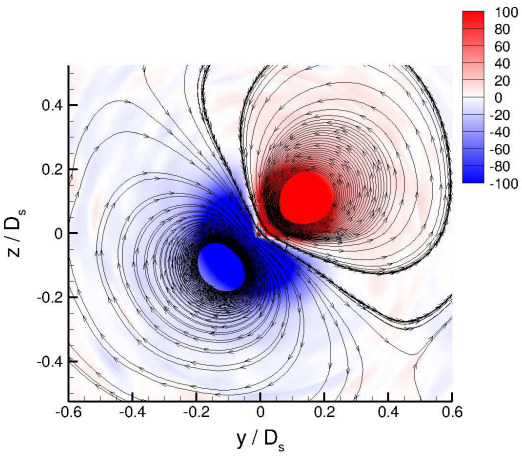

(a) $\langle \omega_x \rangle_{\text{rot}}$

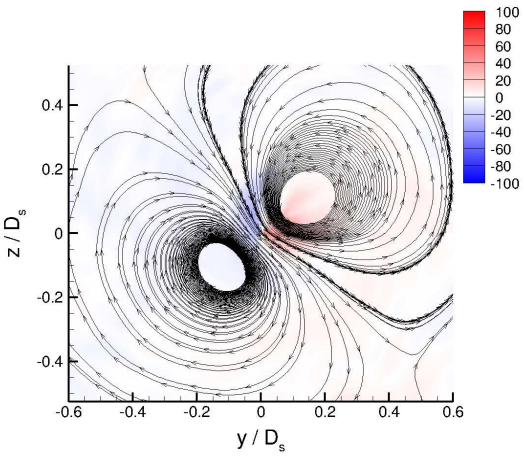

(b) $\langle \omega_r \rangle_{\text{rot}}$

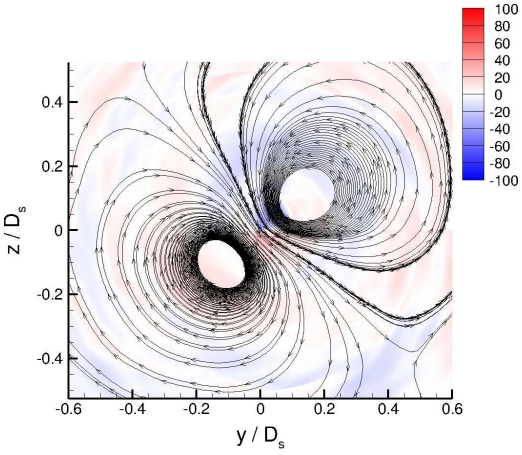

(c) $\langle \omega_\theta \rangle_{\text{rot}}$

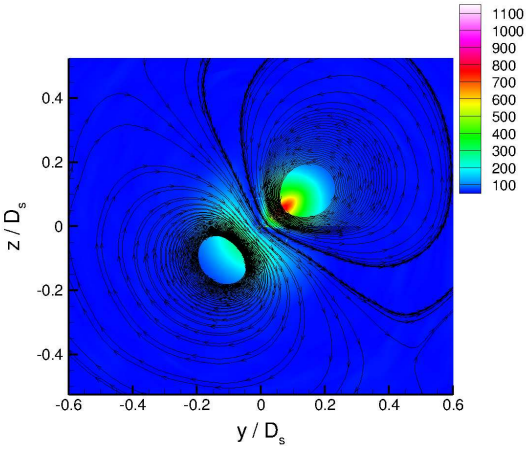

(d) $\langle |\omega| \rangle_{\text{rot}}$

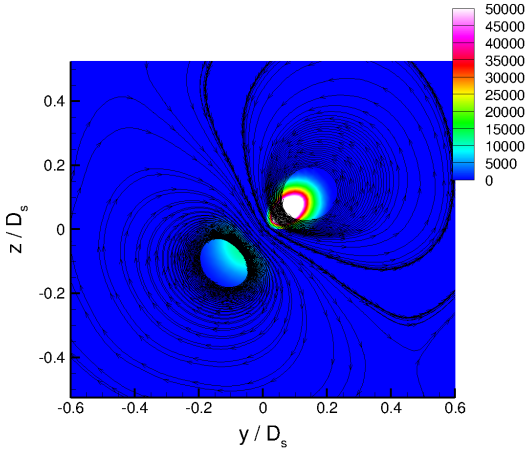

(e) $\langle Q \rangle_{\text{rot}}$

Figure 5.46: Rotationally averaged Reynolds-decomposed streamtraces superimposed on contours of rotationally-averaged vorticity and Q-criterion at $x/D_s = 2.39$

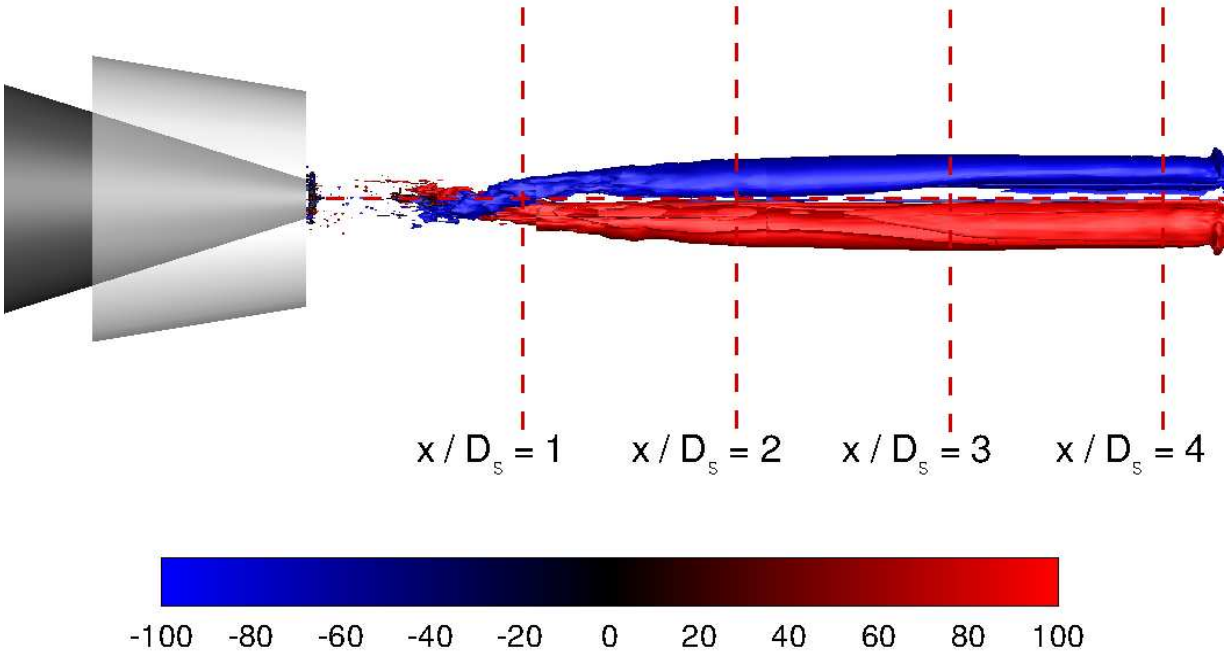

Figure 5.47: Iso-surface of rotationally-averaged Q-criterion $\langle Q \rangle_{\text{rot}} = 1.5 \times 10^3$ coloured by $\langle \omega_x \rangle_{\text{rot}}$ ($r - \theta$ plane at $x/D_s = 2.39$ used as reference for rotational averaging)

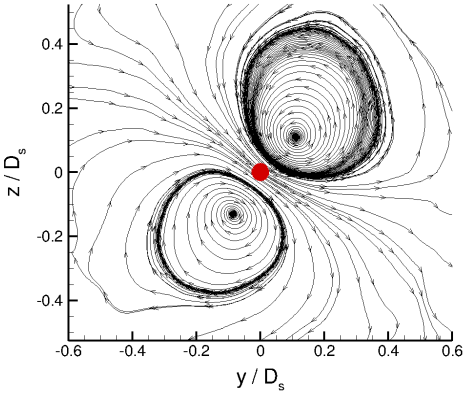

(a) $x/D_s = 1.5$

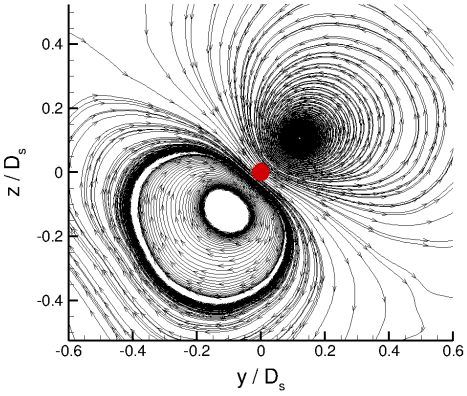

(b) $x/D_s = 2$

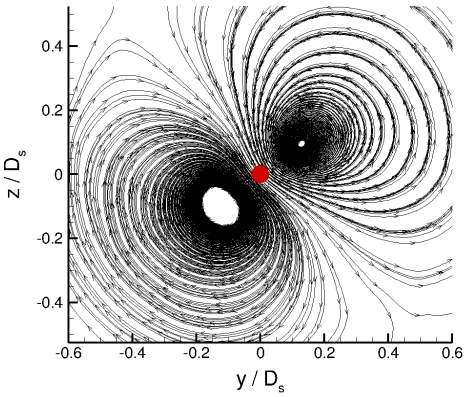

(c) $x/D_s = 2.5$

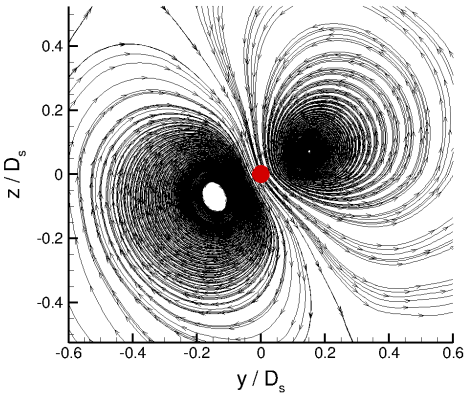

(d) $x/D_s = 3$

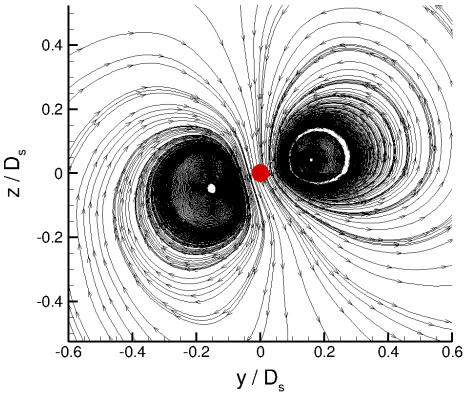

(e) $x/D_s = 3.5$

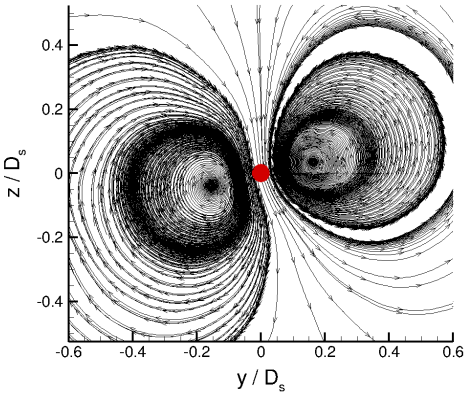

(f) $x/D_s = 4$

Figure 5.48: Rotationally averaged Reynolds-decomposed streamtraces at various axial locations

Chapter 6

Unsteady Reynolds-Averaged Navier-Stokes Results

This chapter presents Unsteady Reynolds-Averaged Navier-Stokes (URANS) calculations of the modular swirler with $\alpha_1 = 30°$. The previous chapter has shown that LES is capable of capturing the unsteady dynamics and instability modes characteristic of this injector in excellent agreement with experiment. To facilitate comparison between LES and URANS-based methods it is convenient, at least initially, to use an identical computational mesh (a mesh density sufficient for LES should be more than sufficient for a URANS prediction). This is considered in Section 6.1 along with the influence of numerical settings (under-relaxation and timestep, Δt), computational mesh (polar and O-grid), CFD solver (Delta and Fluent) and turbulence model ($k - \epsilon$ and RST) on CS development. The most appropriate parameter set derived from these preliminary runs is then selected to compare first and second-order statistics with experiment in Section 6.2. In a similar way to LES, the application of URANS to swirl injectors is only valid if the frequency components associated with *both* near and far-field instability modes are predicted with a high degree of fidelity. A comparison of the frequencies predicted by URANS with expected frequencies derived from experiment [13, 38] is made in Section 6.3.

6.1 Coherent Structure Development

In Dunham et al. [50], the performance of URANS using an eddy viscosity closure was assessed for confined swirl flows similar to those considered here under varying test conditions as discussed in Section 1.3.1. These calculations were performed using the commercial CFD code Fluent (Version 6.2.16) with a standard $k - \epsilon$ turbulence model. It was found that URANS was initially able to capture an experimentally observed vortex structure emerging from within the swirler similar to that shown in Figure 4.18(a); however, as the transient solution progressed the fully self-sustaining solution did not reflect the measured unsteady dynamics. Moreover, spectral analysis of near-field velocity traces suggested that this form of URANS was not able to capture the expected PVC as characterised by an accumulation of fluctuating energy at low frequencies (see

Figure 5.27). One point of concern raised in Section 3.2.3 was that the closed-source nature of commercial solvers makes it difficult to assess whether particular characteristics of a calculation, such as the vortex transition or PVC suppression reported in [50], are to be attributed to the particular characteristics of the selected numerical scheme or even to the manner in which this is implemented in the commercial code. For example, given the vast range of potential end-user applications, a degree of numerical damping or smoothing may be included to improve calculation stability. To circumvent these uncertainties, both in-house (Delta) and commercial (Fluent) CFD codes have been utilised in this thesis as described previously in Sections 3.2.2 and 3.2.3.

Both Delta and Fluent can be selected to utilise the same backward Euler implicit method for temporal discretisation, which offers improved stability over explicit schemes. Since implicit schemes are not restricted by the CFL < 1 limit and it is not expected that URANS predictions need to resolve the high frequency motions present in LES, it was decided to relax the timestep from $\Delta t = 2.0 \times 10^{-6}$ as used for the LES calculations presented in Chapter 5 to $\Delta t = 1.0 \times 10^{-5}$. Based on Equation 3.58, it was found that this gave a maximum CFL number of $\approx$ unity in the vicinity of the centreline and ≈ 0.2 at the swirler exit. Following preliminary investigations with $k - \epsilon$ and RST models (referred to below as URANS cases 1, 6 and 7 in Table 6.3), and based on the reference timescales $T_s = 0.02$s and $T_r = 0.67$s used in Section 5.1.4, it was found that Fluent required an increase in CPU time of $\approx 130\%$ relative to Delta for the same grid and time-step and an eddy viscosity closure (Table 6.1). An increase of $\approx 260\%$ in CPU time was required for an RST closure within Fluent.

Solver	Turbulence Model	CPU Hrs. / T_s	CPU Hrs. / T_r	% Increase CPU Hrs. (approx)
Delta	$k - \epsilon$	1.7	55.8	-
Fluent	$k - \epsilon$	3.9	130.3	130
Fluent	RST	6.1	204.7	260

Table 6.1: Typical computational requirements for URANS simulations based on identical numerical schemes and computational parameters. Calculations performed using 6 64-bit Itanium processors with $\Delta t = 1.0 \times 10^{-5}$ ($T_s/\Delta t = 2 \times 10^3$, $T_r/\Delta t = 67 \times 10^3$).

Based on the requirements detailed in Table 6.1, it was decided to utilise Delta for initial investigations of the influence of computational parameters and numerical grids on CS development, thus minimising the computational effort. Configuration of Fluent with the most appropriate parameter set determined from these preliminary runs then allowed results based on the $k - \epsilon$ model to be compared directly with those from Delta. In this way, uncertainties regarding numerical implementation within Fluent are partially alleviated through verification via an independent code allowing calculations based on the RST model to proceed with increased confidence.

Calculations performed with Fluent generally utilised desktop PCs consisting of a maximum of 6 cores rather than the higher capacity PC cluster used for LULES which used 16 as detailed

in Table 5.2. Assuming a 100% parallelisation efficiency, comparison between Tables 6.1 and 5.2 reveals the typical computational effort required by URANS and LES approaches. For the $k-\epsilon$ model using Delta, the number of CPU hours required to capture a particular flow timescale (T_s, T_r etc) is reduced by around an order of magnitude relative to LES, whilst for the RST model using Fluent the cost is reduced by approximately one-third. As pointed out by Wegner et al.[45], the long integration period required by LES to obtain a statistically-converged ensemble averaged solution (see Section 5.3) is largely avoided in URANS since the solution is of a deterministic nature and just a few periods of the unsteadiness have to be computed. In the present case however it did not prove possible to realise this benefit as characteristic timescales and frequencies associated with important features such as the PVC are large in comparison to the timestep required for temporal accuracy (i.e. such that the local CFL number does not exceed unity) and the acquisition of sample sets of considerable duration is unavoidable.

In Section 5.2 it was found that in order to match experimentally observed values of $\dot{G}_\theta$ and $\dot{m}$ (Table 4.1) at the swirler exit mean radial and swirl velocity in the predictions should be $\langle u_r \rangle_{\text{in}} = 0.78\text{m/s}$ and $\langle u_\theta \rangle_{\text{in}} = 1.484\text{m/s}$. These values were also used in the URANS simulations reported here together with turbulent inlet conditions of $k_{\text{in}} = 10.6 \times 10^{-3} m^2/s^2$ and $\epsilon_{\text{in}} = 168.4 \times 10^{-3} m^2/s^3$ for both $k-\epsilon$ and RST models, these were computed from Equations 3.78 and 3.79 respectively with an assumed 5% turbulence intensity and turbulent lengthscale of 7% of the inlet slot width ($x_{\text{in}} = 0.0153\text{m}$). Integration of the mean velocity profiles of axial and tangential velocity at $x/D_s = 0.02$, (Figures 6.15(a) and 6.18(a)), resulted in the following properties:

	$\dot{m}$	$\dot{G}_x$	$\dot{G}_\theta$	S_{N}	$U_{x,s}$
PIV	2.15	5.26	7.82×10^{-2}	0.80	2.0
$k-\epsilon$	2.08	5.23	7.56×10^{-2}	0.77	1.94
RST	2.26	5.27	8.1×10^{-2}	0.82	2.1

Table 6.2: Swirler exit flow rates $x/D_s = 0.02$

6.1.1 $k-\epsilon$ Turbulence Model URANS Predictions

As discussed in Section 3.2.2, the pressure-correction approach adopted by Delta uses a linkage coefficient, α, between pressure and velocity to reduce the computed change in pressure. Previous work [118] has found that relaxation parameters between 3 and 10 give good convergence behaviour. Based on these recommendation, $\alpha = 10$ was selected for preliminary investigations along with $\Delta t = 1.0 \times 10^{-5}$ and will be referred to as URANS case 1 as detailed in Table 6.3. Following the approach adopted in Section 5.2 for LES predictions, the ability of URANS to capture the experimentally observed unsteady dynamics was assessed by monitoring the progress of the solution at various time-instants. Unlike in LES calculations, which required a considerable

number of timesteps for initial transients to propagate through the computational domain and for the flow to reached a self-sustained state, it was found that in the URANS predictions, the large-scale features such as the CTRZ and CRZ were established soon after solution initialisation. Figure 6.1 for example shows instantaneous circumferentially-averaged streamtraces within the swirl duct, expansion chamber and exhaust duct at various time-instants. At $t/T_s = 50$, which corresponds to roughly 1.5 residence times, T_r, Figure 6.1(a) clearly shows the CTRZ and CRZ, with the reattachment point of the outer shear-layer located at $x_{\mathrm{L}}/D_s \approx 1.7$. Further time-steps resulted in the reattachment location moving upstream as shown in Figures 6.1(b)-(d). Note that this is not the large-scale oscillation of the instantaneous reattachment location predicted by LES (see Figures 5.14 and 5.15) but rather a flow feature of the initial transient. The final location of $x_{\mathrm{L}}/D_s \approx 1.2$ shown in Figure 6.1(d), is upstream of the time-mean location of $x_{\mathrm{L}}/D_s = 1.45$ determined from PIV. These observations are consistent with the findings of Dunham et al. [50] in which reattachment locations from URANS were insensitive to variations in test conditions. In the context of plane flows over a backward facing step, the standard $k-\epsilon$ model underpredicts the reattachment length by up to 20%, however, for flow in an axisymmetric sudden expansion it is predicted to within experimental uncertainty [130]. In the present case which features an axisymmetric expansion, it is likely that the observed underprediction is related to an incorrect response of the $k-\epsilon$ model to strong streamline curvature as already discussed in Section 3.1.1.1. Similarly, Figure 6.2 shows Reynolds-decomposed streamtraces in an $r-\theta$ plane extracted at $x/D_s = 0.02$ at various time-instants. Soon after initialisation (e.g. at $t/T_s = 15$), Figure 6.2(c) shows a vortex pattern appears similar to that shown in Figure 4.18(b), characterised by two clockwise and two counter-clockwise vorticies separated by $\approx \pi$ radians. Since URANS resolves only the coherent, or phase-averaged, component of the turbulent spectrum, Figure 6.2(c) appears much smoother than Figure 4.18(b) and more closely resembles the rotationally-averaged structures presented in Figure 5.39. However, although these structures persisted for an extended duration, they underwent a transitory phase between $t/T_s = 100$ and $t/T_s = 150$ from 4 to 2 vortices, as shown in Figures 6.2(g) and 6.2(h). The vortex pattern at $t/T_s = 150$ was found to characterise the final self-sustaining solution as subsequent time-steps yielded no further changes in the observed features (Figures 6.2(h) to 6.2(l)). The predicted vortical structure consists of one clockwise and one counter-clockwise vortex separated by less than π radians. Unlike the more familiar 4 vortex pattern in which each vortex is defined by an approximately circular streamtrace distribution, vortices from $t/T_s = 150$ onwards are of a more distorted kidney shape. Clearly, the characteristics of the URANS $k-\epsilon$ predicted self-sustaining vortex pattern is not consistent with either PIV or LES. It is, however, remarkably similar to that reported in Dunham et al. [50].

Figure 6.3 shows instantaneous streamtraces in an $r-\theta$ plane at $x/D_s = 2.39$ at various time-instants. Contrary to experiment and LES predictions, the aerodynamic centre is at all times coincident with the geometric centre of the expansion chamber (indicated by the red dot). Large

excursions of the aerodynamic centre from the geometric centre are indicative of a PVC and, therefore, Figure 6.3 suggests that URANS ($k-\epsilon$) has not captured this phenomenon. Again, this is consistent with Dunham et al. [50] in which no PVC was observed for their URANS ($k-\epsilon$) predictions.

Further evidence to support the observations of Figures 6.1 to 6.3 is provided in Figure 6.4; this shows time-histories of axial, radial and tangential velocity components for various points within the computational domain. These points correspond to: flow separation from the inner wall of the swirl duct ($x/D_s = -0.26$, $r/D_s = 0.17$), the rotation of CS at the swirler exit ($x/D_s = 0.02, r/D_s = 0.27$), a location expected to capture evidence of a PVC ($x/D_s = 2.42, r/D_s = 0.0$) and the fluctuating reattachment location of the outer swirler shear-layer ($x/D_s = 1.4, r/D_s = 1.86$). All point were extracted at an angular location of $\theta = \pi$. Inside the swirl duct ($x/D_s = -0.26$, $r/D_s = 0.17$) and in the near-field of the swirler exit ($x/D_s = 0.02$, $r/D_s = 0.27$), all three velocity components oscillate regularly from $t/T_s \approx 150$ onwards. Prior to this, a transitory phase is observed which corresponds to the development of the CS emerging from the swirler as noted in Figure 6.2. In the far-field ($x/D_s = 1.4$ and 2.42), an initial variation in the axial velocity component is observed until $t/T_s \approx 150$ after which no further unsteadiness is observed. This cannot be classified as demonstrating oscillatory behaviour, but merely representing the solution transition from start-up to a self-sustaining state (consistent with Figures 6.1 and 6.3). From Figure 6.4, it can concluded that the flow has reached a fully self-sustaining state by $t/T_s = 150$, which corresponds to approximately 4.5 flow through times, T_r, as discussed in Section 5.1.4. To ensure that initial transients do not contaminate subsequent analysis the early portion of the solution is disregarded and only that from $t/T_s = 150$ onwards utilised.

Following Wegner et al. [45] and Chang and Tavoularis [131], and consistent with assumptions inherent in the URANS framework, total turbulent kinetic energy, k_{tot}, is the sum of modelled, k_{mod}, and resolved, k_{res}, turbulent kinetic energy. The former constitutes the incoherent contribution from the k transport equation whilst the latter constitutes the unsteady resolved CS contribution and is obtained from $k_{\text{res}} = \frac{1}{2}\langle u_i' u_i' \rangle$. Both contributions have to be time-averaged over a period that is sufficiently long to capture a significant number of CS cycles as will be discussed further in Section 6.2.1. By considering modelled and resolved contributions to the total turbulent kinetic energy it is possible to make a quantitative global assessment of the unsteady dynamics captured by URANS which complements the localised point-based analysis presented so far. Figures 6.5(a)-(c) show contours of time-averaged k_{mod}, k_{res} and their ratio, $k_{\text{mod}}/k_{\text{res}}$. These show that k_{mod} dominates k_{res} throughout the near-field of the injector. In the vicinity of the inner wall of the swirl duct, there is a localised region at $x/D_s \approx -0.25$ in which k_{res} is significantly greater ($\approx \times 4$) than k_{mod} which corresponds to a flow separation observed in Figure 6.1. The fact that there is no contribution from k_{mod} in the vicinity of the far-field centreline

is consistent with the conclusion that no PVC is present. The ratio of turbulent to molecular viscosity, ν_t/ν, is shown in Figure 6.5(d) where $\nu_t = C_\mu k^2/\epsilon$ as defined in Equation 3.14. Maximum ratios of $\nu_t/\nu \approx 1750$ are observed within the expansion chamber along the inner shear layer of the swirl stream and close to the geometric centreline. Jochmann et al. [48] quote typical ratios of $\mu_t/\mu \approx 500$ and $\mu_t/\mu \approx 150$ for confined swirl flows at a lower swirl number to that considered here ($S_N = 0.52$) based on standard $k-\epsilon$ and RST (SSG) models respectively. However, they give no indication of where these ratios were observed within the flow. Comparison between Figures 6.5(d) and 5.4(a) reveals that typical levels of URANS $k-\epsilon$ turbulent viscosity are approximately two orders of magnitude greater than the LES sub-grid viscosity, ν_{sgs}. Unlike URANS $k-\epsilon$, maxima of ν_{sgs}/ν derived from LES are not observed at the centreline which suggests a possible explanation for PVC suppression in the case of URANS $(k-\epsilon)$.

6.1.1.1 Influence of Computational Parameters, Numerical Grid and CFD Solver

Following the preliminary investigation described above, it is apparent that URANS $(k-\epsilon)$ is not suitable for capturing even the qualitatively correct details of the unsteady dynamics observed experimentally. However, in order to make a completely definite statement a number of additional numerical tests were undertaken. Firstly, the linkage coefficient between pressure and velocity, α, used by Delta introduces a degree of numerical damping or smoothing which could affect the development and evolution of CS. To investigate whether the value of $\alpha = 10$ used in URANS case 1 exerted a significant influence, two additional simulations were conducted with reduced values of $\alpha = 6$ and 3. These are referred to as URANS cases 2 and 3 (Table 6.3). Further, although the timestep of $\Delta t = 1.0 \times 10^{-5}$ used in URANS case 1 gave only a maximum CFL number of $\approx$ unity, a further simulation was performed with a timestep of $\Delta t = 1.0 \times 10^{-6}$ to ensure that temporal accuracy was sufficient. For this simulation (URANS case 4) the initial linkage coefficient $\alpha = 10$ was used. Unlike LULES, which uses an explicit treatment of flow variables at the centreline, the boundary condition available in Delta was a symmetry condition (defined in Equations 3.73 and 3.74) which ensures no flow or scalar flux across the boundary. To investigate whether this boundary condition might potentially suppress the development of a PVC, an O-grid mesh was used (shown in Figure 6.6). To ensure that only minimal changes were made, the majority of the original polar-type mesh was maintained and modifications restricted to the central region from $r/D_s = 0 - 0.09$. This simulation is referred to as URANS case 5. Finally, in order to answer unresolved issues regarding numerical implementation raised in Section 6.1, a further simulation was performed using Fluent with an identical parameter set as URANS case 1 and this is referred to as URANS case 6.

Figure 6.7 shows Reynolds-decomposed streamtraces at $x/D_s = 0.02$ for URANS cases 2 - 6 at $t/T_s = 150$ (previously determined as a sufficient duration for the solution to reached a fully self-sustaining state). Figure 6.8 shows instantaneous streamtraces at $x/D_s = 2.39$ for URANS

cases 2 - 6 also at $t/T_s = 150$. Clearly, based on evidence presented in these figures, it can be concluded that the computational parameters, numerical grid and CFD solver used in URANS case 1 do not exert any significant influence on near-field or far-field CS development. This failure must therefore be attributed to deficiencies associated with the $k-\epsilon$ model. The fact that $k-\epsilon$ simulations performed with Delta and Fluent with an identical parameter set exhibit good agreement is further confirmation.

6.1.2 Reynolds-Stress Transport Model URANS Predictions

In the previous section, the computational parameters and numerical grid used in URANS case 1 were not found to exert any significant influence on near-field or far-field CS. Furthermore, Delta (URANS case 1) and Fluent (URANS case 6) confirmed that the numerical implementation of the latter played a negligible role. Hence, a further simulation was undertaken with Fluent based on the RST model, using identical computational parameters as URANS case 1. For the remainder of this chapter this simulation will be referred to as URANS case 7 (Table 6.3).

In Figures 5.14 and 6.1 circumferential averaging was applied to LES and URANS ($k-\epsilon$) calculations to provide a clearer picture of flow features in the $x-r$ plane. As already noted, Fluent (version 6.3.26) is a fully unstructured solver and all data outputs are also unstructured. In order to perform a similar circumferential averaging it would be necessary to interpolate the data on to a structured mesh, but this was not attempted due to excessive memory requirements. As an alternative, Figure 6.9 shows instantaneous streamtraces in the $x-r$ plane at $\theta = \pi$ at identical time-instants to Figure 6.1. The transient behaviour of the instantaneous shear layer outer wall reattachment location is quantified via Figure 6.10 which shows x_{L}/D_s as a function of non-dimensional time, t/T_s. Initial development of the CRZ is observed to take place from $t/T_s = 0-50$ in which the reattachment location moves rapidly upstream from $x_{\mathrm{L}}/D_s = 3.3$ to $x_{\mathrm{L}}/D_s = 1.5$. From $t/T_s = 50-100$, the reattachment location continues to move gradually upstream and then oscillates around a mean location of $x_{\mathrm{L}}/D_s \approx 1.25$. Clearly, the fluctuation of the reattachment location predicted by the RST is modest in comparison to that predicted by LES (Figure 5.15), however, it offers some improvement on the $k-\epsilon$ turbulence model which exhibited no oscillatory behaviour.

Figure 6.11 shows Reynolds-decomposed streamtraces in the $r-\theta$ plane at $x/D_s = 0.02$ at identical time-instants to those in Figure 6.2 for the URANS ($k-\epsilon$). The experimentally observed vortex structure, consisting of two clockwise and two counter-clockwise vorticies separated by $\approx \pi$ radians, is firmly established at $t/T_s = 100$. An important aspect of Figure 6.11 it that the vortex pattern does not undergo transition between $t/T_s = 100-150$. This would suggest that the vortex transition observed in Figures 6.2(g)-(h) is not inherent to the URANS approach in general but is rather a specific to the $k-\epsilon$ model. Although the vortex structure observed at

$t/T_s = 100$ is characteristic of the self-sustaining pattern, there is a small degree of variability in the details of each instantaneous realisation. This is in contrast to the $k-\epsilon$ model results in which the vortex pattern reached at $x/D_s = 150$ maintained a fixed spatial structure and rotated with a constant angular velocity, thus giving a completely deterministic solution with respect to time (see Figure 6.4).

Figure 6.12 shows instantaneous streamtraces in the $r-\theta$ plane at $x/D_s = 2.39$ at various time-instants. Contrary to URANS ($k-\epsilon$) predictions, the aerodynamic centre of the flowfield is displaced radially from the geometric centre and varies as a function of time. This demonstrates, albeit qualitatively, the ability of URANS (RST) to capture the PVC phenomenon observed experimentally. In order to facilitate discussions presented later in Section 6.3.2, the vortex detection algorithm of Grosjean et al. [36] (Equation A-24) was used to determine the centre of the PVC and is indicated by the blue dot. Clearly, the computed location is in excellent agreement with the qualitative location deduced from instantaneous streamtraces.

Figure 6.13 shows time-histories of axial, radial and tangential velocity components recorded at identical points to those shown for the $k-\epsilon$ model in Figure 6.4. Inside the swirl duct ($x/D_s = -0.26$, $r/D_s = 0.17$) and in the near-field of the swirler exit ($x/D_s = 0.02$, $r/D_s = 0.27$), the most notable difference between the time-dependent behaviour from $k-\epsilon$ and RST models is that the former displays a repetitive deterministic nature whilst the latter is more characteristic of stochastic turbulence. It is interesting to note that the magnitude of the velocity fluctuations is quite different, with the fluctuating amplitude much larger in the case of the RST model. In the far-field ($x/D_s = 1.4$ and 2.42), $k-\epsilon$ and RST models are again in stark contrast, with the latter demonstrating a time-dependence consistent with experimental observations.

In a similar way to that presented in Figure 6.5, a quantitative global assessment of the unsteady dynamics captured by the RST model was made by examination of the modelled, k_{mod} (obtained from time-averaged modelled Reynolds-stresses transport equations), and resolved, k_{res}, contribution to total turbulent kinetic energy (Figure 6.14). In stark contrast to the $k-\epsilon$ predictions, Figures 6.14(a)-(c) show that k_{res} obtained from the RST model dominates k_{mod} in the injector near-field and inside the swirl duct. The observed difference in k_{res} in these regions can be attributed to the increased magnitude of velocity fluctuation shown in Figures 6.4 and 6.13. Figure 6.14(b) indicates a further zone of resolved fluctuating energy in the vicinity of the far-field centreline which is large in comparison to the modelled contribution. This is further evidence to support Figures 6.12 and 6.13 which suggested that URANS (RST) could capture the PVC phenomena observed experimentally. Although the RST model abandons the eddy viscosity hypothesis, Figure 6.14(d) shows the ratio ν_t/ν (where $\nu_t = C_\mu k^2/\epsilon$ from Equation 3.14) for comparison with Figure 6.5(d). It is interesting to note that although the maximum ratio of

$\nu_t/\nu \approx 1750$ is similar in both cases, levels from the $k-\epsilon$ model are far greater in the vicinity of the swirl stream and far-field centreline in comparison to the RST model. It is likely that the increased levels of ν_t are responsible for the observed damping of CS.

6.1.3 Summary of URANS Test Cases

Table 6.3 summaries the various turbulence models, computational grids and numerical settings used to investigate CS structure development presented in Section 6.1.

Case Name	Solver	Turbulence Model	Grid System	Timestep	Linkage Coefficient
Case 1	Delta	$k-\epsilon$	Structured Polar	1.0×10^{-5}	10
Case 2	Delta	$k-\epsilon$	Structured Polar	1.0×10^{-5}	6
Case 3	Delta	$k-\epsilon$	Structured Polar	1.0×10^{-5}	3
Case 4	Delta	$k-\epsilon$	Structured Polar	1.0×10^{-6}	10
Case 5	Delta	$k-\epsilon$	Structured O-grid	1.0×10^{-5}	10
Case 6	Fluent	$k-\epsilon$	Unstructured Polar*	1.0×10^{-5}	10
Case 7	Fluent	RST	Unstructured Polar*	1.0×10^{-5}	10

Table 6.3: Summary of URANS test cases. *Here unstructured refers to the fact that Fluent treats all numerical grids in an unstructured manner and no explicit boundary conditions were set at the centreline.

6.2 URANS Ensemble Averaged Data

As discussed in Section 6.1, time-histories of axial, radial and tangential velocity presented in Figure 6.4 indicate that simulations performed with the $k-\epsilon$ model reached a self-sustaining, repeating state after $t/T_s = 150$ (≈ 4.5 residence times). Similarly, large-scale features, such as the CRZ development shown in Figure 6.10, computed with URANS (RST) were firmly established by this time. To ensure that initial transients did not contaminate the quantitative analysis presented here, only the portion of the simulations from $t/T_s = 150$ onwards was utilised. In order to facilitate comparison between $k-\epsilon$ and RST models, subsequent analysis is based on URANS cases 6 and 7 (Table 6.3).

The LES ensemble averaged dataset used in Chapter 5 was summarised in Table 5.4 and consisted of a total of 16384 samples (2^{14}) acquired at a frequency of 2kHz ($\Delta T = 0.5$ms). From Section 5.4 this was sufficient to perform a spectral analysis of both near-field and far-field CS which exhibit a broad range of characteristic frequencies. Furthermore, an acceptable number of statistically independent samples were provided, including in regions in which integral timescales were approximately two orders of magnitude larger than the sampling interval (Table 5.5). In order to provide a comparable analysis, an ensemble averaged dataset based on URANS (RST) was acquired with identical properties to those in Table 5.4. It is clear that the $k-\epsilon$ model is not suitable for predicting the expected far-field PVC phenomena. As a result, it was decided only to focus spectral analysis on the higher frequency near-field CS to avoid the necessity of generating excessively large datasets.

6.2.1 Single-Point Statistics

A detailed discussion of radial profile characteristics for mean and r.m.s velocities and shear-stresses obtained from PIV within the dump expansion chamber was presented in Section 4.1. In order to facilitate comparison with URANS, statistics from the conditioned LES dataset ($t/T_s = 125$) presented in Chapter 5 have also been included here. At $x/D_s = 0.02$, both $k-\epsilon$ and RST models exhibit good agreement with experiment in terms of axial velocity across the majority of the swirler exit (Figure 6.15(a)). There are some discrepancies between $0 \leq r/D_s \leq 0.09$ which are probably due to the presence of the inner body of the swirl duct. The radial velocity distribution at this location shown in 6.17(a) predicted by the $k-\epsilon$ model is consistent with measured trends, however, in a similar way to LES, the minimum at $r/D_s \approx 1.7$ and secondary peak at $r/D_s \approx 0.35$ are both overpredicted. This is in contrast to the RST model which is in accordance with PIV across the whole radial extent of the swirler exit. In Section 5.3.2 it was suggested that the radial velocity component at the swirler exit is sensitive to the time-mean location of flow separation from the inner wall of the swirl duct. From the conditioned LES sample, separation occurs at $x/D_s = -0.1$, whilst for $k-\epsilon$ and RST models it is located further upstream at $x/D_s = -0.17$ and $x/D_s = -0.2$ respectively. Thus, the further downstream separation occurs relative to experiment $-0.43 \geq x/D_s \geq -0.27$ [13], the steeper the angle of the exit flow.

Downstream of the swirler exit within the expansion chamber ($x/D_s = 0.27$, $x/D_s = 0.53$ and $x/D_s = 1.06$) the general trend of the $k-\epsilon$ model is an underprediction in the peak magnitude of axial velocity and an overprediction in the peak magnitude of radial velocity relative to experiment (Figures 6.15(b)-(d) and 6.17(b)-(d) respectively). The peak location in both axial and radial velocity components is located further outboard in comparison to PIV, with this discrepancy becoming more pronounced with increasing downstream distance. Similar trends are also observed for the RST model; however, the overall agreement with experiment in terms of the magnitude and location of peak values is improved. The most significant improvement offered by the RST model over the $k-\epsilon$ model is in terms of centreline axial velocities which are consistently underpredicted by the latter. Figure 6.16 shows predicted axial velocity along the centreline of the expansion chamber in comparison to PIV and LES. Close to the swirler exit ($x/D_s \leq 0.4$), the general shape of the CTRZ predicted by the RST model is in good agreement with experiment, however, the peak minima is somewhat underpredicted and the region of rapid axial velocity recovery from $0.4 \leq x/D_s \leq 1.3$ is not captured. Despite these differences, RST is more in accordance with measured trends than $k-\epsilon$ in which the peak minimum of the CTRZ is too far downstream and the recovery of axial velocity is far too slow. As a result, the CTRZ predicted by the $k-\epsilon$ model is much 'stronger' in comparison to experiment. The discrepancies in downstream axial and radial velocity profiles can be attributed to the differences in the mean

reattachment location of the outer shear layer on the outer wall of the expansion chamber; this was shown in Section 5.3.2 to exert a significant influence on the agreement between experiment and LES. The mean reattachment locations of $x_{\mathrm{L}}/D_s = 1.2$ and $x_{\mathrm{L}}/D_s = 1.25$ for $k-\epsilon$ and RST models are upstream of that measured by PIV ($x_{\mathrm{L}}/D_s = 1.45$). The underprediction in the peak magnitude of axial velocity and overprediction in the peak magnitude of radial velocity is consistent with the findings of Section 5.3.2. The mean reattachment location from LES was *downstream* ($x_{\mathrm{L}}/D_s = 1.72$) of the measured location and resulted in an *overprediction* in the peak magnitude of axial velocity and *underprediction* in the peak magnitude of radial velocity. Furthermore, peak values were located *inboard* of experiment. Unlike LES, the instantaneous reattachment location of URANS-based predictions exhibit either no ($k-\epsilon$ model) or weak (RST model) time-dependence and it is therefore not possible to condition statistics in a similar way to that used in Section 5.3.2.

Although differences in time-mean reattachment locations undoubtedly exert some influence on tangential velocity distributions, these are overshadowed by the global effects of the turbulence model. At $x/D_s = 0.02$ and 0.27, Figures 6.18(a)-(b) indicate that in the upstream region tangential velocities predicted by the $k-\epsilon$ model are at least in qualitative agreement with experimental observations, however, at $x/D_s = 0.53$ and 1.06, the solution tends towards a qualitatively incorrect solid-body rotation. In contrast, the overall agreement between experiment and the RST model is favourable. At $x/D_s = 0.02$, 0.27 and 0.53, the correct Rankine-like distribution is captured by the RST model across the majority of forced and free vortex regions. At the latter two locations the peak magnitude is closer to PIV than LES which has a tendency to overpredict this value as already discussed. It should be noted, however, that at these locations the RST model deviates from experiment close to the centreline where the tangential velocity component should increase linearly with radius. The reason for this is unclear, however, it is possibly related to the large-scale unsteadiness of the PVC. In a similar way to LES, largest discrepancies between experiment and the RST model occur at $x/D_s = 1.06$. At this location the magnitude of the peak value is overpredicted relative to PIV and located further inboard.

Examination of modelled and resolved Reynolds stress components as defined above was carried out. Since the modelled stresses are with respect to a Cartesian coordinate basis, the following transformation matrix given by Bower [132] was used to obtain the polar-cylindrical components used throughout this thesis:

$$\begin{bmatrix} \langle u'_r u'_r \rangle & \langle u'_r u'_\theta \rangle & \langle u'_r u'_x \rangle \\ \langle u'_\theta u'_r \rangle & \langle u'_\theta u'_\theta \rangle & \langle u'_\theta u'_x \rangle \\ \langle u'_x u'_r \rangle & \langle u'_x u'_\theta \rangle & \langle u'_x u'_x \rangle \end{bmatrix} = \begin{bmatrix} \cos\theta & \sin\theta & 0 \\ -\sin\theta & \cos\theta & 0 \\ 0 & 0 & 1 \end{bmatrix} \begin{bmatrix} \langle u'_y u'_y \rangle & \langle u'_y u'_z \rangle & \langle u'_y u'_x \rangle \\ \langle u'_z u'_y \rangle & \langle u'_z u'_z \rangle & \langle u'_z u'_x \rangle \\ \langle u'_x u'_y \rangle & \langle u'_y u'_z \rangle & \langle u'_x u'_x \rangle \end{bmatrix} \begin{bmatrix} \cos\theta & -\sin\theta & 0 \\ \sin\theta & \cos\theta & 0 \\ 0 & 0 & 1 \end{bmatrix} \tag{6.1}$$

All second order RST statistics presented in the following are the sum of modelled and resolved contributions and thus can be considered as 'total' quantities. Figures 6.19 to 6.21 show radial profiles of r.m.s axial, radial and tangential stresses respectively. The overall agreement in r.m.s axial velocity between experiment and the RST model is extremely favourable (Figure 6.19). The location and magnitude of peak values in the shear layer arising at the interface of the CTRZ and swirl stream are consistent with measured trends at $x/D_s = 0.02$, 0.27 and 0.53. Further downstream at $x/D_s = 1.06$, the peak magnitude is underpredicted and shifted radially outwards. It is reasonable to assume that this may be attributed to differences in the mean axial velocity component at this location (Figure 6.15(d)) which also exhibits a radial shift. In general, centreline values are well represented although a degree of overprediction is observed at $x/D_s = 0.02$ which again may be attributed to discrepancies in the mean axial velocity (Figure 6.19(a)). Profiles of r.m.s radial velocity from the RST model shown in 6.20 are in general accordance with experiments at all axial locations. In a similar way to LES, the peak magnitude is underpredicted relative to PIV by the RST model at $x/D_s = 1.06$, however, the radial variation is well represented. Profiles of r.m.s tangential velocity shown in Figure 6.21 do not compare as favourably, however, the most salient features are reasonably resolved.

Figures 6.22 to 6.24 show radial profiles of axial-radial, radial-tangential and axial-tangential shear-stresses. Regions of positive and negative correlation of $\langle u'_x u'_r \rangle$ at $x/D_s = 0.02$, 0.27 and 0.53, including the location and magnitude of peak values, are faithfully reproduced by the RST model (Figure 6.22). As already mentioned, since shear-stress distributions in the near-field are firmly linked to CS emerging from the swirl duct, this favourable agreement indicates that RST, like LES, is able to capture important CS details. Further downstream at $x/D_s = 1.06$, the region of zero shear in the forced vortex region is well represented by the RST model. In terms of radial-tangential shear-stress (Figure 6.23), overall levels of agreement between the RST model and experiment are broadly comparable to LES and, at $x/D_s = 0.02$, even offer some improvement. Although it was not possible to obtain axial-tangential shear stress measurements from 2C-PIV, Figure 6.24 indicates a favourable agreement between LES and the RST model.

6.3 Spectral Analysis

Spectral analysis of URANS data was performed in a similar way to Section 5.4 through direct application of the fast Fourier transform (FFT) algorithm of Danielson and Lanczos described by Press et al. [128].

6.3.1 Near Field

For a detailed discussion of near-field spectral characteristics, the reader is referred to Section 4.2.1. Figure 6.25 shows PSDs of axial, radial and tangential velocity components obtained from $k - \epsilon$ and RST models compared against conditioned LES ($t/T_s = 102$) predictions at

$x/D_s = 0.27$, $r/D_s = 0.24$. The expected HWA frequencies of Midgley [13] ($S_t = 0.62$ and 1.24) are indicated by the vertical dashed lines. From RST spectra there is evidence of a peak close to $S_t = 1.24$ in all three velocity components. However, in contrast to LES, the primary HWA frequency of $S_t = 0.62$ has a comparable amplitude to the surrounding turbulent broadband frequencies and cannot be distinguished clearly. Although $k - \epsilon$ spectra contain peaks close to $S_t = 0.62$ and 1.24, this should be viewed as a rather fortuitous outcome given the qualitative differences in CS between experiment and simulation shown in above.

Differences between spectra derived from LES, which agrees well with experiment, and the RST model can be explained by examining the temporal auto-correlations of velocity at $x/D_s = 0.27$, $r/D_s = 0.24$, $\theta = \pi$ shown in Figure 6.26. For the RST model, the autocorrelation of all three components varies sinusoidally with a period between successive peaks (for positive and negative correlation values) of $\tau/T_s \approx 0.67$. This corresponds to $S_t = 1.4$ which has been indicated in Figure 6.26 and is associated with the motion of a vortex *pair*. Autocorrelations derived from LES exhibit a similar periodicity, however there is evidence of an additional timescale of $t/T_s \approx 1.34$ which results from the amplitude variation between alternate peaks of positive correlation values. This corresponds to a Strouhal number of $S_t = 0.7$ which can be observed most clearly in Figure 6.26(c) and is associated with the motion of a *single* vortex. The absence of this timescale in auto-correlations from the RST model implies that it is unable to distinguish between the motion of a single vortex and a vortex pair. This is consistent with the prominence of only the secondary HWA frequency in the velocity spectra. Unlike LES, which preserves the stochastic nature of turbulence, URANS only provides the coherent, or phase-averaged, component of fluctuating motion with the stochastic contribution accounted for via a turbulence model. The absence of this contribution means that the resolved CS are more coherent in both time and space relative to LES and hence the observed differences in velocity spectra and auto-correlations.

It is interesting to note that the amplitude of RST spectra is comparable to LES throughout the majority of the lower frequency range, say $S_t < 3$, whereas that from the $k - \epsilon$ model is much reduced and has a much smoother distribution. At relatively high frequencies, i.e. $S_t > 3$, the RST model does not follow the -5/3 gradient within the inertial subrange suggesting that the rate of energy transfer to successively smaller scales is too rapid. This is to be expected, since URANS makes no attempt to resolve directly any part of the spectrum, and the eddy viscosity levels are larger than the SGS viscosity which leads to rapid dissipation of fluctuating motion. An explanation for the observed differences in $k - \epsilon$ and RST spectral amplitudes is illustrated in Figures 6.5(c) and 6.14(c) which compare the ratio of $k_{\mathrm{mod}}/k_{\mathrm{res}}$. At $x/D_s = 0.27$, Figure 6.5(c) shows that k_{mod} dominates k_{res} in the case of the $k - \epsilon$ model whilst the opposite is the case for the RST model. As the modelled part of the turbulent spectrum, k_{mod}, is not included in Figure 6.25 variations in amplitude are to be expected. The relative smoothness of

$k-\epsilon$ spectra across the frequency range can be explained from Figures 6.4 and 6.13 which show velocity component time-histories at various points within the computational domain for $k-\epsilon$ and RST models respectively. Although none of these points directly coincide with the monitor location used for Figure 6.25 they highlight significant difference between turbulence models. For example, at $x/D_s = 0.02$, $r/D_s = 0.27$, velocity time-histories from the $k-\epsilon$ model shown in Figure 6.4 are of a repetitive deterministic nature whilst those derived from the RST model are (perhaps surprisingly) more characteristic of broadband turbulence.

In addition to the presence of distinct spectral peaks related to coherent vortex motion at relatively high frequency ($S_t > 0.5$), an increase in amplitude at the lower end of the spectra ($0.02 < S_t < 0.1$) has previously been identified as indicative of unsteadiness due to the presence of a PVC. In this region, no increase in $k-\epsilon$ spectra is observed; confirming that the PVC phenomena has not been captured. Far-field spectral characteristics of the RST model are considered in the following subsection.

6.3.2 Far Field

Figures 6.27 to 6.29 show PDSs obtained from all three velocity components at $x/D_s = 2.65$ for various radial locations. The expected precessional frequency of Syred et al. [38] ($S_t = 1.35\times10^{-2}$ - see Section 5.4.2) is indicated by the vertical dashed line. As already noted, the PVC is predominantly aligned in the streamwise direction and the fact that the expected precessional frequency does not appear in RST (or LES) axial velocity spectra shown in Figure 6.27 is unsurprising. From Figures 6.28 and 6.29, which show radial and tangential velocity spectra, a significant accumulation of energy is observed at $S_t = 1.35\times10^{-2}$ at all radial locations. This confirms that, like LES, the RST model is able to predict the frequency characteristics of the PVC. In comparison to LES, the amplitude of far-field URANS velocity spectra is notably reduced throughout the entire frequency range and can be attributed to an increased damping of velocity fluctuations in the vicinity of the centreline.

The time-dependent behaviour of the PVC was investigated for the RST model again using the vortex detection algorithm of Grosjean et al. [36] (Equation A-24). The computed location of the PVC at $x/D_s = 2.39$ was compared with its location deduced from instantaneous streamtraces at various time-instants (Figure 6.12). The angular location (θ_{PVC}) and radial displacement (r_{PVC}) of the PVC for the RST model are shown in Figures 6.30 and 6.31 as a function of non-dimensional time, t/T_s. For clarity, the total record length of the RST ensemble has been divided into two segments from $t/T_s = 0-205$ and $t/T_s = 205-409$ respectively. It should be noted that $t/T_s = 0$ corresponds to the beginning of the sampling interval reached after the initial transitory period ($t/T_s = 0-125$, see Section 6.1.2) rather than solution initialisation. In Section 5.4.2, the sawtooth waveform identified was attributed to the rotational motion of

the PVC about the geometric centreline. Similar behaviour is also observed for the RST model and is most clearly identified between $t/T_s \approx 150 - 300$. The explanation for this is provided in Figure 6.31 which shows that the average radial displacement of the PVC from the centre of the expansion chamber is $\langle r_{\mathrm{PVC}} \rangle / D_x \approx 0.01$. When the instantaneous location of the PVC is relatively close to the centreline, say $r_{\mathrm{PVC}}/D_x < \langle r \rangle / D_x$, even very slight variations in position can lead to the detection of large angular jumps. However, when the PVC is relatively far from the centreline its rotational motion is more clearly defined, which can be observed by examining r_{PVC}/D_x and θ_{PVC} from $t/T_s \approx 150 - 300$. Clearly, the radial displacement of the PVC from RST calculations is relatively modest in comparison to that derived from LES of $\langle r_{\mathrm{PVC}} \rangle / D_x \approx 0.023$ which was in reasonable agreement with PIV measurements (Table 4.2) at 3.5% of the duct diameter. This suggests a higher degree of damping by the RST model relative to LES which is consistent with increased levels of eddy viscosity in the vicinity of the centreline shown in Figures 6.14(d) and 5.4(a) respectively.

6.4 Closure

From results presented in this chapter it can be concluded that $k - \epsilon$ URANS is not suitable for capturing even the correct qualitative details of the modular swirler. Although a Reynolds-decomposition in the near-field revealed an initial vortex structure similar to that observed experimentally this underwent a transitory phase and the final self-sustaining solution reached after further timesteps was inconsistent with experiment. Similarly, the expected PVC in the far-field was not predicted as the aerodynamic centre was coincident with the geometric centre at all times. A thorough investigation into various numerics, computational grids and CFD solvers found that these exerted no influence on CS development. It was suggested that high levels of turbulent viscosity within shear-layers shed from the swirler and in the vicinity of the centreline were a more probable cause of these discrepancies. As a result of qualitative differences and details of the $k-\epsilon$ model first-order statistics and near-field velocity spectra were in poor agreement with experiment.

In contrast to the $k - \epsilon$ model, the qualitative details of the both near and far-field instability modes predicted by the RST were in accordance with experiment. First and second-order statistics derived from an ensemble dataset of identical length to that used for LES showed a good overall agreement with PIV measurements. Although velocity fluctuations in the far-field were suppressed relative to LES due to an increased turbulent viscosity a large accumulation of energy was observed close to the expected precessional frequency of the PVC. From near-field spectral analysis a peak close to $S_t = 1.24$ (vortex *pair*) was present in all three velocity components, however the expected HWA frequency of $S_t = 0.62$ (*single* vortex) had a comparable amplitude to the surrounding turbulent broadband frequencies and could not be clearly distinguished. It was argued that since URANS only provides the coherent, or phase-averaged, component of fluc-

tuating motion the resolved CS are more coherent in both time and space relative to LES which was able to detect both frequencies. As a result of this increase coherence (which was quantified via temporal auto-correlations of velocity) the RST model is unable to distinguish between the motion of a single vortex and a vortex pair and hence the differences in velocity spectra.

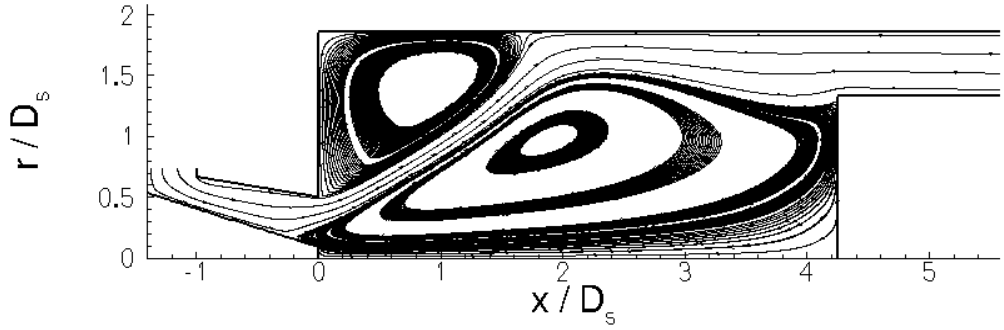

(a) $t/T_s = 50$

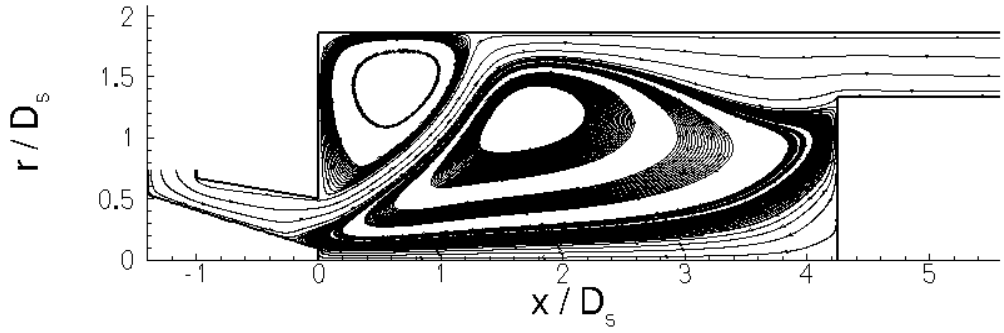

(b) $t/T_s = 100$

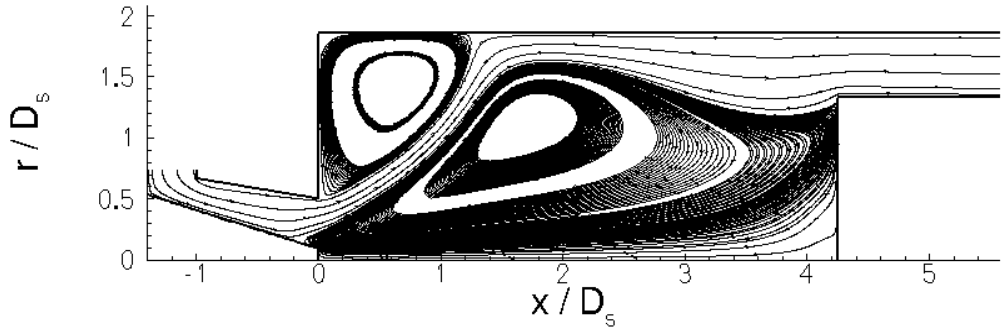

(c) $t/T_s = 150$

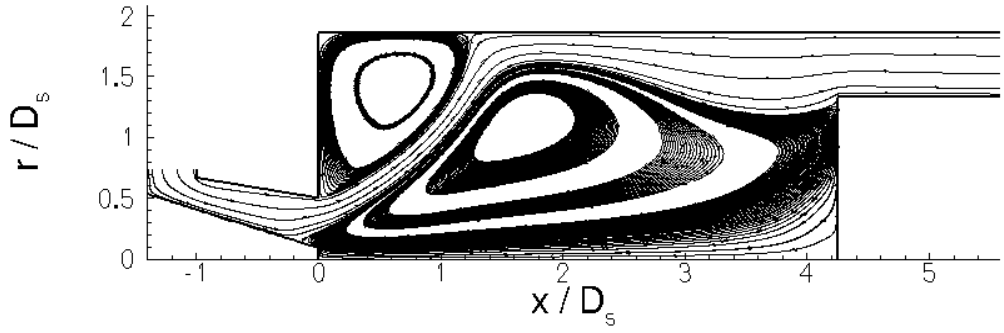

(d) $t/T_s = 300$

Figure 6.1: Instantaneous circumferentially averaged streamtraces in $x - r$ plane at various time instants for URANS case 1.

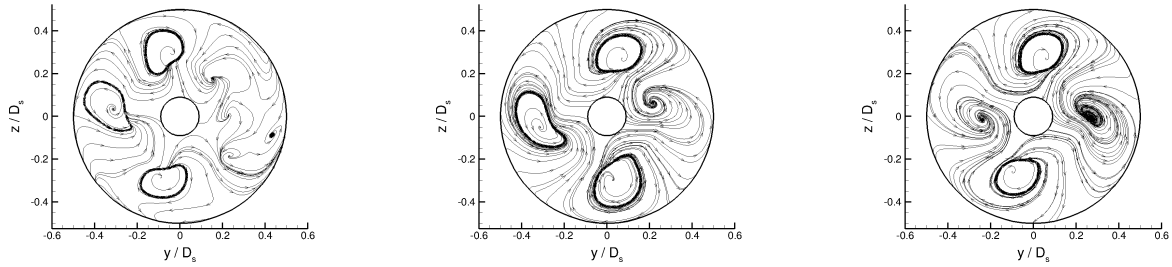

(a) $t/T_s = 5$ (b) $t/T_s = 10$ (c) $t/T_s = 15$

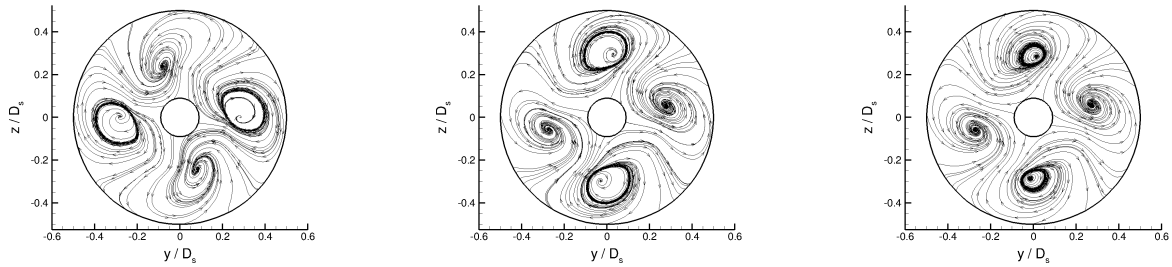

(d) $t/T_s = 25$ (e) $t/T_s = 50$ (f) $t/T_s = 75$

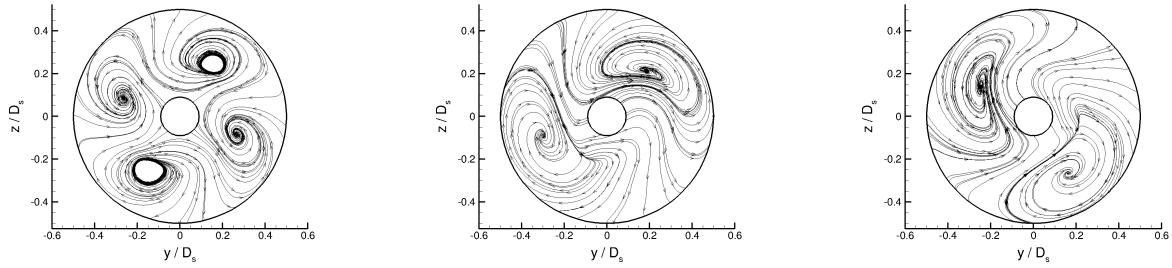

(g) $t/T_s = 100$ (h) $t/T_s = 150$ (i) $t/T_s = 200$

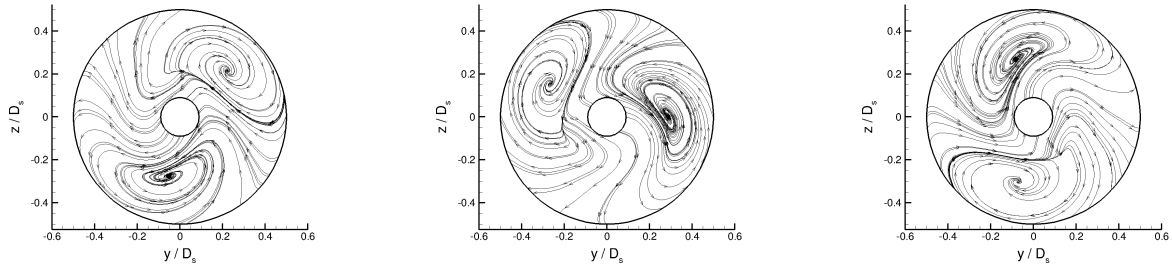

(j) $t/T_s = 250$ (k) $t/T_s = 300$ (l) $t/T_s = 350$

Figure 6.2: Reynolds-decomposed streamtraces at swirler exit ($x/D_s = 0.02$) at various time instants for URANS case 1.

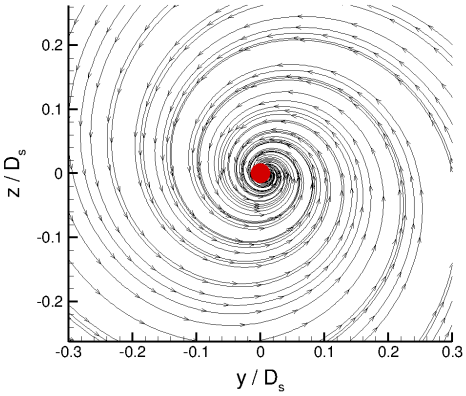

(a) $t/T_s = 50$

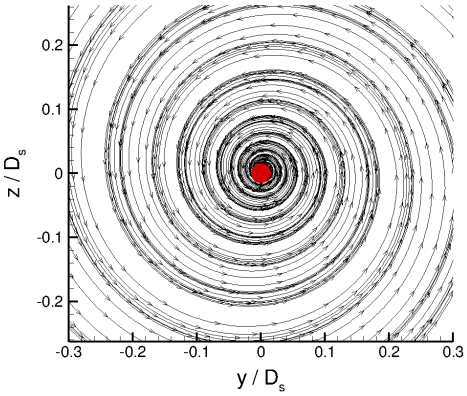

(b) $t/T_s = 100$

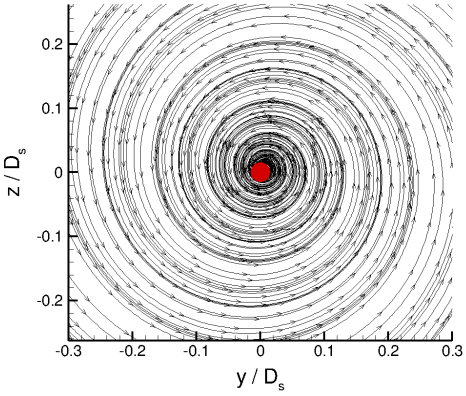

(c) $t/T_s = 150$

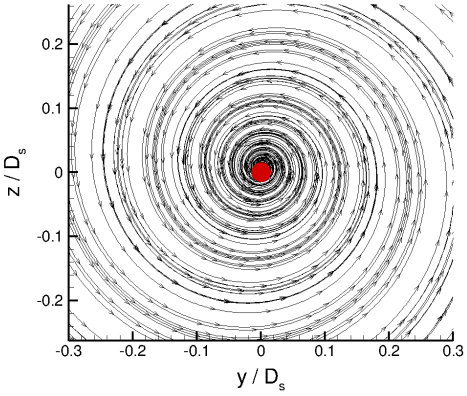

(d) $t/T_s = 200$

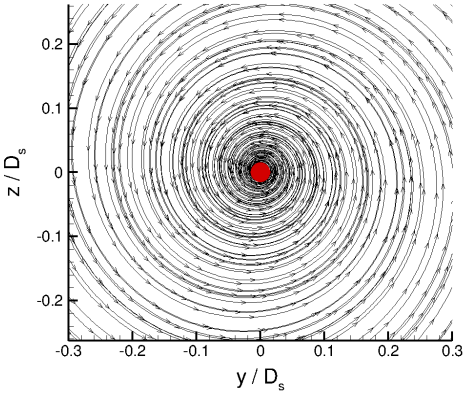

(e) $t/T_s = 250$

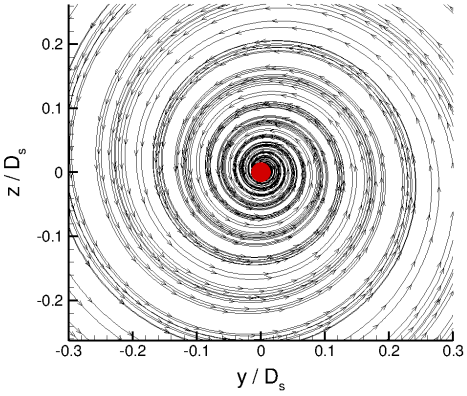

(f) $t/T_s = 300$

Figure 6.3: Instantaneous streamtraces in expansion chamber ($x/D_s = 2.39$) at various time instants for URANS case 1 •- geometric centre

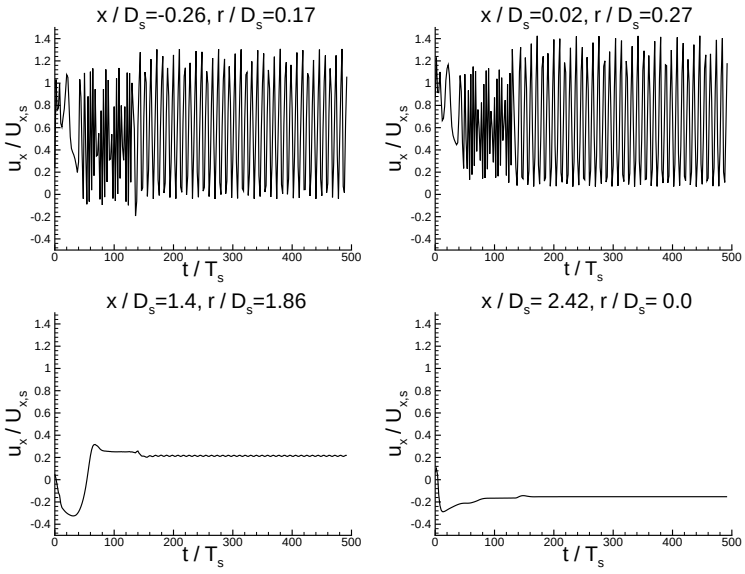

(a) Axial Velocity

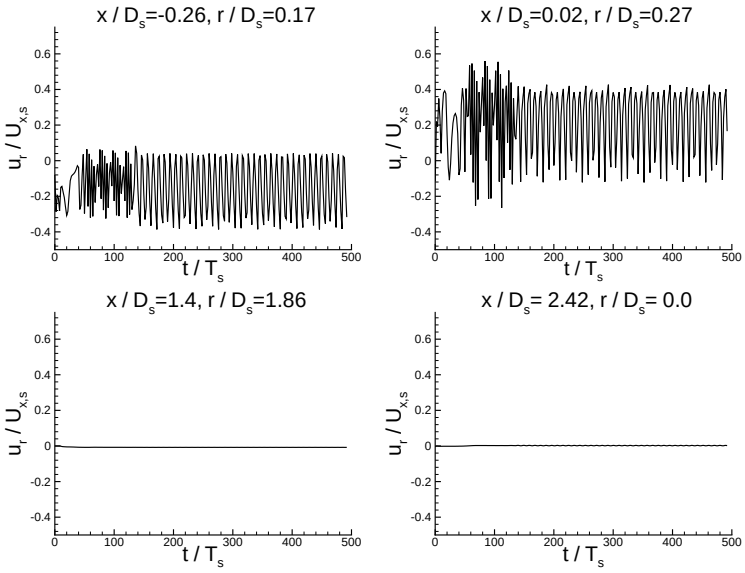

(b) Radial Velocity

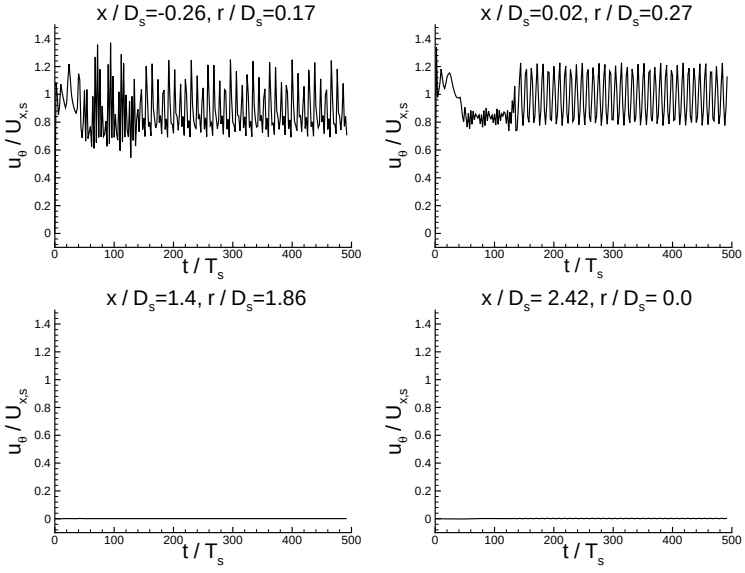

(c) Tangential Velocity

Figure 6.4: Velocity time-histories at various locations for URANS case 1.

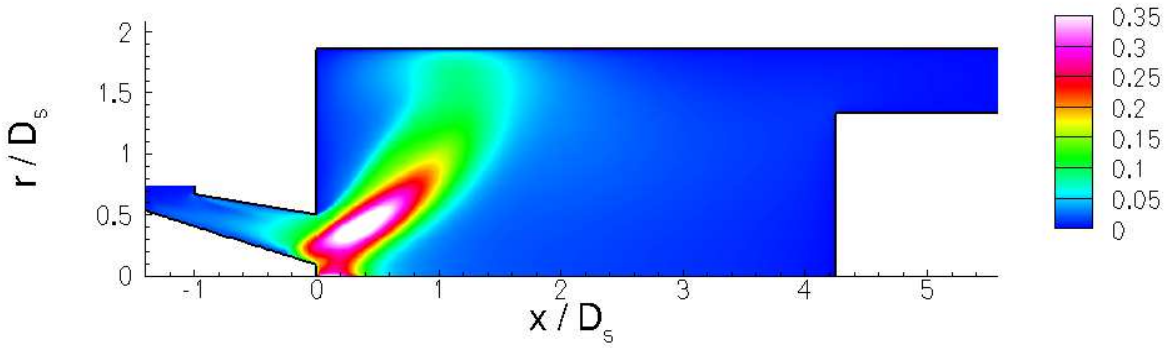

(a) $k_{\mathrm{mod}}/U_{x,s}^2$

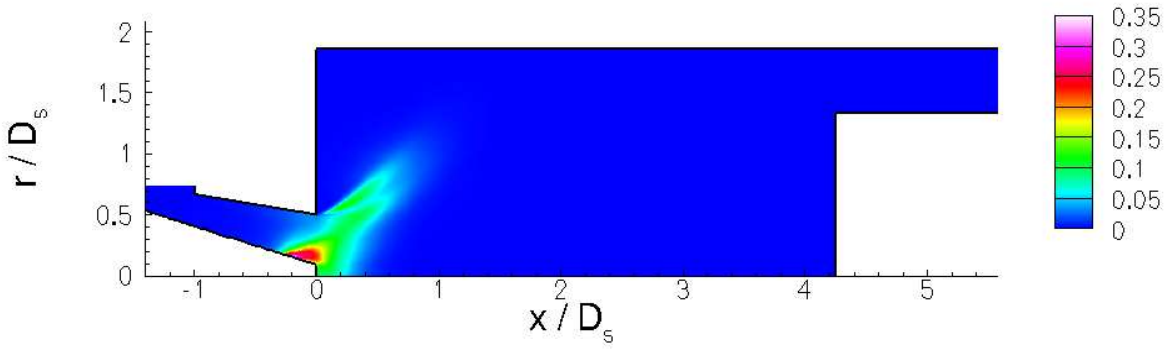

(b) $k_{\mathrm{res}}/U_{x,s}^2$

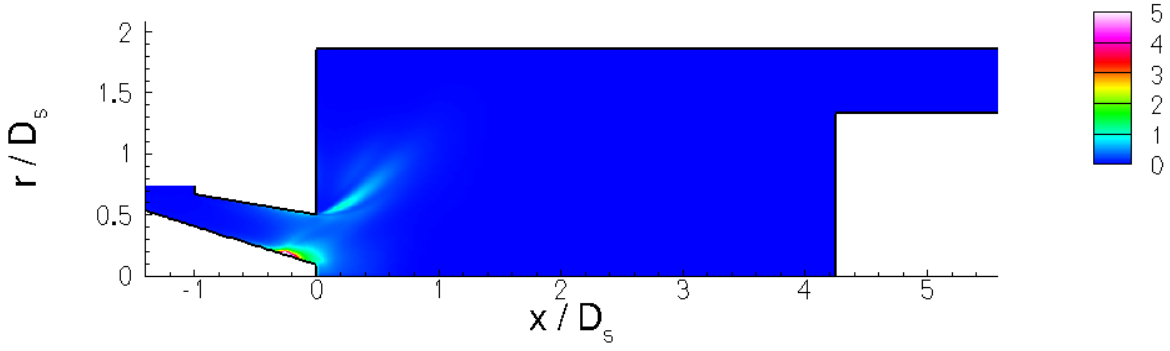

(c) $k_{\mathrm{res}}/k_{\mathrm{mod}}$

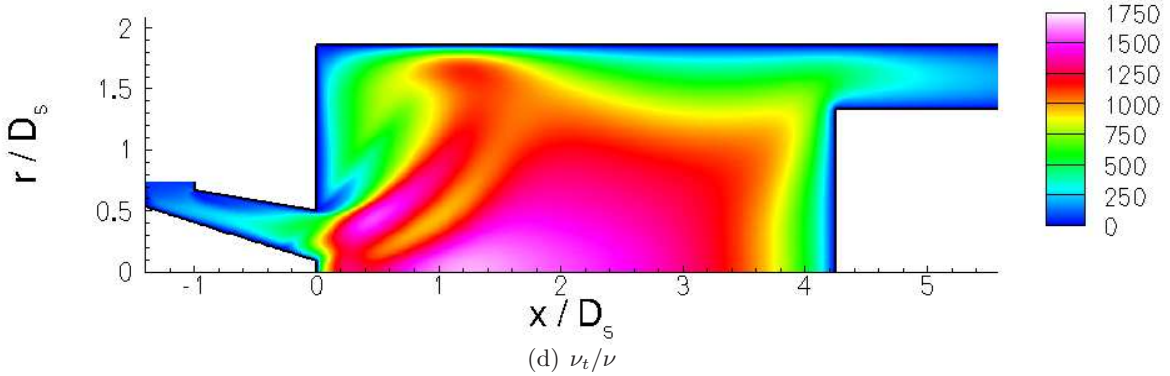

(d) ν_t/ν

Figure 6.5: Contours of time averaged turbulent quantities for URANS case 1.

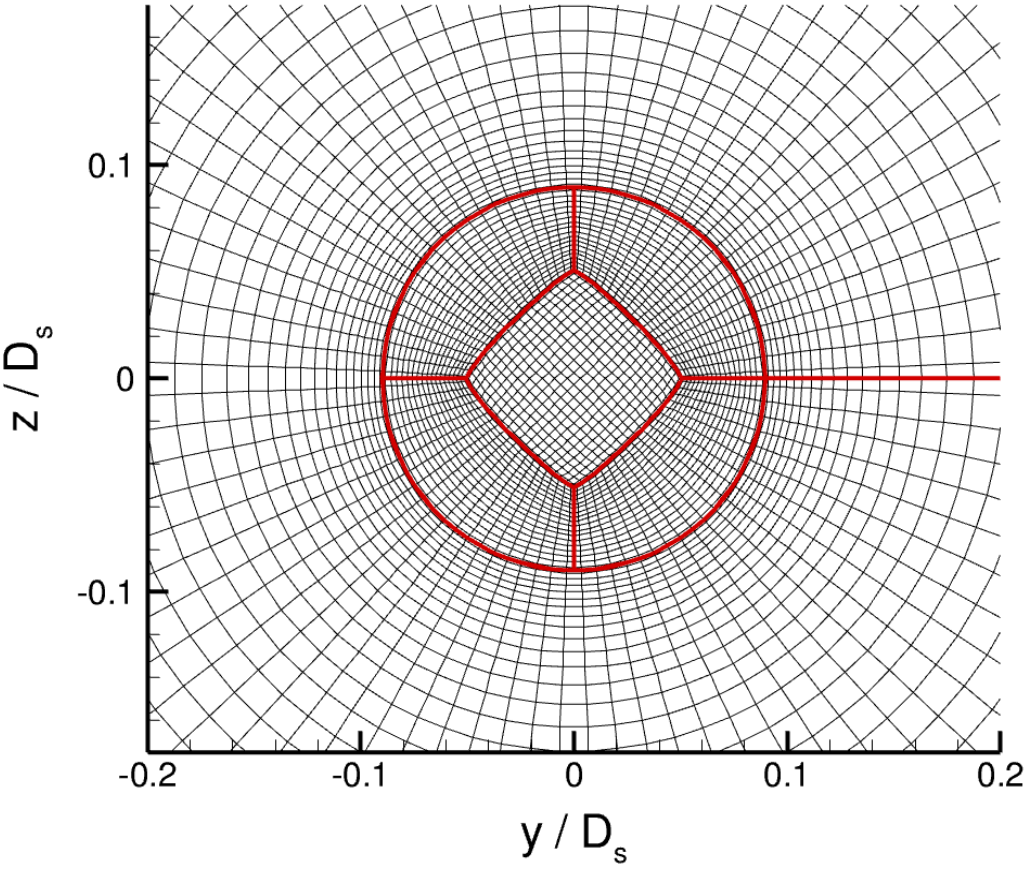

Figure 6.6: O-Grid used for URANS case 5 shown in $r - \theta$ plane.

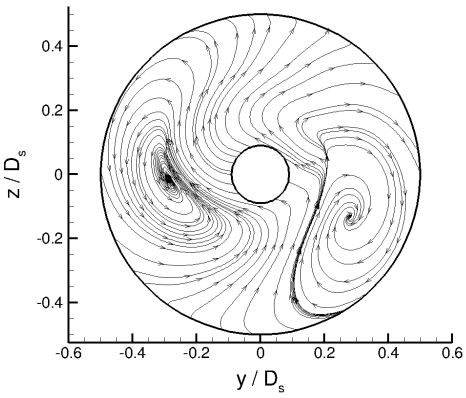

(a) URANS case 2.

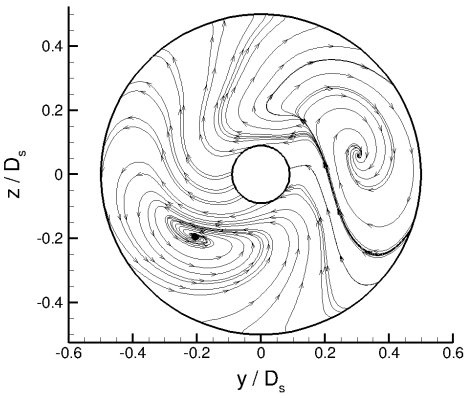

(b) URANS case 3.

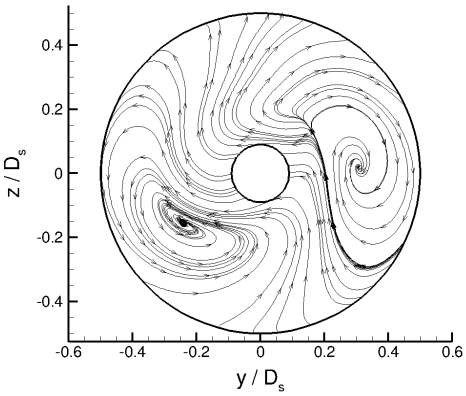

(c) URANS case 4.

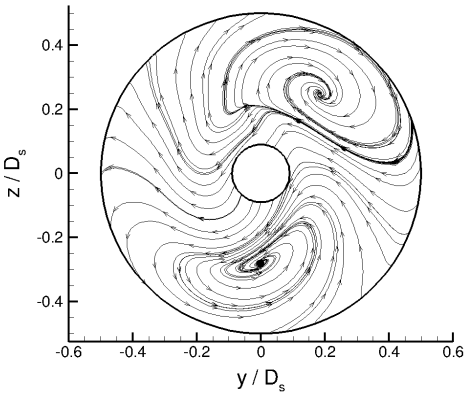

(d) URANS case 5.

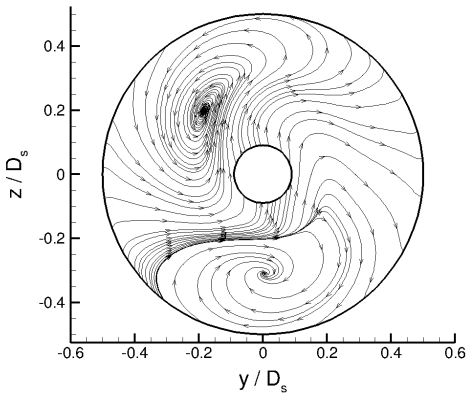

(e) URANS case 6.

Figure 6.7: Reynolds-decomposed streamtraces at $x/D_s = 0.02$, $t/T_s = 150$ for URANS cases 2 - 6.

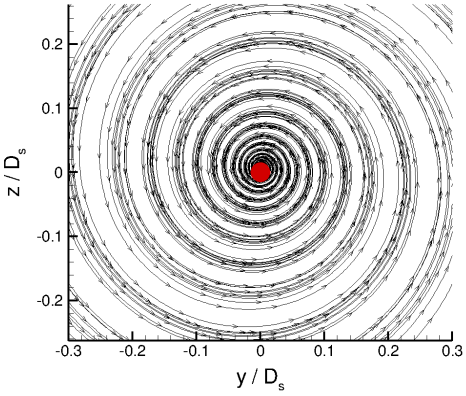

(a) URANS case 2.

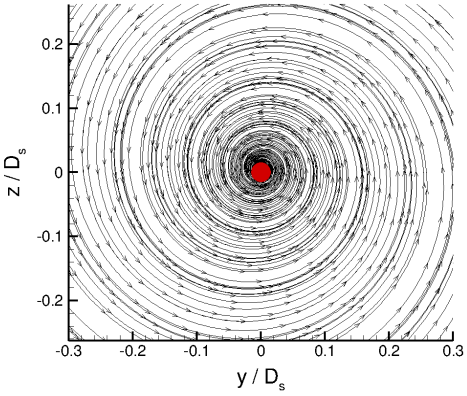

(b) URANS case 3.

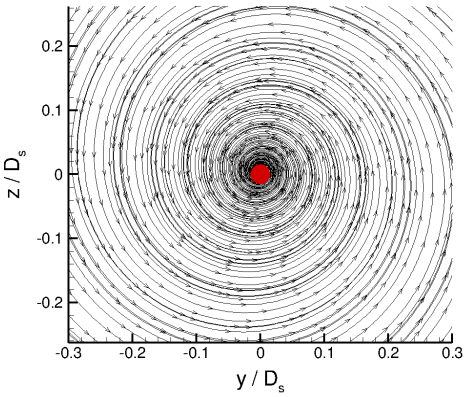

(c) URANS case 4.

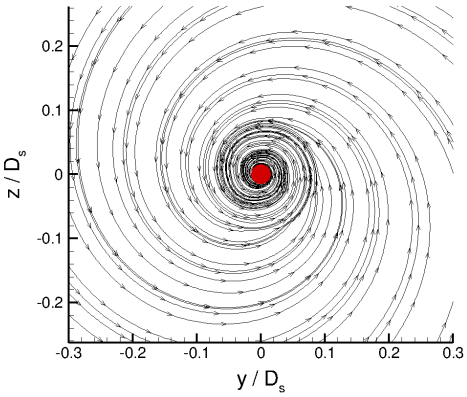

(d) URANS case 5.

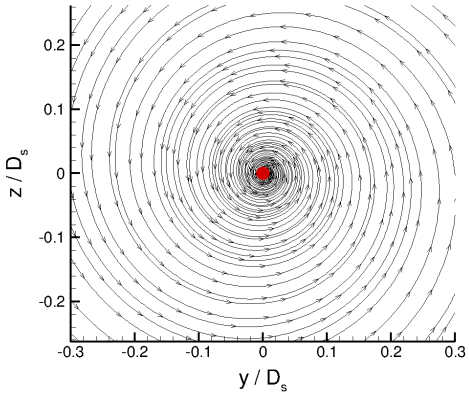

(e) URANS case 6.

Figure 6.8: Instantaneous streamtraces at $x/D_s = 2.39$, $t/T_s = 150$ for URANS cases 2 - 6.

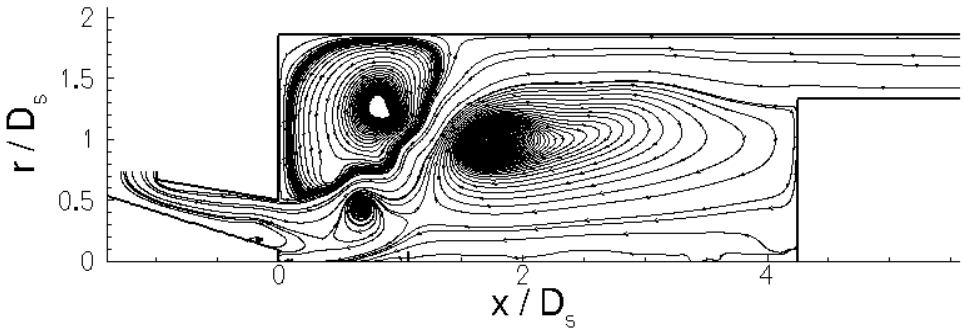

(a) $t/T_s = 50$

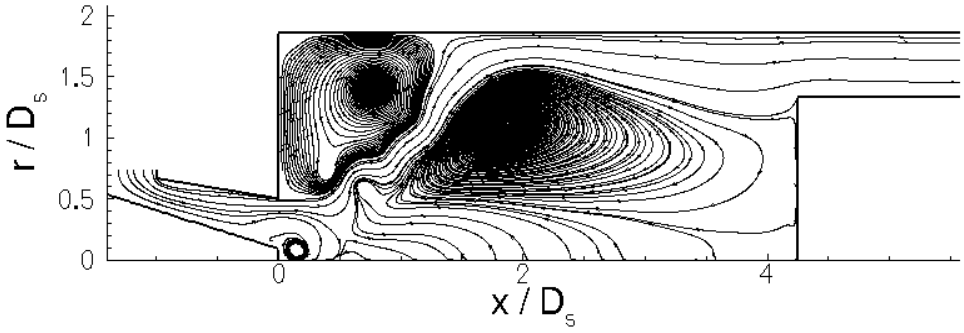

(b) $t/T_s = 100$

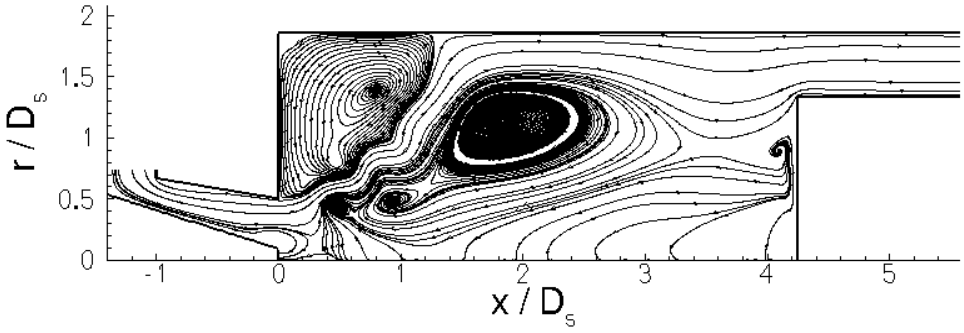

(c) $t/T_s = 150$

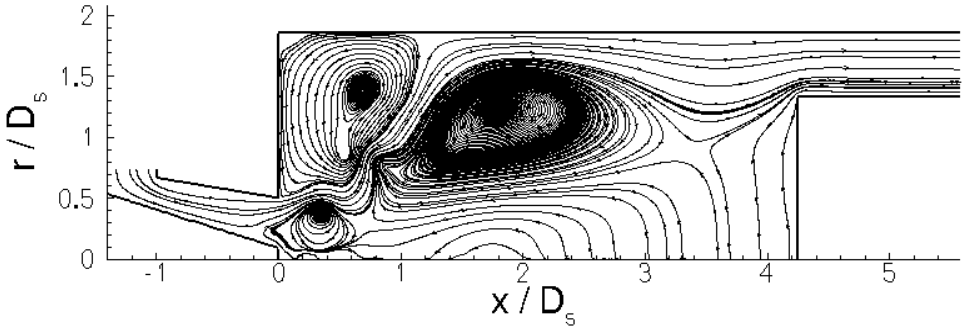

(d) $t/T_s = 300$

Figure 6.9: Instantaneous streamtraces in $x-r$ plane at $\theta = \pi$ at various time instant for URANS case 7.

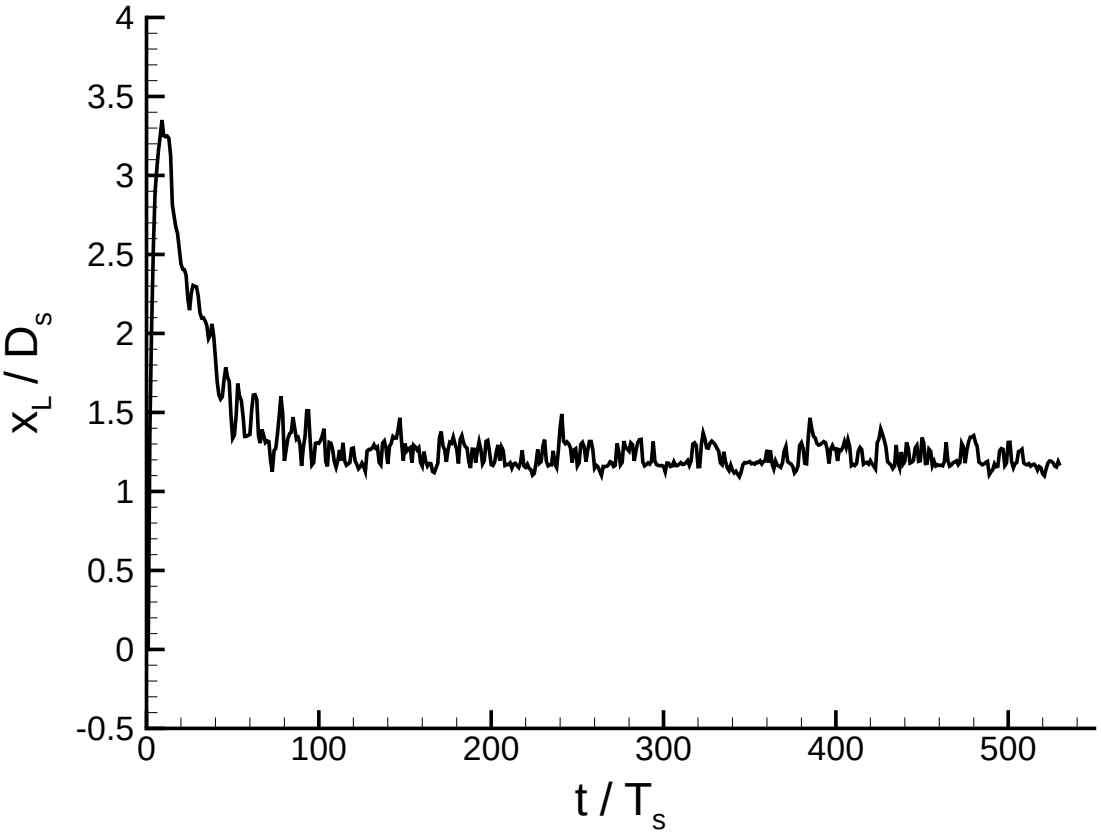

Figure 6.10: Instantaneous reattachment location of outer shear layer at $r/D_s = 1.86$, $\theta = \pi$ for URANS case 7.

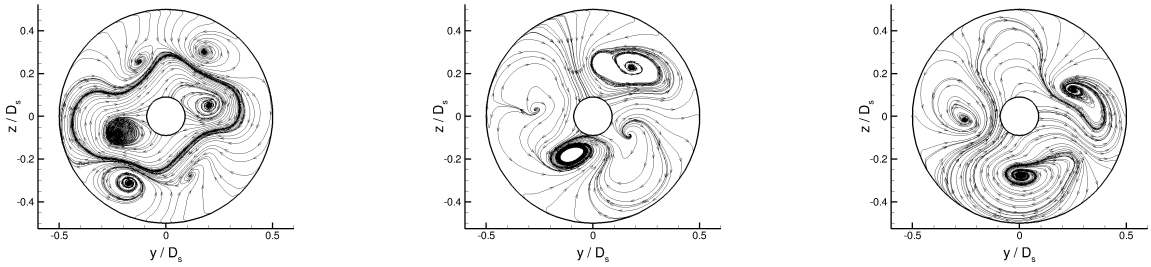

(a) $t/T_s = 5$ (b) $t/T_s = 10$ (c) $t/T_s = 15$

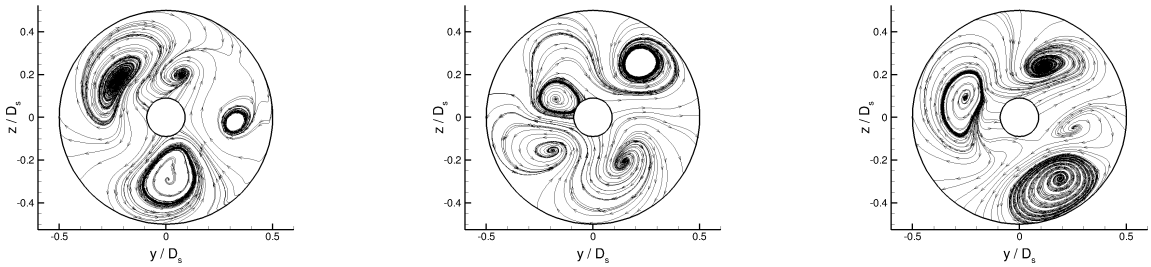

(d) $t/T_s = 25$ (e) $t/T_s = 50$ (f) $t/T_s = 75$

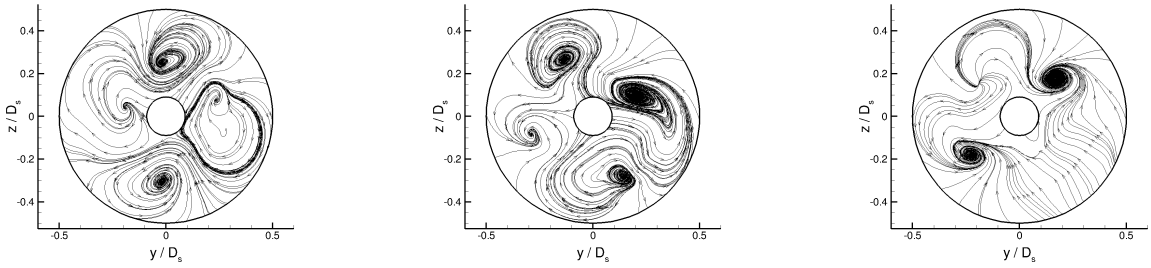

(g) $t/T_s = 100$ (h) $t/T_s = 150$ (i) $t/T_s = 200$

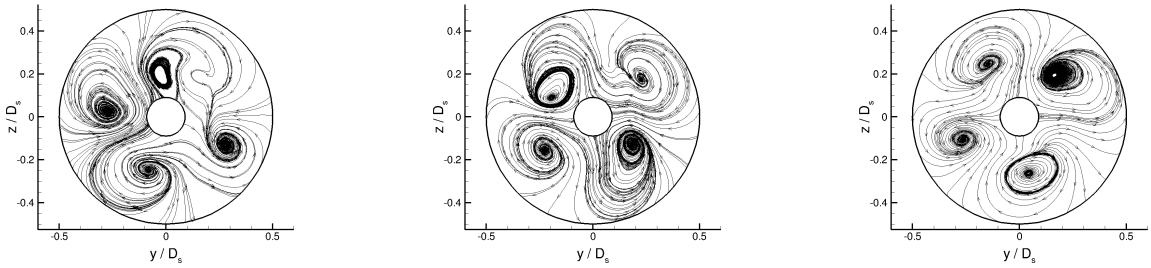

(j) $t/T_s = 250$ (k) $t/T_s = 300$ (l) $t/T_s = 350$

Figure 6.11: Reynolds-decomposed streamtraces at swirler exit ($x/D_s = 0.02$) at various time instants for URANS case 7.

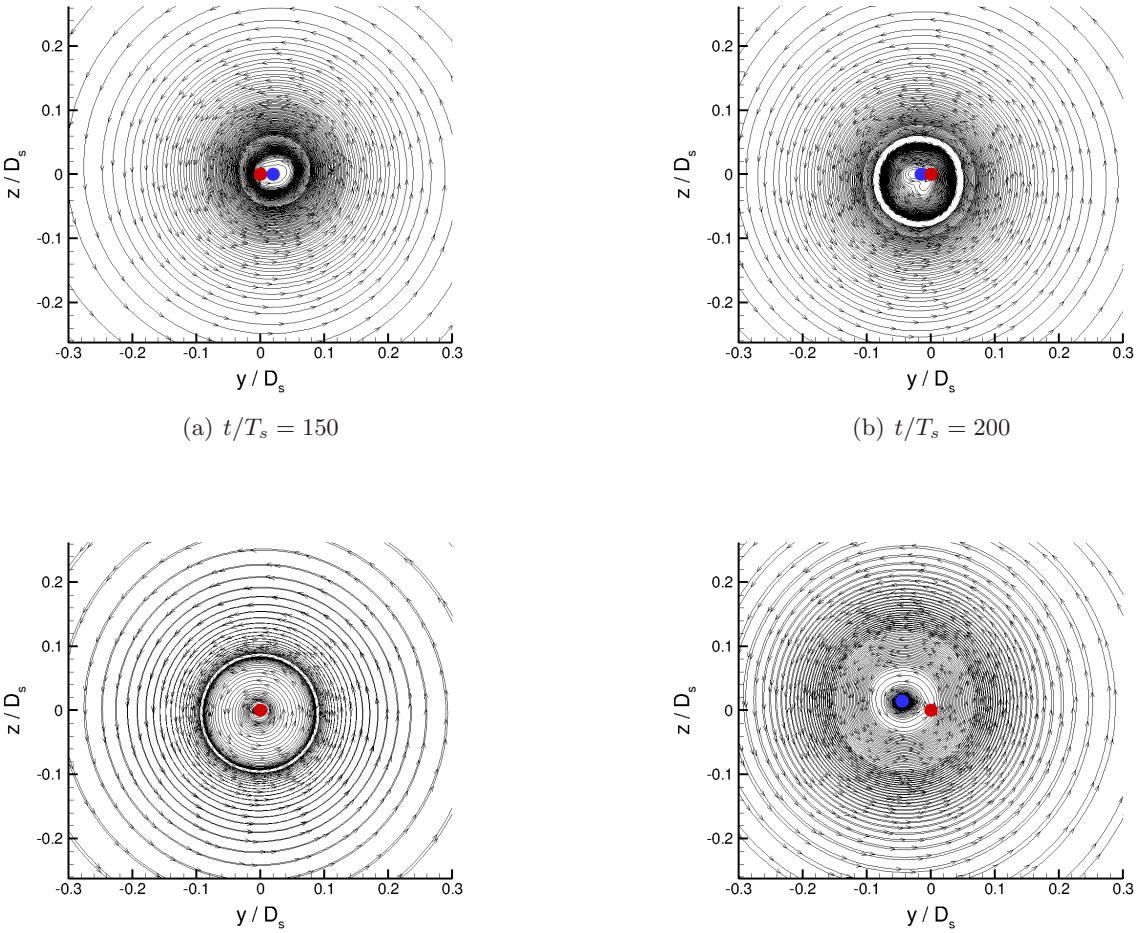

(a) $t/T_s = 150$

(b) $t/T_s = 200$

(c) $t/T_s = 250$

(d) $t/T_s = 300$

Figure 6.12: Instantaneous streamtraces in expansion chamber ($x/D_s = 2.39$) at various time instants for URANS case 7 ●- geometric centre, ●- aerodynamic centre from Equation A-24

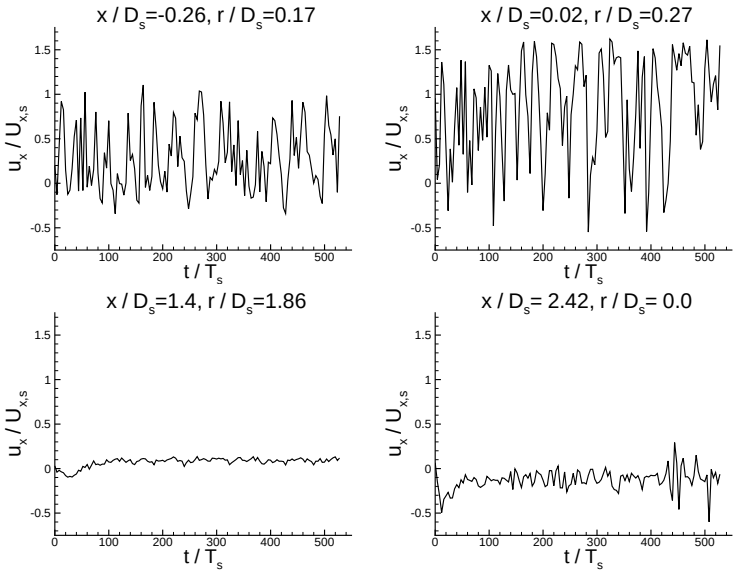

(a) Axial Velocity

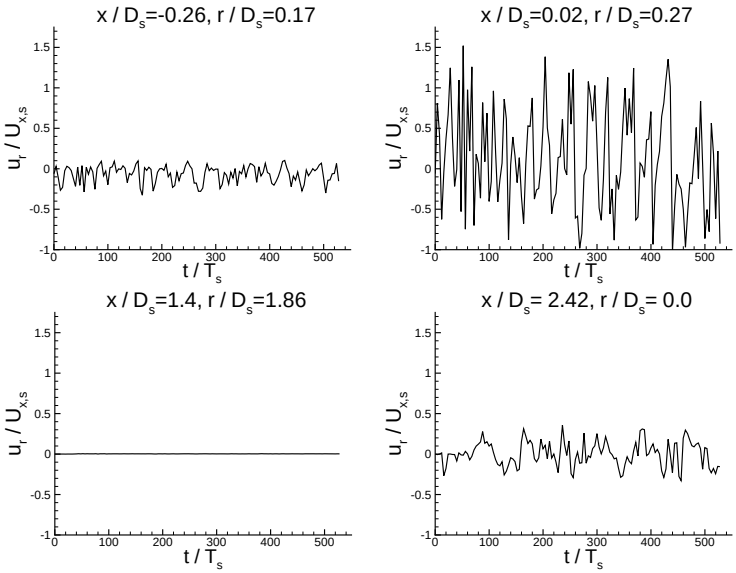

(b) Radial Velocity

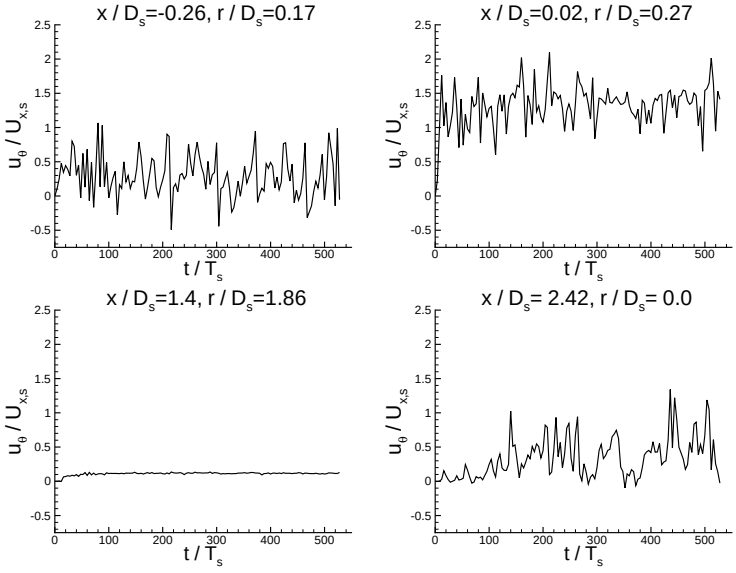

(c) Tangential Velocity

Figure 6.13: Time-histories at various locations for URANS case 7.

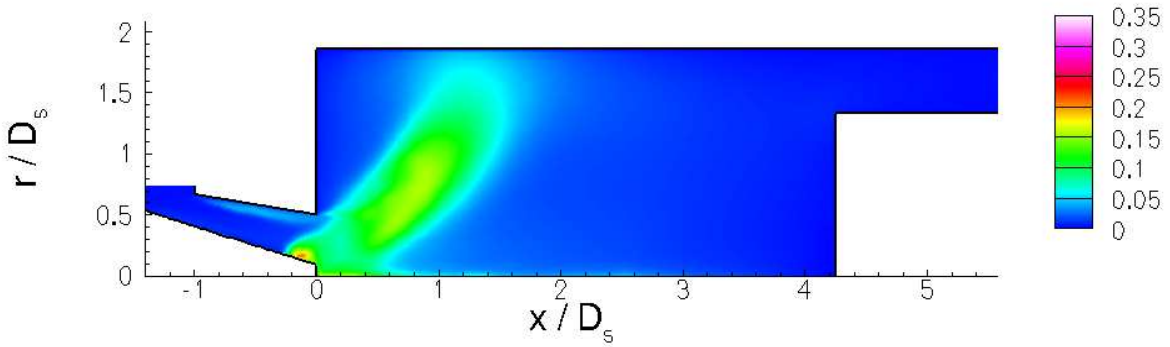

(a) Contours of modeled turbulent kinetic energy, k_{mod}

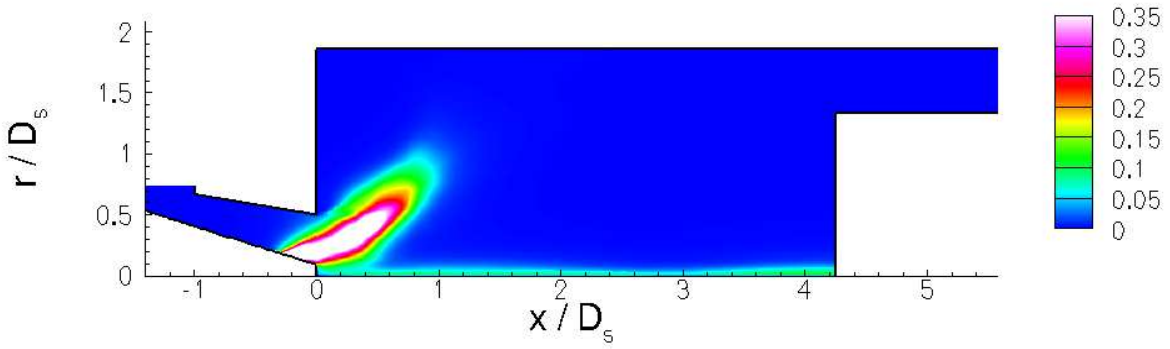

(b) Contours of resolved turbulent kinetic energy, k_{res}

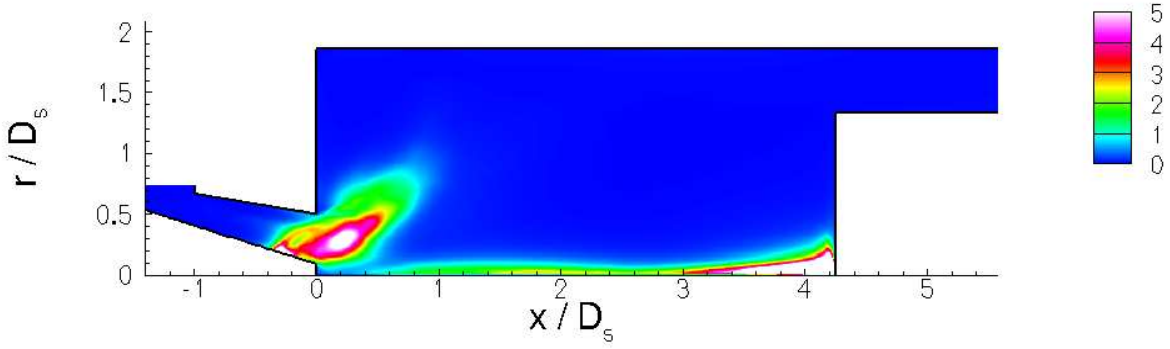

(c) Contours of turbulent kinetic energy ratio, k_{res}/k_{mod}

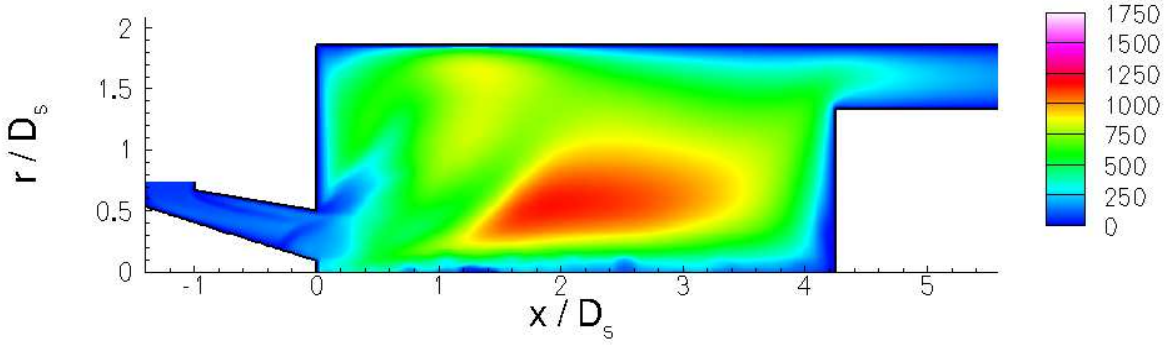

(d) Contours of eddy viscosity ratio, ν_t/ν

Figure 6.14: Contours of time averaged turbulent quantities for URANS case 7.

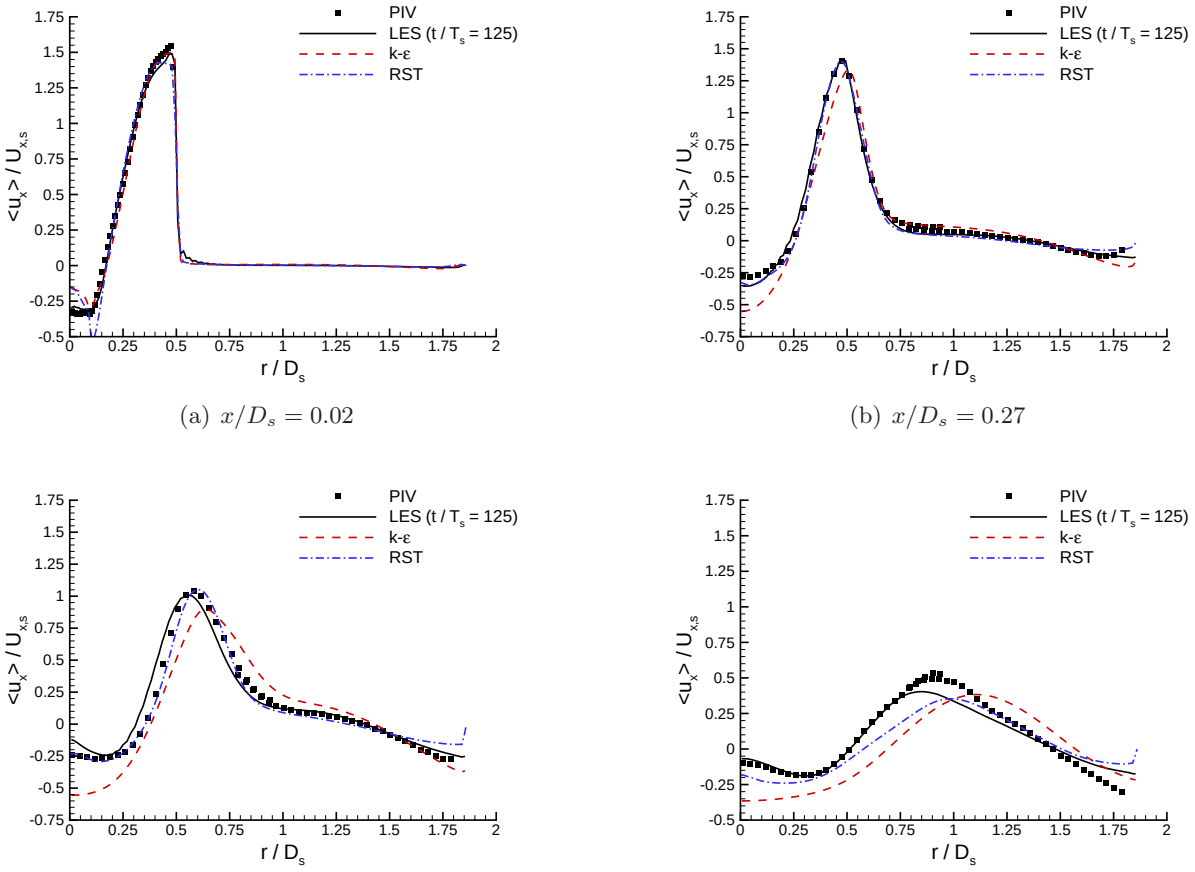

(a) $x/D_s = 0.02$

(b) $x/D_s = 0.27$

(c) $x/D_s = 0.53$

(d) $x/D_s = 1.06$

Figure 6.15: Comparison of mean axial velocity against conditioned LES ($t/T_s = 125$) and PIV at various axial locations in expansion chamber

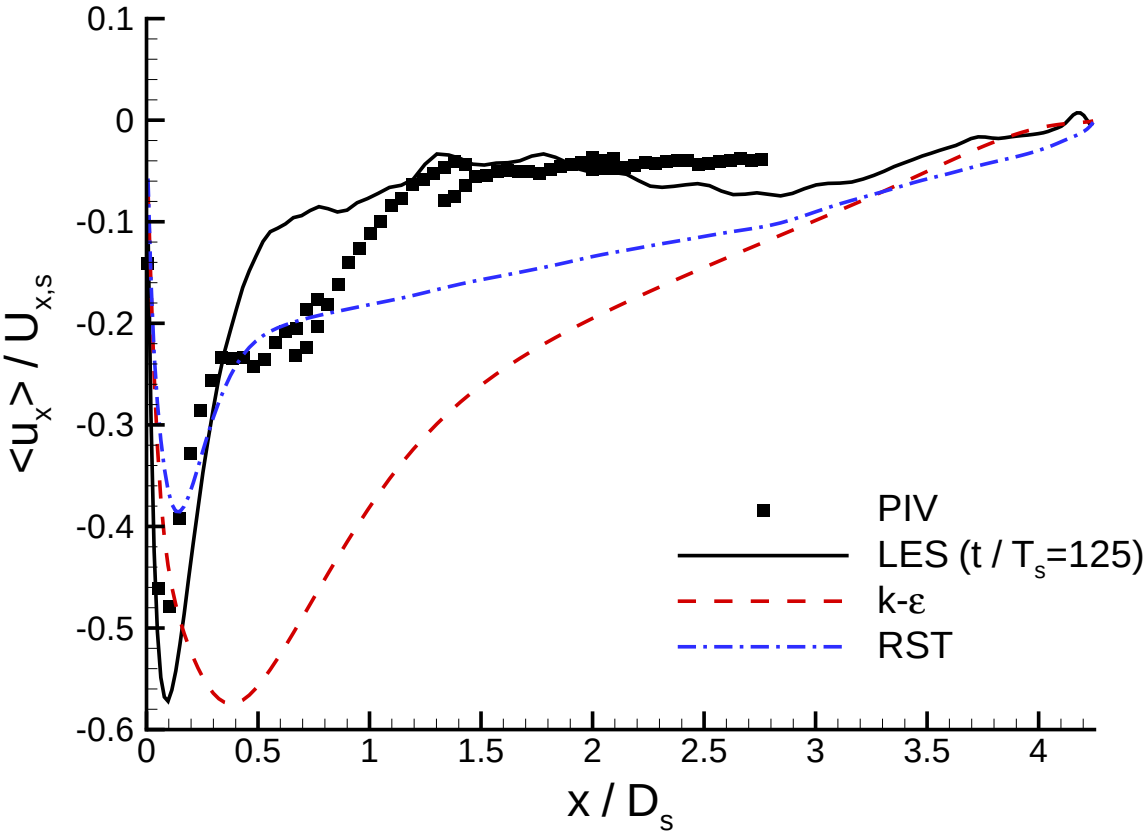

Figure 6.16: Comparison of mean axial centreline velocity against conditioned LES ($t/T_s = 125$) and PIV at various axial locations in expansion chamber

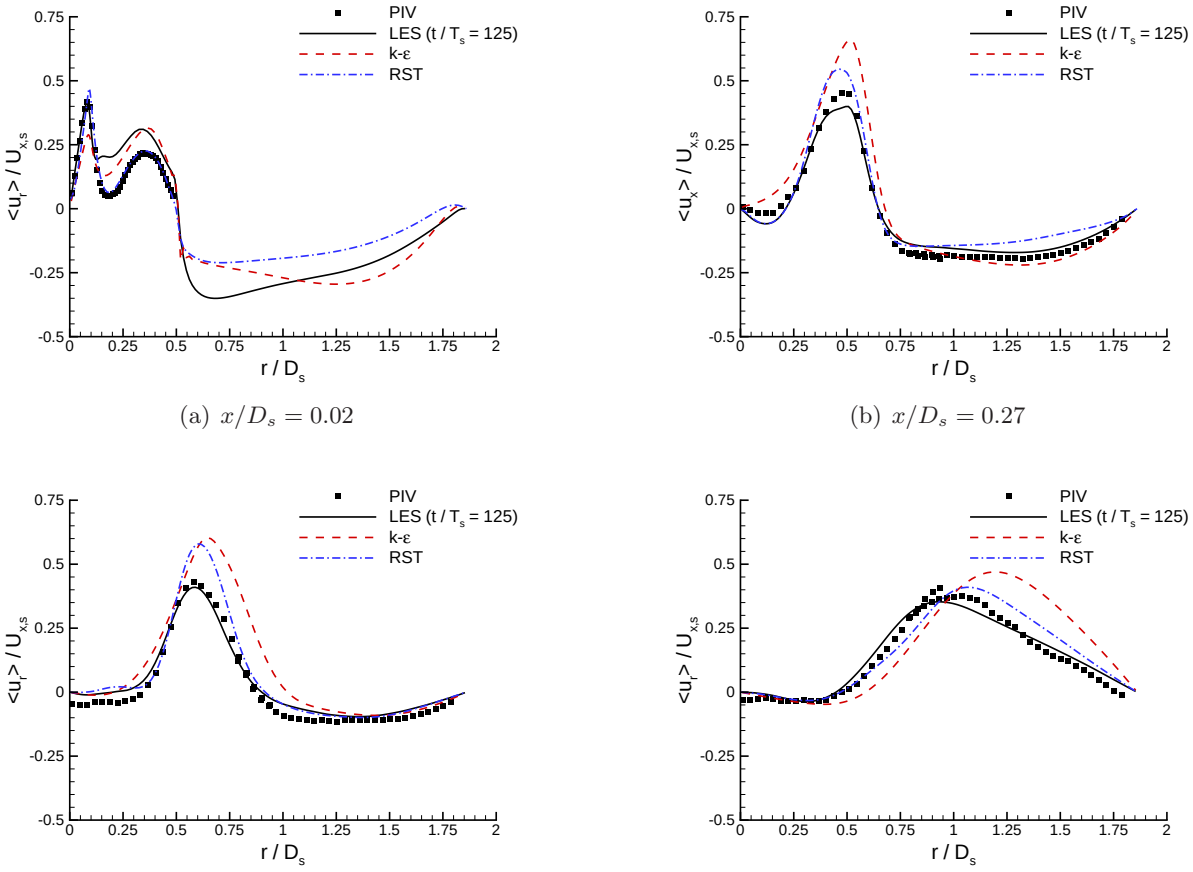

(a) $x/D_s = 0.02$

(b) $x/D_s = 0.27$

(c) $x/D_s = 0.53$

(d) $x/D_s = 1.06$

Figure 6.17: Comparison of mean radial velocity against conditioned LES ($t/T_s = 125$) and PIV at various axial locations in expansion chamber

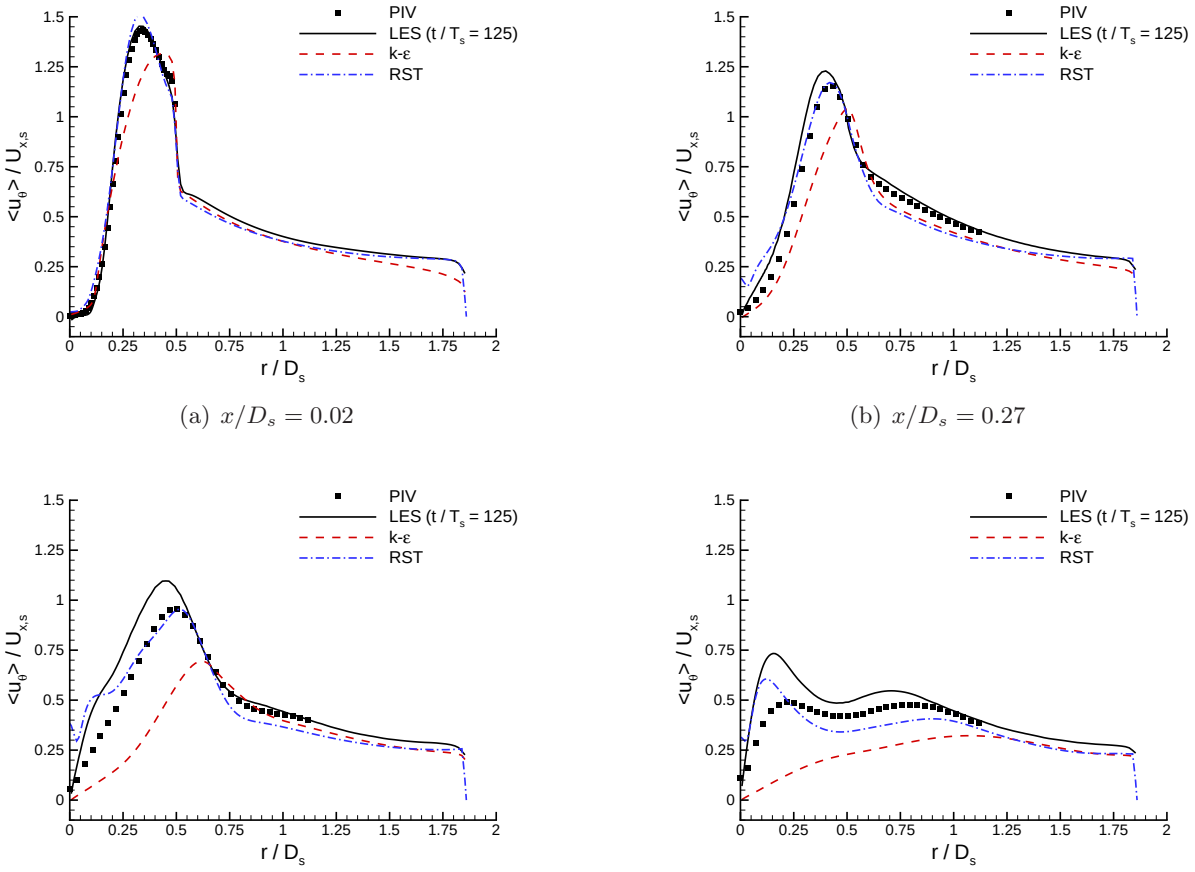

(a) $x/D_s = 0.02$

(b) $x/D_s = 0.27$

(c) $x/D_s = 0.53$

(d) $x/D_s = 1.06$

Figure 6.18: Comparison of mean tangential velocity against conditioned LES ($t/T_s = 125$) and PIV at various axial locations in expansion chamber

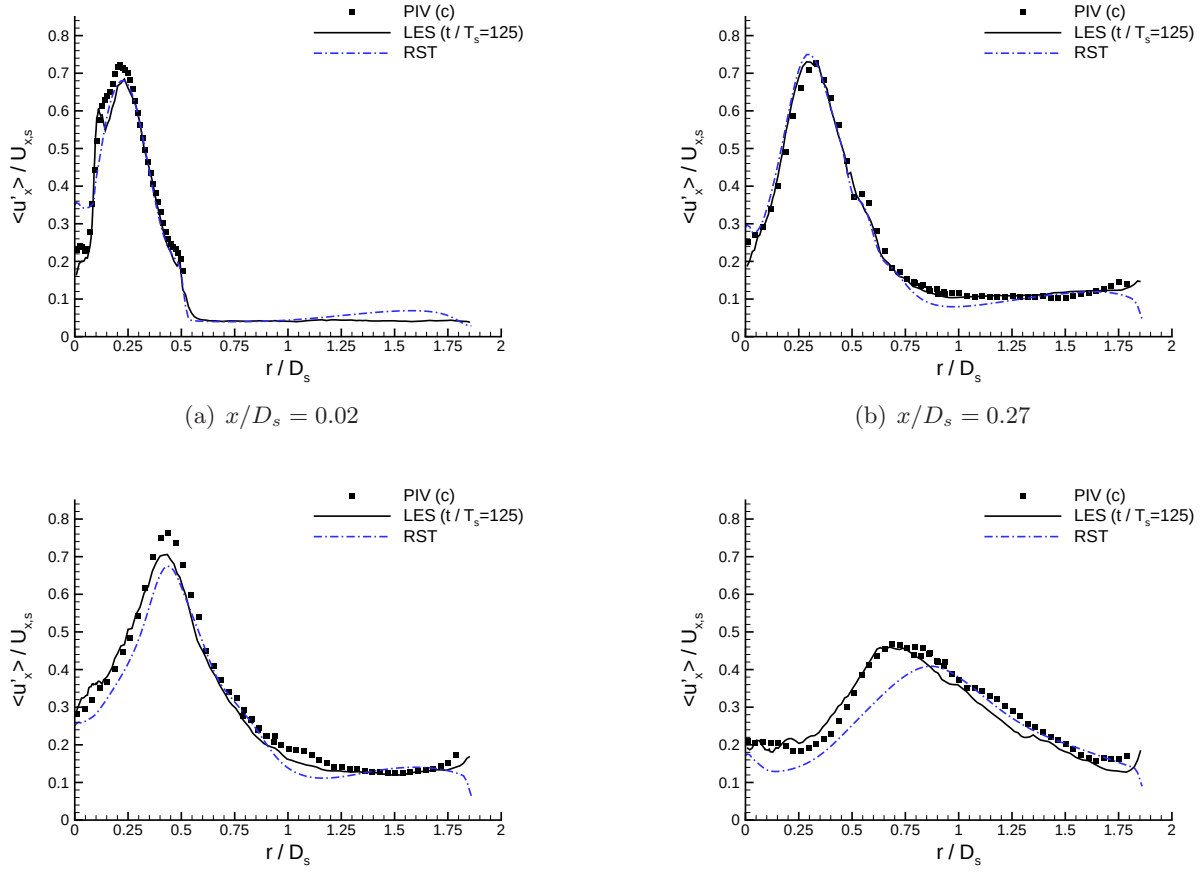

(a) $x/D_s = 0.02$

(b) $x/D_s = 0.27$

(c) $x/D_s = 0.53$

(d) $x/D_s = 1.06$

Figure 6.19: Comparison of r.m.s axial velocity against conditioned LES ($t/T_s = 125$) and corrected PIV at various axial locations in expansion chamber

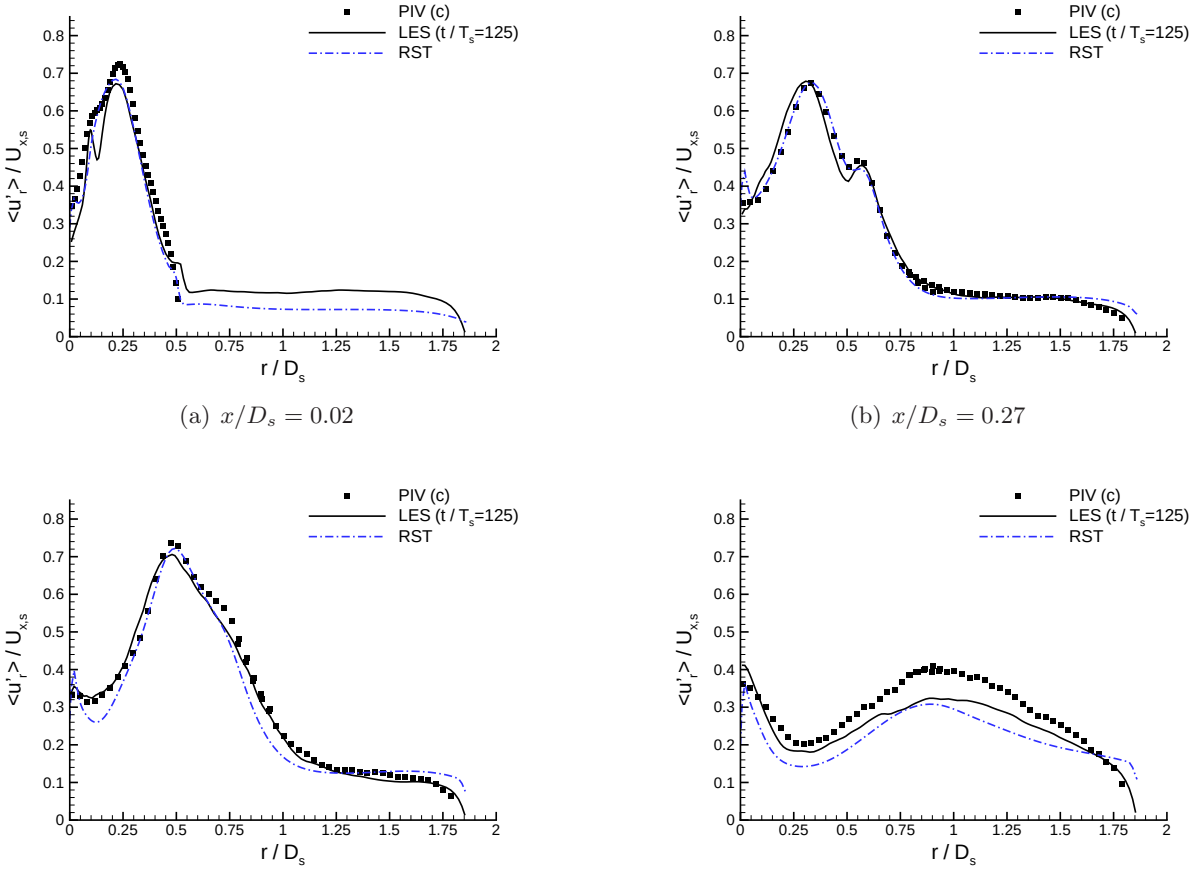

(a) $x/D_s = 0.02$

(b) $x/D_s = 0.27$

(c) $x/D_s = 0.53$

(d) $x/D_s = 1.06$

Figure 6.20: Comparison of r.m.s radial velocity against conditioned LES ($t/T_s = 125$) and corrected PIV at various axial locations in expansion chamber

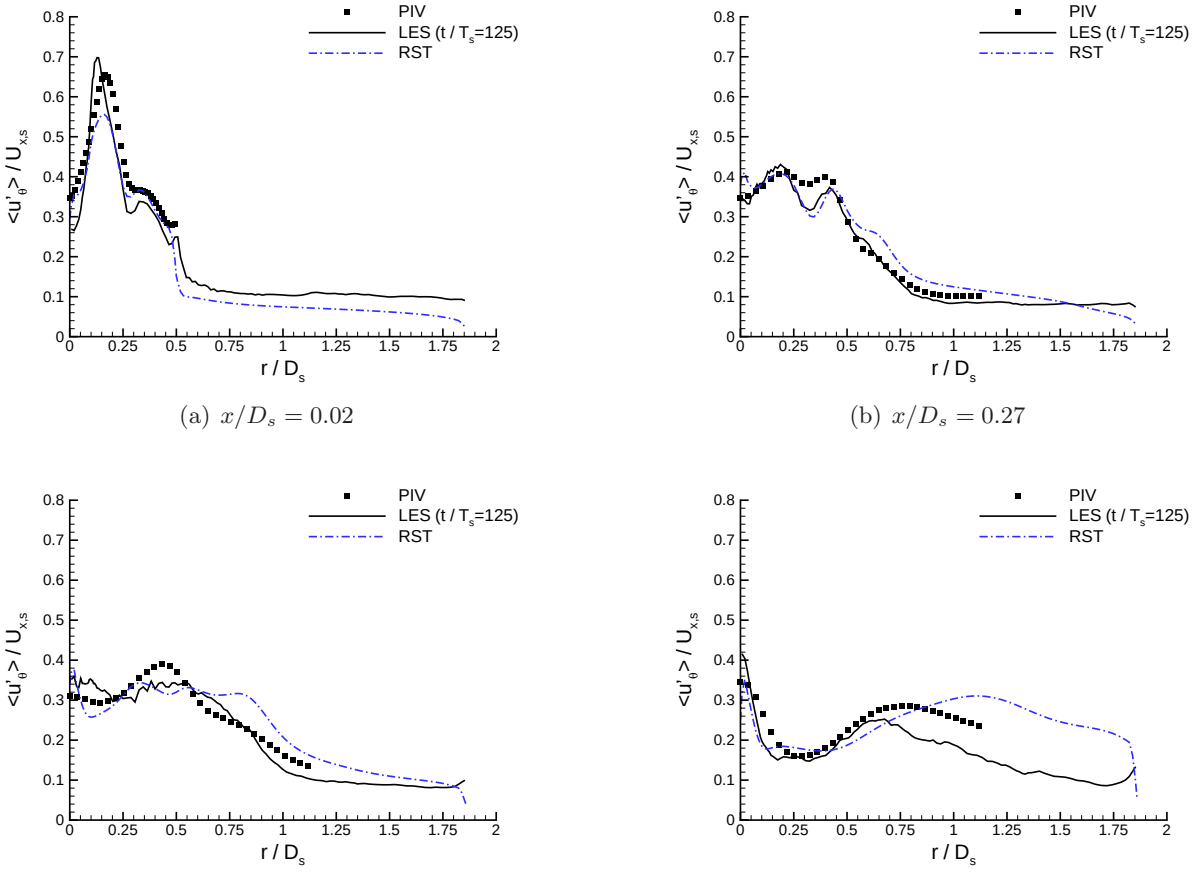

(a) $x/D_s = 0.02$

(b) $x/D_s = 0.27$

(c) $x/D_s = 0.53$

(d) $x/D_s = 1.06$

Figure 6.21: Comparison of r.m.s radial velocity against conditioned LES ($t/T_s = 125$) and corrected PIV at various axial locations in expansion chamber

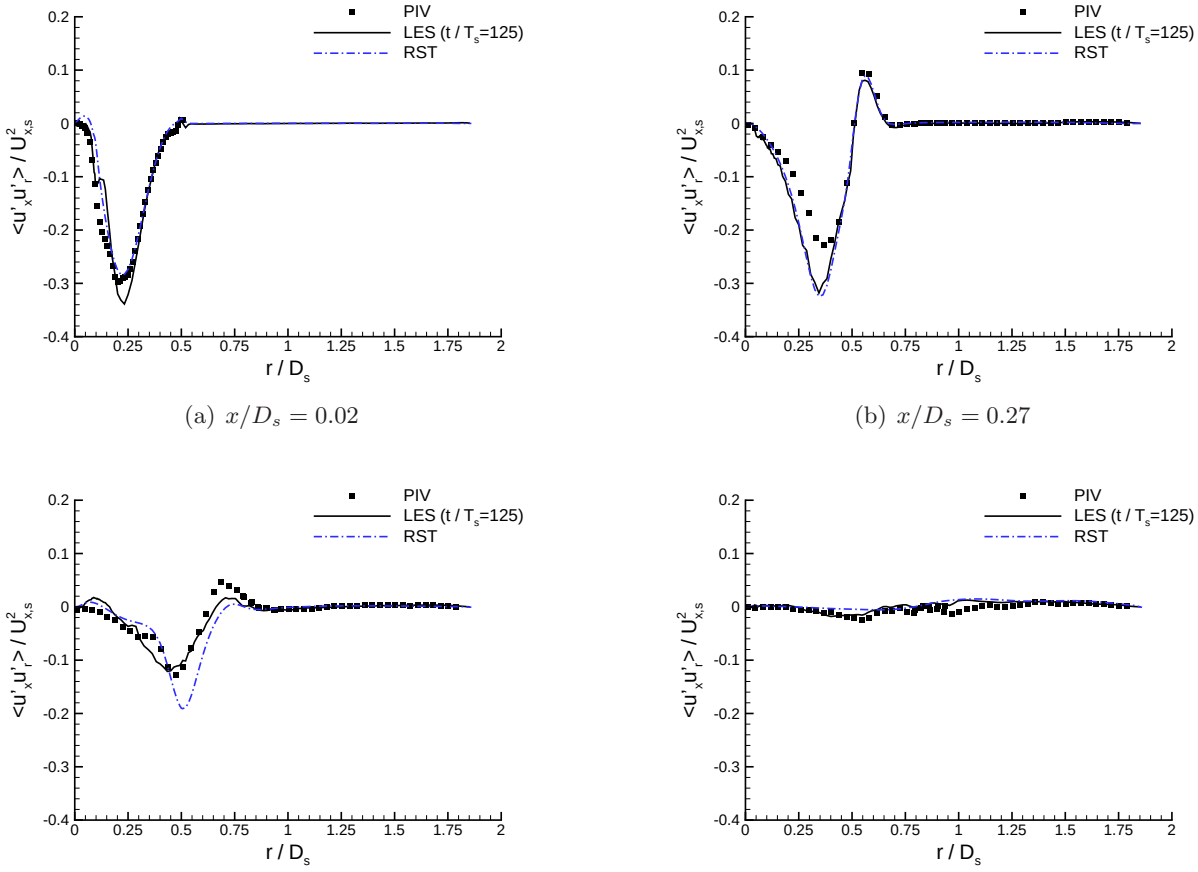

(a) $x/D_s = 0.02$

(b) $x/D_s = 0.27$

(c) $x/D_s = 0.53$

(d) $x/D_s = 1.06$

Figure 6.22: Comparison of axial-radial stress against conditioned LES ($t/T_s = 125$) and PIV at various axial locations in expansion chamber

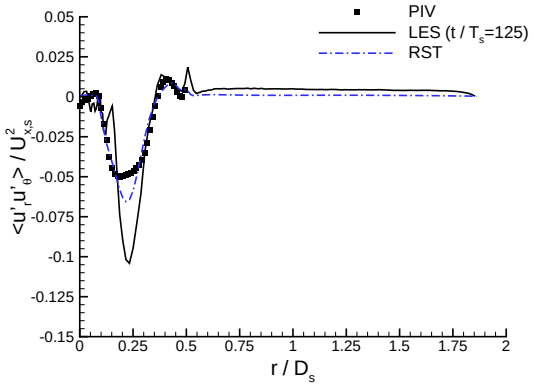

(a) $x/D_s = 0.02$

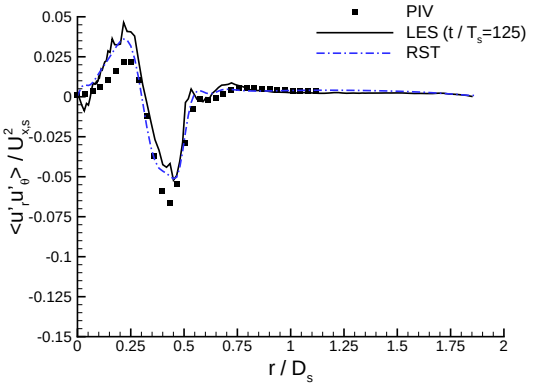

(b) $x/D_s = 0.27$

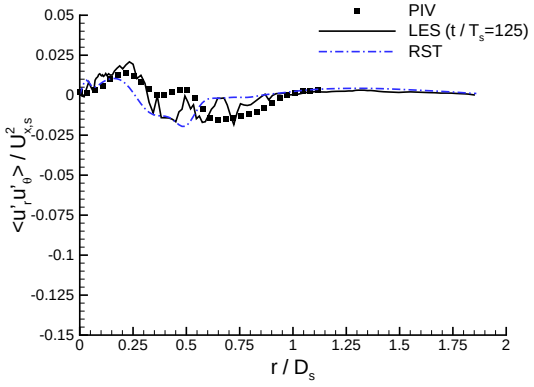

(c) $x/D_s = 0.53$

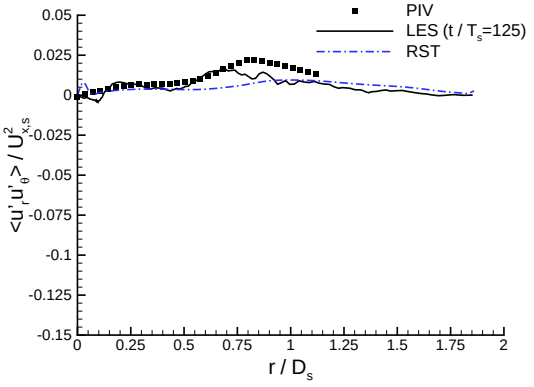

(d) $x/D_s = 1.06$

Figure 6.23: Comparison of radial-tangential stress against conditioned LES ($t/T_s = 125$) and PIV at various axial locations in expansion chamber

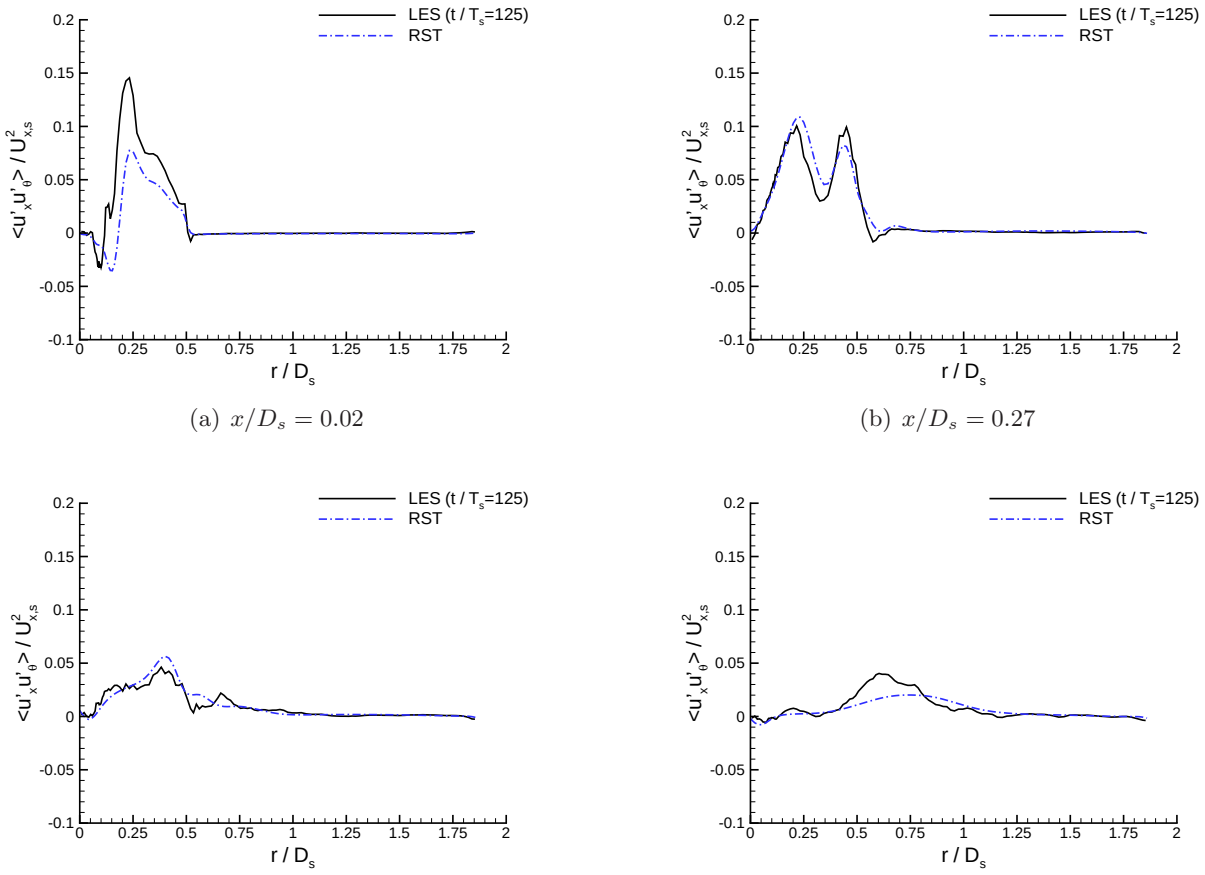

(a) $x/D_s = 0.02$

(b) $x/D_s = 0.27$

(c) $x/D_s = 0.53$

(d) $x/D_s = 1.06$

Figure 6.24: Comparison of axial-tangential stress against conditioned LES ($t/T_s = 125$) at various axial locations in expansion chamber

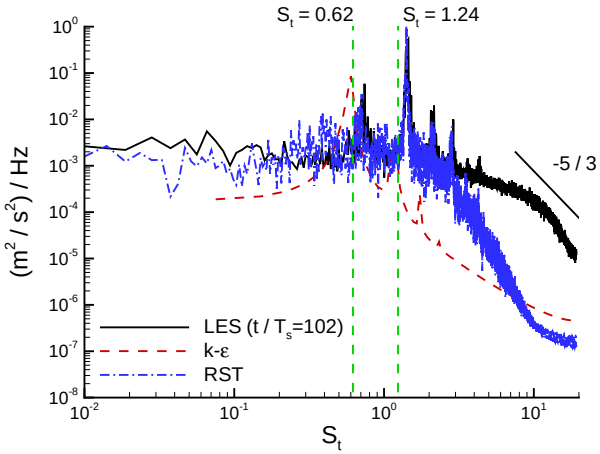

(a) Axial velocity

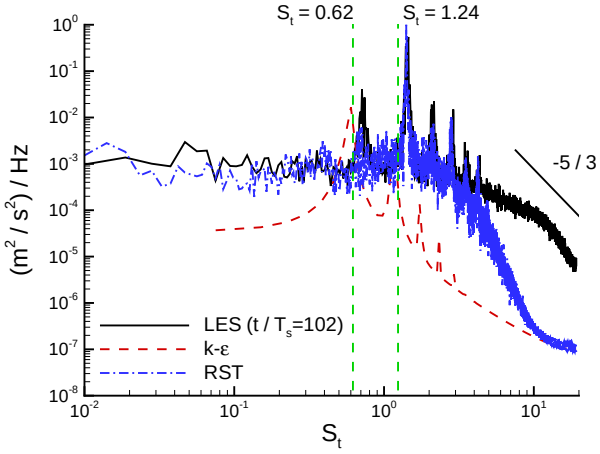

(b) Radial velocity

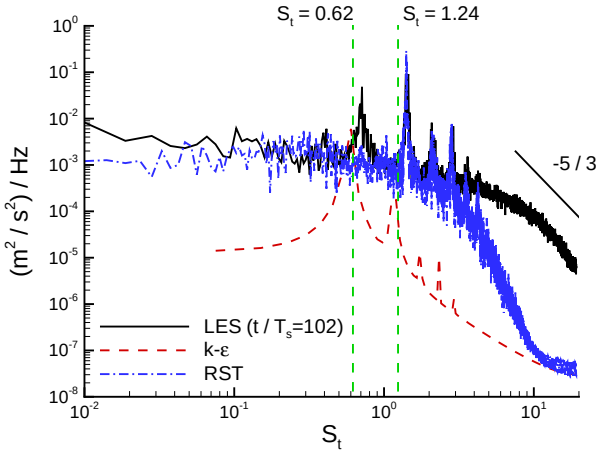

(c) Tangential velocity

Figure 6.25: PSDs of axial, radial and tangential velocity at $x/D_s = 0.27$, $r/D_s = 0.24$ for $k-\epsilon$, RST and conditioned LES ($t/T_s = 102$). Vertical dashed lines indicated expected frequencies of Midgley [13].

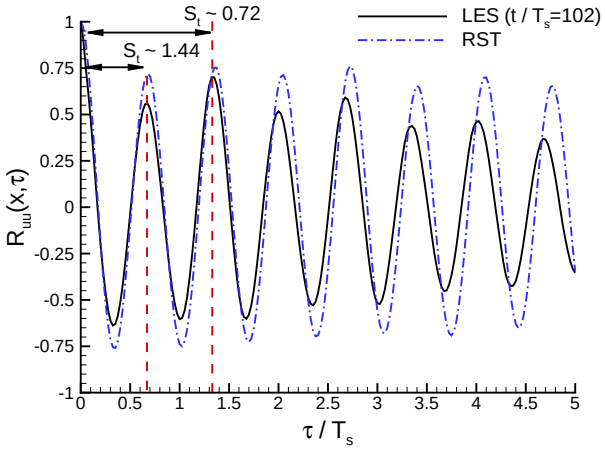

(a) Axial velocity

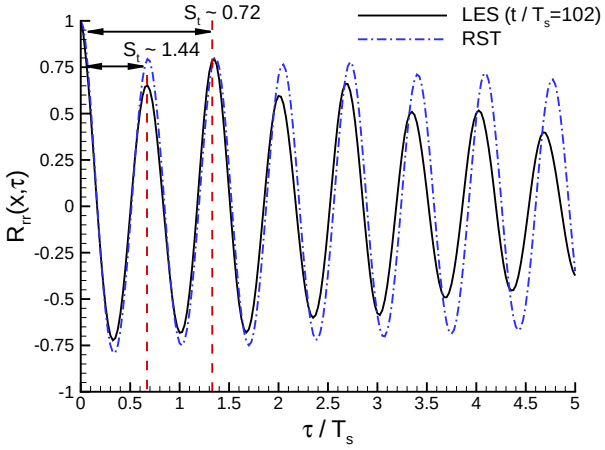

(b) Radial velocity

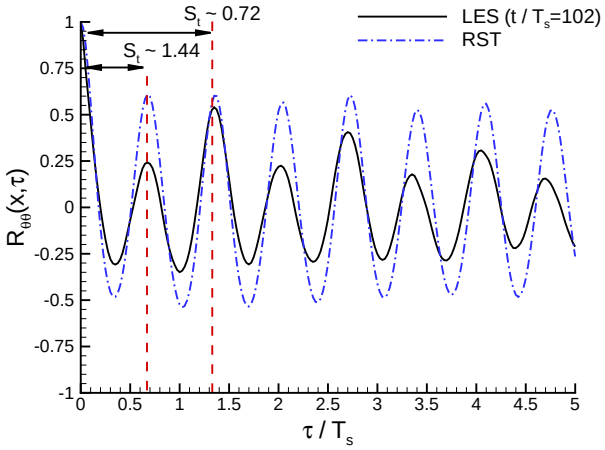

(c) Tangential velocity

Figure 6.26: Autocorrelations for RST model and conditioned LES ($t/T_s = 102$) at $x/D_s = 0.27$, $r/D_s = 0.24$, $\theta = \pi$

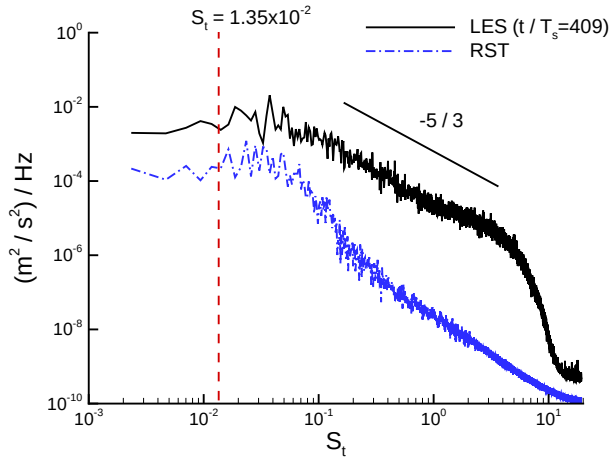

(a) $r/D_s = 0.08$

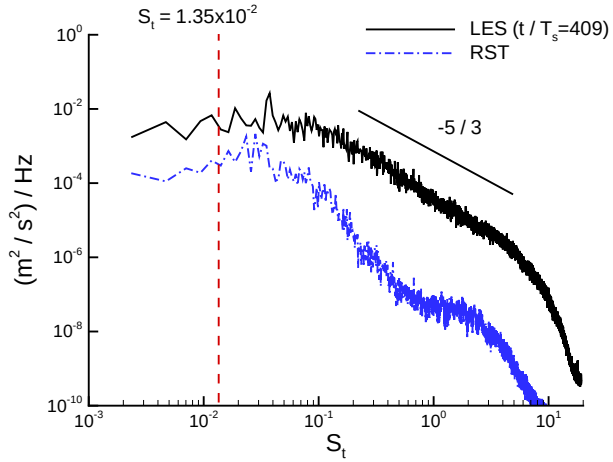

(b) $r/D_s = 0.16$

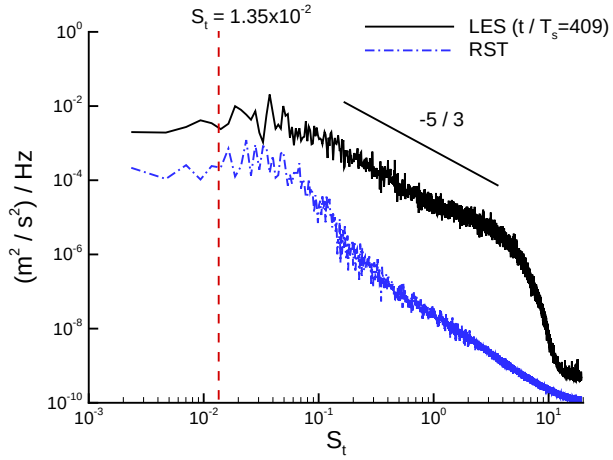

(c) $r/D_s = 0.24$

Figure 6.27: PSD of axial velocity for RST model and complete LES ($t/T_s = 409$) at $x/D_s = 2.65$ for various radial locations. Vertical dashed line indicates expected PVC frequency of Syred et al. [38]

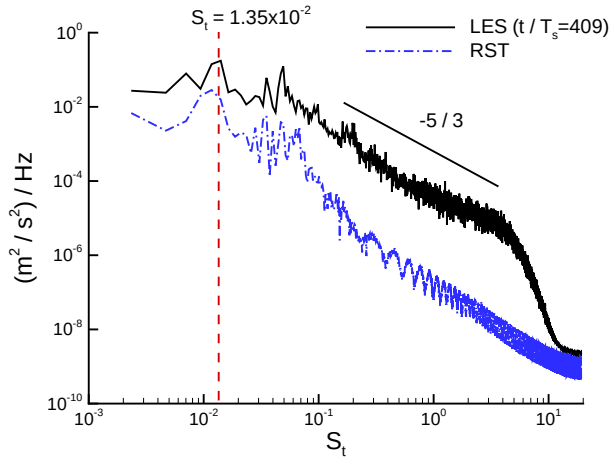

(a) $r/D_s = 0.08$

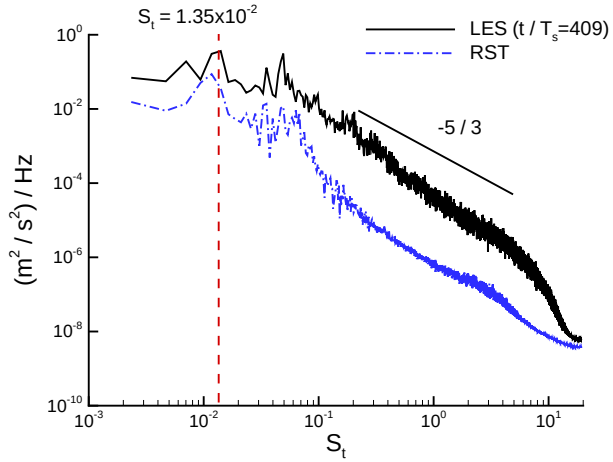

(b) $r/D_s = 0.16$

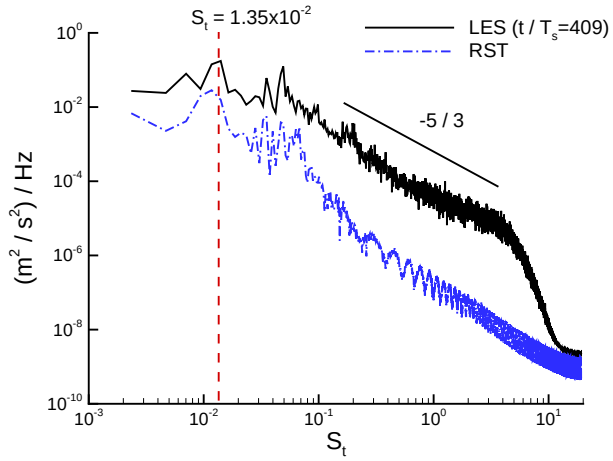

(c) $r/D_s = 0.24$

Figure 6.28: PSD of radial velocity for RST model and complete LES ($t/T_s = 409$) at $x/D_s = 2.65$ for various radial locations. Vertical dashed line indicates expected PVC frequency of Syred et al. [38]

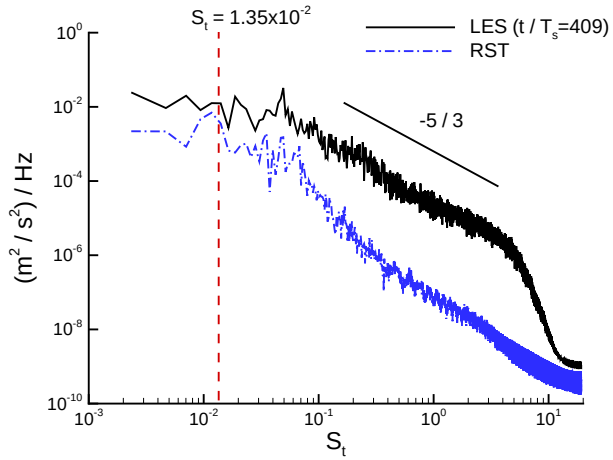

(a) $r/D_s = 0.08$

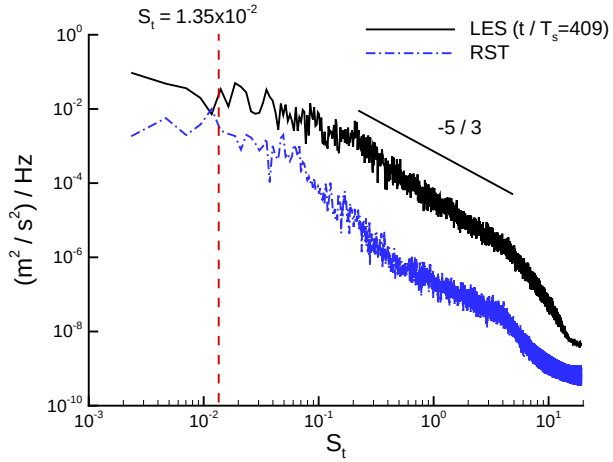

(b) $r/D_s = 0.16$

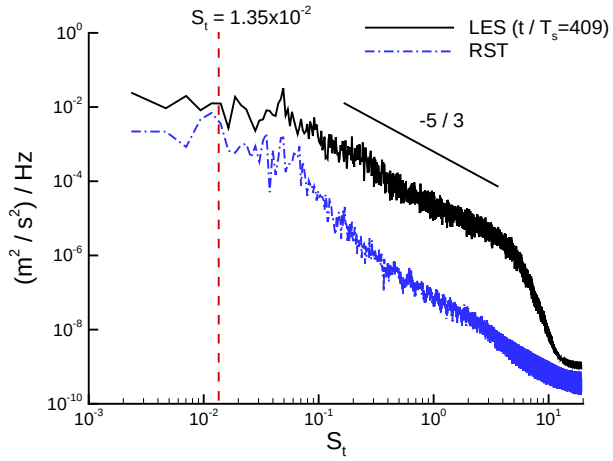

(c) $r/D_s = 0.24$

Figure 6.29: PSD of tangential velocity for RST model and complete LES ($t/T_s = 409$) at $x/D_s = 2.65$ for various radial locations. Vertical dashed line indicates expected PVC frequency of Syred et al. [38]

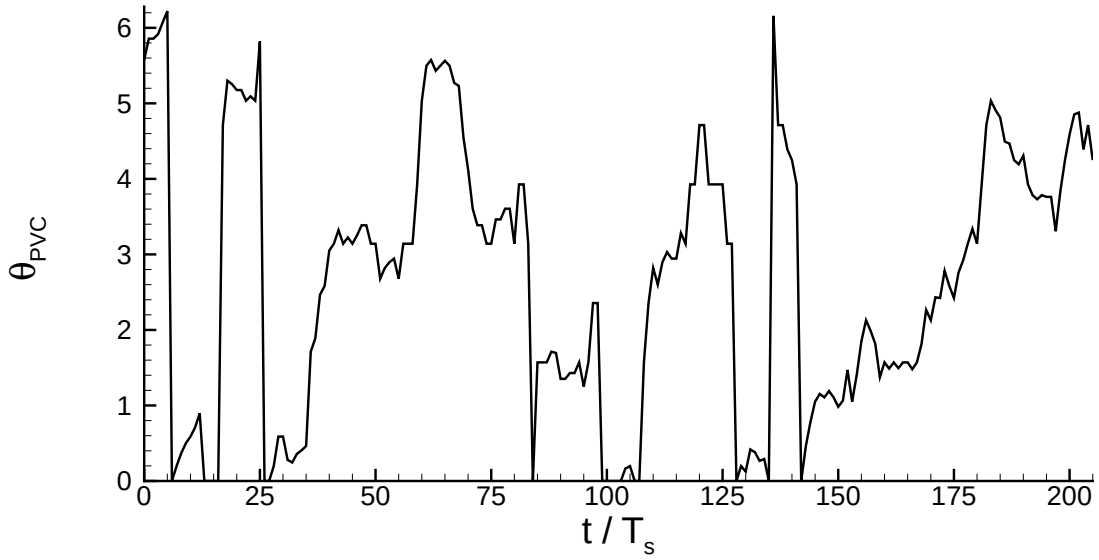

(a) $t/T_s = 0 - 205$

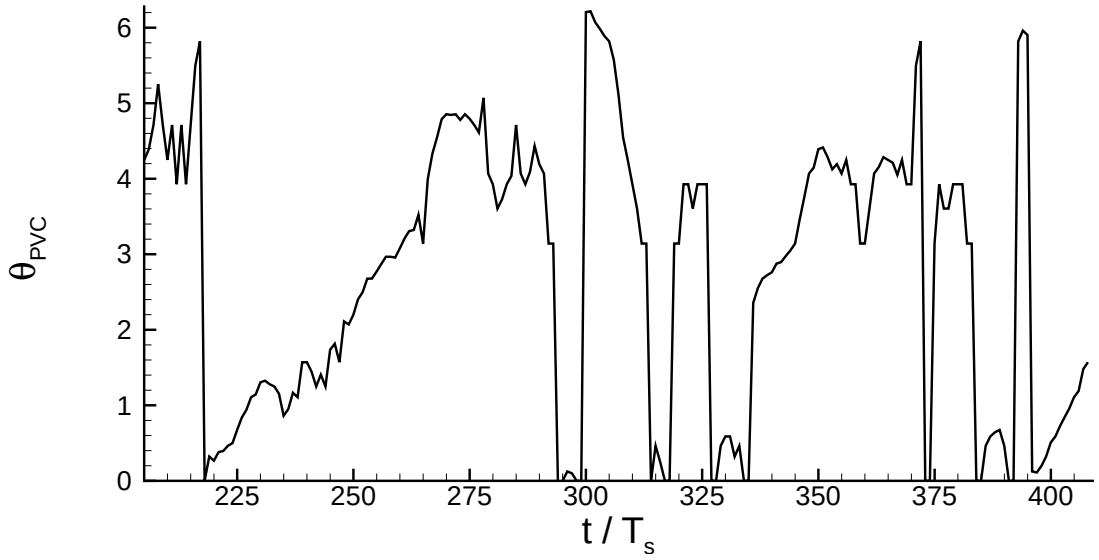

(b) $t/T_s = 205 - 409$

Figure 6.30: Angular location of PVC at $x/D_s = 2.39$ for RST model

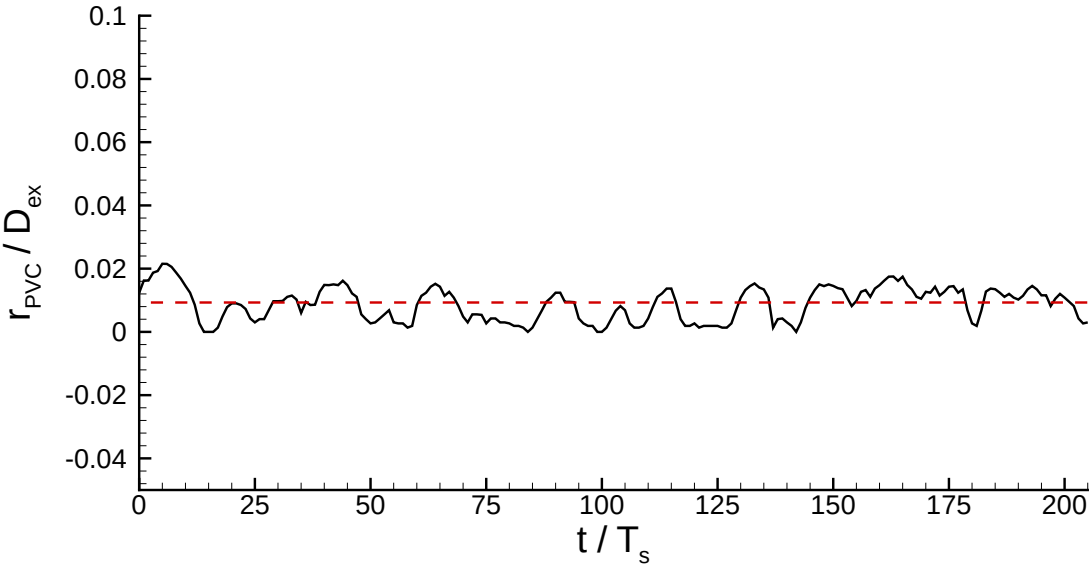

(a) $t/T_s = 0 - 205$

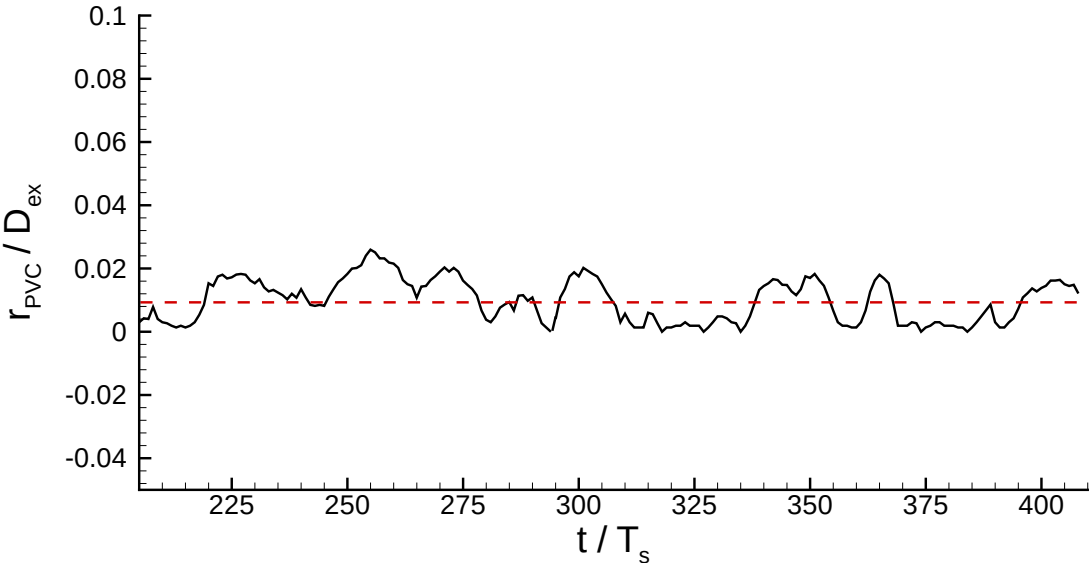

(b) $t/T_s = 205 - 409$

Figure 6.31: Radial displacement of PVC at $x/D_s = 2.39$ for RST model

Chapter 7

Summary, Conclusions and Recommendations

7.1 Summary and Conclusions

The primary objective of this thesis was to assess the suitability of LES and URANS CFD methodologies to flowfields characteristic of swirl-stabilised combustion systems. An essential requirement of this was that frequencies of *all* aerodynamic modes should be predicted with a high degree of fidelity. This is because if any of these frequencies are consistent with prevalent acoustic modes within the combustor there is a potential for flow-acoustic coupling which may reinforce acoustic oscillations and drive combustion instabilities via the Rayleigh criterion (Equation 1.1). This assessment was made under isothermal conditions to avoid the complications that arise in reacting flow. An industrial Turbomeca swirl injector was selected as a suitable test case as this exhibits similar unsteady behaviour under reacting and isothermal conditions [12].

As the level of swirl is known to exert a strong influence on the aerodynamic modes and characteristic frequencies of combustion systems, PIV was used to explore a range of S_{N} by varying the inlet swirl vane angle ($\alpha_1 = 30°, 20°, 15°$ and $10°$) of a derivative of the the Turbomeca design. To ensure the capture of high-quality experimental data, all measurements were performed in water as the reduction in working velocities relative to air allow key instrumentation setup parameters, such as inter-frame time, to be optimised and errors such as particle response time and velocity lag to be reduced through the use of neutrally buoyant tracer particles. Despite a careful adherence to 'best-practice' guidelines [72, 13] there are a number of error sources inherent to the PIV technique that cannot be completely eliminated during acquisition. A procedure was developed in this thesis to account for the effect of perspective error on first-order time-mean statistics and the methodology proposed by Hollis [72] was used to correct for sub-grid filtering effects on r.m.s quantities. Based on a qualitative assessment of instantaneous velocity data and a range of CS eduction techniques it was found that $\alpha_1 = 30°$ contained near (shear-layer

vortices) and far-field (PVC) instability modes which previous studies at similar S_N [13, 38] have shown to exhibit characteristic frequencies which differ by around two orders of magnitude. The coherence of these modes and far-field normal Reynolds-stress anisotropy significantly decreased for $\alpha_1 = 20°$ and $\alpha_1 = 15°$ and no coherent vortex motion was detected for $\alpha_1 = 10°$. From these observations it was decided that $\alpha_1 = 30°$ would be the most challenging test case with which to assess the suitability of LES and URANS.

Following a preliminary LES grid refinement study it was found that the wall-function approach within the swirl duct was not suitable for capturing the near-field CS observed experimentally. However, a further calculation performed with an increased near-wall resolution resulted in the appearance of this feature. In order to validate LES against experiment, an ensemble dataset was collected that included a sufficient number of independent samples for converged first and second-order statistics and an adequate number of PVC cycles for a detailed frequency analysis. Regular monitoring of this revealed a bimodal behaviour at the swirler exit similar to that observed experimentally which was characterised by the presence or absence of CS. It was found that first-order statistics based on all members of ensemble were in reasonable agreement with experiment, however second-order r.m.s quantities were not well represented. It was argued that the most notable discrepancies could be attributed to the details of CS from within the swirler as these contribute significantly to turbulence levels. Since vortex transition occurred on a timescale several orders of magnitude larger than the LES sampling interval this placed severe restrictions on the number of cycles that could be captured. To provide a more representative comparison with experiment, a second 'conditioned' dataset was created corresponding to the period during which CS were observed at the swirler exit. The agreement of first and second-order statistics (including turbulent shear-stresses which were found to be largely unreported in the available literature) of the conditioned set with experiment were found to be much improved. Velocity spectra derived from LES found that the all-important frequency content of near and far-field instability modes was predicted in accordance with experiment.

From volumetric information provided by validated LES predictions it was found that frequencies associated with near-field CS persist throughout the entire swirl duct which may have implications for air-fuel mixing. In the near-field 4 equi-distant helices were identified which formed upstream of the swirler exit with vortex filament windings which opposed the bulk flow. A PDF showed the most probable angle between these and time-mean velocity vectors was close to π radians suggesting the K-H instability as a formative mechanism. A similar helical structure (PVC) was identified in the vicinity of the far-field centreline which also had vortex filament winding opposed to the bulk flow.

Although $k-\epsilon$ URANS performed on an identical grid to LES revealed an initial vortex structure

at the swirler exit similar to that observed experimentally this underwent a transitory phase and the final self-sustaining solution reached after further timesteps was inconsistent with experiment. Similarly, the expected PVC in the far-field was not predicted as the aerodynamic centre was coincident with the geometric centre at all times. A thorough investigation into various numerics (under-relaxation and Δt), computational grids (polar and O-grid) and CFD solvers (Delta and Fluent) found that these exerted no influence on CS development. It was suggested that high levels of turbulent viscosity within shear-layers shed from the swirler and in the vicinity of the centreline were a more probable cause of these discrepancies. As a result of qualitative differences and details of the $k-\epsilon$ model first-order statistics and near-field velocity spectra were in poor agreement with experiment.

In contrast to the $k-\epsilon$ model, the qualitative details of the both near and far-field instability modes predicted by the RST on an identical grid to LES were in accordance with experiment. First and second-order statistics derived from an ensemble dataset of identical length to that used for LES showed a good overall agreement with PIV measurements. Although velocity fluctuations in the far-field were suppressed relative to LES due to an increased turbulent viscosity a large accumulation of energy was observed close to the expected precessional frequency of the PVC. From near-field spectral analysis a peak close to $S_t = 1.24$ (vortex *pair*) was present in all three velocity components, however the expected HWA frequency of $S_t = 0.62$ (*single* vortex) had a comparable amplitude to the surrounding turbulent broadband frequencies and could not be distinguished clearly. It was argued that since URANS only provides the coherent, or phase-averaged, component of fluctuating motion the resolved CS are more coherent in both time and space relative to LES which was able to detect both frequencies. As a result of this increase coherence (which was quantified via temporal auto-correlations of velocity) the RST model is unable to distinguish between the motion of a single vortex and a vortex pair and hence the differences in velocity spectra.

Despite the relatively modest computational cost of URANS which is between one-third (RST) and an order of magnitude ($k-\epsilon$) than that demanded by LES, only LES captures the all-important frequency content in accordance with experiment and, thus, only LES can be recommended for use in swirl injector flows. The increased cost is believed to be an absolutely worthwhile expense because of the high fidelity of the predicted results in the important area of flow instabilities.

7.2 Future Work

Although 2C-PIV is generally well suited to the flows studied in this thesis, the planar nature of the technique makes it difficult to explain fully 3D flow behaviour and companion CFD predictions were necessary for a more complete understanding of the helical instability modes

characteristic of swirl-stabilised combustion systems. Recent developments in image processing algorithms and a continued increase in available computing power now enables the instantaneous measurement of all three velocity components in a complete 3D measurement volume via Tomographic PIV. This technique should be utilised to explore further the highly unsteady flowfield produced by the Turbomeca swirler and verify the CFD results presented here in terms of the predicted spatial structure of the dominant instability modes.

A major focus of the computational work presented in this thesis has been on the ability of LES and URANS CFD methodologies to capture the frequency content of all aerodynamic modes under isothermal conditions. Although this is of great practical importance the next logical steps have to be related to the influence of CS on mixing (passive scalar) in the near and far-field of the swirler and how combustion affects the formation of dominant instability modes and unsteady heat release.

Additional simulations could be performed at the lower levels of swirl investigated experimentally, however, even in the event of an improved performance from URANS the overall suitability of the technique to swirl injector applications would still be under scrutiny based on the calculations presented in this thesis.

The majority of fuel injectors utilised in aeronautical applications typically employ multiple swirl streams for fuel-air mixing and primary zone stabilisation rather than the single stream considered here. It would be of further interest to assess to performance the CFD methodologies for these configurations.

Bibliography

[1] Jeong, J. and Hussain, F., "On the identification of a vortex," *J. Fluid Mech.*, 1995, pp. 69–94.

[2] Mongia, H. C., Held, T. J., Hsiao, G. C., and Pandalai, R. P., "Challenges and progress in controlling dynamics in gas turbine combustors," *Journal of Propulsion and Power*, 2003, pp. 822–829.

[3] Huang, Y. and Yang, V., "Dynamics and stability of lean-premixed swirl-stabilized combustion," *Progress in Energy and Combustion Science*, Vol. 35, 2009, pp. 293–364.

[4] Putnam, A. A., *Combustion-driven oscillations in industry*, Elsevier, 1971.

[5] "ICAO environmental report 2007," *ICAO*, 2007.

[6] Coats, C., "Coherent structures in combustion," *Prog. Energy Combust. Sci.*, Vol. 22, 1996, pp. 427–509.

[7] Pope, S. B., *Turbulent flows*, Cambridge University Press, 2000.

[8] Rogers, D. E. and Marble, F. E., "A mechanism for high frequency oscillations in ramjet combustors and afterburners," *Jet Propulsion*, 1956, pp. 456–462.

[9] Paschereit, C. O., Gutmark, E., and Weisenstein, W., "Structure and control of thermoacoustic instabilities in a gas-turbine combustor," *Combust. Sci. and Tech.*, 1998, pp. 213–232.

[10] Li, G. and Gutmark, J., "Experimental study of large coherent structure in a swirl-dump combustor," *42nd AIAA Aerospace Sciences Meeting and Exhibit 5-8 January 2004, Reno Nevada*, 2004.

[11] Schadow, K. and Gutmark, E., "Combustion instability related to vortex shedding in dump combustor and their passive control," *Progess in Energy and Combustion Science*, Vol. 18, 1992, pp. 117–132.

[12] Janus, B., Dreizler, A., and Janicka, J., "Experimental study on stabilization of lifted swirl falmes in a model gt combustor," *Flow, Turbulence and Combustion*, Vol. 75, 2005, pp. 293–315.

[13] Midgley, K. K., *An isothermal experimental study of the unsteady fluid mechanics of gas turbine fuel injector flowfields*, Ph.D. thesis, Loughborough University, 2005.

[14] Midgley, K. K., Spencer, A., and McGuirk, J. J., "Unsteady flow structures in radial swirler fed fuel injectors," *Journal of Engineering for Gas Turbines and Power*, October 2005, pp. 755–764.

[15] Midgley, K. K., Spencer, A., and McGuirk, J. J., "Vortex breakdown in swirling fuel injector flows," *ASME J. Eng. Gas Turbine Power*, Vol. 130, 2008.

[16] Gupta, A. K., *Swirl flows*, Abacus Press, 1984.

[17] Sloan, D. G., Smith, P. J., and Smoot, L. D., "Modeling of swirl in turbulent flow systems," *Prog. Energy Combust. Sci*, Vol. 12, 1984, pp. 163–250.

[18] Kerr, N. M. and Fraiser, D., "Swirl effects of axi-symmetrical turbulent jets," *J. Inst. Fuel*, Vol. 38, 1965, pp. 519–526.

[19] Ruith, M. R., Chen, P., Meiburg, E., and Maxworthy, T., "Three-dimensional vortex breakdown in swirling jets and wakes: direct numerical simulation," *J. Fluid Mech.*, Vol. 486, 2003, pp. 331–378.

[20] Lucca-Negro, O. and O'Doherty, T., "Vortex breakdown: a review," *Prog. in Energy and Combustion Science*, Vol. 27, 2001, pp. 431–481.

[21] Escuider, M. P., "Vortex breakdown: observations and explanations," *Prog. Aerospace Science*, Vol. 25, 1988, pp. 189–229.

[22] Li, H. and Tomita, Y., "Characteristics of swirling flow in a circular pipe," *Transactions of the ASME*, 1994, pp. 370–373.

[23] Dellenbeck, P., Metzger, D., and Neitzel, G., "Measurements in turbulent swirling flow through an abrupt axi-symmetric expansion," *AIAA*, 1988, pp. 669–681.

[24] Sarpkaya, T., "Vortex breakdown in swirling conical flows," *AIAA*, Vol. 9, 1971, pp. 1792–9.

[25] Sarpkaya, T., "On stationary and travelling breakdowns," *J Fluid Mech*, Vol. 45, 1971, pp. 545–559.

[26] Leibovich, S., "Vortex stability and breakdown: survey and extension," *AIAA Journal*, 1984, pp. 1192–1206.

[27] Faler, J. H. and Leibovich, S., "Disrupted states of vortex flow and vortex breakdown," *Phys Fluids*, Vol. 20, 1977, pp. 1385–1400.

[28] Faler, J. H. and Leibovich, S., "An experimental map of the internal structure of a vortex breakdown," *Journal of Fluid Mechanics*, 1977, pp. 313–335.

[29] Benjamin, T., "Theory of the vortex breakdown phenomenon," *J Fluid Mech*, Vol. 14, 1962, pp. 593–629.

[30] Hall, M. G., "A new approach to vortex breakdown," *Proceedings of the Heat Transactions and Fluid Mechanics Institute, University of California, San Diego, La Jolla*, 1967, pp. 319–340.

[31] Howard, L. N. and Gupta, A. S., "On the hydrodynamic and hyrodmagnetic stability of swirling flows," *J Fluid Mech*, Vol. 14, 1962, pp. 463–476.

[32] Leibovich, S. and Stewartson, K., "A sufficient condition for the instability of columnar vortices," *Journal of Fluid Mechanics*, Vol. 126, pp. 335–356.

[33] Rayleigh, L., "On the dynamics of revolving fluids," *Proceeding of the Royal Society, London*, No. 93, 1916.

[34] Hall, M. G., "Vortex breakdown," *Annual Reviews of Fluid Mechanics*, Vol. 86, 1972, pp. 313.

[35] Leibovich, S., "The structure of vortex breakdown," *Annual Reviews of Fluid Mechanics*, Vol. 10, 1978, pp. 221–246.

[36] Grosjean, N., Graftieaux, L., Michard, M., Hübner, W., Tropea, C., and Volkert, J., "Combining LDA and PIV for turbulence measurements in unsteady swirling flows," *Meas. Sci. Tecnol.*, 1997, pp. 1523–1532.

[37] Claypole, T. and Syred, N., "Coherent structures in swirl generators and combustors," *Proceedings of the Symposium of Vortex Flows, Winter Meeting of ASME, Chicago*, 1980, pp. 47–56.

[38] Syred, N., O'Doherty, T., and Froud, D., "The interaction of the precessing vortex core and reverse flow zone in the exhaust of a swirl burner," *Proceedings of the Institute of Mechanical Engineers, Part A*, Vol. 208, 1994, pp. 27–35.

[39] Syred, N., "A review of oscillation mechanisms and the role of the precessing vortex core (PVC) in swirl combustion systems," *Progress in Energy and Combustion Science*, Vol. 32, pp. 93–161.

[40] Liang, H. and Maxworthy, T., "An experimental investigation of swirling jets," *J. Fluid Mech.*, 2005, pp. 115–159.

[41] Guo, B., Langrish, T. A. G., and Fletcher, D. F., "Simulation of turbulent swirl flow in an axisymmetric sudden expansion," *AIAA Journal*, Vol. 39, 2001, pp. 96–102.

[42] Hallett, W. L. H. and Gunther, R., "Flow and mixing in swirling flow in a sudden expansion." *Canadian Journal of Mechanical Engineering.*, Vol. 62, Feb 1984, pp. 149–155.

[43] Dellenback, P. A., Metzger, D. E., and Neitzel, G. P., "Measurements in turbulent swirling flow through an abrupt axisymmetric expansion." *AIAA*, Vol. 26, No. 6, 1988, pp. 669–681.

[44] Guo, B., Langrish, T., and Fletcher, D. F., "CFD simulation of precession in sudden pipe expansion flows with low inlet swirl," *Appl. Math. Modell*, Vol. 26, 2002, pp. 1–15.

[45] Wegner, B., Maltsev, A., Schneider, C., Sadiki, A., Dreizler, A., and Janicka, J., "Assessement of unsteady RANS in predicting swirl flow instability based on LES and experiments," *International Journal of Heat and Fluid Flow*, Vol. 25, 2004, pp. 528–536.

[46] Scheider, C., Repp, S., Sadiki, A., Dreizler, A., and Janicka, J., "The effect on swirling number variation on turbulent transport and mixing processes in swirling recirculating flows: experimental and numerical investigations," *Second International Symposium on Turbulence and Shear Flow Phenomena*, Vol. 3, 2001, pp. 363–368.

[47] Bowen, P., O'Doherty, T., and Lucca-Negro, O., "Rotating instabilities in swirling and cyclonic flows, part b: theoretical analysis," *Thermal Energy Engineering and the Environment*, edited by D. Zhang and G. Nathan, Department of Chemical Engineering, The University of Adelaide, 1998, pp. 197–220.

[48] Jochmann, P., Sinigersky, A., Hehle, M., Schäfer, O., Koch, R., and Bauer, H. J., "Numerical simulation of precessing breakdown," *International Journal of Heat and Fluid Flow*, Vol. 27, 2006, pp. 192–203.

[49] Speziale, C. G., "Analytical methods for the development of reynolds-stress closures in turbulence," *Annual Review of Fluid Mechanics*, Vol. 23, 1991, pp. 107–157.

[50] Dunham, D., Spencer, A., Dianat, M., and McGuirk, J. J., "Comparison of URANS and LES CFD methodologies for air swirl fuel injectors," *Journal of Engineering for Gas Turbines and Power*, Vol. 130, 2008, pp. 1063–1078.

[51] Tang, G., Yang, Z., and McGuirk, J. J., "Large eddy simulation of flow in lean premixed prevapourised combustor geometries," *Advances in Turbulence VIII*, 2001, pp. 227–230.

[52] Wang, S., Hsieh, S. Y., and Yang, V., "Unsteady flow evolution in swirl injector with radial entry. 1. stationary conditions," *Physics of Fluids*, Vol. 17, 2005.

[53] Tang, G., Yang, Z., and McGuirk, J. J., "Large eddy simulation of isothermal confined swirling flow with recirculation," *Engineering and Turbulence Modelling and Experiments 5*, edited by W. Rodi and N. Fueyo, 2002, pp. 885–894.

[54] Garcia-Villalba, M. and Fröhlich, J., "LES of a free annular swirling jet - dependence of coherent structures on a pilot jet and the level of swirl," *International Journal of Heat and Fluid Flow*, Vol. 27, 2006, pp. 911–923.

[55] Garcia-Villalba, M., Fröhlich, J., and Rodi, W., "Identification and analysis of coherent structures in the near field of a turbulent unconfined annular swirling jet using large eddy simulation," *Physics of Fluids*, Vol. 18, 2006.

[56] Huang, Y. and Yang, V., "Effect of swirl on combustion dynamics in a lean-premixed swirl-stabilized combustor," *Proceedings of the Combustion Instituite*, Vol. 30, 2005, pp. 1775–1782.

[57] Garcia-Villalba, M. Fröhlich, J. and Rodi, W., "Numerical simulations of isothermal flow in a swirl burner," *Proceedings of GT2006 ASME Turbo Expo 2006: Power for Land, Sea and Air May 8-11, 2006, Barcelona, Spain*, 2006, pp. 1–11.

[58] Wegner, B., Staufer, M., Sadiki, A., and Janicka, J., "Study of flow and mixing in a generic gt combustor using les," *Flow Turbulence Combust*, 2007, pp. 911–923.

[59] Roux, S., Lartigue, G., Poinsot, T., Meier, U., and Berat, C., "Studies of mean and unsteady flow in a swirler combustor using experiments, acoustic analysis and large eddy simulations," *Combustion and Flame*, 2005.

[60] Kline, S. and Robertson, S., "Quasi-coherent structures in the turbulent boundary layer part i: status report on a community wide summary of the data," *Proceedings of Zaric Memorial Conference, New York*, 1989, pp. 200–217.

[61] Adrian, R. J., Christensen, K. T., and Liu, Z. C., "Analysis and interpretation of instantaneous turbulent velocity fields," *Experiments in Fluids*, Vol. 29, 2000, pp. 275–290.

[62] Bonnet, J. P., Delville, J., Glauser, M. N., Antonia, R. A., Bisset, D. K., Cole, D. R., Fiedler, H. E., Garmen, J. H., Hilbergy, D., Jong, J., Kevlahan, N. K. R., Ukeiley, L. S., and Vincendeau, E., "Collaborative testing of eddy structure identification methods in free turbulent shear flow," *Experiments in Fluids*, Vol. 25, 1998, pp. 197–225.

[63] Goy, C., James, S., and Rea, S., *Monitoring combustion instabilities: E.ON UK's experience*, Vol. 210 of *Progress in Astronautics and Aeronautics*, chap. 8, 2005, pp. 163–175.

[64] Lefebvre, A. H., *Gas turbine combustion*, Taylor and Francis, 2nd ed., 1998.

[65] Wulff, A. and Hourmouziadis, "Technology review of aeroengine pollutant emissions," *Aerospace Science and Technology*, 1997, pp. 557–572.

[66] Chigier, N. A. and Beer, J. M., *Combustion aerodynamics*, Applied Science Publishers, England, 1972.

[67] S., W., Yang, V., Hsiao, G., and Mongia, H., "Large eddy simulation of gas turbine swirl injector flow dynamics," *Journal of Fluid Mechanics*, Vol. 583, 2007, pp. 99–122.

[68] Lartigue, G., Meier, U., and Berat, C., "Experimental and numerical investigation of self-excited combustion oscillations in a scaled gas turbine combustor," *Applied Thermal Engineering*, Vol. 25, 2004, pp. 1583–1592.

[69] "Modelling of low emissions combustors using large eddy simulations," Tech. rep., 2004, MOLECULES Report.

[70] Escuider, M. P., "Vortex breakdown and the criterion for its occurrence," *Topics in Atmospheric and Oceanographic Sciences: Intense Atmospheric Vortices*, 1982, pp. 247–258.

[71] Spencer, A., *Gas turbine combustor port flows*, Ph.D. thesis, Loughborough University, 1998.

[72] Hollis, D., *Particle image velocimetry in gas turbine combustor flow fields*, Ph.D. thesis, Loughborough University, 2004.

[73] Khezzar, L., "Velocity measurements in near field of radial flow swirler," *Experiments in Thermal and Fluid Science*, 1998.

[74] Adrian, R. J., "Particle-imaging techniques for experimental fluid mechanics," *Annual Review of Fluid Mechanics*, Vol. 23, 1991.

[75] Elghobashi, S., "On predicting particle-laden turbulent flows," *Applied Scientific Research*, Vol. 52, 1994, pp. 309–329.

[76] Raffel, M., Willert, C., and Kompenhaus, J., *Particle image velocimetry*, Springer-Verlag, 1998.

[77] van de Hulst, H. C., *Light scattering by small particles*, John Wiley andsign Sons, Inc., New York (republished 1981 by Dover Publications, New York), 1957.

[78] Shan, J. W., Lang, D. B., and Dimotakis, P. E., "Scalar concentration measurements in liquid-phase flows with pulsed lasers," *Experiments in Fluids*, Vol. 36, 2004, pp. 268–273.

[79] Keane, R. and Adrian, R. J., "Optimisation of particle images velocimeters. part 1: double pulsed systems," *Meas. Sci. Technol*, Vol. 1, 1990, pp. 1202–1215.

[80] Prasad, A. K., "Particle image velocimetry," *Current Science*, Vol. 79, 2000, pp. 51–60.

[81] LaVision, *Tools for DaVis - DaVis FlowMaster software manual for DaVis 7.0*, 2005.

[82] Westerweel, J., "Fundamentals of digital particle image velocimetry," *Measurement Science and Tecnology*, Vol. 8, 1997, pp. 1379–1392.

[83] Westerweel, J., Adrian, R. J., Eggels, J., and Nieuwstadt, F. T. M., "Measurement with particle image velocimetry of fully developed turbulent pipe flow at low Reynolds number,," *Application of Laser Techniques to Fluid Mechanics, Part 1.2*, 1993.

[84] Hoest-Madsen, A. and Nielsen, A. H., "Accuracy of PIV measurements in turbulent flows," *ASME Laser Anemometry*, Vol. 229, 1995.

[85] Hinze, J. O., *Turbulence: An introduction to its mechanism and theory*, McGraw-Hill Book Company, Inc., 1959.

[86] Robinson, M. D., *Unsteady inlet condition generation for large eddy simulation CFD using particle image velocimetry*, Ph.D. thesis, Loughborough University, 2009.

[87] Montgomery, D. C. and Runger, G. C., *Applied statistics and probability for engineers*, John Wiley and Sons, Inc, 1994.

[88] Sagaut, P., *Large eddy simulation for incompressible flows - an introduction*, Springer, 2nd ed., 2004.

[89] Durbin, P., "A perspective on recent developments in RANS modeling," *Engineering Turbulence Modeling and Experiments 5*, edited by W. Rodi and N. Fueyo, Elsevier Sciences Ltd, 2002, pp. 3–16.

[90] Fröhlich, J. and von Terzi, D., "Hybrid LES/RANS methods for the simulation of turbulent flows," *Progress in Aerospace Sciences*, Vol. 44, 2008, pp. 349–377.

[91] Iaccarino, G. A., Ooi, X., Durbin, P., and Behnia, A., "Reynolds averaged simulation of unsteady separated flow," *Int. J. Heat and Fluid Flow*, 2003, pp. 147–156.

[92] Boussinesq, J., "Essai sur la theorie des eaux couranyes," *Mem. Pres. Acad. Sci*, Vol. 23, 1877, pp. 1–680.

[93] Launder, B. E. and Spalding, D. B., "The numerical computation of turbulent flows," *Cpmputer Methods in Applied Mech. and Eng.*, Vol. 3, 1974, pp. 269–289.

[94] Jones, W. P. and Launder, B. E., "The prediction of laminarization with a two-equation model of turbulence," *International Journal of Heat and Mass Transfer*, Vol. 15, 1972, pp. 301–314.

[95] Launder, B. E., Reece, G. J., and Rodi, W., "Progress in the development of a Reynolds-stress turbulence closure," *J. Fluid. Mech.*, Vol. 68, 1975, pp. 537–566.

[96] Daly, B. J. and Harlow, F. H., "Transport equations of turbulence," *Phys. Fluids*, Vol. 13, 1970, pp. 2634–2649.

[97] Rotta, J. C., "Statistische Theorie nichthomogener Turbulenz," *Z. Phys*, Vol. 129, 1951, pp. 547.

[98] Launder, B. E., "Second-moment closure: present... and future?" *Int. J. Heat and Fluid Flow*, Vol. 10, 1989, pp. 282–300.

[99] "Fluent 6.2 user's guide," .

[100] Smagorinsky, J., "General circulation experiments with the primitive equations; i. the basic experiment," *Monthly Weather Review*, Vol. 3, 1963, pp. 99–163.

[101] Clark, R. A., Ferziger, J. H., and Reynolds, W. C., "Evaluation of a subgrid-scale model using an accurately simulated turbulent flow," *J. Fluid. Mech.*, Vol. 91, 1979, pp. 1–16.

[102] Deardorff, J. W., "A numerical study of three-dimensional turbulent channel flow at large Reynolds numbers," *J. Fluid Mech.*, Vol. 41, 1970, pp. 453–480.

[103] Yang, Z. and McGuirk, J. J., "LES of a rotating turbulent pipeflow with two sub-grid-scale models," *Proc. of 1st Symposium on Turbulence and Shear Flow Phenomena, Santa Barbara, USA.*, 1999.

[104] Germano, M., Piomelli, U., Moin, P., and Cabot, W. H., "A dynamic subgrid-scale model eddy viscosity model," *Phys. Fluids A*, Vol. 3, 1991, pp. 1760–1765.

[105] Garcia-Villalba Navaridas, M., *Large eddy simulation of turbulent swirling jets*, Ph.D. thesis, uviversitätsverlag karlsrue, 2006.

[106] Lilly, D. K., "The representation of small-scale turbulence in numerical simulation experiments," *Proc. IBM Scientific Computing Symp. on Environmental Sciences*, 1967, pp. 195–210.

[107] Tang, G., Yang, Z., and McGuirk, J. J., "LES predictions of aerodynamic phenomena in LPP combustors," *ASME Paper 2001-GT-465*, 2001.

[108] Tang, G., Yang, Z., and McGuirk, J. J., "Numerical methods for large-eddy simulation in general coordinates," *International Journal for Numerical Methods in Fluids*, Vol. 46, 2004, pp. 1–18.

[109] Wang, K., *Large eddy simulation of turbulent variable density and reacting flows*, Ph.D. thesis, Loughborough University, 2007.

[110] Pope, S. B., "The calculation of turbulent recirculating flows in general orthogonal coordinates," *Journal of Computational Physics*, Vol. 26, 1978, pp. 192–217.

[111] Moin, P., "Progress in large-eddy simulation of turbulent flows," *AIAA*, 1997.

[112] Schumann, U., "Sub-grid scale model for finite difference simulations of turbulent flow in plane channels and annuli," *Jnl. of Comp. Phys*, Vol. 18, 1975, pp. 376.

[113] McGuirk, J. J. and Page, G. J., "Shock capturing using a pressure-correction method," *AIAA Journal*, Vol. 28, 1990, pp. 1751–1757.

[114] Trumper, M. T., *A study of nozzle exit boundary layers in high speed jet flows*, Ph.D. thesis, Loughborough University, 2006.

[115] Veloudis, I., *A study of subgrid scale modelling and inflow boundary conditions for large eddy simulation of wall-bounded flows*, Ph.D. thesis, Loughborough University, 2007.

[116] Salman, H., Page, G., and McGuirk, J. J., "Prediction of lobed mixer vortical structures with a $k - \epsilon$ turbulence model," *AIAA Journal*, Vol. 41, 2003, pp. 878–887.

[117] Birkby, P. and Page, G., "Numerical predictions of turbulent underexpanded sonic jets using a pressure-based methodology," *Proc Instn Mech Engrs*, Vol. 215, 2001, pp. 165–173.

[118] Page, G. J., "Delta user's guide," Loughborough University.

[119] Rhie, C. M. and Chow, W. L., "Numerical study of the turbulent flow past an airfoil with trailing edge separation," *AIAA*, Vol. 21, 1983, pp. 1525–1532.

[120] Patankar, S. V. and Spalding, D. B., "A calculation procedure for heat, mass and momentum transfer in three-dimensional parabolic flows," *Int. J. Heat and Fluid Flow*, Vol. 12, 1972, pp. 12–19.

[121] Leonard, B. P., "A stable and accurate convective modelling procedure based on quadratic upstream interpolation," *Comput. Methods Appl. Mech. Eng.*, Vol. 19, 1979, pp. 59–98.

[122] Lien, F. S. and Leschziner, M. A., "Assessment of turbulent transport models including non-linear RNG eddy-viscosity formulation and second-moment closure," *Computers and Fluids*, Vol. 23, 1994, pp. 983–1004.

[123] Kitoh, O., "Experimental study of turbulent swirling flow in a straight pipe," *Journal of Fluid Mechanics*, Vol. 225, 1991, pp. 445–479.

[124] Lumley, J. L., "Computational modeling of turbulent flows," *Advances in Appl. Mech*, Vol. 18, 1978, pp. 123–175.

[125] Graftieaux, L., Michard, M., and Grosjean, N., "Combining PIV, POD and vortex identification algorithms for the study of unsteady turbulent swirling flows," *Meas. Sci. Technol.*, 2001, pp. 1422–1429.

[126] Lu, X., Wang, S., Sung, H. G., Hsieh, S. Y., and Yang, V., "Large-eddy simulations of turbulent swirling flows injected into a dump chamber," *Journal of Fluid Mechanics*, Vol. 527, 2005, pp. 171–195.

[127] Durbin, P. A. and Medic, G., *Fluid dynamics with a computational perspective*, Cambridge University Press, 2007.

[128] Press, W. H., Teukolsky, S. A., Vetterling, W. T., and Flannery, B. P., *Numerical recipies in fortran*, Cambridge University Press, 2nd ed., 1992.

[129] Martin, J. E. and Meiburg, E., "On the stability of the swirling jet shear layer," *Phys. Fluids*, Vol. 6, No. 424, 1994.

[130] Nallasamy, M., "Turbulence models and their applications to the prediction of internal flows: a review," *Computers and Fluids*, Vol. 15, No. 2, 1987, pp. 151–194.

[131] Chang, D. and Tavoularis, S., "Unsteady numerical simulations of turbulence and coherent structures in axial flow near a narrow gap," *Transactions of the ASME*, Vol. 127, 2005, pp. 458–466.

[132] Bower, A. F., *Applied mechanics of solids*, CRC, 2009.

[133] Libby, P. A., *Introduction to turbulence*, Taylor & Francis, 1996.

[134] Robinson, M. D., "Xact user's guide," Tech. rep., Loughborough University Department of Aeronautical and Automotive Engineering, 2008.

[135] Hunt, J., Wray, A., and Moin, P., "Eddies, stream, and convergence zones in turbulent flows," *Center for Turbulence Research Report CTR-S88*, 1988, pp. 193–208.

Appendix A

Appropriate methods of presenting experimental and computational data in a concise and descriptive manner are considered in the following sections:

A-1 Statistical Description of Turbulence

A fundamental property of each instantaneous variable of a turbulent flow, $\phi(\vec{x}, t)$, is that it is a stochastic value. Several methods are used to characterise its nature based on single and two-point statistics.

A-1.1 Single-Point Statistics

A-1.1.1 First and Second Moments

The mean, or expected value, of a finite N-point sample collected at discrete time instants, t_k, is defined as:

$$\langle u_i(\vec{x}) \rangle = \frac{1}{N} \sum_{k=1}^{N} u_i(\vec{x}, t_k) \tag{A-1}$$

Reynolds stresses are the components of a symmetric second-order tensor defined as:

$$\langle u_i'(\vec{x}) u_j'(\vec{x}) \rangle = \frac{1}{N} \sum_{k=1}^{N} u_i'(\vec{x}, t_k) u_j'(\vec{x}, t_k) \tag{A-2}$$

where instantaneous velocity fluctuations are obtained via Reynolds decomposition:

$$u_i'(\vec{x}, t_k) = u(\vec{x}, t_k) - \langle u_i(\vec{x}) \rangle \tag{A-3}$$

Normal Reynolds-stresses, which are equal to the variance and nonnegative, are obtained by setting $i = j$. Clearly, r.m.s velocities are simply the square root of the normal Reynolds-stresses, i.e.

$$\langle u_i'(\vec{x})\rangle = \sqrt{\langle u_i'(\vec{x})u_i'(\vec{x})\rangle} \tag{A-4}$$

Reynolds shear-stresses are obtained when $i \neq j$. Turbulent kinetic energy is defined as half the trace of the Reynolds-stress tensor [7], i.e.:

$$k(\vec{x}) = \frac{1}{2}\langle u_i'(\vec{x})u_i'(\vec{x})\rangle \tag{A-5}$$

A-1.1.2 Probability Density Function

The probability density function (PDF) divides the range of a stochastic signal, $\phi(\vec{x}, t)$, into a series of 'bins', a, and is defined as the probability that $\phi(\vec{x}, t)$ is greater than a lower limit, a_1, and less than an upper limit, a_2. For the discrete data considered in this thesis, the PDF is calculated from [133]:

$$P(a) = \lim_{(a_2-a_1)\to 0} \frac{1}{(a_2 - a_1)} \left[\lim_{N\to\infty} \frac{N_a}{N}\right] \tag{A-6}$$

where N_a is the number of samples in bin a.

A-1.1.3 Fourier Analysis

A physical process can be described either in the time domain by specifying the value of some quantity, h, as a function of time, e.g. $h(t)$, or, alternatively, in the frequency domain by specifying its amplitude, H, as a function of frequency, e.g. $H(f)$, where $-\infty < f < \infty$ for a continuous function. Essentially, $h(t)$ and $H(f)$, which are both complex, are different representations of the same function and the Fourier transform and its inverse are used to move back and forth between them. As the data presented in this thesis is obtained from a finite sample set the discrete Fourier transform (DFT) is appropriate and is defined as [128]:

$$H_n = \sum_{k=0}^{N-1} h_k e^{-2\pi jkn/N} \quad n = 0, \ldots, N-1 \tag{A-7}$$

and the inverse discrete Fourier transform (IDFT):

$$h_k = \frac{1}{N}\sum_{n=0}^{N-1} H_n e^{2\pi jkn/N} \quad n = 0, \ldots, N-1 \tag{A-8}$$

All Fourier analysis presented in this thesis was performed using the fast Fourier transform (FFT)

algorithm of Danielson and Lanczos [128] and a rectangular window to truncate the input signal h_k. It is often of interest to assess how much power is contained in a given frequency interval between f and $f + df$. The result is referred to as the power spectral density or PSD. The PSD can be obtained from the DFT of an N-point sample using the periodogram estimate [128] which is defined at $N/2 + 1$ frequencies as:

$$\begin{aligned} P(f_0) &= \frac{1}{N^2} |H_0|^2 \\ P(f_n) &= \frac{1}{N^2} \left[|H_n|^2 + |H_{N-n}|^2 \right] \quad n = 1, 2, \ldots, \left(\frac{N}{2} - 1 \right) \\ P(f_{N/2}) &= \frac{1}{N^2} \left| H_{N/2} \right|^2 \end{aligned} \tag{A-9}$$

It should be noted that $P(f_n)$ does not equal its continuous counterpart $P(f)$ but rather is representative of a whole frequency band extending from halfway from the preceding discrete frequency ($P(f_{n-1})$) to halfway to the next one ($P(f_{n+1})$). To correctly reflect this, each $P(f_k)$ in Equation A-9 is divided by the width of the frequency band which is equal $1/(N\Delta t)$ giving units of power per unit bandwidth.

A-1.2 Two-Point Statistics

Correlation is a measure which quantifies how a property in time and / or space varies in relation to another point in time and / or space. The generalised cross-correlation function (CCF), which is essentially a normalised covariance and denoted R_{ij}, is defined by Hollis [72] as:

$$\text{CCF} = R_{ij}(\vec{x}, \vec{r}, \tau) = \frac{\langle u_i'(\vec{x}, t_k) u_j'(\vec{x} + \vec{r}, t_k + \tau) \rangle}{\sqrt{\langle u_i'(\vec{x}, t_k)^2 \rangle} \sqrt{\langle u_j'(\vec{x} + \vec{r}, t_k)^2 \rangle}}, \quad -1 \leq R_{ij}(\vec{x}, \vec{r}, \tau) \leq 1 \tag{A-10}$$

where $\vec{r}$ and τ are spatial and temporal separations respectively. The generalised CCF can be considered in two simplified forms, namely: the spatial velocity correlation (SVC) and the auto-correlation function (ACF). The SVC is obtained by computing the correlation between two quantities separated in space but at the same instance in time ($\tau = 0$):

$$\text{SVC} = R_{ij}(\vec{x}, \vec{r}) = \frac{\langle u_i'(\vec{x}, t_k) u_j'(\vec{x} + \vec{r}, t_k) \rangle}{\sqrt{\langle u_i'(\vec{x}, t_k)^2 \rangle} \sqrt{\langle u_j'(\vec{x} + \vec{r}, t_k)^2 \rangle}}, \quad -1 \leq R_{ij}(\vec{x}, \vec{r}) \leq 1 \tag{A-11}$$

Similarly, the ACF is obtained by computing the correlation between two quantities separated in time but at the same spatial location ($\vec{r} = 0$):

$$\text{ACF} = R_{ij}(\vec{x}, \tau) = \frac{\langle u_i'(\vec{x}, t_k) u_j'(\vec{x}, t_k + \tau) \rangle}{\sqrt{\langle u_i'(\vec{x}, t_k)^2 \rangle} \sqrt{\langle u_j'(\vec{x}, t_k)^2 \rangle}}, \quad -1 \leq R_{ij}(\vec{x}, \tau) \leq 1 \tag{A-12}$$

In addition to serving as an excellent analysis tool in their own right, correlation functions also form the basis for the derivation of other important fluid dynamic measures. These include integral length, ${}^{k}L_{ij}$, and time, T_{ij}, scales and are considered in the following subsections.

A-1.2.1 Integral Lengthscale

Integral lengthscales, ${}^{k}L_{ij}$ are the simplest measurable statistic containing information on the spatial structure of a turbulent field and are obtained from the SVC (Equation A-11). Mathematically, ${}^{k}L_{ij}$ is defined as:

$$ {}^{k}L_{ij}(\vec{x},\vec{r}) = \int_{0}^{\infty} R_{ij}(\vec{x},\vec{r})d\vec{r} \tag{A-13} $$

In total, 27 integral lengthscales exist in 3D space. Longitudinal lengthscales are defined as the integral of the SVC along a coordinate direction, k, parallel to that of the velocity component, i.e $i = j = k$ in Equation A-13, giving a total of 3 in 3D space. Lateral lengthscales are similarly defined but now the integral is calculated along a coordinate direction normal to that of the velocity component, i.e. $i = j \neq k$ in Equation A-13, and 2 lateral lengthscales exist for each velocity component in 3D space.

For isotropic turbulence the SVC is symmetric about its origin for a particular velocity component and coordinate direction. For the high-Reynolds number flows considered in this thesis, a combination of highly anisotropic inhomogeneous turbulence and the presence of solid boundaries, such as the confining walls of the swirl duct, often result in a SVC that is asymmetric about its origin (Figure A-1(a)). Although it could be argued that in such circumstances two different lengthscales should be quoted; the 'upstream' (negative part of the Δx axis) and 'downstream' (positive part of the Δx axis), it must be borne in mind that Equation A-13 refers to a lengthscale characteristic of an eddy centred at a particular point. The approached used in this thesis is to average the upstream and downstream parts of the integral of the SVC, i.e.

$$ {}^{k}L_{ij} = \frac{w_{\text{up}}\,{}^{k}L_{ij,\text{up}} + w_{\text{down}}\,{}^{k}L_{ij,\text{down}}}{w_{\text{up}} + w_{\text{down}}} \tag{A-14} $$

where w refers to a weighting coefficient characteristic of the averaging and the subscripts up and down refer to the upstream and downstream parts of the integral of the SVC respectively. From the definition given in Equation A-13, ${}^{k}L_{ij}$ is obtained by integrating the SVC from its origin to an infinite displacement. In practice it not possible to integrate to an infinite displacement and instead integration is performed from the origin of the SVC to the point at which it first

crosses the displacement axis. This point is referred to as the first zero crossing (FZC) and is actually a very close approximation to the true definition for most practical flows with relatively localised turbulence [72]. Practical difficulties arise when the SVC is curtailed either artificially or naturally and the FZC is not reached (Figure A-1(b)). In the vicinity of a solid boundary either the upstream or downstream side of the SVC is naturally curtailed. To minimise the effects of sub-grid filtering described in Section 2.3.4 the PIV technique requires very small FoVs as detailed in Tables 2.5 and 2.7 and as a result an artificial curtailment of the SVC is inevitable. In order to account for both natural and artificial curtailment of the SVC, Hollis [72] found that an exponential function of the form $R_{ij} = e^{-x}$ gave a simple but reliable estimate of the missing integral contribution. To assess the amount of real data available from the SVC [72] also developed a confidence weighting of the following form:

$$C = \begin{cases} 0, & R_{\text{curtailed}} > 0.9 \\ 1.125 - 1.25R_{\text{curtailed}}, & 0.1 \leq R_{\text{curtailed}} \geq 0.9 \\ 1, & R_{\text{curtailed}} < 0.1 \end{cases} \tag{A-15}$$

If the function is curtailed at anything greater than 0.9 no confidence can be attributed to the integral for that part of the axis as it relies too heavily on the estimated curve. If the function is curtailed at less than 0.1, entire confidence can be placed on the integral, because the estimated portion is so small. Between the two values, a linear relationship between confidence and the curtailed value exists. The actual lengthscale is then calculated via a confidence weighting and Equation A-14 becomes:

$${}^{k}L_{ij} = \frac{C_{\text{up}}\,{}^{k}L_{ij,\text{up}} + C_{\text{down}}\,{}^{k}L_{ij,\text{down}}}{C_{\text{up}} + C_{\text{down}}} \tag{A-16}$$

Robinson [134] has shown the confidence weighting approach to give a consistent lengthscale distribution close to data boundaries whilst not affecting the calculation away from boundaries.

A-1.2.2 Integral Timescale

The integral timescale is obtained via direct integration of the ACF (Equation A-12) and is given as:

$$T_{ij}(\vec{x}, \tau) = \int_0^\infty R_{ij}(\vec{x}, \tau) d\tau \tag{A-17}$$

In a similar way to the integral lengthscale; as it is not possible to integrate to an infinite temporal separation in practice the upper limit in Equation A-17 is replaced with the FZC. The

only integral timescales considered in practice are when $i = j$ giving a total of 3 in 3D space. Unlike the SVC, the ACF is an even function $R_{ij}(\vec{x}, \vec{\tau}) = R_{ij}(\vec{x}, -\vec{\tau})$ and no weighting, such as that defined in Equation A-14, is required.

A-2 Coherent Structure Detection and Analysis

Although a vortex may elude a precise definition; Kline and Robertson [60] have stated that: *'A vortex exists when instantaneous streamlines mapped onto a plane normal to the core exhibit a roughly circular or spiral pattern, when viewed in a reference frame moving with the centre of the vortex core'*. This provides a valuable means of identifying and characterising coherent structures, however it constitute a subjective approach which, as noted by Pope [7], can lead to controversy over their nature and significance. It is therefore essential that this is combined with qualitative measures and eduction techniques which are the subject of the following subsections.

A-2.1 Vorticity Based Methods

Vorticity, $\vec{\omega}(\vec{x}, t)$, is defined as the curl of velocity [7]:

$$\vec{\omega}(\vec{x}, t) = \nabla \times \vec{u}(\vec{x}, t) \tag{A-18}$$

and equals twice the rate of rotation of the fluid at $(\vec{x}, t)$. In this thesis the components of $\vec{\omega}$ are calculated in a Cartesian (PIV) and polar-cylindrical (CFD) co-ordinate basis. In a Cartesian co-ordinate basis $\vec{\omega}$ has the components:

$$\vec{\omega} = \left[\frac{\partial u_z}{\partial y} - \frac{\partial u_y}{\partial z}\right]\hat{i}_x + \left[\frac{\partial u_x}{\partial z} - \frac{\partial u_z}{\partial z}\right]\hat{i}_y + \left[\frac{\partial u_y}{\partial x} - \frac{\partial u_x}{\partial y}\right]\hat{i}_z \tag{A-19}$$

and in a polar-cylindrical one:

$$\vec{\omega} = \left[\frac{\partial u_\theta}{\partial r} - \frac{1}{r}\frac{\partial u_r}{\partial \theta} + \frac{u_\theta}{r}\right]\hat{i}_x + \left[\frac{1}{r}\frac{\partial u_x}{\partial \theta} - \frac{\partial u_\theta}{\partial x}\right]\hat{i}_r + \left[\frac{\partial u_r}{\partial x} - \frac{\partial u_x}{\partial r}\right]\hat{i}_\theta \tag{A-20}$$

Identification of vorticies in a velocity field, along with the calculation of vortex statistics (size, strength, etc.) is normally accomplished by identifying isolated regions of significant vorticity. However, vorticity not only identifies vortex cores but also any shearing motion present in the flow and can be very noisy. As an alternative, the Q-criterion of Hunt et al. [135] defines vortices in incompressible flow as regions in which vorticity magnitude prevails over strain-rate magnitude:

$$Q = \frac{1}{2}\left(||\boldsymbol{\omega}||^2 - ||\mathbf{S}||^2\right) > 0 \tag{A-21}$$

where $||\boldsymbol{\omega}|| = \sqrt{tr\left(\boldsymbol{\omega}\boldsymbol{\omega}^{\mathrm{T}}\right)}$ and $||\mathbf{S}|| = \sqrt{tr\left(\mathbf{S}\mathbf{S}^{\mathrm{T}}\right)}$. In this thesis S_{ij} and Ω_{ij} are only calculated in a polar-cylindrical co-ordinate basis and have following components:

$$S_{ij} = \begin{bmatrix} \frac{\partial u_x}{\partial x} & \frac{1}{2}\left[\frac{\partial u_x}{\partial r} + \frac{\partial u_r}{\partial x}\right] & \frac{1}{2}\left[\frac{1}{r}\frac{\partial u_x}{\partial \theta} + \frac{\partial u_\theta}{\partial x}\right] \\ \frac{1}{2}\left[\frac{\partial u_r}{\partial x} + \frac{\partial u_x}{\partial r}\right] & \frac{\partial u_r}{\partial r} & \frac{1}{2}\left[\frac{1}{r}\frac{\partial u_r}{\partial \theta} + \frac{\partial u_\theta}{\partial r} - \frac{u_\theta}{r}\right] \\ \frac{1}{2}\left[\frac{\partial u_\theta}{\partial x} + \frac{1}{r}\frac{\partial u_x}{\partial \theta}\right] & \frac{1}{2}\left[\frac{\partial u_\theta}{\partial r} + \frac{1}{r}\frac{\partial u_r}{\partial \theta} - \frac{u_\theta}{r}\right] & \frac{1}{r}\frac{\partial u_\theta}{\partial \theta} + \frac{u_r}{r} \end{bmatrix} \tag{A-22}$$

$$\Omega_{ij} = \begin{bmatrix} 0 & \frac{1}{2}\left[\frac{\partial u_x}{\partial r} - \frac{\partial u_r}{\partial x}\right] & \frac{1}{2}\left[\frac{1}{r}\frac{\partial u_x}{\partial \theta} - \frac{\partial u_\theta}{\partial x}\right] \\ \frac{1}{2}\left[\frac{\partial u_r}{\partial x} - \frac{\partial u_x}{\partial r}\right] & 0 & \frac{1}{2}\left[\frac{1}{r}\frac{\partial u_r}{\partial \theta} - \frac{\partial u_\theta}{\partial r} - \frac{u_\theta}{r}\right] \\ \frac{1}{2}\left[\frac{\partial u_\theta}{\partial x} - \frac{1}{r}\frac{\partial u_x}{\partial \theta}\right] & \frac{1}{2}\left[\frac{\partial u_\theta}{\partial r} - \frac{1}{r}\frac{\partial u_r}{\partial \theta} + \frac{u_\theta}{r}\right] & 0 \end{bmatrix} \tag{A-23}$$

A-2.2 Rotational Averaging

Rotational averaging is a form of conditional averaging whereby a local coordinate system $(x'-y')$ is defined that rotates with a particular flow feature such as the reference vortex shown in Figure A-2. Such an averaging procedure eliminates incoherent turbulence and provides a time-averaged statistical representation of the coherent motions. As flows studied in this thesis are only quasi-periodic it is necessary to determine the location of the reference vortex at each time-instant. The method adopted here is based on that described by Grosjean et al. [36] which maximises the normalised angular momentum according to the following expression and with respect to point P (Figure A-2):

$$f(P) = \frac{1}{(2N+1)^2}\sum_i \frac{\vec{r}_i \times \vec{u}(M_i)}{|\vec{r}_i|\,|\vec{u}(M_i)|} \tag{A-24}$$

whereby P is the proposed vortex centre, $\vec{u}$ is the measured velocity vector at the point M_i and $(2N+1)^2$ is the number of points in the considered area around P and N is the number of layers used. The algebraic value of the function $f(P)$ varies between -1 and 1 for a 2D flowfield. The position P is chosen on the measurement grid until an extremum $f(P)$ is found.

A-2.3 Conditional Averaging

Conditional averaging is used to calculate the ensemble average of a fluctuating turbulent quantity across an area or volume of interest subject to the constraint that the instantaneous fluctuation, $\phi'(\vec{x},t)$, at a fixed point is a factor, k, times greater than the r.m.s value, $\langle\phi'(\vec{x})\rangle$, at that point. This highlights the fluctuations that lie in the 'tails' of the PDF as shown in Figure A-4. Mathematically, the conditionally averaged fluctuations from the positive and negative regions of the PDF, $\langle\phi'_{ca+}(\vec{x},t)\rangle$ and $\langle\phi'_{ca-}(\vec{x},t)\rangle$, may be described as:

$$\langle \phi'_{ca+}(\vec{x}) \rangle = \frac{1}{N_{ca+}} \sum_{k=1}^{N} a_{j+}(t+k)\phi'(\vec{x}, t_k) \quad a_{j+} \quad N_{ca+} = \sum_{k=1}^{N} a_{j+} \tag{A-25}$$

$$\langle \phi'_{ca-}(\vec{x}) \rangle = \frac{1}{N_{ca-}} \sum_{k=1}^{N} a_{j-}(t+k)\phi'(\vec{x}, t_k) \quad a_{j-} \quad N_{ca-} = \sum_{k=1}^{N} a_{j-} \tag{A-26}$$

Conditional averaging essentially phase-locks the flowfield to a high energy containing turbulent event passing a fixed point. When combined with the SVC performed at the same point and based on the same fluctuating quantity it provides a powerful means of identifying the large-scale structures contributing to the correlation. It has been found that a value of $k = 1.5$ [72, 13, 86] is sufficient for this purpose and corresponds to the most extreme $\pm 10\%$ values of the time history [13].

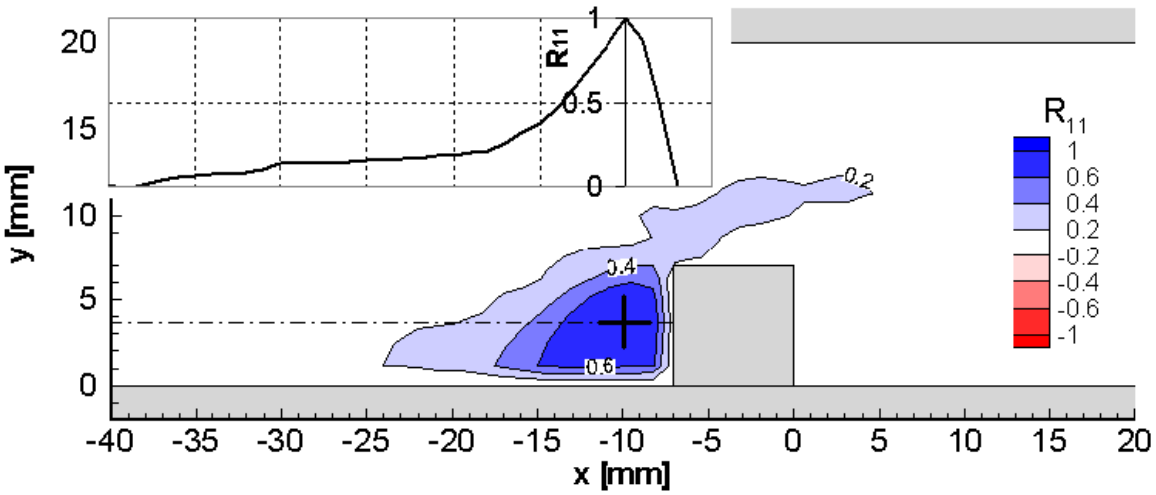

(a) Asymmetric SVC upstream of a step

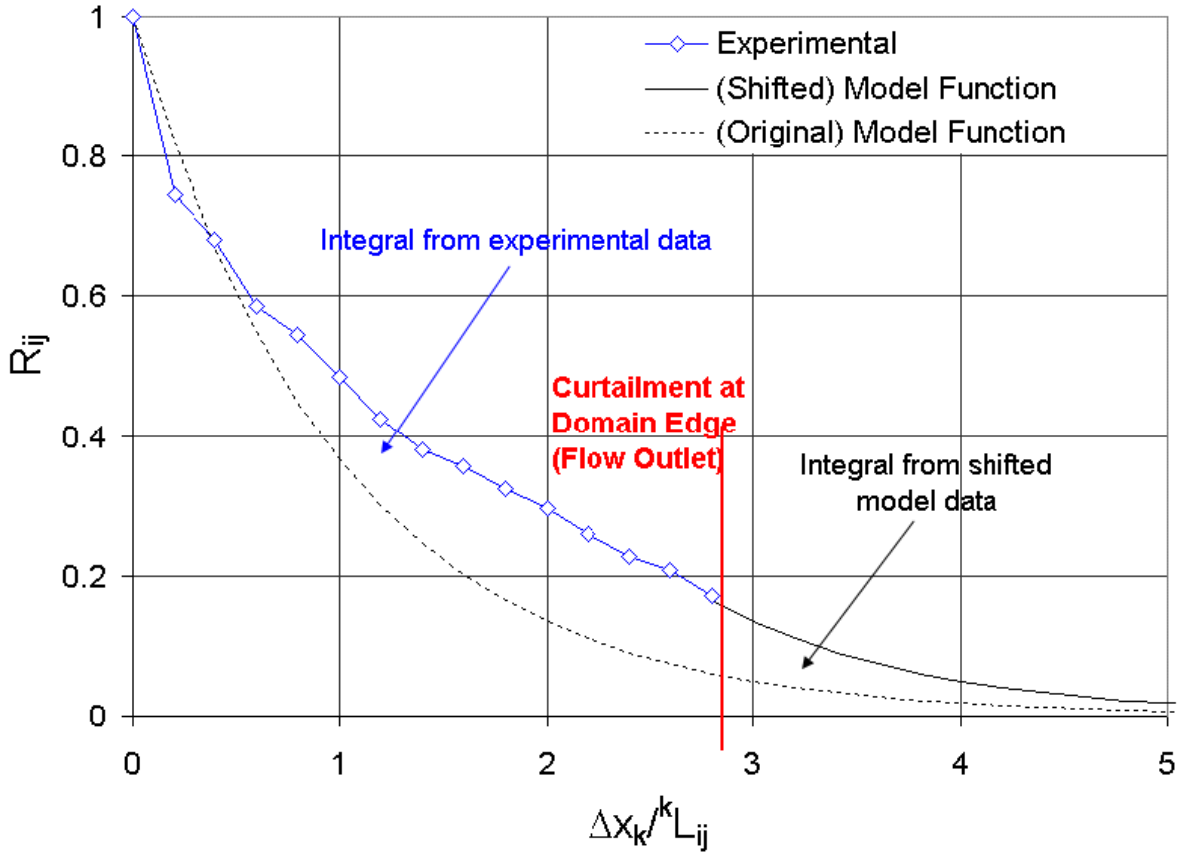

(b) Artificial curtailment of SVC at domain boundary and exponential model ($R_{ij} = e^{-x}$) approximation

Figure A-1: Examples of difficulties encountered in integral lengthscale calculation in engineering flows [72]

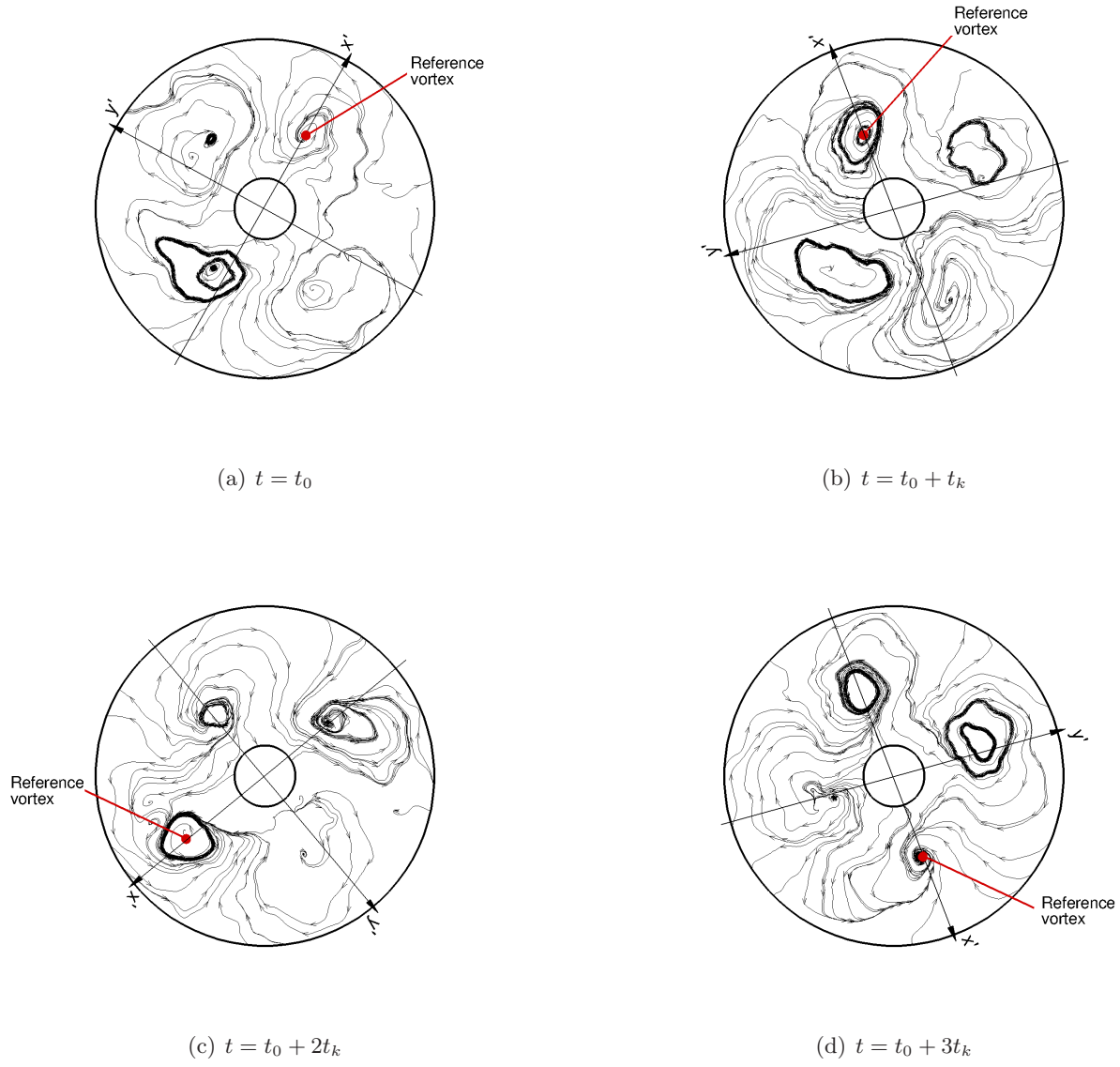

(a) $t = t_0$

(b) $t = t_0 + t_k$

(c) $t = t_0 + 2t_k$

(d) $t = t_0 + 3t_k$

Figure A-2: Illustration of rotational-averaging procedure.

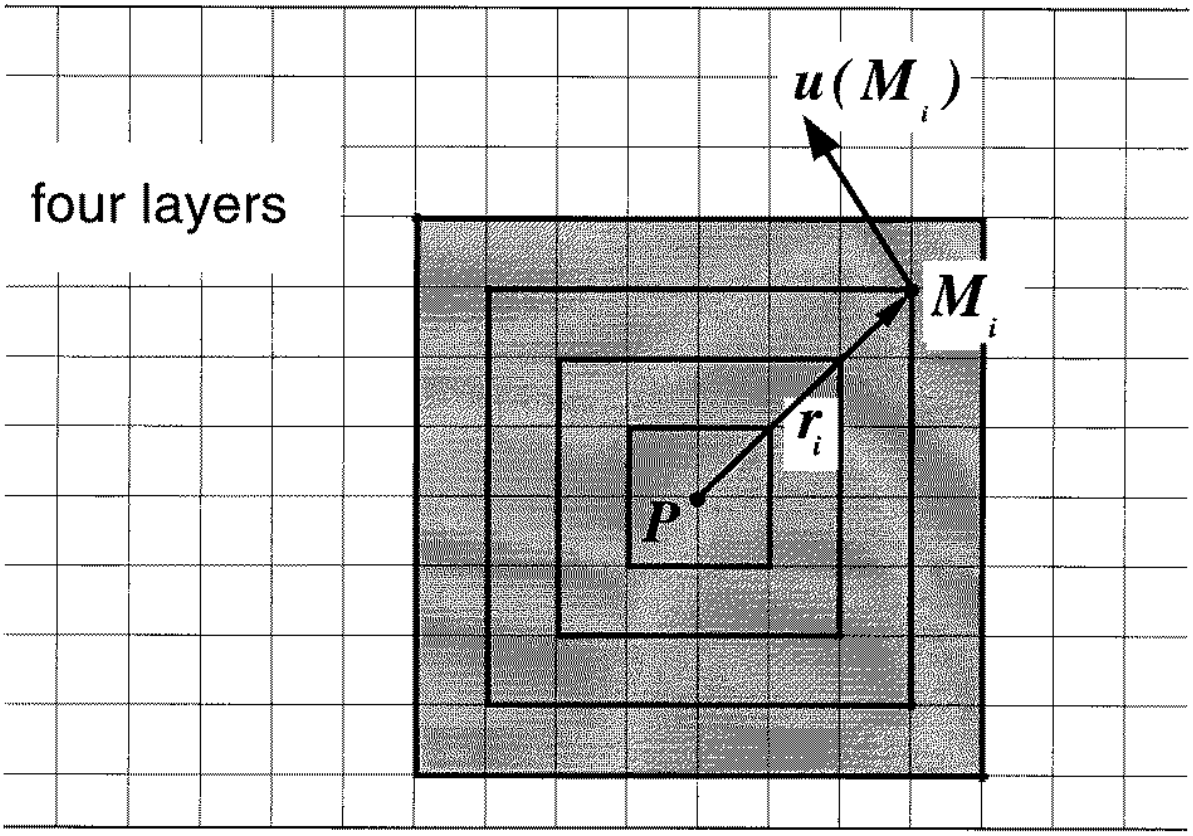

Figure A-3: Method for swirl centre location using normalised angular momentum [36]

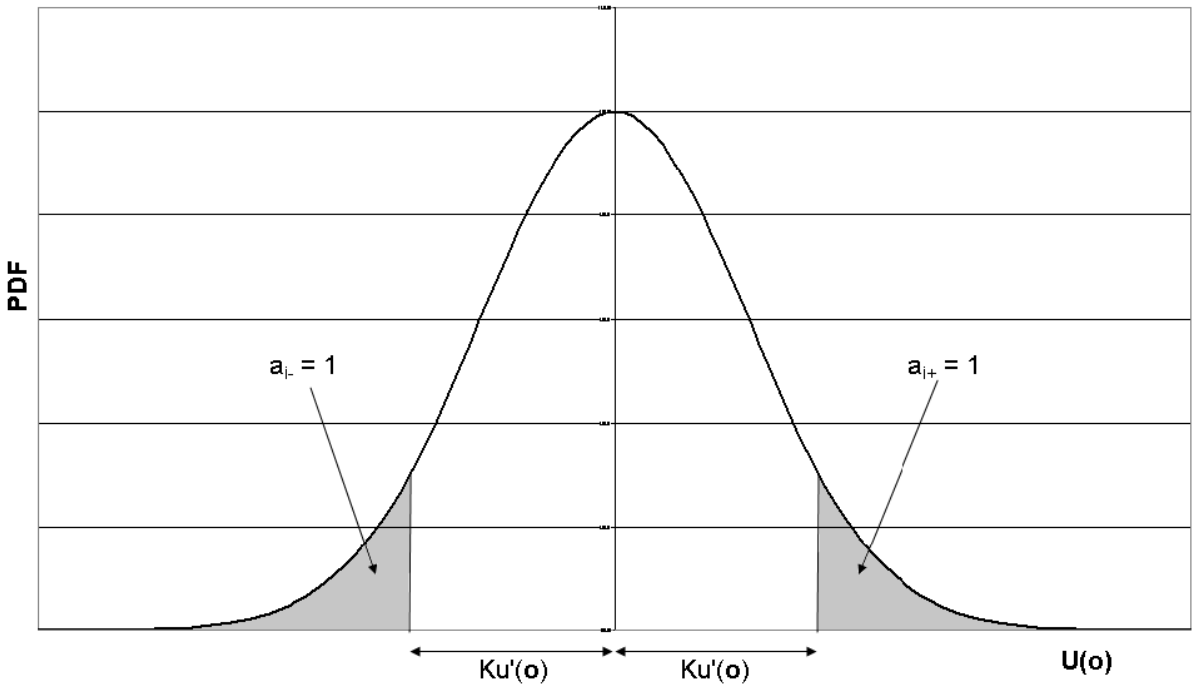

Figure A-4: Conditional averaging of a PDF distribution [72]

Appendix A